THIS WEEK

EDITORIALS

FUTURES Science-fiction fans, can you boil down your story to 200 characters? **p.332**

WORLD VIEW Computer scientists must stand up and be counted **p.333**



POWER UP Wearable battery is a foldable and flexible friend **p.335**

Stem-cell fiasco must be stopped

In the public interest, the Italian health minister should resolve the ongoing uncertainty over a government trial of a controversial therapy.

"This is the end of the matter and we are very happy." That was the reaction of Luca Pani, head of the Italian Medicines Agency, to the news in October that the Italian health minister had halted a government trial of a controversial stem-cell therapy. He is less happy now, and his dissatisfaction should be shared by anyone who cares about the rigorous use of scientific evidence and the protection of vulnerable patients.

Just when Pani and others in Italy were breathing a sigh of relief, an Italian court has thrown an unexpected spanner into the works. The court ruled last week that an expert committee behind a detailed report that demolished the scientific basis for the clinical trial of the claimed treatment was unlawfully biased (see *Nature* http://doi.org/qgr; 2013).

The judgement undermines the October decision made by health minister Beatrice Lorenzin to cancel the trial, which could yet be allowed to proceed. It must not. As *Nature* and independent experts have pointed out many times, there is no evidence that the claimed therapy works, and indeed it could be harmful.

Lorenzin should bring a stop to this uncertainty. She must release the members of the committee who prepared the critical report from a confidentiality agreement. They must be free to give the public their expert opinion on the claims of the Stamina Foundation based in Brescia, which extracts stem cells from a patient's bone marrow, manipulates them and then injects them back into the same patient's blood or spinal cord. And Lorenzin should release to broader scrutiny the protocol that the organization says it will follow to conduct the trial.

Already, members of one patient group have appealed for such openness, arguing that they have waited long enough to understand whether the Stamina method could help them live, and they want to be able to judge for themselves.

Lorenzin has responded that this is not in her power. It is unusual for a government-sponsored clinical trial to be so secretive, and it is natural that many are now asking questions about why the government insisted on confidentiality that would extend well beyond any trial, and why it should not be lifted when it is so clear that this would be in the public interest.

She must act now because things could soon get worse. Last week's ruling by a regional administrative court in Rome said that a new committee should be appointed to take another look at the validity of the trial. To make this successor committee more balanced, the court suggested, it could invite foreign scientists to participate.

This may seem a good idea, but it is venturing onto dangerous ground. There exist powerful international interests that support clinics offering unproven stem-cell therapies in countries such as Mexico and Uganda. Such countries lack the strict regulatory oversight that prevents the exploitation of desperate patients in Europe and the United States — and the clinics would love to see a regulatory loophole open in a European country. In setting up a replacement committee, Lorenzin must go to scientists who are independent of the companies that lobby for looser regulation of stem-cell therapies.

Stamina had been treating seriously ill patients, mostly children, on a 'compassionate basis', since 2007 — until Pani's agency closed its laboratory in Brescia in August 2012 for safety reasons. Some patient groups have lobbied passionately and publicly for access to the therapy that Stamina chief Davide Vannoni claims can cure a range of otherwise deadly diseases.

In November, when it seemed that the clinical trial was finally off the books, Vannoni led a demonstration in front of the parliamentary buildings in Rome, where patients threw their own blood at pictures of the president and prime minister. The emotion of those whose children are fatally ill is a powerful weapon.

"The emotion of those whose children are fatally ill is a powerful weapon."

The judgement — a ruling on an appeal by Stamina — shocked scientists in Italy and should shock scientists elsewhere. It seems not to take into account that the committee was restricted to considering Stamina's clinical protocol and recommending which specific disorders should be treated in any clinical trial. The committee was asked only to assess whether the technical aspects of the proposed study satisfied ethical, clinical and legal standards.

The court argued that the committee lacked balance because most members were known opponents of the Stamina approach. It also complained that the committee had failed to look at documentation of Stamina's claims to treatment successes (something beyond its mandate).

The uncertainty resulting from this latest judgement must be ended. Lorenzin must find the courage to act. ■

Sink or swim?

A rethink on monitoring land-use change is needed to estimate effects on global warming.

During the seven decades of its existence, the Soviet Union was a notorious terra incognita for Western geographers and mapmakers. Information improved when remote-sensing satellites began to circle the globe, but the vast lands of Russia and her former satellite states only became accessible to Western scientists after the end of the cold war.

More than 20 years on, the region continues to surprise. The demise of the Soviet Union and the socio-economic disruption left in its wake resulted in a rural exodus and substantial changes in land use. A study

© 2013 Macmillan Publishers Limited. All rights reserved

by researchers in Germany (F. Schierhorn *et al. Glob. Biogeochem. Cycles* http://doi.org/qg8; 2013) now suggests that the area of cropland abandoned since 1990 is much larger than most people in the West would have guessed (see page 342).

The information that redrew the map was not supplied by sophisticated satellite-borne sensors. Instead, the authors analysed the annual sowing statistics for crops between 1990 and 2009 — which were still hard to come by — and deduced that the area used for grain production in the former Soviet breadbaskets of western Russia, Belarus and Ukraine has decreased by more than one-quarter. This decline is substantially greater than the estimate made, mainly from satellite data, in 2009 by the UN Food and Agricultural Organization.

Why does this decrease matter? Most immediately, millions of hectares of fertile land are lying idle while a growing world population demands more food. As urbanization, desertification and increasing water scarcity constrain the extension of arable land worldwide, this unsown land might look like a precious resource. But as nature gives with one hand, it takes away with the other. These abandoned areas have become important carbon sinks. Substantial amounts of organic carbon have accumulated in their untilled soils and natural vegetation over the past two decades. If intensive agriculture were to resume, this carbon would be rapidly released into the atmosphere as carbon dioxide, contributing to global warming.

The abandoned Eastern European croplands highlight the perennial trade-off between agriculture and climate protection. And they show yet again that the debate over what to do about this needs to be better-informed by more robust data.

Russian soils and forests are a major part of the global terrestrial carbon sink. Russia's last-minute signing of the 1997 Kyoto Protocol on Climate Change (and its possible involvement in a future international agreement) owe much to the prospect of substantial gains from the sale of carbon credits. The possibility that Russia's natural carbon sink has increased is potentially lucrative news for a country whose leaders and scientists often keep a low profile when it comes to global warming.

However, the true size of the Eastern European — and the global — terrestrial carbon sink remains disturbingly uncertain. Discrepancies in various estimates of its size based on changes in land use point to shortcomings in regional and global carbon accounting — a discipline on which any new international climate regime will fundamentally rely. Whether or not the revised estimates on the extent of post-Soviet land abandonment are correct, they underscore the fact that satellite observations of land-use dynamics, in Russia or elsewhere, are no credible guide to a region's carbon balance.

A matter so central to predicting the rate of global warming deserves more attention. But existing remote-sensing technology offers relatively coarse observations of land cover and land-use change, which means that assessments are often little more than good guesses.

"Millions of hectares of fertile land are lying idle while a growing world population demands more food."

Space-borne sensors such as the Moderate Resolution Imaging Spectroradiometer (MODIS) instruments on NASA's Terra and Aqua satellites do provide rough but useful land-cover classifications. But over dry regions such as the south Russian steppes, spectral analysis does not discriminate well. Moreover, the spectral fingerprint of an area tells nothing about its past and current management, such as the application of fertilizer, which affects a soil's carbon-sequestration capacity.

In the absence of reliable satellite observations, land-use dynamics need to be continuously monitored on the ground. A NASA-funded project on land cover and land-use change in western Russia is setting the right tone by incorporating the results of field surveys with remote sensing and statistical modelling. Similar field studies would be desirable in other countries, such as Brazil, Argentina, China and India, where land use is undergoing major transitions.

Ultimately, only improved satellite observations can provide the global data sets required to understand the elusive global carbon sink. The European Space Agency's €400-million (US$551-million) BIOMASS radar mission, selected in spring as Europe's next Earth Explorer mission and scheduled for launch around the end of the decade, could make a real difference — if mainly in the tropics. Emerging space nations, there is a great opportunity to be seized. ■

Futures redux

Can you tell a sci-fi tale in just 200 characters? Then the Nature Futures competition is for you.

As 2013 prepares to gasp its last, this issue follows a venerable tradition and looks back at the myriad events, images and people that made the news and shaped the year's scientific agenda (see page 344). These are collected together with a host of highlights on our website (www.nature.com/2013), where there is even an online quiz to test your memory of what happened in science this year (go.nature.com/izlxfn).

There remains one darkened recess of the *Nature* enterprise that, Scrooge-like, is resolutely refusing to join in. Futures, our science-fiction column, is doggedly pursuing its agenda and is keeping its sights fixed firmly on the, well, future. For more than a decade, Futures authors have been addressing the key questions that any visionary would wish to answer. Is the human race doomed? What are aliens really like? How will technology change the way we live? And can a soft drink really save your life?

Like the famous Time Lord who turned 50 last month, Futures has enjoyed more than one incarnation — although its present form has proved most stable, appearing as it has on the back page of *Nature* since July 2007 (nature.com/futures). So far, Futures has published more than 500 stories — and sadly has been forced to reject more than ten times that number (often because of space constraints, although there was one unfortunate time when a pan-dimensional being from a parallel universe took possession of the editor for a week — apologies to those whose e-mails went unanswered).

As well as watching the skies, Futures has surreptitiously infiltrated the office across the hall, where it has activated the sleeper implanted several years ago behind the filing cabinet in the corner. The result is that from January, sci-fi will return to the pages of *Nature Physics*, offering an extra 12 chances a year to predict what may come to pass. (The submission address is the same: futures@nature.com.)

And the changes don't end there. Back in 2007, we published an anthology of some of the early Futures stories. That too has regenerated, and *Futures 1* (note the '1': there are more planned for 2014) will be available as an eBook from 24 December — ideal, say, for a last-minute virtual stocking filler.

To celebrate this release and the fact that *Nature Physics* is going back to the Futures, we are offering a chance to win a copy of the eBook, plus a year's subscription to *Nature*, in a dazzling competition. Inspired by the brevity of Twitter, we want you to tell a short sci-fi story. And we mean short. No more than 200 characters. This truncated tale can be input at these galactic coordinates: go.nature.com/rnrnxx. The closing date is 31 January 2014.

Robots, extrasolar aliens and genetically modified beings are not eligible to participate — unless you have managed to take over the planet by the closing date. In which case, can we just say how well your new skin suits you, and please allow us to show you the way to the executive suite. ■

➲ NATURE.COM
To comment online, click on Editorials at:
go.nature.com/xhunqv

© 2013 Macmillan Publishers Limited. All rights reserved


CHARLES ARTHUR

Academics should not remain silent on hacking

The revelation that US and British spy agencies have undermined a commonly used encryption code should alarm researchers, says **Charles Arthur**.

Secrecy doesn't come naturally to journalists, but sometimes it is thrust upon us. Earlier this year, there was a room in *The Guardian*'s offices in London that nobody could enter alone. On a table outside by a security guard was a tidy collection of phones and other devices; nothing electronic was allowed. Inside were a coffee maker, a shredder, some paper and a few computers. All were brand new; none had ever been connected to the Internet. None ran Microsoft Windows. All were encrypted; each required two passwords, held by different people.

This is where the biggest news stories of this year lived — away from the Internet. This was where *The Guardian* analysed the 'Snowden files' (classified documents released to the press by former US National Security Agency (NSA) contractor Edward Snowden). These revealed, among other things, that the NSA and the United Kingdom's GCHQ were running enormous efforts to crack encrypted communications online, and that they had worked to undermine the strength of encryption standards such as that used — and recommended — by the US National Institute of Standards and Technology (NIST). (The computers sadly are no more — smashed in *The Guardian* basement on the orders of the British government.)

NIST's standard for random numbers used for cryptography, published in 2006, had been weakened by the NSA. Companies such as banks and financial institutions that rely on encryption to guarantee customer privacy depend on this standard. The nature of the subversions sounds abstruse: the random-number generator, the 'Dual EC DRBG' standard, had been hacked by the NSA so that its output would not be as random as it should have been. That might not sound like much, but if you are trying to break an encrypted message, the knowledge that it is hundreds or thousands of times weaker than advertised is a great encouragement.

It was, to be frank, a big deal. In the world's universities, computer scientists and mathematicians spend their careers trying to develop secure systems, and yet here was evidence of a systematic — and successful — attempt to undermine that work. Executives at companies such as Google, Yahoo, Facebook and Microsoft, which discovered that their internal networks were being tapped and their systems infiltrated, were furious. But a few isolated shouts of protest aside, the academic community has largely been silent.

That's disappointing. Academia is where we expect to hear the free flow of ideas and opinions. Yet it has been the commercial companies that have made the most noise — because the revelations threaten trust in their businesses. Don't academics also see the threat to open expression, and to the flow of dissident ideas from countries where people might fear that their communications are being tapped and, even if encrypted, cracked?

Some get it. Ross Anderson, a security researcher at the University of Cambridge, UK, has been highly critical and outspoken. When I spoke to him in September, soon after the NIST revelation, he called it "a wake-up call for a lot of people" and added: "This has been a 9/11 moment for the community, and it's great that some people are beginning to wake up."

Kenneth White, principal scientist at health-information company Social & Scientific Systems in Silver Spring, Maryland, says: "Just a year ago, such a story would have been derogated by most of my colleagues as unwarranted suspicion at best and outright paranoia at worst. But here we are."

Anderson has an explanation for the muted response: he says that a number of British university departments have been quietly coerced by the GCHQ. The intelligence-gathering agency has a substantial budget, and ropes in academics by offering access to funds that ensures their silence on sensitive matters, Anderson says. (If that sounds like paranoia, then see above.)

I have not been able to confirm his claims, but what are the alternatives? One is that the academics are simply too busy going back over their own work looking to see if they agree with the claimed weaknesses. The other is that they simply don't care enough.

For those who do care, White and Matthew Green, who teaches cryptography at Johns Hopkins University in Baltimore, Maryland, have embarked on an ambitious effort to clean up the mess — one that needs help.

They have created a non-profit organization called OpenAudit.org, which aims to recruit experts to provide technical assistance for security projects in the public interest, especially open-source security software. A similar effort initiated by White and Green is checking the open-source software called TrueCrypt, which is widely used to lock down hard drives during foreign travel (see go.nature.com/nsvdjh).

Concerns over the security of the NIST Dual EC DRBG standard were raised in 2007, but too few academics spoke out then. The events of 2013 must make them rethink. Cryptography rarely reaches the headlines, but now it has done so for all the wrong reasons. For 2014, academics working in cryptography and security should make themselves a promise: 'We won't get fooled again.' And most of all, 'We won't go down quietly.' ■

ACADEMICS IN CRYPTOGRAPHY AND SECURITY SHOULD MAKE THEMSELVES A PROMISE: 'WE WON'T GET FOOLED AGAIN.'

NATURE.COM
Discuss this article online at:
go.nature.com/rklbwy

Charles Arthur *is technology editor of* The Guardian *in London.*
e-mail: charles.arthur@gmail.com

© 2013 Macmillan Publishers Limited. All rights reserved

RESEARCH HIGHLIGHTS

Selections from the scientific literature

NEUROSCIENCE

Cell junk hinders nerve regrowth

Older animals recover slowly from nerve injury because they take longer to clear debris from damaged nerves than younger creatures do.

Hyuno Kang and Jeff Lichtman at Harvard University in Cambridge, Massachusetts, crushed the nerves that transmit signals to muscles in young and old mice, and used high-resolution time-lapse imaging to follow the nerves' regeneration.

Genetic engineering and staining techniques allowed the duo to distinguish cell types and cell debris by colour. The pair found that nerve growth slowed or temporarily halted when the tips of nerve fibres, or axons, hit lingering debris. Young mice broke down these nerve remnants faster than old mice did.

Axons in aged mice regenerated as quickly as those in young animals if their paths were clear of cell junk, so the authors suggest that nerve-injury therapies for older people could target debris-clearance mechanisms.
J. Neurosci. 33, **19480–19491 (2013)**

ASTRONOMY

Galactic clouds swathed in fog

Molecular clouds, where stars are born, are surrounded by a fog of hydrogen that interacts with the clouds. These interactions could affect whether stars form.

In the Plateau de Bure Interferometer Arcsecond Whirlpool Survey, astronomers led by Eva Schinnerer of the Max Planck Institute for Astronomy in Heidelberg, Germany, mapped 1,500 giant molecular clouds in the Whirlpool galaxy, about 7 million parsecs (23 million light years) away. They report in a series of papers that the clouds are not isolated as previously thought, but are embedded in a molecular fog that is much denser than expected and contains 50% of the galaxy's hydrogen.

Clouds that are surrounded by the fog experience decreased pressure when the fog moves relative to larger galactic structures, such as the arms of the spiral galaxy. This reduced pressure lowers the chances of star formation.
Astrophys. J. 779, **42; 43; 44; 45; 46 (2013)**



MEGAN BEST

ANIMAL BEHAVIOUR

Macho chameleons shine the brightest

Male chameleons signal their aggressive intentions and prowess in fighting by adjusting the brightness of their skin colour.

Russell Ligon and Kevin McGraw at Arizona State University in Tempe staged fights between pairs of adult male veiled chameleons (*Chamaeleo calyptratus*; **pictured**) and used high-definition video to track how the animals' skin colour and brightness changed in 28 different patches on the body.

Individuals whose stripes brightened the most were more likely to charge another animal, while chameleons whose heads turned bright more quickly proved the most likely to win a bout.

The two signals could help male chameleons to separate a would-be combatant's motivation to fight from its ability to fight — two factors in competitive behaviour that can have different effects on the outcome of a contest.
Biol. Lett. **http://doi.org/qf9 (2013)**

MOLECULAR BIOLOGY

Microbes meddle with microRNA

Microbes in mouse guts can interfere with infection responses by changing the expression of small RNAs that regulate some genes.

Cristel Archambaud and Pascale Cossart at the Pasteur Institute in Paris and their colleagues looked at the expression of microRNA molecules in the small intestines of mice before and after infection with *Listeria monocytogenes*, a food-borne pathogen. They found reduced expression of six microRNAs after the infection in normal mice, but no decrease was seen for five of the microRNAs in mice without gut microbes, suggesting that the microbiota was responsible for this effect.

The findings suggest that gut microbes regulate the expression of protein-coding genes that are controlled by the microRNAs during infection.
mBio 4, **e00707-13 (2013)**

CANCER

Invasive tumours follow the leader

Tumour cells that lead the charge in invasive breast cancer express two genes that are

© 2013 Macmillan Publishers Limited. All rights reserved

required for invasion, and are distinct from cells that make up the bulk of tumours.

Andrew Ewald at Johns Hopkins University in Baltimore, Maryland, and his colleagues studied mouse and human tumour 'organoids', which consist of hundreds of diverse cancer cells.

They found that cells on the leading edge of the organoids' invasive strands express two genes, *K14* and *p63*. These are normally turned on only in cells that lie at the outer edges of epithelial tissue, which lines cavities and surfaces.

Blocking the expression of *K14* or *p63* in organoids disrupted invasion, suggesting that these and certain other genes in epithelial tissue could be targets for therapies that stop tumours spreading.
Cell **http://doi.org/qhc (2013)**

YONG-HEE LEE/JOO-SEONG KIM/JONGHYEON NOH

GEOSCIENCE

Volcanic lightning made in the lab

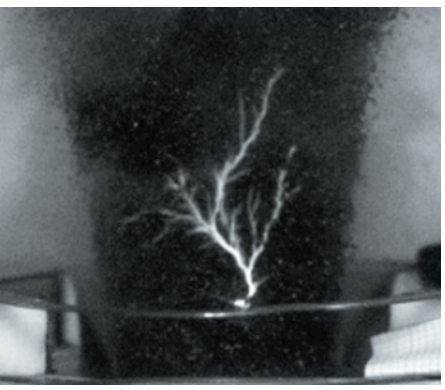
By replicating the lightning seen at the throats of erupting volcanoes, scientists have found that a greater abundance of fine particles spewing out of an eruption creates more lightning.

Corrado Cimarelli of Ludwig Maximilian University in Munich, Germany, and his colleagues simulated a volcanic eruption by placing ash in a shock tube — an instrument that generates blasts. Drastically decompressing the ash caused it to explode upwards into a tank.

High-speed cameras and other instruments captured a rare glimpse of the lightning that formed (**pictured**).

Clustering of charged particles in the ash jet triggers electrical discharges, the authors propose.
Geology **http://doi.org/qfz (2013)**

CORRADO CIMARELLI/MIGUEL ALATORRE IBARGÜENGOITIA



EVOLUTIONARY BIOLOGY

Biofilms block bacterial cheaters

Bacteria that secrete digestive enzymes in communities keep nutrients close at hand to avoid being exploited by cheating neighbours that do not chip in to enzyme production.

Bonnie Bassler and her colleagues at Princeton University in New Jersey studied *Vibrio cholerae*, which causes cholera and secretes an enzyme that digests the natural polymer chitin.

They found that cheaters do not thrive as well as enzyme producers when they are grown in communities called biofilms — probably because the thick sticky film slows the diffusion of nutrients, keeping them close to the producers. Exposing the biofilms to flowing water, which washes away nutrients before they reach the non-producers, also allowed the producers to outcompete the cheaters.

The results suggest ways in which cooperation has evolved in bacterial populations.
Curr. Biol. **http://doi.org/qg9 (2013)**

PHYSIOLOGY

A road block for blood vessels

An alternative way of shutting down blood-vessel growth could lead to better therapies for certain inflammatory and eye diseases.

Stopping the growth of blood vessels is important for treating several diseases, and some therapies aim to block it by inhibiting a protein called VEGF. Peter Carmeliet of the University of Leuven in Belgium and his colleagues found another target: a protein called PFKFB3, which is involved in the breakdown of sugars and helps blood vessels to form.

In embryos of zebrafish (*Danio rerio*), blocking PFKFB3 with a chemical inhibitor reduced vessel sprouting and enhanced the effects of a VEGF-blocking compound. The PFKFB3 inhibitor also hindered vessel growth in mouse models of inflammatory disorders and age-related macular degeneration, a condition that can cause blindness.
Cell Metab. **http://doi.org/qhb (2013)**

COMMUNITY CHOICE

The most viewed papers in science

ELECTRONICS

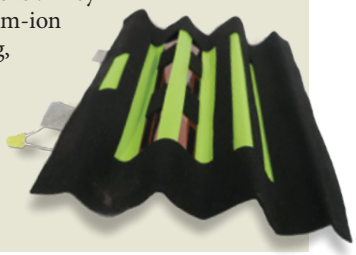
Battery woven into textiles

HIGHLY READ on pubs.acs.org in November

A rechargeable battery has been built into clothing and watch straps and performs as well as inflexible batteries do, even when folded and unfolded repeatedly.

Key to the battery is a flexible current collector — the metal that helps to transfer electrons between battery electrodes and an external circuit. Jang Wook Choi and his colleagues at the Korea Advanced Institute of Science and Technology in Daejeon made their current collector by coating fibres of a woven polyester yarn with nickel. They then attached conventional lithium-ion electrode materials using a strong, flexible polyurethane binder.

The device was also recharged by lightweight solar cells (**pictured,** green) integrated in the battery surface.
Nano Lett. 13, **5753–5761 (2013)**



MICROBIOLOGY

Bacteria adapt to diseased lungs

Bacteria in the lungs of people with cystic fibrosis (CF) adapt to this environment in multiple ways, resulting in a diverse bacterial community even within the same person.

Roy Kishony at Harvard Medical School in Boston, Massachusetts, and his colleagues sequenced multiple isolates of *Burkholderia dolosa* from the lungs of five patients with CF. Genes involved in antibiotic resistance and scavenging iron (a limiting nutrient) showed signs of adaptation. Individual patients harboured microbes with a variety of adaptive mutations in these genes.

In separate work, a team led by Jeremy Dettman at the University of Ottawa, Canada, sequenced *Pseudomonas aeruginosa* isolates from 24 patients with CF and compared their genomes to eight previously sequenced ones. The team found that genes involved in biofilm formation, antibiotic resistance and coping with oxidative stress seemed to help the bacteria adapt to the CF lung. The analysis also showed that a strain with increased antibiotic resistance has spread between North America and the United Kingdom.
Nature Genet. **http://doi.org/qf4 (2013)**
Proc. Natl Acad. Sci. USA **http://doi.org/qf3 (2013)**

NATURE.COM
For the latest research published by *Nature* visit:
www.nature.com/latestresearch

© 2013 Macmillan Publishers Limited. All rights reserved

SEVEN DAYS *The news in brief*

POLICY

US budget deal

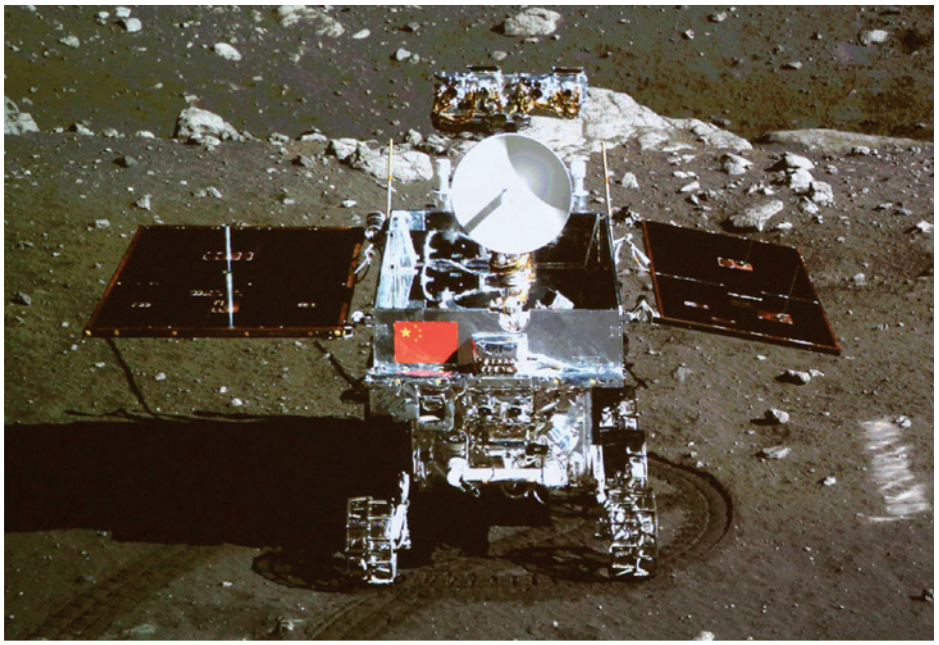
The US government's battles over spending, which culminated in October with a 16-day government shutdown, are close to an end. On 12 December, the House of Representatives approved a measure that would eliminate planned 'sequestration' spending cuts for the next two years — increasing the government's discretionary spending by roughly 4.5% this year, to US$1.012 trillion. The Senate is expected to approve the bill before 20 December, its last scheduled working day this year. That would clear the way for approval by President Barack Obama, who has said he will sign the measure into law.

German reshuffle

German chancellor Angela Merkel's new coalition government, announced on 15 December, includes a new 'super ministry' for energy and the economy, helmed by Sigmar Gabriel. As Merkel's likely vice-chancellor, he will be responsible for advancing the nation's transition to a renewable-energy-dominated economy. Johanna Wanka was renominated as minister for research and education; she has held the post since February, and will oversee a record budget of around €14 billion (US$19 billion) next year. Barbara Hendricks will be the country's new environment minister.

Antibiotics curb

The US Food and Drug Administration has issued guidelines to help phase out the widespread use of antibiotics in livestock — a practice that contributes to the spread of antibiotic-resistant microbes. Under the voluntary plan, pharmaceutical companies have 90 days from 11 December to choose whether to change labels on their drugs so that the medicines cannot be used to boost animals' growth. The guidelines still allow farmers to add drugs to animal feed to prevent outbreaks of disease. See go.nature.com/huzuae for more.



DING LIN/XINHUA NEWS AGENCY/NEWSCOM

China lands rover on Moon

China has become only the third country to soft-land a craft on the Moon — and the first to do so since the Soviet Union in 1976. Its Chang'e 3 spacecraft dropped safely to the surface on 14 December in the northern part of the Mare Imbrium (Sea of Rains), a site that may allow exploration of relatively late-forming basalts that could hold clues to the Moon's evolution. Seven hours later, the Yutu ('Jade rabbit') rover (pictured) drove off the lander: it is due to carry out a three-month tour of the Moon's surface. See go.nature.com/zcrvwq for more.

Shark cull

The government of Western Australia said last week that it would start culling sharks to mitigate risk to humans, after a series of high-profile attacks in the region. Marine researchers have objected to the move, arguing that it could severely damage populations of threatened great white sharks, and that it contradicted scientific advice given to the government last year warning against the environmental impacts of shark-control programmes. See go.nature.com/3eypym for more.

Biofuel delay

A proposal to get the European Union (EU) to limit the use of biofuels made from food crops failed to pass last week, after member-state ministers could not agree on a compromise deal. The EU has previously mandated that, by 2020, 10% of transport fuels must come from renewable sources, but scientists warn that fuels such as biodiesel from palm oil can produce more greenhouse-gas emissions than do fossil fuels (see *Nature* **499,** 13–14; 2013). A final deal to cap food-crop biofuels is now unlikely to be made before 2015, because European Parliament elections in May 2014 will probably set back negotiations.

Israel joins CERN

Israel has become the 21st nation — and the first non-European country — to join CERN, Europe's high-energy physics lab near Geneva, Switzerland. The country spent an obligatory two years as an associate member, ramping up its financial contributions, before it took the expected leap to full membership. The new status

© 2013 Macmillan Publishers Limited. All rights reserved

gives Israel voting rights and removes some previous limits on benefits such as employment opportunities. Brazil also looks set to join, after CERN's council agreed last week that the country had fulfilled criteria for associate membership.

Trawling vote

The European Parliament passed legislation last week to limit deep-sea fishing, but did not approve an amendment banning bottom trawling, in which nets are dragged across or anchored to the sea bed. Some scientists say that the practice causes heavy damage to sensitive ecosystems such as cold-water corals, which are slow to recover. But their arguments failed to sway enough parliament members. See page 341 for more.

FUNDING

Europe funds open

Researchers can now submit proposals for grants from Europe's new funding programme, Horizon 2020 (see go.nature.com/ttiscs). European research commissioner Máire Geoghegan-Quinn launched the programme — which is handing out €7.8 billion (US$10.7 billion) in 2014 — on 11 December. Concerned about high application numbers, the European Research Council has introduced new rules that ban authors of low-quality applications from resubmission for up to two years. And peer-reviewed science articles produced from European funding must be made open to read at an online repository within six months of publication.

Dementia promise

The G8 group of leading industrial countries has agreed to "increase collectively and significantly" its funding for dementia research, with the aim of developing a cure or disease-modifying treatment by 2025 (matching the date set by the United States last year on Alzheimer's disease). The commitments were made on 11 December at a London summit dedicated to dementia. Ahead of the meeting, the United Kingdom said that it would double its annual public and private dementia research funding by 2025; it currently stands at £52 million (US$85 million).

PEOPLE

Charles Vest dies

Mechanical engineer Charles Vest (**pictured**), who served as president of the Massachusetts Institute of Technology (MIT) in Cambridge from 1990 to 2004, died on 12 December, aged

DONNA COVENEY/MIT



72. Under Vest, the university increased its endowment from US$1.4 billion to $5.1 billion; added several research centres, including centres in nanotechnology and genomic medicine; and set up its OpenCourseWare initiative to make course materials freely available online. After leaving MIT, Vest served as president of the US National Academy of Engineering from 2007 until June of this year.

Millionaire prizes

Six biologists, including Robert Langer of the Massachusetts Institute of Technology in Cambridge and Mahlon DeLong of Emory University in Atlanta, Georgia, have each won US$3 million in the latest tranche of Breakthrough Prizes in Life Sciences, announced on 12 December. Two physicists — Michael Green of the University of Cambridge, UK, and John Schwarz of the California Institute of Technology in Pasadena — shared the fundamental-physics award. Internet entrepreneur Yuri Milner, who founded the megaprizes in 2012, initially as a physics award, says that there will be a new mathematics prize next year. See go.nature.com/n5q4ew for more.

COMING UP

19 DECEMBER
The European Space Agency's €1-billion (US$1.4-billion) Gaia spacecraft is scheduled to launch, to make a high-precision map of stars in the Universe.
sci.esa.int/gaia

20 DECEMBER
The US Senate's last scheduled working day — by which time it should have cleared a budget bill that would eliminate cuts from federal science agencies.
go.nature.com/xbybbo

BUSINESS

Water sharing

Israel, Jordan and the Palestinian Authority have signed a water-sharing agreement that may also see brine piped more than 180 kilometres downhill from the Red Sea to replenish the rapidly shrinking Dead Sea. A desalination plant planned for construction in Aqaba, Jordan, would convert Red Sea salt water into fresh water, with its reject brine potentially destined for the Dead Sea — an idea that has been under discussion for decades (see *Nature* http://doi.org/qg7; 2013). The memorandum of understanding was signed in Washington DC on 9 December at the World Bank.

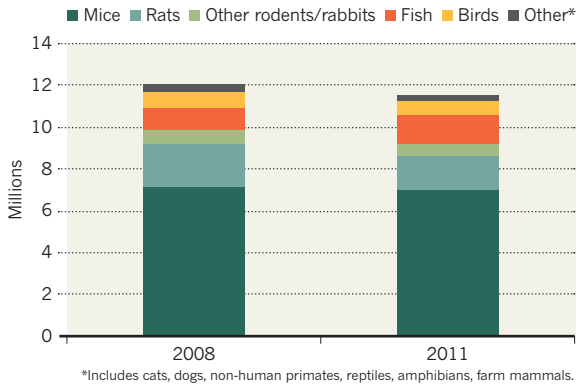
NATURE.COM
For daily news updates see:
www.nature.com/news

TREND WATCH

The number of animals used for scientific purposes in the European Union continues to fall. Half a million fewer animals were used in 2011 than in 2008, according to statistics released on 16 December by the European Commission. The number of mice, the most commonly used species, fell by 1.7%, and rat numbers fell by 24.5%. However, the number of fish rose by 28.5%.

EU ANIMAL USE FALLS

The number of animals used for scientific purposes in Europe fell by 4.3% between 2008 and 2011.



SOURCE: EC

© 2013 Macmillan Publishers Limited. All rights reserved

NEWS IN FOCUS

LAND USE Soviet-era cropland and a dilemma over food versus carbon sinks **p.342**

US FUNDING Foundation research support rises, but not for overheads **p.343**

YEAR IN REVIEW Twelve months of science news at your fingertips **p.344**



***NATURE*'S 10** The people behind major science stories in 2013 **p.357**

DAG MYRESTRAND/STATOIL



At the Sleipner field in the North Sea, waste carbon dioxide is separated from natural gas and injected into a rock formation 800 metres below the seabed.

EMISSIONS

Seabed scars raise questions over carbon-storage plan

Unexpected fractures above the world's biggest storage site could provide path for leaks.

BY RICHARD MONASTERSKY

Like a porpoise on the prowl, the sleek submersible HUGIN tracks its prey with sonar chirps. But the hunter set loose in the waters of the North Sea is not pursuing fish — the robot is trawling for geological clues that could help to determine whether billions of tonnes of carbon dioxide can be stored below the sea floor for centuries, keeping it from warming the planet.

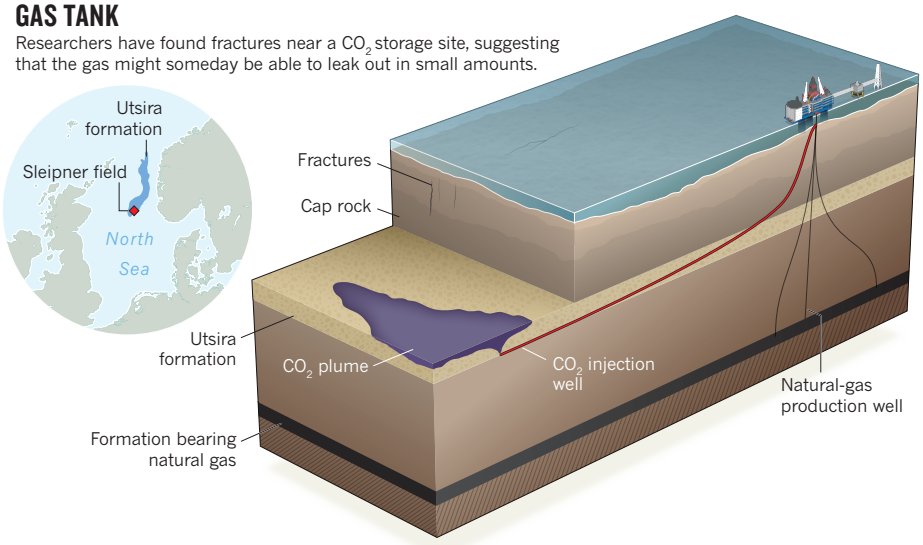
Now, the latest data from the autonomous underwater vehicle and other tools deployed by the European Commission's €10-million (US$13.8-million) ECO_2 research project suggest that the plan might not be so simple. The seabed is fractured and scarred more than researchers had appreciated — providing potential routes for CO_2 to leak from subseabed reservoirs where it is currently being stored. "We are saying it is very likely something will come out in the end," says Klaus Wallmann, ECO_2 coordinator and a marine geochemist at the GEOMAR Helmholtz Centre for Ocean Research in Kiel, Germany.

Such a conclusion could raise problems for the field of carbon capture and storage, especially in Europe, where any suggestion of leakage could reduce public support for the strategy. But ECO_2 researchers say that evidence from oil-industry carbon-storage efforts already under way in the North Sea and Barents Sea suggests no hint of leakage, and that there would be little cause for concern even if there were. "We are very confident that if it were to occur, the rates would be low and the impact would ▶

© 2013 Macmillan Publishers Limited. All rights reserved

GAS TANK

Researchers have found fractures near a CO_2 storage site, suggesting that the gas might someday be able to leak out in small amounts.



JASIEK KRZYSZTOFIAK/*NATURE*

▶ be minimal," says Wallmann, who presented the findings of the ECO_2 team on 9 December at a meeting of the American Geophysical Union in San Francisco, California.

Oil companies have long injected CO_2 into underground formations to enhance oil production, but the ECO_2 project is studying sites where the gas is pumped below the sea floor to keep it out of the atmosphere. One of the biggest operations is in the Sleipner natural-gas field in the North Sea, run by the energy company Statoil, headquartered in Stavanger, Norway.

Since 1996, the company has separated CO_2 gas from the desired hydrocarbons and reinjected up to 1 million tonnes of CO_2 a year into the Utsira formation, a layer of porous sandstone more than 800 metres below the sea floor (see 'Gas tank'). The giant formation, which covers an area of 24,000 square kilometres, has the potential to hold 600 billion tonnes of disposed CO_2. According to Statoil's website, CO_2 in the Utsira is safely contained under "gas-tight cap rock and cannot seep into the atmosphere".

Although the company has rich data about the Utsira formation, less is known about the overlying sedimentary layers. ECO_2 researchers have deployed HUGIN and other tools to fill in the details, using an advanced sonar system and a seismic profiler that sent strong acoustic pulses below the sea floor to reveal hidden geological structures.

The data reveal that the upper sedimentary layers hold many natural scars that might serve as conduits for CO_2 release from the Utsira. At a site 25 kilometres north of the Sleipner injection well, HUGIN found a 3-kilometre-long fracture that is 10 metres wide in places, and runs 150–200 metres deep. Samples of fluids collected within the fracture suggest that methane and fresh water are leaking out from lower layers, says Karin Landschulze, a graduate student in geophysics at the University of Bergen, Norway.

LEAK IMPACT

Because the fracture is so far from the injection site, the disposed CO_2 is unlikely to reach it any time soon, say ECO_2 researchers: since 1996, the CO_2 has spread in a plume and now reaches 3 kilometres north of the injection well. But finding such a large and unexpected fracture in the region raises questions, says Wallmann. "We don't know how it formed, when it formed, and why it formed," he says.

The researchers also discovered smaller vertical features, which they call chimneys and pipes, running through the sedimentary layers. One of these is only about 5 kilometres from the Sleipner CO_2 plume, and it reaches all the way down into the Utsira formation.

The discovery of so many potential leakage paths in the few sites examined has scientists reconsidering how well-contained the Utsira reservoir really is. "We might have to appreciate that there is a much greater chance for some CO_2 to leak out," says Stefan Bünz, a marine geologist at the University of Tromsø in Norway, who participated in the ECO_2 experiment.

Yet neither the ECO_2 project nor Statoil has found any indications that CO_2 has leaked from Sleipner in its 17 years of operation. Furthermore, the ECO_2 team has tested the likely impact of leaks, should they occur, by injecting up to 150 kilograms of CO_2 a day just above the sea floor near Sleipner. They found that the CO_2 completely dissolved within the lower few metres of water, rapidly converting to bicarbonate and dispersing. Only a small amount of the injected gas may have reached the atmosphere, says Wallmann.

The researchers also studied a spot in the Mediterranean Sea where natural vents release about 1 tonne of CO_2 a day. They found that the gas, which acidifies nearby waters, kills off many organisms within a small, 10-metre zone around the vent and reduces species diversity within a radius of about 100 metres, but that effects beyond that distance are limited.

A leak would be much more troubling from a public-relations standpoint, says Landschulze, because carbon capture and storage has been promoted in Europe as being safe. "It would be a disaster for public opinion," she says.

Yet because offshore disposal happens far from population centres, it has some advantages over onshore storage. Germany, Spain and Norway are each running onshore pilot experiments in which they have injected tens of thousands of tonnes of CO_2 into reservoirs underground, but some people have expressed concern about large-scale disposal on land. "I think it's easier to work offshore in the sense that the public perception is not ready for CO_2 storage in their backyards," says hydrogeologist Pascal Audigane of the French Geological Survey in Orléans, who manages a €5-million carbon-storage project in an underground lab in Switzerland.

In the end, the biggest impediments to subseabed CO_2 disposal are probably not leakage, but economics. Disposal makes sense at Sleipner, because the CO_2 has to be separated from natural gas for commercial purposes anyway, and Norway would impose a tax on Statoil if the waste gas were released. But the price of carbon emissions would have to rise in other countries before it becomes worthwhile to pump waste CO_2 from power plants and other sources on land to offshore injection sites. The chances of that happening soon may be slim, but carbon-storage researchers are carrying on with their work in case countries decide to push forwards with major cuts in greenhouse-gas emissions. ■

MORE ONLINE

TOP STORY



Simulation backs string theory's holographic Universe go.nature.com/uvggva

MORE NEWS

- Water seems to flow freely near Martian equator go.nature.com/9zzlzw
- Twitter popularity does not predict citations go.nature.com/xkwyei
- Caribou genetics may impair the animals' ability to cope with climate change go.nature.com/mkdohf

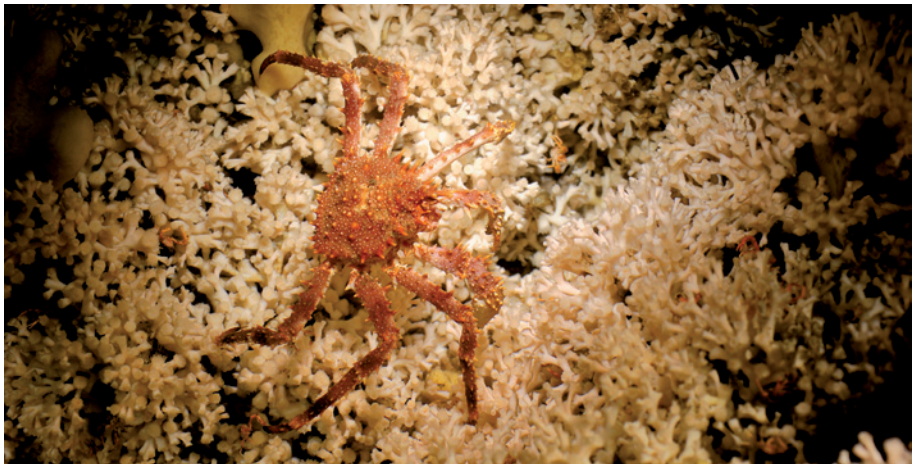
NATURE PODCAST



Neanderthals, the science of pickles and a satirist's look at the year in science nature.com/nature/podcast

MARKUS GANN/SHUTTERSTOCK

© 2013 Macmillan Publishers Limited. All rights reserved



SOLVIN ZANKL/GEOMAR/NATUREPL.COM

Fishing by bottom trawling can damage the delicate ecosystems of deep-sea corals.

SUSTAINABILITY

EU fishing vote foments anger

Failure to impose a ban on deep-sea fishing jeopardizes the future of vulnerable ecosystems, say researchers.

BY DANIEL CRESSEY

Ocean researchers and politicians who had hoped to see restrictions imposed on fishing in the sensitive ecosystems of the deep ocean were left disappointed last week after the European Parliament voted against tougher controls.

A bitterly fought amendment that would have seen deep-sea bottom trawling completely outlawed in the northeast Atlantic failed by just a handful of votes. It came despite Members of the European Parliament (MEPs) backing a package of measures on deep-sea fishing, including restrictions in vulnerable areas.

"The fishing industry lobbied well," says Chris Davies, a UK Liberal Democrat MEP and one of those leading the push for a ban. "If nine MEPs had switched their position the outcome would have been different."

The amendment would have seen a ban on the use of trawl nets, which are dragged across the seabed, and deep-sea gill nets (mesh walls that trap fish by the gills) in waters deeper than 600 metres. Some marine scientists think that such fishing is especially destructive because it damages delicate ecosystems of deep-sea corals and sponges, which take years to recover.

"We might quibble whether high-seas gill-net fishing or dynamite fishing on coral reefs is more destructive," says Julian Koslow, an oceanographer at the Scripps Institution of Oceanography at the University of California, San Diego, in La Jolla. "But the fact is that deep-sea bottom trawling is well documented to have denuded seamounts of highly diverse deep-water coral and sponge reefs wherever this form of fishing has been practised."

The fight for a ban on bottom trawling has intensified in recent weeks. Environmental groups, such as the Deep Sea Conservation Coalition, a consortium of more than 70 non-governmental organizations, have lobbied hard for the amendment. They say that a ban would affect only about 20 fishing vessels registered in Spain and France and have little impact on the wider industry. It is estimated that deep-sea fishing accounts for about 2% of the total European Union (EU) catch (see 'Small fry?').

Opponents of deep-sea fishing also point to an economic analysis in November by the London-based New Economics Foundation think tank. It states that every tonne of deep-sea fish caught costs society around €440 (US$605) in direct costs, such as subsidies, and indirect costs, such as environmental damage.

But the fisheries industry has also been active. Michael Park, chief executive of the Scottish White Fish Producers' Association, a fishing-industry group in Fraserburgh, UK, points to work by the Copenhagen-based International Council for the Exploration of the Sea, which found that the levels of some stocks of deep-sea fish are stable or increasing. Park also says that more vessels than claimed would have been affected by a ban, damaging profitability.

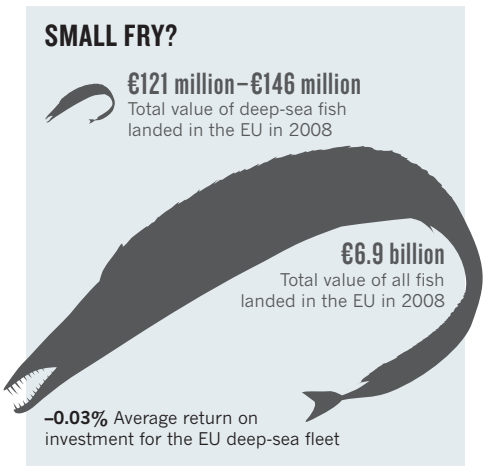
One of the biggest owners of deep-sea fishing vessels, Scapêche in Lorient, France, announced after the EU vote that it would no longer target deep-sea fisheries, although the company has not explained in detail how its practices will change.

Not all deep-sea fishing is harmful, Koslow notes. He says that fishing for the blue grenadier off the coast of New Zealand, and certain deep-sea fish caught with long lines or traps rather than trawls, can be sustainable. But others have proved to be "boom-and-bust fisheries that bring short-term profit to a very small group of fishermen", he says. "They are typically gone within 5 to 10 years, having depleted the resource, and they leave in their wake the destruction of unique and fragile deep-sea ecosystems, which will likely require centuries to millennia to recover."

Other researchers agree. Earlier this year, Les Watling, a biologist at the University of Hawaii at Manoa in Honolulu, wrote in *Nature* that many of the fishing lobby's claims, for example that catches of non-target species were limited, were unscientific "propaganda" (L. Watling *Nature* **501,** 7; 2013).

The European Parliament's legislation will now go to the European Council, which consists of ministers from EU member states, for ratification. In theory, the council could approve the bill quickly, but some environmentalists fear that it may try to shelve the issue. Despite their disappointment over the deep-sea trawling decision, they would like to see some of the other measures in the legislation adopted — such as funding for the conversion of deep-sea trawlers to less damaging fishing methods.

Callum Roberts, a marine conservation biologist at the University of York, UK, says that the vote might have ramifications beyond Europe. The United Nations has been passing resolutions to restrict deep-sea fishing for several years. The implementation of its measures is due for review in 2015. A ban in Europe would have sent a really powerful message that this is "a big problem", says Roberts. ■



SOURCE: PEW ENVIRONMENT GROUP/EC

© 2013 Macmillan Publishers Limited. All rights reserved



MARK MCDONALD/KRT/NEWSCOM

A Soviet-era tractor outside Privolnoye, a Russian town that has been hit hard by a decline in agriculture.

ENVIRONMENT

Quandary over Soviet croplands

Researchers ponder whether Eastern Europe's large areas of abandoned land should be replanted or left as a carbon sink.

BY QUIRIN SCHIERMEIER

The Soviet Union's collapse in 1991 heralded the end of many unprofitable communist industries, along with unprecedented changes in land use. As the free-market economy took hold, large swathes of Soviet cropland were abandoned by farmers and reclaimed by nature, causing a headache for today's policy-makers. Should it be replanted to feed hungry mouths, or left wild to act as a substantial sink for polluting carbon dioxide?

The issue resurfaced this month after a study suggested that the area of cropland abandoned since 1990 in western Russia, Belarus and Ukraine has been severely underestimated. According to figures based on regional sowing statistics, more than one-quarter of former agricultural land in the region is idle. This equates to about 31 million hectares — or an area the size of Poland — and is more than three times the area estimated in 2009 by the United Nations Food and Agricultural Organization mainly on the basis of land-use observations from space.

Such satellite-derived land-cover maps can lack accuracy. So Florian Schierhorn, a geographer at the Leibniz Institute of Agricultural Development in Central and Eastern Europe in Halle, Germany, and his colleagues turned to annual sowing data to map changes in cropland at high spatial and temporal resolution (F. Schierhorn *et al. Glob. Biogeochem. Cycles* http://doi.org/qg8; 2013). Using these maps, they applied an algorithm — based on farming preferences such as soil quality — to decide which sites were most likely to have been cultivated in any given year. They validated their maps using remote-sensing data and images from Google Earth.

"The Soviet Union strived for complete agricultural self-sufficiency," says Schierhorn, and this meant farming even low-quality land. He says that grain production in fertile regions is still substantial, but has dropped sharply in less fertile spots. This is mainly because, after 1990, there was a massive decrease in Soviet animal stock, so less need for animal feed, he adds.

Many sites once used to produce feed could today support wheat varieties and other cereals, Schierhorn says. If fully replanted, he estimates the region's idle land could yield some 90 million tonnes of grain per year — about 35 million tonnes more than Russia's wheat production in 2013. Recultivating only a portion of the land would buffer Russia against its notoriously erratic yields, Schierhorn adds. Ultimately, he says, it would help to satisfy the rising global demand for cereals for food and animal feed — projected to reach 3 billion tonnes by 2050.

The extent of abandonment in western Russia is not clear cut. Kirsten de Beurs, a geographer at the University of Oklahoma in Norman, has often visited the region, and says that some of Schierhorn's data do not fully reflect what is happening on the ground. "We found lots of areas that struggled with abandonment but also a significant number of areas that were taken back into production," she says.

But there is a catch in recultivating idle farmland, in that carbon locked in soils and plants on former agricultural land might be released into the atmosphere. Schierhorn's study estimates, using vegetation modelling, that 470 million tonnes of carbon — which would equate to about one-third of US CO_2 emissions in 2012 if released — have been sequestered between 1990 and 2009 in abandoned cropland in western Russia and Ukraine (see 'Carbon goes wild').

Wild vegetation is taking up carbon at a rate three times greater than previously estimated by some researchers, and the sink could become even more substantial as forests form, the team reports. Abandoned land, says Schierhorn, accounts for about one-third of the carbon sink provided by all forests in western Russia.

But such estimates are shrouded in uncertainty, says Nicolas Vuichard, an ecosystem researcher at the Laboratory of Climate and Environmental Sciences in Gif-sur-Yvette, France. In a 2008 study, he and his team calculated a carbon sink of about 8 million tonnes per year in abandoned cropland in Ukraine, Belarus and western Russia (N. Vuichard *et al. Glob. Biogeochem. Cycles* **22,** GB4018; 2008).

"The strength of a carbon sink depends not only on current biological activity but also on former crop management practices such as fertilizer use," says Vuichard.

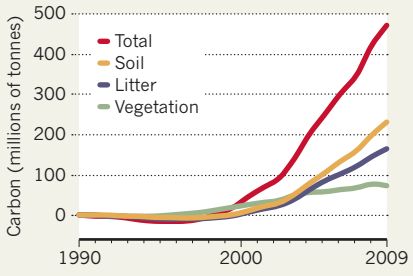
Today, there are signs that abandoned sites in Russia are being replanted: areas sown for crops and cattle fodder have slightly increased in recent years. The trend is encouraging for food production, Schierhorn says — but a full reversal may not be desirable given the trade-offs.

Schierhorn estimates that some 10 million hectares could be recultivated without excess stress on water resources and soils. "The rest," he says, "might better stay untouched." ■

SEE EDITORIAL P.331

CARBON GOES WILD

Amounts of carbon sequestered in abandoned cropland in western Russia and Ukraine rose sharply after 2000 as wild vegetation grew taller and thicker.



SOURCE: F. SCHIERHORN *ET AL. GLOB BIOGEOCHEM. CYCLES* HTTP://DOI.ORG/QG8; 2013

© 2013 Macmillan Publishers Limited. All rights reserved

FUNDING

Charitable grants found lacking

Foundations increasingly fund biomedical research, but are reluctant to pay overhead costs.

BY SARA REARDON

Kimberly Espy was thrilled when neuroscientists at her university won a US$100,000 grant in May from the Bill & Melinda Gates Foundation. The money would allow them to develop a technology to screen for potential drugs against intestinal worm infections — the kind of high-risk endeavour that government agencies often hesitate to fund.

But the grant came with a hitch, says Espy, vice-president for research and innovation at the University of Oregon in Eugene. Like many US philanthropic organizations, the Gates Foundation will add, at most, only 10% to a grant to cover overheads such as building fees, lab technicians and computing support. These indirect costs typically add 40–70% to the price of US research.

And so, to pay these costs, universities have to get creative. In the case of the worm project, says Espy, the university will draw money from tuition fees or other facility funds to supplement the Gates grant. But administrators are increasingly weighing up whether foundation grants are worth it.

"People have been discouraged from applying for grants because the department has to cover the shortfall," says Lita Nelsen, director of the technology-licensing office at the Massachusetts Institute of Technology in Cambridge. "We're at the edge here of turning down money."

In 2012, charities and foundations supported $1.3 billion of US biomedical research — a 79% increase on the previous year — according to a report released on 17 December by Research!America, an advocacy organization based in Alexandria, Virginia. In that time, support from the federal government grew by just 2%. Foundation support comprises just 1% of overall biomedical-research funding — well behind corporate and federal support — but charitable investment has risen steadily since 2001.

With the budget of the US National Institutes of Health (NIH) unlikely to increase much in coming years, philanthropic funding will continue to grow in importance in the United States, says Mary Woolley, head of Research!America. Scientists in other countries already receive a large proportion of their funding from foundations. Some 40% of UK biomedical-research funding, for instance, comes from charities such as the Wellcome Trust, based in London.

For many researchers, the growth in support from foundations is a good thing. Charitable grants have often been the only way for researchers to study rare diseases, for example.

And foundations sometimes offer more flexibility and creativity in the way they award funds, says Richard Insel, chief scientific officer at the Juvenile Diabetes Research Foundation in New York. He says that his foundation has partnered with large drug companies such as Sanofi to hand out joint grants to academic researchers. The companies draw on the charities' expertise in matching researchers to projects, the universities retain the intellectual property of their researchers' discoveries, and the charities increase the chances that therapies for the diseases they champion will make it to market.

But, increasingly, these grants have a hidden cost. Whereas government agencies such as the NIH and industry funders will typically cover all overhead costs, most charities rarely cover more than 10%, says Insel. A 2010 investigation by an advisory board to the multi-campus University of California (UC) found that the UC system loses some $300 million a year by accepting grants that do not cover indirect costs.

"We're at the edge here of turning down money."

Gaps in overheads are particularly problematic for university hospitals, which do not have tuition money to draw on and which shy away from raising patient fees, says Nelsen. She does not blame the foundations, which are trying to fund as much scientific research as possible and which say that it is a university's job to provide its own infrastructure. "Nobody's being a bad guy," she says.

But some scientists are calling for more efforts to convince foundations to change their policies. At an NIH advisory meeting on 5 December, Julio Frenk, a physician at the Harvard School of Public Health in Boston, Massachusetts, suggested to NIH director Francis Collins that the agency should urge foundations to pay these costs. He told Collins, "There needs to be an explanation that universities' costs are real costs, not an illegitimate profit." ■

© 2013 Macmillan Publishers Limited. All rights reserved



2013 IN REVIEW

Shutdowns, lethal viruses, typhoons and meteorites — much of this year's science news seemed to come straight from the set of a Hollywood disaster movie. But there were plenty of feel-good moments, too. Space exploration hit a new high, cash poured in to investigate that most cryptic of human organs, the brain, and huge leaps were made in stem-cell therapies and the treatment of HIV. Here, captured in soundbites, statistics and summaries, is everything you need to know about the science that mattered in 2013.

© 2013 Macmillan Publishers Limited. All rights reserved

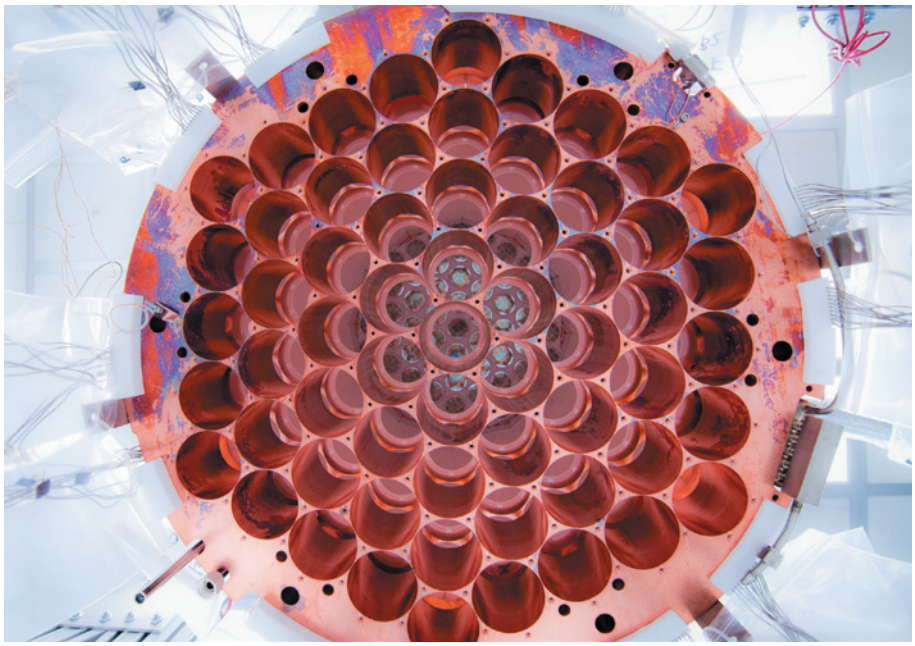
COSMIC MYSTERIES One of the year's most important cosmological results was an experimental no-show. The Large Underground Xenon (LUX, **pictured**) experiment at Sanford Underground Research Facility in Lead, South Dakota — 370 kilograms of liquid xenon almost 1.5 kilometres down in a gold mine — did not see any particles of elusive dark matter flying through Earth. But it put the tightest constraints yet on the mass of dark-matter particles, and their propensity to interact with visible matter. Theoretical physicist Matthew Strassler at Rutgers University in Piscataway, New Jersey, says a consensus is forming that hints of dark matter seen by earlier experiments in the past three years were probably just statistical fluctuations.

Whatever dark matter is, it makes up around 84% of the Universe's total matter, according to observations, released in March, of the Universe's cosmic microwave background (CMB) by the European Space Agency's Planck satellite. Planck's image (**pictured**) also strongly supports the hypothesis of inflation, in which the Universe is thought to have expanded rapidly after the Big Bang. A better probe of inflation might be provided through its predicted influence on how the polarization of CMB photons varies across the sky ('B-mode polarization'). That subtle signal has not been measured yet, but astronomers' hopes were raised by news of the first sighting of a related polarization signal, by the South Pole Telescope, in July. And another Antarctic telescope — the underground IceCube observatory — confirmed this year that the high-energy neutrinos it has detected come from far away in the cosmos, hinting at a new world of neutrino astronomy.

SHUTDOWN! The slow decline of US federal support for research and development — spending is already down 16.3% since 2010 — reached a new nadir in October, when political brinkmanship led the government to shut down for 16 days. Grant money stopped flowing; work halted at major telescopes, US Antarctic bases and most federal laboratories; and key databases maintained by the government went offline. Many government researchers were declared 'non-essential' and barred by law from visiting their offices and laboratories, or even checking their official e-mail accounts. Since the shutdown's end, grant backlogs and missed deadlines have scrambled agency workloads.

Away from the deadlock in the United States, the European Union negotiated a path to a 2014–20 research budget of almost €80 billion (US$110 billion), a 27% rise in real terms over the previous 2007–13 period. And funding in South Korea, China, Germany and Japan continued to increase (the United Kingdom and France saw little change). But Japan's largesse came with the clear understanding that its science investment would bring fast commercial pay-offs. Along similar lines, US Republican politicians are calling for the National Science Foundation to justify every grant it awards as being in the "national interest".

PLANCK: ESA/PLANCK COLLABORATION; LUX: CARLOS H. FAHAM



The Large Underground Xenon dark-matter experiment, deep in a mine in South Dakota.

"WE WANT TO DO OUR JOB AND WE CAN'T, BECAUSE THE GOVERNMENT ISN'T DOING ITS JOB."

Boston University ecologist Robinson Fulweiler on the US government shutdown in October.

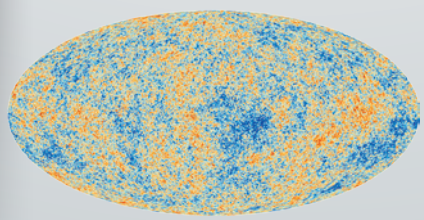
JAE C. HONG/AP



US workers came out in force against the shutdown.

13.82 billion years

AGE OF UNIVERSE AS ESTABLISHED BY THE PLANCK MISSION'S PICTURE OF COSMIC MICROWAVE BACKGROUND (BELOW).



© 2013 Macmillan Publishers Limited. All rights reserved

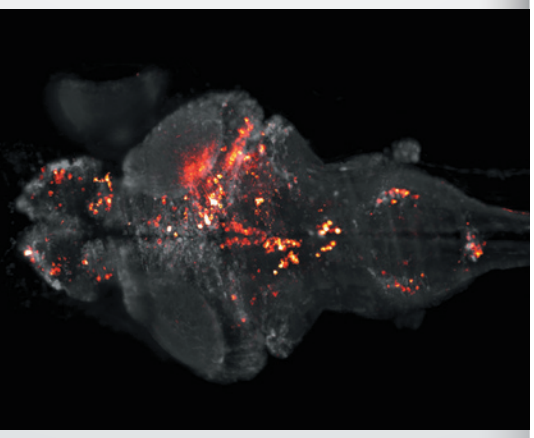
310

km h^{-1}

WIND SPEED OF TYPHOON HAIYAN, ONE OF THE STRONGEST ON RECORD.

400

CO_2 ATMOSPHERIC CONCENTRATION IN PARTS PER MILLION MEASURED AT THE MAUNA LOA VOLCANO IN HAWAII.



Individual neurons flash red in the brain of a larval zebrafish.

MISHA B. AHRENS AND PHILIPP J. KELLER



KAREN L. NYBERG/NASA

Typhoon Haiyan was snapped from the International Space Station as it raced across parts of Asia.

WAVERING ATMOSPHERE Apart from a landmark treaty to cut mercury emissions, signed by more than 90 nations so far, large environmental agreements were low on the political agenda this year. But no one expected to see nations actually regress. Japan renounced any near-term commitment to cut carbon emissions, Canada withdrew from the United Nations convention to combat desertification and the Australian government, elected in September, decided to scrap climate-change agencies and carbon taxes. At least the European Union agreed to end overfishing, reducing catch limits to a level that scientists say is sustainable.

In May, the atmospheric concentration of carbon dioxide temporarily surpassed 400 parts per million for probably the first time in human history. It was no surprise when the Intergovernmental Panel on Climate Change warned in its latest report, published in September, that climate change "unprecedented over decades to millennia" is altering natural environments in ways that could affect billions of people. Typhoon Haiyan's record-breaking wind speeds demonstrated the destructive forces that the atmosphere can unleash — although the jury is out on whether and how much global warming contributed (see page 361).

There were small signs of promise: emissions fell modestly in recent years in the United States and the European Union, and global renewable power generation reached around 5,000 terawatt hours — exceeding the total estimated electricity consumption of China.

In research, the focus was on the apparent slowdown in the rise of global average temperatures over the past 15 years or so. A study published in August supported the idea that the 'missing' heat is being stored in the deep ocean and that surface warming will resume soon. But a November study suggests that the apparent hiatus is a mere statistical artefact produced by incomplete coverage of Arctic regions in global temperature data sets. Stay tuned.

DECADE OF THE BRAIN US neuroscientists were excited and confused in equal measure this April when President Barack Obama unveiled the BRAIN Initiative — the field's equivalent of a Moon shot programme. Those feelings are still running high: what started life as a brain-mapping proposal has rapidly mutated into a more general effort to jump-start new technologies for deciphering the brain, albeit one that lacks clear vision and funding goals. Together with the European Union's €1-billion (US$1.3-billion) decadal project to simulate the human brain with supercomputers, announced in January, Obama's project reflects neuroscience's gradual shift away from molecular and cellular studies towards research on how networks of neurons produce thoughts, memories and actions. "It's starting to become possible to do the kinds of detailed, mechanistic analyses of larger circuits that were unimaginable ten years ago," says Eve Marder, a neuroscientist at Brandeis University in Waltham, Massachusetts.

Among the technical advances helping to make these dreams reality this year was a calcium-sensing dye that researchers used to capture the first images of nerve cells firing in an entire vertebrate brain — that of a transparent zebrafish larva (**pictured**). Efforts to map the brain's architecture got a big boost from CLARITY, a chemical treatment that turns opaque tissue clear and can expose neural circuits without the need for tedious brain slicing. Conventional neuroanatomy approaches also paid off with the completion of BigBrain, the first fine-scale, three-dimensional atlas of a human brain. And the introduction of false memories in mice by using light to stimulate

© 2013 Macmillan Publishers Limited. All rights reserved

genetically modified neurons in the hippocampus suggested that the ability to precisely manipulate neural signals is not that far away.

VANQUISHING VIRUSES The crippling paralytic disease poliomyelitis is now endemic in only three countries, but 2013 offered a reminder that the path to eradication will not be smooth. Although the virus's geographical range in two of the endemic nations, Pakistan and Nigeria, was reduced, efforts to make further progress faced serious opposition, with assassinations of polio-vaccine workers in both countries. No new cases were seen in the third endemic area of southern Afghanistan. But the virus continues to cause sporadic outbreaks elsewhere, with more than 180 cases reported in Somalia. A polio outbreak also began in war-torn Syria, and wild poliovirus persisted in southern Israel, leading to mass vaccinations across the Middle East to try to stop the virus becoming entrenched in the region.

This year also saw the emergence of a new foe: the H7N9 avian influenza virus. An April flare-up in China was quickly brought under control after live bird markets were shut down in the main cities affected (see page 362); the toll stands at 143 lab-confirmed cases and 45 deaths. Scientists are watching closely for any winter resurgence — a job made harder because the virus does not cause visible disease in poultry, and its reservoir species are not yet known. There has been less success in subduing the 'MERS' coronavirus, first reported in September 2012 (see 'A tale of two viruses'). A steady stream of cases has followed — 185 lab-confirmed or suspected, with 74 deaths by 12 December — most in Saudi Arabia, but also more widely in the Middle East and Europe. Researchers have criticized Saudi Arabia's lack of progress in tracking down routes of infection and animal sources — and the case count looks set to rise.

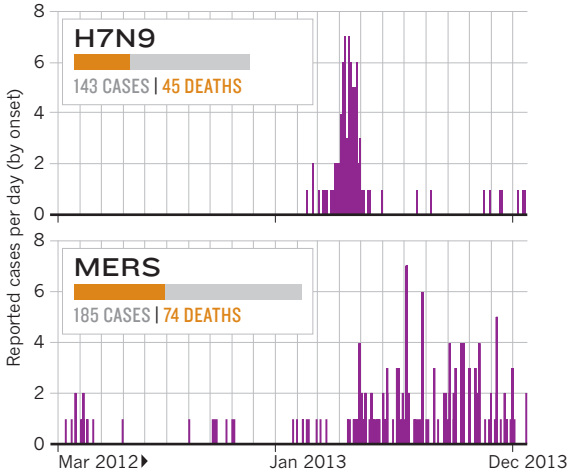
NOORULLAH SHIRZADA/AFP/GETTY



An Afghan health worker gives polio vaccine in an immunization drive earlier this year.

A TALE OF TWO VIRUSES

The outbreak of H7N9 avian flu virus was speedily controlled once live bird markets were identified as the route of transmission to humans. But the route for the MERS coronavirus remains elusive, and so a steady stream of new cases continues.



SOURCE: ANDREW RAMBAUT/WHO

69 years

TIME TAKEN FOR AN EXPERIMENT TO CATCH THE FALL OF A DROP OF TAR PITCH ON CAMERA (A DROP FORMS ONCE EVERY 7–13 YEARS).

−94 °C

THE COLDEST TEMPERATURE EVER RECORDED ON EARTH. NASA SATELLITES PINPOINTED THE LOW IN ANTARCTICA, WHERE THE PREVIOUS RECORD OF −89.2 °C WAS MEASURED IN 1983.

US $13.6 billion

THE YEAR'S LARGEST SCIENCE BUSINESS DEAL SAW THERMO FISHER SCIENTIFIC OF WALTHAM, MASSACHUSETTS, BUY BIOTECH-EQUIPMENT MANUFACTURER LIFE TECHNOLOGIES OF CARLSBAD, CALIFORNIA.

© 2013 Macmillan Publishers Limited. All rights reserved

THE CHELYABINSK METEOR

19 km s^{-1}

INITIAL SPEED OF METEOR IN EARTH'S ATMOSPHERE.

12,000

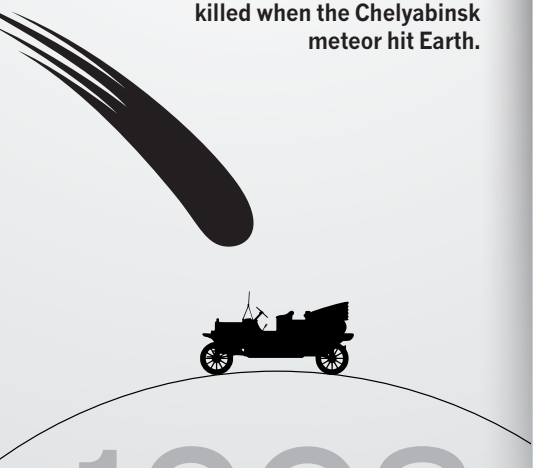
METRIC TONNES, MASS OF METEOR WHEN IT ENTERED THE ATMOSPHERE.

500 kt

TNT ENERGY EQUIVALENT OF RESULTING FIREBALL — ABOUT 30 TIMES THAT OF HIROSHIMA ATOMIC BOMB.

"WE WERE LUCKY."

Astronomer Peter Jenniskens, on the fact that no one was killed when the Chelyabinsk meteor hit Earth.



1908

LAST TIME SUCH A LARGE OBJECT HIT EARTH.



ANTON MELNIKOV/REUTERS/CORBIS

A large piece of the Chelyabinsk meteorite is raised from the bed of Lake Chebarkul in Russia.

THE FINAL FRONTIER The planet-hunting spacecraft Kepler will be remembered for the tantalizing results it produced before going kaput in May: it located more than 3,500 possible extrasolar planets (see page 360). But when a second of Kepler's metal reaction wheels stopped spinning, scientists had to give up their dream of an extended mission for the NASA craft. Other space missions fared better. China, working towards constructing its second space station, saw three astronauts dock with an orbiting laboratory module. NASA's Curiosity rover continued to trundle along on Mars, notching up more than 4.5 kilometres on its odometer on the way to its ultimate mountain destination. As if that weren't enough for the red planet, both India and the United States launched Mars orbiters in November. And by December, China became only the third country ever to send a rover to the Moon.

NASA's Voyager spacecraft left them all in the dust. After a journey of 36 years and 19 billion kilometres, the Voyager 1 probe finally crossed the boundary into interstellar space. The actual transition took place in August 2012, but not until this year were project scientists confident enough to announce the final exit into the void between the stars. Next stop for Voyager 1: drifting past a star in the constellation Camelopardalis, about 40,000 years from now.

GENE PATENTS Nearly 20 years of US patenting practice was turned on its head in June, when the Supreme Court ruled that naturally occurring human genes could not be patented (see page 359). The aftershocks of that decision are only now being felt. The case, brought against medical diagnostics company Myriad Genetics, challenged the validity of patents on two cancer-related genes, *BRCA1* and *BRCA2*, used to protect the company's proprietary tests for breast-cancer susceptibility. Shortly after the Supreme Court's decision was announced, several companies launched competing *BRCA1/2* tests at lower prices. But Myriad, of Salt Lake City, Utah, has already sued six of the firms, arguing that it holds other patents that protect the tests. The effects of the ruling have extended further. In October, a federal court judge cited the Myriad decision in overturning patents held by Sequenom of San Diego, California, on fetal DNA circulating in the blood of pregnant women, which the firm used in some of its prenatal screens. And lawyers report that US patent examiners are rejecting more patents than before on naturally occurring products such as genes and cells.

OPENING UP SCIENCE The drive to make science publications and data more open continued at a rapid clip this year. In February, the United States declared that the results of government-funded research must be made publicly accessible (rather than kept behind paywalls), but researchers have 12 months after publication to comply. By contrast, the United Kingdom wants articles to be made free immediately, although the next few years will see the country use a mixture of the two strategies. (One study found that half of all research papers published in 2011 can already be read for free somewhere on the Internet — the majority not at their publisher's website.) A rumbling undercurrent in the debate concerns the costs of this change, and exactly how much supposedly 'open' research can be reused.

Meanwhile, geneticists founded a global alliance to encourage wider sharing of data on DNA sequences and clinical information. In medical research, the UK government began a shake-up that could see patient medical

© 2013 Macmillan Publishers Limited. All rights reserved

records shared with scientists. And regulatory bodies renewed their efforts to throw open the vaults of data from clinical trials. The European Medicines Agency led the push, but has been stalled by lawsuits from drug firms trying to prevent the release of some of their trial data.

PROGRESS ON HIV Prevention, treatment, cure: the three prongs of HIV research have begun to seem increasingly like part of the same mission. In March, researchers reported that very early antiretroviral therapy had cured an infant of HIV (see page 360), following a January study that found early therapy helps to keep the immune system intact. That prompted the World Health Organization to recommend that treatment begin earlier than previously proposed. But the barrier to cures is still formidable. In July, doctors said that stem-cell transplants had apparently cured two men of HIV — but by December, they revealed the virus had returned. Vaccinologists were buoyed by new structures of a key HIV protein; by the first study to track the development of a broadly neutralizing antibody in a human; and by the demonstration that vaccines based on these antibodies can protect monkeys against the virus. "The past year has been perhaps the most revealing thus far about HIV's secrets," says Bruce Walker of Harvard Medical School in Boston, Massachusetts.

STEM-CELL SUCCESS A decade ago, a huge fanfare greeted South Korean researcher Woo Suk Hwang's claim — later proved fraudulent — to have created stem cells from cloned human embryos. This spring, the feat was accomplished for real, by researchers at Oregon Health and Science University in Beaverton. Yet it stoked much less excitement.

When Hwang was faking his results, hopes were high for therapeutic cloning: creating embryonic stem cells specifically matched to patients (see page 362). But few now think that cloning will be widely needed (although Oregon group leader Shoukhrat Mitalipov is working on clinical applications). This is not just because of concerns over destroying embryos, but also because the same end might be achieved using induced pluripotent stem (iPS) cells, reprogrammed from human adult cells. This year, a Japanese pilot study began recruiting people with the eye disease macular degeneration — the plan is to transplant sheets of retinal epithelial cells, derived from iPS cells, into their eyes. And in November, Japan approved a regenerative-medicine law to speed up approval for iPS-cell and related therapies.

Meanwhile, clinics offering unapproved stem-cell therapies continue to play cat and mouse with regulators. This year, Italy's health minister at first sanctioned a previously banned and unproven treatment for terminally ill patients (based on reinjecting stem cells from bone marrow), then offered money for a clinical trial — before reversing course on the advice of its scientific committee. In a final twist, the committee was ruled unlawfully biased — leaving the issue in limbo (see page 331).

IDENTITY PUZZLES In a year studded with revelations about spying and snooping, the question of what can be gleaned about identity from supposedly anonymized DNA data became an issue in genetics. In January, computational biologist Yaniv Erlich at the Whitehead Institute for Biomedical Research in Cambridge, Massachusetts, revealed how DNA in databases could be cross-referenced with public data to identify research participants. The 'genome hacker' followed this feat by creating a family tree of 13 million individuals going back to the fifteenth century from online genealogy sites.

DNA analysis continued to uncover clues to human ancestry. The 24,000-year-old remains of a Siberian boy suggested that up to one-third of Native American ancestry can be traced back to Europe, for example. Moving tens of thousands of years further back, examination of the Neanderthal and Denisovan genome sequences revealed large amounts of interbreeding between those human-like groups, as well as with modern humans and another unknown archaic population. And in another mystery, a 1.8-million-year-old fossil skull suggested that three separate hominin species may in fact be one. ■

Written by Richard Van Noorden, Jeff Tollefson, Erika Check Hayden, Lauren Morello, Helen Shen, Declan Butler, Heidi Ledford, Alexandra Witze, Eugenie Samuel Reich, Quirin Schiermeier & David Cyranoski



C. ZOLLIKOFER AND M. S. PONCE DE LEON/UNIV. ZURICH

Five skulls found in Dmanisi, Georgia, suggest that varying hominin fossils may not be different species.

QUOTABLES

"IT'LL BE DIFFICULT TO COMPETE WITH THE READY AVAILABILITY AND VERY CHEAP COSTS OF HUMAN POOP."

Tom Moore, a physician in Wichita, Kansas, on efforts to create synthetic pills of faecal bacteria, for curing gut infections.

"ARE WE THERE YET? YES, WE ARE."

Space physicist Ed Stone confirms that the Voyager 1 spacecraft has finally crossed the boundary into interstellar space.



"MOST OF US HAVE LITTLE SENSE OF SOCIAL RESPONSIBILITY."

Phillip Rogaway, a computer scientist at the University of California, Davis, who has sworn not to accept funding from the US National Security Agency and is critical of other researchers' silence.

"IT JUST SEEMS LIKE A GRATUITOUS KILLING OF A MOSQUITO WITH A SLEDGEHAMMER."

Genome policy analyst Misha Angrist, after the US Food and Drug Administration asked personal genetics firm 23andMe to stop marketing its products.

"I HAVE NEVER SEEN SO MANY PHYSICISTS FROM CERN SO WELL DRESSED BEFORE."

Fabiola Gianotti of CERN on the lavish ceremony for the US$3-million physics awards sponsored by Internet billionaire Yuri Milner.

TEST YOUR KNOWLEDGE

Q: THE OLDEST ANCIENT GENOME ON RECORD WAS PUBLISHED THIS YEAR, BUT WAS IT HORSE OR HOMININ?

Find out how much you can recall about the year in science with *Nature*'s end-of-year quiz
go.nature.com/izlxfn

© 2013 Macmillan Publishers Limited. All rights reserved

IMAGES OF THE YEAR

In 2013, our Universe continued to amaze and delight as it was probed and prodded by scientists. During the course of the year, the gaze of researchers ranged near and far, from the vast to the minuscule, providing stunning visions of space and capturing images of the very bonds that tie molecules together. This is our selection of the pictures that highlight science's, and nature's, triumphs.

Images selected by *Nature*'s art and design team
Text by Daniel Cressey

FIRE IN THE SKY

This huge fireball was created by the largest meteor known to hit Earth since the Tunguska rock landed in 1908. Russia was once again the unlucky recipient: the meteor exploded some 30 kilometres above Chelyabinsk in the Urals and shone brighter than the Sun.





MAGIC MOMENT

Reminiscent of an art installation, these γ-ray detectors in Japan captured evidence that calcium atoms with 20 protons and 34 neutrons are stable, identifying 34 as a 'magic number' of nuclear stability.

FLOWER POWER

These images show faint electric fields around an idealized flower. UK researchers found that bees sense these fields: one bee leaves a positive charge behind and others can use it to decide whether to visit the flower.

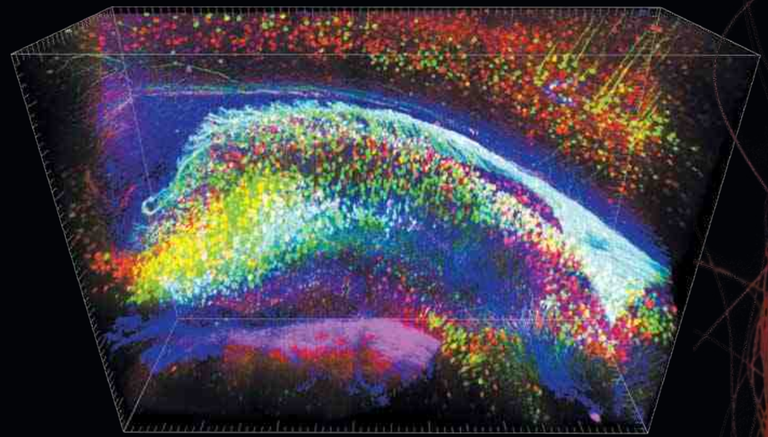


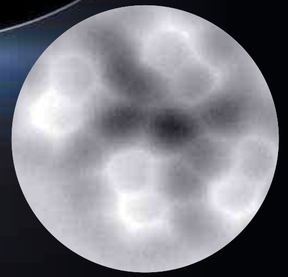
SMALL AND MIGHTY

Made of polyacrylonitrile, these nanofibres seem to defy logic — the thinner they get, the stronger and tougher they become. Made by electrospinning, in which a tiny charge draws fibres from a liquid, their slim build makes them up to ten times stronger than thicker versions currently used in optics and electronics.

MIND READER

This is one of the first 'transparent brains' to be made with CLARITY, a neuroimaging method that renders brains — in this case a mouse hippocampus — transparent by stripping away lipids with detergent. The technique reveals neurons in three-dimensions, instead of conventional two-dimensional slices.





VISUAL LINK

Chemists have become almost blasé about taking images of individual atoms. But with skilful use of atomic force microscopy, researchers in Beijing managed to capture the first pictures of hydrogen bonds, seen here as faint lines between four molecules of 8-hydroxyquinoline.

© 2013 Macmillan Publishers Limited. All rights reserved

FAR OUT

Peer carefully at the lower right of this image and you might just spot the tiny dot that is Earth, seen from more than a billion kilometres away. This vista of Saturn's famous rings backlit by the Sun was assembled from 141 individual images taken by NASA's Cassini probe after it moved into Saturn's shadow in July.



SOLAR STATION

This sci-fi-esque scene offers a glimpse of the future. Solar-power installations — such as this one at the Ivanpah Dry Lake in California, where the Sun's rays boil water to drive a turbine — grew in number and size in 2013. Some estimates predict that this source of energy will soon overtake wind power.



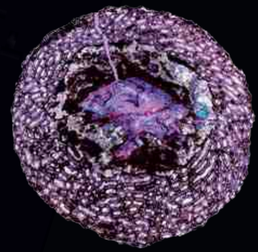
BROUGHT TO LIGHT

The olinguito (*Bassaricyon neblina*) was a rare find: a new land-mammal species discovered in the forests of the Andes. A member of the racoon family, the creature was formally described in August after a search prompted by previously misidentified museum specimens — although it turned out that an olinguito had previously been kept in US zoos.

SATURN: NASA/JPL-CALTECH/SSI; METEOR: MARAT AHMETALIEV; HYDROGEN BOND: IRADIAN QUASCHENSKAAS; BRAIN: HWANGHAN CHUNG & KARL DISSEROTH/HHMI/STANFORD UNIV.; DAY DETECTOR: SATOSHI TAKEUCHI; FLOWERS: DOMINIC CLARKE/GSK/CHEMDRAS; NANOFIBRES: DMITRY PAPKOV/DEL BRENNAN/YURIS DZENIS; SOLAR STATION: JAMES SYLLINGS; OLINGUITO: TUI DE ROY/MINDEN PICTURES/FLPA; GALACTIC WIND: ERIK ROSOLOWSKY/ALMA (NRAO/NAOJ/NRAO); TELESCOPE: DINOSAUR EMBRYO: AARON LEE/ANC; VOLCANO: JOSE JACOME/EPA/CORBIS

BLOWING IN THE WIND

A mass equivalent to nine Suns is blown out from the galaxy NGC 253 every year by a powerful space wind. The ALMA radio telescopes in Chile imaged the carbon monoxide in this wind in unprecedented detail and revealed the extent of the ejection. Regions of low emission intensity are red, and those of high intensity are blue-purple.



ANCIENT YOUNG

Dating to around 195 million years ago, this bone (shown in cross-section) comes from a dinosaur embryo. It is one of about 200 such bones sampled from a bone bed in China. The rare finds offered fresh data on dinosaur development.



OLD FLAMES

Tungurahua in Ecuador has been erupting near-continuously since 2010, and sporadically since at least 7,750 BC. The volcano has provided a wealth of scientific data, including a study this year showing that local settlements were devastated in an eruption in 1,100 BC, making it the site of one of the oldest-known volcanic disasters in the Andes.

© 2013 Macmillan Publishers Limited. All rights reserved

NATURE'S



TEN PEOPLE WHO MATTERED THIS YEAR

FENG ZHANG

TANIA SIMONCELLI

DEBORAH PERSAUD

MICHEL MAYOR

NADEREV SAÑO

VIKTOR GROKHOVSKY

HUALAN CHEN

SHOUKHRAT MITALIPOV

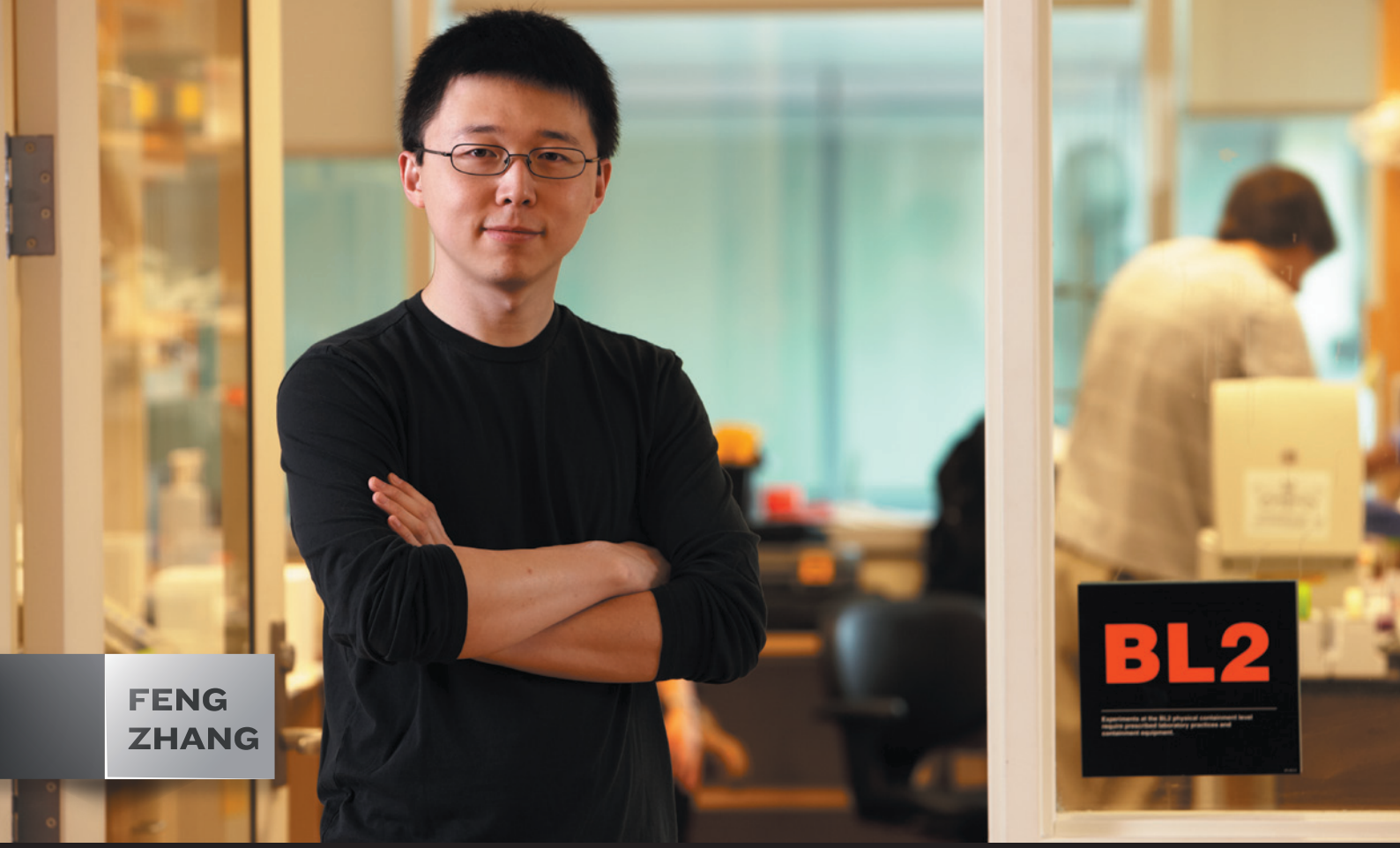
KATHRYN CLANCY

HENRY SNAITH

365 **DAYS:**
the year in science

ILLUSTRATION BY BRYAN CHRISTIE DESIGN

© 2013 Macmillan Publishers Limited. All rights reserved



DNA'S MASTER EDITOR

Borrowing from bacteria, a biologist helps to create a powerful tool for customizing DNA.

BY DANIEL CRESSEY

With a nip here and a tuck there, a DNA-cutting mechanism that bacteria use to protect themselves from viruses became one of the hottest topics in biomedical research in 2013. And a young neuroscientist with a penchant for developing tools helped to make it happen.

Thirty-two-year-old Feng Zhang of the Massachusetts Institute of Technology in Cambridge is among those leading the charge in using a system called CRISPR/Cas to edit genomes cheaply, easily and precisely. In January, his group showed that the system works in eukaryotic cells — ones with membrane-bound nuclei, including those of all animals and plants. This confirmed its potential for tweaking the genomes of mice, rats and even primates to aid research, improve human-disease modelling and develop treatments (L. Cong *et al. Science* **339,** 819–823; 2013).

But as hot as the story has been this year, "the CRISPR craze is likely just starting", says Rodolphe Barrangou, a microbiologist at North Carolina State University in Raleigh.

CRISPRs (clustered regularly interspaced palindromic repeats) are DNA sequences that many bacteria and archaea use to defend themselves. They encode RNAs that can specifically recognize a target sequence in a viral genome. The RNAs work in complex with a CRISPR-associated protein, or Cas, which snips the DNA of the invader.

In 2012, Jennifer Doudna of the University of California, Berkeley, Emmanuelle Charpentier, now at the Helmholtz Centre for Infection Research in Braunschweig, Germany, and colleagues showed that they could reprogram a CRISPR system to cut apart potentially any specific DNA target (M. Jinek *et al. Science* **337,** 816–821; 2012). By controlling how the break is repaired, they can edit a gene — adding, switching or removing parts to change the protein it encodes or disable it altogether.

CRISPR is similar to two earlier genome-editing methods: the zinc-finger nuclease (ZFN) and transcription activator-like effector nuclease (TALEN) systems. But both of those locate target sequences using proteins that are often difficult and costly to produce. CRISPRs use RNA, making them easier to design. Zhang says he feels limited only "by what I can imagine is possible".

Although Charpentier and Doudna are generally credited with kick-starting the growth of CRISPR editing, Zhang demonstrated its vast potential by showing that it works in eukaryotes, a finding independently confirmed by George Church at Harvard Medical School in Boston, Massachusetts (P. Mali *et al. Science* **339,** 823–826; 2013). Zhang says that he had a head start on many of the teams who jumped in: he had been investigating the technique before it was widely reported, and because his lab had previously fine-tuned ZFNs and TALENs to edit DNA, it had procedures in place for perfecting CRISPRs.

Zhang now says that he feels challenged to be creative with other applications. One particularly ambitious project on his slate is to build a library of CRISPRs that can delete any sequence in an organism's entire genome in 100–200 base-pair increments. This could make it easier to investigate the function of non-coding DNA.

But he is most interested in using CRISPR to treat neuropsychiatric conditions such as Huntington's disease and schizophrenia by repairing genes in human tissues. To pursue therapeutic use of the technology, he and other CRISPR pioneers last month launched a company called Editas Medicine, based in Cambridge, that is backed by US$43 million in venture-capital funding. CRISPR "allows us to start to make corrections in the genome", says Zhang. "Because it's easy to program, it will open up the door to addressing mutations that affect few people but are very devastating." ■

KENT DAYTON

© 2013 Macmillan Publishers Limited. All rights reserved



GENE PATENT FOE

A US science-policy expert fought to keep genes open to all.

BY HEIDI LEDFORD

In 2005, Tania Simoncelli managed to shock the senior lawyer at the American Civil Liberties Union (ACLU). Simoncelli, the organization's first science adviser, informed him that companies were snatching up patents on many human genes. "That's ridiculous!" exclaimed the counsel, Chris Hansen. "Who can we sue?"

It would not be that easy. Although the ACLU, a non-profit organization based in New York City, has spent nearly a century suing state and federal agencies for infringing civil rights, it had never challenged a patent. And the prospect seemed daunting in this case: the US Patent and Trademark Office had been issuing patents on human genes for nearly 30 years. But Simoncelli saw the practice as a threat to the right of individuals to access their own medical information, as well as to scientists' ability to do research on the genes.

Over the next four years, Simoncelli helped ACLU's lawyers to pull together a case and identify a suitable target for a suit — Myriad Genetics, a firm based in Salt Lake City, Utah, that had been particularly aggressive in defending its patents on two genes that have been linked to breast cancer. And she rallied a consortium of scientists, patients and physicians to support the suit.

"She's so persuasive," says Hansen. "She's persistent in a way that you don't notice, until suddenly you've agreed with her." Ultimately, the ACLU pursued the lawsuit to the US Supreme Court and, this June, won.

For Simoncelli, the experience offered the kind of interdisciplinary work that she had dreamed of doing since her undergraduate days studying biology and society at Cornell University in Ithaca, New York. "I wanted to be the person who could help bridge the cultures of science and justice," she says.

After Cornell, Simoncelli earned a master's degree in energy and resources from the University of California, Berkeley, then went to work at the ACLU in 2003. Her intention was to stay only two years before leaving to get her PhD in science, technology and society. She stayed for nearly seven — sometimes returning even after she left for the US Food and Drug Administration (FDA) in 2010, using her holiday time to continue work on the lawsuit.

Skipping that PhD was a difficult decision, recalls Sheila Jasanoff, a specialist in science and technology studies at Harvard University in Cambridge, Massachusetts, who taught Simoncelli as an undergraduate and has mentored her ever since. She suspects that Simoncelli has lost out on jobs and at times struggled for respect because she lacks the degree. But at the ACLU she was given the freedom to make her mark. "It was a place where her passion and drive didn't get held back," says Jasanoff.

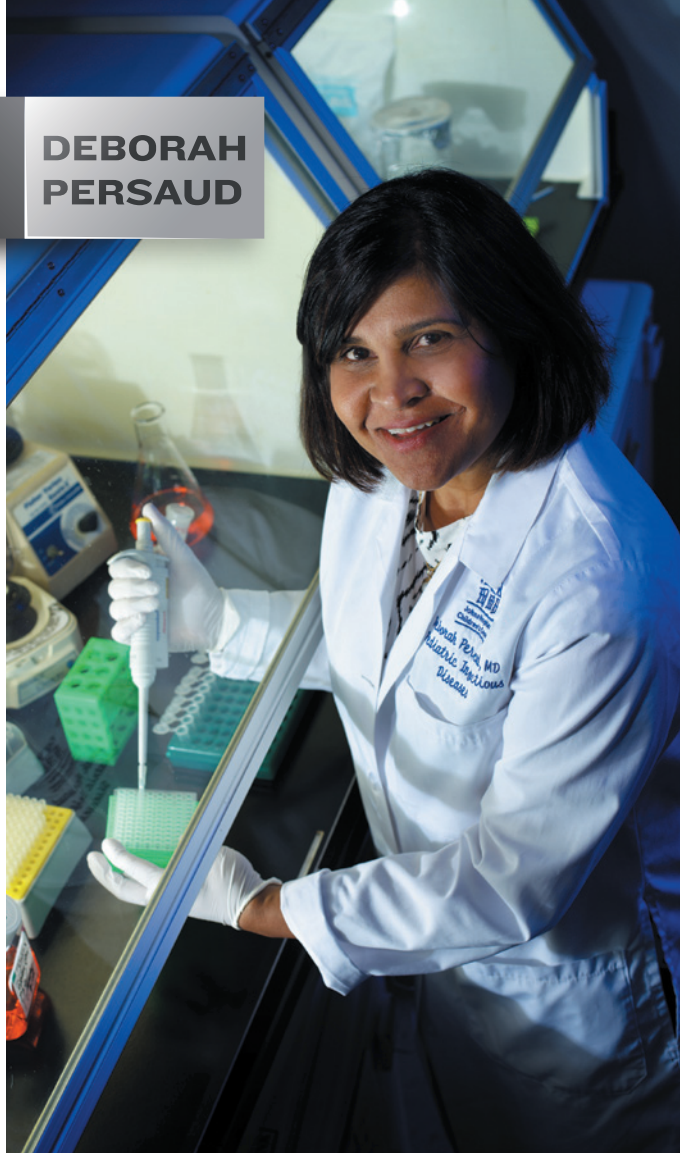
At the FDA, Simoncelli has focused on policy areas such as nutrition and personalized medicine. She is currently working at the White House Office of Science and Technology Policy on forensic science — a project that brings her back to the intersection of science and justice.

"I'm really looking forward to seeing what's next for Tania," says Jasanoff. "She always surpasses my imagination." ■



EERO SIMONCELLI

© 2013 Macmillan Publishers Limited. All rights reserved



JOHNS HOPKINS MEDICINE

VIRAL VICTOR

A virologist provides the strongest evidence yet that infants born with HIV can be cured.

BY SARA REARDON

In March, Deborah Persaud was ready to share the news: a baby born with HIV in Mississippi seemed to be virus-free nearly a year after stopping treatment. Persaud, a serious, soft-spoken virologist at Johns Hopkins Children's Center in Baltimore, Maryland, says she knew that she had to tread delicately. More than 40 similar cases had previously been reported in the literature, and each had fallen apart on closer scrutiny. Genetic analysis revealed that most of the initial tests had generated false positives or had involved specimen mix-ups.

But Persaud and her collaborators, Hannah Gay at the University of Mississippi in Jackson and Katherine Luzuriaga of the University of Massachusetts in Worcester, had done the genetic tests on the Mississippi baby themselves and were ready for the critics. What they were not expecting was the media onslaught that followed their announcement. News outlets around the world jumped on the story, and after a month the three were listed among *Time* magazine's 100 most influential people in the world.

Persaud's role in the case started with a call in September 2012 from Gay, a paediatrician, who was treating a baby born to a woman with HIV. Because the mother had gone untreated for the duration of her pregnancy, Gay gave the baby high doses of three antiretroviral drugs — zidovudine, lamivudine and nevirapine — within hours of birth.

IN SEARCH OF SISTER EARTHS

An astronomer with a flair for technology extends his legacy of discovery.

BY ELIZABETH GIBNEY

Michel Mayor and his team have found hundreds of exoplanets during the past two decades. But 2013 brought the 71-year-old planet-hunter a particularly gratifying discovery: his group determined that the planet Kepler-78b is of a density and size that make it the closest analogue of Earth identified so far.

It is far from an exact match — Kepler-78b orbits so close to its parent star that its surface is molten. But finding a true Earth twin is only a matter of time, says Mayor, an emeritus astronomer at the University of Geneva in Switzerland who is still active in research. Before he truly retires, he says, "I hope to have the possibility to celebrate this discovery."

Mayor has had plenty to celebrate already. In November 1995, he and his then-student Didier Queloz published the first evidence for an exoplanet orbiting a Sun-like star. The evidence was indirect: just a tiny wobble in the motion of the star 51 Pegasi, caused by the gravity of a world half the mass of Jupiter whipping around its orbit every 4.2 days. Since then, teams led by Mayor have discovered a substantial fraction of the 1,050-odd exoplanets known so far. That success is largely due to Mayor's talent for technology, says Geoff Marcy, a rival exoplanet hunter at the University of California, Berkeley. "Year after year, Michel has built an instrument a factor of ten better than the previous one," says Marcy. "Every time he does it, I'm amazed."

A prime example is the High Accuracy Radial Velocity Planet Searcher (HARPS), which Mayor and his team have been operating at the La Silla observatory in Chile since 2003. Able to detect stellar wobbles of less than 1 metre per second, HARPS is the most accurate spectrograph in the world, rivalled only by HARPS-North: a near-identical copy that has been operating on La Palma in the Canary Islands since 2012.

It was with HARPS-North that Mayor and his team determined the density of Kepler-78b, one of thousands of exoplanet candidates compiled by NASA's Kepler spacecraft between 2009 and 2013. Another group, of which Marcy was a member, independently measured Kepler-78b's size and density.

The next step — to find an Earth-like planet that is far enough from its star to harbour liquid water, and potentially life — remains a challenge. But with instruments improving all the time, Mayor predicts that it will happen within five years. He has every intention of remaining a part of that search. "When you are in the dome, looking at the sky with a new instrument for the first time and you start to see that it is working and better than expected," he says, "it is a huge pleasure." ■

© 2013 Macmillan Publishers Limited. All rights reserved

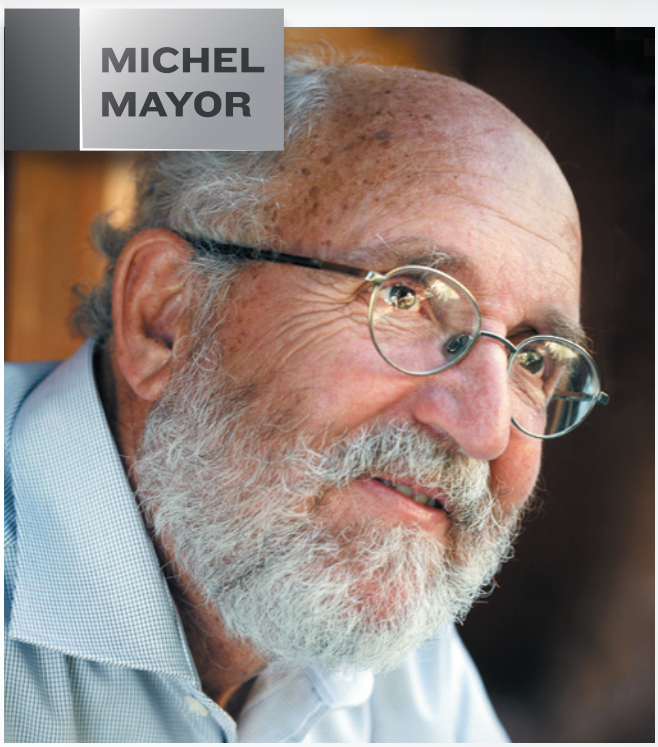
Tests conducted at the time showed that the baby had HIV, and the mother was told to continue the child on treatment. At one check-up, however, Gay found that the baby had not been getting her drugs for five months. Gay tested the child and found no sign of the virus.

To make sure that this was not another false signal, Gay called in Persaud and Luzuriaga. They matched the mother's DNA with the baby's to be sure that she had not been switched in the hospital. They took five separate blood samples for the HIV tests and personally checked each lab result. As they ruled out alternative explanations, it looked more and more likely that the initial blast of drugs had wiped out the virus. They published a paper describing the case in November (D. Persaud *et al. N. Engl. J. Med.* **369,** 1828–1835; 2013), and so far it seems to be standing up to scrutiny.

The media attention after the initial announcement had benefits: it made an ambitious clinical trial more feasible. The International Maternal Pediatric Adolescent AIDS Clinical Trials Group, for which Persaud is a scientific adviser, plans to test these early, heavy drug doses in high-risk infants. HIV transmission rates are low in the United States, so the researchers will need to enrol hundreds of women with the virus to find enough infected infants to make their case.

But many people do not want to wait for the results. Some patients who have been taking antiretrovirals since birth are now wondering whether they, too, can stop taking their drugs. "It comes up in every clinical visit," says Luzuriaga.

For now, people are advised to continue to follow their prescriptions — missing even one daily pill can be hazardous. But if the results hold up, Luzuriaga says that some of the hundreds of children and teenagers treated at birth may one day be able to try ceasing their treatment. In the meantime, Persaud is looking for ways to test whether someone is in remission before such a step is taken. "It's a very high bar," she says, "but it could be the tipping point in HIV therapy for children." ■



RITA SCAGLIA



AP

CLIMATE CONSCIENCE

After Typhoon Haiyan ravaged the Philippines, a diplomat focused the world's attention — briefly — on global warming.

BY JEFF TOLLEFSON

When Naderev Saño offered a tearful statement at the United Nations climate talks in Warsaw in November, he did not know the fate of some of his own relatives, or that of thousands of other fellow Filipinos. The head of the Philippines delegation knew only that his brother was alive and had joined emergency workers collecting dead bodies in the devastating wake of Typhoon Haiyan. He also knew that the colossal cyclone — one of the strongest on record — could be a harbinger of what coastal regions will face in the future.

"What my country is going through as a result of this extreme climate event is madness," Saño said. He pledged to fast during the talks, "until a meaningful outcome is in sight".

His plea for solidarity drew a standing ovation. And he kept his fast for 14 days, until delegates reached a last-minute deal to keep negotiations on track for the next major climate summit, in Paris in 2015.

The pace of international progress on global warming has been glacial. Despite more than two decades of negotiations, atmospheric carbon dioxide levels have continued to rise; in May, the daily average concentration topped 400 parts per million for the first time in Hawaii, where the longest-running record is kept. In September, the Intergovernmental Panel on Climate Change released its fifth assessment of the science underlying global warming, which warned of growing threats from climate-related problems such as sea-level rise, extreme weather and droughts.

Looking back, Saño is not sure what impact his speech had, but he argues that Typhoon Haiyan helped to put the international spotlight squarely on the climate issue. Having done graduate work on climate and disaster response himself, he knows that scientists shy away from attributing any single weather event to global warming. But there is general agreement that warming oceans will fuel more energetic storms, he says, and extreme storms resonate in a way that scientific charts cannot.

"I would hope that beyond the slow climate-change negotiations," he says, "our sacrifice and statement would translate into something more profound." ■

© 2013 Macmillan Publishers Limited. All rights reserved



VIKTOR GROKHOVSKY

METEORITE HUNTER

A Russian researcher tracked the debris from the biggest object to hit our planet in a century.

BY QUIRIN SCHIERMEIER

The event that made 2013 special for Viktor Grokhovsky came without any warning. The mighty meteor that fell to Earth on 15 February had approached our planet from a region of the sky that is inaccessible to ground-based telescopes, so it took astronomers by surprise.

Grokhovsky, a metallurgist at the Ural Federal University in Yekaterinburg, Russia, who has studied meteorites for more than 30 years, was too far away to watch the incoming object light up the morning sky. But when he learned about a powerful explosion that had knocked people off their feet and shattered thousands of windows in the city of Chelyabinsk, he realized that something substantial had hit the planet.

In the days after the impact, Grokhovsky worked feverishly to calculate the meteor's trajectory and predict where fragments might have landed. He supervised searches that unearthed more than 700 pieces of the meteor, weighing a total of 5.5 kilograms. "It was a great satisfaction when it turned out that our initial calculations had been correct," he says.

But his greatest catch came later in the year. Calculations of the meteor's trajectory and a large hole in the ice of a lake to the west of Chelyabinsk had convinced Grokhovsky that the biggest single chunk had landed there. When divers finally searched the lake's muddy bottom in October, they recovered a 570-kilogram boulder.

Thousands of fragments from the meteor are being analysed in labs around the world and they have already begun to reveal their secrets. "It is hard to overestimate the importance of the Chelyabinsk meteor," says Grokhovsky. Because of its size and the damage it caused, it has prompted scientists to increase the odds of similar meteors — or larger ones — striking our planet.

Grokhovsky says that it was a once-in-a-lifetime experience for him. "I was lucky enough to play a part in this exciting story about a space traveller's adventures on Earth." ■

NATALIA NIKITINA

FRONT-LINE FLU SLEUTH

A virologist helped China to quell an outbreak of H7N9 avian flu in humans.

BY DECLAN BUTLER

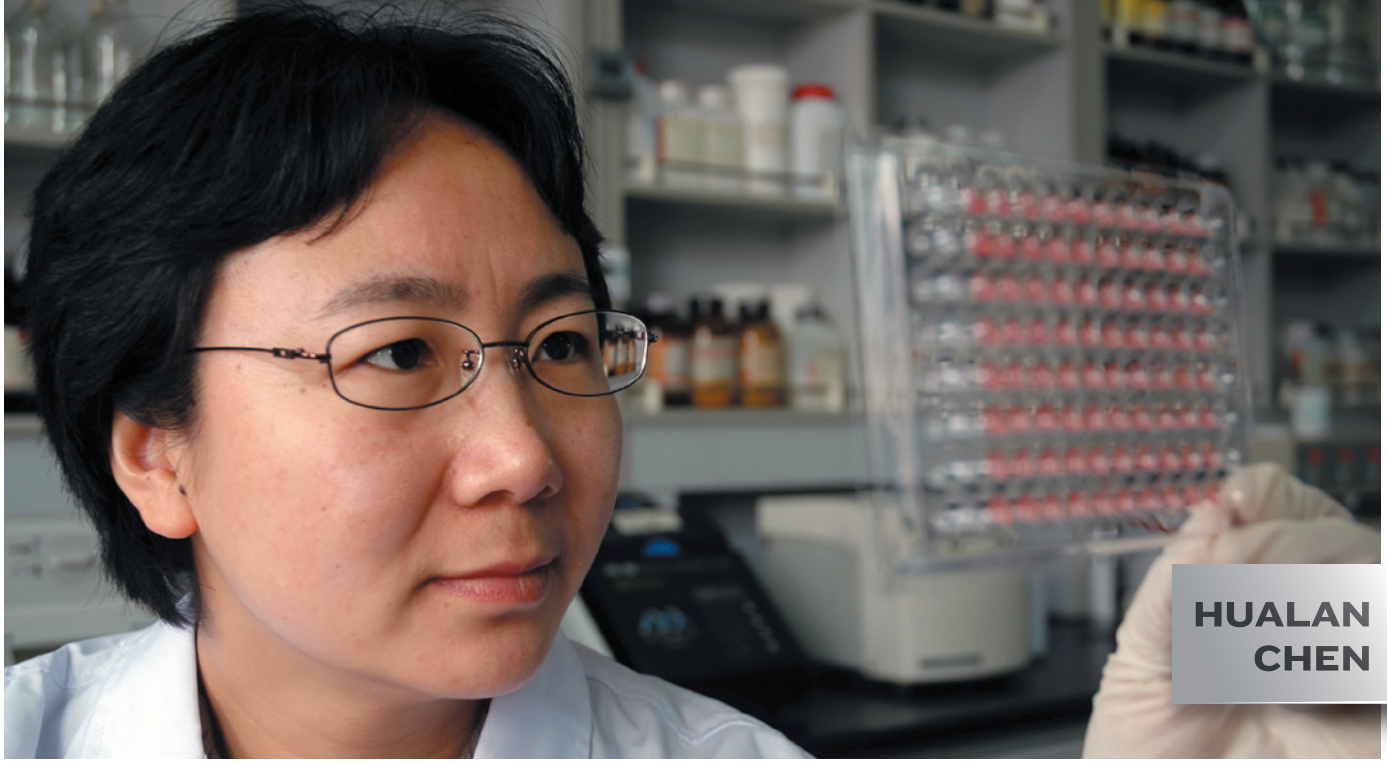
In the early weeks of April, the world's virologists and public-health officials had their eyes fixed on China. An emerging avian influenza virus — H7N9 — was jumping to humans from infected poultry, causing severe disease and deaths, with new cases appearing in Shanghai and neighbouring provinces. Hualan Chen, head of China's National Avian Influenza Reference Laboratory in Harbin, found herself and her lab on the front line of efforts to contain the outbreaks. The scientists pushed all other research aside to focus on H7N9 and to find its route of transmission to humans from birds or other animals. They were so busy, Chen says, that "several lost four to five kilograms during the [first] six weeks".

Less than 48 hours after H7N9 cases were first confirmed (S. Jian-Zhong *et al. Chin. Sci. Bull.* **58,** 1857–1863; 2013), Chen's team, along with researchers at the Shanghai Animal Disease Control Center, collected about 1,000 samples from soil, water, poultry farms and live poultry markets in Shanghai and the neighbouring province of Anhui, where the first cases had occurred. Twenty came up positive for H7N9, all from live markets in Shanghai. Authorities quickly closed live markets in the cities where most cases had been reported, and the rate of new infections immediately plummeted. China's rapid and transparent response has been widely applauded.



SHOUKHRAT MITALIPOV

© 2013 Macmillan Publishers Limited. All rights reserved



HARBIN VETERINARY RES. INST.

The low rate of new cases has continued, with only a handful reported from May through to the end of November, giving Chen and other researchers time to learn more about the virus. They know that H7N9 jumps more easily to humans from birds than does another deadly avian flu virus, H5N1. So far, H7N9 has shown no sign that it can pass from person to person, but Chen believes that it may have this potential.

Chen was so focused on dealing with the H7N9 outbreak that she paid little attention to a brouhaha that erupted in May over the publication of a study that she and Chinese colleagues had done describing the creation of hybrids of avian H5N1 and 2009 pandemic H1N1 flu that could spread easily between guinea pigs (Y. Zhang *et al. Science* **340,** 1459–1463; 2013). The work was reminiscent of controversial research published last year that involved the creation of forms of avian H5N1 that were transmissible between ferrets, prompting a moratorium on similar work that was ultimately lifted in January 2013 (see *Nature* **493,** 460; 2013). Critics argued that Chen's research, like the previous H5N1 studies, had few practical benefits and that the engineered hybrids might spark a pandemic should they escape from the lab.

Chen asserts that these experiments help to illustrate the threats posed by new flu strains; the H5N1 and H1N1 strains she used coexist in many countries, and she thinks that the reassortment carried out in the lab is likely to occur in nature. Similar experiments are needed for H7N9, she adds.

The lull in new H7N9 cases during the summer and autumn may be the result of the initial market closures, or the fact that avian flus typically spread less frequently during warmer months. Winter has now returned to China, and Chen's lab is on the look out for any resurgence. "Influenza virus surveillance is the top priority in our lab," she says. ■

THE CLONING CHIEF

After years of frustration, a biologist has finally developed a line of stem cells from a cloned human embryo.

BY ERIKA CHECK HAYDEN

The hardest part of the cloning advance that Shoukhrat Mitalipov reported in May was not the experiment itself: it was the maze of red tape that came before it.

Since 2007, Mitalipov, a reproductive biologist at Oregon Health & Science University in Portland, had wanted to create cells with the potential to cure any number of diseases — patient-specific stem cells made from embryos cloned from a person's own skin cells. Beyond the technical difficulties, it was a tricky endeavour because it involves harvesting lots of human eggs and using them to create embryos that will then be destroyed. He had to gain approvals from an institutional review board and a stem-cell-research oversight committee. Ultimately, his university built him a new lab, because the cells could not, by law, be derived in his original, federally funded lab space.

Finally, last October, he got started; by Christmas, his lab had succeeded in cloning four cell lines by transferring nuclei into donor eggs. He says that he was able to accomplish the feat, which had long eluded the field, in part because he had spent years perfecting the procedure in monkeys. He had little competition, he says, because heavy regulation had deterred other researchers.

His rush to publish led to problems, notably some duplicated and mislabelled figures in his group's paper (M. Tachibana *et al. Cell* **153,** 1228–1238; 2013). Despite that, researchers such as Dieter Egli of the New York Stem Cell Foundation, who is trying to replicate the work, are optimistic. "My sense is that some of the major conclusions in Mitalipov's paper are likely to stand the test of time," says Egli.

Mitalipov is now seeking federal approval to begin clinical trials of a similar technique, mitochondrial transfer, in women who hope to have children free of mitochondrial diseases. He is also comparing stem cells derived from cloned embryos to those derived from reprogrammed adult cells. He is scrounging for funding and collaborators because federal funders will not pay for research with the cell lines, and the California Institute for Regenerative Medicine will not fund work on lines made the way his were, with eggs harvested from paid donors. And so the work proceeds slowly — just like before. "It feels like we're at the same point where we were a year ago," he says. ■

OREGON HEALTH & SCIENCE UNIV.

© 2013 Macmillan Publishers Limited. All rights reserved



L. BRIAN STAUFFER

AN EYE ON HARASSMENT

An anthropologist unearths disturbing trends in sexual assaults at field sites — and suspects she's just scratching the surface.

BY ALEXANDRA WITZE

Kathryn Clancy loved her doctoral fieldwork in rural Poland. After long days gathering biological specimens from women in a study of reproductive health, she and her fellow scientists — all women — spent their evenings playing board games and listening to pop music. It was "the most magical field experience", says Clancy, an anthropologist at the University of Illinois at Urbana-Champaign.

But years later, she learned that many anthropologists have very different memories of fieldwork. In a halting conversation over coffee, a friend revealed that she had been sexually assaulted by a colleague at a field site run by a university. Clancy decided to take action.

She began in January 2012, by posting stories from her friend and others, anonymized, on her *Scientific American* blog. But she soon realized that anecdotes weren't enough. So she joined forces with three colleagues — Katie Hinde of Harvard University in Cambridge, Massachusetts, Robin Nelson of Skidmore College in Saratoga Springs, New York, and Julienne Rutherford of the University of Illinois at Chicago — to put out a call for data. They asked biological anthropologists to share their stories of field experiences through a web-based survey.

In April this year, Clancy's team dropped a bombshell. During an ethics symposium at a meeting of the American Association of Physical Anthropologists in Knoxville, Tennessee, the team announced that 59% of the 124 survey participants reported experiencing

SUN WORSHIPPER

An energetic physicist pushes a promising solar-cell material into the spotlight.

BY MARK PEPLOW

"I always wanted to be an inventor," says Henry Snaith happily. The 35-year-old physicist at the University of Oxford, UK, has fulfilled that childhood ambition in spectacular style.

This year, Snaith amazed materials researchers by massively boosting the efficiency of solar cells made with perovskite semiconductors (M. Liu *et al. Nature* **501,** 395–398; 2013). For a few years, other researchers have used these materials to make lower-efficiency, complex photovoltaic devices, but Snaith realized that they could be harnessed in a much purer and cheaper design. They are now on the brink of commercialization.

Most of the world's solar cells rely on silicon, and convert roughly 17–25% of the light that falls on them into electricity — almost 10 times better than the humble leaf does through photosynthesis. But their thick chunks of pure silicon make them expensive to build. Thin-film solar cells, containing leaner slivers of other semiconductors, are cheaper but generally less efficient; it has taken decades for their efficiencies to creep above 15%. Perovskite cells combine the best attributes of both.

Snaith's cell — made out of methylammonium lead iodide chloride — already has an efficiency of 15%. "The performance has very quickly got to a high level," says Richard Friend, an optoelectronics researcher at the University of Cambridge, UK, who was Snaith's PhD adviser. Through fine-tuning — changing the balance of chloride and iodide, for example — Snaith thinks that perovskite cells could rival the 29% achieved by crystalline gallium arsenide cells, which are used in many satellites but are much too expensive for widespread use.

The perovskite cells are easy to make. Snaith uses simple techniques such as smearing the readily available ingredients across a coated glass plate (S. D. Stranks *et al. Science* **342,** 341–344; 2013). "I don't think there's a cheaper photovoltaic material," he says. "And the stuff is fundamentally stable. We can stick these devices under a tap and they still work." His team is now working on alternative perovskites that do not contain toxic lead and thus would be easier to dispose of.

Snaith chose solar cells as the focus for his research because they

© 2013 Macmillan Publishers Limited. All rights reserved

FIVE TO WATCH

2014

MASAYO TAKAHASHI
RIKEN CENTER FOR DEVELOPMENTAL BIOLOGY
Induced pluripotent stem cells could get their first test in the clinic. Using cells derived from patients, Takahashi plans to create sheets of retinal cells to treat macular degeneration, a common cause of blindness.

CHRIS FIELD
INTERGOVERNMENTAL PANEL ON CLIMATE CHANGE
As co-chair of the upcoming report on the impacts of climate change, Field hopes to avoid the errors that undercut the Intergovernmental Panel on Climate Change's 2007 report on the same topic, an area that has taken on greater urgency in the intervening years.

JEAN-PIERRE BOURGUIGNON
INCOMING PRESIDENT, EUROPEAN RESEARCH COUNCIL
When the French mathematician replaces Helga Nowotny, he will enjoy a bigger budget but must protect the grant-giving institution from political and bureaucratic pressures.

KOPPILLIL RADHAKRISHNAN
CHAIRMAN, INDIAN SPACE RESEARCH ORGANISATION
India's Mars Orbiter Mission — the country's first attempt to visit that planet — is scheduled to reach orbit in September. All eyes will be on the spacecraft as it travels a route that has, more often than not, ended in failure.

GORDON SANGHERA
CHIEF EXECUTIVE, OXFORD NANOPORE
In February, customers are expected to reveal the first data collected using the UK company's MinION genetic sequencer. If it lives up to its promise, the device could usher in a new era of dramatically faster, cheaper sequencing.

inappropriate sexual comments, and 18% reported physical harassment or assault in the field.

Abuse was systemic, the team found, and frequently played out along lines of power. Young female graduate students were usually the targets; older, more senior men were usually the perpetrators. And sexual harassment was mostly committed by university personnel: postdocs and professors, not local workers hired for the season. Many respondents suggested that work in the field — removed from the norms of family and friends — may be particularly likely to elicit unwanted behaviour. (When Clancy's team later expanded the survey to include 666 respondents in all fieldwork disciplines, from archaeologists to geologists to zoologists, the results were essentially the same.)

Clancy and her colleagues acknowledge that the survey may have drawn an unrepresentative number of people who have been harassed, but even so, the results shocked the anthropological community. A reaction came swiftly. Within days, the American Anthropological Association put out a statement asserting a zero-tolerance policy for sexual harassment. Other professional societies quickly followed suit with similar policies to cover additional venues, such as their professional conferences.

Through their surveys, Clancy and her colleagues learned that many victims didn't report the abuse to authorities, fearing that they would be cut off from data or from access to a field site they needed. Others filed formal complaints but were told to keep quiet or 'just deal with' the situation. Only on rare occasions were reports of abuse followed through to the victim's satisfaction.

The effects of the trauma lingered for many. "Every time you try to do your science, you're reminded of what happened," says Clancy. Some young researchers leave science because of their field experiences, she adds. "There's no doubt in my mind, we are losing very good people."

Clancy, Hinde, Nelson and Rutherford are putting the final touches to a manuscript detailing the field abuse, which Clancy believes is just part of a larger problem. She has been deluged with e-mails asking her to quantify what takes place in other university settings.

Meredith Hastings, a biogeochemist at Brown University in Providence, Rhode Island, and co-founder of the Earth Science Women's Network support group, says that such work is needed to shine a light on an oft-ignored problem in the research world. "You don't recognize how widespread these issues are," she says, "until somebody speaks up." ■

occupied a happy middle ground in clean energy: wind power, he reckoned, involved too much engineering, and nuclear fusion seemed too distant. Photovoltaic research was just right — plenty of room for improvement, with new discoveries delivering immediate, practical benefits.

He is not alone in his quest. Michael Grätzel at the Swiss Federal Institute of Technology in Lausanne pioneered dye-sensitized solar cells more than 20 years ago, and is now getting spectacular results using perovskites in them (J. Burschka *et al. Nature* **499,** 316–319; 2013). "The whole photovoltaic community is excited about it," says Grätzel. "The perovskites are kind of magic." Snaith did his postdoctoral research with Grätzel, and says that they are still very friendly "but there's certainly competition there".

Solar-cell manufacturers are starting to take an interest in perovskites, but Snaith hopes he has a jump on the competition. In 2010, he co-founded Oxford Photovoltaics, which aims to incorporate transparent perovskite cells into windows. By 2017, the company hopes to glaze large buildings for not much more than the price of conventional glass.

Snaith is also looking forward to his next invention. If photovoltaic power really takes off, he notes, we will need a better way to store solar power for a rainy day. "Once things calm down a bit," he says, "I'll be looking to adapt our work to make better battery electrodes." ■



DOUGLAS FRY/PIRANHA PHOTOGRAPHY

© 2013 Macmillan Publishers Limited. All rights reserved

COMMENT

CONSERVATION Four views of the US Endangered Species Act as it turns 40 **p.369**

MICROBIOLOGY Harold McGee on festive feasting's debt to fermentation **p.372**

EDUCATION Why Victorian primers taught science by way of fairies **p.374**

OBITUARY Adrienne Asch, bioethics pioneer, remembered **p.377**

ILLUSTRATION BY SCOTT GARRETT



Together to the next frontier

As emerging players jostle old ambitions, **Nigel Lockyer** calls for the next generation of particle-physics projects to be coordinated on a global scale.

This year was a watershed for particle physics. The decades-long quest to discover the Higgs boson is essentially complete. Still abuzz after a Nobel prize for the Higgs prediction, the particle-physics community is feeling satisfied. It is time to pause, reflect and consider what comes next.

The Higgs boson is the last puzzle piece in the standard model of particle physics, but the model does not explain some fundamental aspects of our Universe. From the neutrino's very small mass to dark matter and dark energy, we know there is more going on. But where might the next clue lurk?

We really don't know. Each physicist has his or her own opinion, and countries and regions are preparing to explore different strategies to identify the territories ripest for exploration. What we do know is that the next generation of particle accelerators will be expensive. And requests for government funding will run up against fiscal constraint around the globe.

NATURE.COM
See *Nature*'s special issue on the Large Hadron Collider:
nature.com/lhc

As the incoming director of the Fermi National Accelerator Laboratory (Fermilab) in Batavia, Illinois, I have spent the past six months in discussions about the future of US particle physics. But particle physics is an international pursuit, with projects in and participants from many different countries. The United States is well positioned to take the lead in some areas, such as neutrino physics, but the global landscape is uncertain. Resources need to be pooled, and new players are emerging. China's and India's talent, infrastructure and ambitions must now be factored into the global equation.

We are at a critical moment for the field. Each country and major project ▶

© 2013 Macmillan Publishers Limited. All rights reserved

must take into account its impact on the overall enterprise. The opportunity is enormous: a truly coherent approach to accelerate progress and combine disparate strengths. But the risks are just as large: failing to agree on major efforts, losing international partners and sacrificing progress in a downward spiral of too many partially approved projects.

BEYOND THE HIGGS

The high-energy frontier neighbouring the Higgs will soon be within reach of the Large Hadron Collider (LHC) at CERN, Europe's particle-physics lab near Geneva, Switzerland — currently the highest-energy accelerator in the world. When it turns on again in early 2015 after a two-year upgrade, the machine will operate close to its design energy of 14 teraelectronvolts (TeV) — roughly twice that at which the Higgs was discovered. Now that the standard model is complete, any new particles found will revolutionize our view of physics.

Beyond that, there are plans to upgrade the LHC in the 2020s to provide even brighter beams and detectors capable of handling the enormous rates of data that will be produced. Even modest upgrades will cost around US$1 billion, requiring contributions from non-member as well as member states.

Other frontiers hold promise. We still do not understand how neutrinos interact, the origin of their tiny masses or their role in the early Universe. Fermilab is heading a US proposal to build a long neutrino-beam experiment, running 1,300 kilometres from Fermilab to the Homestake mine in South Dakota. An ambitious 35-kilotonne liquid argon detector located nearly 1,500 metres below the surface emerged as the preferred project when the US community met in Minnesota for a ten-day planning symposium in July. It would help us to understand neutrino masses and whether these particles contribute to the matter–antimatter asymmetry of the Universe.

With the total construction budget nearing $1 billion, the experiment will require international partners — a new approach for US domestic science. The US Department of Energy's Office of Science has indicated that it would support such a major proposal if there was involvement from Europe and Asia.

A long-baseline neutrino experiment is necessary, somewhere. Alternatives are on the table: one in Europe would see neutrinos travelling from CERN to Finland; another has neutrinos travelling across Japan. But the world can afford only one.

Japan is perhaps the stiffest competitor, with leading programmes in neutrino physics, a bottom-quark ('b-quark') factory and kaon and muon experiments. The country hopes to host the International Linear Collider (ILC) — a 30-kilometre-long, 500-gigaelectronvolt electron–positron collider to study the Higgs boson that would surpass the LHC in terms of precision in the late 2020s. It is hoped that construction will begin later this decade.

Japan is about to begin a campaign to sign up support for this international project, which would require US and European participation. Most particle physicists support the ILC but many would like to see what discoveries will come out of the upgraded LHC first. If no new particles emerge, then the higher precision available to the ILC would make building it even more attractive. If another discovery is made at the LHC, then the community might need a different machine to explore the new energy regime.

PASSING THE BATON

Given that we are not sure which is the next fertile energy range, many particle physicists believe that we should aim as high as possible. Some argue for an even higher-energy lepton collider, such as a muon collider or the Compact Linear Collider (a European higher-energy competitor to the ILC) that would reach 3–5 TeV. Europe is assembling a team to design a 100-TeV proton–proton collider, with a 100-kilometre-circumference tunnel, to probe any particles that may be discovered by the upgraded LHC and at energies beyond. This machine could start up in the 2030s.

And the United States still has ambitions to host a high-energy frontier machine, after turning off the Fermilab's Tevatron accelerator in 2011 and failing to realize the Superconducting Super Collider in the 1990s. Perhaps the high-energy baton could be passed back to the United States. Fermilab is still a world leader in high-field magnets for proton accelerators, which would be necessary for any 100-TeV proton–proton collider.

"If China does jump ahead, it will change the landscape of science."

To add to the suspense, there is the changing role of China. Historically a small player in particle physics, it last year stepped onto the world stage with impressive results in reactor-driven neutrino physics, including showing that two of the three types of neutrinos mix together much more than expected. This large mixing implies that fundamental symmetry differences between neutrinos and antineutrinos might be observable in a long-baseline experiment, telling us about matter and antimatter imbalances in the early Universe. Emboldened, might the Chinese leapfrog the world by hosting the 100-TeV machine? Construction of the machine would be cheaper in China, although the nation would need help from the rest of the world to design and build it.

If China does jump ahead, it will change the landscape of science, levelling the playing field with the emerging economies. Discussions about global progress in particle physics would need to explicitly include heads of state from China and India as well as North America, Europe and Japan.

GLOBAL CONVERSATION

Physicists do not care where they do their research. But the vast scale of particle-physics projects means that all new mega-accelerators require global planning, agreement and joint construction. Governments around the world will have to make unprecedented financial investments in other countries, challenging the traditional political calculus in which public tax dollars are primarily spent at home for direct, short-term benefit.

Governments are trying to understand which models best suit their national interests. There is less talk of 'brain gain and drain' and more of 'brain circulation'. Countries and intellectual communities thrive by participating in the global conversation, not necessarily by owning most of the players.

Care must be taken to ensure the health of major regional laboratories, such as CERN, Fermilab and the High Energy Accelerator Research Organization (KEK) in Tsukuba, Japan: these are the only places where large particle-physics projects are currently feasible. Demands from emerging economies such as China to host other projects will challenge the long-term plans of the existing leaders. Scientists in the United States and Europe will have to find out how best to use international competition as a spur for advancing projects on their own soil while still being good international partners. This may become tricky.

Higgs bosons are not export-controlled, nor are pictures of deep space from advanced telescopes. But the technologies developed, often through international collaborations, may have dual use — for defence applications or for economic gains, for example, as well as for basic science. Countries will have to decide how to oversee and exploit these opportunities responsibly.

Particle-physics leaders need to be more vocal and aggressive in defining and defending the global programme. After all, a suite of global particle-physics facilities helps us to understand how the Universe works. ■

Nigel Lockyer *is director of the Fermi National Accelerator Laboratory in Batavia, Illinois.*
e-mail: lockyer@fnal.gov

© 2013 Macmillan Publishers Limited. All rights reserved



AFLO/NATUREPL.COM

The Endangered Species Act at 40

On the anniversary of a landmark piece of US legislation, four experts weigh in on what has worked and what needs to change.

NOAH GREENWALD

Cherish the act's proven power

Endangered species programme director, Center for Biological Diversity

The US Endangered Species Act (ESA) is the reason that there are bald eagles from coast to coast, grizzly bears in the Yellowstone ecosystem and American alligators in the southeastern United States. The act remains our best tool for saving species and their habitats and practically our only way of helping declining populations to recover.

Since it came into effect in 1973, the ESA has had unqualified success at saving species from extinction. So far, only ten of the more than 1,500 species protected under the ESA (see 'On the list') have gone extinct, and eight of these were probably extinct before they received protection. A 2006 analysis[1] found that, were it not for the ESA, as many as 227 US species would have disappeared.

This landmark law is also putting animals and plants on the path to recovery. An analysis[2] of all federally protected species in the northeast found that more than 90% were stabilized or improving since being put on the list; more than 80% were on track to meet recovery goals set by scientists.

The ESA has been criticized for mandating protection of individual species rather than of ecosystems. Yet it has driven some of the most successful efforts in ecosystem management, most notably the Northwest Forest Plan adopted in 1994. These land-use policies have protected forested and aquatic habitats for northern spotted owls, marbled murrelets and Pacific salmonids.

Too often, those who advocate moving away from the firm protections of the act argue for flexible ecosystem management not to advance conservation, but to avoid economic conflicts. In practice, saving a species can mean saving an entire ecosystem. That helps wildlife and people who depend on clean water, clean air and the other benefits that functioning ecosystems provide.

AMY W. ANDO

Focus on the bigger picture

Professor of environmental and natural resource economics, University of Illinois at Urbana–Champaign

The ESA has accomplished important victories. However, it causes regulators to stand by until species are near the brink of extinction, and so engenders counterproductive cycles of support and endangerment. Protection can be withdrawn without eliminating the forces that led the species to be imperilled. The ESA can help species threatened by direct human action such as hunting — as it did for the American bison (*Bison bison*). But most species are in decline because of diffuse threats such as invasive species, large-scale land conversion and climate change, over which the act has little power. Efforts to use the ESA to protect the polar bear (*Ursus maritimus*) from melting sea ice cannot, for example, force an international agreement on greenhouse-gas emissions.

"Policies to protect individual species should not be based on indiscriminate rules."

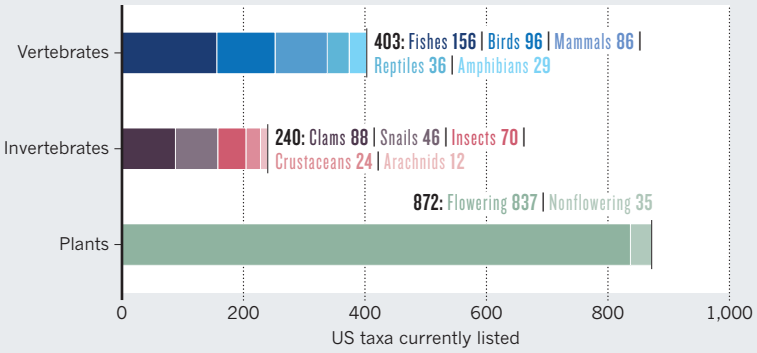
Furthermore, a conservation policy that counts all species as having equal value can be counterproductive. Mandatory expenditures perceived by the public as having little value could exhaust society's desire to commit resources to conservation and actually reduce the sum of government and private citizens' conservation efforts. For instance, ESA policies to preserve a small, unalluring fish known as the delta smelt (*Hypomesus transpacificus*) has led to controversial water-use restrictions in California, feeding anti-conservation sentiment.

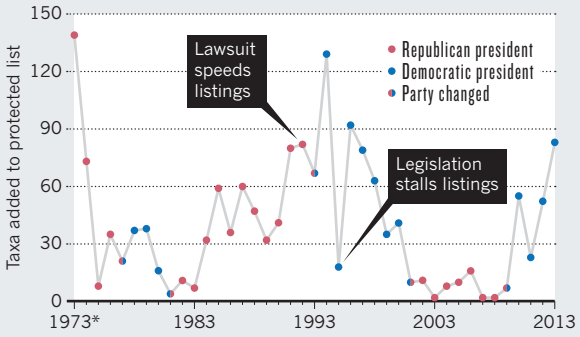
Policies to protect individual species should not be based on indiscriminate

© 2013 Macmillan Publishers Limited. All rights reserved

ON THE LIST

The number of species granted protection by the US Endangered Species Act vacillates with politics and litigation.





*1973 includes species listed under predecessor legislation.
Taxa refers to species, subspecies and certain populations with distinct genetic compositions.

SOURCE: US FISH AND WILDLIFE SERVICE

rules. They should be justified case by case, according to the value society places on the species, either for the part it plays in a natural community, or because of the place it holds in people's hearts and lives. For example, freshwater mussels filter out dangerous bacteria; sea turtles inspire awe with their epic migrations. Effective and secure conservation policy will acknowledge these different types of value.

STUART H. M. BUTCHART

Clarify extinction risk

Head of science, BirdLife International

The ESA is one of the most powerful pieces of nature legislation in the world. But it has shortcomings. The act's criteria for listing species as threatened and endangered are remarkably vague. Classifications include terms that lack precise legal or biological meaning, for example, 'in danger of', 'likely' and 'foreseeable future'. The resulting legal wrangling costs too much time and money. The phrase 'significant portion of its range' is particularly problematic, prompting lengthy arguments in courts and countless pages of legal documents. In the past decade, dozens of challenges to listing decisions have focused on the term.

To be more effective, ESA assessments should incorporate what is widely accepted as the most authoritative system for systematically categorizing species by extinction risk: the Red List of Threatened Species maintained by the International Union for Conservation of Nature (IUCN), the largest global coalition of environmental organizations. This list uses objective, quantitative criteria that account for uncertainty and gaps in data. For example, species with a population size of fewer than 50 mature individuals are classified as critically endangered.

Regulators in other countries have taken note. Canada's ESA equivalent, the Species at Risk Act, uses the IUCN Red List system to determine extinction risk; individual species are then listed by explicitly taking into account other societal considerations, such as the perceived economic or even political costs associated with listing. This separates the science and policy aspects of setting conservation priorities. A similar practice might help to unblock the current logjam at the US Fish and Wildlife Service.

Most of the agency's decisions to review how a species should be listed are initiated not because of scientific uncertainty, but because of lawsuits brought by individuals or interest groups hoping to alter legal protection for particular species. Costly legal arguments caused by ambiguities in the listing process leave the agency with few resources for proactive steps that would help it to fulfil its primary mission to save species.

JOHN TSCHIRHART

Account for economics

Professor of economics, University of Wyoming

Economic impacts of conservation plans cause many of the controversies surrounding the ESA. To manage endangered species effectively, we need sophisticated, integrated models that evaluate ecosystem and economic trade-offs. If these describe unanticipated economic beneficiaries, conservation plans could have unexpected champions.

Many governments use complex economic models called computable general equilibrium models. These can predict how a tax or tariff policy might affect various industries and how those effects would ripple out to other industries and to consumers' incomes. Few models consider the effects of conservation policies. Those that do are usually narrow in scope and restricted to a single species.

That is not surprising: ecosystem models that cover multiple species and their effects on each other are relatively new, yet they can reveal unexpected insights. Such large-scale general ecosystem models have, for example, forecast that an increase in pollock (*Theragra*) levels in Alaskan fisheries could decrease levels of sea otters, even though the species do not interact directly[3]. More pollock swells populations of their predators, sea lions, which in turn boosts populations of their predators, killer whales, which also feed on otters. Although most ecological modelling considers only two or three species at once, integrated models are emerging, and these will be essential to manage endangered species effectively.

"The biggest benefits will come when ecosystem models are integrated into economic ones."

The biggest benefits will come when ecosystem models are integrated into economic ones. Ecological and economic variables are, after all, interdependent. For instance, policies that keep chicken-farm waste from reaching rivers might produce economic benefits in the recreation and fishing industries. Pollock-fishing losses could be outweighed by gains in tourism as more sightseers go to watch sea lions cavort. Economic modelling will not always show net gains for conservation policies, but the current models rarely capture gains at all. ■

1. Scott, J. M., Goble, D. D., Svancana, L. K. & Pidgorna, A. in *The Endangered Species Act at Thirty* Vol. 1 (eds Goble, D. D., Scott, J. M. & Davis, F. W.) Ch. 2 (Island, 2006).
2. Suckling, K. *Measuring the Success of the Endangered Species Act* (Centre for Biological Diversity, 2006).
3. Finnoff, D. & Tschirhart, J. *Res. Energy Econ.* **30,** 91–114 (2008).

© 2013 Macmillan Publishers Limited. All rights reserved



CHEMISTRY

A festive ferment

Harold McGee surveys a seething array of microbially transformed treats — from beard beer and grasshopper sauce to extreme herring and armpit cheese.

Rare is the holiday meal that does not owe many of its pleasures to invisible cooks with tongue-twisting names. Do you enjoy charcuterie and pickles? Bread with cultured butter? A drizzle of vinaigrette on this or that? A bit of cheese? Some chocolates? Wine, beer or cider? Then raise a glass to *Saccharomyces cerevisiae*, *Leuconostoc mesenteroides* and their ilk, the fungi and bacteria that do the real work of turning blandness into piquant delight.

As a technology rather than a metabolic mode, fermentation is the managed microbial transformation of raw plant and animal materials into foods that resist spoilage. Above all, it has been a method of preserving the bounty of a harvest or hunt for nourishment in leaner times. Peoples across the planet have applied it to nearly everything edible, from fruits, vegetables, meats and milks to animal hides in the Sudan and fish heads in the Arctic.

The most common food fermentations develop spontaneously, because the microbes responsible are ubiquitous and thrive on sugars in nutrient-rich materials such as plant tissues and animal secretions. As these first exploiters multiply, they release a number of chemical weapons that suppress their competition, and so can delay or prevent the growth of microbes that spoil foods with disgusting or toxic by-products. The weapons include antimicrobial peptides, lactic and acetic acids, and alcohols, all harmless to us in moderation and some addictively appealing. So shredded cabbage and milk readily turn sour, crushed fruits get heady, and instead of the putrid and inedible, we end up with sauerkraut, clabbered milk and wine.

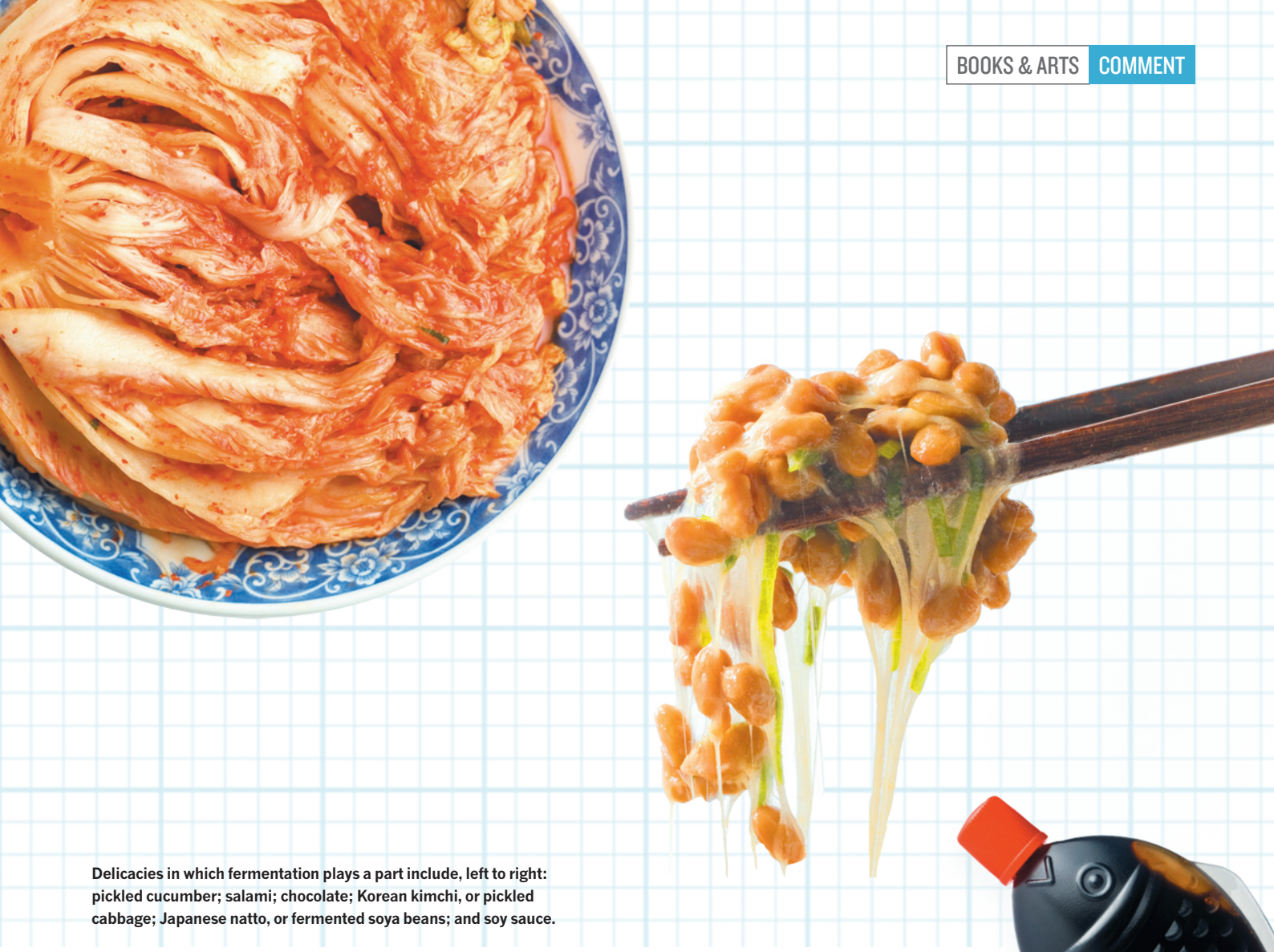
Today we easily preserve raw foods simply by chilling or freezing them, which slows all biological activity. Yet fermented foods remain popular because they offer intensified, complex flavours. Stilton is more savoury than a spoonful of milk, chorizo tastier than steak tartare. The microbes themselves generate complexity by turning sugars into acids and alcohols, and by breaking down flavourless macromolecules — starch, proteins and fats — into their component sugars, amino acids and fatty acids. These building blocks have flavours of their own and serve as precursors to a host of other small molecules that we can taste or smell. The food's own enzymes can do similar flavour-generating work from within in the extended time that fermentation buys them. Eventually these changes go too far and the food becomes unappealing — effectively spoiled. That point is hard to define, and foods such as Chinese stinky tofu and Swedish surströmming, or extreme herring, delight fans by flirting with it.

MICROBIAL TEAMWORK

Food fermentations generally involve a community of various microbes growing at the same time or in succession, but it is convenient to group them loosely by dominant organisms. By far the largest group of fermentations uses the lactic acid bacteria or LAB, most of which associate with plants and secrete pleasantly tart lactic acid. The LAB produce an impressive array of our favourite foods. Among them are yogurt,

CUCUMBER: WESTEND61/ALAMY; SALAMI: MARC WUCHNER/CORBIS; CHOCOLATE: OKSIX/SHUTTERSTOCK.COM; KIMCHI: IMAGEMORE/GETTY; NATTO: TAKAO ONOZATO/AFLO/GETTY; SOY SAUCE: EMMANUEL LATTES/ALAMY

© 2013 Macmillan Publishers Limited. All rights reserved



Delicacies in which fermentation plays a part include, left to right: pickled cucumber; salami; chocolate; Korean kimchi, or pickled cabbage; Japanese natto, or fermented soya beans; and soy sauce.

cheese and cultured creams such as crème fraiche; sauerkraut, Korean kimchi and other pickled vegetables; dry-cured salamis and similar sausages; Asian fish sauces; and the rice–lentil batters for two South Indian and Sri Lankan specialities, the crêpe-like dosa and plump idli.

A second main group of food fermentations stems from the yeasts, pre-eminently *S. cerevisiae*, which produce alcohols and carbon dioxide from fruit juices and other sugar-rich liquids: hence wine and beer and their distillates, brandies and whiskies. If given the chance, certain bacteria will feed on alcohol, produce acetic acid, and turn wine into vinegar — or transform bland and astringent cocoa beans in their fermented fruit pulp into the makings of richly flavoured chocolate. In thick doughs and batters made from grain, which contain enough sugar to support only limited yeast growth, the alcohols get cooked out and it is the gas that matters. It turns the dense mass into a light foam with a structure that is stabilized by heat to make leavened breads, from Ethiopian injera to Italian panettone.

NATURE.COM
For a Nature Podcast on fermented foods, see:
go.nature.com/elfmp6

A third group is based on an Asian method for fermenting starchy foods, mainly the seeds of grains and legumes, which yeasts and LAB cannot utilize directly. Some time before the second century BC, Chinese brewers domesticated a species of *Aspergillus* mould to convert the starch into fermentable sugars, at the same time generating its own distinctive aromas. It is with the help of this *Aspergillus* culture, called *qu* in China and *koji* in Japan, that sake and other alcohols are made from rice. It is also how miso paste and soy sauces including tamari are made from soya beans and grains. Because Western brewers have always prepared grains very differently, by 'malting' or partly germinating them to develop their own starch-digesting enzymes, the *koji* fermentation has been little known outside Asia until the past decade.

MODERN REVIVAL

Today's manufactured versions of fermented foods are often just approximated: many 'pickles' are just vegetables drenched in acids such as vinegar. But do-it-yourselfers have kept home fermentation alive, and in recent years foodies and artisans have been rediscovering its magic. Pickles and vinegars are especially straightforward to craft, and their variations and labels seem to be growing logarithmically — as is the baffling popularity of kombucha, sweetened tea fermented with what is known among enthusiasts as a SCOBY. These symbiotic communities of bacteria and yeasts are solid cellulosic aggregates that have been found to include as many as 20 microbial genera. In my experience, too many cooks. I am partial to flavoured sauerkrauts (beets and ginger, Indian spices) and local fresh natto, soya beans fermented and made slimy by *Bacillus subtilis*, much superior to frozen imports.

Professional cooks have also caught the fermenting bug, with restaurants now proudly offering their own distinctive pickles and cured meats. And a handful of programmatically innovative restaurants have successfully adapted *koji* fermentation ▶

© 2013 Macmillan Publishers Limited. All rights reserved

to Western ingredients. In New York City, the Momofuku restaurant group's Culinary Lab has focused on miso- and tamari-like pastes and sauces made from non-soya bases such as cashews, pistachios, chickpeas and spelt. Copenhagen's renowned Noma and the affiliated Nordic Food Lab have had good results with a yellow-pea 'peaso', a barley *koji* roasted to a chocolate brown and versions of fish sauces made from grasshoppers and from *koji*-treated beef.

These experiments with fusion fermentation are probably just a taste of things to come. The James Beard Foundation, a New York-based organization of professional chefs, gave its award for the best reference book of 2013 to Sandor Ellix Katz's 500-page *The Art of Fermentation* (Chelsea Green Publishing), a jaw-dropping survey of possibilities from abará (Nigerian steamed or boiled fermented cowpeas) to zur (Polish sour rye porridge soup).

"Provocation rather than flavour has motivated experiments with what might be called personal fermentation."

Outside the restaurant world, provocation rather than flavour has motivated experiments with what might be called personal fermentation. After the Rogue Ales brewery in Newport, Oregon, failed to find beerworthy wild yeasts in its hop yard, it turned to a different local niche: a strain cultured from the brewmaster's hair follicles now goes into the making of its speciality Beard Beer. And noting that we regularly devastate our own microbiome to suppress its production of the same odours that we enjoy in fermented foods, biologist Christina Agapakis and artist Sissel Tolaas have developed an exhibit to help us to better appreciate our unsanitized selves: cheeses made from milk inoculated with swabs of volunteers' hands, feet, noses and armpits (see A. King *Nature* **503,** 196; 2013).

After a centuries-long stationary phase during which traditional food cultures slowly developed in isolation from each other, the world crock has been stirred and things are really bubbling. Will new fermentations grace our future holiday spreads? Even the possibility is worth toasting. ■

Harold McGee *is the author of* McGee On Food & Cooking *and* Keys to Good Cooking, *both published by Hodder & Stoughton.*
e-mail: harold@curiouscook.com



CALIFORNIA DIGITAL LIB.

A forest of the Carboniferous period as depicted in *The Fairy-Land of Science*.

EDUCATION

Fairylands of science

Melanie Keene revisits two Victorian children's science primers that harnessed interest in the supernatural.

© 2013 Macmillan Publishers Limited. All rights reserved

Correspondence

Policy tips: six more practical pointers

Politicians are likely to dismiss the excellent 'Twenty tips for interpreting scientific claims' after a few lines, simply because these tips are not geared to their everyday needs (W. J. Sutherland *et al. Nature* **503,** 335–337; 2013). I have some other suggestions for them.

Science is open-minded, but not empty-headed. Just because there is no definitive answer to a problem does not mean that any alternative is equally good. Not all evidence may point in one direction. Trust the weight of evidence.

Avoid 'false balance' on scientific issues. There will always be naysayers. That is fine in politics, in which everyone is entitled to their opinions, but not in science, in which one produces the evidence or holds one's peace.

Science is not decided by vote. Most scientists have little expertise outside their own fields. Let people who really understand the issues help you to evaluate the evidence.

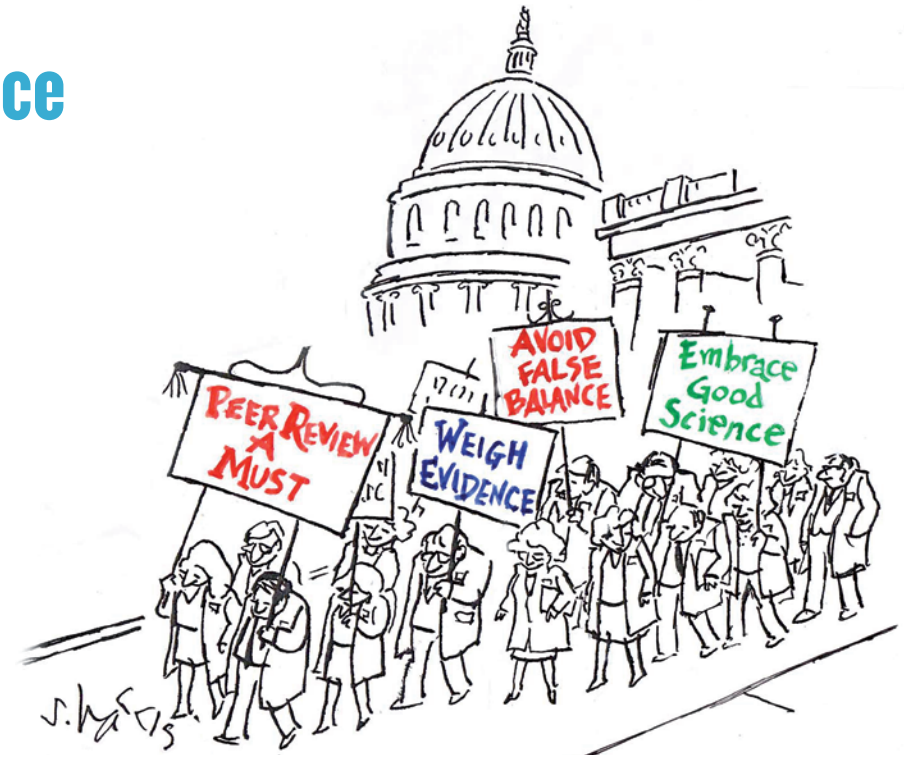
Enlist the best advice on scientific issues. Do not rely on 'independent scholars' and think-tank policy wonks for advice and referrals. Every country has academies of science and excellent universities to consult.

Steer clear of science that has not been peer reviewed. Conscientious analysis by our peers makes science work. It does not ensure certitude, but it beats the alternative.

Championing good science makes you look good. Know-nothings and anti-intellectuals will try to undermine your principled support of some scientific issues. Turn their ignorance against them by showing the consequences of following their path.

Non-scientists could also consult undsci.berkeley.edu for an introduction to how science is done.

Kevin Padian *Museum of Paleontology, University of California, Berkeley, USA.*
kpadian@berkeley.edu



Policy tips: heed risks of uncertainty

William Sutherland and colleagues' 20 tips for non-scientists on how to interpret scientific evidence could do more harm than good in the hands of policy-makers (*Nature* **503,** 335–337; 2013).

My experience in natural-resource management taught me that emphasizing uncertainty can lead policy-makers to dismiss evidence rather than to embrace it. On one occasion when I testified before Congress, I was told to come back only when I was 100% certain of my information. Practically speaking, this might be viewed as an excuse for political inaction.

For policy-makers, assessing the potential risks and benefits of policy action or inaction should be critical. For instance, when scientific uncertainty about the likelihood of a severe weather event is high but the consequences are potentially dire, there is a large risk in taking no protective action.

Rather than trying to teach non-scientists how to interpret uncertainty in our results, let's do a better job of helping them to understand the possible consequences of what they do or don't do.

Andrew A. Rosenberg *Center for Science and Democracy, Union of Concerned Scientists, Cambridge, Massachusetts, USA.*
arosenberg@ucsusa.org

Life sciences lag in stringent standards

Initiatives to ensure scientific reproducibility in life-science research (M. Bissell *Nature* **503,** 333–334; 2013) should demand strict standards, such as the use of only authenticated cell lines or the validation of commercially available antibodies. Setting guidelines for standards brings diverse stakeholders together and fosters an environment for adherence.

Carefully devised standards have underpinned advances in industries such as engineering and technology — from Wi-Fi to building bridges. It is time for the life-sciences community to catch up.

Leonard Freedman *Global Biological Standards Institute, Washington DC, USA.*
lfreedman@gbsi.org

EU fructose claim ignores risks

After a long discussion within and between member states, the European Union (EU) register of authorized health claims for foodstuffs will be expanded in January 2014 to include the claim: "consumption of foods containing fructose leads to a lower blood glucose rise compared to foods containing sucrose or glucose" (see go.nature.com/tf2iov). This claim fails to mention some potentially harmful effects of fructose metabolism (see, for example, C. A. Lyssiotis and L. C. Cantley *Nature* **502,** 181–182; 2013, and R. H. Lustig *et al. Nature* **482,** 27–29; 2012).

As the European Food Safety Authority noted during the authorization process (see go.nature.com/dbjkxm), there is evidence that a high intake of fructose can lead to metabolic complications such as abnormal lipid levels, resistance to insulin and increased visceral adiposity.

Companies will be able to use this claim to promote sweetened foods and drinks, as long as at least 30% of the glucose or sucrose is replaced by fructose. Only stronger evidence for the risks of high fructose intake can stop this.

Igor Pravst *Nutrition Institute, Ljubljana, Slovenia.*
igor.pravst@nutris.org

© 2013 Macmillan Publishers Limited. All rights reserved

Adrienne Asch

(1946–2013)

Bioethicist who fought for disability rights in reproductive technologies.

Adrienne Asch was a brilliant, feisty bioethicist and feminist who grappled with the impacts of human reproductive technologies on disability rights and social inequality. A groundbreaking scholar, teacher and activist, Asch questioned the practice of parents using prenatal testing and selective abortion to choose their children's traits and exclude those predicted to have disabilities.



NATIONAL FEDERATION OF THE BLIND

Asch, who died from cancer on 19 November, was born in New York City in 1946. Premature at birth, she developed retinopathy as a result of too much oxygen in her incubator, and soon lost her vision. She later attended public schools and sat in the same classrooms as sighted children in Ramsey, New Jersey. In 1969, after graduating from Swarthmore College in Pennsylvania with a bachelor's degree in philosophy, Asch had trouble getting hired because she was blind — and this inspired her interests in disability rights. She received a master's degree in social work from Columbia University in New York in 1973, and in 1981 she earned a certificate from the Institute for Contemporary Psychotherapy, where she trained as a family therapist.

Asch's career as a bioethicist began in the early 1980s, when she was investigating employment-discrimination cases for the New York State Division of Human Rights and conducting a private psychotherapy practice. At a bioethics meeting at the New York City Bar Association, she objected to the absence of speakers with disabilities participating in a debate about withholding life-saving treatment for babies born with spina bifida or Down's syndrome.

Her comments led to conference invitations and her involvement in a project on the care of imperilled newborns at the Hastings Center, a bioethics think tank in Garrison, New York. Two decades later, Asch was part of the working group that developed the Hastings Center guidelines for end-of-life care. At her urging, the guidelines were informed by consultation with representatives from disabilities communities. It is thanks in large part to Asch that bioethicists and researchers have begun to engage people with disabilities as valued, peer participants.

In 1988, as a doctoral student in social psychology at Columbia, she published *Women with Disabilities: Essays in Psychology, Culture and Politics,* co-edited with Michelle Fine, a social psychologist now at the City University of New York. It represented key features of her work — the intersection of feminism and disability rights, attention to the experiences of women with disabilities and resistance to demeaning stereotypes.

In 1994, two years after receiving her PhD, Asch became a professor of women's studies and biology, ethics, and the politics of human reproduction at Wellesley College in Massachusetts. In 2005, she was recruited by Yeshiva University in New York to direct its Center for Ethics. She also taught courses in epidemiology and population health and in family and social medicine at Albert Einstein College of Medicine in New York.

In addition to writing many scholarly articles and book chapters, Asch co-edited two influential books: *Prenatal Testing and Disability Rights* (2000) and *The Double-Edged Helix: Social Implications of Genetics in a Diverse Society* (2002). Her scholarship and advocacy were fuelled by a deep conviction that people with disabilities are as valuable as those with able bodies, their lives as worthwhile and their rights equal in every respect.

A just society, she argued, must eliminate pervasive discrimination, not children with disabling traits. Asch was a staunch supporter of a woman's right to abortion, but distinguished between abortions to avoid having any child and those to avoid having a child with particular features. She pushed for parental decisions, social policies and bioethics debates to be based on genuine experiences rather than tragic myths and fears. Asch was especially instrumental in shifting genetic counselling away from a prevention-based model, which steers prospective parents to select against disabling traits, towards a social model, which provides information about life with a disabling condition.

Asch had an endearing ability to be at once gracious and confrontational, passionate and prickly. She was always open to differing views, but she never compromised her insistence on absolute respect for the lives and perspectives of people with disabilities. She was known for asking probing questions to identify common values and expose disagreements that needed to be hashed out.

As feminist scholars who wrote about the bioethics of reproduction and inequality, Adrienne and I crossed paths frequently beginning in the late 1980s. Her cogent arguments helped me to incorporate disability studies in my own writing on genetic selection and the devaluation of black women's childbearing. In 2008, we participated in a workshop for an issue of *Signs: Journal of Women in Culture and Society* on reproductive and genetic technologies. Adrienne asked why scholars who write about disability rights fail to cite scholars who have disabilities. Her questions made me think more seriously about the experts I relied on and more deeply about the role of disability in my own work and life.

In many bioethics meetings, Adrienne was the only person with a visible disability. Her unmistakable voice compelled the rest of us to confront how disability-rights arguments affected our commitment to social justice and human equality. Yet, Adrienne wanted mainly for us to see her and others with disabilities as unremarkable. As she put it in a 2006 interview: "I'm neither unhappy nor proud. I just am." ■

Dorothy Roberts *is a professor of Africana studies, law and sociology at the University of Pennsylvania, Philadelphia, Pennsylvania.*
e-mail: dorothyroberts@law.upenn.edu

© 2013 Macmillan Publishers Limited. All rights reserved

EARTH SCIENCE

Erosion by cooling

The thermal history of thousands of rock samples convincingly confirms the idea that climate cooling accelerates the rate of erosion at Earth's surface — and implicates glaciers in particular. SEE LETTER P.423

DAVID LUNDBEK EGHOLM

On page 423 of this issue, Herman *et al.*[1] report an analysis of mountain-range erosion rates which shows that global cooling in the past 6 million years has accelerated the destruction of mountains. This result reignites a long-lived debate about links between climate, topography and plate tectonics.

The high topography of Earth's mountain ranges is made when plate tectonics force the continental plates to slowly collide. However, erosion by rivers, glaciers and landslides constantly counteracts this mountain-building process by breaking down bedrock and moving the resulting sediment to lower elevations, where it accumulates in sedimentary basins or oceans. The structure of mountain ranges therefore reflects a complex balance between constructive and destructive forces.

Although we can measure current changes in topography using the Global Positioning System, finding out what happened in the past and obtaining data that span the extremely long timescales of these processes are major challenges. An intriguing question relates to how climate influences the erosion processes, and thereby the elevation and morphology of mountain ranges[2,3].

About 6 million years ago, Earth's global climate started a strong cooling trend that led to glaciations in high mountain ranges and at high latitudes[4]. Extensive ice masses then developed at the beginning of the Quaternary period (the most recent 2.6 million years). It has long been recognized that the volume of sediment that has accumulated in the oceans within the past few million years far exceeds that measured for any other period of a similar length[5], which points to increased erosion rates during the Quaternary[6]. But some have questioned whether this observation is biased by the difficulty of measuring the correct volume of older sediments and, therefore, whether surface processes truly led to faster erosion when the global climate cooled and started to fluctuate[7]. Herman *et al.* address this question by analysing new information: the thermal history of rocks.

Using a technique known as thermochronology, the thermal history of a rock sample can be reconstructed from the relative concentrations of certain noble gases within it or from the distribution of damage trails produced by radioactive decay[8]. Specifically, thermochronology allows the dating of the time when a rock cooled to a 'closure' temperature — the temperature below which gaseous isotopes no longer diffuse out of the rock and/or when damage trails stop annealing. This, in turn, provides an estimate of how fast erosion brought the rock closer to the surface, because temperature decreases with distance from the centre of the Earth. Closure temperatures vary from 70 to 250 °C, depending on the specific thermochronometer used.

By combining several thermochronometers that had different closure temperatures, Herman and colleagues implemented a clever approach to determine past changes in erosion rate. They compiled a global set of nearly 18,000 thermochronology data points and then used an algorithm to reconstruct patterns of erosion rate for several time intervals. The results reveal that the erosion of Earth's mountain ranges did indeed accelerate globally as the climate cooled, confirming the information provided by sediment volumes.

The progressive increase in erosion rate is most pronounced at intermediate latitudes (30° to 50°) within the past 2 million years. Herman and co-workers therefore propose that glaciers are the main driver of the accelerated erosion because, at these latitudes, many high-elevation landscapes were glaciated for the first time. Their conclusion is supported by the fact that glaciers are known to have left their distinctive imprint on the morphology of landscapes within a fairly short period. For example, the substantial landscape modifications that formed the spectacular glacial fjord systems of Norway, Greenland, western North America, Chile and New Zealand (Fig. 1) must have occurred within a few million years. Glaciers are efficient agents of erosion because they can abrade and quarry bedrock as they slide down through steep topography.

The hypothesis that climate change was the main driver of recent increased mountain-range erosion has provoked intense debates[9,10]. Sudden pulses of erosion have conventionally been attributed to changes in tectonic activity rather than climate. Many geologists have therefore interpreted the increased erosion of the recent past as a product of tectonic uplift — even in places where no direct evidence of tectonic plate movements exists.

Unfortunately, Herman and colleagues'



DAVID WALL/ALAMY

Figure 1 | Carved by glaciers. Herman *et al.*[1] demonstrate that erosion processes, including those that led to the formation of glacial fjords (here at Bradshaw Sound Fjordland National Park, New Zealand), accelerated globally over the past 6 million years.

© 2013 Macmillan Publishers Limited. All rights reserved

analysis cannot resolve what happened in these controversial regions. The reason is that erosion rates in these areas were generally low before they started to increase less than 10 million years ago, but the authors' thermochronological method requires total erosion to be high enough to uncover rocks from depths that are associated with closure temperatures. This amounts to kilometre-scale erosion, even for the thermochronometers that have the lowest closure temperatures. Such levels of erosion are generally reached only in areas where tectonic uplift has maintained high erosion rates for a long period, which is why the researchers' analysis is limited to areas where substantial tectonic activity happens today or occurred at about the time of global cooling.

Even with this limitation, Herman *et al.* convincingly demonstrate the global scale of the recent erosion phenomenon. Their results suggest that climate drives erosion, because, unlike tectonic activity, climate can change synchronously on a global scale. ■

David Lundbek Egholm *is in the Department of Geoscience, Aarhus University, 8000 Aarhus, Denmark.*
e-mail: david@geo.au.dk

1. Herman, F. *et al. Nature* **504,** 423–426 (2013).
2. Montgomery, D. R., Balco, G. & Willett, S. D. *Geology* **29,** 579–582 (2001).
3. Molnar, P. *Annu. Rev. Earth Planet. Sci.* **32,** 67–89 (2004).
4. Zachos, J., Pagani, M., Sloan, L., Thomas, E. & Billups, K. *Science* **292,** 686–693 (2001).
5. Hay, W. W., Sloan, J. L. & Wold, C. N. *J. Geophys. Res.* **93,** 14933–14940 (1988).
6. Zhang, P., Molnar, P. & Downs, W. R. *Nature* **410,** 891–897 (2001).
7. Willenbring, J. K. & von Blanckenburg, F. *Nature* **465,** 211–214 (2010).
8. Reiners, P. W., Ehlers, T. A. & Zeitler, P. K. *Rev. Miner. Geochem.* **58,** 1–18 (2005).
9. Ruddiman, W. F. & Kutzbach, J. E. *J. Geophys. Res.* **94,** 18409–18427 (1989).
10. Molnar, P. & England, P. *Nature* **346,** 29–34 (1990).

CANCER

Discrepancies in drug sensitivity

Large panels of human cancer cell lines have been profiled at the DNA, RNA and pharmacological levels to accelerate the search for cancer therapies. But two of those large data sets show only partial concordance. SEE ANALYSIS P.389

JOHN N. WEINSTEIN & PHILIP L. LORENZI

Despite obvious limitations in their ability to model clinical disease, cultured cell lines remain central to research on cancer. But a study by Haibe-Kains *et al.*[1] on page 389 of this issue reveals apparent inconsistencies between two large studies of the sensitivity of hundreds of cell lines to dozens of drugs. The findings sound a note of caution about the interpretation of data from such projects, but do not undermine their value.

The first cell-line panel used for large-scale screening of compounds for anticancer activity was the NCI-60, a diverse set of 60 human lines that has been used to screen more than 100,000 compounds since 1988 (ref. 2). Because the same lines have been profiled at the DNA, RNA, protein and chromosomal levels, molecular aberrations in the cells can be correlated with their sensitivity to drugs[3]. But 60 is a relatively small number. So it was exciting when, in March 2012, the Cancer Cell Line Encyclopedia (CCLE)[4] and Cancer Genome Project (CGP)[5] were published, presenting gene-expression profiles and drug-sensitivity assays for 1,036 cell lines and 24 drugs, and 727 cell lines and 138 drugs, respectively. The publications also contained information on gene-copy number and genome sequence for some of the cell lines, and protein-level data have since been added to the mix. Those extensive databases are being used in numerous laboratories to guide research on the molecular mechanisms of cancer, to generate hypotheses for the development of new therapies, and in conjunction with clinical studies[6].

Haibe-Kains *et al.* analysed the relationships between gene expression and drug sensitivity for 471 cell lines, 15 drugs and 12,187 genes that were in both the CCLE and CGP data sets. They found a rather low correlation between the two. Both original studies were carefully done and carefully documented; there is no implication that the apparent discrepancy involved error on the part of either team. So what is the source of the difference? In principle, it could be due to differences in the gene-expression profiles, pharmacological assays, computational methods or any combination thereof.

The authors found that the gene-expression profiles, which were obtained from microarray studies, showed quite good concordance between the two projects, whereas the pharmacological assays did not (Fig. 1). But that should come as no surprise. The pharmacological assay used by the CGP (the CellTiter 96 AQueous One Solution Cell Proliferation Assay from Promega) measures metabolic activity in terms of a reductase-enzyme product after a 72-hour incubation of cells with a drug; that used by the CCLE (the CellTiter-Glo assay from Promega) measures metabolic activity by assessing levels of the energy-transfer molecule ATP, after 72–84 hours of incubation. Both assays provide indices of the drug's activity against the cells, but they would not be

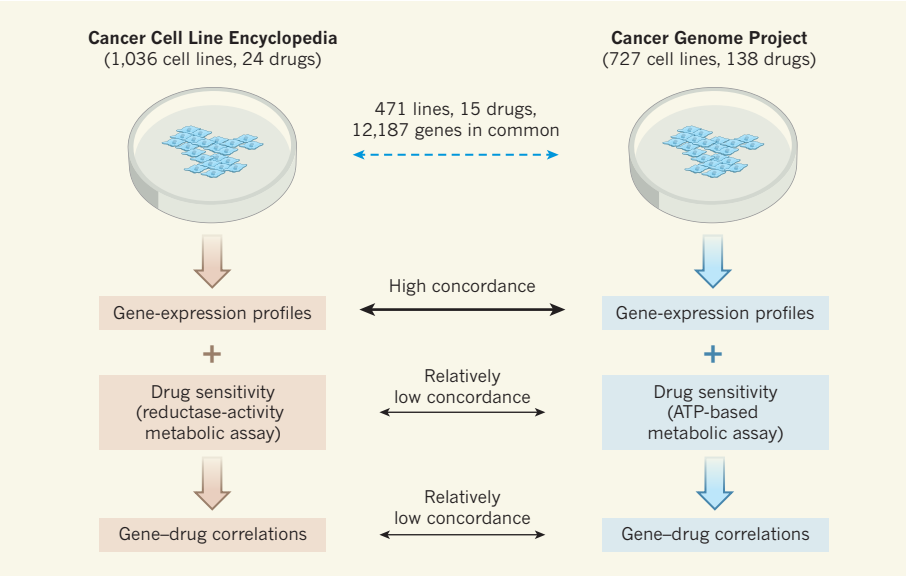


Figure 1 | Study comparison. The Cancer Cell Line Encyclopedia[4] and Cancer Genome Project[5] data provide rich resources for the cancer research community. Haibe-Kains *et al.*[1] analysed the concordance of the two data sets from several perspectives and identified a high concordance between the gene-expression data sets, but a relatively low correspondence between drug-sensitivity assays. That apparent difference propagates into the gene–drug correlations found by the two studies.

© 2013 Macmillan Publishers Limited. All rights reserved

expected to mirror each other across all cell and drug types, even if run in parallel (and neither may be the best indicator of cell viability).

Furthermore, many variables can affect the quantitative results obtained in such assays. For example, drug sensitivities can diverge if different batches of fetal bovine serum (an ingredient of cell-culture medium that varies in its content of cytokines and other biologically active molecules) are used. The time and conditions of the cells' incubation before the drug is added, the coating on the plastic culture wells, intra-study batch or trend effects and other such arcane factors can all be influential. In this case, the intrinsic sensitivities of the two assays as analysed were also different: for 12 of the 15 drugs in question, the CCLE assay was not sensitive enough to reach its endpoint for a large fraction of the cell types; in the CGP study, a mathematical extrapolation was used to obtain quantitative results in such cases. Haibe-Kains *et al.* performed extensive analyses to take account of such issues, but more experimental data would be required to pin down the true reasons for the discrepancies they highlight. Overall, if there is any surprise about the discordance between the two pharmacological data sets, it is quantitative, rather than qualitative.

An interesting question not directly addressed by Haibe-Kains and colleagues is whether the drugs would cluster into two separate groups on the basis of response data from the two different projects or whether they would intermingle — in other words, whether the between-assay differences were greater than the within-assay differences among drugs.

Given the differences, which pharmacological assay represents the 'truth'? The probable answer is either both or neither, depending on one's purpose. If the aim is to predict clinical efficacy, then neither assay will be 'correct' in most cases. The well-worn dictum "all models are wrong, some models are useful"[7] applies with a vengeance in this context; there are too many differences between cultured cells and patients, particularly in terms of the delicate balance between beneficial and toxic effects of anticancer drugs.

In our view, the more appropriate uses of cell-line pharmacological data are for hypothesis generation and for elaborating on existing hypotheses, rather than for formal statistical prediction. Clues obtained by correlating drug-sensitivity patterns with molecular profiles will sometimes illuminate cellular mechanisms and pathways that advance our basic understanding, even if they are not directly predictive for the clinic. The CCLE and CGP authors each use their drug-response data to tell several provocative molecular stories, and there is considerable overlap between the two sets of stories. Indeed, the statistical tests presented in both studies suggest that the patterns of response they observe are quite robust, even if the individual drug-response measurements are not. The patterns can be highly instructive about mechanisms of action.

Haibe-Kains *et al.* make a plea for standardization of pharmacological assays among researchers. Standardization is without doubt useful for comparison of studies and for quality assurance, once a research community has decided what the standards should be. In this particular case, however, the more immediately productive enterprise would be a joint effort by the teams to pin down the reason(s) for the differences between assays. We strongly suspect that the two teams have already generated a great deal of the relevant information, and additional experiments could be done in parallel between the two — to support the activities of the many researchers who are using, or will use, these rich data resources. ■

John N. Weinstein *and* **Philip L. Lorenzi**
are in the Department of Bioinformatics and Computational Biology and the Department of Systems Biology, University of Texas MD Anderson Cancer Center, Houston, Texas 77030, USA.
e-mail: jweinste@mdanderson.org

1. Haibe-Kains, B. *et al. Nature* **504,** 389–393 (2013).
2. Shoemaker, R. H. *et al. Prog. Clin. Biol. Res.* **276,** 265–286 (1988).
3. Weinstein, J. N. *et al. Science* **275,** 343–349 (1997).
4. Barretina, J. *et al. Nature* **483,** 603–607 (2012).
5. Garnett, M. J. *et al. Nature* **483,** 570–575 (2012).
6. The Cancer Genome Atlas Research Network *et al. Nature Genet.* **45,** 1113–1120 (2013).
7. Box, G. E. P. in *Robustness in Statistics: Proceedings of a Workshop* (eds Launer, R. L. & Wilkinson, G. N.) 201–236 (Academic, 1979).

This article was published online on 27 November 2013.

SPACE PHYSICS

A fast lane in the magnetosphere

A marriage between satellite observations and modelling has shown that acceleration of electrons in the magnetosphere can be explained by scattering of these particles by plasma oscillations known as chorus waves. SEE LETTER P.411

MARY K. HUDSON

Both dramatic dropout[1] and increase[2,3] in the flux of high-energy electrons trapped in Earth's dipole-like magnetic field have been reported along with the formation of a storage ring[4] — a third 'radiation belt' nested between the usual inner and outer zones of million-electronvolt ionized particles (plasma) that surround Earth. This ring lies in a region called the slot, which is formed by scattering of electrons by plasma waves and their loss to the atmosphere[5,6]. On page 411 of this issue, Thorne *et al.*[7] present convincing evidence for local acceleration of electrons by the same type of plasma wave or oscillation that causes electron loss — called a whistler wave because of its occurrence in the audio frequency range. This mode of oscillation occurs in two types depending on the density of the cold plasma in the inner region of the magnetosphere: 'hiss' and 'chorus'. These colourful names go back to the early days of listening to these modes with audio-range radio receivers[8,9].

Figure 1 shows a classic picture of Earth's magnetosphere and the wave modes originally sketched by Thorne and Kennel[10]. These have subsequently been augmented with other plasma-wave types[11,12] that affect the radiation-belt electrons, including ultra-low frequency and electromagnetic ion cyclotron (EMIC) waves. Electrons and ions transported from the tail of the magnetosphere excite chorus and EMIC waves at the dawn and dusk sides of the magnetosphere (right and left parts of the figure), respectively.

In their study, Thorne and colleagues report observations taken by the Van Allen Probes launched last year[13]. The satellites recorded a rapid electron-acceleration event that occurred during a disturbance of Earth's magnetosphere, known as a geomagnetic storm, on 8–9 October 2012. The authors modelled these observations and showed that chorus waves can explain this acceleration event. What allows these waves to interact so effectively with electrons is the right-hand rotation of the waves' electric field, which occurs in the same direction as electron gyration, allowing electrons to be accelerated. Such polarization of the electric field allows the waves to resonate with the electron gyration, causing either electron loss to the atmosphere or rapid acceleration, depending on the energy of electrons and their relative velocity parallel and perpendicular to the magnetic field. The energy of electrons interacting with the chorus depends on the density of the cold plasma, which co-rotates with Earth.

A dramatic loss of the entire outer-zone million-electronvolt electrons had been observed on 8 October 2012 (ref. 4). Thorne and colleagues' analysis now reveals a rapid rebuilding and enhancement of the outer

© 2013 Macmillan Publishers Limited. All rights reserved

AGU

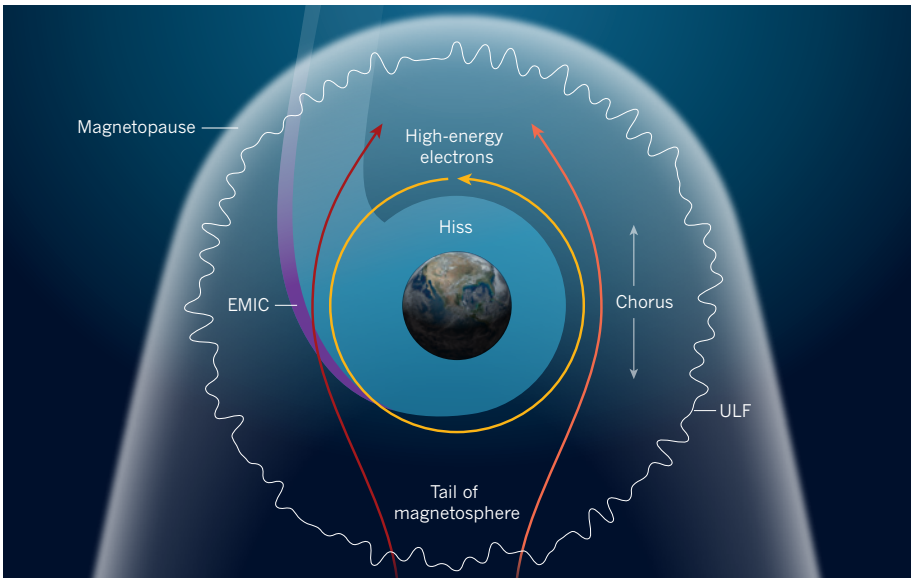


Figure 1 | Plasma waves in the magnetosphere. A projection of the equatorial plane of Earth's magnetosphere and the distribution of plasma waves[12]. Hiss plasma waves are confined to the region of cold plasma (pale blue region), which co-rotates with Earth. This region can extend to the dayside of the magnetopause (the outer edge of the magnetosphere) in plumes (pale blue tail) during strong plasma convection from the tail of the magnetosphere. Electrons and ions transported (red arrows) from the tail excite electromagnetic ion cyclotron (EMIC) waves around the dusk side (left) of the magnetosphere and chorus waves around its dawn side (right). The yellow circular arrow shows the direction of high-energy electron drift around Earth. Ultra-low-frequency (ULF) waves are also shown. Thorne and colleagues' study[7] suggests that chorus waves caused an event of rapid electron acceleration that occurred during a geomagnetic storm on 8–9 October 2012. (Figure adapted from ref. 12.)

zone on 9 October in six-dimensional (phase-) space, extended to include the velocity dimension (see Extended Data Fig. 4, where the enhancement is illustrated as a peak on the dawn side of the magnetosphere). The authors compared this enhancement with a phase-space density distribution that peaks at a greater distance from Earth than the observed enhancement does. Observations from the Van Allen Probes have shown[3] the rapid development of this peak now modelled by the authors, but the peak had been difficult to explain with radial diffusion in phase-space density from greater distance to where the peak is located — long the paradigm for replenishment of the outer-zone electrons[14]. The authors' modelling now demonstrates that this effect can cause the peak.

Thorne and colleagues' study represents a breakthrough in understanding the complex interplay of radiation-belt electrons with plasma waves, which affects the electrons' acceleration and loss. More investigations in this field should combine the type of analysis performed by Thorne *et al.* with models of radial transport that include measured electric and magnetic-field amplitudes in the ultra-low-frequency wave regime[15], which oscillate with the longitudinal-drift period of electrons[14]. Future work should also incorporate the effects of large-amplitude coherent whistler waves[16], which have been observed in improved high-resolution measurements from the Van Allen Probes[17]. ■

Mary K. Hudson *is in the Department of Physics and Astronomy, Dartmouth College, Hanover, New Hampshire 03755-3528, USA.*
e-mail: mary.k.hudson@dartmouth.edu

1. Turner, D. L., Shprits, Y., Hartinger, M. & Angelopoulos, V. *Nature Phys.* **8,** 208–212 (2012).
2. Horne, R. B. *et al. Nature* **437,** 227–230 (2005).
3. Reeves, G. D. *et al. Science* **341,** 991–994 (2013).
4. Baker, D. N. *et al. Science* **340,** 186–190 (2013).
5. Kennel, C. F. & Petschek, H. E. *J. Geophys. Res.* **71,** 1–28 (1966).
6. Lyons, L. R. & Thorne, R. M. *J. Geophys. Res.* **78,** 2142–2149 (1973).
7. Thorne, R. M. *et al. Nature* **504,** 411–414 (2013).
8. Morgan, M. G. & Allcock, G. McK. *Nature* **177,** 30–31 (1956).
9. Helliwell, R. A. *Whistlers and Related Ionospheric Phenomena* (Stanford Univ. Press, 1965).
10. Thorne, R. M. & Kennel, C. F. *J. Geophys. Res.* **76,** 4446–4453 (1971).
11. Summers, D., Thorne, R. M. & Xiao, F. *J. Geophys. Res.* **103,** 20487–20500 (1998).
12. Shprits, Y. Y., Li, W. & Thorne, R. M. *J. Geophys. Res.* **111,** A12206 (2006).
13. Kessel, R. L., Fox, N. J. & Weiss, M. *Space Sci. Rev.* **179,** 531–543 (2012).
14. Fälthammar, C.-G. *J. Geophys. Res.* **70,** 2503–2516 (1965).
15. Loto'aniu, T. M. *et al. J. Geophys. Res.* **115,** A12245 (2010).
16. Cattell, C. *et al. Geophys. Res. Lett.* **35,** L01105 (2008).
17. Wygant, J. R. *et al. Space Sci. Rev.* **179,** 183–220 (2013).

PLANT BIOLOGY

Witchcraft and destruction

The discovery of a protein that is targeted for degradation by the 'witch' hormones called strigolactones reveals a mechanism by which shoot architecture is controlled in rice plants. SEE ARTICLES P.401 & P.406

STEVEN M. SMITH

The mythical old hag Striga gained succour by drawing the life force from her young victims. Today, she lends her name to the witchweeds of the genus *Striga* and to the strigolactone compounds that trigger these plants to parasitize their unsuspecting host plants. But these compounds typically play a more positive part in plant biology — as hormones that control the development of roots and shoots to coordinate the capture of mineral nutrients from the soil with that of carbon from the atmosphere. The strigolactone receptor is a curious protein because it simultaneously perceives and destroys the hormone. In two papers[1,2] in this issue, a target of this receptor in rice is reported to be the novel protein DWARF53, the strigolactone-dependent destruction of which blocks the outgrowth of secondary shoots.

Strigolactones were first discovered in root exudates through their ability to stimulate seed germination of the root-parasitic plant *Striga hermonthica*[3]. The compounds were later shown to promote the formation of mutually beneficial symbioses between plant roots and fungi[4]. More recently, it was discovered that strigolactones are involved in the control of plant development[5,6]. In response to nutrient limitation, strigolactones are produced in the roots[7], where they promote the growth of lateral roots and root hairs, and they are transported to the shoots, where they repress the outgrowth of lateral buds or secondary shoots[8]. These outcomes increase the capture of mineral nutrients by the roots, while at the same time reducing the shoots' demand for resources.

© 2013 Macmillan Publishers Limited. All rights reserved

Mutant plants that are strigolactone deficient or insensitive have multiple secondary shoots and often a short primary stem. In rice, these plants are typically described as dwarf mutants. Genetic analysis of these plants has led to the identification of enzymes involved in strigolactone biosynthesis[9] and of the rice strigolactone receptor DWARF14 (D14)[10]. The receptor is an α/β-fold hydrolase enzyme that uses a catalytic triad of amino acids to simultaneously perceive and hydrolyse strigolactones, in conjunction with an F-box protein[11] that in rice is known as DWARF3 (D3)[3]. Because the function of F-box proteins is to select other proteins for degradation, this interaction suggests that D14 and D3 might form a complex that targets other proteins for removal. Just such a target protein has now been identified.

Jiang *et al.*[1] (page 401) and Zhou *et al.*[2] (page 406) studied a rice dwarf mutant known as *d53*, which was described 36 years ago[12]. Both groups of authors show that these plants are strigolactone insensitive, and they have succeeded in the difficult task of identifying the mutated gene. They show that the D53 protein has sequence similarities to Clp ATPase enzymes and to heat-shock protein 101, which suggests that it has a role in protein–protein interactions. They also reveal that the *d53* mutation involves the deletion of five amino acids and substitution of one other in the D53 protein, which could potentially cause the protein to malfunction.

Both papers present evidence for strigolactone-dependent interactions between D53 and D14, and between D14 and D3, and show that the catalytic triad of D14 is essential for this strigolactone function. Interaction between the three proteins leads to D53 being tagged with ubiquitin — a regulatory protein that marks proteins for destruction — and destroyed (Fig. 1). In the absence of D14 or strigolactone, D53 and D3 can still interact, but this does not lead to destruction of D53. Furthermore, the mutant D53 protein is neither ubiquitinated nor degraded even in the presence of D14 and strigolactone, which seems to explain why *d53* plants produce multiple secondary shoots (tillers).

Both groups go on to show that D53 is located in the nucleus and that it contains putative EAR sequences; these are thought to interact with proteins of the TOPLESS family, which are involved in repression of gene transcription in several plant-hormone signalling pathways. Indeed, Jiang *et al.* show that D53 interacts with two rice TOPLESS proteins, raising the possibility that D53 in concert with TOPLESS proteins could regulate the expression of genes that determine shoot architecture. The *d53* mutant also exhibits downregulation of the gene *FC1*, an orthologue of the maize (corn) *TB1* and thale cress (*Arabidopsis*) *BRC1* genes, which are known to repress secondary-shoot growth. Thus, it seems likely that D53 acts in the nucleus to regulate the expression of genes involved in secondary-shoot growth.

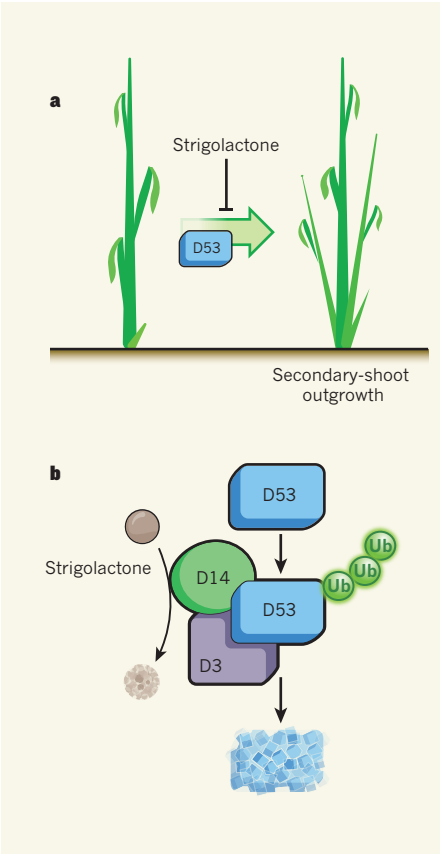


Figure 1 | Repression of secondary-shoot growth by strigolactones. **a**, Strigolactone hormones can inhibit the outgrowth of secondary shoots when nutrients are in short supply. Jiang *et al.*[1] and Zhou *et al.*[2] have found that, in rice, this is achieved by destruction of the protein D53, which otherwise promotes secondary-shoot growth. **b**, The authors show that binding and hydrolysis of strigolactone by its receptor D14 leads to the recruitment of D53 into a complex of D14 and another protein, D3. These protein interactions result in the ubiquitination (indicated by Ub) and subsequent destruction of D53.

Strigolactones control numerous aspects of plant development, so might D53 have a broader role? *D53* belongs to a small gene family, other members of which could regulate different aspects of development. Support for this idea comes from a recent study of *Arabidopsis*[13]. MAX2 is the *Arabidopsis* orthologue of D3 and is required not only for the control of shoot development, in conjunction with the *Arabidopsis* D14, but also for seedling growth, together with the D14-like protein KAI2. A gene (*SMAX1*) has been identified[13] that encodes a protein that works in conjunction with MAX2 and is required for seedling growth but not for secondary-shoot growth; *SMAX1* is a homologue of *D53*, indicating that these genes provide examples of functional specialization within a gene family.

Although Jiang *et al.* indicate that D53 acts as a repressor of strigolactone action, it is conceptually easier to think of strigolactones as repressors of D53. What is remarkable is that nutrient limitation in the roots does not simply limit shoot growth by default, but instead the root dispatches the strigolactone signal to impose a brake on shoot growth by destroying the D53 protein. These findings reveal remarkable similarities between strigolactones and their receptors, and the perception and signalling mechanisms of several other classes of plant hormone, including auxins, jasmonates and gibberellins. For example, the rice gibberellin receptor GID1 is also a member of the α/β-fold hydrolase family, and by binding the protein SLR1 recruits it into a complex with an F-box protein (SLY1) for ubiquitination and destruction. Another twist to the story comes from the recent report[14] that rice D14 exhibits strigolactone-dependent interaction with SLR1, suggesting a mechanism for the coordination of strigolactone and gibberellin signalling during the control of shoot development. This will be an exciting area for further research.

The discovery that strigolactones have a central role in regulating resource allocation and growth in plants has far-reaching consequences. Agriculturalists need to boost yields while decreasing their dependency on finite resources, such as phosphate, and on fossil fuels for nitrogen-based fertilizers. We have already seen the development of higher-yielding nitrogen-dependent crop varieties with modified gibberellin action. It is now clear that strigolactones might be exploited to generate crop varieties with improved resource allocation under nutrient-limiting conditions. ■

Steven M. Smith *is at the Australian Research Council Centre of Excellence in Plant Energy Biology, and the School of Chemistry and Biochemistry, University of Western Australia, Perth, Western Australia 6009, Australia.*
e-mail: steven.smith@uwa.edu.au

1. Jiang, L. *et al. Nature* **504,** 401–405 (2013).
2. Zhou, F. *et al. Nature* **504,** 406–410 (2013).
3. Xie, X., Yoneyama, K. & Yoneyama, K. *Annu. Rev. Phytopathol.* **48,** 93–117 (2010).
4. Akiyama, K., Matsuzaki, K. & Hayashi, H. *Nature* **435,** 824–827 (2005).
5. Umehara, M. *et al. Nature* **455,** 195–200 (2008).
6. Gomez-Roldan, V. *et al. Nature* **455,** 189–194 (2008).
7. Umehara, M., Hanada, A., Magome, H., Takeda-Kamiya, N. & Yamaguchi, S. *Plant Cell Physiol.* **51,** 1118–1126 (2010).
8. Brewer, P. B., Koltai, H. & Beveridge, C. A. *Mol. Plant* **6,** 18–28 (2013).
9. Alder, A. *et al. Science* **335,** 1348–1351 (2012).
10. Arite, T. *et al. Plant Cell Physiol.* **50,** 1416–1424 (2009).
11. Hamiaux, C. *et al. Curr. Biol.* **22,** 2032–2036 (2012).
12. Iwata, N., Satoh, H. & Omura, T. *Japan. J. Breed.* **27** (suppl. 1), 250–251 (1977).
13. Stanga, J. P., Smith, S. M., Briggs, W. R. & Nelson, D. C. *Plant Physiol.* **163,** 318–330 (2013).
14. Nakamura, H. *et al. Nature Commun.* **4,** 2613 (2013).

This article was published online on 11 December 2013.

© 2013 Macmillan Publishers Limited. All rights reserved

2013 EDITORS' CHOICE

Adapted extracts from selected News & Views articles published this year.

FISHERIES

CLIMATE CHANGE AT THE DINNER TABLE

Mark R. Payne (*Nature* 497, 320–321; 2013)

Marine species tend to occupy the full range of temperatures that they can tolerate physiologically, and therefore, on a broad scale, their distributions closely track temperature boundaries in the ocean. Thus, over the multi-decadal to centennial scale, warming, acidification and deoxygenation of the oceans are expected to change the species composition of fish communities in a given region. However, Cheung *et al.* present startling evidence that global fisheries catches have already changed in a manner associated with the warming trend. Furthermore, they suggest that catch composition in tropical regions has stabilized, implying that these regions have already become too hot for all but the warmest-water species. The fact that the catch composition seems to have reached the terminal hot-water state in these regions means that further warming may reduce fishery yields, if it has not already done so.

Nature **497,** 365–368 (2013).

NEUROSCIENCE

THE UNITS OF A SONG

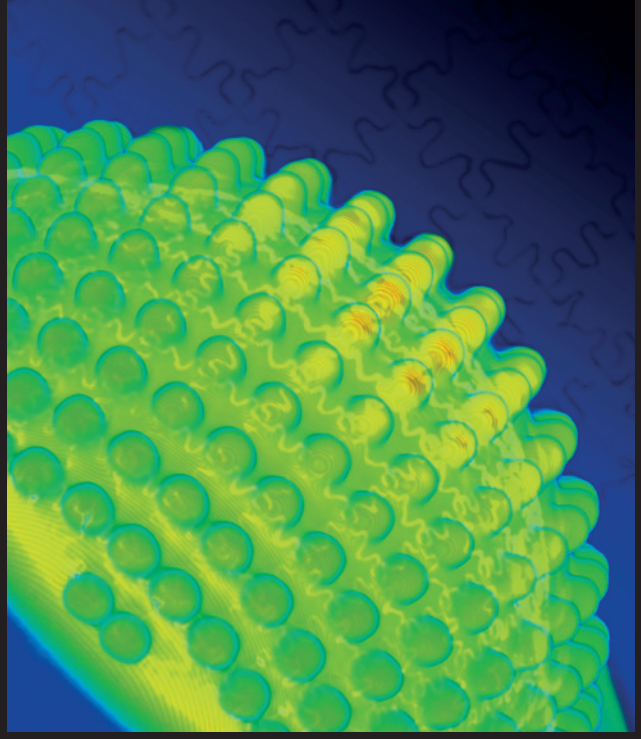
Todd W. Troyer (*Nature* 495, 56–57; 2013)

What is the basic unit of speech? This question has vexed speech and language researchers for decades, and similar questions have challenged those who study songbirds. Whereas behavioural evidence supports the grouping of songs into 100–250-millisecond vocalizations called syllables, neurophysiological data suggest that the premotor areas at high levels in the hierarchy of motor neurons in the brain act more like a clock, providing a continuous stream of activity on a 10-millisecond timescale. Amador *et al.* reconcile these data, providing evidence that the song code generated by HCV motor neurons in zebra finches (*Taeniopygia guttata*) is indeed broken into discrete 'gestures', which are significantly shorter than song syllables. Although the clock and gesture hypotheses lead to different views of the motor code for song, it is possible that, whereas bursting activity in HVC neurons tends to align with gesture transitions, enough HVC neurons are active throughout each gesture to sustain clock-like functionality.

Nature **495,** 59–64 (2013).



ANDREW WALMSLEY/NATURE PICTURE LIBRARY



UNIV. ILLINOIS

OPTICAL DEVICES

SEEING THE WORLD THROUGH AN INSECT'S EYES

Alexander Borst & Johannes Plett (*Nature* 497, 47–48; 2013)

Flies are usually treated with disdain. Most commonly associated with spreading disease, they are at best considered simply annoying. Conversely, flies have also inspired mankind for centuries. An early report along these lines dates back to the seventeenth century, when the young René Descartes, while lying sick in bed, observed a fly walking along the ceiling of his room. Thinking about how he could describe the path of the fly in quantitative terms, he came up with what have become known as Cartesian coordinates. The most recent example of such insect-inspired research is described by Song *et al.* — the authors have transferred the design of an insect's compound eye to a digital camera. The result is a small, artificial faceted eye with a near-hemispheric field of view, but without off-axis aberration and with an almost infinite depth of field. It could prove a stepping stone towards autonomous navigation of micro aerial vehicles, in their manifold possible uses.

Nature **497,** 95–99 (2013).

GLOBAL HEALTH

PERSUASIVE EVIDENCE ON HIV POLICY

Grace John-Stewart (*Nature* 495, 452–453; 2013)

As emergency investment to fight HIV/AIDS evolves into a long-term response, it remains crucial to measure the direct and indirect benefits of HIV treatment to sustain investment. Two studies published in *Science* (Tanser *et al.* and Bor *et al.*) show a large increase in the overall population life expectancy and a decrease in new cases of HIV infection after expanded use of antiretroviral therapy in South Africa. Population studies such as these, which involve individuals who may have much lower drug adherence than those participating in carefully controlled clinical trials, are a powerful complement to clinical trials. They give us a sense of impact in the 'real world'. The new studies focus on a fairly specific real world — one in which HIV prevalence was staggeringly high, allowing detection of the impact of therapy on overall adult life expectancy. Nonetheless, the studies are persuasive in the larger landscape of global HIV. These data should persuade policy-makers to sustain or increase investment in this form of therapy.

Science **339,** 961–965, 966–971 (2013).

© 2013 Macmillan Publishers Limited. All rights reserved

QUANTUM PHYSICS

THE RIGHT AMBIENCE FOR A SINGLE SPIN

Michael E. Flatté (*Nature* 503, 205–206; 2013)

Anyone whose dinner at a favourite restaurant has been ruined by noisy neighbours understands the disruption caused by too much interaction with one's environment. Most electronic spins in a solid are also buffeted by naturally occurring 'noises'. The resilience of single-spin dynamics to these noises is quantified by the spin coherence time or the closely related zero-field spin lifetime. Just as one might make modifications that soundproof a restaurant and thus improve the ambience for diners, so using methods to reduce the noises influencing a single spin leads to long spin coherence times. Unfortunately, these methods also limit the materials in which long spin coherence times can be observed. Miyamachi *et al.* demonstrate an approach to making a single spin deaf to the dominant noises around it. With a single holmium atom adsorbed on the surface of platinum, they measured a spin lifetime that exceeded 6 minutes — a remarkably high value for any solid-state spin system.

Nature **503,** 242–246 (2013).

EARTH SCIENCE

MAINLY IN THE PLAIN

James W. Kirchner & Ken L. Ferrier (*Nature* 495, 318–319; 2013)

On million-year timescales, landscapes disappear, gradually consumed by physical erosion and chemical dissolution. How quickly these processes transform Earth's surface has been a question of great interest to geologists and geochemists. But they may have mostly been looking for the answer in the wrong places, Willenbring *et al.* report in *Geology*. Geologists have focused their attention on steep terrain, where rapid erosion is thought to drive rapid chemical weathering. However, Willenbring and colleagues say that there is just not enough mountainous terrain to account for much of the global flux of sediment (from erosion) or solutes (from chemical weathering) reaching the oceans. This argument is likely to arouse interest, and some measure of controversy. There are details in the paper that one can argue over. Nonetheless, the authors' analysis suggests that more geologists should climb down from their beloved mountains, to explore the erosion and weathering of the surrounding lowlands.

Geology **41,** 343–346 (2013).



RACHID DAHNOUN/AURORA OPEN/CORBIS IMAGES

SOCIAL SCIENCE

THE MATHEMATICS OF MURDER

Adeline Lo & James H. Fowler (*Nature* 501, 170–171; 2013)

The mass killing on 14 December 2012 at Sandy Hook Elementary School in Newtown, Connecticut, has revived an enduring controversy about gun control in the United States. Gun-control advocates believe that widespread gun ownership increases the rate of gun-related crime and homicide, whereas critics argue that gun availability decreases gun violence because potential assailants are less likely to commit such crimes if they believe citizens are armed. But who is right? Writing in *PLoS ONE*, Wodarz and Komarova describe a mathematical model designed to answer exactly this question. In an extremely cautious way, they suggest that more guns make things worse. This is social science at its very best. Rather than crafting yet another highly abstract formal model, the authors create a model that is directly relevant to this issue. And rather than overly emphasizing their model's results, they conduct an exercise in caution, highlighting the importance of grounding models in sound and accurate assumptions.

PLoS ONE **8,** e71606 (2013).



MICHAEL DURHAM/MINDEN PICTURES/FLPA

FORUM: Genetics

A SOCIAL REARRANGEMENT

(*Nature* 493, 612–613; 2013)

Some worker fire ants (*Solenopsis invicta*) will tolerate multiple queens in their colony, but others only one. It turns out that this behaviour is governed by a gene cluster on an unusual pair of chromosomes. Two scientists describe what these findings mean to the fields of social evolution, genetics and beyond.

GENES AND QUEENS

Andrew F. G. Bourke

Social evolution — the evolution of behaviours that have effects beyond the individual — requires genetic variation to influence social behaviour. The fire ant's social polymorphism is associated with inheritance of variants of the gene *Gp-9*, but Wang *et al.* show that *Gp-9* sits within a supergene containing other genes that are differentially expressed between the two colony forms. The system shows that a multifaceted social trait can be under genetic influence.

CHROMOSOME MYSTERIES

Judith E. Mank

At first glance, it might be difficult to see what, if anything, fire-ant behaviour can tell us about the evolution of sex chromosomes. However, Wang and colleagues show that the fire-ant 'social chromosomes' are, in many ways, similar to X and Y chromosomes. At least one massive inversion on the chromosome that encompasses *Gp-9* prevents recombination between the two chromosome forms, in much the same way as we think inversions might prevent recombination between the X and Y chromosomes.

Nature **493,** 664–668 (2013).

© 2013 Macmillan Publishers Limited. All rights reserved

doi:10.1038/nature12831

Inconsistency in large pharmacogenomic studies

Benjamin Haibe-Kains[1,2], Nehme El-Hachem[1], Nicolai Juul Birkbak[3], Andrew C. Jin[4], Andrew H. Beck[4]*, Hugo J. W. L. Aerts[5,6,7]* & John Quackenbush[5,8]*

Two large-scale pharmacogenomic studies were published recently in this journal. Genomic data are well correlated between studies; however, the measured drug response data are highly discordant. Although the source of inconsistencies remains uncertain, it has potential implications for using these outcome measures to assess gene–drug associations or select potential anticancer drugs on the basis of their reported results.

Patients with cancer often exhibit heterogeneous responses to anticancer treatments, and evidence indicates that response is determined in part by patient-specific alterations in the somatic cancer genome and changes in gene expression[1]. Cancer cell line studies have long been used to test the efficacy of therapeutic agents and to explore genomic factors associated with drug response[2,3]. A number of studies have searched for gene expression signatures predictive of response; however, most only tested a limited number of genes, a small panel of drugs, or assayed drug response in a small number of cell lines[2,4,5].

Results from two large-scale pharmacogenomic studies—the Cancer Genome Project (CGP)[6] and the Cancer Cell line Encyclopedia (CCLE)[7]—were recently reported in this journal. The CGP tested 138 anticancer drugs against 727 cell lines whereas the CCLE tested the response of 24 drugs against 1,036 cell lines (Extended Data Fig. 1); of these, 15 drugs (Extended Data Fig. 1a, b) and 471 cell lines were tested in both (Extended Data Fig. 1d, e). There was overlap between both data sets for mutations in 64 genes (Extended Data Fig. 1g) and expression of 12,153 genes (Extended Data Fig. 1h). The overlap allows assessment of consistency between these independent data sets and the potential to infer genomic models predictive of drug response.

We downloaded, curated and annotated the genomic and pharmacological data from the CGP and CCLE studies (Methods). We first compared expression profiles between the 61 biological replicates in CGP and observed very high correlation (median Spearman's rank correlation of 0.97; Fig. 1a), indicating excellent reproducibility within the same study.

We then compared gene expression profiles of the 471 cell lines shared between studies. Despite the use of different array platforms (Affymetrix GeneChip HG-U133A in CGP and HG-U133PLUS2 in CCLE), the expression profiles of identical cell lines were significantly better correlated than between different cell lines (median correlation of 0.85 versus 0.34 for identical and different cell lines, respectively; two-sided Wilcoxon rank-sum test P value $<1\times10^{-16}$). For 467 cell lines, the most highly correlated gene expression profile was with the same cell line; only four (MOG-G-CCM, SNB19, SW1990 and SW403) were more highly correlated with another cell line (Fig. 1b). This small discordance between the CGP and CCLE is probably due to experimental artefacts, measurement error, or divergence of the four cell lines. We tested consistency based on

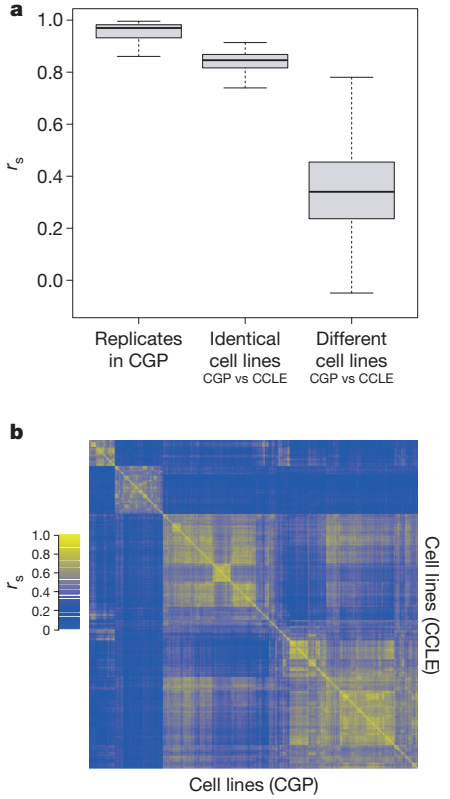


Figure 1 | Consistency between gene expression profiles of cell lines in CGP[6] and CCLE[7] studies. a, Box plot representing the Spearman's rank correlation coefficients of the biological replicates in CGP, and identical and between different cell lines from CGP and CCLE data sets. The box and horizontal bar within represent the interquartile range and median of the correlation coefficients, respectively. The whiskers extend to the most extreme data point, which is no more than 1.5 times the interquartile range from the box. **b**, Heat map representing the Spearman's rank correlations between gene expression profiles of cell lines; the order of cell lines is identical in rows (CCLE) and columns (CGP).

[1]Institut de Recherches Cliniques de Montréal, University of Montreal, Montreal, Quebec, Canada. [2]Ontario Cancer Institute, Princess Margaret Cancer Centre, University Health Network, Toronto, Ontario M5G 2M9, Canada. [3]Center for Biological Sequence Analysis, Department of Systems Biology, Technical University of Denmark, 2800 Kgs. Lyngby, Denmark. [4]Department of Pathology, Beth Israel Deaconess Medical Center and Harvard Medical School, Boston, Massachusetts 02215, USA. [5]Department of Biostatistics and Computational Biology and Center for Cancer Computational Biology, Dana-Farber Cancer Institute, Boston, Massachusetts 02215, USA. [6]Department of Radiation Oncology & Radiology, Dana-Farber Cancer Institute, Brigham and Women's Hospital, Harvard Medical School, Boston, Massachusetts 02215, USA. [7]Department of Radiation Oncology, Maastricht University, Maastricht 6200 MD, The Netherlands. [8]Department of Cancer Biology, Dana-Farber Cancer Institute, Boston, Massachusetts 02215, USA.
*These authors contributed equally to this work.

©2013 Macmillan Publishers Limited. All rights reserved

the tissue from which the cell line was derived (Supplementary Fig. 1). We found the highest correlation with cell lines from the urinary tract (median correlation of 0.87) and the lowest for those of the upper aerodigestive tract (median Spearman's rank correlation of 0.79).

We compared the reported presence of mutations for 64 genes in the shared 471 cell lines and found better agreement between identical cell lines than between different cell lines (two-sided Wilcoxon rank-sum test P value $<1\times10^{-16}$; Extended Data Fig. 2), although not perfect agreement (median Cohen's kappa (κ) of 0.65), which might be due to the different sequencing platforms and software used to call genomic variants in the two studies. Agreement in mutation profiles was higher in pancreatic cell lines, although the difference was not significant (Supplementary Fig. 2).

We then compared drug sensitivity phenotype measurements. In the CGP[6] study, drug screening was performed at two sites: the Massachusetts General Hospital (MGH) and the Wellcome Trust Sanger Institute (WTSI). As a control, camptothecin, an inhibitor of DNA enzyme topoisomerase I, was screened at both sites using the same experimental protocol in 252 cell lines. The IC_{50} (concentration in micromolar (μM) at which the drug inhibited 50% of the maximum cellular growth)[8] for camptothecin had significant but only fair correlation (Spearman's rank correlation coefficient (r_s) = 0.58. P value = 1.5×10^{-23}, Extended Data Fig. 3, see Methods for definition of 'fair' and qualitative description of correlation).

We compared drug sensitivity measures between CGP[6] and CCLE[7] for 15 drugs (Extended Data Fig. 1a, b) tested on the 471 shared cell lines (Extended Data Fig. 1d, e). Both CGP and CCLE measured cell line drug sensitivity using IC_{50} and AUC (area under the activity curve measuring dose response), also referred to as activity area[8]; however, the two studies used different experimental protocols (summarized in Supplementary Information). Differences include the pharmacological assay used, the range of drug concentrations tested, and choice of an estimator for summarizing the drug dose–response curve.

In both studies, the IC_{50} could not be estimated in many cases, as drug concentration necessary to inhibit 50% of growth was not reached. In CGP, IC_{50} was estimated using a Bayesian sigmoid model for drug response. In contrast, CCLE reported the maximum concentration for inactive compounds (referred to as placeholder values) rather than the extrapolated IC_{50}. AUC measures do not require extrapolation and can always be estimated from the dose–response curve.

For each of the 15 drugs assayed by both CGP and CCLE studies, we ranked the response of the 471 shared cell lines (Fig. 2a) and computed Spearman's rank correlation coefficient (see Methods) for the reported IC_{50} (Fig. 2b). We found a single drug, 17AAG (an HSP90 inhibitor), with moderate correlation ($r_s = 0.61$; Extended Data Table 1a), and another, PD0325901 (a MEK inhibitor), with fair correlation ($r_s = 0.53$; Extended Data Table 1a) between studies.

To test whether extrapolation decreased the correlations between studies, we filtered out all IC_{50} values exceeding the maximum tested drug concentrations. We observed only small increases in correlation for PLX4720, PD0325901 and paclitaxel and decreases for 17AAG and AZD6244, although the number of measurements was small (Extended Data Fig. 4). We also compared reported AUC measures (Fig. 2b, Extended Data Table 1b and Extended data Fig. 5) and found that only two drugs yielded fair correlations (17AAG with $r_s = 0.58$ and PD0325901 with $r_s = 0.55$).

We compared correlations computed from IC_{50} and AUC (Fig. 2b) and found that AUC is more concordant between CGP and CCLE (median Spearman's rank correlation of 0.28 and 0.35 for IC_{50} and AUC, respectively)

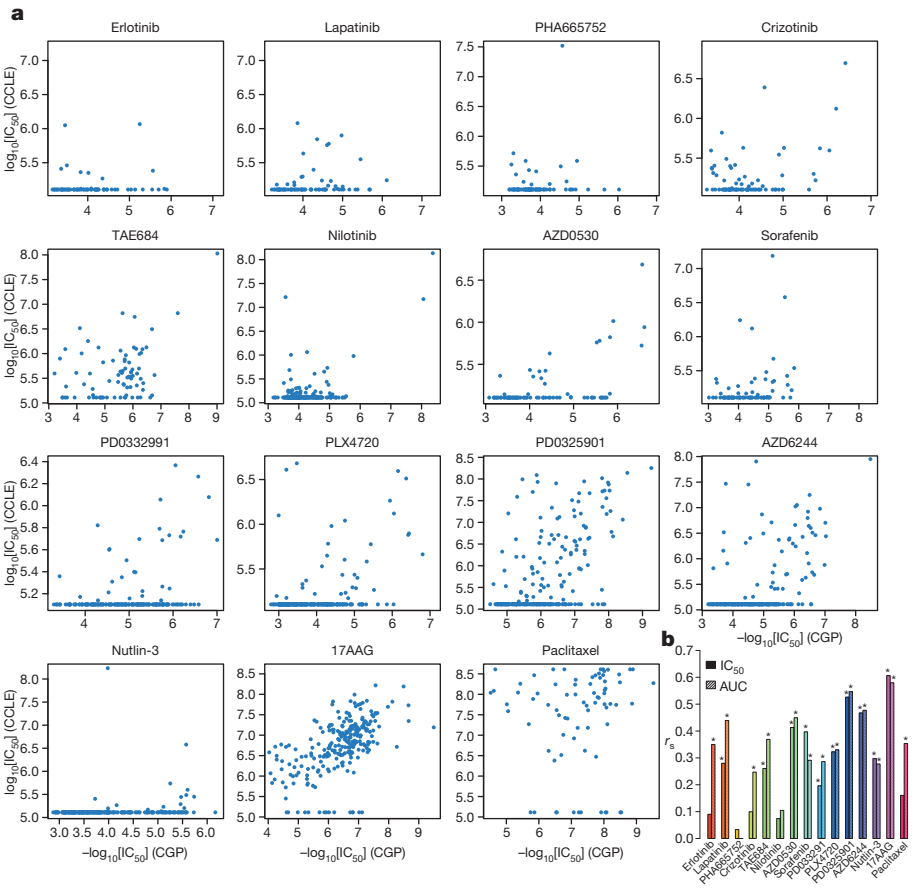


Figure 2 | Consistency between drug sensitivity data published in CGP and CCLE studies. a, Scatter plots reporting the drug sensitivity (IC_{50}) measured in the 471 cell lines and for the 15 drugs investigated both in CGP and CCLE. **b**, Bar plot representing the Spearman's rank correlation coefficient for IC_{50} and AUC drug sensitivity measures; significance is reported using an asterisk if two-sided P value <0.05.

©2013 Macmillan Publishers Limited. All rights reserved

but that the difference was not significant (two-sided Wilcoxon signed rank test P value = 0.3). The vast majority of drugs yielded poor concordance ($r_s < 0.5$) for both IC_{50} and AUC, which suggests that the lack of consistency of the drug response cannot be solely explained by the choice of the estimator of drug sensitivity.

We tested whether drug response correlation depended on tissue source. We found that both IC_{50} and AUC measures tend to be more consistent in cell lines originating from urinary tract (Supplementary Fig. 3); this difference is significant for AUC (two-sided Kruskal–Wallis test P value = 0.024; Supplementary Fig. 3b). However, owing to the small number of urinary tract cell lines (10), only three drugs (PD0325901, nutlin-3 and 17AAG) showed a statistically significant moderate correlation (Supplementary Fig. 4).

In addition to IC_{50} and AUC, we also compared sensitivity using the waterfall method described in the CCLE study[7]. For each compound, we considered the shape of the rank-ordered plot of response values (log-transformed IC_{50} or AUC) to assign cell lines into resistant, intermediate and sensitive classes (referred to as drug sensitivity calls; see Methods). Such drug sensitivity calls were estimated from IC_{50} and AUC values and compared using Cohen's κ (see Methods). Again, the drug sensitivity calls for both IC_{50} and AUC estimates (Supplementary Tables 1 and 2) had a poor agreement between studies ($\kappa < 0.5$; Supplementary Fig. 5).

Despite the discordance in drug sensitivity measures between CGP and CCLE, we tested whether the association between drug response and genomic features might be consistent across data sets. This is important because the identification of genomic predictors of drug response was the primary goal of both the CGP[6] and CCLE[7] studies.

We estimated gene–drug associations by fitting, for each gene, a linear regression model including gene expression as predictor of drug sensitivity, controlled for tissue source (see Methods). Linear models were fitted using both IC_{50} and AUC measures (Supplementary Data 2–5). Here too, we observed poor correspondence between studies; the best correlation with IC_{50} data was observed for PD0325901 and 17AAG (r_s of 0.36 and 0.38, respectively; Fig. 3a, Supplementary Fig. 6 and Extended Data Table 1a); for the vast majority of drugs, correlations were slightly better when AUC measures were used to estimate gene–drug associations, but the best correlation was still poor ($r_s = 0.46$ for PD0325901; Fig. 3a, Extended Data Table 1b and Extended Data Fig. 6). Although correlations significantly depended on tissue source (two-sided Kruskal–Wallis test P value <0.006), only drugs screened in haematopoietic/lymphoma tissue and urinary tract yielded slightly higher correlation than all tissues combined for both IC_{50} and AUC (Supplementary Figs 7 and 8).

We tested whether these poor correlations could be due to genes unrelated to drug sensitivity by focusing on genes statistically associated with drug sensitivity (false discovery rate (FDR) <20%) in at least one data set. Overall, whereas the correlations were better than those computed using all genes, they were still low. For IC_{50}, only AZD6244 and 17AAG yielded a moderate correlation ($r_s = 0.65$ and $r_s = 0.63$, respectively; Fig. 3b, Extended Data Table 1a and Supplementary Fig. 9). Using AUC and this subset of genes, we found that PD0332991 had a fair correlation, and five drugs had a moderate correlation between studies (PD0325901, AZD6244, nilotinib, 17AAG and nutlin-3; Fig. 3b, Extended Data Table 1b and Supplementary Fig. 10). However the correlations for the remaining drugs remained poor (Fig. 3b, Extended Data Table 1 and Supplementary Figs 8 and 9) and did not significantly depend on tissue source (two-sided Kruskal–Wallis test P value >0.064; Supplementary Figs 11 and 12).

We recognize that activation of drug response through specific gene functional classes may be more predictive than individual genes. We

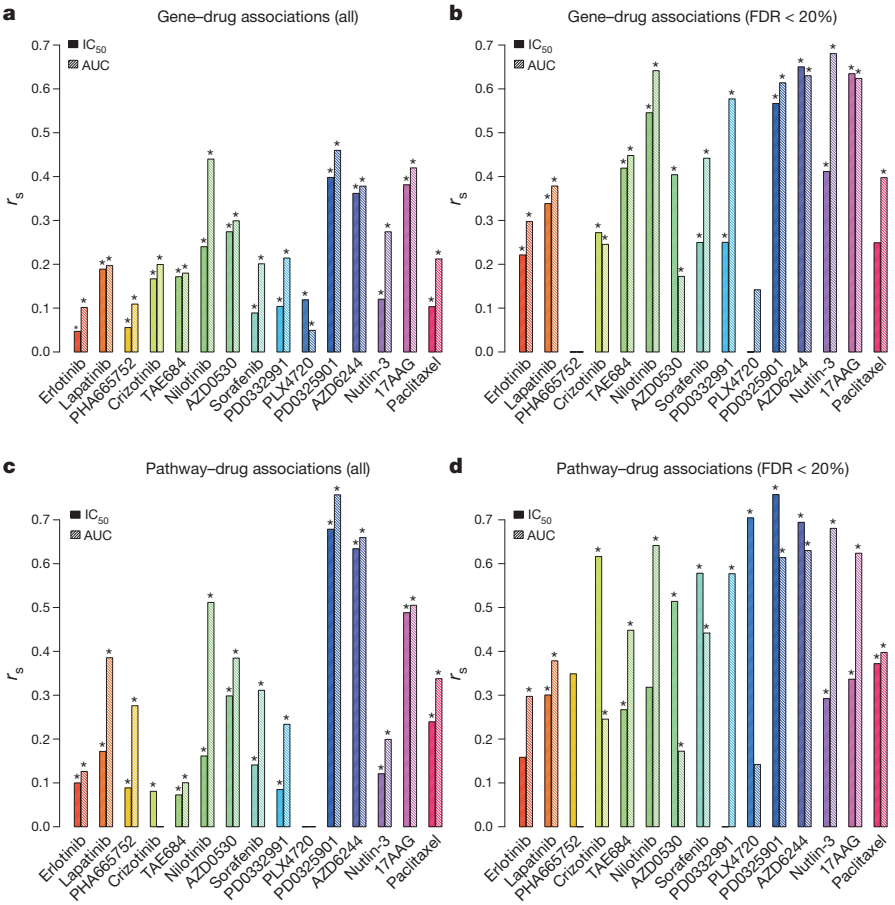


Figure 3 | Consistency of associations of genomics features with drug sensitivity. **a**–**d**, The bars represent the Spearman's rank correlation coefficients computed from all (**a**) and significant (**b**) (FDR <20%) gene–drug associations, and all (**c**) and significant (**d**) (FDR <20%) pathway–drug associations, as estimated in CGP[6] and CCLE[7] data sets. Significance is reported using an asterisk if one-sided P value <0.05.

©2013 Macmillan Publishers Limited. All rights reserved

therefore used the previously computed gene–drug associations to rank genes by the significance of their association with drug sensitivity and searched for over-represented Gene Ontology (GO) terms using pre-ranked gene set enrichment analysis (GSEA)[9]. We compared the normalized enrichment scores computed for CGP and CCLE for the 15 drugs screened in both studies (see Methods).

For IC_{50}, there was poor correlation of GSEA enrichment scores for drugs, except for AZD6244 and PD0325901, which yielded fair correlation ($r_s = 0.63$ for AZD6244 and $r_s = 0.68$ for PD0325901; Fig. 3c, Extended Data Table 1a, Supplementary Fig. 13, and Supplementary Data 6 and 7). When using AUC, two drugs yielded fair correlations (nilotinib and 17AAG), AZD6244 yielded moderate correlation, and PD0325901 yielded substantial correlation ($r_s = 0.76$; Fig. 3c, Extended Data Table 1b, Extended Data Fig. 7, and Supplementary Data 8 and 9). These correlations significantly depended on tissue source (two-sided Kruskal–Wallis test P value $< 7 \times 10^{-4}$; Supplementary Fig. 14) where median drug correlations computed from IC_{50} were higher in breast, urinary tract, haematopoietic/lymphoma and lung cell lines compared to all tissues combined (Supplementary Figs 14 and 15).

We repeated the analyses, this time focused on the GO classes that were statistically significantly enriched (FDR <20% for normalized enrichment score) among genes associated with drug response in at least one of the two studies. Using IC_{50}, most correlations increased slightly, except for 17AAG and PD0332991, with PLX4720 and PD0325901 yielding moderate correlation (Fig. 3c, d, Extended Data Table 1a and Supplementary Fig. 16). For AUC, we observed fair correlation for paclitaxel and sorafenib, moderate correlation only for lapatnib, and substantial correlation for PD0325901 and AZD6244 (Fig. 3d, Extended Data Table 1b and Supplementary Fig. 17).

These pathway-based correlations are the best observed in our analysis as almost half of the drugs exhibited a correlation greater than 0.5, although they are still quite poor. When stratifying by tissue source, only drugs screened in lung cancer cell lines yielded slightly higher median correlation compared to all tissues combined (Supplementary Figs 18 and 19).

We then performed similar analyses using mutation data of the 64 genes sequenced by both CGP and CCLE (Extended Data Fig. 1g). We observed that few mutations were significantly associated with drug response (Supplementary Data 11–13), which partly explains the poor correlation between mutation–drug associations ($r_s < 0.5$; Extended Data Fig. 8 and Supplementary Figs 20 and 21).

To test whether genomic data or drug response measures are the likely source of the poor correlations, we used identical (therefore perfectly correlated) gene expression data for the 471 cell lines while keeping the original drug sensitivity measures in each study, but did not find improved correlations for (significant) gene–drug associations (see 'GeneCGP fixed' and 'GeneCCLE fixed' in Fig. 4). However, when using identical drug phenotypes with the original gene expression data, correlations significantly increased in all cases (two-sided Kruskal–Wallis test P value <0.01, see 'DrugCGP fixed' and 'DrugCCLE fixed' in Fig. 4) and yielded almost perfect correlation for significant gene–drug associations with AUC (median Spearman's rank correlation >0.83). Results were similar for pathway–drug associations (Supplementary Fig. 22). These results clearly demonstrate that the discordance between studies stems from the drug sensitivity measurements.

We also investigated the impact of the choice of pharmacological assay across study and compared CGP and CCLE drug sensitivity data with those published in ref. 10 in a panel of 319 cell lines (the GlaxoSmithKline cell line collection (GSK)). Reference 10 used the same pharmacological assay used by the CCLE (Cell Titer Glo Luminescent Cell Viability Assay kit from Promega), but other parameters in the experimental protocols differ from those in either CGP[6] or CCLE[7] and yet another model was used to estimate IC_{50} values (model 205 in XLfit in Microsoft Excel).

Among the 15 drugs shared between CGP and CCLE, only two, lapatinib and paclitaxel, were tested by the GSK study[10] on a common set of 194 cell lines. As might be expected based on the assay used, the

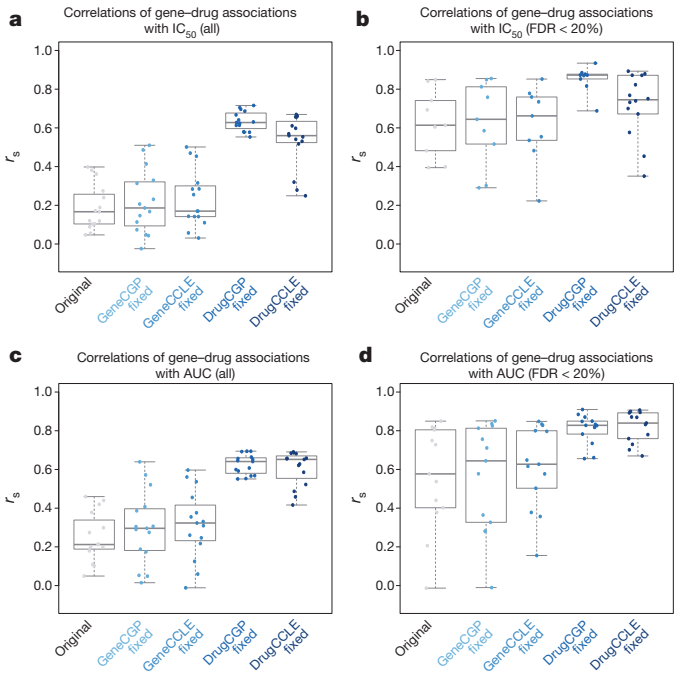


Figure 4 | Effects on consistency by intermixing CGP[6] and CCLE[7] data. **a–d**, The box plots report the correlations between all (**a**) and significant (**b**) (FDR <20%) gene–drug associations with IC_{50}, and all (**c**) and significant (**d**) (FDR <20%) gene–drug associations with AUC. Each box represents the data sets used to compute correlations: 'Original' refers to the original data sets; 'GeneCGP fixed' refers to ($CGP_g + CGP_d$) versus ($CGP_g + CCLE_d$); 'GeneCCLE fixed' refers to ($CCLE_g + CGP_d$) versus ($CCLE_g + CCLE_d$); 'DrugCGP fixed' refers to ($CGP_g + CGP_d$) versus ($CCLE_g + CGP_d$); 'DrugCCLE fixed' refers to ($CGP_g + CCLE_d$) versus ($CCLE_g + CCLE_d$) where subscript g and d stand for gene expression and drug sensitivity data, respectively. The box and horizontal bar within represent the interquartile range and median of the Spearman's rank correlation coefficients, respectively. The whiskers extend to the most extreme data point, which is no more than 1.5 times the interquartile range from the box.

GSK data set IC_{50} measurements were more consistent with those of CCLE ($r_s = 0.42$ and 0.36 for lapatinib and paclitaxel, respectively; Supplementary Fig. 23a) than CGP ($r_s = 0.24$ and 0.10 for lapatinib and paclitaxel, respectively; Supplementary Fig. 23b), but here too the overall consistency was rather poor (and similar to the observed consistency between CCLE and CGP).

We then performed the same analysis but focusing on drugs and cell lines shared only by two studies. For lapatinib and paclitaxel, screened by CCLE and the GSK data set in 249 common cell lines, we observed fair to poor correlations (Extended Data Fig. 9a). Five drugs and 231 cell lines were screened both in CGP and the GSK data set[10] (Extended Data Fig. 1c); for these we observed poor correlation (r_s ranging from 0.12 to 0.30; Extended Data Fig. 9b).

These results add further evidence that the inconsistency between studies stems from the use of different pharmacological assays, but there is no clear evidence to conclude which of the three approaches is more accurate. Indeed, even if we observed perfect correlation between the GSK data set[10] and either the CGP[6] or CCLE[7] drug response assays, all that would indicate is a consistency in measurement, but not necessarily which provided the most meaningful assay of drug response or which could best be translated to *in vivo* response.

Our analysis of these three large-scale pharmacogenomic studies points to a fundamental problem in assessment of pharmacological drug response. Although gene expression analysis has long been seen as a source of 'noisy' data, extensive work has led to standardized approaches to data collection and analysis and the development of robust platforms for measuring expression levels. This standardization has led to substantially

©2013 Macmillan Publishers Limited. All rights reserved

higher quality, more reproducible expression data sets, and this is evident in the CCLE and CGP data where we found excellent correlation between expression profiles in cell lines profiled in both studies.

The poor correlation between drug response phenotypes is troubling and may represent a lack of standardization in experimental assays and data analysis methods. However, there may be other factors driving the discrepancy. As reported by the CGP, there was only a fair correlation ($r_s < 0.6$) between camptothecin IC_{50} measurements generated at two sites using matched cell line collections and identical experimental protocols. Although this might lead to speculation that the cell lines could be the source of the observed phenotypic differences, this is highly unlikely as the gene expression profiles are well correlated between studies.

Although our analysis has been limited to common cell lines and drugs between studies, it is not unreasonable to assume that the measured pharmacogenomic response for other drugs and cell lines assayed are also questionable. Ultimately, the poor correlation in these published studies presents an obstacle to using the associated resources to build or validate predictive models of drug response. Because there is no clear concordance, predictive models of response developed using data from one study are almost guaranteed to fail when validated on data from another study[11], and there is no way with available data to determine which study is more accurate. This suggests that users of both data sets should be cautious in their interpretation of results derived from their analyses.

Clearly the investment in these projects warrants additional work to resolve the discrepancies in drug response phenotype so that the wealth of data that has been generated can be used to its fullest advantage. Our findings support the need for standardization of drug-response measurements or development of new, robust drug sensitivity assays; without such assays, it will not be possible to identify reliably genomic predictors of drug response or to identify effectively a drug's mechanism of action.

METHODS SUMMARY

To ensure reproducibility of our analysis, we developed an automated pipeline in R that can generate all the results, figures and tables of the paper (Supplementary Data 1). Gene expression, mutation and drug sensitivity data were downloaded from the CGP (http://www.cancerrxgene.org), CCLE (http://www.broadinstitute.org/ccle/) and GlaxoSmithKline (http://cbiit.nci.nih.gov/ncip) websites. Drug sensitivity measures, which are IC_{50} and AUC values, were set to a common scale ($-\log_{10}$(M) for IC50 and [0,1] for AUC) across studies. We assessed the gene/mutation–drug associations using a linear regression model controlled for tissue source. We used these associations to generate drug-specific gene ranking for pre-ranked gene set enrichment analyses (GSEA[9]). We used Spearman's rank correlation coefficients (r_s)[12] to assess consistency between CGP and CCLE with qualitative descriptions of r_s values associated with intervals: $r_s < 0.5$, poor; $0.5 \le r_s < 0.6$, fair; $0.6 \le r_s < 0.7$, moderate; $0.7 \le r_s < 0.8$, substantial; and $r_s \ge 0.8$, almost perfect consistency.

Online Content Any additional Methods, Extended Data display items and Source Data are available in the online version of the paper; references unique to these sections appear only in the online paper.

Received 15 April; accepted 7 November 2013.
Published online 27 November 2013.

1. Roden, D. M. & George, A. L. Jr. The genetic basis of drug response. *Nature* **1,** 37–44 (2002).
2. Shoemaker, R. H. The NCI60 human tumour cell line anticancer drug screen. *Nature Rev. Cancer* **6,** 813–823 (2006).
3. Weinstein, J. N. Drug discovery: Cell lines battle cancer. *Nature* **483,** 544–545 (2012).
4. Heiser, L. M. *et al.* Subtype and pathway specific responses to anticancer compounds in breast cancer. *Proc. Natl Acad. Sci. USA* **109,** 2724–2729 (2012).
5. Yamori, T. Panel of human cancer cell lines provides valuable database for drug discovery and bioinformatics. *Cancer Chemother. Pharmacol.* **52** (Suppl. 1), 74–79 (2003).
6. Garnett, M. J. *et al.* Systematic identification of genomic markers of drug sensitivity in cancer cells. *Nature* **483,** 570–575 (2012).
7. Barretina, J. *et al.* The Cancer Cell Line Encyclopedia enables predictive modelling of anticancer drug sensitivity. *Nature* **483,** 603–607 (2012).
8. Wu, R. & Lin, M. *Statistical and Computational Pharmacogenomics* (Chapman and Hall/CRC, 2010).
9. Subramanian, A. *et al.* Gene set enrichment analysis: A knowledge-based approach for interpreting genome-wide expression profiles. *Proc. Natl Acad. Sci. USA* **102,** 15545–15550 (2005).
10. Greshock, J. *et al.* Molecular target class is predictive of *in vitro* response profile. *Cancer Res.* **70,** 3677–3686 (2010).
11. Papillon-Cavanagh, S. *et al.* Comparison and validation of genomic predictors for anticancer drug sensitivity. *J. Am. Med. Inform. Assoc.* **20,** 597–602 (2013).
12. Spearman, C. The proof and measurement of association between two things. *Int. J. Epidemiol.* **39,** 1137–1150 (2010).

Supplementary Information is available in the online version of the paper.

Acknowledgements We thank J. Archambault for his insightful comments on the comparative study between experimental protocols used in the large pharmacogenomic studies investigated in this work. The authors would like to thank the investigators of the Cancer Genome Project, the Cancer Cell Line Encyclopedia and the GlaxoSmithKline cell line study who have made their invaluable data available to the scientific community. N.E.-H. was supported by an IRCM doctoral fellowship. A.H.B. was supported by an award from the Klarman Family Foundation and by support from NIH grant CA087969. N.J.B. was funded The Villum Kann Rasmussen Foundation. J.Q. was supported grants from the Dr Miriam and Sheldon G. Adelson Medical Research Foundation and from the NCI GAME-ON Cancer Post-GWAS initiative (U19 CA148065-01).

Author Contributions B.H.-K. conceived the study with major contributions from N.J.B., H.J.W.L.A. and J.Q. B.H.-K. and N.E.-H. collected and curated the gene expression profiles and drug phenotypic data. A.C.J. and A.H.B. collected and curated the mutation data. B.H.-K. performed all the analyses and wrote the code with contributions from N.E.-H. and A.C.J. N.E.-H., A.C.J. and A.H.B. compared the experimental protocols of the pharmacogenomic studies. B.H.-K., A.H.B., H.J.W.L.A. and J.Q. supervised the study. B.H.-K., A.H.B., H.J.W.L.A. and J.Q. wrote the manuscript with contributions from N.E.-H. and N.J.B. All authors discussed the results and commented on the manuscript.

Author Information The R code enables one to download and process the pharmacogenomic data and to generate all the results presented in the paper and its Supplementary Information. Reprints and permissions information is available at www.nature.com/reprints. The authors declare no competing financial interests. Readers are welcome to comment on the online version of the paper. Correspondence and requests for materials should be addressed to B.H.-K. (bhaibeka@uhnresearch.ca).

©2013 Macmillan Publishers Limited. All rights reserved

METHODS

To ensure reproducibility of our analysis, we developed an automated pipeline in R that can generate all the results, figures and tables of the paper (Supplementary Data 1).

Data retrieval and curation. We retrieved and curated data from three large pharmacogenomic studies, namely the Cancer Genome Project (CGP)[6], the Cancer Cell Line Encyclopedia (CCLE)[7] and the GlaxoSmithKline cell line collection (ref. 10).

For CGP, gene expression data (raw Affymetrix CEL files) were downloaded from ArrayExpress (http://www.ebi.ac.uk/arrayexpress/experiments/E-MTAB-783/). Drug sensitivity measurements, mutation data and cell lines annotations were downloaded from the CGP website (http://www.cancerrxgene.org/downloads/). Drug information was collected from Supplementary Information of ref. 6. Minimum and maximum screening concentrations (μM) for each drug/cell line were extracted from gdsc_compounds_conc_w2.csv available on the CGP website. The natural logarithm of IC_{50} measurements were retrieved from column '*_IC_50' of gdsc_manova_input_w2.csv available on the CGP website. The AUC measurements were retrieved from gdsc_manova_input_w2.csv in column '*_AUC'. Coding variants in 68 genes were also extracted from gdsc_manova_input_w2.csv.

For CCLE, gene expression, mutation data cell line annotations and drug information were downloaded from the CCLE website (http://www.broadinstitute.org/ccle). Drug sensitivity data were downloaded from the addendum published by ref. 13. Screening concentrations (μM) for each drug/cell line were extracted from Supplementary Table 11 in column 'Doses (μM)'. IC_{50} measurements were retrieved from Supplementary Table 11 in column 'IC_{50} μM (norm)'. AUC measurements were retrieved from Supplementary Table 11 in column 'ActArea (norm)'. Coding variants in 1,667 genes (column 'Protein Change') measured using the Oncomap3 and hybrid capture platforms were extracted from CCLE_Oncomap3_2012-04-09.maf and CCLE_hybrid_capture1650_hg19_NoCommonSNPs_NoNeutralVariants_CDS_2012.05.07.maf, respectively.

For the GlaxoSmithKline cell line collection, gene expression data and cell line annotations were downloaded from the National Cancer Informatics Program website (http://cbiit.nci.nih.gov/ncip). IC_{50} measurements and drug information were downloaded from Supplementary Table 2 (stab_2.xls) of ref. 10.

Cell line annotations. Cell line names were harmonized in CGP, CCLE and GSK to match identical cell lines; this was done through manual search over alternative names of cell lines, as reported in the corresponding cell line annotation files and online databases such as hyperCLDB (http://bioinformatics.istge.it/hypercldb/) and BioInformationWeb (http://bioinfoweb.com). We identified 471 cancer cell lines being investigated both in CGP and CCLE, 231 cell lines shared between CGP and GSK, 249 cell lines shared between CCLE and GSK, and 194 cell lines shared by all three studies (Extended Data Fig. 1c). To annotate the tissue of origin of each cell line, we chose the nomenclature used in CGP; CCLE and GSK tissue type information was therefore updated to follow this nomenclature, which resulted in 24 tissue types.

Drug sensitivity data. Drug sensitivity measures, which are IC_{50} and AUC values, were set to common scale ($-\log_{10}$(M) for IC_{50} and [0,1] for AUC) across studies so that high values are representative of cell line sensitivity to drugs. For CGP, extracted IC_{50} measures (x) were transformed using $-\log_{10}(\exp(x)/10^6)$, and AUC measures were left untransformed. For CCLE, extracted IC_{50} measures (x) were transformed into logarithmic scale, $-\log_{10}(x/10^6)$, and AUC measures were divided by the number of drug concentrations tested (8). For GSK, extracted IC_{50} measures (x) were transformed using $-\log_{10}(x/10^3)$.

We also discretized the drug sensitivity measures into three categories (resistant, intermediate and sensitive) using the waterfall method described in the CCLE study[7]. The full procedure, as provided by K. Venkatesan (personal communication), is described below. (1) Extract the drug sensitivity measurements, either IC_{50} or AUC. (2) Sort increasing log IC_{50} values (or AUC) of the cell lines to generate a waterfall distribution. (3) If the waterfall distribution is nonlinear (Pearson correlation coefficient to the linear fit ≤0.95), estimate the major inflection point of the log IC_{50} curve as the point on the curve with the maximal distance to a line drawn between the start and end points of the distribution. (4) If the waterfall distribution appears linear (Pearson correlation coefficient to the linear fit >0.95), then use the median IC_{50} instead. (5) Cell lines within a fourfold IC_{50} (or within a 1.2-fold AUC) difference centred around this inflection point are classified as being intermediate, cell lines with lower IC_{50} (or AUC) values than this range are defined as sensitive, and those with IC_{50} (or AUC) values higher than this range are called resistant. (6) Require at least $x = 5$ sensitive and $x = 5$ resistant cell lines after applying these criteria.

Using this approach we generated drug sensitivity calls for all drugs in CGP and CCLE (Supplementary Tables 1 and 2).

Gene expression data. Raw gene expression profiles (Affymetrix CEL format) for 789 CGP, 1,036 CCLE and 950 cell lines were downloaded, respectively, from ArrayExpress[14] (E-MTAB-783), CCLE (http://www.broadinstitute.org/ccle/) and NCIP (http://cbiit.nci.nih.gov/ncip) websites. Gene expression data were normalized with frozen RMA[15] using the Bioconductor Chip Description File (CDF) definitions (hthgu133a from CGP, and hgu133plus2 for CCLE and GSK). We then used the R package jetset[16], which maps Affymetrix probe sets to unique Entrez gene IDs by selecting the best probe set for each gene; subsequent analyses were restricted to the 12,153 probe sets common to the CGP, CCLE and GSK arrays. For replicates in CGP and GSK, the CEL files were ordered by hybridization date and the first experiment was selected. To compare gene expression profiles of cell lines 1,000 genes with the most variant expression values were selected in CGP and CCLE data sets (471 shared cell lines; Extended Data Fig. 1d).

Mutation data. Missense mutations in 64 protein-coding genes sequenced in 431 cell lines both in CGP and CCLE were downloaded from their respective website. Similarly to CGP and CCLE studies[6,7], mutation data were discretized to represent the presence or absence of missense mutation in a given gene in a given cell line.

Gene–drug associations. We assessed the association between gene expression and drug response, referred to as gene–drug association, using a linear regression model controlled for tissue source:

$$Y = \beta_0 + \beta_i G_i + \beta_t T$$

where Y denotes the drug sensitivity variable, G_i and T denote the expression of gene i and the tissue type, respectively, and β values are the regression coefficients. The strength of gene–drug association is quantified by β_i, above and beyond the relationship between drug sensitivity and tissue source. The variables Y and G are scaled (standard deviation equals to 1) to estimate standardized coefficients from the linear model. Significance of the gene–drug association is estimated by the statistical significance of β_i (two-sided t-test).

Pathway–drug associations. For each drug, genes were ranked according to the statistical significance of their gene–drug association (Student's t statistic). We then used this drug-specific gene ranking to perform pre-ranked gene set enrichment analyses (GSEA[9] version 2.0.13) to assess enrichment of gene ontology terms[17] curated in MSigDB[9] (c5.all.v4.0.entrez.gmt). Only pathways for which corresponding gene sets contained between 15 genes and 250 genes were considered for further analysis (913 gene sets). We used the resulting normalized enrichment (NES[9]) scores to quantify the strength of pathway–drug associations.

Measures of consistency. We computed Spearman's rank correlation coefficients (r_s)[12] to assess the consistency between CGP and CCLE drug phenotypes (IC_{50} and AUC measures), gene/mutation–drug associations (coefficient β) and pathway–drug associations (normalized enrichment scores). We used Cohen's kappa (κ) coefficient[18] to assess consistency between CGP and CCLE drug sensitivity calls (resistant, intermediate, sensitive) and mutation data. We used the following qualitative descriptions of correlation coefficient (r_s) values associated with intervals: $r_s < 0.5$, poor consistency; $0.5 \le r_s < 0.6$, fair consistency; $0.6 \le r_s < 0.7$, moderate consistency; $0.7 \le r_s < 0.8$, substantial consistency; and $r_s \ge 0.8$, almost perfect consistency. Same qualitative descriptions were used for Cohen's kappa (κ) coefficient.

13. Barretina, J. *et al.* Addendum: The Cancer Cell Line Encyclopedia enables predictive modelling of anticancer drug sensitivity. *Nature* **492,** 290 (2012).
14. Parkinson, H. *et al.* ArrayExpress–a public database of microarray experiments and gene expression profiles. *Nucleic Acids Res.* **35,** D747–D750 (2007).
15. McCall, M. N., Bolstad, B. M. & Irizarry, R. A. Frozen robust multiarray analysis (fRMA). *Biostatistics* **11,** 242–253 (2010).
16. Li, Q., Birkbak, N. J., Győrffy, B., Szallasi, Z. & Eklund, A. C. Jetset: selecting the optimal microarray probe set to represent a gene. *BMC Bioinformatics* **12,** 474 (2011).
17. Ashburner, M. *et al.* Gene ontology: tool for the unfication of biology. *Nature Genet.* **25,** 25–29 (2000).
18. Sim, J. & Wright, C. C. The kappa statistic in reliability studies: use, interpretation, and sample size requirements. *Phys. Ther.* **85,** 257–268 (2005).

©2013 Macmillan Publishers Limited. All rights reserved

ARTICLE

doi:10.1038/nature12776

Astrocytes mediate synapse elimination through MEGF10 and MERTK pathways

Won-Suk Chung[1], Laura E. Clarke[1]*, Gordon X. Wang[2]*, Benjamin K. Stafford[3], Alexander Sher[4], Chandrani Chakraborty[1], Julia Joung[1], Lynette C. Foo[5], Andrew Thompson[6], Chinfei Chen[6], Stephen J. Smith[2] & Ben A. Barres[1]

To achieve its precise neural connectivity, the developing mammalian nervous system undergoes extensive activity-dependent synapse remodelling. Recently, microglial cells have been shown to be responsible for a portion of synaptic pruning, but the remaining mechanisms remain unknown. Here we report a new role for astrocytes in actively engulfing central nervous system synapses. This process helps to mediate synapse elimination, requires the MEGF10 and MERTK phagocytic pathways, and is strongly dependent on neuronal activity. Developing mice deficient in both astrocyte pathways fail to refine their retinogeniculate connections normally and retain excess functional synapses. Finally, we show that in the adult mouse brain, astrocytes continuously engulf both excitatory and inhibitory synapses. These studies reveal a novel role for astrocytes in mediating synapse elimination in the developing and adult brain, identify MEGF10 and MERTK as critical proteins in the synapse remodelling underlying neural circuit refinement, and have important implications for understanding learning and memory as well as neurological disease processes.

Astrocytes constitute at least one-third of human brain cells, yet we do not completely understand their function[1]. To understand their functions better, we previously performed gene expression analysis on purified mouse astrocytes and found that they are enriched in genes for phagocytic pathways[2], including two phagocytic receptors, *Megf10* and *Mertk*. MEGF10 is an orthologue of *Drosophila* Draper[3,4] and *Caenorhabditis elegans* CED-1 (ref. 5) that help to mediate axon pruning by glia cells in flies and phagocytosis of apoptotic cells in nematodes. MEGF10 has also been shown to mediate phagocytosis *in vitro*[6] and *in vivo*[7], and the function of MEGF10 requires other proteins, such as GULP1 and ABCA1 (refs 6, 8). MERTK is a member of the MER/AXL/TYRO3 receptor kinase family that mediates shedding of the photoreceptor outer segment by retinal pigment epithelial cells[9,10]. MERTK works with the integrin pathway[11] to regulate CrKII/DOCK180/Rac1 modules in controlling rearrangement of the actin cytoskeleton on phagocytosis[12]. Both MEGF10 and MERTK function as engulfment receptors by recognizing 'eat me signals', such as phosphatidylserine, presented in target debris[13,14]. Because astrocytes highly express phagocytic receptors as well as all their other interacting proteins listed above[2], and one astrocyte has been shown to ensheath thousands of synapses, we reasoned that astrocytes mediate synapse elimination within the developing and adult central nervous system (CNS) through the MEGF10 and/or MERTK phagocytic pathways.

Localization of MEGF10 and MERTK to astrocytes

We first investigated whether MEGF10 and MERTK proteins were present in astrocytes *in vivo*. We found that MEGF10 protein was localized to developing astrocytes visualized by *Aldh1l1-EGFP* transgene expression[2] in the postnatal day 5 (P5) dorsal lateral geniculate nucleus (dLGN) (Fig. 1a). Staining for β-galactosidase driven by the endogenous *Megf10* locus in *Megf10*$^{-/-}$ alleles confirmed specific expression by astrocytes (Fig. 1b). MERTK protein expression was highly localized to developing astrocytes in the P5 dLGN (Fig. 1c), as well as to microglia and endothelial cells (Extended Data Fig. 1). Functional MEGF10 and MERTK proteins were absent in the *Megf10*$^{-/-}$ and *Mertk*$^{-/-}$ postnatal brains (Fig. 1f), confirming the specificity of antibodies. Both *Megf10* and *Mertk* messenger RNA expression and immunoreactivity persisted in adult astrocytes (data not shown and Extended Data Fig. 2).

Astrocytes phagocytose synapses *in vitro* and *in vivo*

We next investigated whether astrocytes could phagocytose synapses and neural debris *in vitro*. Using purified astrocytes with the immunopanning method[15], we developed an *in vitro* engulfment assay, where we cultured astrocytes in the presence of synaptosomes, which are isolated nerve terminals, and found that astrocytes efficiently engulfed synaptosomes (Fig. 1d and Supplementary Video 1). To determine whether these engulfed synaptosomes were targeted to lysosomes, we conjugated the synaptosomes with a pH-sensitive dye, pHrodo, and found that pHrodo-conjugated synaptosomes were efficiently engulfed by astrocytes where they produced bright-red fluorescence (Fig. 1e). The engulfment ability of astrocytes was highly dependent on the presence of secreted factors, as addition of astrocyte-conditioned media (ACM), 5% serum or protein S (a bridging molecule that bridges phosphatidylserine–MERTK interaction)[9] greatly increased the amount of synaptosomes engulfed by astrocytes, whereas addition of fresh media (unconditioned astrocyte growth media, AGM) did not (Fig. 1g). These findings indicate that astrocytes have strong phagocytic capacity that is regulated by secreted, extracellular molecules.

Next, we purified astrocytes from the *Megf10*$^{-/-}$ and *Mertk*$^{-/-}$ postnatal cerebral cortex and performed the *in vitro* engulfment assay. Using image (Fig. 1h) and fluorescence-activated cell sorting (FACS) (Extended Data Fig. 3a, c, e) analysis, we found that *Megf10*$^{-/-}$ and *Mertk*$^{-/-}$ astrocytes each displayed about 50% reduction in their relative engulfment ability. We also compared the phagocytic capacity of enriched microglial populations using FACS analysis, and found

[1]Department of Neurobiology, Stanford University, School of Medicine, Stanford, California 94305, USA. [2]Department of Molecular and Cellular Physiology, Stanford University, School of Medicine, Stanford, California 94305, USA. [3]Department of Ophthalmology and Visual Sciences, University of Michigan, Ann Arbor, Michigan 48105, USA. [4]Santa Cruz Institute of Particle Physic and Department of Physics, University of California, Santa Cruz, California 95064, USA. [5]Institute of Molecular and Cell Biology, A *Star, 61 Biopolis Drive, Proteos Building, 138673 Singapore. [6]Children's Hospital, Harvard Medical School, 300 Longwood Avenue, CLS12250, Boston, Massachusetts 02115, USA.
*These authors contributed equally to this work.

©2013 Macmillan Publishers Limited. All rights reserved

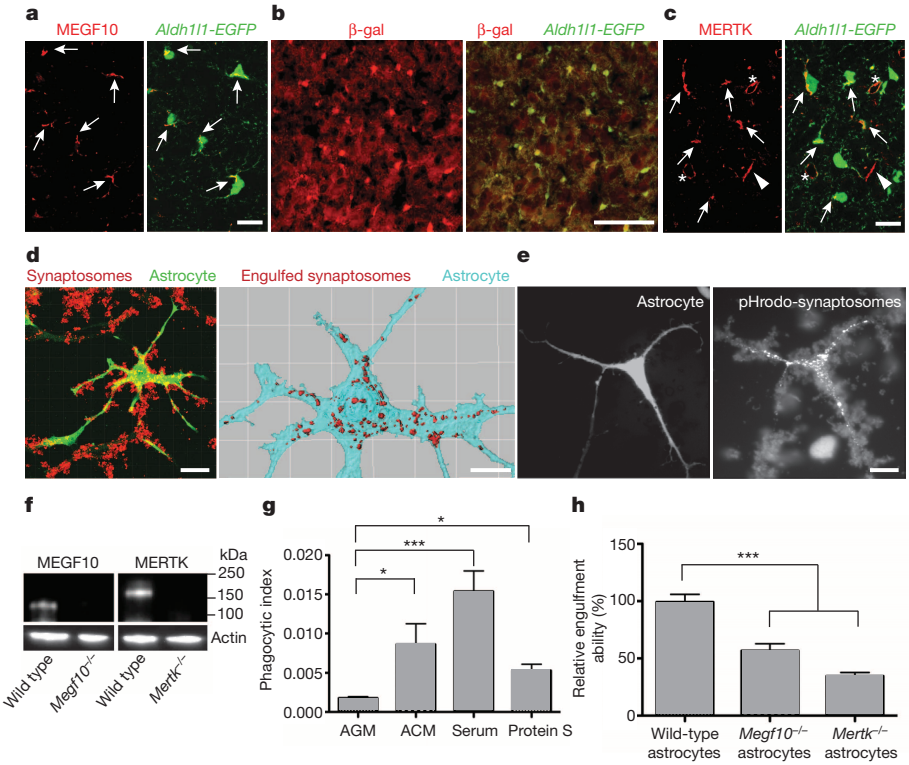


Figure 1 | Localization of MEGF10 and MERTK to astrocytes and their phagocytic roles in purified astrocytes. **a**, Confocal images showing specific MEGF10 (red) localization to astrocytes (green, arrows). **b**, β-gal (red) expression driven by endogenous *Megf10* locus in astrocytes (green). **c**, Confocal images showing MERTK (red) localization to astrocytes (green, arrows) as well as microglia (arrowheads) and endothelial cells (asterisks). **d**, Three-dimensional surface rendering before (left) or after (right) subtracting synaptosomes (red) outside of the astrocytic volume (cyan). **e**, pHrodo-conjugated synaptosomes (right) engulfed by astrocytes (left). **f**, Western blotting showing the absence of functional MEGF10 and MERTK proteins in the brains of P5 *Megf10*$^{-/-}$ and *Mertk*$^{-/-}$ mice, respectively. **g**, Compared to AGM, addition of ACM, 5% serum or protein S significantly increased the phagocytic index of astrocytes. **h**, Purified *Megf10*$^{-/-}$ and *Mertk*$^{-/-}$ astrocytes showed a 42% and 64% reduction in the engulfment ability, respectively. Representative data from three independent experiments are shown (**g**, **h**). $*P < 0.05$, $***P < 0.001$, one-way ANOVA. Error bars indicate s.e.m. Scale bar: 20 μm (**a**, **c**, **d** (left), **e**); 100 μm (**b**); 10 μm (**d** (right)).

that unlike *Megf10*$^{-/-}$ microglia (Extended Data Fig. 3b, f), *Mertk*$^{-/-}$ microglia exhibited a 25% reduction in the relative engulfment ability (Extended Data Fig. 3d, f). Thus, MEGF10 and MERTK are each required for astrocyte-mediated phagocytosis.

To find out whether astrocytes, and their MEGF10 and MERTK pathways, mediate developmental synapse elimination *in vivo*, we took advantage of the retinogeniculate system, a classical model of developmental synapse elimination[16,17]. Initially, axonal projections from retinal ganglion cells (RGCs) form excessive synapses with neurons in the dLGN. During the first week of postnatal development, projections from the contra- and ipsilateral eyes are segregated in the dLGN, so that a single LGN neuron receives RGC inputs from only one eye. Subsequently, all but one or two RGC inputs onto each LGN neuron are removed and the remaining RGC inputs are stabilized. Both of these synapse refinement processes are dependent on spontaneous retinal wave activity[17,18], although how neural activity promotes elimination of synapses is not well understood.

To visualize synapse elimination, RGC projections and their presynaptic compartments were labelled by injecting Alexa594- and Alexa647-conjugated CTB (CTB-594 and CTB-647) into the contra- and ipsilateral eyes of *Aldh1l1-EGFP* transgenic mice at P4, respectively (Fig. 2a). The dLGNs were subsequently imaged at P6 using confocal microscopy (Fig. 2b). Notably, we found a significant amount of CTB-labelled neural debris inside of EGFP-expressing astrocytes (Fig. 2c). Most of the CTB-labelled neural debris engulfed by astrocytes co-localized with LAMP2, a specific marker for late endosome/lysosomes (Fig. 2d)[19], indicating that they are in the process of active degradation.

To find out whether the neural debris engulfed by astrocytes contained synaptic material, first, we used confocal and structured illumination microscopy to examine the P5 dLGN. We found that antibodies to specific presynaptic proteins, including synaptophysin and VGlut2 (Extended Data Fig. 4), whose mRNAs are not expressed at all by astrocytes[2], labelled puncta present within astrocytes. Using array tomography (AT), a super-resolution imaging technique visualizing synaptic protein expression with sub-100-nm volumetric resolution[20], we found that astrocytes engulfed much of the CTB-labelled debris as well as synaptic material immunolabelled for both presynaptic (Bassoon) and postsynaptic (PSD-95 and GluR1) proteins (Extended Data Fig. 5). Moreover, putative synapses that contained both CTB-positive presynaptic, and PSD-95-positive (Fig. 2e) or GluR1-positive (Fig. 2f) postsynaptic proteins were frequently found adjoined together inside of astrocytes, indicating that entire synapses had been engulfed. To examine cellular details of the engulfed synapses by astrocytes, the P5 dLGN was also imaged with serial block-face scanning electron microscopy (SBEM, Fig. 2g–j). We found many incidents showing double-membrane-bound inclusions with vesicles that are the same size as the presynaptic vesicles (Fig. 2g–j) being completely surrounded by astrocytic cytoplasm identified by the presence of glycogen granules (Fig. 2j and Supplementary Video 2)[21]. The inner membrane of the engulfed presynaptic material within astrocytes displayed irregular morphology (Fig. 2h, i), suggesting that the material was in the process of active degradation. Some of the inclusion seems to be in the further process of degradation as it was found in structures with the characteristics of lysosomal bodies[21] (Fig. 2h–j). These data indicate that astrocytes actively engulf synapses and suggest that astrocytes are actively helping to mediate retinogeniculate refinement.

We next developed an image-processing algorithm that allowed us to visualize only the engulfed puncta inside of astrocytes (Fig. 3a). By measuring the phagocytic index at different time points, we found that the highest amount of astrocyte-mediated phagocytosis occurs at the peak period of eye-specific segregation before P6 (Fig. 3d), indicating that there is a critical developmental time window for synapse elimination by astrocytes.

To determine whether MEGF10 and MERTK are required for astrocyte-mediated synapse elimination, we next measured the phagocytic index of astrocytes in the *Megf10*$^{-/-}$ and *Mertk*$^{-/-}$ dLGNs (Fig. 3b, c). As we had observed *in vitro*, we found that astrocytes *in vivo* in the *Megf10*$^{-/-}$ and *Mertk*$^{-/-}$ dLGNs displayed a 45% and 58% reduction, respectively, in their relative engulfment ability compared to wild type (Fig. 3e). Furthermore, astrocytes in the *Megf10*$^{-/-}$; *Mertk*$^{-/-}$ dLGNs showed a further decrease in their relative engulfment ability of about 85% (Fig. 3e), indicating that MEGF10 and MERTK work in parallel to mediate synapse elimination in developing brains.

Recently, it has been shown that microglial cells also mediate synapse elimination in the developing retinogeniculate system[22]. To investigate the relative contributions of microglia and astrocytes in

©2013 Macmillan Publishers Limited. All rights reserved

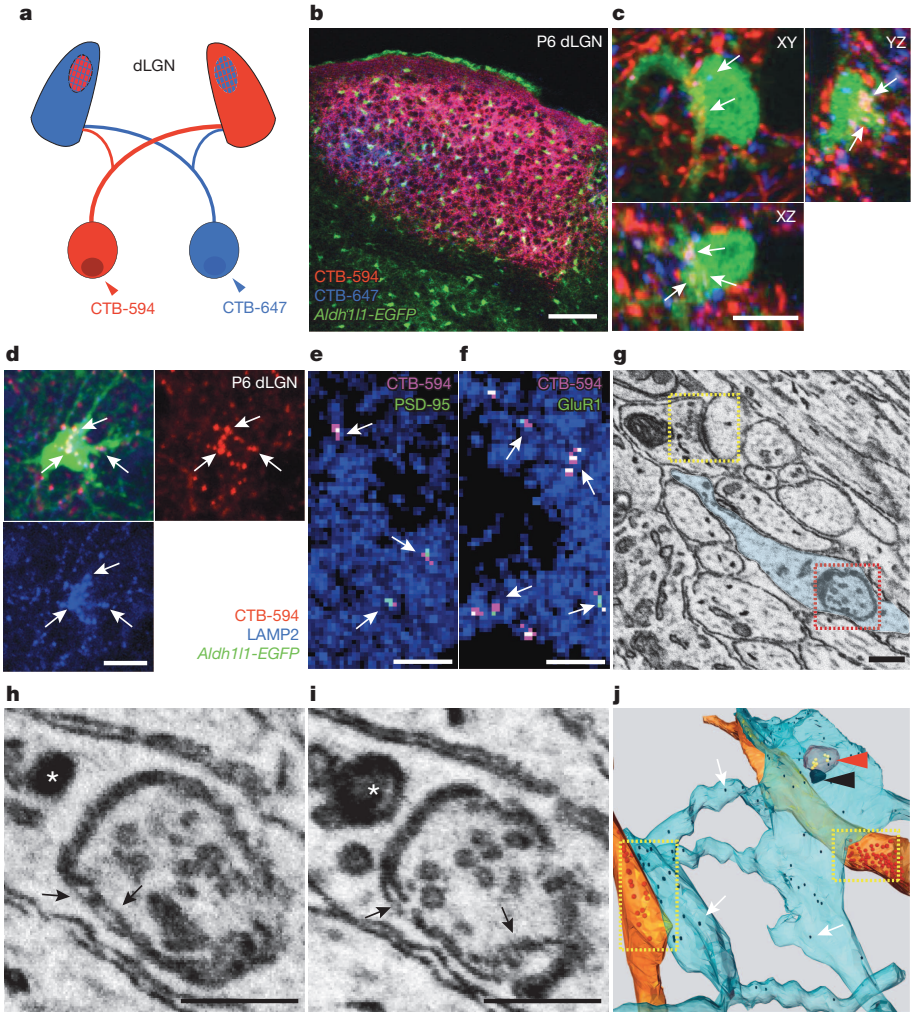


Figure 2 | Astrocytes mediate synapse elimination in the developing dLGN. **a**, Schematic diagram of anterograde RGC labelling with CTB-594 (red) and CTB-647 (blue), projecting to the developing dLGN. **b**, Contralateral (red) and ipsilateral (blue) projections in the P6 dLGN from *Aldh1l1-EGFP* (green) transgenic animals. Scale bar: 100 μm. **c**, Confocal optical sections through *xy*, *xz* and *yz* axes showing CTB-labelled debris (arrows) inside astrocytes (green). Scale bar: 10 μm. **d**, 3D-max projection showing that CTB-labelled debris (red, arrows) engulfed by astrocytes (green) was co-localized with LAMP2-positive lysosomes (blue). Scale bar: 10 μm. **e**, **f**, 3D-max projection AT images showing engulfed putative synapses (arrows) in astrocytes (blue). Engulfed putative synapses are defined as EYFP (blue) enveloped CTB-594 (magenta) and PSD-95 (**e**) or GluR1 (**f**) (green) that are within 200 nm of each other. Scale bar: 5 μm. **g**, Low-magnification SBEM micrograph showing an intact synapse (yellow rectangle; note the presynaptic vesicles and postsynaptic density) and astrocytic process (cyan) containing engulfed presynaptic material (red rectangle; note the vesicles that are the same size as the presynaptic vesicles). **h**, **i**, Consecutive high-magnification SBEM micrographs showing the engulfed presynaptic structure with irregular double-membrane morphology (arrows) and second inclusion (asterisks). **j**, Three-dimensional reconstruction of SBEM micrographs confirmed that astrocytic processes (cyan) with glycogen granules (arrows) fully engulfed presynaptic material (red arrowhead) as well as the second inclusion (black arrowhead). Synaptic vesicles in the intact synapse (yellow rectangles), in the axons (orange) and the engulfed presynaptic material are shown in red and yellow spheres, respectively. Scale bar: 0.4 μm (**g**, **h**, **i**).

synapse elimination, we measured the phagocytic indices of astrocytes and microglia together during P3–P9. Only during P3–P6, microglia engulfed more CTB-labelled debris than astrocytes per unit cell volume (Extended Data Fig. 6c). However, we found that astrocytes significantly outnumbered microglia by 10-, 7-, 6- and 4-fold at P5, P6, P7 and P9, respectively (Extended Data Fig. 6a, b). As a result, the total amount of engulfed CTB-labelled debris in a given imaging field was much greater in astrocytes (Extended Data Fig. 6d) during P3–P9, indicating that the total amount of synaptic pruning by astrocytes could exceed that by microglia in the developing LGN.

It is important to note that MERTK protein is localized to astrocytes as well as to microglia (Fig. 1c and Extended Data Fig. 1). Therefore, to determine whether MERTK contributes to the phagocytic function of microglia in the developing dLGN, we examined the phagocytic index of microglia in the *Mertk*$^{-/-}$ dLGN during P3–P6. Unexpectedly, we found that the *Mertk*$^{-/-}$ microglia displayed a transient increase in the amount of engulfed CTB-labelled debris compared to wild type only during P4–P5 (Extended Data Fig. 7). Thus, our *in vivo* data indicate that MERTK is dispensable for the phagocytic function of microglia in the developing dLGN, and that microglia can compensate to some extent for reduced astrocyte-mediated phagocytosis of synapses.

Neural circuit pruning and refinement by astrocytes

What is the role of astrocyte-mediated phagocytosis of synapses? Astrocytes could be removing axonal and synaptic debris produced from already retracting pre- and postsynaptic compartments that are no longer functional. Alternatively, astrocytes could actively promote synapse disassembly and clearance of unwanted synapses, leaving strong inputs intact for further stabilization. To address this issue, we labelled contra- and ipsilateral projections with CTB-594 and CTB-488, respectively, at P29 and examined the dLGN at P30 when eye-specific segregation is fully accomplished. We found that in *Megf10*$^{-/-}$; *Mertk*$^{-/-}$ mice, eye-specific segregation failed to occur properly (Fig. 3f, g). The overlap between contra- and ipsilateral projections was significantly increased compared to wild-type and single-knockout mice, indicating incomplete segregation (Fig. 3g). Consistent with this finding, the area of dLGN occupied by ipsilateral projections was significantly increased in *Megf10*$^{-/-}$; *Mertk*$^{-/-}$ mice (Fig. 3h). Because photoreceptors in the *Mertk*$^{-/-}$ retina show progressive degeneration starting from P25 (refs 9, 10), we examined spontaneous retinal waves that drive eye-specific segregation and found that they were intact in the P6 *Megf10*$^{-/-}$; *Mertk*$^{-/-}$ retina (Extended Data Fig. 8), indicating that incomplete eye-specific segregation was not due to any retinal defects.

To measure directly whether the number of functional retinogeniculate synapses is increased in *Megf10*$^{-/-}$; *Mertk*$^{-/-}$ mice, we performed electrophysiology with acute brain slices of P15–18 mice. Figure 4a, b shows the excitatory postsynaptic currents (EPSCs) from dLGN neurons of wild-type and *Megf10*$^{-/-}$; *Mertk*$^{-/-}$ littermates, respectively, in response to incremental increases in optic tract stimulation. The visually discernible 'steps' in the current traces were counted and compared between wild-type and *Megf10*$^{-/-}$; *Mertk*$^{-/-}$ neurons (Fig. 4c). As previously reported[18,23], we found that by P18 most (91%) of wild-type neurons were innervated by between 1–4 inputs. In contrast, *Megf10*$^{-/-}$; *Mertk*$^{-/-}$ neurons received a larger number of

©2013 Macmillan Publishers Limited. All rights reserved

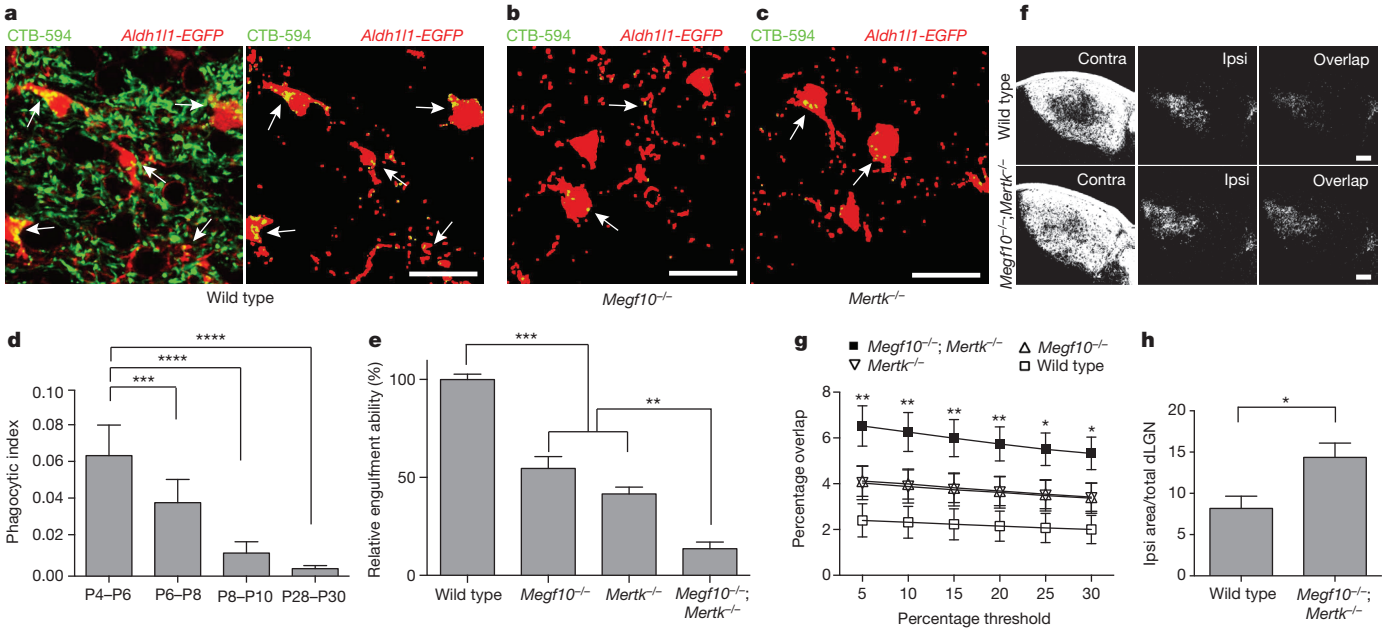
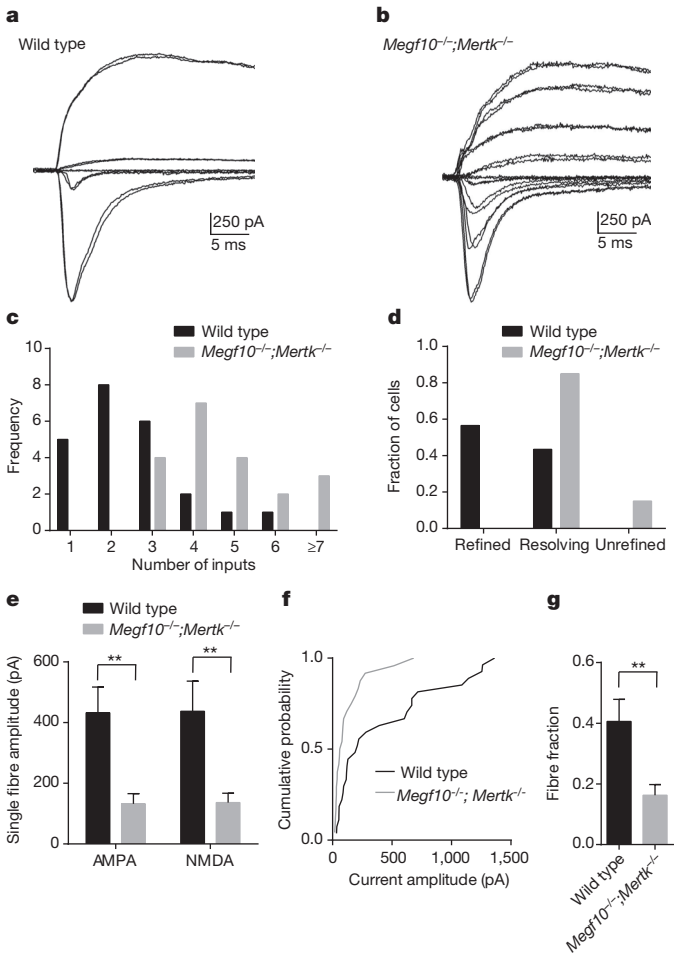


Figure 3 | Astrocytes mediate developmental synapse pruning and remodelling through MEGF10 and MERTK pathways. **a**, Confocal images of the wild-type P6 dLGN before and after subtracting CTB-594 (pseudo-coloured green) outside of astrocytes (pseudo-coloured red). **b**, **c**, In *Megf10*$^{-/-}$ (**b**) and *Mertk*$^{-/-}$ (**c**) mice, the amount of engulfed CTB-594 (green) by astrocytes (red) was significantly reduced (arrows). **d**, The highest astrocyte-mediated phagocytosis occurs during P4–P6. $n = 3$ mice per age. **e**, *Megf10*$^{-/-}$ and *Mertk*$^{-/-}$ mice showed significantly reduced astrocyte-mediated phagocytosis (45% and 58% reduction, respectively), which was further reduced in *Megf10*$^{-/-}$; *Mertk*$^{-/-}$ mice (85% reduction). $n = 4$ mice per group. **f**, **g**, Overlap between contra- and ipsilateral projections was significantly increased in *Megf10*$^{-/-}$; *Mertk*$^{-/-}$ mice at P30 (**f**), independently from the threshold value used in the analysis (**g**). $n = 4$ mice per group. **h**, The area of dLGN occupied by ipsilateral projections was significantly increased in P30 *Megf10*$^{-/-}$; *Mertk*$^{-/-}$ mice. $n = 4$ mice per group. $^{*}P < 0.05$, $^{**}P < 0.01$, $^{***}P < 0.001$, $^{****}P < 0.0001$, one-way ANOVA for all except **h** (*t*-test). NS, not significant. Error bars indicate s.e.m. Scale bar: 20 μm (**a**–**c**); 100 μm (**f**).



inputs, as shown by a rightward shift in the distribution of the number of inputs (Fig. 4c). As a result, wild-type neurons fell into either the refined or the resolving category (Fig. 4d), whereas we found no fully refined *Megf10*$^{-/-}$; *Mertk*$^{-/-}$ neurons at this age, and most *Megf10*$^{-/-}$; *Mertk*$^{-/-}$ neurons remained multiply innervated (Fig. 4d), indicating a significant deficit in synapse elimination.

Next, we used minimal stimulation to measure the synaptic properties of individual fibres. We found that the mean amplitude of AMPA (α-amino-3-hydroxy-5-methyl-4-isoxazole propionic acid) and NMDA (*N*-methyl-D-aspartate) single-fibre responses were significantly reduced in *Megf10*$^{-/-}$; *Mertk*$^{-/-}$ neurons (Fig. 4e) with a leftward shift in a cumulative distribution plot compared to wild-type neurons (Fig. 4f). We also compared the fibre fraction ratios by quantifying the contribution of each single fibre EPSC to the maximal evoked response and found that the fibre fraction ratio was significantly reduced in *Megf10*$^{-/-}$; *Mertk*$^{-/-}$ neurons (Fig. 4g), with each fibre contributing only 16.3 ± 0.03% of the total innervation compared to 40.6 ± 0.07% in wild-type cells. Taken together, these data indicate that these neurons are innervated by a greater number of

Figure 4 | dLGN neurons are abnormally innervated by multiple weak inputs in *Megf10*$^{-/-}$; *Mertk*$^{-/-}$ mice. **a**, **b**, Representative traces of superimposed EPSCs evoked by increasing intensities of optic tract stimulation recorded from individual wild-type (**a**) and *Megf10*$^{-/-}$; *Mertk*$^{-/-}$ (**b**) dLGN neurons at P15–18. **c**, *Megf10*$^{-/-}$; *Mertk*$^{-/-}$ neurons receive a significantly larger number of inputs ($P = 0.003$). **d**, Most *Megf10*$^{-/-}$; *Mertk*$^{-/-}$ neurons were in the resolving or unrefined category, whereas most wild-type neurons were in the refined category. **e**, *Megf10*$^{-/-}$; *Mertk*$^{-/-}$ neurons had significantly smaller AMPA ($P = 0.002$) and NMDA ($P = 0.008$) single-fibre currents. **f**, *Megf10*$^{-/-}$; *Mertk*$^{-/-}$ neurons had significantly more small-amplitude single-fibre AMPA current responses in cumulative probability histograms ($P = 0.023$). **g**, *Megf10*$^{-/-}$; *Mertk*$^{-/-}$ neurons had a significantly reduced mean fibre fraction ($P = 0.005$). Recordings were obtained from 23 wild-type cells and 20 *Megf10*$^{-/-}$; *Mertk*$^{-/-}$ cells. $^{**}P < 0.01$, *t*-test except **c** and **f** (Kolmogorov–Smirnov test). Error bars indicate s.e.m.

©2013 Macmillan Publishers Limited. All rights reserved

weak inputs and demonstrate that astrocytes contribute to normal neural circuit pruning and refinement in the developing CNS by phagocytosing weak synapses through MEGF10 and MERTK pathways.

Neural activity promotes synapse pruning by astrocytes

Retinogeniculate segregation does not occur when retinal wave activity is blocked[17,24], raising the question of whether neural activity has a role in astrocyte-mediated synapse elimination. To find out, we intraocularly injected epibatidine, a potent agonist for neuronal nicotinic acetylcholine receptors, to block specifically the spontaneous retinal waves[17,25,26]. Previous work has shown that injecting epibatidine binocularly blocks eye-specific segregation in dLGN, whereas injecting epibatidine monocularly preserves eye-specific segregation, inducing the affected weaker projections to lose their territory preferentially. When we injected epibatidine binocularly, the total amount of both engulfed contra- (CTB-594) and ipsilateral (CTB-647) projections by astrocytes was significantly reduced (Fig. 5a, b, d), whereas the ratio of engulfed contra- versus ipsilateral projections was unchanged compared to control injections (Fig. 5e). Notably, when epibatidine was injected monocularly to the contralateral eye of the wild-type mice, astrocytes engulfed the weaker projections preferentially (Fig. 5c, d), significantly increasing the ratio of engulfed contra- versus ipsilateral projections by astrocytes (Fig. 5e). This preferential engulfment of weaker projections was significantly reduced in the *Megf10*$^{-/-}$ and *Mertk*$^{-/-}$ background (Fig. 5d, e). These data show that retinal activity strongly promotes synapse elimination by enhancing the amount of astrocyte-mediated phagocytosis via the MEGF10 and MERTK pathways in the dLGN.

Synapse elimination by astrocytes in adult brains

Synapses in the adult brain, especially dendritic spines, are dynamic structures that turn over rapidly during activity-dependent synaptic plasticity induced by learning and memory[27–29]. Because MEGF10 and MERTK are highly localized to astrocytes in the adult CNS and not just the developing CNS (Extended Data Fig. 2), we next asked whether synapse engulfment and elimination by astrocytes persists in the adult CNS. By using AT, we analysed EYFP-expressing astrocytes in the 1- and 4-month-old somatosensory cortex by immunostaining with astrocyte- and synapse-specific antibodies (Extended Data Fig. 9). Three-dimensional (3D)-max projection AT images revealed that both putative excitatory (puncta containing Bassoon and PSD-95) and inhibitory (puncta containing Gephyrin and VGAT) synapses were robustly engulfed by astrocytes throughout the 1- and 4-month-old cortex (Fig. 6a–c). Notably, we found that more excitatory synapses were engulfed by 1-month-old than 4-month-old cortical astrocytes (Fig. 6d), probably due to a higher rate of developmental synapse pruning of excitatory projections in the younger brains[30]. In contrast, engulfed putative inhibitory synapses showed about the same density within 1- and 4-month-old cortical astrocytes (Fig. 6d). These data show that engulfment of both excitatory and inhibitory synapses by astrocytes continues in the adult CNS.

Concluding remarks

Our findings demonstrate that astrocytes actively contribute to the activity-dependent synapse elimination that mediates neural circuit refinement in the developing CNS by phagocytosing synapses via the MEGF10 and MERTK pathways, and that astrocytes continue to engulf synapses in the adult CNS. These findings reveal a previously unknown role for astrocytes, provide new information about the mechanisms underlying neural circuit refinement during development, and add to the growing evidence that substantial synapse turnover and remodelling occurs in the adult CNS. Astrocytes thus share with microglia the ability to actively engulf and eliminate synapses in response to neural activity, but synapse engulfment by astrocytes is independent of complement protein C1q (ref. 31 and data not shown), and uses distinct phagocytic pathways from microglia. Astrocytes in *Drosophila* also phagocytose synapses, indicating that the phagocytic function of astrocytes is evolutionarily conserved[32]. These findings have important implications and raise many questions. How does neural activity control the rate of astrocyte-mediated synapse phagocytosis, do astrocytes and microglia phagocytose different synapse types or circuits, and how do astrocytes decide which synapses to engulf? Because MEGF10 and MERTK phagocytic receptors initiate the engulfment process by recognizing phosphatidylserine presented by target debris, an important question is whether the weak synapses that need to be eliminated present 'eat me signals' locally and if so what their identities are. Most notably, our findings suggest that the activity-dependent engulfment of synapses by astrocytes has an active role in

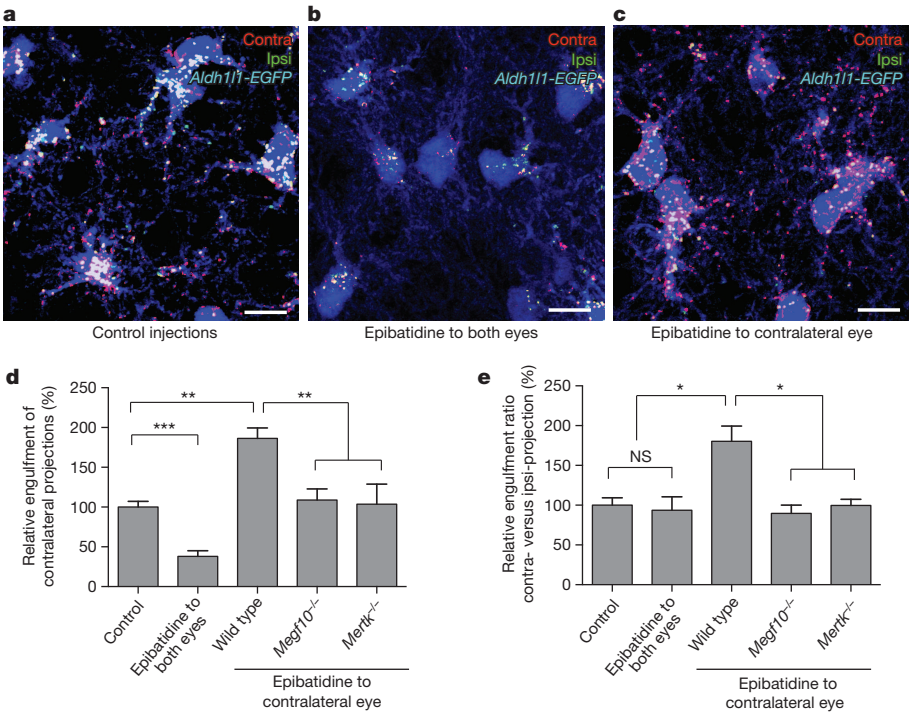


Figure 5 | Neural activity promotes astrocyte-mediated synapse elimination through MEGF10 and MERTK. **a**–**c**, 3D-max projection confocal images showing CTB-594-labelled contralateral (red) and CTB-647-labelled ipsilateral (green) debris engulfed by astrocytes (blue) in P6 dLGN, comparing control (**a**), binocular (**b**) and monocular (**c**) injections. Red and green debris co-localized in astrocytes (blue) appears as bright yellow. **d**, Relative engulfment of contralateral projections by astrocytes was significantly reduced after binocular epibatidine injections whereas it was significantly increased after monocular epibatidine injections to the wide-type contralateral eye. However, this increased engulfment was reduced in the *Megf10*$^{-/-}$ or *Mertk*$^{-/-}$ background. **e**, In binocular epibatidine injection cases, the ratio of engulfed contralateral versus ipsilateral projections by astrocytes was unchanged compared to control injections whereas it was significantly increased after monocular epibatidine injections to wild-type contralateral eye. However, this increased ratio of engulfed contralateral versus ipsilateral projections was reduced in the *Megf10*$^{-/-}$ or *Mertk*$^{-/-}$ background. $n = 4$ mice per treatment. $^{*}P < 0.05$, $^{**}P < 0.01$, $^{***}P < 0.001$, one-way ANOVA. NS, not significant. Error bars indicate s.e.m. Scale bar: 10 μm (**a**–**c**).

©2013 Macmillan Publishers Limited. All rights reserved

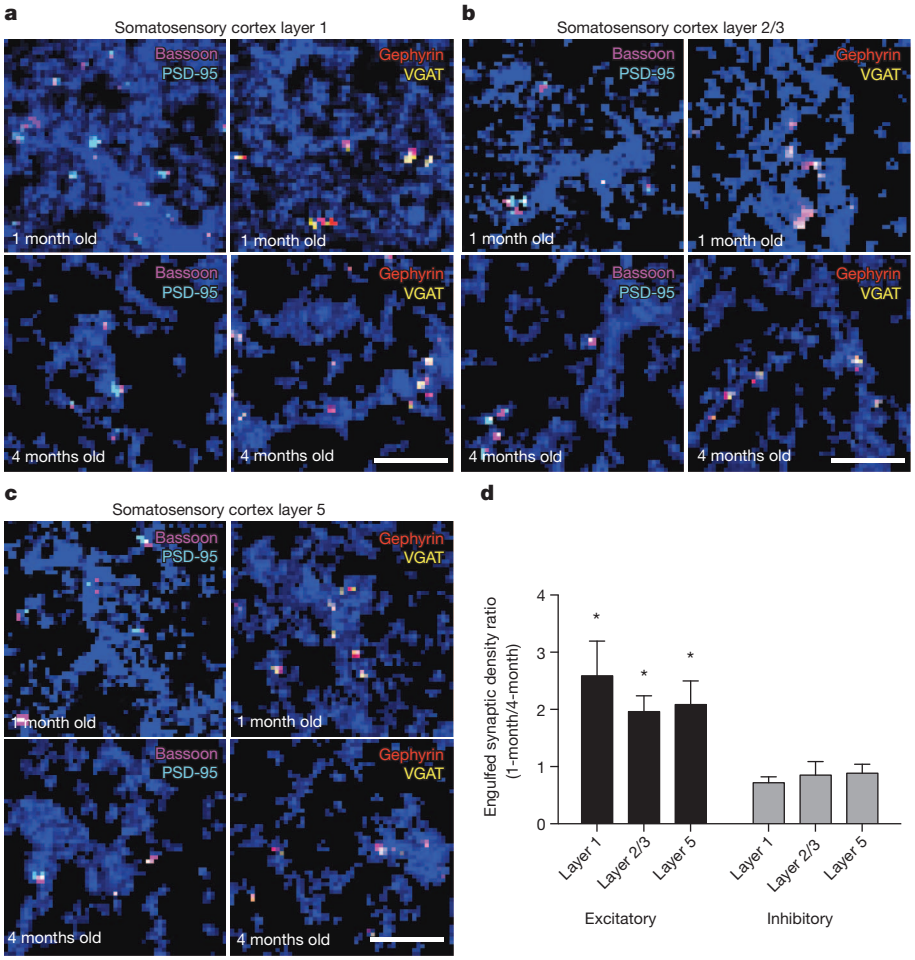


Figure 6 | Astrocytes in the adult cortex continuously engulf synapses. **a**–**c**, 3D-max projection AT images showing EYFP-labelled cortical astrocytes (blue) and engulfed putative excitatory synapses (Bassoon, magenta, and PSD-95, cyan) and inhibitory synapses (VGAT, yellow, and Gephyrin, red) from layers 1 (**a**), 2/3 (**b**) and 5 (**c**) of the 1- and 4-month-old mouse somatosensory cortex (total volume = 60 μm by 60 μm by 2.8 μm). Engulfed synapses were defined as EYFP (blue) enveloped presynaptic and postsynaptic puncta that were within 200 nm of each other. Scale bar: 2.5 μm. **d**, The density ratio of engulfed excitatory and inhibitory synapses by astrocytes between the 1-month-old and 4-month-old cortex. $n = 3$ mice per age. $^*P < 0.05$, *t*-test. Error bars indicate s.e.m.

continually remodelling the synaptic architecture of our brains. Whether such remodelling underlies learning and memory, and whether a declining rate of synapse engulfment by astrocytes throughout life could contribute to critical period plasticity during development or to synaptic senescence and neurodegeneration with ageing, are important questions for future study.

METHODS SUMMARY

All procedures were conducted in accordance with the animal care standards set forth by the National Institutes of Health and approved by Stanford University's Administrative Panel on Laboratory Animal Care. Astrocytes and microglial cells were purified from P4–P6 mouse cortex and cultured in serum-free conditions. All experiments with mutants were performed blindly without knowledge of their genotype.

Online Content Any additional Methods, Extended Data display items and Source Data are available in the online version of the paper; references unique to these sections appear only in the online paper.

Received 11 March; accepted 11 October 2013.
Published online 24 November 2013.

1. Barres, B. A. The mystery and magic of glia: a perspective on their roles in health and disease. *Neuron* **60,** 430–440 (2008).
2. Cahoy, J. D. *et al.* A transcriptome database for astrocytes, neurons, and oligodendrocytes: a new resource for understanding brain development and function. *J. Neurosci.* **28,** 264–278 (2008).
3. Ziegenfuss, J. S. *et al.* Draper-dependent glial phagocytic activity is mediated by Src and Syk family kinase signalling. *Nature* **453,** 935–939 (2008).
4. MacDonald, J. M. *et al.* The *Drosophila* cell corpse engulfment receptor Draper mediates glial clearance of severed axons. *Neuron* **50,** 869–881 (2006).
5. Zhou, Z., Hartwieg, E. & Horvitz, H. R. CED-1 is a transmembrane receptor that mediates cell corpse engulfment in *C. elegans*. *Cell* **104,** 43–56 (2001).
6. Hamon, Y. *et al.* Cooperation between engulfment receptors: the case of ABCA1 and MEGF10. *PLoS ONE* **1,** e120 (2006).
7. Wu, H. H. *et al.* Glial precursors clear sensory neuron corpses during development via Jedi-1, an engulfment receptor. *Nature Neurosci.* **12,** 1534–1541 (2009).
8. Kinchen, J. M. *et al.* Two pathways converge at CED-10 to mediate actin rearrangement and corpse removal in *C. elegans*. *Nature* **434,** 93–99 (2005).
9. Prasad, D. *et al.* TAM receptor function in the retinal pigment epithelium. *Mol. Cell. Neurosci.* **33,** 96–108 (2006).
10. Duncan, J. L. *et al.* An RCS-like retinal dystrophy phenotype in mer knockout mice. *Invest. Ophthalmol. Vis. Sci.* **44,** 826–838 (2003).
11. Finnemann, S. C. Focal adhesion kinase signaling promotes phagocytosis of integrin-bound photoreceptors. *EMBO J.* **22,** 4143–4154 (2003).
12. Wu, Y., Singh, S., Georgescu, M. M. & Birge, R. B. A role for Mer tyrosine kinase in αvβ5 integrin-mediated phagocytosis of apoptotic cells. *J. Cell Sci.* **118,** 539–553 (2005).
13. Tung, T. T. *et al.* Phosphatidylserine recognition and induction of apoptotic cell clearance by *Drosophila* engulfment receptor Draper. *J. Biochem.* **153,** 483–491 (2013).
14. Hochreiter-Hufford, A. & Ravichandran, K. S. Clearing the dead: apoptotic cell sensing, recognition, engulfment, and digestion. *Cold Spring Harb. Perspect. Biol.* **5** (2013).
15. Foo, L. C. *et al.* Development of a method for the purification and culture of rodent astrocytes. *Neuron* **71,** 799–811 (2011).
16. Shatz, C. J. & Sretavan, D. W. Interactions between retinal ganglion cells during the development of the mammalian visual system. *Annu. Rev. Neurosci.* **9,** 171–207 (1986).
17. Penn, A. A., Riquelme, P. A., Feller, M. B. & Shatz, C. J. Competition in retinogeniculate patterning driven by spontaneous activity. *Science* **279,** 2108–2112 (1998).
18. Hooks, B. M. & Chen, C. Distinct roles for spontaneous and visual activity in remodeling of the retinogeniculate synapse. *Neuron* **52,** 281–291 (2006).
19. Cuervo, A. M. & Dice, J. F. A receptor for the selective uptake and degradation of proteins by lysosomes. *Science* **273,** 501–503 (1996).
20. Wang, G. & Smith, S. J. Sub-diffraction limit localization of proteins in volumetric space using Bayesian restoration of fluorescence images from ultrathin specimens. *PLOS Comput. Biol.* **8,** e1002671 (2012).
21. Peters, A., Palay, S. L., Webster, H. & d. *The Fine Structure of the Nervous System: the Neurons and Supporting Cells* (Saunders, 1976).
22. Schafer, D. P. *et al.* Microglia sculpt postnatal neural circuits in an activity and complement-dependent manner. *Neuron* **74,** 691–705 (2012).

©2013 Macmillan Publishers Limited. All rights reserved

23. Chen, C. & Regehr, W. G. Developmental remodeling of the retinogeniculate synapse. *Neuron* **28,** 955–966 (2000).
24. Shatz, C. J. & Stryker, M. P. Prenatal tetrodotoxin infusion blocks segregation of retinogeniculate afferents. *Science* **242,** 87–89 (1988).
25. Stellwagen, D. & Shatz, C. J. An instructive role for retinal waves in the development of retinogeniculate connectivity. *Neuron* **33,** 357–367 (2002).
26. Huberman, A. D., Stellwagen, D. & Chapman, B. Decoupling eye-specific segregation from lamination in the lateral geniculate nucleus. *J. Neurosci.* **22,** 9419–9429 (2002).
27. Xu, T. *et al.* Rapid formation and selective stabilization of synapses for enduring motor memories. *Nature* **462,** 915–919 (2009).
28. Yang, G., Pan, F. & Gan, W. B. Stably maintained dendritic spines are associated with lifelong memories. *Nature* **462,** 920–924 (2009).
29. Roberts, T. F., Tschida, K. A., Klein, M. E. & Mooney, R. Rapid spine stabilization and synaptic enhancement at the onset of behavioural learning. *Nature* **463,** 948–952 (2010).
30. Paolicelli, R. C. *et al.* Synaptic pruning by microglia is necessary for normal brain development. *Science* **333,** 1456–1458 (2011).
31. Stevens, B. *et al.* The classical complement cascade mediates CNS synapse elimination. *Cell* **131,** 1164–1178 (2007).
32. Tasdemir-Yilmaz, O. & Freeman, M. R. Astrocytes engage unique molecular programs to engulf pruned neuronal debris from distinct subsets of neurons. *Genes Dev.* (in the press).

Supplementary Information is available in the online version of the paper.

Acknowledgements We thank D. Vollrath for discussions and MERTK antibody. We also thank H. M. Lee for helping us set up electrophysiology experiments as well as for discussions. Part of the data was acquired at Stanford Neuroscience Microscopy Service (NMS), supported by NIH NS069375. W.-S.C. was supported in part by a postdoctoral fellowship from the Damon Runyon Cancer Research Foundation (DRG 2020-09). L.E.C. was supported in part by an EMBO ALTF fellowship. This work was supported by grants from the NIH (5 R21NS072556, B.A.B.) and a Brain Disorder Award from the Mcknight Foundation to B.A.B. We thank V. and S. Coates for their generous support.

Author Contributions W.-S.C. and B.A.B. designed the experiments and wrote the paper. W.-S.C. performed experiments and analysed data. L.E.C. performed and analysed electrophysiology recordings from LGN neurons with support from A.T. and C. Chen. G.X.W. performed and analysed array tomography experiments. B.K.S. performed and analysed spontaneous retinal wave recording with support from A.S. C. Chakraborty, J.J., L.C.F. and S.J.S. provided technical support.

Author Information Reprints and permissions information is available at www.nature.com/reprints. The authors declare no competing financial interests. Readers are welcome to comment on the online version of the paper. Correspondence and requests for materials should be addressed to W.-S.C. (wschung@stanford.edu).

©2013 Macmillan Publishers Limited. All rights reserved

METHODS

Animals. *Megf10*$^{tm1(KOMP)Vlcg}$ and B6;129-*Mertk*^{tm1Grl}/J (ref. 33) mice were obtained from KOMP and Jackson Laboratories, respectively. *Aldh1l1-EGFP* (ref. 2) and *CX3CR1-EGFP* (ref. 22) transgenic lines were used to visualize astrocytes and microglia, respectively. For array tomography, a reporter line [*Gt(ROSA)26Sor*$^{tm3(CAG-EYFP)Hze}$/J] and *cre* lines [Tg(*GFAP-cre*)25Mes/J for the dLGN and Tg(*Gfap-cre*)77.6Mvs/J for the cortex] from Jackson Laboratories were crossed together to get astrocyte-specific EYFP expression. All lines were maintained by breeding with C57BL/6 mice. All experiments with mutants were performed blindly without knowledge of their genotype.

Immunohistochemistry. Animals were anaesthetized with a ketamine (100 mg kg^{-1})/xylazine (20 mg kg^{-1}) cocktail, and perfused with PBS followed by 4% paraformaldehyde. Brains were dissected out, post-fixed overnight in 4% paraformaldehyde at 4 °C and transferred to 30% sucrose for 24 h. After embedding brain tissues with OCT compound (Tissue-Tek), 10 μm tissue sections were prepared by Leica cryostats. The following antibodies were used: MEGF10 (rabbit polyclonal from Sigma and Millipore), MERTK (goat polyclonal Biotin conjugated from R&D, rabbit polyclonal: gift from D. Vollrath), β-galactosidase (chicken polyclonal from Abcam and Aves Labs), GFP (chicken polyclonal from Aves Labs), LAMP2 (rat monoclonal from Abcam), synaptophysin (mouse monoclonal from Millipore), VGlut2 (guinea-pig polyclonal from Millipore), BSL (biotin-conjugated BSL from Vector Labs), IBA1 (rabbit polyclonal from Wako and mouse monoclonal Millipore), Bassoon (mouse monoclonal from Abcam), PSD-95 (rabbit monoclonal from Cell Signaling Technology), gephyrin (mouse monoclonal from Biosciences Pharmingen) and VGAT (mouse monoclonal from Synaptic Systems). Staining for MEGF10 and MERTK was achieved by using Tyramide Signal Amplification (TSA) system from PerkinElmer. Staining for other antibodies was performed as described previously[31] with appropriate secondary antibodies conjugated with Alexa fluorophore (Invitrogen). Images were acquired using Zeiss LSM510 inverted confocal, Zeiss AxioImager fluorescence microscopy and Applied Precision OMX V4 structured illumination super-resolution microscopy.

Synaptosome purification. Synaptosomes were purified by percoll gradient from the adult mouse brains as described previously[34]. To obtain red fluorescent synaptosomes, *Gt(ROSA)26Sor*$^{tm9(CAG-tdTomato)Hze}$/J line from Jackson Laboratories was crossed to ubiquitous *cre* line (heat-shock-promoter-driven *cre* line), and the tdTomato-expressing adult brains were used for purifying synaptosomes. To obtain pHrodo-conjugated synaptosomes, synaptosomes purified from the wild-type adult brains were incubated with pHrodo red, succinimidyl ester (Invitrogen) in 0.1 M sodium carbonate (pH 9.0) at room temperature with gentle agitation[35]. After 2-h incubation, unbound pHrodo was washed out by multiple rounds of centrifugation and pHrodo-conjugated synaptosomes were re-suspended with isotonic buffer containing 5% DMSO for subsequent freezing.

***In vitro* engulfment assay with astrocytes.** Astrocytes were purified from the P4–P6 *Aldh1l1-EGFP* mouse cortex and cultured in serum-free conditions as described previously[15]. Astrocytes at 3–5 days *in vitro* were washed twice with PBS and incubated with appropriate media (see below) containing either tdTomato-expressing or pHrodo-conjugated synaptosomes. For tdTomato-expressing synaptosomes, after incubating with synaptosomes for 4 h, astrocytes were fixed with 4% paraformaldehyde and imaged by confocal microscopy to obtain optical *z*-stacks. Imaris software (BITPLANE) was used to process confocal *z*-stacks to reveal engulfed synaptosomes by astrocytes. For pHrodo-conjugated synaptosomes, live astrocytes were imaged with epifluorescence microscopy after incubating with synaptosomes for 4 h to reveal engulfed pHrodo-conjugated synaptosomes. For testing secreted factors on astrocyte-mediated phagocytosis, pHrodo-conjugated synaptosomes were incubated with purified astrocytes for 24 h in the presence of fresh astrocyte growth media (AGM: 50% neurobasal, 50% DMEM, glutamine, pyruvate, NAC and penicillin-streptomycin, 5 ng ml^{-1} HBEGF), astrocyte-conditioned media (ACM, see below), 5% fetal calf serum (FCS) in AGM or protein S (1 μg ml^{-1}, Abcam) in AGM. To compare phagocytic capacity of astrocytes between wild types and mutants, astrocytes were purified from the P4–P6 wild-type, *Megf10*$^{-/-}$ or *Mertk*$^{-/-}$ cortex and astrocytes at 3–5 days *in vitro* were incubated with pHrodo-conjugated synaptosomes for 24 h in the presence of 5% serum. We used two different methods to quantify the phagocytic capacity: image processing and FACS analysis. For image processing analysis, we took 10 images per well using ×20 objective lens from a random area of the 24-well plates and calculated the phagocytic index by measuring the area of engulfed synaptosomes normalized by the area of astrocytes, using FIJI. Relative engulfment ability was calculated by normalizing the phagocytic index of mutant astrocytes by that of wild-type astrocytes. For FACS analysis, astrocytes were trypsinized, collected by centrifugation, and re-suspended in Dulbecco's PBS (DPBS) containing 0.02% BSA. Live astrocytes were analysed at room temperature by the LSR 2 analyser at the Stanford Shared FACS Facility on the basis of their pHrodo expression intensity. The phagocytic index was calculated by measuring the percentage of the cell population showing strong pHrodo intensity ($>3 \times 10^4$ in pHrodo intensity). Relative engulfment ability was calculated by normalizing the phagocytic index of mutant astrocytes by that of wild-type astrocytes.

***In vitro* engulfment assay with microglia.** To compare phagocytic capacity of microglia between wild types and mutants, enriched microglial cell population was purified from the P4–P6 wild-type, *Megf10*$^{-/-}$ or *Mertk*$^{-/-}$ cortex by the immunopanning method[15] with slight modification. Briefly, cortex from 3–4 mice per genotype were dissected in DPBS and the meninges were removed. Single-cell suspension was produced by dissociating the tissues with papain, and placed in the panning plate coated with rat anti-mouse CD45 (BD Pharmingen). After 20 min, the plate was washed thoroughly to remove any unbound cell, and microglia were collected by trypsinization and centrifugation. Microglia cultured with ACM (see below) at 3–5 days *in vitro* were incubated with pHrodo-conjugated synaptosomes for 24 h in the presence of 5% serum for subsequent FACS analysis. FACS analysis with enriched microglial cells showed two distinct cell populations with low and strong pHrodo intensity. The phagocytic index was calculated by measuring the percentage of the cell population showing strong pHrodo intensity ($>3 \times 10^4$ in pHrodo intensity). Relative engulfment ability was calculated by normalizing the phagocytic index of mutant astrocytes by that of wild-type astrocytes.

Astrocyte-conditioned media. Purified astrocytes were plated in a 10-cm plate and cultured in AGM. After 2 days *in vitro*, old media was replaced with conditioning media (50% neurobasal, 50% DMEM without phenol red, glutamine, pyruvate, NAC and penicillin-streptomycin) and astrocytes were cultured for an additional 7 days to enrich secreted factors from astrocytes. Any dead cell and debris were removed by centrifugation.

***In vivo* engulfment assay.** *Aldh1l1-EGFP* (ref. 2) and *CX3CR1-EGFP* (ref. 22) transgenic lines were used to visualize astrocytes and microglia, respectively, in all *in vivo* engulfment assays, except for the experiments determining the relative contributions of microglia and astrocytes in synapse elimination shown in Extended Data Fig. 6 (in this case, microglia were labelled by IBA1-immunostaining and astrocytes were labelled by *Aldh1l1-EGFP* on the same brain sections). Pups were anaesthetized with isoflurane and 1 μl of cholera toxin-β subunit (CTB) conjugated with Alexa594 and 647 (Invitrogen, 1 mg ml^{-1} in normal saline) were injected into the contralateral and ipsilateral eyes, respectively. After 1–2 days (depending on experiments), mice were perfused with PBS followed by 4% paraformaldehyde and brains were dissected, postfixed overnight for 4 °C and transferred to 30% sucrose for 24 h. The 50 μm floating coronal sections containing dLGN were mounted on slide glasses and used for the analysis. For each animal, two medial-most dLGN were chosen. For each dLGN, two fields (the tip and medial portions of dLGN that contain both contra- and ipsilateral projections) were imaged using Zeiss LSM510 inverted confocal microscopy to obtain 50–70 consecutive optical sections with 0.3 μm interval thickness. FIJI was used to remove outliers (radius 2.0 pixels and threshold 20) from all channels and subtract background from CTB images (rolling bar radius 50 pixels). An image-processing algorithm (Matlab, Mathworks) was used to localize CTB-labelled debris engulfed by glia cells by subtracting CTB-labelled projections outside of glia cells. The phagocytic index was calculated by measuring the total volume of engulfed CTB-labelled debris normalized by the total volume of glia cells in a given *z*-stack. Relative engulfment ability was calculated by normalizing the phagocytic index of experimental groups to control group.

Intraocular injections of epibatidine. P3 *Aldh1l1-EGFP* pups were anaesthetized with isoflurane and 1 μl of epibatidine (Sigma, 1 mM in normal saline) was injected either binocularly or monocularly (for monocular injections, epibatidine was injected into the contralateral eye). Control eyes were also injected with 1 μl of normal saline. Mice received the second intraocular injections of CTB-594 (contralateral) and CTB-647 (ipsilateral) at P4, and the third intraocular injections of epibatidine at P5. The dLGN was collected at P6 for analysis.

Eye segregation analysis. P29 *Megf10* and *Mertk* single/double knockout, and wild-type siblings were anaesthetized with isoflurane and 1 μl of CTB-594 and CTB-488 (Invitrogen, 1 mg ml^{-1} in normal saline) were injected into the left and right eyes, respectively, and the dLGN was harvested at P30. Tissues were prepared and analysed as previously described[36,37].

Array tomography. Tissue preparation, array creation and immunohistochemistry have been described in detail previously[38]. In short, a small piece of tissue (~2 mm high by 1 mm wide by 1 mm deep), in our case P5 dLGN and 1- and 4-month-old somatosensory cortical tissues, was microwave fixed in 4% paraformaldehyde. The fixed tissue was then dehydrated in graded steps of ethanol, and then embedded in LR White resin overnight at 50 °C. The embedded tissue was sectioned on an ultramicrotome at a thickness of 70 nm and placed as a ribbon array directly on gelatin- or carbon-coated glass coverslips.

For image registration and processing, image stacks from AT were imported into FIJI and aligned using both rigid and affine transformations with the Register

©2013 Macmillan Publishers Limited. All rights reserved

Virtual Stacks plugin. The aligned image stacks were further registered across image sessions using FIJI and TrackEM. The aligned and registered image stacks were imported into Matlab and deconvolved using the native implementation of Richardson–Lucy deconvolution with empirical or theoretical PSFs with 10 iterations[20]. Custom functions were written to automate and facilitate this work-flow. Blind deconvolution is also natively implemented in Matlab. Matlab native function (regionprops) was used to calculate the centres of mass of puncta in the image volumes using 26 neighbourhood 3D connected component analyses with an assumed background threshold that is 0.1 of the total dynamic range, which is 6,553.5 for a 16-bit image, and is in line with previous background thresholds used for AT analysis[20]. Custom functions were implemented to facilitate the handling and processing of the data. In Fig. 6 where engulfed synapses by astrocytes were imaged, engulfed excitatory synapses were defined as EYFP (blue) enveloped Bassoon (magenta) and PSD-95 (cyan) that were within 200 nm of each other. Engulfed inhibitory synapses were defined as EYFP (blue) enveloped VGAT (yellow) and Gephyrin (red) that were within 200 nm of each other. The density of engulfed synapses was calculated as the total number of engulfed synapses divided by the volume of EYFP in the image volume.

Serial block face scanning electron microscopy. P5 wild-type animals were perfused transcardially with 0.1 M sodium cacodylate buffer containing 4% PFA and 2% glutaraldehyde. dLGN tissues were dissected out and post-fixed overnight with the same fixative. Subsequent tissue processing and image acquisition were performed by Renovo Neural.

Spontaneous retinal wave recording. Retinal preparations were isolated from P6 mice as previously described[39] and maintained at 34–35 °C. Recordings were analysed offline to isolate the spikes of different cells, as described previously. Briefly, candidate spikes were detected using a threshold on each electrode, and the voltage waveforms on the electrode and nearby electrodes around the time of the spike were extracted. Spikes were projected into the first five principal component dimensions, where an expectation maximization algorithm was used to sort spikes based on a mixture of Gaussians model.

For wave and burst detection, waves and burst occurrences in the spike trains of neurons were detected using modified Poisson surprise algorithms as described previously. Briefly, the time-varying spike count for each neuron was calculated using a 1-s bin. When the probability that a Poisson spike train would generate the spike count calculated for a given bin was $<10^{-5}$, a neuron was considered to be bursting. A wave was considered to have started when >5% of all neurons were bursting. A wave was considered to have ended when <2.5% of all neurons were still bursting. To detect bursts, the spike train of each neuron was analysed. Whenever 3 spikes were found for which the interspike interval (ISI) was less than half the mean ISI of the neuron, the algorithm calculated the initial probability that a Poisson spike train would generate three spikes in a time bin defined by the first and last spike. Spikes were then added one at a time, and the probability was re-calculated. Spikes were added until either the probability increased above the initial value, or the next spike occurred at a time that was greater the mean ISI of the neuron after the preceding spike. If the minimum probability calculated was $<10^{-4}$, then a neuron was considered to have fired a burst.

Wave and burst parameters were calculated as described previously[39]. Briefly, wave speed was calculated by binning each wave into 1-s intervals. The centre of mass of all neurons that were active, weighted by the number of spikes each neuron fired, was calculated for each bin. The distance between centres of mass calculated for successive bins was used to calculate a wave speed. The total wave speed was the average of all wave speeds calculated for successive bins. Wave width was calculated by binning each wave into 1-s intervals and finding all the neurons that burst 1 s before or after a given bin. The width was defined as the maximum distance between neurons bursting before and after the bin. The width of a wave was the average of all these widths calculated for all bins. Burst durations and burst spike rates were computed by averaging all values over the entire recording for each neuron. The time spent spiking above 10 Hz was computed by summing all ISIs <100 ms within a burst. To quantify how high-frequency spiking was distributed among wave bursts and non-wave bursts, we calculated the percentage of the total time spent spiking above 10 Hz that occurred during wave bursts or during non-wave bursts. The correlation index was computed as described previously using a 100-ms coincidence interval.

For wave directionality, the directional bias of individual neurons, as well as each preparation, was calculated as described previously. Briefly, each burst that a neuron fired that occurred during a wave was analysed. Any bursts that occurred 0.5 s before (pre) or after (post) this burst were identified, and the weighted centres of mass of pre- and post-bursts were calculated. Each spike fired by the burst under investigation was assigned the angle between the pre- and post-burst centres of mass (burst spike angle). A neuron was said to have a directional bias if the distribution of all burst spike angles deviated significantly from circular uniformity (Rayleigh test; $P < 0.05$). The directional bias of each neuron was defined as the normalized vector sum of all its burst spike angles. A preparation was said to have a directional bias if the directional bias of all neurons deviated significantly from circular uniformity (Rayleigh test; $P < 0.01$). The directional bias of each preparation was defined as the normalized vector sum of the directional bias of all neurons.

Electrophysiology. Mice aged P15–18 were killed and the brain was rapidly removed and placed into ice-cold choline-based cutting solution containing (in mM): $NaHCO_3$ 26, glucose 25, choline chloride 130, KCl 2.5, NaH_2PO_4 1.25, $MgCl_2$ 7, $CaCl_2$ 0.5. Angled parasagittal brain slices (250 μm) were prepared, using a sapphire blade, according to the method of Turner and Salt, with adaptations[18,23]. This method preserves the optic tract and dLGN, and generally only one slice is obtained per animal. After cutting, slices were incubated at 31 °C for 20 min in choline-based cutting solution followed by 20 min in isotonic saline solution (in mM: NaCl 125, $NaHCO_3$ 25, KCl 2.5, NaH_2PO_4 1.25, glucose 25, $MgCl_2$ 1, $CaCl_2$ 2). Oxygenation was continuously supplied during cutting, recovery and recording. Slices were transferred to a recording chamber and dLGN relay neurons were identified under DIC optics based on their large size and by their number of dendrites (three or more dendrites). Whole-cell voltage-clamp recordings were performed at room temperature in isotonic saline solution containing the $GABA_A$ receptor antagonist GABAzine (10 μM), to block local inhibitory circuits. Patch electrodes with a resistance of 2–2.5 MΩ were filled with an internal solution containing (in mM): CsCl 130, NaCl 4, HEPES 10, EGTA 5, $CaCl_2$ 0.5, MgATP 4, Na_2GTP 0.5, QX-341 5 (to suppress voltage-gated sodium channels), pH adjusted to 7.2 with CsOH. A bipolar simulating electrode, filled with isotonic saline solution, was placed in the optic tract next to the vLGN, in a location that optimized the maximal evoked current. The optic tract was stimulated at intensities of 0–200 μA (duration 0.5 ms), with inter-trial intervals of 30 s. The membrane potential of LGN neurons was clamped at either −70 mV or +40 mV, to measure responses mediated predominantly by AMPA or NMDA receptors, respectively.

Two methods were used to quantify the number of retinal afferents connected to the relay neurons in the dLGN: the fibre fraction method and the step-counting method. For the fibre fraction method, we recorded the single-fibre response by reducing the stimulus intensity until no response could be detected and then increasing the stimulus intensity in small increments (0.5-μA increments) to recruit a single fibre (minimal stimulation). Next, we increased the stimulus intensity to excite the bulk of the optic tract (maximal stimulation) to determine the maximal evoked response. The fibre fraction was calculated by dividing the single fibre current response by the maximal current response, thereby estimating the fraction of the cell's total retinogeniculate input contributed by a single fibre. For the step-counting method, we recorded the synaptic responses of dLGN neurons while varying the stimulus intensity from the minimal stimulation to the maximal stimulation to recruit individual axonal inputs. Separate fibres were interpreted as clusters of postsynaptic current responses recruited by an increase in stimulation. This stimulus–response profile allowed an estimation of the number of afferents to each dLGN neuron. Cells were categorized into three groups; refined (1–2 steps), resolving (3–6 steps) and unrefined (7 or more steps), depending on the number of steps detected in their stimulus-response profile.

Statistical analysis. All statistical analyses were done using GraphPad Prism 6 software.

Most of the data were analysed by one-way ANOVA followed by Dunnett's multiple post-hoc tests for comparing more than three samples, and two-sample un-paired *t*-test for comparing two samples with 95% confidence. Two-sample Kolmogorov–Smirnov test with 95% confidence was used for electrophysiology experiments in Fig. 4c, f.

33. Lu, Q. *et al.* Tyro-3 family receptors are essential regulators of mammalian spermatogenesis. *Nature* **398,** 723–728 (1999).
34. Dunkley, P. R., Jarvie, P. E. & Robinson, P. J. A rapid Percoll gradient procedure for preparation of synaptosomes. *Nature Protocols* **3,** 1718–1728 (2008).
35. Beletskii, A. *et al.* High-throughput phagocytosis assay utilizing a pH-sensitive fluorescent dye. *Biotechniques* **39,** 894–897 (2005).
36. Datwani, A. *et al.* Classical MHCI molecules regulate retinogeniculate refinement and limit ocular dominance plasticity. *Neuron* **64,** 463–470 (2009).
37. Jaubert-Miazza, L. *et al.* Structural and functional composition of the developing retinogeniculate pathway in the mouse. *Vis. Neurosci.* **22,** 661–676 (2005).
38. Micheva, K. D., Busse, B., Weiler, N. C., O'Rourke, N. & Smith, S. J. Single-synapse analysis of a diverse synapse population: proteomic imaging methods and markers. *Neuron* **68,** 639–653 (2010).
39. Stafford, B. K., Sher, A., Litke, A. M. & Feldheim, D. A. Spatial-temporal patterns of retinal waves underlying activity-dependent refinement of retinofugal projections. *Neuron* **64,** 200–212 (2009).

©2013 Macmillan Publishers Limited. All rights reserved

ARTICLE

doi:10.1038/nature12870

DWARF 53 acts as a repressor of strigolactone signalling in rice

Liang Jiang[1]*, Xue Liu[1]*, Guosheng Xiong[1]*, Huihui Liu[1]*, Fulu Chen[1], Lei Wang[1], Xiangbing Meng[1], Guifu Liu[1], Hong Yu[1], Yundong Yuan[1], Wei Yi[2], Lihua Zhao[2], Honglei Ma[2], Yuanzheng He[3], Zhongshan Wu[3], Karsten Melcher[3], Qian Qian[4], H. Eric Xu[2,3], Yonghong Wang[1] & Jiayang Li[1]

Strigolactones (SLs) are a group of newly identified plant hormones that control plant shoot branching. SL signalling requires the hormone-dependent interaction of DWARF 14 (D14), a probable candidate SL receptor, with DWARF 3 (D3), an F-box component of the Skp–Cullin–F-box (SCF) E3 ubiquitin ligase complex. Here we report the characterization of a dominant SL-insensitive rice (*Oryza sativa*) mutant *dwarf 53* (*d53*) and the cloning of *D53*, which encodes a substrate of the SCF^{D3} ubiquitination complex and functions as a repressor of SL signalling. Treatments with GR24, a synthetic SL analogue, cause D53 degradation via the proteasome in a manner that requires D14 and the SCF^{D3} ubiquitin ligase, whereas the dominant form of D53 is resistant to SL-mediated degradation. Moreover, D53 can interact with transcriptional co-repressors known as TOPLESS-RELATED PROTEINS. Our results suggest a model of SL signalling that involves SL-dependent degradation of the D53 repressor mediated by the D14–D3 complex.

SLs are a group of terpenoid lactones that were first known for their function in rhizosphere parasitic and symbiotic interactions[1,2]. Recently, SLs have been identified as plant hormones that inhibit axillary bud outgrowth in diverse plant species[3,4]. Deficiencies in SL production and perception lead to excessive outgrowth of axillary buds[5,6]. Studies with branching mutants—*more axillary growth* (*max*) in *Arabidopsis*[7–13], *tillering dwarf mutants* (*d* mutants) in rice[14–20], *ramosus* (*rms*) in pea[8,21] and *decreased apical dominance* (*dad*) in petunia[22–24]—have identified key players in SL biosynthesis and signalling, indicating the largely conserved mechanisms underlying the role of SL in regulating axillary bud outgrowth[5,6]. In addition, SLs are also involved in regulating stem secondary growth, leaf senescence, seed germination and root development[6]. The diverse roles of SLs enable plants to coordinate their internal developmental program and the surrounding environment[5,6].

Rice tillers are specialized branches that determine grain yields and tillering is a model system for elucidating molecular mechanisms that regulate axillary buds[25]. In rice, three DWARF proteins (D27, D17 and D10) are enzymes required for converting all-*trans*-β-carotene to carlactone, a precursor of SLs[15–17,26], whereas the other two DWARF proteins (D14 and D3) have central roles in SL perception and signalling[14,18–20]. *D14* encodes a member of α/β-hydrolase fold family protein and is proposed to be a candidate SL receptor[18–20,27,28], and *D3* encodes a Leu-rich repeat F-box protein and participates in SL perception[14]. D14 has a canonical α/β-hydrolase fold structure and disruption of the hydrolase activity of D14 homologue DAD2 in petunia abolishes SL-induced interaction between DAD2 and PhMAX2A, one of the D3 homologues in petunia, indicating that SL-mediated interaction of DAD2 with PhMAX2A may trigger the SCF E3 ligase to target an unknown substrate for ubiquitination and degradation[24,27–29]. Previous study identified a dominant tillering dwarf mutant *dwarf 53* (*d53*)[30], and the *D53* locus was primarily mapped to the short arm of chromosome 11 (ref. 31). In this study, we show that rice DWARF 53 (D53) is an important component involved in SL signalling, in which D53 acts as a substrate of the SCF^{D3} ubiquitination complex and functions as a repressor of SL signalling.

Characterization of a SL signalling mutant

To elucidate the SL biosynthetic and signalling pathways, we have identified various tillering dwarf mutants. Among them, a dominant mutant, *e9*, which exhibited dwarf and high tillering phenotypes, was of particular interest (Fig. 1a and Extended Data Fig. 1a, b). Previous studies have shown that SLs can inhibit the tillering phenotype of the SL-deficient mutant *d27*, whereas SL signalling mutants including *d3* are resistant to SL treatment[4,17]. Like the *d3* mutant, *e9* is resistant to exogenous application of GR24, a synthetic SL analogue (Fig. 1b and Extended Data Fig. 1c). The expression of *D10*, which is subject to a feedback regulation in the mutants defective in SL biosynthesis and signalling[16], is markedly increased in *e9* (Extended Data Fig. 1d). Moreover, quantitative analysis of the SLs produced in root exudates showed that 2′-*epi*-5-deoxystrigol (*epi*-5DS) in *e9* was ~30% higher than that in the wild type (Fig. 1c and Extended Data Fig. 1e). These results suggested that *e9* is probably involved in SL signalling rather than in SL biosynthesis.

Map-based cloning of the *D53* gene

To isolate the *E9* gene, we took a map-based cloning approach (Extended Data Fig. 2a). *E9* was pin-pointed within a 273-kilobase region between markers Ds3 and K81114 on chromosome 11, which is consistent with the reported region of the dominant dwarf and high tillering locus *d53* (refs 30, 31). Sequencing of the genomic DNA from both *e9* and *d53* within this region revealed an identical mutation that has a 15-base-pair deletion at the third exon of *LOC_Os11g01330*, which results in an in-frame deletion of amino acids 813–817 (Gly-Lys-Thr-Gly-Ile) and an amino acid substitution at 812 (R to T) (Extended Data Fig. 2b). Therefore, *e9* was referred to as *d53* thereafter. To verify whether the mutation of *LOC_Os11g01330* is responsible for the phenotype of *d53*, the plasmid harbouring a 7,452-base-pair genomic fragment of

[1]State Key Laboratory of Plant Genomics and National Center for Plant Gene Research (Beijing), Institute of Genetics and Developmental Biology, Chinese Academy of Sciences, Beijing 100101, China. [2]VARI-SIMM Center, Center for Structure and Function of Drug Targets, CAS-Key Laboratory of Receptor Research, Shanghai Institute of Materia Medica, Chinese Academy of Sciences, Shanghai 201203, China. [3]Laboratory of Structural Sciences, Van Andel Research Institute, 333 Bostwick Avenue Northeast, Grand Rapids, Michigan 49503, USA. [4]State Key Laboratory of Rice Biology, China National Rice Research Institute, Chinese Academy of Agricultural Sciences, Hangzhou 310006, China.
*These authors contributed equally to this work.

©2013 Macmillan Publishers Limited. All rights reserved

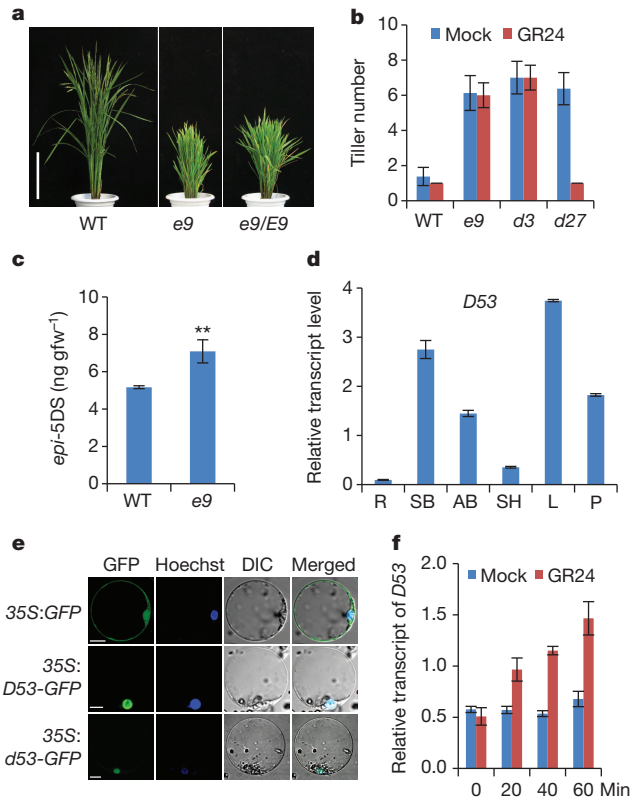


Figure 1 | *D53* acts as a negative regulator in SL signalling. **a**, Phenotypes of *e9* mutants. Scale bars, 20 cm. **b**, Tiller numbers of 4-week-old seedlings of wild-type, *e9*, *d3* and *d27* treated with or without 1 μM GR24. Values are means ± s.d. ($n = 10$). **c**, Comparison of *epi*-5DS contents in wild-type and *e9* root exudates. Values are means ± s.d. ($n = 3$), $^{**}P < 0.01$ (Student's *t*-test). gfw^{-1}, per gram fresh weight. **d**, *D53* transcript levels in various organs, including roots (R), shoot bases of seedlings (SB), axillary buds (AB), sheaths (SH), young leaves (L) and young panicles (P). Values are means with ± s.d. of three independent experiments. **e**, Subcellular localization of *35S:GFP* (top), *35S:D53-GFP* (middle) and *35S:d53-GFP* (bottom) in rice protoplasts. Scale bars, 10 μm. **f**, *D53* transcripts upon 20 μM GR24 treatment in wild-type seedlings revealed by quantitative (q)PCR. Values are means with ± s.d. of three independent experiments.

LOC_Os11g01330 from *d53* was introduced into Nipponbare (Extended Data Fig. 2c). All the nine independent transgenic lines exhibited the same phenotype as *d53* (Extended Data Fig. 2d, e). Thus the mutation of *LOC_Os11g01330* is responsible for the phenotype of *d53*.

The *D53* gene encodes a protein that belongs to the double Clp-N motif-containing P-loop nucleoside triphosphate hydrolase superfamily and shares 96.5% identity with *LOC_Os12g01360* (D53-like) in rice and 36–41% to a subfamily of D53-like (or SUPPRESSOR OF MORE AXILLARY GROWTH2 1-LIKE (SMXL)) proteins recently identified in *Arabidopsis*[32], which also show extended homology to HEAT SHOCK PROTEIN 101 (HSP101) (Extended Data Figs 3 and 4). In addition to the Clp homologous region, D53 also contains three putative ethylene-responsive element binding factor-associated amphiphilic repression (EAR) motifs (Extended Data Fig. 4), which have been proposed to be essential for proteins that interact with the TOPLESS class of transcriptional co-repressors in a number of plant hormone-signalling pathways[33,34]. *D53* is mainly expressed in the shoot bases of seedlings, young leaves, axillary buds and young panicles (Fig. 1d). Subcellular

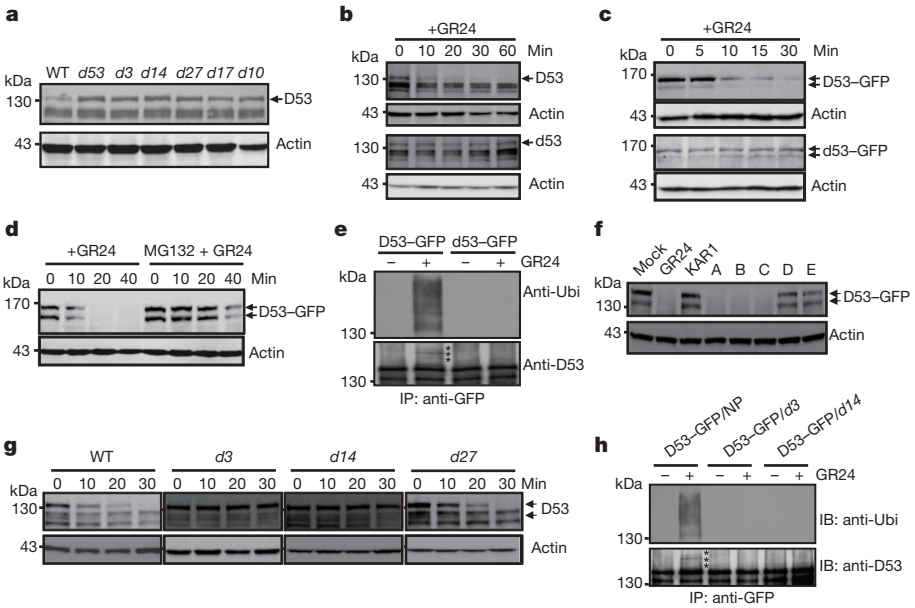


Figure 2 | SL-induced D53 degradation by the ubiquitin proteasome system. **a**, Protein levels of D53 in seedlings of wild-type and *d* mutants detected by immunoblotting with anti-D53 antibodies. **b**, D53 protein levels in 3-week-old seedlings of the wild type (top) and *d53* mutant (bottom) upon 10 μM GR24 treatment detected by immunoblotting with anti-D53 antibodies. **c**, Protein levels of D53–GFP in calli of *Act:D53-GFP* and *Act:d53-GFP* transgenic lines at different time points of GR24 (5 μM) treatment, as detected by immunoblotting with anti-GFP antibody. **d**, D53–GFP protein levels at different time points of GR24 treatment (10 μM) in the presence or absence of MG132 (50 μM), as detected by immunoblotting with anti-GFP antibody. **e**, Analysis of D53–GFP and d53–GFP ubiquitination in response to GR24 (10 μM) treatment. Top, immunoblot with anti-ubiquitin (Ubi) antibody. Bottom, immunoblot with anti-D53 antibodies. Asterisks indicate ubiquitinated D53–GFP proteins. **f**, D53–GFP protein levels in *Act:D53-GFP* transgenic calli treated with 10 μM GR24, KAR1 or SL mimics, as detected by immunoblotting with anti-GFP antibody. A, 4-[(2,5-dihydro-4-methyl-5-oxo-2-furanyl)oxy]benzonitrile; B, 5-(4-bromophenoxy)-3-methyl-2(5*H*)-furanone; C, 5-(4-iodophenoxy)-3-methyl-2(5*H*)-furanone; D, 3,3a,4,8b-tetrahydro-3-(hydroxymethylene)-2*H*-Indeno[1,2-*b*]furan-2-one (ABC rings of GR24); E, 5-hydroxy-3-methyl-2(5*H*)-furanone (D ring of GR24). **g**, D53 protein levels in calli of wild-type, *d3*, *d14* and *d27* upon 5 μM GR24 treatment at different time points, detected by immunoblotting with anti-D53 antibodies. **h**, Analysis of D53–GFP ubiquitination in *d14* and *d3* under GR24 (10 μM) treatment. Top, immunoblotting with a monoclonal anti-ubiquitin antibody. Bottom, immunoblotting with anti-D53 antibodies. Asterisks indicate ubiquitinated D53–GFP. Actin contents were used as loading controls in all the immunoblotting analyses. NP, Nipponbare.

©2013 Macmillan Publishers Limited. All rights reserved

localization observation revealed that both D53–green fluorescent protein (GFP) and d53–GFP were localized to nuclei, indicating that localization of the mutant protein is unaffected (Fig. 1e).

SL-mediated degradation of D53

To understand the role of D53 in the SL signalling pathway, we first examined the expression of *D53* in relation to SL signalling. As shown in Fig. 1f, activation of SL signalling by the treatments of GR24 in wild-type plants upregulated *D53* transcription. By contrast, deficiency in SL biosynthesis and signalling as shown in *d* mutants resulted in down-regulation of *D53* transcription (Extended Data Fig. 5), suggesting that *D53* expression may be subjected to a negative feedback control of SL signalling. In parallel, we examined the D53 protein levels in *d53* and other *d* mutants that are defective in SL biosynthesis or signalling. In contrast to the transcript levels, the protein levels were increased not only in *d53*, but also in all *d* mutants tested (Fig. 2a). Moreover, the D53 protein levels decreased rapidly upon GR24 treatment in wild-type seedlings (Fig. 2b, top panel), even though its transcription is increased (Fig. 1f). The disappearance of the corresponding D53 protein in *d53* is much attenuated (Fig. 2b, bottom panel). Consistent with this, the d53–GFP protein level was not reduced in the transgenic calli by the treatments of GR24 whereas the D53–GFP protein was rapidly degraded upon GR24 treatment (Fig. 2c). However, unlike D53, the protein levels of D14–GFP and D3–GFP remained stable upon GR24 treatment (Extended Data Fig. 6). Furthermore, the GR24-induced degradation of D53 was strongly attenuated by the treatment of the proteasome inhibitor MG132 (Fig. 2d), indicating that ubiquitination might be involved in the degradation of D53. Polyubiquitination of D53–GFP, but not d53–GFP, was indeed induced by GR24 (Fig. 2e), demonstrating that D53 was polyubiquitinated and degraded via the ubiquitin proteasome system in response to GR24. Furthermore, we found that the degradation of D53 was induced by GR24 and several other SL mimics that are active in SL signalling and inhibition of shoot branching[35,36], but not by the KAR1 and ABC- or D-ring of GR24, which are inactive in SL signalling[35–37] (Fig. 2f and Extended Data Fig. 7). Together, these results indicate that the protein stability of D53 is negatively correlated with the signalling status of the SL pathway, leading us to propose that D53 could function as a repressor of SL signalling. This hypothesis is consistent with the dominant phenotype of *d53*, in which the mutated protein is insensitive to SL-mediated degradation.

Formation of a D14–D3–D53 complex

To understand the relationship between D53 and other two SL signalling components, D3 and D14, we constitutively expressed *D53-GFP* or knocked down the *D53* expression level in *d3* and *d14* mutants, respectively. The results showed that overexpression of *D53-GFP* had

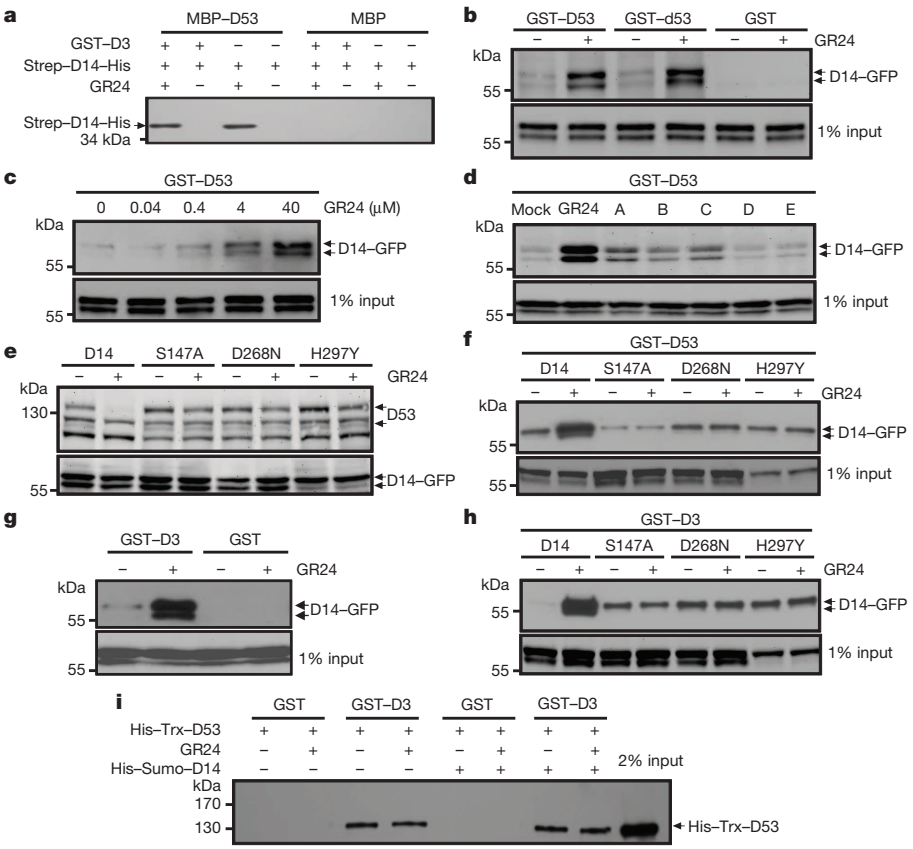


Figure 3 | Interactions among D3, D14 and D53. **a**, *In vitro* pull-down assay using maltose-binding protein (MBP)–D53, GST–D3 and Strep–D14–His recombinant proteins in the presence or absence of 10 μM GR24. **b**, Pull-down assays using recombinant GST–D53 or GST–d53 and lysates prepared from *Act:D14-GFP/d14* calli in the absence or presence of 20 μM GR24. **c**, Pull-down assay using recombinant GST–D53 and lysates prepared from *Act:D14-GFP/d14* calli in the presence of GR24 at indicated concentrations. **d**, Pull-down assay using recombinant GST–D53 and lysates of *Act:D14-GFP/d14* calli treated with 20 μM GR24 or SL mimics. **e**, D53 levels in the 10 μM-GR24-treated calli transformed with *D14* mutated at the Ser-His-Asp catalytic triad sites, revealed by immunoblotting with anti-D53 antibodies. D14, *Act:D14-GFP/d14*; S147A, *Act:D14(S147A)-GFP/d14*; D268N, *Act:D14(D268N)-GFP/d14*; H297Y, *Act:D14(H297Y)-GFP/d14*. **f**, Pull-down assay using recombinant GST–D53 and lysates of the calli transformed with *D14* mutated at its catalytic triad sites in the absence or presence of 20 μM GR24. **g**, Pull-down assay using recombinant GST–D3 and lysates of *Act:D14-GFP/d14* calli in the absence or presence of 20 μM GR24. **h**, Pull-down assay using recombinant GST–D3 and lysates of transgenic calli transformed with *D14* mutated at its catalytic triad sites in the absence or presence of 20 μM GR24. **i**, Pull-down assay using recombinant GST–D3 and His–Trx–D53 in the absence or presence of 5 μM GR24 or His–Sumo–D14 recombinant proteins. The D14 recombinant proteins in **a** were detected with anti-His antibody, GFP-fusion proteins in (**b**–**d** and **f**–**h**) were revealed with anti-GFP antibody, and His–Trx–D53 was detected with anti-D53 antibodies.

©2013 Macmillan Publishers Limited. All rights reserved

little effect on the phenotypes of *d3* and *d14* (Extended Data Fig. 8a–c), whereas the decreased expression of *D53* obviously reduced the tiller number of *d3* and *d14*, respectively (Extended Data Fig. 9), indicating that the reduction of *D53* expression could partially rescue the signalling defects of *d3* and *d14* and that the result is consistent with its negative role in SL signalling. In addition, D53–GFP could not be degraded in *d3* and *d14* plants even in the presence of GR24 (Extended Data Fig. 8d). These results suggest that *D53* may act downstream of *D3* and *D14*. Moreover, when GR24 was applied, degradation of D53 was detected in the wild-type and SL-biosynthesis mutant *d27*, but not in *d3* and *d14* (Fig. 2g). Importantly, the ubiquitination of D53 could also be detected in the D53–GFP transgenic plants in the wild type but not in the background of *d3* and *d14* (Fig. 2h). Taken together, these results demonstrate that SL-induced degradation of D53 is dependent on intact functions of D3 and D14.

To unravel the underlying mechanism of D53 as a repressor in SL signalling, we first examined whether D53 can interact with D14. As shown in Fig. 3a, b, D53 was shown to interact with D14 by pull-down assay. Notably, the d53 protein was still able to interact with D14, indicating that the mutation sites in *d53* may be essential for ubiquitination and stability of D53, but not for its interaction with D14 (Fig. 3b). Importantly, the interaction between D53 and D14 was enhanced by GR24 in a dose-dependent manner (Fig. 3c). In addition, active SL mimics could also enhance the interaction between D53 and D14 (Fig. 3d), which is consistent with their biological functions. To address whether the hydrolase activity of D14 is required for the degradation of D53 and its interaction with D53, we mutated the sites of the Ser-His-Asp catalytic triad and found that mutation at any site of the triad could attenuate the SL-induced degradation of D53 (Fig. 3e) and weaken the interaction between D53 and D14 (Fig. 3f). These results indicate that the perception of SL by D14 is essential for the SL-induced degradation of D53.

We then tested whether the perception of SL requires the interaction between D3 and D14 by performing a pull-down assay. As shown in Fig. 3g, D14–GFP was co-purified with the GST–D3 fusion protein and GR24 could enhance the interaction. Similar to the interaction between D14 and D53, any mutation in the Ser-His-Asp catalytic triad of D14 could also weaken the GR24-induced interaction between D3 and D14 (Fig. 3h), consistent with previous study in petunia[24].

The findings indicating that D14 can interact with both D53 and D3 suggest that D53 may also interact with D3. As shown in Fig. 3i, the histidine (His)–thioredoxin (Trx)–D53 protein could interact with GST–D3 in the *in vitro* pull-down assay with or without the presence of His–small ubiquitin-like modifier (Sumo)–D14 and GR24, suggesting that D53 could be directly targeted by D3 and that hormone-dependent association of D14 with D3 and D53 could trigger D53 ubiquitination and degradation.

Interaction of D53 with TPR proteins

TOPLESS (TPL) and TPL-related proteins (TPRs) have been reported to function as co-repressors in various plant hormone signalling and developmental pathways[33,34,38,39]. The EAR motif is a hallmark of the TPL and TPR interaction proteins[33,34,38,39]. Scanning of the D53 amino acid sequence revealed that D53 harbours three possible EAR motifs: ^{578}Leu-Val-Leu-Asn-Leu^{582} (EAR1), ^{799}Leu-Asp-Leu-Asn-Leu^{803} (EAR2) and ^{976}Phe-Asp-Leu-Asn-Leu-Pro^{981} (EAR3) (Extended Data Fig. 4). There are three TPL/TPR proteins in rice, namely TPR1 (LOC_Os01g15020), TPR2 (LOC_Os08g06480) and TPR3 (LOC_Os03g14980). Among them, TPR2 (also known as ASP1, OsREL2 or OsLIS-L1) has been reported to function in tiller and spikelet development[40–42]. As shown in Fig. 4a, the interactions between D53 and rice TPR proteins were detected by two-hybrid assays in mammalian cells, and the interaction between D53 and TPR2 was further verified by a pull-down assay (Fig. 4b). These results suggest that TPR proteins may be the downstream regulators of SL signalling.

Discussion

In this study, we have identified the *D53* gene that encodes a substrate of the SCF^{D3} ubiquitination complex, and revealed that D53 functions as a repressor of SL signalling. These results allow us to establish a model of SL signalling that is centred around a D14–D3–D53 signalling axis (Fig. 5). In the presence of SLs, perception of SL by D14 and the SCF^{D3} complex leads to ubiquitination of D53 and its subsequent degradation by the ubiquitin proteasome system, which in turn releases the repression of downstream target genes (Fig. 5). In the *d53* plant, the mutated D53 protein is resistant to ubiquitination and degradation, leading to the accumulation of d53, which blocks SL signalling and results in dwarf and high tillering phenotypes. The signalling paradigm of SLs

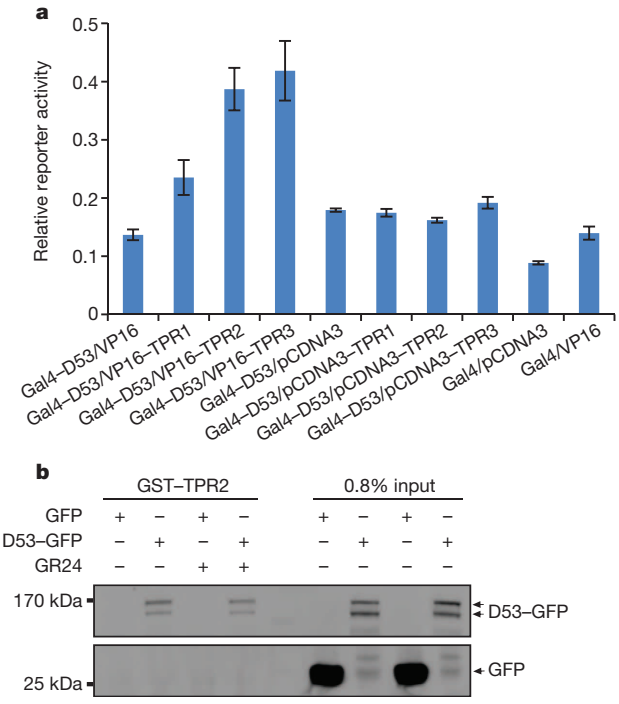


Figure 4 | Interaction of D53 with TPR proteins. a, Mammalian two-hybrid assays showing interaction of D53 with TPR proteins. Values are means ± s.d. of three independent experiments. VP16, herpes simplex virus virion protein 16. **b**, Pull-down assay for GST–TPR2 and lysates of *Act:D53-GFP* calli in the absence or presence of 10 μM GR24. D53–GFP and GFP were detected with the monoclonal anti-GFP antibody.

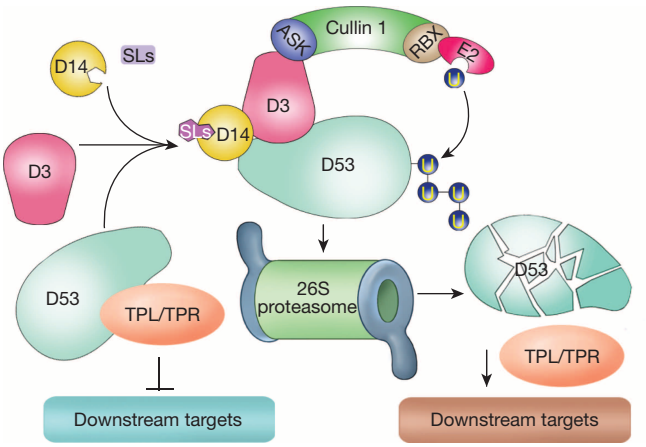


Figure 5 | A proposed model of D53 action. In the absence of SLs, D53 is stable and may recruit TPL/TPR proteins and repress downstream responses. In the presence of SLs, perception of SL leads to SCF^{D3}-mediated ubiquitination of D53 and its subsequent degradation by the proteasome system, which in turn releases the repression of downstream responses.

©2013 Macmillan Publishers Limited. All rights reserved

is still emerging as SLs are a relatively new class of plant hormone for which many knowledge gaps still exist. Identification of D53 as a repressor of SL signalling adds a critical piece of information that helps to paint the whole picture of the SL signalling pathways.

Moreover, our work has also provided an important paradigm for understanding signalling pathways of other plant hormones, for example, karrikins, a class of plant growth regulators found in the smoke of burning plants[37]. Karrikin signalling involves MAX2 and KAI2, a D14-like α/β-hydrolase[13,37]. It is probable that a similar protein to D53 could serve as the repressor of karrikin signalling. Indeed, multiple D53-like proteins are found in rice and in *Arabidopsis*[32]. We propose that these proteins could serve as repressors of signalling by karrikin and other plant hormones, in a similar way to D53 in SL signalling.

METHODS SUMMARY

The rice mutant *e9*/*d53* and other *d* mutants/alleles were identified in the Nipponbare background. *E9/D53* was isolated by map-based cloning. The *D53* function was verified by *D53:d53* and *D53* interference RNA (RNAi) transformants. The subcellular localization of D53 was observed by transient expression of D53–GFP in rice protoplasts. For SL analysis, the SL-containing fraction was eluted, collected and dried, then samples reconstituted in acetonitrile and subjected to ultra-performance liquid chromatography–tandem mass spectrometry analysis. To detect *D53* expression and D53 degradation, chemical treatments were performed in hydroponic cultured seedlings or transgenic calli in liquid medium, the transcripts of *D53* were determined by qPCR and the abundance of D53 was detected by western blot. The ubiquitination of D53 was performed by detection of immunoprecipitated D53–GFP and d53–GFP fusion proteins with anti-ubiquitin and anti-D53 antibodies. For pull-down assays, the recombinant GST–D53, MBP–D53, His–Trx–D53, GST–D3, Strep–D14–His and GST–TPR2 were expressed in *Escherichia coli* BL21 (DE3) cells and purified through GSTrap HP column, MBPTrap HP column, or HisTrap HP column. For mammalian two-hybrid assays, Gal4-fusion constructs were co-transfected with VP16-fusion constructs and reporter plasmids into AD293 cells. Luciferase/Renilla relative activities were measured using Dual Luciferase Kit.

Online Content Any additional Methods, Extended Data display items and Source Data are available in the online version of the paper; references unique to these sections appear only in the online paper.

Received 9 July; accepted 6 November 2013.

Published online 11 December 2013.

1. Cook, C. E., Whichard, L. P., Turner, B., Wall, M. E. & Egley, G. H. Germination of witchweed (*Striga lutea Lour.*): isolation and properties of a potent stimulant. *Science* **154,** 1189–1190 (1966).
2. Akiyama, K., Matsuzaki, K. & Hayashi, H. Plant sesquiterpenes induce hyphal branching in arbuscular mycorrhizal fungi. *Nature* **435,** 824–827 (2005).
3. Gomez-Roldan, V. *et al.* Strigolactone inhibition of shoot branching. *Nature* **455,** 189–194 (2008).
4. Umehara, M. *et al.* Inhibition of shoot branching by new terpenoid plant hormones. *Nature* **455,** 195–200 (2008).
5. Domagalska, M. A. & Leyser, O. Signal integration in the control of shoot branching. *Nature Rev. Mol. Cell Biol.* **12,** 211–221 (2011).
6. Ruyter-Spira, C., Al-Babili, S., van der Krol, S. & Bouwmeester, H. The biology of strigolactones. *Trends Plant Sci.* **18,** 72–83 (2013).
7. Stirnberg, P., van De Sande, K. & Leyser, O. *MAX1* and *MAX2* control shoot lateral branching in *Arabidopsis*. *Development* **129,** 1131–1141 (2002).
8. Sorefan, K. *et al. MAX4* and *RMS1* are orthologous dioxygenase-like genes that regulate shoot branching in *Arabidopsis* and pea. *Genes Dev.* **17,** 1469–1474 (2003).
9. Booker, J. *et al.* MAX3/CCD7 is a carotenoid cleavage dioxygenase required for the synthesis of a novel plant signaling molecule. *Curr. Biol.* **14,** 1232–1238 (2004).
10. Booker, J. *et al. MAX1* encodes a cytochrome P450 family member that acts downstream of *MAX3/4* to produce a carotenoid-derived branch-inhibiting hormone. *Dev. Cell* **8,** 443–449 (2005).
11. Stirnberg, P., Furner, I. J. & Leyser, O. MAX2 participates in an SCF complex which acts locally at the node to suppress shoot branching. *Plant J.* **50,** 80–94 (2007).
12. Waters, M. T., Brewer, P. B., Bussell, J. D., Smith, S. M. & Beveridge, C. A. The *Arabidopsis* ortholog of rice DWARF27 acts upstream of MAX1 in the control of plant development by strigolactones. *Plant Physiol.* **159,** 1073–1085 (2012).
13. Waters, M. T. *et al.* Specialisation within the DWARF14 protein family confers distinct responses to karrikins and strigolactones in *Arabidopsis*. *Development* **139,** 1285–1295 (2012).
14. Ishikawa, S. *et al.* Suppression of tiller bud activity in tillering dwarf mutants of rice. *Plant Cell Physiol.* **46,** 79–86 (2005).
15. Zou, J. *et al.* The rice *HIGH-TILLERING DWARF1* encoding an ortholog of *Arabidopsis MAX3* is required for negative regulation of the outgrowth of axillary buds. *Plant J.* **48,** 687–698 (2006).
16. Arite, T. *et al. DWARF10*, an *RMS1/MAX4/DAD1* ortholog, controls lateral bud outgrowth in rice. *Plant J.* **51,** 1019–1029 (2007).
17. Lin, H. *et al.* DWARF27, an iron-containing protein required for the biosynthesis of strigolactones, regulates rice tiller bud outgrowth. *Plant Cell* **21,** 1512–1525 (2009).
18. Arite, T. *et al. d14*, a strigolactone-insensitive mutant of rice, shows an accelerated outgrowth of tillers. *Plant Cell Physiol.* **50,** 1416–1424 (2009).
19. Gao, Z. *et al. Dwarf 88*, a novel putative esterase gene affecting architecture of rice plant. *Plant Mol. Biol.* **71,** 265–276 (2009).
20. Liu, W. *et al.* Identification and characterization of *HTD2*: a novel gene negatively regulating tiller bud outgrowth in rice. *Planta* **230,** 649–658 (2009).
21. Johnson, X. *et al.* Branching genes are conserved across species. Genes controlling a novel signal in pea are coregulated by other long-distance signals. *Plant Physiol.* **142,** 1014–1026 (2006).
22. Snowden, K. C. *et al.* The *Decreased apical dominance1/Petunia hybrida CAROTENOID CLEAVAGE DIOXYGENASE8* gene affects branch production and plays a role in leaf senescence, root growth, and flower development. *Plant Cell* **17,** 746–759 (2005).
23. Simons, J. L., Napoli, C. A., Janssen, B. J., Plummer, K. M. & Snowden, K. C. Analysis of the *DECREASED APICAL DOMINANCE* genes of petunia in the control of axillary branching. *Plant Physiol.* **143,** 697–706 (2007).
24. Hamiaux, C. *et al.* DAD2 is an α/β hydrolase likely to be involved in the perception of the plant branching hormone, strigolactone. *Curr. Biol.* **22,** 2032–2036 (2012).
25. Wang, Y. & Li, J. Molecular basis of plant architecture. *Annu. Rev. Plant Biol.* **59,** 253–279 (2008).
26. Alder, A. *et al.* The path from β-carotene to carlactone, a strigolactone-like plant hormone. *Science* **335,** 1348–1351 (2012).
27. Zhao, L. H. *et al.* Crystal structures of two phytohormone signal-transducing α/β hydrolases: karrikin-signaling KAI2 and strigolactone-signaling DWARF14. *Cell Res.* **23,** 436–439 (2013).
28. Kagiyama, M. *et al.* Structures of D14 and D14L in the strigolactone and karrikin signaling pathways. *Genes Cells* **18,** 147–160 (2013).
29. Smith, S. M. & Waters, M. T. Strigolactones: destruction-dependent perception? *Curr. Biol.* **22,** R924–R927 (2012).
30. Iwata, N. & Omura, T. Studies on the trisomics in rice plants (*Oryza sativa* L.). VI. An accomplishment of a trisomic series in *japonica* rice plants. *Jpn. J. Genet.* **59,** 199–204 (1984).
31. Wei, L. R., Xu, J. C., Li, X. B., Qian, Q. & Zhu, L. H. Genetic analysis and mapping of the dominant dwarfing dene *D-53* in rice. *J. Integr. Plant Biol.* **48,** 447–452 (2006).
32. Stanga, J. P., Smith, S. M., Briggs, W. R. & Nelson, D. C. *SUPPRESSOR OF MORE AXILLARY GROWTH2 1* controls seed germination and seedling development in *Arabidopsis*. *Plant Physiol.* **163,** 318–330 (2013).
33. Szemenyei, H., Hannon, M. & Long, J. A. TOPLESS mediates auxin-dependent transcriptional repression during *Arabidopsis* embryogenesis. *Science* **319,** 1384–1386 (2008).
34. Pauwels, L. *et al.* NINJA connects the co-repressor TOPLESS to jasmonate signalling. *Nature* **464,** 788–791 (2010).
35. Fukui, K. *et al.* New branching inhibitors and their potential as strigolactone mimics in rice. *Bioorg. Med. Chem. Lett.* **21,** 4905–4908 (2011).
36. Fukui, K., Ito, S. & Asami, T. Selective mimics of strigolactone actions and their potential use for controlling damage caused by root parasitic weeds. *Mol. Plant* **6,** 88–99 (2013).
37. Nelson, D. C. *et al.* F-box protein MAX2 has dual roles in karrikin and strigolactone signaling in *Arabidopsis thaliana*. *Proc. Natl Acad. Sci. USA* **108,** 8897–8902 (2011).
38. Causier, B., Ashworth, M., Guo, W. & Davies, B. The TOPLESS interactome: a framework for gene repression in *Arabidopsis*. *Plant Physiol.* **158,** 423–438 (2012).
39. Long, J. A., Ohno, C., Smith, Z. R. & Meyerowitz, E. M. TOPLESS regulates apical embryonic fate in *Arabidopsis*. *Science* **312,** 1520–1523 (2006).
40. Yoshida, A., Ohmori, Y., Kitano, H., Taguchi-Shiobara, F. & Hirano, H. Y. *Aberrant spikelet and panicle1*, encoding a TOPLESS-related transcriptional co-repressor, is involved in the regulation of meristem fate in rice. *Plant J.* **70,** 327–339 (2012).
41. Kwon, Y. *et al. OsREL2*, a rice TOPLESS homolog functions in axillary meristem development in rice inflorescence. *Plant Biotechnol. Rep.* **6,** 213–224 (2012).
42. Gao, X. *et al. OsLIS-L1* encoding a lissencephaly type-1-like protein with WD40 repeats is required for plant height and male gametophyte formation in rice. *Planta* **235,** 713–727 (2012).

Supplementary Information is available in the online version of the paper.

Acknowledgements We thank K. Yoneyama for assistance in SL analysis and C. Yan for SL measurement. This work was supported by grants from Ministry of Science and Technology of the People's Republic of China (2012AA10A301) and National Natural Science Foundation of China (31025004, 90817108 and 91217311).

Author Contributions L.J., X.L., G.X. and H.L. designed research, performed experiments, analysed data and wrote the paper; F.C., L.W., X.M., H.Y., Y.Y., G.L., W.Y., L.Z., H.M., Y.H., Z.W. and K.M. performed some of the experiments. Q.Q. provided and planted the rice materials. J.L., Y.W. and H.E.X. designed research, analysed data and wrote the paper. J.L. conceived and supervised the project.

Author Information The sequence of DWARF53 coding region has been deposited in the GenBank database under accession number KF23088. Reprints and permissions information is available at www.nature.com/reprints. The authors declare no competing financial interests. Readers are welcome to comment on the online version of the paper. Correspondence and requests for materials should be addressed to J.L. (jyli@genetics.ac.cn), Y.W. (yhwang@genetics.ac.cn) or H.E.X. (Eric.Xu@vai.org).

©2013 Macmillan Publishers Limited. All rights reserved

METHODS

Plant materials. A naturally occurring rice mutant *e9* was isolated from a Nipponbare (*Oryza sativa* L. ssp. *japonica*) population in Hangzhou, China in 2005. The *e9* mutant was then backcrossed to Nipponbare four times. Cloning and sequencing of *e9* indicated that it has an identical mutation to *d53*, suggesting that *e9* might originally have resulted from a natural pollination by *d53*-carrying plants[30,43] in the field. All other *d* mutants/alleles in the Nipponbare background (*d27*, *d17*, *d10*, *d14* and *d3*) used in this study were isolated by our laboratory and the mutation sites of the mutants are shown in Extended Data Fig. 5b.

Map-based cloning. To map the *e9* locus, *e9* mutant plants were crossed to NJ06 (*indica*) and 142 recessive individual plants showing normal tillering phenotype from F_2 populations were used for primary mapping. *E9* was pin-pointed to the region between makers Ds3 and K81114 (Extended Data Fig. 2a and Supplementary Table 1), which is consistent with the mapping result of the previously reported *D53* locus[31]. To find out the mutation site, we amplified the corresponding fragments from *e9* and *d53*, respectively. The average length of the PCR products was 1.5 kb. By comparison of the sequence between *e9* and *d53*, only one mutation in the exon was identified in both *e9* and *d53*.

Rice hydroponic culture. Rice seeds were de-hulled and sterilized with 2.5% (v/v) sodium hypochlorite for 30 min, rinsed five times with sterile water, and then germinated for 30 h in sterile water at 37 °C in darkness. Germinated seeds were transferred into a hydroponic culture medium (pH 5.5) and cultured at 28 °C, 70% relative humidity under fluorescence white light (150–200 $\mu M\ m^{-2}\ s^{-1}$) with a 16 h light/8 h dark photoperiod for 5 days, and grown under the same condition in hydroponic culture medium without Pi for an additional 14 days (total 3 weeks). The hydroponic solution was renewed every 3 days.

SL analysis. SL analyses in rice root exudates were performed according to the previously described method with minor modifications[4,17]. For each sample, 50 ml hydroponic culture medium from total 500 ml was loaded to a pre-equilibrated Oasis HLB 3cc cartridge (Waters) after adding 1 ng d_6-5DS as an internal standard and the column was washed with de-ionized water. The SLs-containing fraction was eluted with acetone, collected and dried up under nitrogen gas, then reconstituted in acetonitrile and subjected to UPLC–MS/MS analysis, which consists of a triple quadruple tandem mass spectrometer (Quattro Premier XE; Waters) and an Acquity Ultra Performance Liquid Chromatograph (Acquity UPLC; Waters) equipped with a reverse phase column (BEH-C18, 2.1 × 100 mm, 1.7 μm; Waters). The gradient started with 50% mobile phase A (99.5% H_2O plus 0.5% acetic acid) and increased mobile phase B (99.5% ACN plus 0.5% acetic acid) from 50% to 70% in 5 min at 25 °C with a flow rate of 0.4 ml min^{-1}. MS parameters were set to the following values: desolvation gas flow, 800 l h^{-1}; capillary voltage, 3.8 kV; cone voltage, 24 V; desolvation temperature, 350 °C; source temperature, 110 °C; collision energy, 14 V, using multiple reaction monitoring (MRM) 331 > 216 transition for the *epi*-5DS detection and MRM 337 > 222 transition for the d_6-5DS detection. Data were analysed with MassLynx software (V.4.1). The *epi*-5DS concentrations of rice exudates were calculated by comparing the MRM relative response of *epi*-5DS with the d_6-5DS ones then divided by the fresh rice roots weight. The peak area values of *epi*-5DS versus the internal standard in the wild type were 55.9 versus 231.1, 51.7 versus 204.63 and 40.8 versus 162.8. The peak area values of *epi*-5DS versus the internal standard in *e9* were 68.5 versus 246.9, 57.3 versus 169.3 and 74.3 versus 241.4. The fresh root weights of the wild type and *e9* mutant were 0.48 g and 0.43 g, respectively. The *epi*-5DS concentrations of rice exudates were calibrated by comparing the MRM relative response of *epi*-5DS with that of d_6-5DS and multiplying by the dilution ratio (500:50) and then dividing by the fresh rice root weight.

Plasmid construction and transformation. To construct the *D53*:*d53* plasmid, a 7,452-base pair (bp) genomic fragment from the 1,769-bp 5′-upstream sequence to the 1,002-bp 3′-downstream was amplified using primers d53GenF and d53GenR (Supplementary Table 2), digested with BamHI and HindIII, and cloned into the binary vector pCAMBIA1300. No additional mutation was found by sequencing. To construct the *Act*:*D53-GFP* and *Act*:*d53 -GFP* plasmids, the full-length coding sequences of *D53* and *d53* were amplified using primers ActD53GFPF and ActD53GFPR (Supplementary Table 2), digested by ApaI and SpeI, and then ligated into the binary vector AHLG. To generate the plasmids of *Act*:*D3-GFP* and *Act*:*D14-GFP*, the full-length coding sequences of *D3* and *D14* were amplified with primers ActD3GFPF and ActD3GFPR, ActD14GFPF and ActD14GFPR, respectively (Supplementary Table 2). Two insertions were digested by AapI and XbaI, and ligated into the binary vector AHLG. The *Act*:*D14(S147A)-GFP*, *Act*:*D14(D268N)-GFP* and *Act*:*D14(H297Y)-GFP* plasmids were derived from *pAct:D14-GFP* by site-directed mutagenesis (Supplementary Table 2). To generate the *D53*-RNAi plasmid, two inverted fragments of D53 were amplified by two pairs of primers (D53RNAi1F and D53RNAi1R; D53RNAi2F and D53RNAi2R), digested by BamHI/KpnI and SacI/SpeI, and cloned into pTCK303 (ref. 44). All plasmids were introduced into *Agrobacterium tumefaciens* strain EHA105 and transformed into indicated rice recipients as reported previously[45].

qPCR. Total RNAs from various organs were extracted using a TRIzol kit according to the user's manual (Invitrogen). Total RNAs (2.5 μg) were treated with DNase I and used for complementary DNA synthesis with Superscript III RT kit (Invitrogen). qPCR experiments were performed with gene-specific primers D53RT and D10RT (Supplementary Table 1) in the reaction system of SsoFast EvaGreen supermix (Bio-Rad) on the CFX96 Real-time system (Bio-Rad) following the manufacturer's instructions. The rice actin gene was used as an internal control.

Protoplast transient expression assay. To generate *35S:D53-GFP* and *35S:d53-GFP* plasmids, full-length coding sequences of *D53* and *d53* were amplified using primers 35SD53GFPF and 35SD53GFPR (Supplementary Table 2), digested by BamHI and HindIII, and inserted into the vector pBI221. The plasmids of *35S:GFP*, *35S:D53-GFP* and *35S:d53-GFP* were introduced into rice leaf protoplasts as described[46]. After overnight incubation in the dark at 28 °C, nuclei were stained with Hoechst 33342 as described[47]. The signals of GFP and Hoechst 33342 were observed under a confocal microscope at excitation wavelengths of 488 and 405 nm, respectively (FluoView 1000; Olympus).

Antibody preparation. A DNA fragment encoding D53 amino acid residues 251–700 amplified by primers D53antigenF and D53antigenR (Supplementary Table 2) was cloned into pDONR222 by integrative reaction (Invitrogen) and then to the destination vector pET-55-DEST (Invitrogen) by excisive reaction. The recombinant protein was expressed in *E. coli* BL21 cells and purified by Ni-sepharose (GE Healthcare). The purified proteins were used to raise polyclonal antibodies in rabbit and the anti-D53 serum was affinity purified before use. 1:1,000 ~1:2,000 dilution of the antibody was used for protein blotting. The specificity of D53 antibodies was confirmed by western blot analysis with *Act:D53–GFP* transgenic seedlings (Extended Fig. 10).

Chemical treatment of rice seedlings and calli. To detect D53 degradation, seedlings were grown on hydroponic solution (pH 5.5)[48] in a greenhouse for 3 weeks. After the treatment with 10 μM GR24 (Chiralix), shoot bases were collected and frozen at −80 °C until protein gel blot analysis. For detecting D53 abundance, calli of wild-type and transgenic lines were cultured on solid medium[49] for 6 days at 28 °C and then transferred into a liquid medium[50]. After treatment with the indicated concentrations of GR24 or other SL-like chemicals, calli were collected at the times indicated and frozen at −80 °C until immunoblotting.

***In vivo* ubiquitination assay.** Transgenic calli of *Act*:*D53-GFP*, *Act*:*d53-GFP*, *Act*:*D53-GFP/d3* and *Act*:*D53-GFP/d14* were cultured on solid medium[49] for 6 days at 28 °C and then transferred into a liquid medium[50]. The calli were pre-treated with 50 μM MG132 (Calbiochem) for 1 h and then supplemented with or without 10 μM GR24 for 3 min. Total proteins were extracted in the extraction buffer (50 mM sodium phosphate buffer, pH 7.0, 150 mM NaCl, 10% glycerol, 0.1% NP-40, 50 μM MG132, 1 × complete protease inhibitor cocktail). The lysates were centrifuged at 18,000*g* for 20 min at 4 °C. The supernatant was taken for immunoprecipitation experiments. In brief, 30 μl of anti-GFP monoclonal antibody-conjugated agarose (MBL) was added into 1.5 ml total extracted proteins and incubated at 4 °C for 3 h with gentle rotation. The beads were washed three times with the extraction buffer without NP-40 and then eluted with 30 μl of the SDS–PAGE sample buffer for protein blotting. Mouse anti-ubiquitin monoclonal antibody (Cell signaling) was used at a 1:3,000 dilution and rabbit anti-D53 polyclonal antibodies were used at a 1:2,000 dilution.

Preparation of recombinant proteins. To prepare different tag-fused D53 recombinant proteins, various expression vectors were constructed. To construct the GST–D53 plasmid, a synthesized codon-optimized *D53* coding sequence was inserted into the vector pGEX-6p-1 (GE healthcare). To construct the MBP–D53 plasmid, the full-length coding sequence (CDS) of *D53* was amplified from rice cDNAs by primers MBPD53F and MBPD53R (Supplementary Table 2), digested with BamHI and HindIII, and inserted into the vector pMAL-c2x. To construct the His–Trx–D53 plasmid, the full-length codon-optimized CDS of *D53* coding sequence was digested with BamHI and NotI and inserted into the vector His–Trx. To construct the GST–D3 plasmid, the full-length CDS of *D3* was amplified by primers GST–D3F and GST–D3R (Supplementary Table 2), digested by EcoR I and SalI, and inserted into the vector pGEX-6p-1. To construct the Strep–D14–His plasmid, the full-length CDS of *D14* was amplified by primers StrepD14-HISF and StrepD14-HISR (Supplementary Table 2), cloned into pDONR222 by BP reaction (Invitrogen), and then recombined to pET-55-DEST by LR reaction (Invitrogen). To construct the plasmid that expresses GST–TPR2 (*LOC_Os08g06480*), the coding sequence of *TPR2* was synthesized, sub-cloned into pDONR222 by BP reaction (Invitrogen), and recombined to pET-60-DEST by LR reaction (Invitrogen). To produce recombinant proteins, each expression plasmid constructed above was introduced into *E. coli* BL21 (DE3) cells. In brief, bacterial cells were cultured in the 2YT broth at 37 °C to reach 0.8 (OD_{600}) and then continuously cultured at 16 °C for 15 h after adding 1 mM isopropyl-β-D-thiogalactopyranoside (IPTG). Cells were collected and lysed by JNBIO high pressure homogenizer (Beijing, Shunxinwangchang Co) at 4 °C. Lysates of the above recombinant proteins were centrifuged at 16,000*g* for

©2013 Macmillan Publishers Limited. All rights reserved

30 min and the supernatants were loaded onto a 5-ml GSTrap HP column (GE healthcare), MBPTrap HP column (GE healthcare) or HisTrap HP column (GE healthcare) according to their fused-tags. The purified recombinant proteins finally desalted by a PD-10 column (GE healthcare).

Pull-down assays. Total proteins were extracted from calli treated with or without GR24 before collection by extraction buffer (50 mM sodium phosphate buffer, pH 7.0, 150 mM NaCl, 10% glycerol, 0.1% NP-40, 50 μM MG132, 1 × complete protease inhibitor cocktail) and cell debris was removed by centrifugation at 17,000*g* for 20 min at 4 °C. For the GST–D53, GST–D3 or GST–TPR2 pull-down assay, 0.5–1 μg glutathione agarose-bound GST fusion proteins were added to the crude extract and incubated at 4 °C for 2 h with gentle rotation. Glutathione beads (GE healthcare) were collected by brief centrifugation, washed three times in the above buffer without NP-40, then re-suspended in SDS–PAGE sample buffer and subjected to SDS–PAGE electrophoresis and immunoblotting. For an *in vitro* MBP–D53 pull-down assay, ~0.3 μg recombinant MBP–D53 proteins bound to MBP beads were incubated with ~0.2 μg Strep–D14–His or Strep–D14–His plus GST–D3 (~0.2 μg each) at 4 °C for 2 h, and washed three times with PBS. GFP fusion proteins were detected by a monoclonal anti-GFP antibody (Roche) and Strep–D14–His by a monoclonal anti-His antibody (Abmart). For an *in vitro* GST–D3 pull-down assay, 12 μg recombinant GST–D3 protein bound to glutathione beads and incubated with ~1 μg His–Trx–D53 with or without 5 μM GR24 and His–Sumo–D14 (~10 μg each) at 4 °C for 15 min, and washed four times with PBS. His–Trx–D53 was detected by anti-D53 antibodies.

Mammalian two-hybrid assay. To construct the Gal4–D53 plasmid, the *D53* full-length CDS was generated from pUC57-D53 (synthesized codon-optimized *D53* cDNA in the pUC plasmid) digested with EcoRI and XhoI, and ligated into the EcoRI/SalI double-digested Gal4 plasmid pM (Clontech). To construct VP16–TPR1, VP16–TPR2 and VP16–TPR3, full-length coding sequences of *TPR1*, *TPR2* and *TPR3* were yielded from pLexA-N-fusion plasmids (synthesized codon-optimized *TPR* cDNAs in the pLexA-N plasmid), and inserted into EcoRI/SalI double-digested pVP16 (Clontech). The pcDNA3-derived plasmids were constructed by inserting EcoRI/SalI-digested TPR1, TPR2 and TPR3 into EcoRI/XhoI-digested pcDNA3. Gal4-fusion constructs (25 ng) were co-transfected with VP16-fusion constructs (25 ng), together with 100 ng pG5-Luc, 5 ng phRG-TK/Renilla (Promega) into AD293 cells in the 24-well-plate via Fugen6 (Promega) according to the manufacturer's manual. Cells were collected 24 h after transfection with 1 × passive lysis buffer (Promega). Luciferase/Renilla activities were measured with the Dual Luciferase Kit (Promega) and data were plotted as relative activities (Luciferase activity:Renilla activity).

43. Iwata, N., Satoh, N. & Omura, T. Linkage studies in rice. Linkage groups for 6 genes newly described. *Jpn. J. Breed.* **27** (suppl.), 250–251 (1977).
44. Wang, Z. *et al.* A practical vector for efficient knockdown of gene expression in rice (*Oryza sativa* L.). *Plant Mol. Biol. Rep.* **22,** 409–417 (2004).
45. Hiei, Y., Ohta, S., Komari, T. & Kumashiro, T. Efficient transformation of rice (*Oryza sativa* L.) mediated by *Agrobacterium* and sequence analysis of the boundaries of the T-DNA. *Plant J.* **6,** 271–282 (1994).
46. Bart, R., Chern, M., Park, C. J., Bartley, L. & Ronald, P. C. A novel system for gene silencing using siRNAs in rice leaf and stem-derived protoplasts. *Plant Methods* **2,** 13 (2006).
47. Kierzkowski, D. *et al.* The *Arabidopsis* CBP20 targets the cap-binding complex to the nucleus, and is stabilized by CBP80. *Plant J.* **59,** 814–825 (2009).
48. Kamachi, K., Yamaya, T., Mae, T. & Ojima, K. A role for glutamine synthetase in the remobilization of leaf nitrogen during natural senescence in rice leaves. *Plant Physiol.* **96,** 411–417 (1991).
49. Chu, C. C. *et al.* Establishment of an efficient medium for anther culture of rice through comparative experiments on nitrogen-source. *Sci. China* **18,** 659–668 (1975).
50. Gamborg, O. L., Miller, R. A. & Ojima, K. Nutrient requirements of suspension cultures of soybean root cells. *Exp. Cell Res.* **50,** 151–158 (1968).

©2013 **Macmillan Publishers Limited. All rights reserved**

ARTICLE

doi:10.1038/nature12878

D14–SCF^{D3}–dependent degradation of D53 regulates strigolactone signalling

Feng Zhou[1,2], Qibing Lin[2], Lihong Zhu[1], Yulong Ren[2], Kunneng Zhou[1], Nitzan Shabek[3,4], Fuqing Wu[2], Haibin Mao[3,4], Wei Dong[2], Lu Gan[2], Weiwei Ma[2], He Gao[1], Jun Chen[2], Chao Yang[1], Dan Wang[2], Junjie Tan[2], Xin Zhang[2], Xiuping Guo[2], Jiulin Wang[2], Ling Jiang[1], Xi Liu[1], Weiqi Chen[5], Jinfang Chu[5], Cunyu Yan[5], Kotomi Ueno[6], Shinsaku Ito[6], Tadao Asami[6], Zhijun Cheng[2], Jie Wang[2], Cailin Lei[2], Huqu Zhai[2], Chuanyin Wu[2], Haiyang Wang[2], Ning Zheng[3,4] & Jianmin Wan[1,2]

Strigolactones (SLs), a newly discovered class of carotenoid-derived phytohormones, are essential for developmental processes that shape plant architecture and interactions with parasitic weeds and symbiotic arbuscular mycorrhizal fungi. Despite the rapid progress in elucidating the SL biosynthetic pathway, the perception and signalling mechanisms of SL remain poorly understood. Here we show that DWARF 53 (D53) acts as a repressor of SL signalling and that SLs induce its degradation. We find that the rice (*Oryza sativa*) *d53* mutant, which produces an exaggerated number of tillers compared to wild-type plants, is caused by a gain-of-function mutation and is insensitive to exogenous SL treatment. The *D53* gene product shares predicted features with the class I Clp ATPase proteins and can form a complex with the α/β hydrolase protein DWARF 14 (D14) and the F-box protein DWARF 3 (D3), two previously identified signalling components potentially responsible for SL perception. We demonstrate that, in a D14- and D3-dependent manner, SLs induce D53 degradation by the proteasome and abrogate its activity in promoting axillary bud outgrowth. Our combined genetic and biochemical data reveal that D53 acts as a repressor of the SL signalling pathway, whose hormone-induced degradation represents a key molecular link between SL perception and responses.

Shoot branching (tillering in crops) is a major determinant of plant architecture and crop yield, which is under the integrated control of hormonal, developmental and environmental factors[1–3]. Although the existence of a root-derived transmissible shoot-repressing signal was proposed more than 70 years ago[4], the identity of this signal(s) has remained elusive. Recent studies with branching mutants in several plant species have demonstrated that SLs, a specific group of terpenoid lactones, are the long-sought branching-repressing hormones, whose function are highly conserved in both monocots and dicots[5,6]. In addition to repressing shoot branching, SLs also have a role in regulating root growth, leaf senescence and flower development[7]. SLs also act as exogenous signals to promote the symbiosis between land plants and arbuscular mycorrhizal fungi[8] and stimulate the germination of the parasitic weeds *Striga* and *Orobanche*, which are serious agricultural pests in many parts of the world[9].

Previous studies have shown that *DWARF 3* (*D3*), *D10*, *D14* (also known as *HIGH-TILLERING DWARF 2, HTD2* and *D88*), *D17* (also known as *HTD1*) and *D27* in rice[10–14], *MORE AXILLARY GROWTH 1* (*MAX1*), *MAX2*, *MAX3* and *MAX4* in *Arabidopsis*[15–17], *RAMOSUS 1* (*RMS1*), *RMS4* and *RMS5* in pea[18] and *DECREASED APICAL DOMINANCE 1* (*DAD1*), *DAD2* and *DAD3* in petunia[7,19] are involved in either the biosynthesis or signalling of SLs. Among these genes, *MAX3*/*RMS5*/*D17*/*DAD3*, *MAX4*/*RMS1*/*D10*/*DAD1*, *MAX1* in *Arabidopsis* and *D27* in rice encode the carotenoid cleavage dioxygenase 7 (CCD7), CCD8, CYP711A1 (a cytochrome P450) and a novel β-carotene isomerase, respectively, and are involved in the sequential cleavage of β-carotene and synthesis of SLs[20]. By contrast, *MAX2*/*RMS4*/*D3* and *D14*/*DAD2*, which encode an F-box protein and a protein of the α/β-hydrolase superfamily, respectively, probably have a role in SL signalling[12,19,21]. The structural similarity between MAX2/RMS4/D3 proteins with the auxin receptor TRANSPORT INHIBITOR RESPONSE 1 (TIR1)[22,23] and jasmonate receptor CORONATINE INSENSITIVE 1 (COI1)[24], and D14/DAD2 proteins with the gibberellin receptor GIBBERELLIN INSENSITIVE DWARF 1 (GID1)[25], has sparked the speculation that both MAX2/RMS4/D3 and D14/DAD2 could be candidates for the SL receptors[26] and that binding and hydrolysis of SLs by D14/DAD2 (refs 19, 27, 28) might be required for triggering proteasome-mediated degradation of an unknown repressor by the Skp1–Cullin–F-box-containing (SCF)^{MAX2} complex[29,30]. However, the identity of such a repressor and its regulatory mechanisms in SL signalling have remained unknown.

In this study, we identified a gain-of-function rice mutant, *d53*, which displays a SL-insensitive and increased-tillering phenotype. Map-based cloning revealed that *D53* encodes a protein sharing predicted features with the class I Clp ATPase proteins and that it can form a complex with the α/β hydrolase protein D14 and the F-box protein D3. We show that SLs induce D53 degradation by the proteasome–ubiquitin pathway in a D14- and D3-dependent manner. Our studies establish D53 as a repressor of the SL signalling pathway, whose hormone-induced degradation is essential for SL signalling.

d53 is a rice SL-insensitive mutant

Previous studies have identified several rice mutants defective in SL biosynthesis or signalling[10–14]. Because of their highly branched and dwarf phenotype, these mutants were termed '*d* mutants', such as *d3*, *d10*, *d14*, *d17* and *d27*. The rice *d53* mutant[31] also displayed reduced height and increased tillering, as well as thinner stem and shorter crown root, compared to the wild-type strain (Fig. 1a, b and Extended Data Fig. 1a, b).

[1]National Key Laboratory for Crop Genetics and Germplasm Enhancement, Jiangsu Plant Gene Engineering Research Center, Nanjing Agricultural University, Nanjing 210095, China. [2]National Key Facility for Crop Gene Resources and Genetic Improvement, Institute of Crop Science, Chinese Academy of Agricultural Sciences, Beijing 100081, China. [3]Department of Pharmacology, University of Washington, Seattle, Washington 98195, USA. [4]Howard Hughes Medical Institute, Box 357280, University of Washington, Seattle, Washington 98195, USA. [5]National Centre for Plant Gene Research (Beijing), Institute of Genetics and Developmental Biology, Chinese Academy of Sciences, 1-2 Beichen West Road, Beijing 100101, China. [6]Department of Applied Biological Chemistry, The University of Tokyo, 1-1-1 Yayoi, Bunkyo, Tokyo 113-8657, Japan.

©2013 Macmillan Publishers Limited. All rights reserved

Kinetic analysis showed that at the heading stage, the total tiller number of *d53* was about three times that of the wild type, resulting from an increase in both higher-order and high-node tillers (Fig. 1c and Extended Data Fig. 1c, d). Histological analysis revealed that the sizes of vascular bundles and parenchyma cells in internodes were largely comparable between *d53* and wild-type plants, implying that the shortening and thinning of the *d53* stem were mainly caused by a reduction in cell number (Extended Data Fig. 1e–h). The phenotypes of F_1 heterozygous plants were intermediate between the homozygous parental plants (Extended Data Fig. 2a–g). Genetic analyses of an F_2 population derived from a cross of *d53* and the wild-type parent (Norin 8) showed that the normal, intermediate and dwarf plants segregated as 1:2:1 (33:58:28, $\chi^2 = 0.09$, $P > 0.05$), indicating that the *d53* mutation behaved in a semi-dominant manner (Extended Data Fig. 2h).

The phenotypic similarity between *d53* and the previously reported rice *d* mutants prompted us to examine whether *d53* is defective in SL-mediated inhibition of axillary bud outgrowth. Quantitative PCR with reverse transcription (qRT–PCR) analysis showed that expression of *D10* (encoding CCD8) was similarly upregulated in *d53* (Fig. 1d) as in other *d* mutants, owing to feedback regulation in the SL pathway[11]. In addition, expression of an inhibitor of axillary bud outgrowth, *FINE CULM 1* (*FC1*)[32], which is orthologous to the maize *TEOSINTE BRANCHED1* (*TB1*)[33] and the *Arabidopsis BRANCHED 1* (*BRC1*)[34], was also similarly downregulated in the *d53*, *d14* and *d27* mutants (Fig. 1d), suggesting that *D53* is probably involved in SL biosynthesis or signalling. Moreover, exogenous application of a SL analogue, GR24, effectively inhibited the outgrowth axillary buds of *d27*, but not *d14* or *d53* (Fig. 1e and Extended Data Fig. 3a–c). Further, measurement of SLs produced in the root exudates showed that *d53* accumulated markedly higher levels of *2′-epi*-5-deoxystrigol (*epi*-5DS), a native SL of rice, than the wild-type cultivar Norin 8 (Fig. 1f). These results indicate that *d53* is a SL-insensitive mutant.

D53 acts as a repressor of SL signalling

D53 was previously mapped to the terminal region of the short arm of rice chromosome 11 (ref. 35). To decipher the molecular defect in *d53*, we isolated *D53* by a map-based cloning approach. Using an F_2 population of ~ 12,000 plants generated from the cross between Ketan Nangka and the mutant, we further delimited the *D53* locus to a 34-kilobase DNA region on the bacterial artificial chromosome (BAC) clone OSJNBa0032J07, which contains three putative genes (Fig. 2a). Sequence analysis revealed a single-nucleotide substitution and 15-nucleotide deletion in the third exon of LOC_Os11g01330 in *d53*, which resulted in an amino acid substitution (R812T) and deletion of five amino acids (^{813}GKTGI^{817}) (Fig. 2b). To verify that this mutation caused the tillering dwarf phenotype, we generated transgenic plants expressing the wild-type or mutant *D53* gene under the control

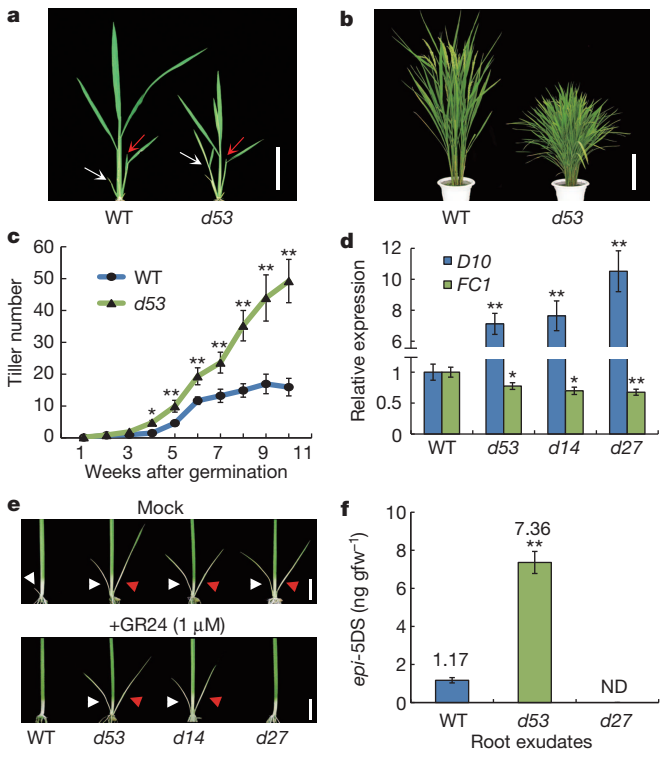


Figure 1 | Phenotype of *d53* mutant. **a**, **b**, Phenotype of wild type (WT) and *d53* mutant at 4-week-old seedling stage (**a**) or heading stage (**b**). White arrows indicate the first tillers in *d53*, which is usually absent in wild type, and red arrows show the second tillers. **c**, Comparison of tillering kinetics at different developmental stages. **d**, qRT–PCR assay showing altered expression of *D10* and *FC1* in *d* mutants. **e**, Responses of rice seedlings to GR24 treatment. Red and white arrowheads indicate the first and second tillers, respectively. **f**, Liquid chromatography–tandem mass spectrometry (LC–MS/MS) measurement of *epi*-5DS levels in root exudates. gfw, per gram fresh weight; ND, not detected. Scale bars, 5 cm (**a**), 30 cm (**b**), 2 cm (**e**). Values are means ± s.d. (**c**, $n = 30$ plants; **d**, **f**, $n = 3$ replicates). The Student's *t*-test analysis indicates a significant difference (compared with wild type, $*P < 0.05$, $**P < 0.01$).

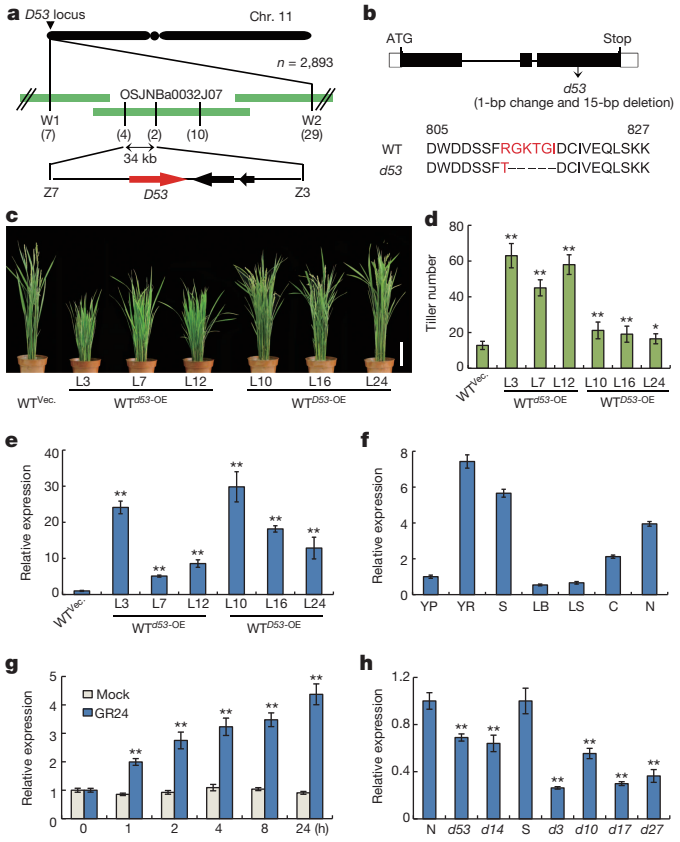


Figure 2 | Map-based cloning and characterization of *D53*. **a**, *D53* was fine-mapped on chromosome 11. The numbers of recombinants are shown in brackets. **b**, Molecular lesions in *d53* mutant. **c**, Phenotypic comparison of *pAct1::D53-GFP* and *pAct1::d53-GFP* transgenic plants. Vector (Vec.), *pAct1::GFP* control. L, independent transgenic line. Scale bar, 10 cm. **d**, **e**, Tiller number (**d**) and relative expression of *D53* (**e**) of transgenic plants in **c**. OE, overexpression. **f**, *D53* expression in various organs, including young panicles (YP), young roots (YR), shoots (S), leaf blades (LB), leaf sheaths (LS), culms (C) and nodes (N). **g**, GR24 treatment induces *D53* expression. **h**, Relative expression levels of *D53* in two wild-type varieties Norin 8 (N) and Shiokari (S), and six rice *d* mutants. Each value in **d**–**h** represents the mean ± s.d. (**d** and **f**–**h**, $n = 3$ replicates; **e**, $n = 20$ plants). The Student's *t*-test analysis indicates a significant difference (compared with control, $*P < 0.05$, $**P < 0.01$).

©2013 Macmillan Publishers Limited. All rights reserved

of rice *ACTIN 1* promoter (*pAct1*), in a wild-type background. Notably, all transgenic plants expressing the mutant *d53* gene showed a more exaggerated tillering phenotype than those expressing the wild-type *D53* gene. The severity of tillering phenotype in these transgenic plants was correlated with the expression level of the transgene. Notably, overexpression of the wild-type *D53* gene also caused a moderate increase in tillering, compared to the vector control plants (Fig. 2c–e). These observations suggested that the D53 protein acts as a repressor in the SL-mediated branching-inhibition pathway and that the dominant tillering phenotype of the *d53* mutant was most likely caused by a gain-of-function mutation in *d53*. To further confirm this, we generated *D53* knockdown transgenic plants using an RNA interference (RNAi) approach. As expected, reducing *D53* expression in a *d53* background markedly reduced the tiller number (Extended Data Fig. 3d, e). Taken together, these data support the proposition that the *d53* mutation enhances D53 activity in repressing SL signalling.

D53 is predicted to encode a protein of 1,131 amino acids. A BLAST search identified a closely related homologue of D53 (designated D53-like, LOC_Os12g01360) with 96.6% amino acid sequence identity in the rice genome. Further, D53-like proteins were found in other monocots and dicots, but not in lower plants, animals or microbes, indicating that the D53-like clade is specific to higher plants (Extended Data Fig. 4). Sequence analysis by the HHpred structure prediction server revealed that D53 shares a similar secondary structure composition, despite low primary sequence homology, to proteins of the class I Clp ATPase family, which are characterized by an N-terminal domain, a D1 ATPase domain, an M domain and a D2 ATPase domain[36]. Notably, the D2 domain of D53 contains a highly conserved linear sequence, Phe-Asp-Leu-Asn-Leu, which closely matches the ethylene-responsive element binding factor-associated amphiphilic repression (EAR) motif (Extended Data Fig. 5), which is known to interact with the TOPLESS family of proteins and is involved in transcriptional repression[37].

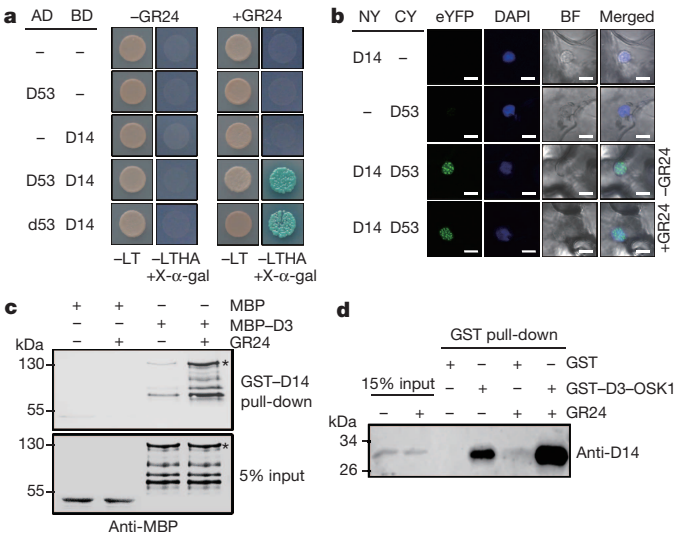


Figure 3 | GR24 promotes the D53–D14 and D14–D3 interaction. a, Y2H assay showing that D53 and d53 interact with D14 in the presence of GR24. Yeast transformants were spotted on the control medium (SD −Leu/−Trp (−LT)) and selective medium (SD −Leu/−Trp/−His/−Ade (−LTHA) plus X-α-gal). AD, activating domain; BD, binding domain; SD, synthetic dropout. **b**, BiFC analysis of D53 and D14. The positions of nuclei are indicated by DAPI (4′,6-diamidino-2-phenylindole) staining. eYFP, enhanced yellow fluorescent protein. NY and CY stand for the N terminus and C terminus of eYFP, respectively. BF, bright-field image. Scale bars, 10 μm. **c**, *In vitro* pull-down assay of recombinant maltose binding protein (MBP)–D3 or MBP using resins containing GST–D14. Asterisks indicate the full-length MBP–D3 protein. **d**, Pull-down assay showing co-immunoprecipitation of D14 from the *d3* mutant plant extracts, using GST–D3–OSK1 as the bait. 'Input' shows that roughly equal amounts of total plant proteins were used.

qPCR analysis revealed that *D53* was widely expressed in the examined rice tissues (Fig. 2f). A *D53*-promoter-driven GUS (β-glucuronidase) reporter gene (*pD53::GUS*) assay showed that GUS staining was observed in the vasculature in roots, shoots, leaves, leaf sheaths, nodes, internodes and young panicles, preferentially in the parenchyma cells surrounding the xylem (Extended Data Fig. 6a–h). Moreover, *D53* expression was upregulated by GR24 treatment in wild-type plants, but downregulated in six *d* mutants, suggesting that expression of *D53* is regulated by SL signalling (Fig. 2g, h). The D53–green fluorescent protein (GFP) fusion protein is exclusively localized to the nucleus in rice protoplasts and the *pAct1::D53-GFP* transgenic root cells (Extended Data Fig. 6i–p).

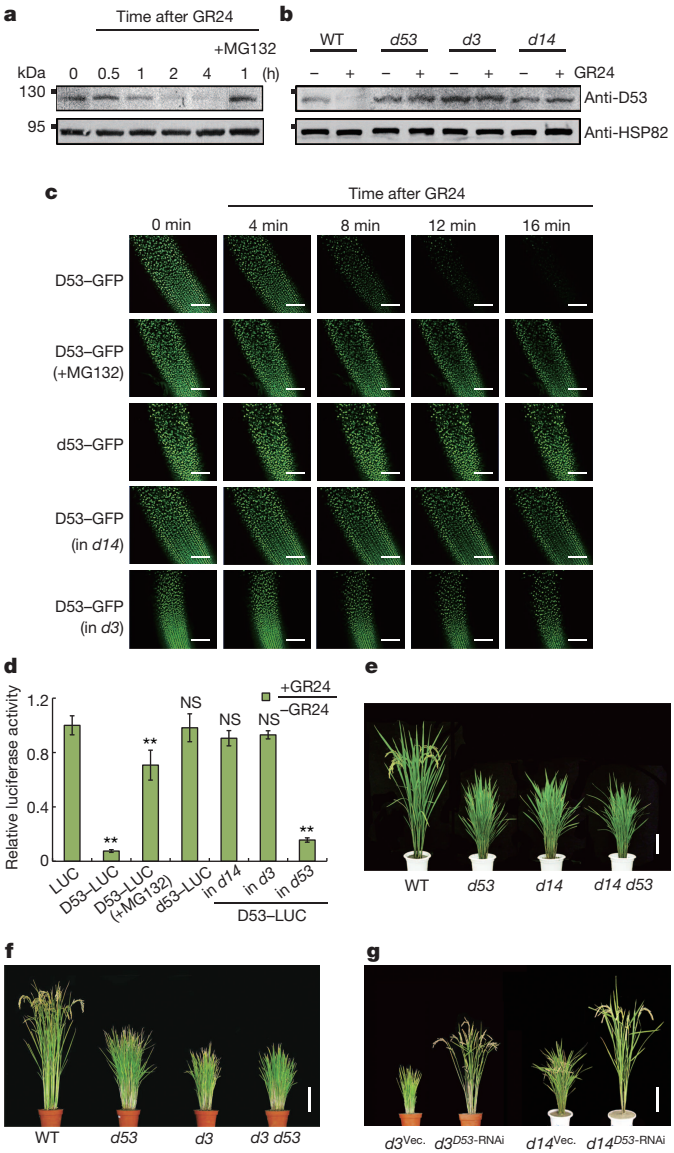


Figure 4 | GR24 promotes D14- and D3-dependent proteasomal degradation of D53. a, **b**, Western blot analysis showing that GR24 promotes D53 protein degradation in wild type (**a**), but not in *d* mutants (**b**). 10 μg of total protein was applied in each lane. **c**, Confocal scanning images showing different degradation patterns of D53–GFP and d53–GFP fusion proteins in wild-type, *d3* or *d14* backgrounds. **d**, Relative luciferase activity of D53–LUC or d53–LUC in wild-type, *d14*, *d3* or *d53* protoplasts. Values are means ± s.d. of three independent experiments. The double asterisks represent significant difference compared with control (LUC) determined by the Student's *t*-test at $P < 0.01$. NS, not significant. **e**, **f**, Phenotype of *d14 d53* (**e**) and *d3 d53* (**f**) double mutants. **g**, Phenotypes of *D53*-RNAi transgenic plants in *d3* and *d14* backgrounds. Scale bars, 100 μm (**c**), 20 cm (**e**–**g**).

©2013 Macmillan Publishers Limited. All rights reserved

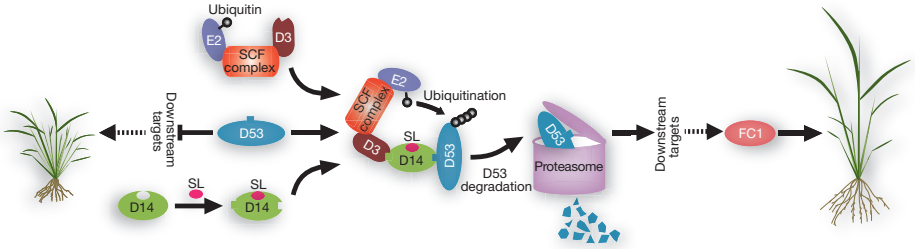


Figure 5 | A schematic model depicting that SL promotes D14–SCF^{D3}-mediated degradation of D53. Bioactive SL binding induces a conformational switch in D14 for SCF^{D3} and D53 binding, which in turn promotes D53 protein polyubiquitination. Degradation of D53 protein via the ubiquitin-proteasome pathway leads to expression of SL-responsive genes (such as *FC1*) and SL responses.

SLs promote D53–D14 and D14–D3 interaction

Previous studies have identified the F-box protein D3 and the α/β hydrolase D14 as two key components of SL signalling in rice[10,12], of which D14 and its orthologues in *Arabidopsis* (AtD14) and petunia (DAD2) have been proposed to directly participate in SL perception[19,27,28]. A yeast two-hybrid (Y2H) assay showed that both D53 and d53 could physically interact with D14 in the presence of GR24 (Fig. 3a). Domain deletion analysis indicated that the D1 domain of D53 was essential for the GR24-dependent D53–D14 interaction. Interestingly, its binding activity was inhibited by the M and D2 domains, although their negative effect can be overcome by the N domain (Extended Data Fig. 7). We verified the D53–D14 interaction in *Nicotiana benthamiana* leaf cell nucleus both in the presence or absence of exogenously applied GR24 using a bimolecular fluorescence complementation (BiFC) assay (Fig. 3b). The observed interaction between D53 and D14 in the absence of exogenously applied GR24 might be due to the effect of endogenous SLs present in the tobacco leaf cells. Consistent with the previously reported GR24-depedent interaction between DAD2 and PhMAX2A (an orthologue of D3 in petunia) in yeast[19], our *in vitro* pull-down assay also revealed a direct physical interaction between D14 and D3 in a GR24-dependent manner (Fig. 3c). Furthermore, using recombinant glutathione *S*-transferase (GST)–D3–OSK1 fusion protein as the bait, our *in vitro* pull-down assay showed that D14 could be more efficiently co-immunoprecipitated from *d3* plant extracts in the presence of exogenously applied GR24 (Fig. 3d). Together, these results suggest that SLs may act to promote complex formation among D14, D3 and D53, linking D53 to the hormone-perception components of the SL signalling pathway.

GR24 promotes D53 protein degradation

To investigate how SL regulates D53, we performed a set of additional experiments. Both western blot analysis and fluorescence microscopy examination showed that GR24 treatment induced rapid degradation of the D53 protein in wild-type cells, but not in *d3* or *d14* mutant cells (Fig. 4a–c). We further showed that D53 was degraded by the proteasome, as a proteasome inhibitor, MG132, but not other protease inhibitors, effectively blocked GR24-induced D53–GFP degradation (Fig. 4c, d and Extended Data Fig. 8a, b). Notably, unlike the wild-type D53–GFP fusion protein, the mutant d53–GFP fusion protein appeared to be stable in the presence of GR24 (Fig. 4c and Extended Data Fig. 8b). Interestingly, we noted that D53–GFP and D53–luciferase (LUC) were still degraded in the *d53* mutant cells, but not in *d3* or *d14* mutant cells (Fig. 4d and Extended Data Fig. 8c), indicating that the D53 degradation pathway was still operational in the *d53* mutant. Together, these results suggest that SL triggers proteasome-mediated degradation of D53 in a D14- and D3-dependent manner. Importantly, the insensitivity of d53 protein to SL-triggered turnover is consistent with the observed dominant gain-of-function mutant phenotype of *d53*.

To provide genetic support for the functional relationship between *D53*, *D3* and *D14*, we generated *d3 d53* and *d14 d53* double mutants. The *d3* mutant had more tillers and it was shorter than the *d14* and *d53* single mutants (Extended Data Fig. 9a). The *d14 d53* double mutants exhibited a dwarf tillering phenotype resembling the *d14* and *d53* parental plants, whereas the *d3 d53* double mutant exhibited a dwarf tillering phenotype resembling *d3* (Fig. 4e, f and Extended Data Fig. 9a). The lack of obvious additive effects among these mutants suggests that *D3*, *D14* and *D53* act in the same signalling pathway. To further test their epistatic relationship, we knocked down *D53* gene expression in the *d3* and *d14* backgrounds. As shown in Fig. 4g and Extended Data Fig. 9b–d, the mutant phenotype of *d3* and *d14* was restored to nearly wild-type levels, demonstrating that *D53* acts downstream of *D3* and *D14*, and that accumulation of D53 protein is responsible for blocking SL signalling and conferring the dwarf tillering phenotype in these mutants.

Discussion

It has been speculated that perception of SLs triggers the degradation of putative repressors by the SCF^{MAX2} ubiquitin ligase complex to suppress shoot branching[21,29,30]. In this study, we established that D53 acts as a repressor of SL signalling in rice. Consistent with the previous observation of GR24-dependent interaction between DAD2 and PhMAX2A (ref. 19), we found that GR24 also promotes the interaction between D14 with D53 and D3 (Fig. 3). Further, we showed that D53 is targeted for degradation by the proteasome in a D14- and D3-dependent manner (Fig. 4a–d and Extended data Fig. 8). Together, these data collectively support the notion that SL perception by D14 acts to promote ubiquitination of D53 by the D14–SCF^{D3} ubiquitin ligase, and subsequent degradation of D53 by the proteasome, leading to the propagation of SL signal and downstream physiological responses (Fig. 5). Our findings revealed a remarkable similarity between the hormonal perception and signalling mechanism of SL and several other classes of plant hormones, including auxin, jasmonate and gibberellin[25,38–40].

Interestingly, a recent study reported that a *D53* homologue in *Arabidopsis*, *SMAX1*, acts downstream of *MAX2* (orthologue of rice *D3*) in repressing the seed germination and seedling photomorphogenesis phenotypes of *max2*, but not the lateral root formation, axillary shoot growth, or senescence phenotypes of *max2* (ref. 41). Further, as observed for *D53*, three closest homologues of *D53* in *Arabidopsis* (designated *SMXL6*, *SMXL7* and *SMXL8*) were also induced by GR24 treatment[41], suggesting that *D53* and its homologues have a broad role in regulating different developmental processes and that the D3/D53 functional module is conserved between monocots and dicots. Consistent with this notion, the SL-analogous compounds known as karrikins also use a MAX2- and KAI2 (D14-LIKE)-dependent pathway to regulate seed germination and seedling growth[29,42]. The identification and characterization of *D53* in SL signalling now sets the stage for further dissection of the mechanisms by which SLs regulate plant form and its complex interactions with parasitic weeds and symbiotic arbuscular mycorrhizal fungi[3].

METHODS SUMMARY

The Methods provide detailed information about all experimental procedures, including description of plant materials and growth conditions, map-based cloning of *D53*, vector construction and plant transformation, rice hydroponic culture

©2013 Macmillan Publishers Limited. All rights reserved

and LC/MS–MS measurement of *epi*-5DS, qRT–PCR, histological analysis and GUS staining, Y2H assay, *in vivo* degradation assay, BiFC assays, recombinant protein preparation, *in vitro* pull-down assays and transient expression assays.

Online Content Any additional Methods, Extended Data display items and Source Data are available in the online version of the paper; references unique to these sections appear only in the online paper.

Received 9 July; accepted 15 November 2013.
Published online 11 December 2013.

1. Wang, Y. & Li, J. Branching in rice. *Curr. Opin. Plant Biol.* **14,** 94–99 (2011).
2. Domagalska, M. A. & Leyser, O. Signal integration in the control of shoot branching. *Nature Rev. Mol. Cell Biol.* **12,** 211–221 (2011).
3. Ruyter-Spira, C., Al-Babili, S., van der Krol, S. & Bouwmeester, H. The biology of strigolactones. *Trends Plant Sci.* **18,** 72–83 (2013).
4. Dun, E. A., Brewer, P. B. & Beveridge, C. A. Strigolactones: discovery of the elusive shoot branching hormone. *Trends Plant Sci.* **14,** 364–372 (2009).
5. Gomez-Roldan, V. *et al.* Strigolactone inhibition of shoot branching. *Nature* **455,** 189–194 (2008).
6. Umehara, M. *et al.* Inhibition of shoot branching by new terpenoid plant hormones. *Nature* **455,** 195–200 (2008).
7. Snowden, K. C. *et al.* The *Decreased apical dominance1/Petunia hybrida CAROTENOID CLEAVAGE DIOXYGENASE8* gene affects branch production and plays a role in leaf senescence, root growth, and flower development. *Plant Cell* **17,** 746–759 (2005).
8. Akiyama, K., Matsuzaki, K. & Hayashi, H. Plant sesquiterpenes induce hyphal branching in arbuscular mycorrhizal fungi. *Nature* **435,** 824–827 (2005).
9. Cook, C. E., Whichard, L. P., Turner, B., Wall, M. E. & Egley, G. H. Germination of witchweed (*Striga lutea* Lour.): isolation and properties of a potent stimulant. *Science* **154,** 1189–1190 (1966).
10. Ishikawa, S. *et al.* Suppression of tiller bud activity in tillering dwarf mutants of rice. *Plant Cell Physiol.* **46,** 79–86 (2005).
11. Arite, T. *et al. DWARF10*, an *RMS1/MAX4/DAD1* ortholog, controls lateral bud outgrowth in rice. *Plant J.* **51,** 1019–1029 (2007).
12. Arite, T. *et al. d14*, a strigolactone-insensitive mutant of rice, shows an accelerated outgrowth of tillers. *Plant Cell Physiol.* **50,** 1416–1424 (2009).
13. Zou, J. *et al.* The rice *HIGH-TILLERING DWARF1* encoding an ortholog of *Arabidopsis* MAX3 is required for negative regulation of the outgrowth of axillary buds. *Plant J.* **48,** 687–698 (2006).
14. Lin, H. *et al.* DWARF27, an iron-containing protein required for the biosynthesis of strigolactones, regulates rice tiller bud outgrowth. *Plant Cell* **21,** 1512–1525 (2009).
15. Stirnberg, P., van de Sande, K. & Leyser, H. M. O. *MAX1* and *MAX2* control shoot lateral branching in *Arabidopsis*. *Development* **129,** 1131–1141 (2002).
16. Booker, J. *et al.* MAX3/CCD7 is a carotenoid cleavage dioxygenase required for the synthesis of a novel plant signaling molecule. *Curr. Biol.* **14,** 1232–1238 (2004).
17. Sorefan, K. *et al. MAX4* and *RMS1* are orthologous dioxygenase-like genes that regulate shoot branching in *Arabidopsis* and pea. *Genes Dev.* **17,** 1469–1474 (2003).
18. Beveridge, C. A. Long-distance signalling and a mutational analysis of branching in pea. *Plant Growth Regul.* **32,** 193–203 (2000).
19. Hamiaux, C. *et al.* DAD2 is an α/β hydrolase likely to be involved in the perception of the plant branching hormone, strigolactone. *Curr. Biol.* **22,** 2032–2036 (2012).
20. Alder, A. *et al.* The path from β-carotene to carlactone, a strigolactone-like plant hormone. *Science* **335,** 1348–1351 (2012).
21. Stirnberg, P., Furner, I. J. & Leyser, H. M. O. MAX2 participates in an SCF complex which acts locally at the node to suppress shoot branching. *Plant J.* **50,** 80–94 (2007).
22. Dharmasiri, N., Dharmasiri, S. & Estelle, M. The F-box protein TIR1 is an auxin receptor. *Nature* **435,** 441–445 (2005).
23. Kepinski, S. & Leyser, O. The *Arabidopsis* F-box protein TIR1 is an auxin receptor. *Nature* **435,** 446–451 (2005).
24. Sheard, L. B. *et al.* Jasmonate perception by inositol-phosphate-potentiated COI1-JAZ co-receptor. *Nature* **468,** 400–405 (2010).
25. Ueguchi-Tanaka, M. *et al. GIBBERELLIN INSENSITIVE DWARF1* encodes a soluble receptor for gibberellin. *Nature* **437,** 693–698 (2005).
26. Beveridge, C. A. & Kyozuka, J. New genes in the strigolactone-related shoot branching pathway. *Curr. Opin. Plant Biol.* **13,** 34–39 (2010).
27. Zhao, L. H. *et al.* Crystal structures of two phytohormone signal-transducing α/β hydrolases: karrikin-signaling KAI2 and strigolactone-signaling DWARF14. *Cell Res.* **23,** 436–439 (2013).
28. Nakamura, H. *et al.* Molecular mechanism of strigolactone perception by DWARF14. *Nature Commun.* **4,** 2613 (2013).
29. Waters, M. T. *et al.* Specialisation within the DWARF14 protein family confers distinct responses to karrikins and strigolactones in *Arabidopsis*. *Development* **139,** 1285–1295 (2012).
30. de Saint Germain, A., Bonhomme, S., Boyer, F. D. & Rameau, C. Novel insights into strigolactone distribution and signalling. *Curr. Opin. Plant Biol.* **16,** 583–589 (2013).
31. Iwata, N., Satoh, H. & Omura, T. Linkage studies in rice. Linkage groups for 6 genes newly described. *Jpn J. Breed.* **27** (suppl.), 250–251 (1977).
32. Takeda, T. *et al.* The *OsTB1* gene negatively regulates lateral branching in rice. *Plant J.* **33,** 513–520 (2003).
33. Doebley, J., Stec, A. & Hubbard, L. The evolution of apical dominance in maize. *Nature* **386,** 485–488 (1997).
34. Aguilar-Martínez, J. A., Poza-Carrión, C. & Cubas, P. *Arabidopsis BRANCHED1* acts as an integrator of branching signals within axillary buds. *Plant Cell* **19,** 458–472 (2007).
35. Wei, L., Xu, J., Li, X., Qian, Q. & Zhu, L. Genetic analysis and mapping of the dominant dwarfing gene *D-53* in rice. *J. Integr. Plant Biol.* **48,** 447–452 (2006).
36. Wang, F. *et al.* Structure and mechanism of the hexameric MecA-ClpC molecular machine. *Nature* **471,** 331–335 (2011).
37. Pauwels, L. *et al.* NINJA connects the co-repressor TOPLESS to jasmonate signalling. *Nature* **464,** 788–791 (2010).
38. Gray, W. M., Kepinski, S., Rouse, D., Leyser, O. & Estelle, M. Auxin regulates SCF^{TIR1}-dependent degradation of AUX/IAA proteins. *Nature* **414,** 271–276 (2001).
39. Thines, B. *et al.* JAZ repressor proteins are targets of the SCF^{COI1} complex during jasmonate signalling. *Nature* **448,** 661–665 (2007).
40. Chini, A. *et al.* The JAZ family of repressors is the missing link in jasmonate signalling. *Nature* **448,** 666–671 (2007).
41. Stanga, J. P., Smith, S. M., Briggs, W. R. & Nelson, D. C. *SUPPRESSOR OF MORE AXILLARY GROWTH2 1* controls seed germination and seedling development in *Arabidopsis*. *Plant Physiol.* **163,** 318–330 (2013).
42. Nelson, D. C. *et al.* F-box protein MAX2 has dual roles in karrikin and strigolactone signaling in *Arabidopsis thaliana*. *Proc. Natl Acad. Sci. USA* **108,** 8897–8902 (2011).

Acknowledgements We thank T. Omura for providing the *d53* mutant, and Z.-Y. Wang and C. Lin for reading of the manuscript. We also thank X. Li for providing the *d3* mutant, W. Liu for providing the *htd2* mutant and I. Takamure for providing the *d10*, *d17* and *d27* mutants. This work was supported by the National Transgenic Science and Technology Program (2011ZX08009-003), 863 National High-tech R&D Program of China (2012AA101100, 2012AA10A301), Jiangsu Province 333 Program (BRA2012126) and National Natural Science Foundation of China (90917017). N.Z. is a Howard Hughes Medical Institute investigator and is supported by the National Science Foundation.

Author Contributions F.Z., L.Z., X.L., Z.C. and H.Z. performed genetic analysis and mapping of *D53*; Q.L., Y.R., N.S., F.W. and H.M. performed the protein interaction experiments; X.Z., X.G. and L.J. performed the genetic transformation; C.W., Jiulin.W., Chao.Y., Jie.W. and C.L. performed the construction and identification of double mutants; K.U., S.I., and T.A. performed the synthesis of d_6-5DS; W.C., Jinfang.C., and Cunyu.Y. performed the determination of SLs; K.Z., Y.R. and L.G. performed the degradation experiments; F.Z., H.G. and W.D. performed the Y2H and qRT–PCR experiments; Jun.C., D.W., J.T. and W.M. performed the phenotypic analysis and painted the model picture. Jianmin.W., N.Z. and H.W. directed the project and wrote the manuscript.

Author Information The GenBank accession number for the *D53* nucleotide sequence is KF709434. Reprints and permissions information is available at www.nature.com/reprints. The authors declare no competing financial interests. Readers are welcome to comment on the online version of the paper. Correspondence and requests for materials should be addressed to Jianmin.W. (wanjm@njau.edu.cn or wanjianmin@caas.cn), N.Z. (nzheng@u.washington.edu) or H.W. (wanghaiyang@caas.cn).

©2013 Macmillan Publishers Limited. All rights reserved

METHODS

Plant materials and growth conditions. The wild-type rice (*Oryza sativa* L. subspecies *japonica*) varieties used in this study were Norin 8 (for *d53*, *d14* and *d27*), Akumuro (for *d3*), Shiokari (for *d10* and *d17*) and Kitaake (for transformation analyses). The *d53*-carrying line, KL908, was initially identified from a mutant library of Norin 8 mutagenized by ^{60}Co-γ irradiation[31]. The *d27* and *d14* mutants were described previously[14,43]. The *d3* mutant used in this work carries a premature stop codon (unpublished data). The *d14 d53* and *d3 d53* double mutants were generated by crossing their respective parental lines and identified by genotyping from their respective F_2 or F_3 populations.

Rice plants were cultivated in the experimental field at the Nanjing Agricultural University in Nanjing in the natural growing seasons. For qRT–PCR, GR24 treatment, SL analyses and transient expression assay, the seedlings of wild-type and mutants were grown in climate chambers (HP1500GS, Ruihua) at 70% humidity, under long-day conditions with daily cycles of 14 h of light at 30 °C and 10 h of dark at 25 °C. Light was provided by fluorescent white-light tubes (400–700 nm, 250 μmol m^{-2} s^{-1}).

Map-based cloning of *D53*. To map the *D53* locus, the *d53* mutant was crossed with a polymorphic *javanica* variety, Ketan Nangka. Rough mapping was performed with simple sequence repeat (SSR) markers W1 (5′-GGATGATGAGA TCCTAATGTAGAA-3′ and 5′-CATCCTTGGAAAATAGTGGG-3′) and W2 (5′-GGCTTCATCTTTGGCGACC-3′ and 5′-CCGGATTCACGAGATAAACT CTC-3′) using 242 normal plants obtained in the F_2 population. Using 2,893 normal plants, *D53* was finally mapped to a region between the SSR marker Z7 (5′-C AGAGACCAAGCAACAGAG-3′ and 5′-GGAGACGTGTGAGCTACAAC-3′) and a derived cleaved amplified polymorphic sequence (dCAPS) marker Z3 (5′-G TTACCGCTCCTCCTCAGC-3′ and 5′-AGTAAAAATGTGGAGGGGCA-3′).

Vector construction and plant transformation. To generate the *pAct1::D53-GFP* and *pAct1::d53-GFP* constructs, full-length complementary DNAs (cDNAs) of *D53* and *d53* were amplified, and the PCR products were then cloned into the binary vector AHLG[44] using the In-Fusion Advantage PCR Cloning Kit (Clontech) and sequenced (Biomed). The *pAct1::GFP*, *pAct1::D53-GFP* and *pAct1::d53-GFP* constructs were introduced into the wild-type variety Kitaake. The *pAct1::D53-GFP* transgene was introduced into *d3* and *d14* backgrounds by genetic crosses.

To knock down the *D53* gene, the *D53*-RNA interference (*D53*-RNAi) vector was constructed using a 475-base pair cDNA fragment. The PCR fragment was cloned into the p*EASY*-Blunt cloning vector (TransGen), and the gene-specific fragment was prepared by double digestion with KpnI-SacI and PstI-BamHI, respectively, and then the PCR products were ligated to both sides of the *FAD2* intron in the binary vector pCUbi1390-$^{\Delta}$FAD2 in opposite orientation[45] and sequenced. The resultant constructs D53-RNAi and the control vector pCUbi1390-$^{\Delta}$FAD2 were separately introduced into *d53*, *d3* and *d14* mutants.

To analyse the expression pattern of the *D53* gene, a 2.7-kilobase promoter fragment was cloned into the binary vector pCAMBIA-1381Z and sequenced to create the *pD53::GUS* reporter gene construct, which was then introduced into wild-type rice cultivar Norin 8. All transgenic rice plants were generated using *Agrobacterium*-mediated transformation of rice calli, as described previously[46].

Rice hydroponic culture and LC/MS–MS analysis of *epi*-5DS. Preparation of hydroponic culture solution and treatment with GR24 (http://www.chiralix.com/) were performed as described previously[6]. In brief, surface-sterilized rice seeds were incubated in sterile water at 30 °C in the dark for 2 days. The germinated seeds were transferred into hydroponic culture medium solidified with 0.5% agar and cultured at 30 °C for 5 days. The 1-week-old seedlings were then transferred to a plastic pot containing hydroponic culture solution (500 ml) and grown for an additional 7 days (total 2 weeks) or 28 days (total 5 weeks). The hydroponic culture solution with or without 1 μM GR24 was renewed every week. For SL analysis, the 1-week-old seedlings were grown in hydroponic culture medium without P_i for an additional 14 days (total 3 weeks).

SL analysis in rice root exudates was performed according to a previously described method[14] with minor modifications. For each sample, the weight of fresh rice roots was recorded and 50 ml hydroponic culture medium was loaded onto a pre-equilibrated Oasis HLB 3cc cartridges (Waters) after adding 1 ng d_6-5DS as the internal standard. Subsequently, the columns were washed with de-ionized water. The SL-containing fraction, eluted with acetone, was collected and dried up under nitrogen gas, then reconstructed in acetonitrile and subjected to UPLC–MS/MS analysis. The UPLC–MS/MS system consists of a triple quadruple tandem mass spectrometer (Quattro Premier XE; Waters MS Technology) and an Acquity Ultra Performance Liquid Chromatograph (Acquity UPLC; Waters) equipped with a reverse phase column (BEH-C18, 2.1 × 100 mm, 1.7 μm; Waters). Mobile phase A (99.95% H_2O + 0.05% acetic acid) and mobile phase B (99.95% ACN + 0.05% acetic acid) were pumped at a rate of 0.4 ml min^{-1}. The gradient started with 50% A and increased B from 50% to 70% in 5 min. The column temperature was set to 25 °C. MS parameters were set to the following values: desolvation gas flow, 800 L h^{-1}; capillary voltage, 3.8 kV; cone voltage, 24 V; desolvation temperature, 350 °C; source temperature, 110 °C; collision energy 14 V, using multiple reaction monitoring (MRM) transition of m/z 331 > 216 for the *epi*-5DS detection, and MRM transition of m/z 337 > 222 for the d_6-5DS detection. Data were analysed with MassLynx software (V.4.1). The *epi*-5DS concentrations of rice exudates were calculated by comparing the MRM relative response of *epi*-5DS with the d_6-5DS ones then divided by the weight of fresh rice roots.

qRT–PCR. Total RNA was extracted using the RNeasy Plant Mini Kit (QIAGEN). Then, 20 μl cDNA was synthesized using 1 μg RNA with the QuantiTect Reverse Transcription Kit (QIAGEN). qRT–PCR (20 μl reaction volume) was carried out using 0.5 μl cDNA, 0.2 μM of each gene-specific primer and SYBR Premix Ex Taq Kit (TaKaRa) in an ABI PRISM 7900HT (Applied Biosystems) according to the manufacturer's instructions. The rice ubiquitin gene was used as the internal control. The gene-specific primers used for qRT–PCR are: ubiquitin gene (LOC_Os03g13170) (5′-AACCAGCTGAGGCCCAAGA-3′ and 5′-ACGATTGATTTAACCAGTCCA TGA-3′); *D53* gene (5′-CCAAGCAGTTTGAAGCGAC-3′ and 5′-CCGCAAGTT TATCAAAGTCAA-3′); *D10* gene (5′-CGTGGCGATATCGATGGT-3′ and 5′-CG ACCTCCTCGAACGTCTT-3′); *FC1* gene (5′-CGACAGCGGCAGCTACTAC-3′ and 5′-GCGAATTGGCGTAGACGA-3′). Data from three replicates were analysed following the relative quantification method[47].

Histological analysis and GUS staining. Culm segments of rice were fixed in FAA (formalin/acetic acid/50% ethanol, 2:1:17 (v/v/v)) overnight, followed by a series of dehydration and infiltration, and embedded in paraffin (Paraplast Plus; Sigma-Aldrich). The tissues were sliced into 8–12-μm sections with a microtome (Leica RM2265), and affixed to microscope slides. Paraffin was removed from the sections using xylene, and the sections were dehydrated through a gradient ethanol series, and stained with toluidine blue. Sections were viewed under a light microscope (Leica DM5000B) and photographed using a Micro Colour charge-coupled device camera (Leica DFC490).

GUS histochemical staining was performed according to a method described previously[48]. Various tissues or hand-cut sections of *pD53::GUS* T_1 generation transgenic plants were incubated in a staining solution containing 100 mM $NaPO_4$ buffer, pH 7.0, 2 mM X-Gluc, 0.5 mM $K_3Fe(CN)_6$, 0.5 mM $K_4Fe(CN)_6$, 0.1% Triton X-100 and 10 mM Na_2-EDTA at 37 °C. Samples were vacuum-infiltrated briefly at the initiation of staining with X-Gluc solution. After staining, the staining solution was removed and the sample was washed with several changes of 50% ethanol until the tissue became clear. Images were taken directly or under the stereomicroscope.

Y2H assay. Coding regions of the rice *D53*, *d53* and various domain deletion variants of *D53* were cloned into the Y2H 'prey' vector pGADT7 (Clontech). The coding region of rice *D14* was cloned into the Y2H 'bait' vector pGBKT7 (Clontech). Bait and prey constructs were co-transformed into the yeast (*Saccharomyces cerevisiae*) strain Y2HGold (Clontech) and the resultant yeast stains were grown on SD −Leu/−Trp plates for 3 days at 30 °C. Interactions between bait and prey were examined on the control media −LT (SD −Leu/−Trp) and selective media −LTHA (SD−Leu/−Trp/−His/−Ade) or −LTHA plus X-α-gal in the presence or absence of 5 μM GR24. Plates were incubated for 4 days at 30 °C. Yeast strains containing *D53*, *d53* or *D14* in combination with pGADT7 or pGBKT7 were used as controls.

Antibody preparation. For detection of D53, a His-fused protein-specific polypeptide (amino acids 963–1,112 of D53 protein) was expressed in *BM*Rosetta (DE3) cells (Biomed), and then affinity purified. Subsequently, the recombination protein was injected into rabbits to produce polyclonal antibodies against D53 (Abmart). For detection of D14 protein, a His-fused polypeptide (amino acids 153–302 of D14) was expressed in *BM*Rosetta (DE3) cells. Purified fusion protein was injected into rats to produce polyclonal antibodies against D14 (Abmart). The loading control used is anti-HSP82 antibody (Beijing Protein Innovation).

***In vivo* degradation assay of D53.** One-week-old rice seedlings were treated with or without 5 μM GR24 and collected at different time points. To block proteasomal protein degradation, seedlings were pre-treated with 40 μM MG132 for 2 h. Total protein was extracted and denatured in the SDS sample buffer containing 5% β-mercaptoethanol (β-ME) at 95 °C for 10 min. Western blots were performed using the antiserum against D53 and visualized by an enhanced horseradish peroxidase-diaminobenzidine (HRP-DAB) substrate kit (Tiangen).

The *pAct1::D53-GFP* and *pAct1::d53-GFP* transgenic plants were treated with 5 μM GR24 with or without the following inhibitors: MG132 (40 μM), AEBSF (500 μM), pepstatin A (1 μM) or leupeptin (20 μM). GFP fluorescence in nuclei of transgenic root cells was observed and imaged with a Zeiss LSM 700 laser scanning confocal microscope.

BiFC assay. The full-length *D14* and *D53* cDNAs were cloned into the binary vectors pSPYNE173 and pSPYCE(M) to create the D14-NY and D53-CY vectors, respectively. For transient expression, *A. tumefaciens* strain EHA105 carrying the gene of interest (at an OD_{600} of 0.1) was co-infiltrated with p19 strain into a 5-week-old *N. benthamiana* leaf as described previously[49]. After 2 days, infiltrated leaves were sprayed with (+) or without (−) 5 μM GR24 24 h before leaf excision. The

©2013 Macmillan Publishers Limited. All rights reserved

eYFP and DAPI fluorescent signals of the infiltrated leaves were monitored sequentially using a laser confocal scanning microscope. The wavelengths for eYFP and DAPI were 514 and 405 nm for excitation, and 527 and 488 nm for detection, respectively.

Recombinant protein preparation. The full-length open reading frames of D3–OSK1 and D14 were cloned into the pGEX4T-1 vector, generating a fusion with the GST protein. The full-length cDNA of D3 was cloned into the pMAL-c2x vector to generate a fusion with MBP. Expression of GST, GST–D3–OSK1, GST–D14, MBP and MBP–D3 in BL21 Rosetta cells was induced with 0.1 mM isopropyl-β-D-thiogalactoside at 20 °C for 16 h. Fusion proteins were purified using GST Bind Resin (Novagen) or amylose-affinity chromatography (New England Biolabs) according to the manufacturer's protocols and quantified by the Bio-Rad protein assay reagent.

Pull-down assays. One-week-old rice seedlings were pre-treated with 40 μM MG132 for 1 h and then treated with or without 5 μM GR24 for 30 min. Total proteins were subsequently extracted in a radioimmunoprecipitation assay (RIPA) buffer (50 mM Tris-HCl, pH 7.2, 150 mM NaCl, 10 mM $MgCl_2$, 1 × complete protease inhibitor cocktail, Roche) containing 40 μM MG132. After centrifugation (16,000*g* at 4 °C), the supernatant was collected. Total protein concentration was determined by the Bradford protein assay kit (Bio-Rad). Roughly equal amounts of purified GST and GST–D3–OSK1 fusion proteins (about 50 μg) were affixed to GST Bind Resin and then mixed with 300 μl of plant extract (containing 1.5 mg total proteins). After being gently shaken at 25 °C for 15 min, the resin was washed five times with RIPA buffer. During all the procedures, 5 μM GR24 was added to the assay mixture for GR24-treated seedlings and was not added to the protein samples from seedlings not treated with GR24. Proteins were detected with anti-D14 antibodies at 1:1,000 dilution and visualized with enhanced chemiluminescence reagent (GE Healthcare).

For *in vitro* pull-down, GST–D14 (5 μg) was incubated with MBP–D3 (6 μg) or MBP (2 μg) at 25 °C for 15 min in 300 μl of binding buffer (20 mM Tris-HCl, pH 7.6, 2.5 mM β-ME and 0.1 M NaCl) with or without 10 μM GR24. After incubation, 20 μl of GST resin was added. After further incubation at 25 °C for 15 min, the resin was washed five times with the washing buffer (20 mM Tris-HCl, pH 7.5, 500 mM NaCl and 0.5% Triton X-100). The washing buffer also contains 10 μM GR24 where appropriate. After washing, 40 μl of 1 × SDS–PAGE sample buffer were added, the mixture was denatured, and the sample was loaded on a 8% SDS–PAGE gel, and proteins were detected by the HRP-conjugated anti-MBP antibody (New England Biolabs) and visualized with enhanced chemiluminescence reagent (GE Healthcare).

Transient expression assays. The *D53*, *d53*, *D3* and *D14* full-length cDNAs were cloned into the vector pA7-GFP or pGreenII 0800-LUC to generate D53–GFP or D53–LUC recombinant plasmids for transient expression assays, respectively. Plasmids DNA was prepared using the Plasmid Midi Kits (Qiagen) according to the manufacturer's instructions. For preparation of rice protoplasts, the sterilized seeds were germinated and grown in climate chambers for 7–10 days. Green tissues from the stem and sheath of 40–60 rice seedlings were used. The protoplasts isolation and polyethyleneglycol (PEG) -mediated transfections procedure were carried out as described previously[50]. GFP fluorescence from protoplasts was observed and imaged as described above. For measurement of the relative luciferase activity, protoplasts were incubated overnight and then treated with or without 5 μM GR24 for 4 h. For MG132 treatment, 40 μM MG132 was added to the sample and incubated for 1 h before addition of GR24. Activities of firefly luciferase (fLUC) and Renilla luciferase (rLUC) were determined with the Dual-Glo Luciferase Assay System (Promega). The data were represented as the ratio of fLUC/rLUC activty.

43. Liu, W. *et al.* Identification and characterization of *HTD2*: a novel gene negatively regulating tiller bud outgrowth in rice. *Planta* **230,** 649–658 (2009).
44. Itoh, H., Ueguchi-Tanaka, M., Sato, Y., Ashikari, M. & Matsuoka, M. The gibberellin signaling pathway is regulated by the appearance and disappearance of SLENDER RICE1 in nuclei. *Plant Cell* **14,** 57–70 (2002).
45. Zhou, K. *et al. Young Leaf Chlorosis 1*, a chloroplast-localized gene required for chlorophyll and lutein accumulation during early leaf development in rice. *Planta* **237,** 279–292 (2013).
46. Hiei, Y., Ohta, S., Komari, T. & Kumashiro, T. Efficient transformation of rice (*Oryza sativa* L.) mediated by *Agrobacterium* and sequence analysis of the boundaries of the T-DNA. *Plant J.* **6,** 271–282 (1994).
47. Livak, K. J. & Schmittgen, T. D. Analysis of relative gene expression data using real-time quantitative PCR and the $2^{-\Delta\Delta C}{}_T$ method. *Methods* **25,** 402–408 (2001).
48. Jefferson, R. A., Kavanagh, T. A. & Bevan, M. W. GUS fusions: β-glucuronidase as a sensitive and versatile gene fusion marker in higher plants. *EMBO J.* **6,** 3901–3907 (1987).
49. Waadt, R. *et al.* Multicolor bimolecular fluorescence complementation reveals simultaneous formation of alternative CBL/CIPK complexes *in planta*. *Plant J.* **56,** 505–516 (2008).
50. Zhang, Y. *et al.* A highly efficient rice green tissue protoplast system for transient gene expression and studying light/chloroplast-related processes. *Plant Methods* **7,** 30 (2011).

©2013 Macmillan Publishers Limited. All rights reserved

LETTER

doi:10.1038/nature12889

Rapid local acceleration of relativistic radiation-belt electrons by magnetospheric chorus

R. M. Thorne[1], W. Li[1], B. Ni[1], Q. Ma[1], J. Bortnik[1], L. Chen[1], D. N. Baker[2], H. E. Spence[3], G. D. Reeves[4], M. G. Henderson[4], C. A. Kletzing[5], W. S. Kurth[5], G. B. Hospodarsky[5], J. B. Blake[6], J. F. Fennell[6], S. G. Claudepierre[6] & S. G. Kanekal[7]

Recent analysis of satellite data obtained during the 9 October 2012 geomagnetic storm identified the development of peaks in electron phase space density[1], which are compelling evidence for local electron acceleration in the heart of the outer radiation belt[2,3], but are inconsistent with acceleration by inward radial diffusive transport[4,5]. However, the precise physical mechanism responsible for the acceleration on 9 October was not identified. Previous modelling has indicated that a magnetospheric electromagnetic emission known as chorus could be a potential candidate for local electron acceleration[6–10], but a definitive resolution of the importance of chorus for radiation-belt acceleration was not possible because of limitations in the energy range and resolution of previous electron observations and the lack of a dynamic global wave model. Here we report high-resolution electron observations[11] obtained during the 9 October storm and demonstrate, using a two-dimensional simulation performed with a recently developed time-varying data-driven model[12], that chorus scattering explains the temporal evolution of both the energy and angular distribution of the observed relativistic electron flux increase. Our detailed modelling demonstrates the remarkable efficiency of wave acceleration in the Earth's outer radiation belt, and the results presented have potential application to Jupiter, Saturn and other magnetized astrophysical objects.

A strong and rapid electron acceleration event occurred during a geomagnetic storm on 9 October 2012. The data in Fig. 1a–c show that the storm was triggered by two interplanetary magnetic clouds[13] with large negative B_z (the z component of the interplanetary magnetic field), which produced effective coupling with the Earth's magnetosphere and sustained geomagnetic activity[14]. The first dip in SYM-H (an index of geomagnetic disturbance, see Fig. 1 legend for details) on 8 October was associated with large solar wind dynamic pressure, which compressed the magnetopause inward to $<8\,R_E$ above Earth's surface[15] (R_E, Earth radius). Interestingly, the fluxes of relativistic radiation-belt electrons observed by the Relativistic Electron–Proton Telescope (REPT)[11] (Fig. 1e–g) on the NASA Van Allen probes were reduced during the first dip in SYM-H, and only exhibited a dramatic increase during the second dip in SYM-H on 9 October when the solar wind dynamic pressure decreased and the magnetopause moved out to $>10\,R_E$. Intense whistler-mode chorus emissions (Fig. 1d) were observed in the region outside the plasmasphere (a high-density extension of the Earth's ionosphere) by the Electric and Magnetic Field Instrument Suite and Integrated Science (EMFISIS) wave instrument[16] on Van Allen probe A. Chorus intensification occurred during the injection of low-energy (<30 keV) plasma sheet electrons into the inner magnetosphere during the period of enhanced electric field and associated plasma convection associated with the intervals of negative B_z. Here we use the high-resolution data available from the Van Allen probes to provide a definitive test of whether chorus can account for the observed variability in electron fluxes during the 9 October storm and thus explain the associated peak in electron phase space density[1] (Fig. 1h) during the second dip in SYM-H.

The chorus observations obtained from EMFISIS were confined to a limited range of magnetic local time (MLT) near dawn and on the dayside. Figure 2b shows the amplitude B_w of chorus at locations along the orbit of both Van Allen probes. The waves intensified during each period of southward B_z (Fig. 2a) with peak intensities occurring in the spatial region $3.5 < L < 6$ (L is the maximum radial extent, in R_E, of the dipole magnetic field). However, previous statistical studies of chorus have shown that chorus is found over a broad range of MLT extending from the nightside through dawn to the dayside, with peak wave intensities generally found near the Equator on the nightside[17,18]. Chorus is excited following the injection of low-energy (1–30 keV) plasma sheet electrons into the inner magnetosphere during geomagnetically disturbed periods[19], and the resulting electron scattering leads to precipitation into the atmosphere[20]. Recent studies have shown that scattering by chorus emissions is the dominant mechanism responsible for the global distribution of the pulsating and diffuse auroral precipitation[21,22]. The ratio between the precipitated and trapped fluxes measured by low altitude POES satellites (Fig. 2c) is approximately proportional to the power spectral intensity of magnetospheric chorus[23]. Consequently, we have developed a quantitative algorithm (described in Supplementary Information) to convert the measured POES flux ratios at different MLT (Extended Data Fig. 1) to obtain a dynamic global model of chorus wave amplitudes as a function of L, MLT and time during the 9 October storm[12]. This global wave model was used to evaluate rates of electron scattering in pitch angle and energy (averaged over the bounce and drift orbits of electrons in the Earth's magnetic field) shown in Extended Data Fig. 2 based on the parameters listed in Extended Data Table 1.

To simulate the dynamical evolution of the relativistic electron population during the 16-h interval of the storm when chorus waves were intense, we solve the two-dimensional Fokker–Planck equation

$$\frac{\partial f}{\partial t} = \frac{1}{G}\frac{\partial}{\partial \alpha_{eq}} G\left(\langle D_{\alpha_{eq}\alpha_{eq}}\rangle \frac{\partial f}{\partial \alpha_{eq}} + p\langle D_{\alpha_{eq}p}\rangle \frac{\partial f}{\partial p}\right) + \frac{1}{G}\frac{\partial}{\partial p} G\left(p\langle D_{\alpha_{eq}p}\rangle \frac{\partial f}{\partial \alpha_{eq}} + p^2\langle D_{pp}\rangle \frac{\partial f}{\partial p}\right) \quad (1)$$

where f is electron phase space density (PSD), and $\langle D_{\alpha_{eq}\alpha_{eq}}\rangle$, $\langle D_{\alpha_{eq}p}\rangle$ and $\langle D_{pp}\rangle$ are drift and bounce averaged electron diffusion coefficients for pitch angle (α_{eq}), mixed pitch angle and momentum (p), and momentum, respectively (measured in units of s^{-1}). Here $G = p^2T(\alpha_{eq})\sin(\alpha_{eq})\cos(\alpha_{eq})$, and $T(\alpha_{eq}) \approx 1.30 - 0.56\sin(\alpha_{eq})$ is the normalized bounce period. Integration is performed over the energy range 100 keV–30 MeV, using initial conditions taken from electron flux measurements obtained from both the Magnetic Electron Ion Spectrometer (MagEIS)[24] and REPT[11]

[1]Department of Atmospheric and Oceanic Sciences, University of California, Los Angeles, California 90095-1565, USA. [2]Laboratory for Atmospheric and Space Research, University of Colorado, Boulder, Colorado 80303-7814, USA. [3]Each Institute for the Study of Earth, Oceans, and Space, University of New Hampshire, Durham, New Hampshire 03824-3525, USA. [4]Space Science and Applications Group, Los Alamos National Laboratory, Los Alamos, New Mexico 87544, USA. [5]Department of Physics and Astronomy, University of Iowa, Iowa City, Iowa 52242-1479, USA. [6]The Aerospace Corporation, Los Angeles, California 90245-4609, USA. [7]NASA Goddard Space Flight Center, Greenbelt, Maryland 20771, USA.

©2013 Macmillan Publishers Limited. All rights reserved

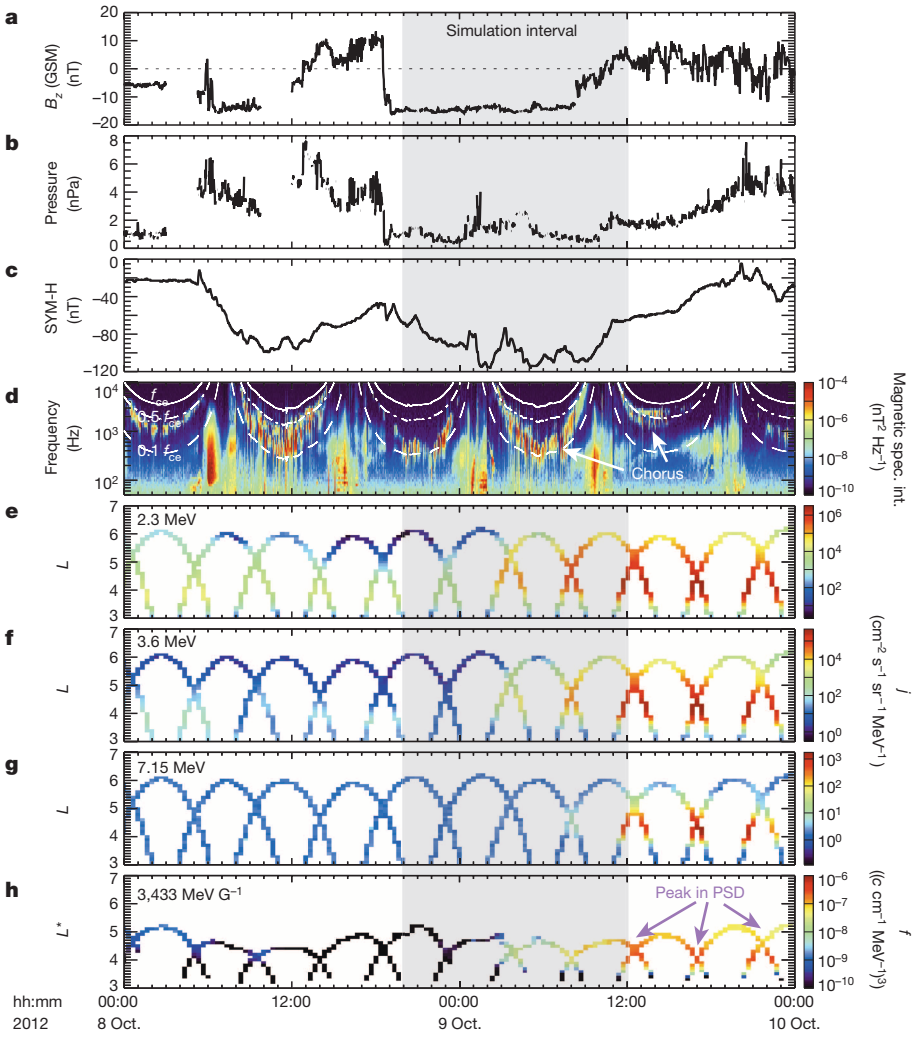


Figure 1 | Conditions leading to rapid relativistic electron acceleration on 9 October 2012. **a**, B_z in the Geocentric Solar Magnetospheric (GSM) system (where the x axis is directed from the Earth to the Sun and the y axis is defined to be perpendicular to the Earth's magnetic dipole axis) showing the prolonged period of southward directed field (light grey shading), which leads to enhanced convective injection of plasma sheet electrons into the inner magnetosphere. **b**, Solar wind dynamic pressure. **c**, SYM-H, which is a longitudinally symmetric (SYM) disturbance index describing the horizontal (H) component of geomagnetic disturbance fields at mid-latitudes with 1-min resolution. **d**, Magnetic spectral intensity (Magnetic spec. int., colour scale) of highly-structured whistler-mode chorus waves as a function of frequency observed by the EMFISIS instrument on Van Allen probe A. Superimposed white lines demarcate the electron gyrofrequency f_{ce}, $0.5f_{ce}$ and $0.1f_{ce}$. Intense chorus emissions measured by the EMFISIS instrument on the Van Allen probes are excited over the frequency range (0.1–0.8) f_{ce} in the region outside the plasmapause during intervals of negative B_z. **e**–**g**, Differential fluxes (j, colour scale) of relativistic electrons measured by the REPT instrument on the Van Allen probes (**e**, 2.3 MeV; **f**, 3.6 MeV; **g**, 7.15 MeV) as a function of L showing a rapid increase over the radial range $3.5 < L < 5.5$ where chorus emissions are strong. **h**, The phase space density ($f = j/p^2$; colour scale) of 3,433 MeV G^{-1} relativistic electrons, where p is the relativistic electron momentum, showing peaks in the inner magnetosphere indicative of local wave acceleration[2,3] rather than radial diffusive acceleration. Phase space density (PSD) is plotted as a function of L^*, which remains invariant over the electron drift orbit in a distorted magnetic field[1], and becomes equal to L for a dipole field. For the TS05 magnetic field model adopted[1], the value of L^* is smaller than the value of L shown in **e**–**g**.

instruments approximately 2 h before 20:00 UT on 8 October, when Van Allen probe B travelled through $L \approx 5$. The simulation is relatively insensitive to the initial high-energy distribution, and for the results shown in Fig. 3 we adopt a smooth spline fitting to the measured energy spectrum (Extended Data Fig. 3). Our simulation of the dynamic response of relativistic electrons to chorus scattering (Fig. 3e) agrees well with the observations obtained from the REPT instrument (Fig. 3a). Specifically, we are able to account for both the magnitude and the timing of the relativistic (2–7 MeV) electron flux enhancement as a function of energy. The delayed enhancement of the higher energy electrons is a characteristic feature of local wave acceleration[25]. As further confirmation of the dominance of chorus scattering to electron acceleration during this storm, we also show in Fig. 3 a comparison between the simulated pitch angle distribution (Fig. 3f–h) and REPT observation (Fig. 3b–d) during the acceleration interval. The most rapid flux enhancement occurs over the pitch angle range above 50°, where momentum diffusion rates maximize (Extended Data Fig. 2). Also the pitch angle distributions above ~50° become essentially flat owing to the larger rates of pitch angle scattering. Finally, the large gradients towards the loss cone below 50° are a direct result of the more rapid acceleration compared to scattering loss into the atmosphere for such high-energy electrons.

Previous attempts to quantify the role of chorus emissions in causing radiation-belt electron acceleration have been limited to one-dimensional simulations of energy diffusion using empirical estimates for the rate of electron loss to the atmosphere[8], or to the use of statistical models for the global distribution of chorus intensities and plasma densities[25]. The simulations presented here utilize a novel time-varying data-driven model for chorus intensity[12] and also incorporate *in situ* plasma density observations from the Van Allen probes. Our two-dimensional simulation of energy, pitch angle, and mixed energy-pitch angle scattering also allows us to simultaneously treat both the local stochastic acceleration and electron loss to the atmosphere. We did not include the process of radial diffusion because this requires the future development of global radial diffusion coefficients based on ultra-low frequency wave power. However, because our simulation provides excellent agreement with the observed dynamical evolution of both the energy and pitch angle distribution of the highly relativistic electron population (that was unavailable before the REPT observations), it is clear that radial diffusion is of secondary importance to relativistic electron acceleration during this storm.

Our results provide quantitative confirmation of the remarkable efficiency of local electron acceleration by chorus emissions in the heart of the outer radiation belt. The physical processes involved are schematically illustrated in Extended Data Fig. 4. Together with the previous detailed analysis of peaks in electron phase space density[1], our study establishes that local stochastic acceleration by chorus emissions was the dominant process responsible for electron acceleration during the 9 October 2012 storm. The particular solar wind conditions leading to the dramatic acceleration included a relatively weak solar wind pressure with the magnetopause boundary outside 10 R_E (thus minimizing loss to the boundary[26]), and an extended period of strongly southward-directed interplanetary magnetic field. The latter both maintained enhanced convection of plasma sheet electrons into the inner magnetosphere leading to intense chorus excitation, and also led to significantly

©2013 Macmillan Publishers Limited. All rights reserved

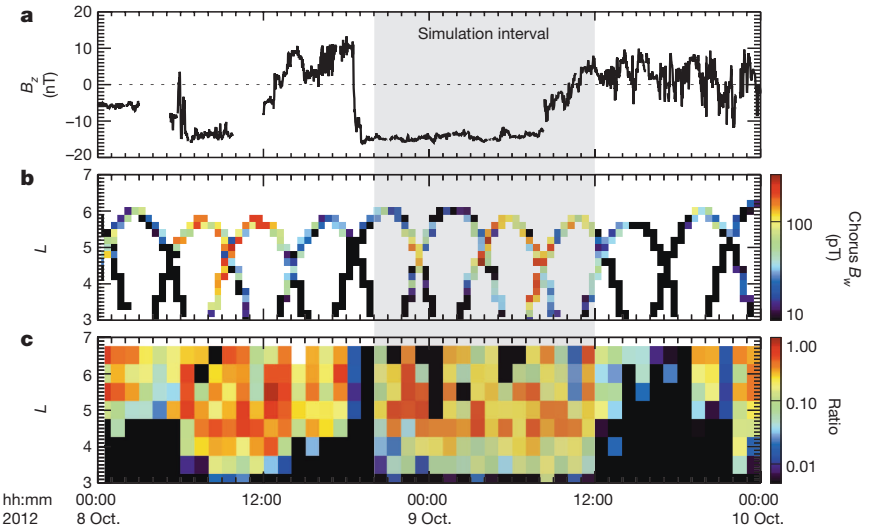


Figure 2 | Modelling the global distribution of chorus and electron scattering rates. **a**, Interplanetary B_z. **b**, Magnetic amplitude B_w (colour scale) of chorus emissions integrated over (0.1–0.5) f_{ce} obtained from EMFISIS on both Van Allen probes as a function of L showing the intensification on the dawn and dayside during intervals of strongly negative B_z. **c**, The ratio between the precipitated and trapped flux (colour scale) of 30–100 keV electrons as a function of L observed on multiple POES spacecraft in the 04-08 MLT sector. The ratio is controlled by the rate of pitch angle scattering and can be used to infer the amplitude of scattering chorus as a function of L and MLT on a global scale[12]. When near-conjugate measurements with the Van Allen probes are available, the inferred wave amplitudes from POES agree well with direct *in situ* EMFISIS observations. POES data at other MLT (Extended Data Fig. 1) are consequently used to develop a global model for chorus wave intensity as described in the Supplementary Information. In each 4-h MLT sector we also adopt a realistic model for the frequency distribution of chorus and its wave normal distribution based on previous statistical studies[17,29]. Plasma density is modelled using a statistical MLT distribution outside the plasmapause[30] scaled to *in situ* density values obtained from the EMFISIS instruments on each Van Allen probe. Adopted model parameters and resultant diffusion coefficients at $L = 5$, near the drift shell where peaks in electron phase space density are observed (Fig. 1h), are shown in Extended Data Fig. 2 and Extended Data Table 1. However, the stochastic acceleration process occurs over a broad spatial region ($3.5 < L < 6$) where chorus emissions are either directly observed (Fig. 2b) or inferred from the POES data.

reduced plasma density, which is conducive to more efficient local momentum diffusion[25]. The absence of acceleration for electrons of energy $E > 1$ MeV during the first dip in SYM-H is probably associated with rapid outward radial diffusion of any accelerated electrons and subsequent loss to the magnetopause[27] associated with strongly enhanced solar wind pressure. The local acceleration process described

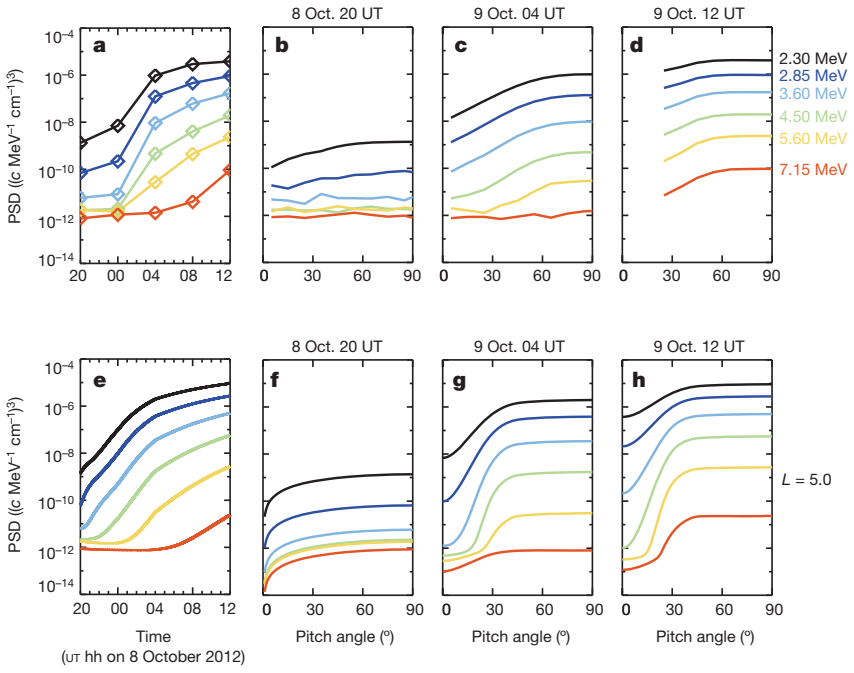


Figure 3 | Comparison of Fokker–Planck simulation results with observations. **a**, Increase of perpendicular electron phase space density (PSD) as a function of UT observed by REPT during the acceleration event at energies from 2.30 MeV to 7.15 MeV at $L = 5$. **b–d**, Observed evolution of the relativistic electron PSD as a function of pitch angle at 8 h intervals (shown above panels) during the simulation. **e**, The Fokker-Planck simulation of phase space density using the global wave model of chorus is able to account for both the magnitude and the timing of the observed (**a**) relativistic electron acceleration. Momentum scattering rates tend to peak at pitch angles between 60° and 80° (see Extended Data Fig. 2) and the rate of local stochastic flux increase becomes larger than the rate of loss to the atmosphere for energies above a few hundred keV. This property allows the stochastic build-up of the high-energy tail of the electron population even though losses to the atmosphere are still occurring[25]. **f–h**, Fokker-Planck simulation results of the electron PSD as a function of pitch angle during the acceleration event showing the development of flat pitch angle distributions at large pitch angles, which are a characteristic signature of chorus scattering at relativistic energies. This feature, together with the observed peaks in phase space density[1], provides a definitive confirmation of the dominance of chorus scattering over inward radial diffusion in causing electron acceleration during this storm.

©2013 Macmillan Publishers Limited. All rights reserved

here is a universal physical process, which should also be effective in the magnetospheres of Jupiter[28], Saturn and other magnetized plasma environments in the cosmos.

Online Content Any additional Methods, Extended Data display items and Source Data are available in the online version of the paper; references unique to these sections appear only in the online paper.

Received 26 August; accepted 18 November 2013.

1. Reeves, G. D. *et al.* Electron acceleration in the heart of the Van Allen radiation belts. *Science* **341,** 991–994 (2013).
2. Green, J. C. & Kivelson, M. G. Relativistic electrons in the outer radiation belt: differentiating between acceleration mechanisms. *J. Geophys. Res.* **109,** A03213 (2004).
3. Chen, Y., Reeves, G. D. & Friedel, R. H. W. The energization of relativistic electrons in the outer Van Allen belt. *Nature Phys.* **3,** 614–617 (2007).
4. Ukhorskiy, A. Y., Sitnov, M. I., Takahasi, K. & Anderson, B. J. Radial transport of radiation belt electrons due to stormtime Pc5 waves. *Ann. Geophys.* **27,** 2173–2181 (2009).
5. Perry, K. L., Hudson, M. K. & Elkington, S. R. Incorporating spectral characteristics of Pc5 waves into three-dimensional modelling and the diffusion of relativistic electrons. *J. Geophys. Res.* **110,** A03215 (2005).
6. Horne, R. B. & Thorne, R. M. Potential wave modes for electron scattering and stochastic acceleration to relativistic energies during magnetic storms. *Geophys. Res. Lett.* **25,** 3011–3014 (1998).
7. Summers, D., Thorne, R. M. & Xiao, F. Relativistic theory of wave-particle resonant diffusion with application to electron acceleration in the magnetosphere. *J. Geophys. Res.* **103,** 20487–20500 (1998).
8. Summers, D. *et al.* Model of the energization of outer-zone electrons by whistler-mode chorus during the October 9, 1990 geomagnetic storm. *Geophys. Res. Lett.* **29,** 2174–2197 (2002).
9. Horne, R. B. *et al.* Wave acceleration of electrons in the Van Allen radiation belts. *Nature* **437,** 227–230 (2005).
10. Thorne, R. M. Radiation belt dynamics: the importance of wave-particle interactions. *Geophys. Res. Lett.* **37,** L22107 (2010).
11. Baker, D. N. *et al.* The relativistic electron-proton telescope (REPT) instrument on board the Radiation Belt Storm Probes (RBSP) spacecraft: characterization of Earth's radiation belt high-energy particle populations. *Space Sci. Rev.* **179,** 337–381 (2013).
12. Li, W. *et al.* Constructing the global distribution of chorus wave intensity using measurements of electrons by the POES satellites and waves by the Van Allen probes. *Geophys. Res. Lett.* **40,** 4526–4532 (2013).
13. Baker, D. N. *et al.* Coronal mass ejections, magnetic clouds, and relativistic magnetospheric electron events: ISTP. *J. Geophys. Res.* **103,** 17279–17291 (1998).
14. McPherron, R. L. & Baker, D. N. Factors influencing the intensity of magnetospheric substorms. *J. Atmos. Terr. Phys.* **55,** 1091–1122 (1993).
15. Shue, J.-H. *et al.* Magnetopause location under extreme solar wind conditions. *Geophys. Res. Lett.* **103,** 17691–17700 (1998).
16. Kletzing, C. A. *et al.* The Electric and Magnetic Field Instrument Suite and Integrated Science (EMFISIS) on RBSP. *Space Sci. Rev.* **179,** 127–181 (2013).
17. Meredith, N. P. *et al.* Global models of lower band and upper band chorus from multiple satellite observations. *J. Geophys. Res.* **117,** A10225 (2012).
18. Li, W. *et al.* Global distribution of whistler-mode chorus waves observed on the THEMIS spacecraft. *Geophys. Res. Lett.* **36,** L09104 (2009).
19. Li, W. *et al.* THEMIS analysis of observed electron distributions responsible for chorus excitation. *J. Geophys. Res.* **115,** A00F11 (2010).
20. Ni, B., Thorne, R. M., Shprits, Y. Y. & Bortnik, J. Resonant scattering of plasma sheet electrons by whistler-mode chorus: contributions to diffuse auroral precipitation. *Geophys. Res. Lett.* **35,** L11106 (2008).
21. Nishimura, Y. *et al.* Identifying the driver of pulsating aurora. *Science* **330,** 81–84 (2010).
22. Thorne, R. M., Ni, B., Tao, X., Horne, R. B. & Meredith, N. P. Scattering by chorus waves as the dominant cause of diffuse auroral precipitation. *Nature* **467,** 943–946 (2010).
23. Kennel, C. F. & Petschek, H. E. Limit on stably trapped particle fluxes. *J. Geophys. Res.* **71,** 1–28 (1966).
24. Blake, J. B. *et al.* The Magnetic Electron Ion Spectrometer (MagEIS) instruments aboard the Radiation Belt Storm Probes (RBSP) spacecraft. *Space Sci. Rev.* **179,** 383–421 (2013).
25. Horne, R. B. *et al.* Timescales for radiation belt electron acceleration by whistler mode chorus waves. *J. Geophys. Res.* **110,** A03225 (2005).
26. Kataoka, R. & Miyoshi, Y. Magnetosphere inflation during the recovery phase of geomagnetic storms as an excellent magnetic confinement of killer electrons. *Geophys. Res. Lett.* **35,** L06S09 (2008).
27. Turner, D. L., Shprits, Y., Hartinger, M. & Angelopoulos, V. Explaining sudden losses of outer radiation belt electrons during geomagnetic storms. *Nature Phys.* **8,** 208–212 (2012).
28. Horne, R. B. *et al.* Gyro-resonant electron acceleration at Jupiter. *Nature Phys.* **4,** 301–304 (2008).
29. Li, W. *et al.* Global distribution of wave amplitudes and wave normal distributions of chorus waves with high-resolution THEMIS wave observations. *J. Geophys. Res.* **116,** A12205 (2011).
30. Sheeley, B. W., Moldwin, M. B., Rassoul, H. K. & Anderson, R. R. An empirical plasmasphere and trough density model: CRRES observations. *J. Geophys. Res.* **106,** 25631–25641 (2001).

Supplementary Information is available in the online version of the paper.

Acknowledgements This work was supported by JHU/APL contracts 967399 and 921647 under NASA's prime contract NAS5-01072. The analysis at UCLA was supported by the EMFISIS sub-award 1001057397:01 and by the ECT sub-award 13-041. We thank OMNIweb for providing geomagnetic indices and solar wind parameters used in this study and the NOAA POES team for providing POES electron data.

Author Contributions R.M.T. developed the project, directed the theoretical analysis, and was mainly responsible for writing the paper. W.L. conducted the data analysis on electrons and chorus waves and helped construct the global model of chorus. B.N. developed the method to infer wave intensity using POES electron data, performed the wave modelling, and evaluated the diffusion coefficients. Q.M. performed the Fokker–Planck simulations. J.B. and L.C. assisted with the global wave modelling. D.N.B. and S.G.K. provided the REPT data. H.E.S. and G.D.R. led the RBSP-ECT energetic particle team and G.D.R. and M.G.H. provided the phase space density. M.G.H. was responsible for the electron pitch angle data. C.A.K., W.S.K. and G.B.H. provided the EMFISIS wave data. J.B.B., J.F.F. and S.G.C. provided the MagEIS data.

Author Information Reprints and permissions information is available at www.nature.com/reprints. The authors declare no competing financial interests. Readers are welcome to comment on the online version of the paper. Correspondence and requests for materials should be addressed to R.M.T. (rmt@atmos.ucla.edu).

©2013 Macmillan Publishers Limited. All rights reserved

LETTER

doi:10.1038/nature12801

Dissipative production of a maximally entangled steady state of two quantum bits

Y. Lin[1]*, J. P. Gaebler[1]*, F. Reiter[2], T. R. Tan[1], R. Bowler[1], A. S. Sørensen[2], D. Leibfried[1] & D. J. Wineland[1]

Entangled states are a key resource in fundamental quantum physics, quantum cryptography and quantum computation[1]. Introduction of controlled unitary processes—quantum gates—to a quantum system has so far been the most widely used method to create entanglement deterministically[2]. These processes require high-fidelity state preparation and minimization of the decoherence that inevitably arises from coupling between the system and the environment, and imperfect control of the system parameters. Here we combine unitary processes with engineered dissipation to deterministically produce and stabilize an approximate Bell state of two trapped-ion quantum bits (qubits), independent of their initial states. Compared with previous studies that involved dissipative entanglement of atomic ensembles[3] or the application of sequences of multiple time-dependent gates to trapped ions[4], we implement our combined process using trapped-ion qubits in a continuous time-independent fashion (analogous to optical pumping of atomic states). By continuously driving the system towards the steady state, entanglement is stabilized even in the presence of experimental noise and decoherence. Our demonstration of an entangled steady state of two qubits represents a step towards dissipative state engineering, dissipative quantum computation and dissipative phase transitions[5–7]. Following this approach, engineered coupling to the environment may be applied to a broad range of experimental systems to achieve desired quantum dynamics or steady states. Indeed, concurrently with this work, an entangled steady state of two superconducting qubits was demonstrated using dissipation[8].

Trapped ions are one of the leading experimental platforms for quantum information processing, and advanced protocols using unitary quantum gates have been demonstrated (see, for example, refs 9, 10). However, decoherence and dissipation from coupling to the environment remains a challenge. One approach to overcome this relies on active feedback[11–17]. Such feedback techniques may be extended to quantum error correction, which can stabilize entangled states or realize fault-tolerant quantum computations. This will, however, require high-fidelity quantum gates and large qubit overheads that are beyond the reach of current experiments[2]. Recently, a complementary approach has been proposed to create entangled states or perform quantum computing by engineering the continuous interaction of the system with its environment[5–7,18–28]. In our experiment, we take a step towards harnessing dissipation for quantum information processing by producing an entangled state that is inherently stabilized against decoherence by the applied interactions in a setting fully compatible with quantum computation. With this technique, we realize maximally entangled steady states with a fidelity of $F = 0.75(3)$ by simultaneously applying a combination of time-independent fields. We also demonstrate that a stepwise application of these fields can speed up the dynamics of the scheme and achieve a fidelity of $F = 0.89(2)$ after approximately 30 repetitions. In both cases, the errors can be attributed to known experimental imperfections. Although these errors lead to a lower fidelity for entanglement preparation in our system as compared to unitary gates[10], the dissipative technique is much less sensitive to certain sources of experimental noise—for example, laser intensity fluctuations common to both qubits—and so may lead to improved performance in other trapped-ion systems where this is the dominant error. In the Supplementary Information we model the errors for the dissipative entanglement preparation and propose how they can be reduced.

Our scheme uses an ion chain with two qubit ions and at least one 'coolant' ion for sympathetic cooling[29] of the qubit ions' motion. We consider a normal motional mode of this ion chain having frequency ν and mean motional quanta $\bar{n}$. We cool the motional mode to $\bar{n} \approx 0$ by laser-cooling the coolant ion (or ions) and thus effectively couple the vibration to a zero-temperature bath with the phonon loss rate denoted by κ. As depicted in Fig. 1, we consider four energy levels of each qubit ion ($^9Be^+$), where $|\uparrow\rangle$ and $|\downarrow\rangle$ are the qubit 'spin' states, $|a\rangle$ is an auxiliary state and $|e\rangle$ is a fast-decaying excited electronic state. A sideband excitation, with Hamiltonian $H_s \equiv \Omega_s(|\uparrow\rangle_1\langle\downarrow| + |\uparrow\rangle_2\langle\downarrow|)b^+ + \text{h.c.}$ in the atomic and motional rotating frame, couples the two ions' spins via their motion (here Ω_s denotes the Rabi frequency, b^+ is the motional-mode Fock-state creation operator, the number subscripts denote the qubit ion number, and h.c. is the Hermitian conjugate). A carrier interaction with Hamiltonian $H_c \equiv \Omega_c(|a\rangle_1\langle\uparrow| + |a\rangle_2\langle\uparrow|) + \text{h.c.}$ drives the $|\uparrow\rangle \leftrightarrow |a\rangle$ transition of each ion with Rabi frequency Ω_c, and a repump laser incoherently drives $|a\rangle \rightarrow |\downarrow\rangle$, $|\uparrow\rangle$ by coupling to the intermediate state $|e\rangle$ at a rate γ (see Fig. 1a). All the above transitions are homogeneously driven for both qubit ions, such that individual addressing is not needed for this scheme. These couplings ensure that the maximally entangled singlet state $|S\rangle \equiv \frac{1}{\sqrt{2}}(|\uparrow\downarrow\rangle - |\downarrow\uparrow\rangle)$ is the only steady state of the effective dynamics[30] in the regime $\gamma, \kappa, \Omega_c \ll \Omega_s$.

For an intuitive understanding of the scheme, we first consider only the sideband excitation and the sympathetic cooling (blue lines in Fig. 1a), which, when applied together, have two dark states that are not affected by the interactions $|\uparrow\uparrow\rangle|0\rangle$ and $|S\rangle|0\rangle$. The remaining basis states of the qubits, $|\downarrow\downarrow\rangle$ and $|T\rangle \equiv \frac{1}{\sqrt{2}}(|\uparrow\downarrow\rangle + |\downarrow\uparrow\rangle)$, are driven by H_s and eventually pumped to $|\uparrow\uparrow\rangle|0\rangle$ by the combination of the sideband drive and the sympathetic cooling (Fig. 1b). The effect of adding the carrier drive H_c is to couple the $|\uparrow\uparrow\rangle$ state to a combination of the $|\uparrow a\rangle$, $|a\uparrow\rangle$ and $|aa\rangle$ states and the $|S\rangle$ state to the $|S_a\rangle \equiv \frac{1}{\sqrt{2}}(|a\downarrow\rangle - |\downarrow a\rangle)$ state. However, assuming the ions are in the ground state of motion, the dressed states of the sideband Hamiltonian H_s containing $|S_a\rangle$ have eigenenergies $\pm\Omega_s$, while $|S\rangle$, $|\uparrow\uparrow\rangle$, $|\uparrow a\rangle$ and $|a\uparrow\rangle$ are dark states of H_s with zero eigenenergy. Thus, the transition from $|S\rangle|0\rangle$ to $|S_a\rangle|0\rangle$ is shifted out of resonance with the carrier drive and therefore suppressed for $\Omega_c \ll \Omega_s$. On the other hand, the transitions from the $|\uparrow\uparrow\rangle|0\rangle$ state to the $|\uparrow a\rangle|0\rangle$ and $|a\uparrow\rangle|0\rangle$ states are not energy shifted and remain resonant. The repumping laser incoherently transfers the state $|a\rangle$ back to the $|\uparrow\rangle$ and $|\downarrow\rangle$ qubit manifold. Thus, the combination

[1]National Institute of Standards and Technology, 325 Broadway, Boulder, Colorado 80305, USA. [2]QUANTOP, The Niels Bohr Institute, University of Copenhagen, Blegdamsvej 17, DK-2100 Copenhagen Ø, Denmark.

*These authors contributed equally to this work.

©2013 Macmillan Publishers Limited. All rights reserved

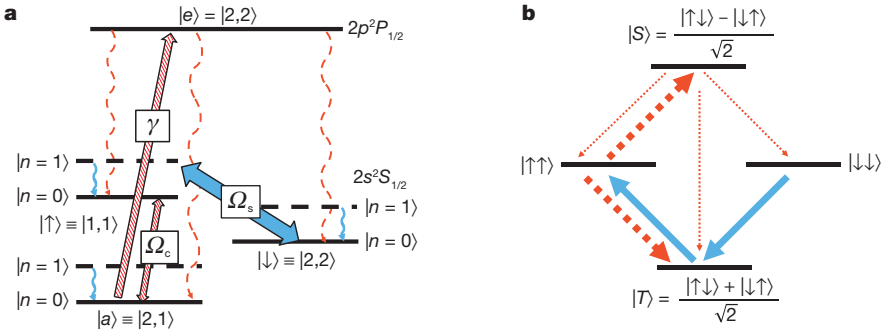


Figure 1 | Energy levels and entanglement preparation scheme. a, The internal energy levels (not to scale) of $^{9}Be^{+}$ are shown as thick solid black lines for the ground motional state and dashed lines for the first excited motional state. The couplings needed to produce steady-state entanglement are shown with blue arrows for the strong sideband coupling (Ω_s) and sympathetic cooling, and by patterned and dashed red arrows for the weak microwave coupling (Ω_c), repumping (γ), and spontaneous emission from the $|e\rangle$ state. Wavy arrows depict the dissipative processes. **b**, Four spin states that span the $|\uparrow\rangle$, $|\downarrow\rangle$ qubit manifold of the two $^{9}Be^{+}$ ions are shown as horizontal lines. Transfer processes that are accomplished by the sideband drive and sympathetic cooling are shown as blue arrows, whereas processes that occur by coupling the $|\uparrow\rangle$ state to the auxiliary $|a\rangle$ state followed by excitation with the repumping beam and decay by spontaneous emission are shown as dashed red arrows. Processes shown as thin dotted red lines are shifted out of resonance owing to the strong sideband coupling, leading to accumulation of population in the maximally entangled state $|S\rangle$ in steady state. Further details about the rates for each process are given in Supplementary Information.

of H_c and the repumping beam create a process to pump $|\uparrow\uparrow\rangle$ to $|S\rangle$ as well as a depumping process from $|S\rangle$ to $|\downarrow\downarrow\rangle$, $|T\rangle$ and $|\uparrow\uparrow\rangle$, although the latter is significantly slower (Fig. 1b). In the limit where the rate of pumping other states into $|S\rangle$ is much greater than the depumping rate from $|S\rangle$, the steady state will approach $|S\rangle$. The ratio of these rates can be made arbitrarily high by reducing the values of γ, κ and Ω_c compared to Ω_s and in steady state the fidelity of the maximally entangled state $|S\rangle$ can approach unity (see Supplementary Information). Fluctuations in the values of these parameters do not reduce the fidelity of the entangled state as long as the values of γ, κ and Ω_c remain small compared to Ω_s, which is in contrast to the method of entanglement preparation via unitary gates.

For our experimental implementation, we confine a $^{9}Be^{+}$–$^{24}Mg^{+}$–$^{24}Mg^{+}$–$^{9}Be^{+}$ four-ion chain in a linear radio-frequency Paul trap[10]. The two $^{9}Be^{+}$ ions serve as qubit ions while the two $^{24}Mg^{+}$ ions are used for sympathetic cooling. The ion chain lies along the axis of the trap, the axis of weakest confinement, and has an extent of approximately 11 μm. We label the four-ion axial modes {1, 2, 3, 4}, and they have mode frequencies $\nu_{1-4} \approx \{2.0, 4.1, 5.5, 5.8\ \mathrm{MHz}\}$, respectively. An internal-state quantization magnetic field $B \approx 11.964$ mT is applied along a direction that is at 45° to the trap axis, which breaks the degeneracy of the magnetic sub-levels of $^{9}Be^{+}$ and $^{24}Mg^{+}$. As depicted in Fig. 1a, we utilize the $^{9}Be^{+}$ internal states $|F = 1, m_F = 1\rangle \equiv |\uparrow\rangle$, $|2, 2\rangle \equiv |\downarrow\rangle$ and $|2, 1\rangle \equiv |a\rangle$. To create the sideband coupling term H_s, we apply two 313 nm laser beams in a Raman configuration tuned approximately 270 GHz below the $2s\ ^{2}S_{1/2}$ to $2p\ ^{2}P_{1/2}$ transition with a frequency difference equal to $f_0 + \nu_3$ where $f_0 \approx 1.018$ GHz is the resonant transition frequency between the $|\downarrow\rangle$ and $|\uparrow\rangle$ states. The two beams are derived from the same laser and frequency-shifted using acousto-optic modulators. The difference wave vector of the two beams is parallel to the trap axis. Microwaves are used to drive resonant transitions between the $|\uparrow\rangle$ state and the $|a\rangle$ state ($f \approx 1.121$ GHz) to create H_c. We also apply a repump laser beam to drive the $|a\rangle$ state to the $2p\ ^{2}P_{1/2}|2, 2\rangle$ state, which subsequently spontaneously emits a photon and decays to $|\uparrow\rangle$, $|\downarrow\rangle$ or $|a\rangle$ with a branching ratio of approximately 5:4:3. Phonon excitations due to the photon recoil are removed by the sympathetic cooling. To cool the $^{24}Mg^{+}$ ions, a Doppler cooling beam, two Raman-sideband beams, and a repump beam co-propagate with the $^{9}Be^{+}$ Raman beams. These beams ($\lambda \approx 280$ nm) interact negligibly with the internal states of the $^{9}Be^{+}$ ions. We initialize each experiment by first applying Doppler cooling to $^{9}Be^{+}$ and $^{24}Mg^{+}$, followed by $^{24}Mg^{+}$ sideband cooling of all the axial modes to near the ground state of motion. An optical pumping pulse initializes the $^{9}Be^{+}$ ions to the $|\downarrow\downarrow\rangle$ state. We then apply the dissipative entanglement preparation operations, as detailed below. Finally, we perform spin-state analysis to measure the populations of the $|S\rangle$, $|T\rangle$, $|\uparrow\uparrow\rangle$ and $|\downarrow\downarrow\rangle$ spin states (see Methods).

We implement the entanglement scheme using mode 3, where the $^{9}Be^{+}$ ions oscillate in phase with each other but out of phase with the $^{24}Mg^{+}$ ions (which oscillate in phase). In one implementation of the experiment, we apply the laser-induced sideband excitation, microwave-induced carrier excitation, repumping and sympathetic cooling simultaneously (see Methods for parameter values) for a duration t and obtain a steady-state singlet state fidelity of 0.75(3), as shown in Fig. 2.

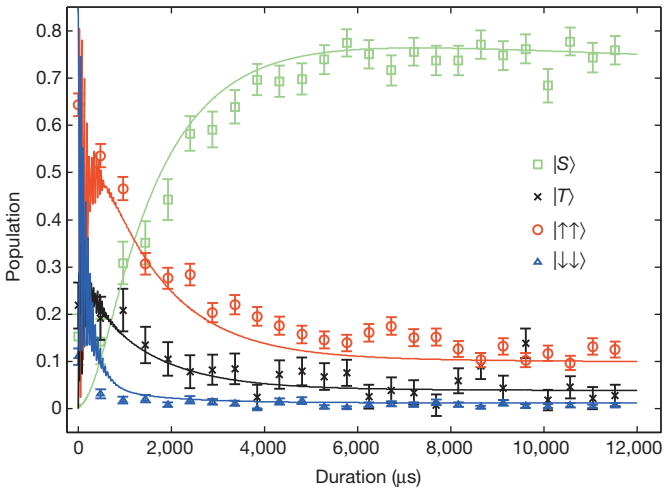


Figure 2 | Steady-state entanglement. Measured populations of the singlet, triplet, $|\uparrow\uparrow\rangle$ and $|\downarrow\downarrow\rangle$ states (respectively squares, crosses, circles and triangles) are shown as a function of duration; the duration is the length of time during which all elements of the dissipative entanglement scheme are applied simultaneously. The system reaches a steady state with a 0.75(3) population in the target singlet state after a few milliseconds. The solid lines are the result of a simulation based on the experimental parameters (see Methods). The slow decrease in the singlet state fidelity at long times visible in the simulation is due to a leak of the qubits to spin states outside the $|\uparrow\rangle$, $|\downarrow\rangle$, $|a\rangle$ manifold caused by spontaneous emission from the lasers that generate the sideband coupling (see Methods and Supplementary Information). Strictly speaking this depumping means that the state is only a quasi-steady state. For our parameters there is, however, a clear separation of the preparation and depumping timescales, justifying the description as a steady state. Data are shown as mean ± s.d.

©2013 Macmillan Publishers Limited. All rights reserved

We model the experiment (solid lines in Fig. 2) taking into account: (1) the additional spontaneous emission due to the off-resonant $^9Be^+$ sideband laser beams, (2) the position fluctuations of those beams at the ions' location, which leads to unequal sideband Rabi rates for the two $^9Be^+$ ions, (3) off-resonant coupling of the sideband excitation to other motional modes, and (4) heating processes (see Methods). The model is in close agreement with the data and suggests that the resulting state is an incoherent mixture of $|S\rangle$ and other states (mainly $|\uparrow\uparrow\rangle$) and the dominant errors come from the spontaneous emission induced by the sideband laser beams and unequal sideband Rabi rates.

We also implement the scheme in a stepwise manner. In this case, we can take advantage of coherences to speed up the entanglement creation process and thereby reduce the effect of the spontaneous emission induced by the $^9Be^+$ sideband laser beams. Specifically, we apply a sequence of steps, with each step consisting of a coherent pulse with $H_{coh} = H_s + H_c$ followed by the dissipative processes of repumping and sympathetic cooling, applied sequentially (the order does not matter). In the steady-state entanglement procedure outlined above, we required Ω_c, γ, $\kappa \ll \Omega_s$ to suppress transitions from $|S\rangle$ to $|S_a\rangle$. However, when H_{coh} is applied without any dissipation, ions initially in the $|S\rangle$ state will oscillate between $|S\rangle$ and a superposition of $|S\rangle$ and $|S_a\rangle$, which is dressed by H_s, with a period of $2\pi/\sqrt{\Omega_s^2+\Omega_c^2}$, assuming the ions are in the motional ground state. Thus, by applying H_{coh} for a full oscillation period the interaction will be an identity operation for the $|S\rangle$ state while all other states will be partially transferred to the auxiliary level $|a\rangle$, which can then be repumped to create $|S\rangle$. However, if $n \neq 0$ some population will be transferred out of the $|S\rangle$ state because the oscillation period is dependent on n. By taking advantage of the coherent evolution, we relax the requirement Ω_c, γ, $\kappa \ll \Omega_s$ and the entanglement preparation timescale can be shortened, which reduces the error due to spontaneous emission induced by the sideband laser beams. During the coherent process, the entangled state $|S\rangle$ is no longer strictly a steady state; however, if the ratio Ω_c/Ω_s is small, the evolution of the state away from $|S\rangle$ will be correspondingly small and $|S\rangle$ remains an approximate steady state.

The results of the stepwise experiment are shown in Fig. 3. We obtain the singlet state with fidelity 0.89(2). We use the same model as for the continuous case to predict the outcome of the stepwise scheme, and find good agreement with the data (solid lines in Fig. 3), with the largest sources of error coming from heating processes, unequal sideband Rabi rates, spontaneous emission caused by the $^9Be^+$ sideband lasers and off-resonant coupling of the sideband to mode 4.

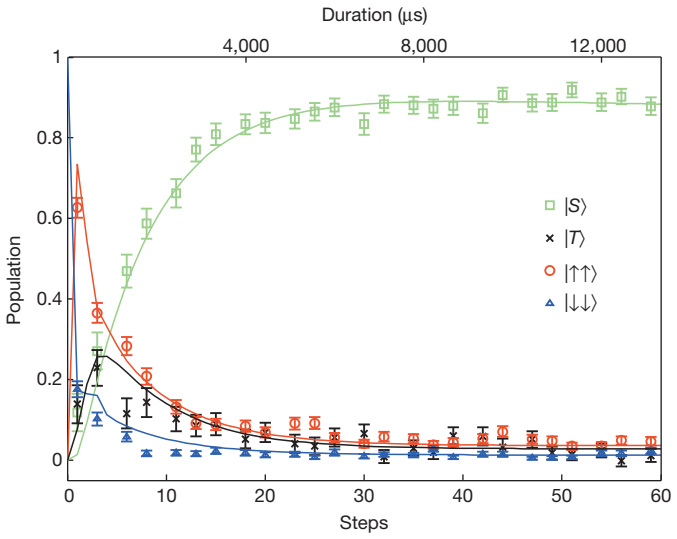


Figure 3 | Entanglement with stepwise scheme. The measured populations of the singlet, triplet, $|\uparrow\uparrow\rangle$ and $|\downarrow\downarrow\rangle$ states (respectively squares, crosses, circles and triangles) are shown as a function of the number of applied steps. Each step has a duration of approximately 220 μs. The solid lines are the results of a model (see Methods). Data are shown as mean ± s.d.

We have presented deterministic steady-state pumping into a maximally entangled state with fidelities that are limited by known experimental imperfections. This result can be extended to other systems where two-qubit quantum logic gates may not be feasible owing to strong dissipation[22], and represents a step towards harnessing dissipation for quantum information processing.

METHODS SUMMARY

The Methods section includes detailed descriptions of (1) the state detection and analysis procedure, (2) the experimental parameters for continuous and stepwise implementation of the scheme, and (3) the theoretical model used to produce the solid lines in Figs 2 and 3.

Online Content Any additional Methods, Extended Data display items and Source Data are available in the online version of the paper; references unique to these sections appear only in the online paper.

Received 18 July; accepted 16 October 2013.
Published online 24 November 2013.

1. Nielsen, M. A. & Chuang, I. L. *Quantum Computation and Quantum Information* (Cambridge Univ. Press, 2000).
2. Ladd, T. D. *et al.* Quantum computers. *Nature* **464,** 45–53 (2010).
3. Krauter, H. *et al.* Entanglement generated by dissipation and steady state entanglement of two macroscopic objects. *Phys. Rev. Lett.* **107,** 080503 (2011).
4. Barreiro, J. T. *et al.* An open-system quantum simulator with trapped ions. *Nature* **470,** 486–491 (2011).
5. Kraus, B. *et al.* Preparation of entangled states by quantum Markov processes. *Phys. Rev. A* **78,** 042307 (2008).
6. Diehl, S. *et al.* Quantum states and phases in driven open quantum systems with cold atoms. *Nature Phys.* **4,** 878–883 (2008).
7. Verstraete, F., Wolf, M. M. & Cirac, J. I. Quantum computation and quantum-state engineering driven by dissipation. *Nature Phys.* **5,** 633–636 (2009).
8. Shankar, S. *et al.* Autonomously stabilized entanglement between two superconducting quantum bits. *Nature* http://dx.doi.org/10.1038/nature12802 (this issue).
9. Lanyon, B. P. *et al.* Universal digital quantum simulation with trapped ions. *Science* **334,** 57–61 (2011).
10. Hanneke, D. *et al.* Realization of a programmable two-qubit quantum processor. *Nature Phys.* **6,** 13–16 (2010).
11. Sayrin, C. *et al.* Real-time quantum feedback prepares and stabilizes photon number states. *Nature* **477,** 73–77 (2011).
12. Vijay, R. *et al.* Stabilizing Rabi oscillations in a superconducting qubit using quantum feedback. *Nature* **490,** 77–80 (2012).
13. Ristè, D., Bultink, C. C., Lehnert, K. W. & DiCarlo, L. Feedback control of a solid-state qubit using high-fidelity projective measurement. *Phys. Rev. Lett.* **109,** 240502 (2012).
14. Brakhane, S. *et al.* Bayesian feedback control of a two-atom spin-state in an atom-cavity system. *Phys. Rev. Lett.* **109,** 173601 (2012).
15. Schindler, P. *et al.* Quantum simulation of dynamical maps with trapped ions. *Nature Phys.* **9,** 361–367 (2013).
16. Campagne-Ibarcq, P. *et al.* Persistent control of a superconducting qubit by stroboscopic measurement feedback. *Phys. Rev. X* **3,** 021008 (2013).
17. Ristè, D. *et al.* Deterministic entanglement of superconducting qubits by parity measurement and feedback. *Nature* **502,** 350–354 (2013).
18. Poyatos, J. F., Cirac, J. I. & Zoller, P. Quantum reservoir engineering with laser cooled trapped ions. *Phys. Rev. Lett.* **77,** 4728–4731 (1996).
19. Plenio, M. B., Huelga, S., Beige, A. & Knight, P. L. Cavity-loss-induced generation of entangled atoms. *Phys. Rev. A* **59,** 2468–2475 (1999).
20. Clark, S., Peng, A., Gu, M. & Parkins, S. Unconditional preparation of entanglement between atoms in cascaded optical cavities. *Phys. Rev. Lett.* **91,** 177901 (2003).
21. Parkins, A. S., Solano, E. & Cirac, J. I. Unconditional two-mode squeezing of separated atomic ensembles. *Phys. Rev. Lett.* **96,** 053602 (2006).
22. Kastoryano, M. J., Reiter, F. & Sørensen, A. S. Dissipative preparation of entanglement in optical cavities. *Phys. Rev. Lett.* **106,** 090502 (2011).
23. Cho, J., Bose, S. & Kim, M. S. Optical pumping into many-body entanglement. *Phys. Rev. Lett.* **106,** 020504 (2011).
24. Bermudez, A., Schaetz, T. & Plenio, M. B. Dissipation-assisted quantum information processing with trapped ions. *Phys. Rev. Lett.* **110,** 110502 (2013).
25. Leghtas, Z. *et al.* Stabilizing a Bell state of two superconducting qubits by dissipation engineering. *Phys. Rev. A* **88,** 023849 (2013).
26. Reiter, F., Tornberg, L., Johansson, G. & Sørensen, A. S. Steady state entanglement of two superconducting qubits by engineered dissipation. *Phys. Rev. A* **88,** 032317 (2013).
27. Cormick, C., Bermudez, A., Huelga, S. F. & Plenio, M. B. Dissipative ground-state preparation of a spin chain by a structured environment. *New J. Phys.* **15,** 073027 (2013).
28. Ticozzi, F. & Viola, L. Steady-state entanglement by engineered quasi-local Markovian dissipation: Hamiltonian-assisted and conditional stabilization.

©2013 Macmillan Publishers Limited. All rights reserved

Quantum Inform. Comput. (in the press); preprint at http://arXiv.org/abs/1304.4270 (2013).
29. Barrett, M. D. *et al.* Sympathetic cooling of $^{9}Be^{+}$ and $^{24}Mg^{+}$ for quantum logic. *Phys. Rev. A* **68,** 042302 (2003).
30. Reiter, F. & Sørensen, A. S. Effective operator formalism for open quantum systems. *Phys. Rev. A* **85,** 032111 (2012).

Supplementary Information is available in the online version of the paper.

Acknowledgements This research was funded in part by the Office of the Director of National Intelligence (ODNI), Intelligence Advanced Research Projects Activity (IARPA). All statements of fact, opinion or conclusions contained herein are those of the authors and should not be construed as representing the official views or policies of IARPA or the ODNI. This work was also supported by ONR, by the NIST Quantum Information Program, and by the European Union's Seventh Framework Program through SIQS (grant no. 600645) and through the ERC grant QIOS (grant no. 306576). We thank D. Allcock and B. Sawyer for comments on the manuscript and E. Knill for conversations. F.R. acknowledges conversations with B. Lanyon, R. Blatt and J. Home and support from the Studienstiftung des deutschen Volkes. This Letter is a contribution of NIST and is not subject to US copyright.

Author Contributions Y.L. and J.P.G. performed the experiments, analysed the data and developed the numerical model. F.R. proposed the entanglement scheme and developed the analytic rate model described in Supplementary Information under the guidance of A.S.S. T.R.T. contributed to the numerical model and the experimental apparatus. R.B. contributed to the experimental apparatus. D.L. and D.J.W. directed the experiments. All authors provided important suggestions for the experiments, discussed the results and contributed to the manuscript.

Author Information Reprints and permissions information is available at www.nature.com/reprints. The authors declare no competing financial interests. Readers are welcome to comment on the online version of the paper. Correspondence and requests for materials should be addressed to Y.L. (yiheng.lin@colorado.edu).

©2013 Macmillan Publishers Limited. All rights reserved

METHODS

Spin-state fidelity measurement. To detect the populations of the $|S\rangle$, $|T\rangle$, $|\uparrow\uparrow\rangle$ and $|\downarrow\downarrow\rangle$ states, we need to obtain the relevant elements of the density matrix ρ describing the state of the two $^9Be^+$ ions during the experiment. Because each ion may be found in any of the three ground states $|\uparrow\rangle$, $|\downarrow\rangle$, $|a\rangle$ (Fig. 1), the density matrix has dimensions 9×9. The singlet-state population is given by $\frac{1}{2}(\rho_{\uparrow\downarrow,\uparrow\downarrow}+\rho_{\downarrow\uparrow,\downarrow\uparrow})-\mathrm{Re}(\rho_{\uparrow\downarrow,\downarrow\uparrow})$ and the triplet-state population is given by $\frac{1}{2}(\rho_{\uparrow\downarrow,\uparrow\downarrow}+\rho_{\downarrow\uparrow,\downarrow\uparrow})+\mathrm{Re}(\rho_{\uparrow\downarrow,\downarrow\uparrow})$. The fidelity of the target entangled state, F, is equal to the singlet-state population. For the steady-state fidelity, we report the average fidelity measured between 6 and 12 ms for the continuous case and between 35 and 59 steps in the stepwise case. We first measure the populations of the $|\downarrow\rangle$ state by collecting fluorescence photons from the laser-induced cycling transition $|\downarrow\rangle\leftrightarrow 2p\,^2P_{3/2}|3,3\rangle$ of both $^9Be^+$ ions together. We apply this detection beam for 250 μs and collect photon counts with a photomultiplier tube (approximately 30 counts are registered per ion in the $|\downarrow\rangle$ state). We repeat the experiment and detection 400 times to obtain a histogram. We fit the histogram of counts to a Poisson distribution to obtain the probabilities to measure both ions, one ion and zero ions in the $|\downarrow\rangle$ state denoted by P_2, P_1 and P_0, respectively. Specifically, these probabilities are related to the density matrix as follows: $P_2=\rho_{\downarrow\downarrow,\downarrow\downarrow}$, $P_1=\rho_{\downarrow\uparrow,\downarrow\uparrow}+\rho_{\uparrow\downarrow,\uparrow\downarrow}+\rho_{a\downarrow,a\downarrow}+\rho_{\downarrow a,\downarrow a}$, and $P_0=\rho_{\uparrow\uparrow,\uparrow\uparrow}+\rho_{a\uparrow,a\uparrow}+\rho_{\uparrow a,\uparrow a}+\rho_{aa,aa}$. We repeat the entanglement preparation scheme and perform a microwave π pulse on the $|\downarrow\rangle\leftrightarrow|\uparrow\rangle$ transition followed by the same detection procedure to obtain: $P_{2,\pi}=\rho_{\uparrow\uparrow,\uparrow\uparrow}$, $P_{1,\pi}=\rho_{\uparrow\downarrow,\uparrow\downarrow}+\rho_{\downarrow\uparrow,\downarrow\uparrow}+\rho_{a\uparrow,a\uparrow}+\rho_{\uparrow a,\uparrow a}$, and $P_{0,\pi}=\rho_{\downarrow\downarrow,\downarrow\downarrow}+\rho_{a\downarrow,a\downarrow}+\rho_{\downarrow a,\downarrow a}+\rho_{aa,aa}$. Thus, assuming the population of the $|aa\rangle$ state is negligible (see below), we have $\rho_{\uparrow\downarrow,\uparrow\downarrow}+\rho_{\downarrow\uparrow,\downarrow\uparrow}=P_1-(P_{0,\pi}-P_2)$. To obtain the off-diagonal elements, we perform the same experiment but with a microwave π/2 pulse on the $|\downarrow\rangle\leftrightarrow|\uparrow\rangle$ transition before the detection to obtain $P_{2,\frac{\pi}{2}}$, $P_{1,\frac{\pi}{2}}$ and $P_{0,\frac{\pi}{2}}$. The phase of the microwave is randomized in each experiment. It can be shown that $\mathrm{Re}(\rho_{\uparrow\downarrow,\downarrow\uparrow})=-1/2+2P_{0,\frac{\pi}{2}}+\frac{1}{2}(P_2-P_0)+\frac{1}{2}(P_{2,\pi}-P_{0,\pi})$, which gives the last piece of information needed to obtain the populations of the $|S\rangle$ and $|T\rangle$ states.

Owing to spontaneous Raman scattering caused by the sideband laser beams, it is possible that the $^9Be^+$ ions could be transferred to a hyperfine state outside the $|\uparrow\rangle$, $|\downarrow\rangle$, $|a\rangle$ manifold. However, this detection procedure does not distinguish these states from the $|a\rangle$ state. Our model predicts that the probability to find at least one ion outside the three-state manifold is at most 5% for the data in Fig. 2 and 3% for the data in Fig. 3. In future experiments, this population could be brought back to the three-state manifold with additional repump beams.

To calculate the singlet fidelity above, we assumed that the probability to find both atoms outside the $|\uparrow\rangle$, $|\downarrow\rangle$ qubit manifold was negligible. For the data in Figs 2 and 3 we measured the probability to find at least one ion outside the qubit manifold state, given by $P_0+P_{0,\pi}-(P_2+P_{2,\pi})$, to be 7(5)% and 2(2)% respectively for the steady state. We expect the probability to find both ions outside the qubit manifold to be of the order of the square of the probability to find one ion outside the qubit manifold, which is therefore small. Furthermore, our theoretical model predicts the probability of finding both ions outside the qubit manifold to be at most 1% for the continuous implementation and 0.05% for the stepwise implementation.

Experimental parameters. For the continuous implementation of the scheme shown in Fig. 2, the sideband Rabi rate was $\Omega_s=2\pi\times 7.8(1)$ kHz and the microwave Rabi rate was $\Omega_c=2\pi\times 0.543(6)$ kHz. The 1/e time for the repump beam to deplete the $|a\rangle$ state was 88 μs. The 1/e time for continuous sympathetic sideband cooling of mode 3 was 203 μs; this was determined from an exponential fit of the average Fock-state occupation number $\bar{n}$ versus sympathetic cooling time from the initial Doppler-cooled value of $\bar{n}\approx 2.5$ to a steady-state value, with cooling on, of $\bar{n}=0.11(1)$. The continuous sympathetic cooling was achieved by applying the laser-induced Raman sideband for the $^{24}Mg^+$ ions that couples the electronic ground states $\left|F=\frac{1}{2},m_F=-\frac{1}{2}\right\rangle|n\rangle\leftrightarrow\left|\frac{1}{2},\frac{1}{2}\right\rangle|n-1\rangle$ simultaneously with a repump beam that transfers $\left|\frac{1}{2},\frac{1}{2}\right\rangle|n\rangle\rightarrow\left|\frac{1}{2},-\frac{1}{2}\right\rangle|n\rangle$. The continuous sympathetic cooling off-resonantly cooled the other axial modes 1, 2 and 4 with 1/e times of approximately 1,300 μs, 294 μs and 181 μs to thermal states with average Fock state occupation numbers of approximately 2.9, 0.95 and 0.12, respectively. The Rabi rate for the $^{24}Mg^+$ sideband transition on mode 3 was $\sim 2\pi\times 11.9$ kHz and the repumping rate was $\sim 2\pi\times 625$ kHz (corresponding to a 1/e repump time of 1.6 μs). The repumping rate was made significantly stronger than the sideband rate to eliminate any coherent dynamics between the $^{24}Mg^+$ spins and ion-crystal motion.

We implemented the stepwise scheme in the following way: in each step we first sympathetically cooled each of the modes of the $^9Be^+$–$^{24}Mg^+$–$^{24}Mg^+$–$^9Be^+$ chain with $^{24}Mg^+$ Raman sideband cooling[31,32], followed by application of H_{coh} for a duration $t_{2\pi}$, and at the end of each step we applied the repumping beam. The populations of the qubit state were measured at the end of each step and plotted in Fig. 3. The $^9Be^+$ sideband Rabi rate was $\Omega_s=2\pi\times 8.4(1)$ kHz and the microwave Rabi rate was $\Omega_c=2\pi\times 1.24(6)$ kHz. The repumping beam had a 1/e time of approximately 3 μs and was turned on for 6 μs in each step. In each step, two sympathetic cooling cycles were applied to mode 1, which has the largest heating rate, and one cycle was applied to each of the remaining modes, with mode 3 being the last. A sympathetic cooling cycle consists of a single motion subtracting sideband pulse applied to the $^{24}Mg^+$ ions followed by a repump pulse. The five cooling cycles were applied for a total duration of ~100 μs in each step.

In both cases, the ion spacing was set by adjusting the strength of the harmonic confinement, such that $\Delta_k z=2\pi m$ where $\Delta_k\approx\frac{2\pi\sqrt{2}}{313\times 10^{-9}}\ m^{-1}$ is the wavevector difference of the $^9Be^+$ Raman sideband lasers, z is the distance between the $^9Be^+$ ions, and m is an integer, such that the phase of the sideband excitation was equal on both ions. For our confinement strength, $z\approx 11$ μm such that the value of m was near 300. For modes where the qubit ions move in phase, the integer value of m ensures H_s is as defined in the main text. However, in the general case $H_s\equiv\Omega_s(|\uparrow\rangle_1\langle\downarrow|+e^{i\phi}|\uparrow\rangle_2\langle\downarrow|)b^+ + \mathrm{h.c.}$, where ϕ is the phase difference between the two $^9Be^+$ ions of the sideband coupling, and the steady state of the system (including the cooling, repumping and microwave carrier) is $|D_\phi\rangle\equiv\frac{|\uparrow\downarrow\rangle-e^{i\phi}|\downarrow\uparrow\rangle}{\sqrt{2}}$.

Numerical model. We modelled our experiment using a master equation with a coherent component describing the $^9Be^+$ sideband and microwave carrier drives and Lindblad operators describing the sympathetic cooling, repumping and spontaneous emission due to the $^9Be^+$ sideband lasers. The coherent Hamiltonian is

$$H_{coh}\equiv\Omega_s\left[\left(1-\frac{r}{2}\right)|\uparrow\rangle_1\langle\downarrow|+\left(1+\frac{r}{2}\right)|\uparrow\rangle_2\langle\downarrow|\right)b^+ + \Omega_c\left(|a\rangle_1\langle\uparrow|+|a\rangle_2\langle\uparrow|\right)+\mathrm{h.c.}$$

where r describes the Rabi-rate imbalance of the sideband on the two ions. The Lindblad operator describing sympathetic cooling is given by $L_\kappa=\sqrt{\kappa}b$, and the repumping is given by $L_{\gamma_{j,a}}$, where j is either the $|\uparrow\rangle$ or $|\downarrow\rangle$ state and $L_{\gamma_{j,a}}=\sqrt{\gamma_{j,a}}|a\rangle$. Heating processes that limit the sympathetic cooling are modelled with a Lindblad operator $L_{\kappa_h}=\sqrt{\kappa_h}b^\dagger$, where κ_h is determined experimentally by measuring $\bar{n}$ for mode 3 after sympathetic cooling (no other interactions are turned on). The heating rate is given by $\kappa_h=\frac{\kappa\bar{n}}{1+\bar{n}}$. For the continuous cooling used for the data in Fig. 2 we found $\bar{n}=0.11(1)$ and for the stepwise case of Fig. 3 we found $\bar{n}=0.08(1)$. We take into account spontaneous emission that incoherently changes population from the state i to the state j ($i\neq j$) caused by the $^9Be^+$ sideband laser beams with Lindblad operators of the form $L_{j,i}=\sqrt{\Gamma_{j,i}}|j\rangle\langle i|$, where $\Gamma_{j,i}$ can be calculated using the Kramers-Heisenberg formula[33]. The error caused by Rayleigh scattering ($i=j$) is negligible[34]. Off-resonant coupling to mode 4 is taken into account with an additional Hamiltonian term $H_4=\Omega_s\frac{\eta_4}{\eta_3}\left(|\uparrow\rangle_1\langle\downarrow|-|\uparrow\rangle_2\langle\downarrow|\right)c^+e^{-i\delta t}+\mathrm{h.c.}$, where c^+ is the raising operator for the fourth mode, $\delta\approx 2\pi\times 250$ kHz is the splitting between modes 3 and 4, and $\eta_3=0.180$ and $\eta_4=0.155$ are the Lamb-Dicke parameters of modes 3 and 4, respectively. The continuous implementation of the scheme is modelled by numerically solving a master equation that includes all terms for a variable duration and a given value of r. We then obtain the theoretical prediction shown in Fig. 2 by averaging simulations with different values of r using a Gaussian distribution with an r.m.s. value of 0.014. This r.m.s. value was determined from fits to qubit Rabi flopping curves for a single $^9Be^+$ ion and for the $^9Be^+$–$^{24}Mg^+$–$^{24}Mg^+$–$^9Be^+$ ion chain. Percent-level fluctuations of Ω_s cause negligible changes to the predicted fidelity. The result of the calculation at the end of each step is plotted in Fig. 3. In both cases, the initial state of the $^9Be^+$ ions was taken to be $|\downarrow\downarrow\rangle|n=0\rangle$. The particular initial state chosen affects the dynamics only at short times and does not affect the steady state. All numerical models were implemented by use of the quantum optics toolbox[35].

31. Monroe, C. *et al.* Resolved-sideband Raman cooling of a bound atom to the 3D zero-point energy. *Phys. Rev. Lett.* **75,** 4011–4014 (1995).

©2013 Macmillan Publishers Limited. All rights reserved

32. Jost, J. D. *et al.* Entangled mechanical oscillators. *Nature* **459,** 683–685 (2009).
33. Ozeri, R. *et al.* Errors in trapped-ion quantum gates due to spontaneous photon scattering. *Phys. Rev. A* **75,** 042329 (2007).
34. Uys, H. *et al.* Decoherence due to elastic Rayleigh scattering. *Phys. Rev. Lett.* **105,** 200401 (2010).
35. Tan, S. M. A computation toolbox for quantum and atomic optics. *J. Opt. B* **1,** 424–432 (1999).

©2013 **Macmillan Publishers Limited. All rights reserved**

LETTER

doi:10.1038/nature12802

Autonomously stabilized entanglement between two superconducting quantum bits

S. Shankar[1], M. Hatridge[1], Z. Leghtas[1], K. M. Sliwa[1], A. Narla[1], U. Vool[1], S. M. Girvin[1], L. Frunzio[1], M. Mirrahimi[1,2] & M. H. Devoret[1]

Quantum error correction codes are designed to protect an arbitrary state of a multi-qubit register from decoherence-induced errors[1], but their implementation is an outstanding challenge in the development of large-scale quantum computers. The first step is to stabilize a non-equilibrium state of a simple quantum system, such as a quantum bit (qubit) or a cavity mode, in the presence of decoherence. This has recently been accomplished using measurement-based feedback schemes[2–5]. The next step is to prepare and stabilize a state of a composite system[6–8]. Here we demonstrate the stabilization of an entangled Bell state of a quantum register of two superconducting qubits for an arbitrary time. Our result is achieved using an autonomous feedback scheme that combines continuous drives along with a specifically engineered coupling between the two-qubit register and a dissipative reservoir. Similar autonomous feedback techniques have been used for qubit reset[9], single-qubit state stabilization[10], and the creation[11] and stabilization[6] of states of multipartite quantum systems. Unlike conventional, measurement-based schemes, the autonomous approach uses engineered dissipation to counteract decoherence[12–15], obviating the need for a complicated external feedback loop to correct errors. Instead, the feedback loop is built into the Hamiltonian such that the steady state of the system in the presence of drives and dissipation is a Bell state, an essential building block for quantum information processing. Such autonomous schemes, which are broadly applicable to a variety of physical systems, as demonstrated by the accompanying paper on trapped ion qubits[16], will be an essential tool for the implementation of quantum error correction.

Here we implement a proposal[17], tailored to the circuit quantum electrodynamics (cQED) architecture[18], for stabilizing entanglement between two superconducting transmon qubits[19]. Each transmon consists of a Josephson junction capacitively shunted to form an anharmonic oscillator whose lowest two levels are used as the qubit. The qubits are dispersively coupled to an open cavity that acts as the dissipative reservoir. The cavity in our implementation is furthermore engineered to decay preferentially into a 50-Ω transmission line that we monitor on demand. We show, using two-qubit quantum state tomography and high-fidelity single-shot readout, that the steady state of the system reaches the target Bell state with a fidelity of 67%, which is well above the 50% threshold that signifies entanglement. The fidelity can be further improved by monitoring the cavity output and performing conditional tomography when the output indicates that the two qubits are in the Bell state[17]. We implemented this protocol by means of post-selection and demonstrated that the fidelity increased to ~77%.

Our cQED set-up (Fig. 1a) consists of two individually addressable qubits, Alice and Bob, coupled dispersively to a three-dimensional (3D) rectangular copper cavity. The set-up is described by the dispersive Hamiltonian[20]

$$\frac{H}{\hbar}=\omega_{\mathrm{A}}^{0}a^{\dagger}a+\omega_{\mathrm{B}}^{0}b^{\dagger}b+\omega_{\mathrm{c}}^{\mathrm{gg}}c^{\dagger}c-\frac{1}{2}\alpha_{\mathrm{A}}(a^{\dagger}a)^{2}-\frac{1}{2}\alpha_{\mathrm{B}}(b^{\dagger}b)^{2}-\chi_{\mathrm{A}}a^{\dagger}ac^{\dagger}c-\chi_{\mathrm{B}}b^{\dagger}bc^{\dagger}c \quad (1)$$

Here a, b and c are respectively the annihilation operators of the Alice and Bob qubits and the cavity mode; $a^{\dagger}$, $b^{\dagger}$ and $c^{\dagger}$ are the corresponding creation operators; ω_{A}^{0} and ω_{B}^{0} are the Alice and Bob qubit angular frequencies when there are no photons in the cavity; $\omega_{\mathrm{c}}^{\mathrm{gg}}$ is the cavity frequency when both qubits are in the ground state (see Methods for experiment parameters); α_{A} and α_{B} are respectively the Alice and Bob

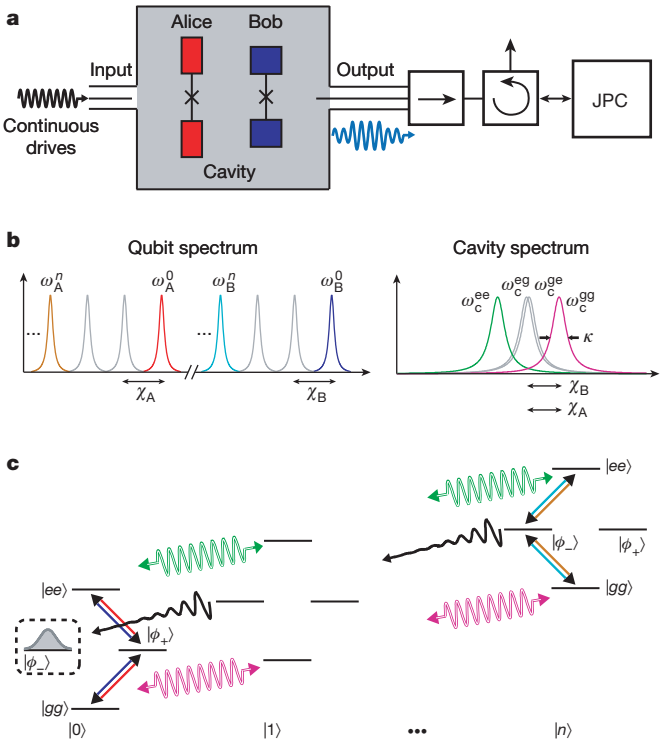


Figure 1 | Bell state stabilization set-up schematic and frequency landscape of autonomous feedback loop. **a**, The qubits (Alice and Bob) are coupled to the fundamental mode of a 3D cavity. Six continuous drives applied to the cavity input stabilize the Bell state $|\phi_{-},0\rangle$. The cavity output jumps between low and high amplitude depending on whether the qubits are in the desired Bell state or not. The output is monitored by a quantum-limited amplifier (JPC). **b**, Spectra of the qubits and cavity coupled with nearly equal dispersive shifts (χ_{A} and χ_{B}); κ is the cavity linewidth. Colours denote transitions that are driven to establish the autonomous feedback loop. **c**, Effective states of the system involved in the feedback loop. Qubit states consist of the odd-parity states in the Bell basis $\{|\phi_{-}\rangle, |\phi_{+}\rangle\}$ and the even-parity computational states $\{|gg\rangle, |ee\rangle\}$. Cavity states, arrayed horizontally, are the photon-number basis kets $|n\rangle$. Sinusoidal double lines represent the two cavity tones whose amplitudes create on average $\bar{n}$ photons in the cavity when the qubits are in even-parity states. The cavity level populations are Poisson distributed with mean $\bar{n}$ and we show only $|n\rangle$ such that $n \approx \bar{n}$. Straight double lines represent four tones on qubit transitions. Collectively, the six tones and the cavity decay (decaying sinusoidal lines) drive the system towards the 'dark' state, $|\phi_{-},0\rangle$, which builds up a steady-state population.

[1]Department of Applied Physics and Physics, Yale University, New Haven, Connecticut 06520, USA. [2]INRIA Paris-Rocquencourt, Domaine de Voluceau, BP 105, 78153 Le Chesnay Cedex, France.

©2013 Macmillan Publishers Limited. All rights reserved

qubit anharmonicities; and χ_A and χ_B are the respective dispersive couplings, which are designed to be nearly equal. The cavity linewidth, κ, and the qubit decoherence rates, $\Gamma_1^{A,B}$ and $\Gamma_\phi^{A,B}$, are smaller than χ_A and χ_B, such that the system operates in the strong-dispersive limit of cQED[21], where ω_A^n and ω_B^n, the qubit transition frequencies for different cavity photon occupancies, n, are clearly resolved. As described in Fig. 1b, by applying six continuous drives, four at qubit transitions and two at cavity transitions, an effective feedback loop is established that forces the two qubits into the Bell state $|\phi_-\rangle \equiv (|ge\rangle - |eg\rangle)/\sqrt{2}$ with zero photons in the cavity.

The feedback loop shown in Fig. 1c can be broken down into two parts that operate continuously and concurrently: the first is equivalent to a measurement process, and the second is equivalent to qubit rotations conditioned on the measurement outcome. The measurement process, implemented by two drives at the cavity frequencies, ω_c^{gg} and ω_c^{ee}, together with the approximately equal dispersive shifts, distinguishes the even-parity manifold, where the qubits are parallel, from the odd-parity manifold, where they are antiparallel. The odd-parity manifold is conveniently described in the Bell basis $\{|\phi_-\rangle, |\phi_+\rangle\}$, which contains our target state, $|\phi_-\rangle$. The drives, together with cavity dissipation, can be regarded as implementing a continuous projective measurement of the state of the two qubits that leaves the odd-parity manifold unaffected[22,23]. The drives are resonant when the qubits are in $|gg\rangle$ or $|ee\rangle$, such that an average of $\bar{n}$ photons at ω_c^{gg} or ω_c^{ee} continuously traverse the cavity every lifetime, $1/\kappa$. However, when the qubits have odd parity, both drives are far off-resonance because $\chi_A, \chi_B \gg \kappa$, thus leaving the cavity almost empty of photons. As a result, the average number of photons in the cavity, the pointer variable 'observed' by the environment[1], projects the even-parity manifold into $|gg\rangle$ and $|ee\rangle$, and distinguishes them from the odd-parity manifold, which is left unperturbed.

The second part of the feedback loop uses the photon-number splitting (quantized light shifts) of the qubit transitions in the strong-dispersive limit to implement conditional qubit rotations. Two drives are applied selectively at the zero-photon qubit frequencies, ω_A^0 and ω_B^0, with amplitudes set to give equal Rabi frequencies of $\Omega^0 \approx \kappa \ll \chi_A, \chi_B$. The phases of these drives set, by definition, the x axis of each qubit's Bloch sphere. The action of these drives is described by the effective unitary rotation operator $(a + a^\dagger) \otimes I^B + I^A \otimes (b + b^\dagger)$ on the two qubit subspace, where I^A and I^B are the respective identity matrices. Therefore, they rotate the undesired Bell state, $|\phi_+, 0\rangle$, into the even-parity manifold, leaving the desired one, $|\phi_-, 0\rangle$, untouched. Thus, any population in $|\phi_+, 0\rangle$ is eventually pumped out by the combined action of the zero-photon qubit drives and the cavity drives.

To re-pump population into the target Bell state, $|\phi_-, 0\rangle$, two more drives with equal Rabi frequencies, Ω^n, are applied at $\omega_A^0 - n(\chi_A + \chi_B)/2$ and $\omega_B^0 - n(\chi_A + \chi_B)/2$, which are near the n-photon qubit frequencies, ω_A^n and ω_B^n, shown in Fig. 1b. The phase of the drive on Alice is set to be along the x axis of its Bloch sphere, whereas that on Bob is set to be antiparallel to its x axis, resulting in the effective unitary rotation operator $(a + a^\dagger) \otimes I^B - I^A \otimes (b + b^\dagger)$ (see Methods for details on the phase control of qubit drives). Thus, as long as $n \approx \bar{n}$, these two drives shuffle population from $|gg, n\rangle$ and $|ee, n\rangle$ into the state $|\phi_-, n\rangle$. The latter state is unaffected by the cavity drives and therefore decays irreversibly, at a rate κ, to the desired target Bell state, $|\phi_-, 0\rangle$.

Thus, when all six drives are turned on, the continuously operating feedback loop forces the two qubits into $|\phi_-\rangle$ even in the presence of error-inducing relaxation ($\Gamma_1^{A,B}$) and dephasing ($\Gamma_\phi^{A,B}$) processes. As shown in Extended Data Fig. 4, simulations indicate that the drive amplitudes should be optimally set to give Rabi frequencies $\Omega^0 \approx \Omega^n \approx \kappa/2$ and $\bar{n} \approx 3-4$. For these parameters, the two qubits are expected to stabilize into the target state at a rate of order $\kappa/10$, which can be understood from the successive combination of transition rates, each of which is of order κ. With the experimental parameters in our implementation, the feedback loop is expected to correct errors and stabilize the two qubits into $|\phi_-\rangle$ with a time constant of about 1 μs.

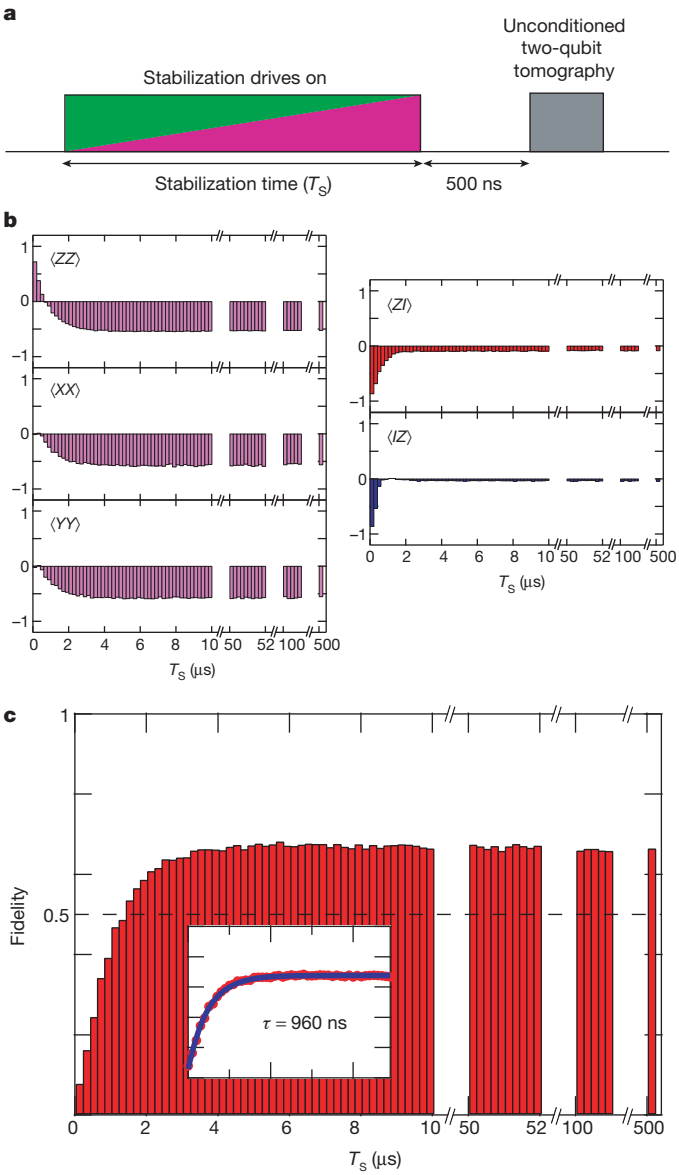


Figure 2 | Convergence of two qubit-state to the target Bell state. **a**, The six drives are turned on during the stabilization period for time T_S. Next, the drives are turned off and the system is left idle for 500 ns, allowing any remaining cavity photons to decay away. Finally, two-qubit tomography is performed using single-qubit rotations followed by single-shot joint readout. The system is then allowed to reach thermal equilibrium by waiting at least $5T_1$ before repetition. **b**, Time variation of the relevant Pauli operator averages, showing the system's evolution from thermal equilibrium (nearly $|gg\rangle$) towards $|\phi_-\rangle$. The system remains in this steady state for an arbitrarily long time, as demonstrated by data acquired at T_S = 50, 100 and 500 μs. **c**, Fidelity to the target state $|\phi_-\rangle$ as a function of stabilization time, T_S. The dashed line at 50% is the entanglement threshold. The fidelity converges to 67% with a time constant, τ, of about ten cavity lifetimes, in good agreement with the theoretical prediction; inset, F for T_S = 0–10 μs (red circles), with exponential fit (blue line).

The fidelity of the stabilized state to $|\phi_-\rangle$ is determined by the competition between the correction rate, $\kappa/10$, and the rates, $\Gamma_1^{A,B} = 1/T_1^{A,B}$ and $\Gamma_\phi^{A,B} = 1/T_\phi^{A,B}$, at which the Alice–Bob system decoheres out of the target state. Thus, to achieve a high-fidelity entangled state, the system–reservoir parameters χ_A, χ_B and κ have to be engineered such that $\chi_A = \chi_B > \kappa$, while maintaining $\kappa \gg \Gamma = \max\left(\Gamma_1^{A,B}, \Gamma_\phi^{A,B}\right)$. In the present experiment, we built on recent advances in the coherence of superconducting qubits achieved by using 3D cavities[24] to obtain $\chi/\kappa \approx 4$ and $\kappa/\Gamma \approx 100$ simultaneously, satisfying both requirements.

©2013 Macmillan Publishers Limited. All rights reserved

The protocol of the experiment consists of applying the six continuous drives for a length of time T_S (Fig. 2a) and verifying the presence of entanglement by performing two-qubit state tomography. State tomography is realized by applying one of a set of 16 single-qubit rotations and then performing joint qubit readout[25], implemented here using single-shot measurements. As described in Fig. 1a, Extended Data Fig. 1 and Methods, the dispersive joint two-qubit readout is implemented by pulsing the cavity at ω_c^{gg} and recording the cavity output for 240 ns using a nearly quantum-limited microwave amplification chain. The first amplifier in the chain is a Josephson parametric converter (JPC) operated as a phase-preserving amplifier[26], which performs single-shot projective readout of the state of the two qubits with a fidelity of more than 96% in our experiment (Extended Data Fig. 2 and Methods). The averages of the 16 two-qubit Pauli operators $\langle AB\rangle$, where A and B are each one of the four single-qubit operators $\{I, X, Y, Z\}$ for Alice and Bob, respectively, are calculated by repeating the tomography 5×10^5 times per operator, resulting in a statistical imprecision of about 0.2%.

Tomography results as a function of the duration of the stabilization interval, T_S, are illustrated in Fig. 2b, showing the expected convergence of the system to the Bell state $|\phi_-\rangle$. For $T_S = 0$, the Pauli operator averages are $\langle ZI\rangle = \langle IZ\rangle = 0.86$ and $\langle ZZ\rangle = 0.72$, indicating that the system is mostly in $|gg\rangle$ when no drives are present. With increasing T_S, the single-qubit averages tend to zero, whereas the two-qubit averages $\langle ZZ\rangle$, $\langle XX\rangle$ and $\langle YY\rangle$ stabilize at negative values, whose sign is characteristic of $|\phi_-\rangle$. The autonomous feedback loop operation was verified with snapshots taken for values of T_S up to 500 μs, indicating that the steady state of the two qubits remains stable for times well in excess of the timescales of decoherence processes.

The fidelity, F, of the measured state to the target, $|\phi_-\rangle$, is $F = \mathrm{Tr}(\rho_{target}\rho_{meas})$, where $\rho_{target} = |\phi_-\rangle\langle\phi_-|$ and ρ_{meas} is obtained from the measured set of two-qubit Pauli operators. As shown in Fig. 2c, F stabilizes at 67%, which is well above the threshold of 50% that indicates the presence of entanglement. Entanglement is also evidenced by the non-zero concurrence[27], $C = 0.36$. The exponential rise of F with a time constant of 960 ns (Fig. 2c, inset), or approximately ten cavity lifetimes, is in good agreement with the expected 1-μs correction time constant of the autonomous feedback loop.

As expected, the steady state reached by the autonomous feedback loop is impure. By analysing the density matrix constructed from tomography, we calculate that it contains 67% weight in $|\phi_-\rangle\langle\phi_-|$ and that the weights in the undesired states $|gg\rangle\langle gg|$, $|ee\rangle\langle ee|$ and $|\phi_+\rangle\langle\phi_+|$ are 15%, 10% and 8%, respectively. However, the reservoir (cavity output) contains information on the qubits' parity that can be exploited. Thus, the state fidelity can be conditionally enhanced by passively monitoring this output and performing tomography only when the loop indicates that the qubits are in an odd-parity state (eliminating weights in the even-parity states $|gg\rangle\langle gg|$ and $|ee\rangle\langle ee|$). A version of this protocol (Fig. 3) is implemented in essence by passively recording the cavity output at ω_c^{gg} for the last 240 ns of the stabilization period (measurement M_1 in Fig. 3a). A reference histogram for M_1 (Fig. 3b) shows Gaussian distributions separated by two standard deviations, allowing us to remove any $|gg\rangle\langle gg|$ component present in the ensemble at the end of the stabilization period, by applying an exclusionary threshold, I_m^{th}/σ. We again perform single-shot tomography (measurement M_2 in Fig. 3a) after 100 ns and post-select M_2 for trials where M_1 indicates that the qubits are not in the state $|gg\rangle\langle gg|$ ($M_1 = \overline{GG}$), in the process keeping ~1% of counts. This conditioned tomography improves F to 77% ($C = 0.54$), in good agreement with a simple estimate of $67/(67 + 10 + 8) = 79\%$ when the weight of $|gg\rangle\langle gg|$ is removed. Additionally monitoring the cavity output at ω_c^{ee} could straightforwardly improve the conditioned fidelity to 90%, and would be achievable through modest improvements of the Josephson amplifier bandwidth. Thus, in addition to fully autonomous Bell state stabilization, we have demonstrated that, in principle, real-time electronics monitoring can significantly increase the Bell state purity.

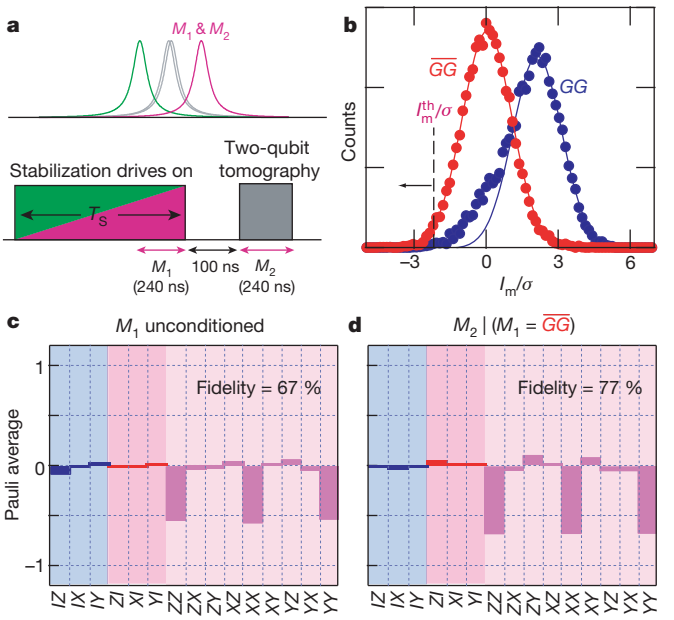


Figure 3 | Fidelity improved by monitoring the feedback loop. **a**, Pulse sequence consisting of a $T_S = 10$-μs period followed by two-qubit tomography. Here, the cavity output at ω_c^{gg} is recorded during the last 240 ns of the stabilization period (M_1). The outcomes obtained during M_1 are used to condition the tomography in post-processing. After waiting 100 ns for any cavity photons to decay away, two-qubit state tomography is performed using a second 240-ns-long measurement (M_2) similar to that used in the unconditioned tomography (Fig. 2). **b**, Reference histogram for M_1, with qubits prepared in thermal equilibrium (denoted GG) and after a π-pulse on Alice (denoted $\overline{GG}$). The standard deviation, σ, of the Gaussian distributions scales the horizontal axis of measurement outcomes, I_m. **c**, Complete set of Pauli operator averages measured by tomography without conditioning, as in Fig. 2, showing a fidelity of 67% to $|\phi_-\rangle$. **d**, Tomography conditioned on M_1 being $\overline{GG}$, that is, outcomes I_m/σ during $M_1 < I_m^{th}/\sigma = -2.2$, resulting in an increased fidelity of 77%.

We now address the basic imperfections of our experiment that limit the current value of the steady-state, unconditioned fidelity to 0.67. First, the fidelity measured by tomography is ~0.05 less than the theoretical steady-state value during the stabilization period, owing to the 500-ns wait time before tomography, during which the state decays under the influence of T_1 and T_ϕ. This wait period, which was introduced to ensure that the single-qubit rotations during tomography are not perturbed by residual cavity photons, can be reduced with conditioned tomography (to 100 ns; see Fig. 3a) because there will be fewer cavity photons when the qubits are in the target state. As shown in Methods, owing to this wait period the fidelity measured by tomography is not expected to be affected by extraneous systematic errors in calibration of single-qubit rotations (Extended Data Fig. 3). Furthermore, we also show that the fidelity is unaffected by the measurement infidelity of the readout. Instead, the sources of error are intrinsically determined by the environmental couplings inherent in the system and its coupling to the reservoir.

Although it might be supposed that mismatch between χ_A and χ_B would be a dominant cause for infidelity through measurement-induced dephasing[23], simulations (Methods) indicate that the present 10% mismatch contributes only 0.02 to the infidelity. This robust property of the feedback loop is achieved by setting the cavity drives on ω_c^{gg} and ω_c^{ee} transitions, which mitigate the measurement-induced dephasing, by comparison with the more straightforward irradiation between ω_c^{ge} and ω_c^{eg} proposed in usual parity measurement[8,22,23]. The dominant mechanism for infidelity turns out to be the T_1 and T_ϕ processes, which contribute 0.12 and 0.08, respectively. The severity of these processes may actually be enhanced in the presence of cavity drives, which tend to shorten T_1 in transmon qubits[28]. The remaining infidelity

©2013 Macmillan Publishers Limited. All rights reserved

can possibly be attributed to this shortening of T_1, in combination with the presence of $|f\rangle$ (second excited state) population in each qubit due to finite qubit temperature. Overall, the dominant sources of infidelity (T_1 and T_ϕ) are likely to be mitigated in future experiments by expected improvements in qubit coherence (Methods), which will allow a larger ratio κ/Γ and, thus, fidelities in excess of 90%.

We have demonstrated the stabilization of two-qubit entanglement that makes a Bell state available for indefinite time, using a completely autonomous protocol. Although the fidelity to the Bell state does not presently exceed that needed for violation of Bell's inequality, straightforward improvements to the set-up should allow it[17]. In addition to sufficiently coherent qubits, the resources required, consisting of matching dispersive couplings and six pure tones sent through the same input line, are modest in comparison with the hardware that would be needed in a conventional measurement-based scheme to stabilize $|\phi_-\rangle$. Although the pure tones can be generated using microwave modulation techniques from three sources only, the tolerance to imperfections in the matching of the couplings amounts to about 10%, which can be easily achieved in superconducting qubit design. A primary virtue of our protocol is that it can be extended to larger systems because it assumes only that the system Hamiltonian can be precisely engineered (a general requirement for all quantum information implementations) and that abundant, off-the-shelf room-temperature microwave generators are available. Moreover, the protocol can take advantage of any available high-fidelity readout capability by passively monitoring the cavity outputs, enabling purification by real-time conditioning as demonstrated by our 30% reduction in state infidelity using a Josephson amplifier.

Therefore, autonomous feedback is uniquely suited to exploiting all available state-of-the-art hardware and is an ideal platform on which to construct more complicated protocols. Possible avenues for future experiments include implementing a 'compound' Bell state stabilization protocol, using a four-qubit quantum register operating two independent autonomous stabilization loops complemented by an entanglement distillation step[29]. The quantum engineering concept implemented in our experiment could also be applied to autonomously stabilize a coherent two-state manifold of Schrödinger cat states of a superconducting cavity[30], thus possibly achieving a continuous version of qubit quantum error correction.

METHODS SUMMARY

Alice and Bob are single-junction 3D transmons with qubit frequencies $\omega_A^0/2\pi = 5.238$ GHz and $\omega_B^0/2\pi = 6.304$ GHz, anharmonicities $\alpha_A/2\pi = 220$ MHz and $\alpha_B/2\pi = 200$ MHz, relaxation times $T_1^A = 16$ μs and $T_1^B = 9$ μs, and pure dephasing times $T_\phi^A = 11$ μs and $T_\phi^B = 36$ μs, respectively. They are coupled to a rectangular cavity ($\omega_c^{gg}/2\pi = 7.453$ GHz) with nearly equal dispersive couplings, $\chi_A/2\pi = 6.5$ MHz and $\chi_B/2\pi = 5.9$ MHz, that are larger than the cavity linewidth, $\kappa/2\pi = 1.7$ MHz. The set-up is mounted on the base of a dilution refrigerator (Extended Data Fig. 1) and controlled using heavily attenuated and filtered microwave lines. The room-temperature microwave set-up generates all microwave drives in a manner that is insensitive to drifts in generator phases. Single-shot joint readout with fidelity of 96% was performed using a JPC (Extended Data Fig. 2). We checked, by performing tomography of Clifford states, that the measured fidelity of the Bell state was not significantly altered by systematic errors in single-qubit rotations and measurements (Extended Data Fig. 3). The choice of drive amplitudes used for Bell state stabilization was guided by Lindblad master equation simulations (Extended Data Fig. 4). These simulations also provided an error budget analysis for the steady-state infidelity suggesting that the dominant source of infidelity is the finite times T_1 and T_ϕ.

Online Content Any additional Methods, Extended Data display items and Source Data are available in the online version of the paper; references unique to these sections appear only in the online paper.

Received 18 July; accepted 22 October 2013.
Published online 24 November 2013.

1. Nielsen, M. A. & Chuang, I. L. *Quantum Computation and Quantum Information* (Cambridge Univ. Press, 2004).
2. Sayrin, C. *et al.* Real-time quantum feedback prepares and stabilizes photon number states. *Nature* **477,** 73–77 (2011).
3. Vijay, R. *et al.* Stabilizing Rabi oscillations in a superconducting qubit using quantum feedback. *Nature* **490,** 77–80 (2012).
4. Ristè, D., Bultink, C. C., Lehnert, K. W. & DiCarlo, L. Feedback control of a solid-state qubit using high-fidelity projective measurement. *Phys. Rev. Lett.* **109,** 240502 (2012).
5. Campagne-Ibarcq, P. *et al.* Persistent control of a superconducting qubit by stroboscopic measurement feedback. *Phys. Rev. X* **3,** 021008 (2013).
6. Krauter, H. *et al.* Entanglement generated by dissipation and steady state entanglement of two macroscopic objects. *Phys. Rev. Lett.* **107,** 080503 (2011).
7. Brakhane, S. *et al.* Bayesian feedback control of a two-atom spin-state in an atom-cavity system. *Phys. Rev. Lett.* **109,** 173601 (2012).
8. Ristè, D. *et al.* Deterministic entanglement of superconducting qubits by parity measurement and feedback. *Nature* **502,** 350–354 (2013).
9. Geerlings, K. *et al.* Demonstrating a driven reset protocol for a superconducting qubit. *Phys. Rev. Lett.* **110,** 120501 (2013).
10. Murch, K. W. *et al.* Cavity-assisted quantum bath engineering. *Phys. Rev. Lett.* **109,** 183602 (2012).
11. Barreiro, J. T. *et al.* An open-system quantum simulator with trapped ions. *Nature* **470,** 486–491 (2011).
12. Poyatos, J. F., Cirac, J. I. & Zoller, P. Quantum reservoir engineering with laser cooled trapped ions. *Phys. Rev. Lett.* **77,** 4728–4731 (1996).
13. Kerckhoff, J., Nurdin, H. I., Pavlichin, D. S. & Mabuchi, H. Designing quantum memories with embedded control: photonic circuits for autonomous quantum error correction. *Phys. Rev. Lett.* **105,** 040502 (2010).
14. Kastoryano, M. J., Reiter, F. & Sørensen, A. S. Dissipative preparation of entanglement in optical cavities. *Phys. Rev. Lett.* **106,** 090502 (2011).
15. Sarlette, A., Raimond, J. M., Brune, M. & Rouchon, P. Stabilization of nonclassical states of the radiation field in a cavity by reservoir engineering. *Phys. Rev. Lett.* **107,** 010402 (2011).
16. Lin, Y. *et al.* Dissipative production of a maximally entangled steady state of two quantum bits. *Nature* http://dx.doi.org/10.1038/nature12801 (this issue).
17. Leghtas, Z. *et al.* Stabilizing a bell state of two superconducting qubits by dissipation engineering. *Phys. Rev. A* **88,** 023849 (2013).
18. Wallraff, A. *et al.* Strong coupling of a single photon to a superconducting qubit using circuit quantum electrodynamics. *Nature* **431,** 162–167 (2004).
19. Schreier, J. A. *et al.* Suppressing charge noise decoherence in superconducting charge qubits. *Phys. Rev. B* **77,** 180502 (2008).
20. Nigg, S. E. *et al.* Black-box superconducting circuit quantization. *Phys. Rev. Lett.* **108,** 240502 (2012).
21. Schuster, D. I. *et al.* Resolving photon number states in a superconducting circuit. *Nature* **445,** 515–518 (2007).
22. Lalumière, K., Gambetta, J. M. & Blais, A. Tunable joint measurements in the dispersive regime of cavity QED. *Phys. Rev. A* **81,** 040301 (2010).
23. Tornberg, L. & Johansson, G. High-fidelity feedback-assisted parity measurement in circuit QED. *Phys. Rev. A* **82,** 012329 (2010).
24. Paik, H. *et al.* Observation of high coherence in Josephson junction qubits measured in a three-dimensional circuit QED architecture. *Phys. Rev. Lett.* **107,** 240501 (2011).
25. Filipp, S. *et al.* Two-qubit state tomography using a joint dispersive readout. *Phys. Rev. Lett.* **102,** 200402 (2009).
26. Bergeal, N. *et al.* Phase-preserving amplification near the quantum limit with a Josephson ring modulator. *Nature* **465,** 64–68 (2010).
27. Wootters, W. K. Entanglement of formation of an arbitrary state of two qubits. *Phys. Rev. Lett.* **80,** 2245–2248 (1998).
28. Slichter, D. H. *et al.* Measurement-induced qubit state mixing in circuit QED from up-converted dephasing noise. *Phys. Rev. Lett.* **109,** 153601 (2012).
29. Reichle, R. *et al.* Experimental purification of two-atom entanglement. *Nature* **443,** 838–841 (2006).
30. Leghtas, Z. *et al.* Hardware-efficient autonomous quantum memory protection. *Phys. Rev. Lett.* **111,** 120501 (2013).

Acknowledgements Facility use was supported by the Yale Institute for Nanoscience and Quantum Engineering and the National Science Foundation (NSF) MRSEC DMR 1119826. This research was supported by the Office of the Director of National Intelligence (ODNI), Intelligence Advanced Research Projects Activity (IARPA) W911NF-09-1-0369, by the US Army Research Office W911NF-09-1-0514, and by the NSF DMR 1006060 and DMR 0653377. M.M. acknowledges partial support from the Agence National de la Recherche under the project EPOQ2 ANR-09-JCJC-0070. S.M.G. and Z.L. acknowledge support from the NSF DMR 1004406. All statements of fact, opinion or conclusions contained herein are those of the authors and should not be construed as representing the official views or policies of IARPA, the ODNI or the US government.

Author Contributions S.S. performed the experiment and analysed the data with assistance from M.H. and Z.L. Z.L. proposed the autonomous feedback protocol and performed numerical simulations under the guidance of M.M. K.M.S., A.N. and L.F. contributed to the experimental apparatus, and U.V. contributed to the theoretical modelling under the guidance of S.M.G. M.H.D. supervised the project. S.S., M.H. and M.H.D. wrote the manuscript. All authors provided suggestions for the experiment, discussed the results and contributed to the manuscript.

Author Information Reprints and permissions information is available at www.nature.com/reprints. The authors declare no competing financial interests. Readers are welcome to comment on the online version of the paper. Correspondence and requests for materials should be addressed to S.S. (shyam.shankar@yale.edu) or M.H.D. (michel.devoret@yale.edu).

©2013 Macmillan Publishers Limited. All rights reserved

METHODS

Qubit–cavity implementation. The two transmon qubits were fabricated with double-angle-evaporated Al/AlO_x/Al Josephson junctions, defined using the bridge-free electron-beam lithography technique[31,32], on double-side-polished 3 mm-by-10 mm chips of *c*-plane sapphire. They were coupled to the TE_{101} mode of a rectangular copper cavity. The room-temperature junction resistances (Alice, 7.5 kΩ; Bob, 5.6 kΩ), antenna pad dimensions (Alice, 1.4 mm by 0.2 mm; Bob, 0.68 mm by 0.36 mm) and cavity dimensions (35.6 mm by 21.3 mm by 7.6 mm) were designed using finite-element simulations and black-box circuit quantization analysis[20] to give Alice and Bob qubit frequencies of $\omega_A^0/2\pi = 5.238$ GHz and $\omega_B^0/2\pi = 6.304$ GHz, qubit anharmonicities of $\alpha_A/2\pi = 220$ MHz and $\alpha_B/2\pi = 200$ MHz, a cavity frequency of $\omega_c^{gg}/2\pi = 7.453$ GHz, and nearly equal dispersive couplings of $\chi_A/2\pi = 6.5$ MHz and $\chi_B/2\pi = 5.9$ MHz. The cavity was coupled to input and output transmission lines with quality factors $Q_{IN} \approx 100{,}000$ and $Q_{OUT} = 4{,}500$, such that its linewidth, $\kappa/2\pi = 1.7$ MHz, was set predominantly by Q_{OUT}.

As shown in the experiment schematic (Extended Data Fig. 1), the cavity and the JPC set-up was mounted on the base stage of a cryogen-free dilution refrigerator (Oxford Triton200). As is common practice for superconducting qubit experiments, the cavity and JPC were shielded from stray magnetic fields by aluminium and cryogenic μ-metal (Amumetal A4K) shields. The input microwave lines going to the set-up were attenuated at various fridge stages and filtered using commercial 12-GHz reflective, low-pass filters and home-made, lossy Eccosorb filters. The attenuators and filters serve to protect the qubit and cavity from room-temperature thermal noise and block microwave or optical frequency signals from reaching the qubit. The output line of the fridge consisted of reflective and Eccosorb filters as well as two cryogenic isolators (Quinstar CWJ1019K) at the base to attenuate noise coming down from higher-temperature stages. In addition, a cryogenic HEMT amplifier (Low Noise Factory LNF-LNC7_10A) at the 3 K stage provided 40 dB of gain to overcome the noise added by the following room-temperature amplification stages.

Relaxation times were measured to be $T_1^A = 16$ μs and $T_1^B = 9$ μs, and coherence times measured with a Ramsey protocol were $T_2^A = 8$ μs and $T_2^B = 12$ μs, resulting in dephasing times of $T_\phi^A = 11$ μs and $T_\phi^B = 36$ μs. Black-box quantization analysis of the qubit–cavity system suggest that the relaxation times were limited by the Purcell effect[33]. Coherence times did not improve using an echo pulse, suggesting that they were limited by thermal photons present in the fundamental and higher modes of the cavity[34] as well as by non-zero qubit temperature (~75 mK).

Control of stabilization drives. The room-temperature set-up must generate and control microwave tones in a manner such that the experiment is insensitive to drifts in the phase between microwave sources over the timescale of the experiment. Although all sources are locked to a common rubidium frequency standard (SRS FS725), they drift apart in phase on a timescale of a few minutes. Therefore, for example, the four Rabi drives on the qubits during Bell state stabilization cannot be produced by four separate sources because the phase of the drives need to be controlled precisely. The phase drift was eliminated by using one microwave source per qubit and generating the desired frequencies using single-sideband modulation (Extended Data Fig. 1). The qubit drives were produced by sources f_{Alice} and f_{Bob} (Vaunix Labbrick LMS-802), set 100 MHz below the respective zero-photon qubit frequencies. For Bell state stabilization, these tones were mixed using IQ mixers (Marki IQ4509) with 100-MHz and 82-MHz sine waves produced by a Tektronix AWG5014C arbitrary waveform generator (AWG). The mixer outputs at the desired frequencies can be expressed mathematically as $A_A^0 \cos\left(\omega_A^0 t + \phi_A^{arb} + \phi_A^0\right)$, $A_B^0 \cos\left(\omega_B^0 t + \phi_B^{arb} + \phi_B^0\right)$, $A_A^n \cos\left(\omega_A^n t + \phi_A^{arb} + \phi_A^n\right)$ and $A_B^n \cos\left(\omega_B^n t + \phi_B^{arb} + \phi_B^n\right)$. Here ϕ_A^{arb} and ϕ_B^{arb} are respectively the arbitrary phases of the microwave sources f_{Alice} and f_{Bob}, which can drift during an experiment, and ϕ_A^0, ϕ_B^0, ϕ_A^n and ϕ_B^n are set by the AWG as well as the length of the cables going to the qubit–cavity system, and are therefore fixed over the course of the experiment. The relationship between the drive phases required for the stabilization protocol is $\phi_A^0 - \phi_A^n = \phi_B^0 - \phi_B^n + \pi$. This is achieved in experiment by fixing ϕ_A^0, ϕ_A^n and ϕ_B^0 and sweeping ϕ_B^n.

The cavity drives for stabilization were generated by two sources (Agilent E8267 and N5183), f_c^{GG} set to ω_c^{gg} and f_c^{EE} set to $\omega_c^{ee} = \left(\omega_c^{gg} - \chi_A - \chi_B\right)$. These drives could potentially also be produced using a single microwave source and single-sideband modulation, but this was not done because control over the phase of these drives was not important for the stabilization protocol.

Joint readout implementation with JPC. The joint readout of the qubits used for tomography was implemented with high-fidelity single-shot measurements[35] by pulsing the cavity input for 500 ns using the source f_c^{GG} (msmt) (Agilent N5183) set at ω_c^{gg} (Extended Data Fig. 1). The transmitted microwave pulse was directed via two circulators (Quinstar CTH1409) to the JPC amplifier, reflected with gain and then amplified at 3 K. This was followed by further signal processing at room temperature. The JPC was biased at ω_c^{gg} to provide a reflected power gain of 20 dB in a bandwidth of 6 MHz. A noise rise of 6 dB was recorded when the amplifier was switched on, implying that 80% of the noise measured at room temperature was amplified quantum fluctuations originating from the base stage of the fridge.

The circulators also provide reverse isolation, which prevents amplified quantum fluctuations output by the JPC from impinging on the cavity and causing dephasing. In our experiment, the T_2 of the qubits was found to decrease to 3 μs when the amplifier was turned on, suggesting that either this reverse isolation was insufficient or that the pump tone was accidentally aligned with a higher mode of the cavity. Therefore, the amplifier was turned on 100 ns before the cavity pulse was applied and turned off 1 μs after the cavity had finished ringing down. This pulsing of the JPC ensured that the excess dephasing was absent during the stabilization period of the experiment described in the main text. Rather, it was present only during the tomography phase, when it was less important.

The output of the fridge at ω_c^{gg} had to be shifted to radio frequencies (<500 MHz) before it could be digitized using commercial hardware. This processing was performed in a manner that was insensitive to drifts in digitizer offsets and generator phases over the timescale of the experiment. As shown in Extended Data Fig. 1, the fridge output was demodulated using an image-reject mixer (Marki IRW0618) with a local oscillator (Agilent N5183), set 50 MHz above f_c^{GG} (msmt), to produce a signal centred in frequency domain at 50 MHz. A copy of the cavity input that did not pass through the dilution refrigerator was also demodulated to give a reference copy for comparison. The signal and reference were digitized (in an Alazar ATS9870 analogue-to-digital converter) and finally digitally demodulated in the PC to give in-phase and quadrature signals ($I(t)$, $Q(t)$). This room-temperature analogue and digital signal processing ensured that the measured ($I(t)$, $Q(t)$) were insensitive to drifts in digitizer offsets and generator phases.

A 240-ns section of the cavity response after ring-up was averaged to give a measurement outcome (I_m, Q_m). Reference histograms along the I_m axis are shown in Extended Data Fig. 2a. These reference histograms were produced using qubits initialized in $|gg\rangle$, by a heralding measurement[36], with a fidelity of 99.5%. The histogram labelled *GG* was recorded using this initialized state, whereas that labelled $\overline{GG}$ was recorded after a π-pulse on Alice. Similar $\overline{GG}$ histograms could be produced after a π-pulse on Bob or on both qubits. The two histograms are fitted with Gaussian distributions; of the two, the *GG* histogram has a standard deviation that is smaller by a factor of ~0.75, owing to amplifier saturation, resulting in a larger amplitude. However, the areas under each histogram are identical, as expected. The different standard deviations imply that the threshold (I_m^{th}/σ) distinguishing outcomes associated with *GG* from those associated with $\overline{GG}$ cannot be set symmetrically between the two distributions. Rather, $I_m^{th}/\sigma = 5$, shifted towards *GG*, ensuring that the error induced by the overlap of the distributions are equal. Because the Gaussians are separated by 5.5 standard deviations, the indicated threshold would imply a readout fidelity of 99.5% calculated from the overlap of the distributions.

These well-separated Gaussian distributions indicate that the readout implements a close-to-ideal measurement of the observable $|gg\rangle\langle gg|$. However, excess counts are observed in $\overline{GG}$ when the qubits are prepared in $|gg\rangle$, and vice versa, owing to T_1 events as well as transitions induced by the measurement tone. These errors reduce the fidelity from that calculated simply from the overlap of the two distributions. Thus, the total measurement fidelity of the observable $|gg\rangle\langle gg|$, summarized by the diagram in Extended Data Fig. 2b, is found to be 96% for the state $|gg\rangle$ and 97% for states $|ge\rangle$, $|eg\rangle$ and $|ee\rangle$.

Calibration of systematic errors in tomography. Standard two-qubit tomography is performed by applying one of a set of four single-qubit rotations (Id, $R_x(\pi)$, $R_x(\pi/2)$, $R_y(\pi/2)$) on each qubit, followed by the readout of the observable $|gg\rangle\langle gg|$ (refs 25, 37). To implement these rotations, the AWG shapes a 100-MHz sine wave with a 6σ-long Gaussian envelope with $\sigma = 12$ ns and DRAG correction[38,39]. The outputs of the IQ mixers (Extended Data Fig. 1) are thus Gaussian pulses resonant on the zero-photon qubit transition frequencies. The resulting 16 measured observables are expressed in the Pauli basis, and the Pauli operator averages are calculated by matrix inversion. The density matrix constructed from the Pauli operator averages is then used to calculate the fidelity of the measured state to a desired target, as described in the main text.

The ability of the tomography to represent faithfully the state of the two qubits is limited by systematic errors in the readout, in single-qubit rotations and by qubit decoherence. Although these errors have been individually reduced below 1% in superconducting qubit experiments[40], they are in the few per cent range in our system owing to insufficient combined optimization. We have estimated a worst-case combined effect of these errors on the tomography by preparing the qubits in one of 36 possible two-qubit Clifford states and then performing tomography to extract the fidelity to the target state. The fidelity of the measured state to the target (Extended Data Fig. 3) varies from a maximum of 94% for the state $|-Z, -Z\rangle$, which is least susceptible to errors from relaxation and decoherence, to a minimum of 87% for the state $|+Y, +Z\rangle$, which is among the most susceptible. The

©2013 Macmillan Publishers Limited. All rights reserved

average fidelity of 90% across all 36 states is in good agreement with that expected from the aggregate of few-per-cent errors arising from readout, rotations and decoherence. This fidelity, which is substantially higher than the maximum fidelity to the Bell state we estimate in the main text, leads us to believe that systematic errors in the tomography do not significantly alter the maximum measured fidelity to $|\phi_-\rangle$, of 77%.

Simulation of the stabilization protocol. The stabilization protocol consists of six drives whose amplitudes need to be optimized for maximum fidelity. We now describe simulations which suggest that this is not such a daunting task because the continuous-drive protocol is robust against modest errors in the amplitudes. As described in the theory proposal[17], the dynamics of the system comprising two qubits, coupled to the cavity (the reservoir) in the presence of drives, qubit decay and qubit dephasing can be simulated using the Lindblad master equation

$$\frac{\mathrm{d}\rho(t)}{\mathrm{d}t} = -\frac{i}{\hbar}[H(t),\rho(t)] + \kappa D[a]\rho(t) + \sum_{j=\mathrm{A,B}}\left(\frac{1}{T_1^j}D[\sigma_-^j]\rho(t) + \frac{1}{2T_\phi^j}D[\sigma_z^j]\rho(t)\right)$$

where

$$H(t) = \left(\chi_\mathrm{A}\frac{\sigma_z^\mathrm{A}}{2} + \chi_\mathrm{B}\frac{\sigma_z^\mathrm{B}}{2}\right)a^\dagger a + 2\varepsilon_\mathrm{c}\cos\left(\frac{\chi_\mathrm{A}+\chi_\mathrm{B}}{2}t\right)\left(a+a^\dagger\right) + \Omega^0\left(\sigma_x^\mathrm{A}+\sigma_x^\mathrm{B}\right) + \Omega^n\left(\mathrm{e}^{-in(\chi_\mathrm{A}+\chi_\mathrm{B})t/2}\left(\sigma_+^A-\sigma_+^B\right)+\mathrm{c.c.}\right)$$

is the Hamiltonian of the driven system in the rotating frame of the two qubits (ω_A^0, ω_B^0) and the cavity mode ($(\omega_\mathrm{c}^{\mathrm{gg}}+\omega_\mathrm{c}^{\mathrm{ee}})/2$). The qubits are considered to be perfect two-level systems rather than the anharmonic oscillators assumed in the main text, and therefore we use Pauli operators σ_z, σ_x and $\sigma_+ = \sigma_x + i\sigma_y$. The qubit dephasing rate is $1/T_\phi^{\mathrm{A,B}} = 1/T_2^{\mathrm{A,B}} - 1/2T_1^{\mathrm{A,B}}$, the Lindblad super-operator is defined for any operator O as $D[O]\rho = O\rho O^\dagger - (1/2)O^\dagger O\rho - (1/2)\rho O^\dagger O$, and ε_c is the amplitude of the drive on the cavity, which is taken to equal $\kappa\sqrt{\bar{n}}/2$, where $\bar{n}$ is the number of photons circulating in the cavity. The Lindblad equation is solved numerically for $\rho(t)$ assuming that $\rho(0) = |gg\rangle\langle gg|$. The steady-state fidelity to $|\phi_-\rangle$ is estimated as $\mathrm{Tr}((|\phi_-\rangle\langle\phi_-| \otimes I_\mathrm{c})\rho(\infty))$. The system was empirically found to have reached a steady state at $t = 10\,\mu\mathrm{s}$, and so $\rho(\infty)$ is taken to be $\rho(10\,\mu\mathrm{s})$.

The drive amplitudes are swept in the simulation to optimize fidelity; a representative result shown in Extended Data Fig. 4 for our system characteristics indicates that a broad range of cavity drive amplitudes greater than three photons and Rabi drive amplitudes greater than $\kappa/2$ should lead to fidelities of around 70%. The dependence of the fidelity on drive amplitudes can be qualitatively understood as follows. As discussed in the main text, the two cavity drives perform a quasi-parity measurement of the state of the qubits. The parity measurement rate is $\bar{n}\kappa/2$ for $\chi_\mathrm{A}, \chi_\mathrm{B} \gg \kappa$, which increases with cavity drive amplitude. Thus, the fidelity is smaller at low $\bar{n}$ owing to the slow measurement of parity compared with the error rate induced by decoherence. However, the fidelity drops at high $\bar{n}$ owing to the unwanted dephasing between $|\phi_-\rangle$ and $|\phi_+\rangle$ induced by the mismatch between χ_A and χ_B. Next, we see that the Rabi rates required for highest fidelity increase with $\bar{n}$. This effect arises from a quantum Zeno-like competition[41] between the parity measurement, which pins the qubits in the odd- or even-parity subspace, and the Rabi drives, which try to induce transitions between these subspaces. The ratio of the rates of these processes is the quantum Zeno parameter, which must not be too large if the photon-number-selective Rabi drives are to correct the system fast enough. For our optimal parameters, $\bar{n} = 3$ and $\Omega^0 = \Omega^n = \kappa/2$, the quantum Zeno parameter is 3, that is, not much greater than 1. In this intermediate regime, the feedback loop does not respond to errors through fully resolved discrete quantum jumps between the various states, but rather through a quasi-continuous evolution. Moreover as seen in Extended Data Fig. 4, this continuous feedback strategy is insensitive to small errors in setting the drive amplitudes, a favourable quality for the experimental realization.

In the experiment, the drive amplitudes for the cavity and zero-photon qubit transitions were pre-calibrated with Ramsey and Rabi experiments so that they could be set to $\bar{n} = 3$ and $\Omega^0 = \kappa/2$. However, Ω^n and the phase of the n-photon Rabi drives cannot be easily calibrated; instead they were individually swept till the fidelity was maximized. As a final optimization, $\bar{n}$ and Ω^0 were also swept; the fidelity improved by 1–2% for $\bar{n} = 3.7$ and $\Omega^0 = \kappa/2$, marginally different from the originally chosen parameters. Overall, we found that the drive amplitudes could be varied by about 20% without reducing the fidelity by more than 1%. Thus, this result as well as the good agreement for the steady-state maximum fidelity of 67% indicates that the Lindblad simulation captures most of the physics of our experiment.

Sources of steady-state infidelity. The Lindblad simulation provides an error budget analysis for the steady-state infidelity, indicating directions for improvement. We first set $\chi_\mathrm{A} = \chi_\mathrm{B} = 5.9\,\mathrm{MHz}$ and $T_1 = T_2 = \infty$, and then individually introduce the imperfections into the simulation. The ideal fidelity with drive amplitudes $\bar{n} = 3$ and $\Omega^0 = \Omega^n = \kappa/2$ is 97%, limited by the finiteness of $\bar{n}$. Introducing the ~10% χ mismatch reduces this fidelity by only 2%, indicating the robustness of the protocol to the difference between χ_A and χ_B. However, individually adding T_1 and T_ϕ processes reduces the fidelity by 12% and 8% respectively. Thus, we find that the dominant sources of infidelity are the decoherence processes inherent to the qubits and their coupling to the environment.

The T_1 values of the qubits are believed to be Purcell limited[33] (implying that κT_1 is constant) and potentially could be a factor of ten greater in the 3D cQED architecture[24]. However, this improvement cannot be achieved by reducing κ, because that would concurrently reduce the feedback correction time and, thus, the steady-state fidelity. Instead, T_1 must be improved using a Purcell filter[42], which results in a larger κT_1 and, thus, an overall improvement in the fidelity. Such a filter has been implemented in the 3D architecture used by our group recently and will be an immediate upgrade to the current set-up.

The current limit on T_ϕ is believed to be set by dephasing arising from thermal photons in the fundamental and higher modes of the cavity. This dephasing is given by $\kappa T_\phi \approx 1/n_\mathrm{th}$, where n_th is the thermal occupancy of the cavity modes. The value of n_th calculated to give our T_2, $n_\mathrm{th} = 10^{-2}$, can be reduced by at least an order of magnitude[34], allowing larger κT_ϕ and, thus, an improved fidelity.

Other sources of infidelity are ~4% $|f\rangle$ (second excited state) population of the qubits, owing to finite temperature, as well as undesired qubit transitions that are induced by the cavity drives[28] which decrease T_1. The $|f\rangle$ state population could be reduced in future experiments by additional drives on the $|e\rangle \leftrightarrow |f\rangle$ transitions. However, the T_1 reduction remains an insufficiently understood effect that requires further investigation. Nevertheless, these effects are not likely to limit the fidelity by more than 10%.

31. Lecocq, F. *et al.* Junction fabrication by shadow evaporation without a suspended bridge. *Nanotechnology* **22,** 315302 (2011).
32. Rigetti, C. *Quantum Gates for Superconducting Qubits* 174–176. PhD thesis, Yale Univ. (2009).
33. Houck, A. A. *et al.* Controlling the spontaneous emission of a superconducting transmon qubit. *Phys. Rev. Lett.* **101,** 080502 (2008).
34. Sears, A. P. *et al.* Photon shot noise dephasing in the strong-dispersive limit of circuit QED. *Phys. Rev. B* **86,** 180504 (2012).
35. Hatridge, M. *et al.* Quantum back-action of an individual variable-strength measurement. *Science* **339,** 178–181 (2013).
36. Johnson, J. E. *et al.* Heralded state preparation in a superconducting qubit. *Phys. Rev. Lett.* **109,** 050506 (2012).
37. Chow, J. M. *et al.* Detecting highly entangled states with a joint qubit readout. *Phys. Rev. A* **81,** 062325 (2010).
38. Motzoi, F., Gambetta, J. M., Rebentrost, P. & Wilhelm, F. K. Simple pulses for elimination of leakage in weakly nonlinear qubits. *Phys. Rev. Lett.* **103,** 110501 (2009).
39. Reed, M. D. *Entanglement and Quantum Error Correction with Superconducting Qubits* Ch. 5. PhD thesis, Yale Univ. (2013).
40. Devoret, M. H. & Schoelkopf, R. J. Superconducting circuits for quantum information: an outlook. *Science* **339,** 1169–1174 (2013).
41. Itano, W. M., Heinzen, D. J., Bollinger, J. J. & Wineland, D. J. Quantum Zeno effect. *Phys. Rev. A* **41,** 2295–2300 (1990).
42. Reed, M. D. *et al.* Fast reset and suppressing spontaneous emission of a superconducting qubit. *Appl. Phys. Lett.* **96,** 203110 (2010).

©2013 Macmillan Publishers Limited. All rights reserved

LETTER

doi:10.1038/nature12877

Worldwide acceleration of mountain erosion under a cooling climate

Frédéric Herman[1,2], Diane Seward[3], Pierre G. Valla[1,2], Andrew Carter[4], Barry Kohn[5], Sean D. Willett[2] & Todd A. Ehlers[6]

Climate influences the erosion processes acting at the Earth's surface. However, the effect of cooling during the Late Cenozoic era, including the onset of Pliocene–Pleistocene Northern Hemisphere glaciation (about two to three million years ago), on global erosion rates remains unclear[1–4]. The uncertainty arises mainly from a lack of consensus on the use of the sedimentary record as a proxy for erosion[3,4] and the difficulty of isolating the respective contributions of tectonics and climate to erosion[5–7]. Here we compile 18,000 bedrock thermochronometric ages from around the world and use a formal inversion procedure[8] to estimate temporal and spatial variations in erosion rates. This allows for the quantification of erosion for the source areas that ultimately produce the sediment record on a timescale of millions of years. We find that mountain erosion rates have increased since about six million years ago and most rapidly since two million years ago. The increase of erosion rates is observed at all latitudes, but is most pronounced in glaciated mountain ranges, indicating that glacial processes played an important part. Because mountains represent a considerable fraction of the global production of sediments[9], our results imply an increase in sediment flux at a global scale that coincides closely with enhanced cooling during the Pliocene and Pleistocene epochs[10,11].

The Earth's continental topography reflects the balance between tectonics and climate, and their interaction through erosion. Therefore, any change in either climate or tectonics is expected to lead to a change in topography and erosion rates. In that context, Late Cenozoic global cooling represents one of the best-documented major shifts in climate. During this transition, the climate cooled and evolved towards high-amplitude oscillating conditions that are associated with the waxing and waning of continental ice sheets in the Northern Hemisphere and alpine glaciers throughout the Pliocene and Pleistocene epochs[10,11]. As a consequence of these oscillations, the climate's influence on erosion became highly variable. In particular, it continuously switched between fluvial and (peri)glacial processes in many mid- to high-latitude, high-elevation regions[1,2]. Several studies have documented locally an increase of erosion in response to this climate transition[12–18], although the timing and magnitude of this erosional shift vary with latitude. However, whether this effect can explain the apparent global increase in sediment accumulation remains a subject of debate. The controversy comes from an observed increase in sediment accumulation rates, which may be biased by the incompleteness of the sedimentary record[3,4].

To address this issue, we quantify erosion rates at an unprecedented global scale directly from bedrock using low-temperature thermochronometry. Thermochronometry exploits the diffusion behaviour of noble gases through crystals, or damage trails produced by the spontaneous fission of ^{238}U contained in target minerals, to interpret measured apparent ages in terms of the travel time of a rock from a given closure temperature (at which diffusion/annealing becomes negligible) to the surface (see ref. 19 for a review). The passage of a rock through a temperature field near the Earth's surface gives its thermochronometric age, which can be converted into a cooling history and subsequently into an erosion rate integrated over the timescale provided by the measured age. We compiled data from across the globe for four low-temperature thermochronometric systems: apatite (U–Th)/He, apatite fission track, zircon (U–Th)/He and zircon fission track, which have approximate closure temperatures of 70 °C, 110 °C, 180 °C and 250 °C, respectively[19]. Taken together, these thermochronometers enable the tracking of bedrock erosion from typical crustal depths of about 8–10 km (ref. 19) up to the surface. Furthermore, by using multiple thermochronometers, and taking note of the information contained in the elevation at which bedrock samples were acquired, we are able to resolve recent variability in erosion rates. In total, 17,833 thermochronometric ages were compiled worldwide (Extended Data Fig. 1). Unlike sediment accumulation budgets[3,4], which are subject to many assumptions about transport and deposition, thermochronometry provides a first-order unbiased estimate of erosion in the bedrock source regions.

To estimate the rates of erosion in space and time, we perform a formal analysis of the compiled thermochronometric data using a new approach[8] based on linear inverse theory (Methods). This procedure enables the efficient treatment of a large number of spatially distributed data and provides an explicit definition of variance and resolution, which can be used to determine where erosion rates are well resolved both in space and time. We focus on the results from the past 8 million years (Myr), for which resolution is high enough to resolve potential changes in erosion rates (that is, where we might see variations associated with the onset of Pliocene–Pleistocene Northern Hemisphere glaciation). A limitation to our approach is that we do not consider complexities in the data related to small-scale tectonic structures. We expect such regional effects to be negligible at a global scale (Methods). Similarly, we do not consider uncertainties on the kinetic parameters of each thermochronometric system.

Results indicate that erosion rates vary globally since 8 Myr ago within four orders of magnitude, ranging from less than 0.01 mm yr^{-1} up to about 10 mm yr^{-1} (Fig. 1 and Supplementary Video). The slowest-eroding regions (<0.01 mm yr^{-1}) for which we have thermochronometric data are cratonic areas of central and western Australia, central North America and eastern Scandinavia. Rates are higher (0.01–0.1 mm yr^{-1}) in the passive margins of southeastern Australia, Brazil, the eastern USA, western Scandinavia, Madagascar, South Africa, Sri Lanka, southern India, the Tibetan plateau and its margins, and the Altiplano. Most of these thermochronometric age-derived erosion rates are integrated over several tens to hundreds of million years and, therefore, have insufficient resolution to reveal temporal variations associated with the Late Cenozoic cooling and Pliocene–Pleistocene glaciation. As an illustration, the authors of ref. 18 recently used the Pliocene–Pleistocene offshore sediment record and a palaeo-topographic reconstruction to identify an increase in erosion by a factor of 20 (from ~0.01 mm yr^{-1} up to ~0.2 mm yr^{-1}) during the Pliocene–Pleistocene in western Scandinavia, which they attributed to a switch from fluvial to glacial erosion. Even with this

[1]Institute of Earth Sciences, University of Lausanne, CH-1015 Lausanne, Switzerland. [2]Department of Earth Sciences, Swiss Federal Institute of Technology, Sonneggstrasse 6, CH-8092 Zürich, Switzerland. [3]School of Geography, Environment and Earth Sciences, Victoria University, PO Box 600, Wellington, New Zealand. [4]Department of Earth and Planetary Science, Birkbeck University of London, Malet Street, Bloomsbury, London WC1E 7HX, UK. [5]School of Earth Sciences, University of Melbourne, Victoria 3010, Australia. [6]Department of Geosciences, University of Tübingen, Wilhelmstrasse 56, D-72074 Tübingen, Germany.

©2013 Macmillan Publishers Limited. All rights reserved

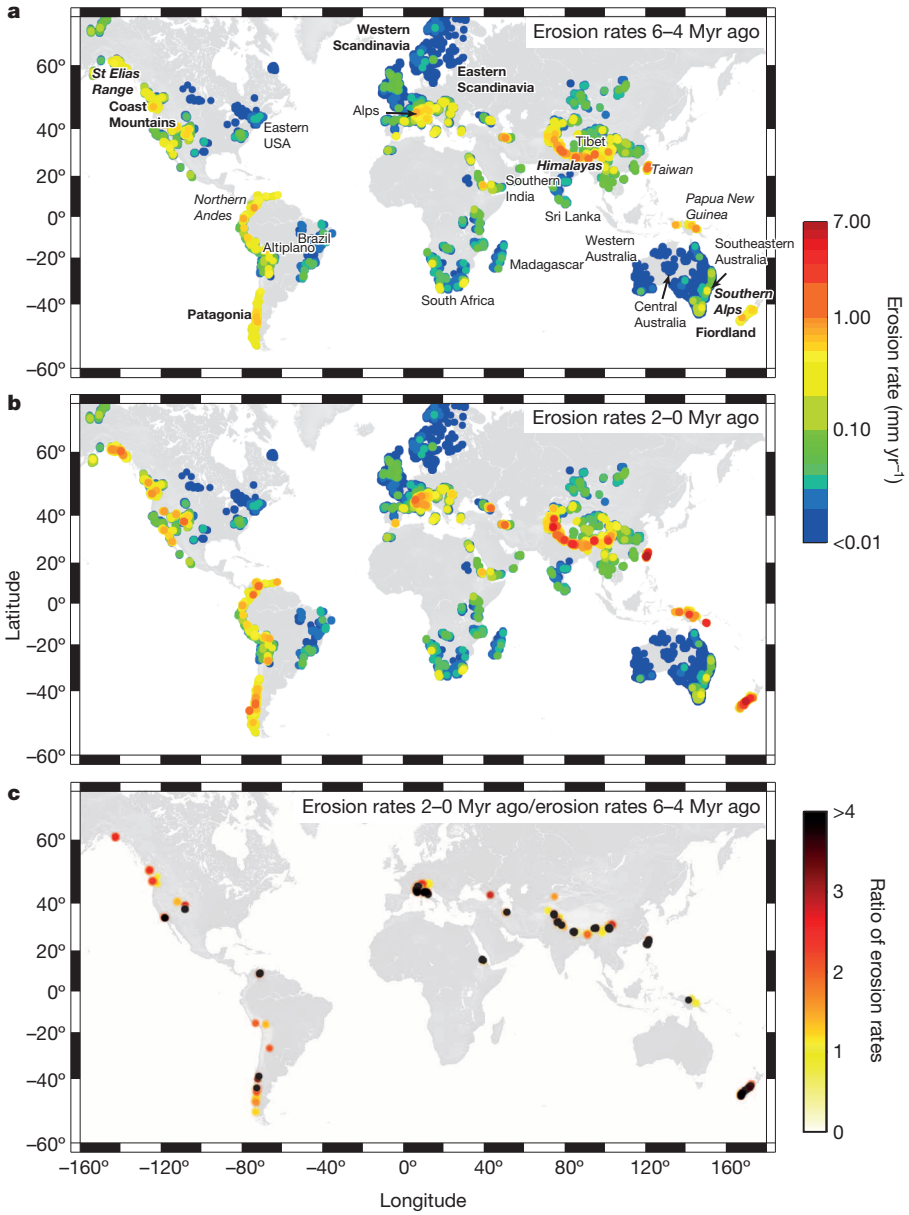


Figure 1 | Erosion rates and their variations over the past 6 Myr, resolved into 2-Myr time steps. **a**, Erosion rates between 6 Myr ago and 4 Myr ago. **b**, Erosion rates between 2 Myr ago and 0 Myr ago. **c**, Ratio of erosion rates between 2–0 Myr ago and 6–4 Myr ago, where resolution is higher than 0.25. We use a time step length of 2 Myr for ages younger than 40 Myr ago, and a 40-Myr time step for ages older than 40 Myr ago. The initial geotherm is equal to 26 °C km^{-1}. We use a thermal diffusivity equal to 30 km^2 Myr^{-1} and a 50-km vertical extent. The a priori erosion rates are set to 0.35 ±0.1 mm yr^{-1} in tectonically active mountain ranges and 0.01 ±0.01 mm yr^{-1} in tectonically inactive regions. Italic font indicates tectonically active mountain ranges and boldface font indicates glaciated ranges mentioned in the text.

significant increase in rate, the total erosion remains too small to be detected by any of the thermochronometric systems we have considered (Fig. 1).

Erosion rates are significantly higher (2–7 mm yr^{-1}) in several tectonically active mountainous areas (Fig. 1) (for example, the Southern Alps of New Zealand, Taiwan, Papua New Guinea, the Himalayas and the St Elias Range of Alaska). These orogens also receive significant precipitation[7], which can sustain high erosion rates. These areas are either glaciated or exhibit threshold hillslopes, dominated by landslides, which are a characteristic of high erosion rates[20]. Also, we observe rates higher than 1 mm yr^{-1} in some tectonically quiescent orogens such as the western European Alps, the Coast Mountains of British Columbia, Fiordland in New Zealand or northern Patagonia. In contrast with some of the more tectonically active areas, we observe high rates only in quiescent areas where the topography was heavily affected by glacial erosion[12–18].

Our results highlight an increase in erosion during the Late Cenozoic in most mountain ranges (Figs 1b and c, 2 and 3). The majority of the increase in erosion rates we detect is based on the difference in cooling from apatite fission track to apatite (U–Th)/He closure depth. Our results therefore depend partly on the thermal model and kinetic parameters we prescribe for each system in the inversion scheme. We first evaluate the significance of this erosion rate increase by computing the ratio of erosion rates 2–0 Myr ago to those 6–4 Myr ago, limiting our analysis to regions where the thermochronological cooling history is well resolved (that is, resolution is higher than 0.25, which is chosen arbitrarily; see Methods). The distribution of erosion rates shows that more than 80% of the regions with high-resolution values exhibit an increase, with an erosion rate ratio between >1 and 4 (Fig. 2). This increase is observed at all latitudes, but is more pronounced at latitudes outside the intertropical zone (inset of Fig. 2). The increase of erosion rate in low-latitude, non-glaciated regions (that is, <25°) may locally correspond to recent tectonic activity (for example, Papua New Guinea, Taiwan, the Red Sea or the northern Andes) but may also be associated with enhanced climatic variability[1,2]. Interestingly, we do not observe an increase of erosion rate in tectonically inactive regions at low latitudes. It may be that either the increase is not sufficiently large to be resolved by the thermochronometric data we compiled or there is a bias related to the spatial distribution of ages and the location of mountain ranges on Earth (such as that there are fewer mountain ranges at latitudes below 25°). At intermediate latitudes of 25°–50°, substantial changes in erosion rates are observed. In the Himalayas, rates have been consistently high over the past 8 Myr, but have increased in the northern high-elevation glaciated regions of the Greater Himalaya Sequence during the past 4 Myr,

©2013 Macmillan Publishers Limited. All rights reserved

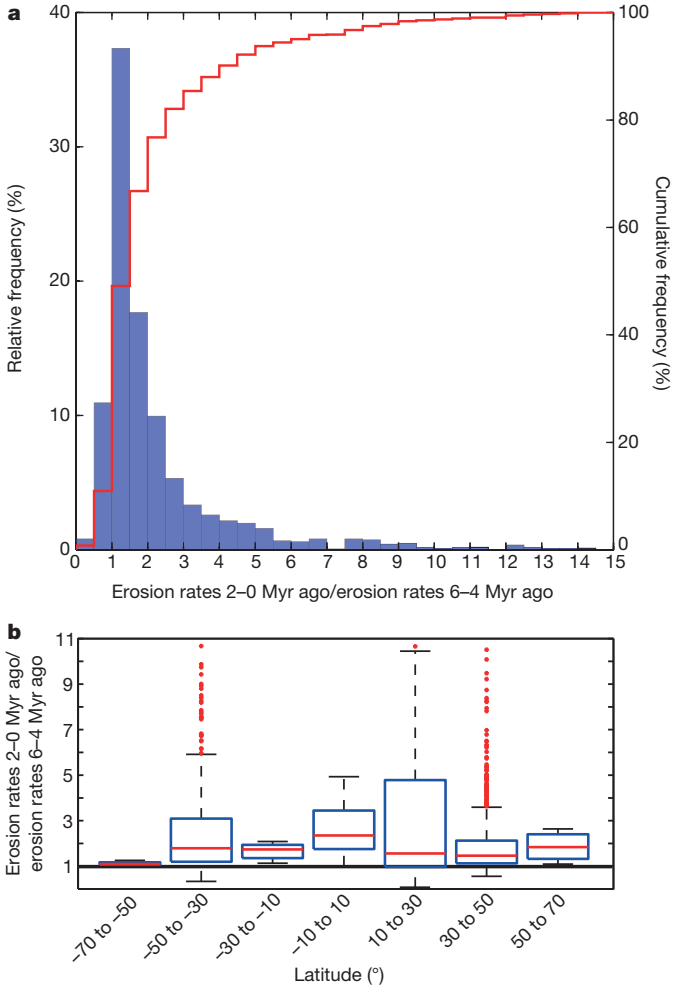


Figure 2 | Relative frequency and cumulative distributions of the ratio of erosion rates between 2–0 Myr ago and 6–4 Myr ago. **a**, Blue bars depict the relative frequency and the red line the cumulative distribution. The reported values are computed only at locations where the erosion rate is estimated and the resolution is higher than 0.25. Values higher than 1 indicate an increase of erosion rates and lower than 1 indicate a decrease. **b**, A box-and-whisker plot of the data used in this calculation distributed over latitude (using 20° intervals). The red line in each box is the median, the edges of the box are the 25th and 75th percentiles, the whiskers extend to the most extreme data points not considered outliers, and outliers are plotted as red dots.

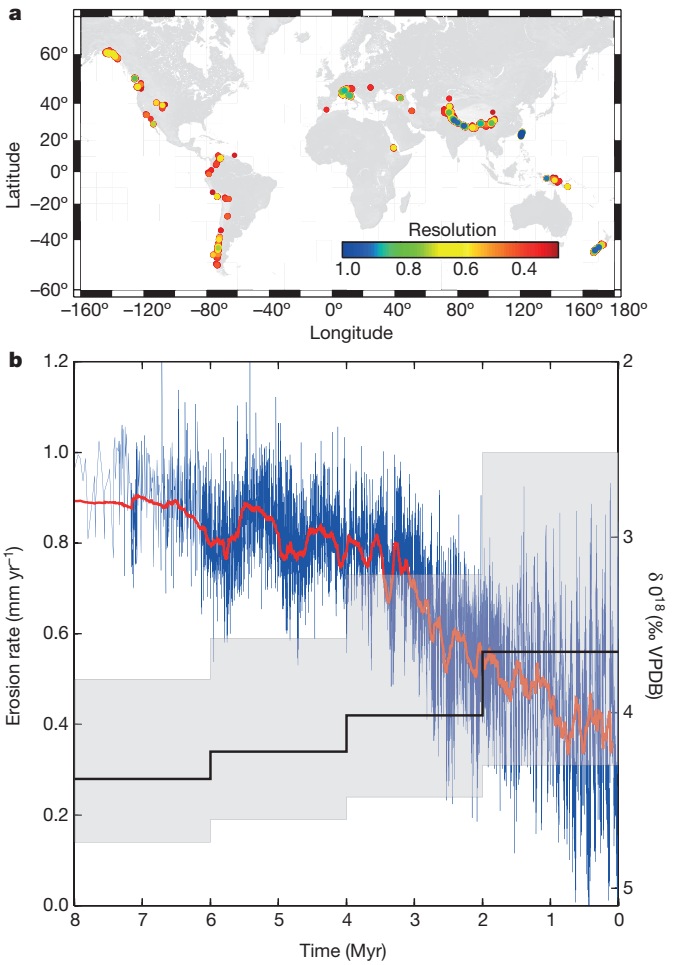


Figure 3 | Mountain erosion rates and $\delta^{18}O$ measurements during the Late Cenozoic era. **a**, Resolution is higher than 0.25 for the past 2 Myr. **b**, Erosion rate is computed at locations shown in **a**. The median (black line) and standard deviation (grey area) are estimated from the distributions of erosion rates over each 2-Myr time interval. (There is no weighting correction for areal coverage, except from using the solution at the grid points; see Methods.) The blue line depicts the raw $\delta^{18}O$ data compilation[11], whereas the red line corresponds to the moving average. VPDB, the Vienna Pee-Dee belemnite standard.

in spite of steady convergence rates[21]. In the past 2 Myr, very large changes in erosion rates are observed at latitudes above 30° (for example, the European Alps, Patagonia, Alaska, the South Island of New Zealand and the Coast Mountains of British Columbia). These areas are highly variable in their tectonic activity, but they have all been glaciated in the past few million years. This further suggests that glacial erosion has played an important part globally.

Collapsing erosion rates in mountainous areas to a median and variance over each 2-Myr time interval (Fig. 3) reveals an increase in mountain erosion rates since about 6 Myr ago, by nearly a factor of two for the Pleistocene compared to the Pliocene. This change shows a clear temporal correspondence with further cooling and increased amplitude of glacial cycles, as indicated by the global compilation of benthic foraminifera $\delta^{18}O$ measurements[11], which serve as a proxy for reconstructing global climate fluctuations. Such a short-term shift in erosion rates must be climate-driven, given that a global acceleration in tectonic activity is unlikely[1,2].

The global increase in erosion has been attributed primarily to enhanced climate variability during the Late Cenozoic era and the Pliocene–Pleistocene epoch[1,2]. Such variability may play a part in low-latitude regions where fluvial erosion dominates. Recent modelling and observational studies suggest that erosion can be promoted by an increase in both mean runoff and discharge variability[22,23]. However, our inversion of thermochronometric data does not have enough resolving power to reveal large changes in erosion rates in areas that are both fluvial-dominated and tectonically inactive. In terms of the effects of glaciers and ice caps on erosion rates, strong nonlinear feedbacks exist between glacial erosion, landscape hypsometry, net mass ice balance, climate and tectonics, all of which make attributing an increase of erosion mainly to climatic oscillations less obviously justifiable. In fact, modelling efforts have shown that glacial erosion predominantly increases in response to increased ice accumulation area owing to enhanced climate cooling[24,25], surface uplift or both[25]. Although repeated alteration between fluvial and glacial processes may have played a part[1,2], the pronounced cooling during the Pliocene–Pleistocene would be sufficient to induce an increase of erosion rates in glaciated mountain regions.

Our observations establish that the rates at which mountainous landscapes have eroded increased globally during the Late Cenozoic and that this increase correlates with further cooling and an increase of the amplitude of climate cycles. This effect is observed not only in tectonically active mountain ranges, but also in relatively inactive orogens that have experienced glacial erosion (for example, the western Alps, the Coast Mountains of British Columbia, Patagonia). This increase

©2013 Macmillan Publishers Limited. All rights reserved

has global implications under the assumption that mountains dominate global sediment production[9]. Recently, the authors of ref. 26 suggested that mountains have less of a role in erosion than do flat terrains. However, they derived and used a biased relationship between slope and denudation that led to an underestimation of sediment production from steep terrains (J. K. Willenbring, personal communication, 2013).

Furthermore, our inferred increase in the Late Cenozoic erosion rates supports an erosional feedback on climate, that is, the carbon dioxide (CO_2) cycle and its connections to Pliocene–Pleistocene cooling. Late Cenozoic cooling has been related to decreasing atmospheric CO_2, including a sharp drop in CO_2 at about 3 Myr ago (refs 27 and 28). Two main mechanisms linked to increased erosion could contribute to this CO_2 drawdown. First, an increase in physical erosion could lead to increased silicate weathering, which serves as a CO_2 sink (see ref. 29, for example), although some authors have recently argued that weathering is not necessarily associated with physical erosion[30,31]. Second, burial of terrestrial organic carbon[31] can be very efficient at sequestering CO_2 in the ocean. This process is clearly correlated with physical erosion rate[32] and may explain the tight temporal connection we observe between a change in climate and erosion. Either or both of these mechanisms could result in a strong positive feedback between climate and erosion, in which carbon dioxide removal from the atmosphere is enhanced by erosion, thereby promoting cooling.

METHODS SUMMARY

Inversion of thermochronological data. We use the method developed by ref. 8 to invert thermochronometric data sets. It exploits the information contained in both age–elevation profiles and multi-thermochronometric systems strategies. In this approach, the depth to the closure temperature is an integral of erosion rate from the thermochronometric age to the present day. This closure depth is computed using a one-dimensional thermal model combined with a spectral solution that accounts for the effects of topography on the isotherms. Erosion rate is parameterized as a piecewise constant function over fixed time intervals. A thermochronometric age is thus represented by a linear equation, and a suite of n thermochronometric ages becomes a linear system of equations:

$$A\dot{e} = z_c \tag{1}$$

where z_c is a vector of length n describing the different closure depths, $\dot{e}$ is a vector of unknown erosion rates and A is a sparse matrix whose components have units of time. To solve these independent equations, we impose a condition that erosion rates are correlated in space by defining an a priori covariance matrix, C. This matrix is constructed using the separation distance d between the ith and jth data points and an exponential correlation function:

$$C_{ij} = \sigma_e^2 e^{-\frac{d}{\lambda}} \tag{2}$$

where λ is a specified correlation length that we fix equal to 30 km. The a priori variance for the erosion rate, σ_e^2, serves primarily as a weighting factor. In turn, the maximum likelihood estimate for the erosion rate, $\dot{e}$, is given by:

$$\dot{e} = \dot{e}_{pr} + CA^T(ACA^T + C_\varepsilon)^{-1}(z_c - A\dot{e}_{pr}) \tag{3}$$

where $\dot{e}_{pr}$ is the a priori expected value of the erosion rate and C_ε is a diagonal matrix containing the estimated data uncertainty. We calculated a parameter resolution matrix, R, as:

$$R = CA^T\,(ACA^T + C_\varepsilon)^{-1}A \tag{4}$$

which permits us to establish when changes in erosion rates are well resolved. This is integrated across the spatial dimension. Results at data locations are then interpolated on a regular grid for visualization and to reduce weight due to the sampling density.

Online Content Any additional Methods, Extended Data display items and Source Data are available in the online version of the paper; references unique to these sections appear only in the online paper.

Received 16 June; accepted 13 November 2013.

1. Zhang, P., Molnar, P. & Downs, W. R. Increased sedimentation rates and grain sizes 2–4 Myr ago due to the influence of climate change on erosion rates. *Nature* **410,** 891–897 (2001).
2. Molnar, P. Late Cenozoic increase in accumulation rates of terrestrial sediment: how might climate change have affected erosion rates? *Annu. Rev. Earth Planet. Sci.* **32,** 67–89 (2004).
3. Schumer, R. & Jerolmack, D. J. Real and apparent changes in sediment deposition rates through time. *J. Geophys. Res.* **114,** F00A06 (2009).
4. Willenbring, J. K. & von Blanckenburg, F. Long-term stability of global erosion rates and weathering during late-Cenozoic cooling. *Nature* **465,** 211–214 (2010).
5. von Blanckenburg, F. The control mechanism of erosion and weathering at basin scale from cosmogenic nuclides in river sediments. *Earth Planet. Sci. Lett.* **237,** 462–479 (2005).
6. Whipple, K. X. The influence of climate on the tectonic evolution of mountain belts. *Nature Geosci.* **2,** 97–104 (2009).
7. Champagnac, J.-D., Molnar, P., Sue, C. & Herman, F. Tectonics, climate, and mountain topography. *J. Geophys. Res.* **117,** B02403 (2012).
8. Fox, M., Herman, F., Willett, S. D. & May, A. D. A linear inversion method to infer exhumation rates in space and time from thermochronometric data. *Earth Surf. Dynam. Discuss.* **1,** 207–259 (2013).
9. Milliman, J. D. & Syvitski, J. P. M. Geomorphic/tectonic control of sediment discharge to the ocean: the importance of small mountainous rivers. *J. Geol.* **100,** 525–544 (1992).
10. Shackleton, N. J. & Opdyke, N. D. Oxygen isotope and paleomagnetic evidence for early Northern Hemisphere glaciation. *Nature* **270,** 216–219 (1977).
11. Zachos, J., Pagani, M., Sloan, L., Thomas, E. & Billups, K. Trends, rhythms, and aberrations in global climate 65 Ma to present. *Science* **292,** 686–693 (2001).
12. Shuster, D. L., Ehlers, T. A., Rusmore, M. E. & Farley, K. A. Rapid glacial erosion at 1.8 Ma revealed by $^4He/^3He$ thermochronometry. *Science* **310,** 1668–1670 (2005).
13. Berger, A. L. *et al.* Quaternary tectonic response to intensified glacial erosion in an orogenic wedge. *Nature Geosci.* **1,** 793–799 (2008).
14. Vernon, A. J., van der Beek, P. A., Sinclair, H. D. & Rahn, M. K. Increase in late Neogene denudation of the European Alps confirmed by analysis of a fission track thermochronology database. *Earth Planet. Sci. Lett.* **270,** 316–329 (2008).
15. Thomson, S. N. *et al.* Glaciation as a destructive and constructive control on mountain building. *Nature* **467,** 313–317 (2010).
16. Shuster, D. L., Cuffey, K. M., Sanders, J. W. & Balco, G. Thermochronometry reveals headward propagation of erosion in an alpine landscape. *Science* **332,** 84–88 (2011).
17. Valla, P. G. *et al.* Late Neogene exhumation and relief development of the Aar and Aiguilles Rouges massifs (Swiss Alps) from low-temperature thermochronology modeling and $^4He/^3He$ thermochronometry. *J. Geophys. Res.* **117,** F01004 (2012).
18. Steer, P., Huismans, R. S., Valla, P. G., Gac, S. & Herman, F. Bimodal Plio-Quaternary glacial erosion of fjords and low-relief surfaces in Scandinavia. *Nature Geosci.* **5,** 635–639 (2012).
19. Reiners, P. W. & Brandon, M. T. Using thermochronology to understand orogenic erosion. *Annu. Rev. Earth Planet. Sci.* **34,** 419–466 (2006).
20. Montgomery, D. R. & Brandon, M. T. Topographic controls on erosion rates in tectonically active mountain ranges. *Earth Planet. Sci. Lett.* **201,** 481–489 (2002).
21. Thiede, R. C. & Ehlers, T. A. Large spatial and temporal variations in Himalayan denudation. *Earth Planet. Sci. Lett.* **371–372,** 278–293 (2013).
22. Lague, D., Hovius, N. & Davy, P. Discharge, discharge variability, and the bedrock channel profile. *J. Geophys. Res.* **110,** F04006 (2005).
23. DiBiase, R. A. & Whipple, K. X. The influence of erosion thresholds and runoff variability on the relationships among topography, climate, and erosion rate. *J. Geophys. Res.* **116,** F04036 (2011).
24. Pedersen, V. K. & Egholm, D. L. Glaciations in response to climate variations preconditioned by evolving topography. *Nature* **493,** 206–210 (2013).
25. Sternai, P., Herman, F., Valla, P. G. & Champagnac, J.-D. Spatial and temporal variations of glacial erosion in the Rhone valley (Swiss Alps): insights from numerical modeling. *Earth Planet. Sci. Lett.* **368,** 119–131 (2013).
26. Willenbring, J. K., Codilean, A. T. & McElroy, B. Earth is (mostly) flat: apportionment of the flux of continental sediment over millennial time scales. *Geology* **41,** 343–346 (2013).
27. Seki, O. *et al.* Alkenone and boron-based Pliocene pCO_2 records. *Earth Planet. Sci. Lett.* **292,** 201–211 (2010).
28. Bartoli, G., Hönisch, B. & Zeebe, R. E. Atmospheric CO_2 decline during the Pliocene intensification of Northern Hemisphere glaciations. *Paleoceanography* **26,** PA4213 (2011).
29. Raymo, M. E., Ruddiman, W. F. & Froelich, P. N. Influence of late Cenozoic mountain building on ocean geochemical cycles. *Geology* **16,** 649–653 (1988).
30. Moore, J., Jacobson, A. D., Holmden, C. & Craw, D. Tracking the relationship between mountain uplift, silicate weathering, and long-term CO_2 consumption with Ca isotopes: southern Alps, New Zealand. *Chem. Geol.* **341,** 110–127 (2013).
31. West, A. J., Galy, A. & Bickle, M. Tectonic and climatic controls on silicate weathering. *Earth Planet. Sci. Lett.* **235,** 211–228 (2005).
32. Galy, V. *et al.* Efficient organic carbon burial in the Bengal fan sustained by the Himalayan erosional system. *Nature* **450,** 407–410 (2007).

Supplementary Information is available in the online version of the paper.

Acknowledgements We thank J.-D. Champagnac and M. Brandon for discussions throughout the study. We also thank S. Jaccard and P. Molnar for their feedback on the manuscript and K. Huntington for her constructive review. The computations presented here were performed on the Brutus facility at ETH Zurich, Switzerland. F.H. was funded by SNF grant PP00P2_138956.

Author Contributions F.H. designed the study and carried out the data interpretation. F.H., D.S., P.G.V., A.C., B.K. and T.A.E. contributed to compiling the data. All authors contributed to writing the paper.

Author Information Reprints and permissions information is available at www.nature.com/reprints. The authors declare no competing financial interests. Readers are welcome to comment on the online version of the paper. Correspondence and requests for materials should be addressed to F.H. (frederic.herman@unil.ch).

©2013 Macmillan Publishers Limited. All rights reserved

METHODS

Inversion of thermochronological data. We use the method recently developed by ref. 8 to invert thermochronometric data sets. It exploits the information contained in both age–elevation profiles and multi-thermochronometric systems strategies. In this approach, we express the depth to the closure temperature as the integral of erosion rate from the thermochronometric age to present-day as:

$$\int_0^{\tau} \dot{e}(t)\mathrm{d}t = z_c \quad (1)$$

where z_c is the closure depth, τ is the thermochronometric age and $\dot{e}$ the erosion rate. We wish to solve for $\dot{e}$, which can be achieved given that the depth of closure is estimated. To that end, we use a one-dimensional thermal model that solves the heat transfer equation using the finite difference method, which we combine with a spectral solution that accounts for the effects of topography on the shape of the isotherms[33]. The initial condition is a linear unperturbed geotherm. We then compute the depth of closure by extracting the cooling history of each sample and using Dodson's approximation[34]. Both the temperature field and Dodson's approximation depend on the solution (that is, estimated erosion rates), which implies that the problem is weakly nonlinear. We obtain the solution by direct iteration on the procedure we discuss below. Convergence occurs typically after a few iterations.

To obtain a useful numerical solution for equation (1), we discretize the integral. It becomes a summation in which erosion rate is parameterized as a piecewise constant function over fixed time intervals. A thermochronometric age is thus represented by a linear equation, and a suite of n thermochronometric ages becomes a linear system of independent equations:

$$A\dot{e} = z_c \quad (2)$$

where z_c becomes a vector of length n describing the different closure depths, $\dot{e}$ is a vector of unknown erosion rates and A is a sparse matrix whose components have units of time. This leads to an under-determined inverse problem, which can be solved by regularization (see ref. 35, for example). To that end, we impose the condition that erosion rates are correlated in space by defining an a priori covariance matrix, C. This covariance matrix is constructed for all time intervals using the horizontal distance d between the ith and jth data points, and an exponential correlation function:

$$C_{ij} = \sigma_e^2 e^{-\frac{d}{\lambda}} \quad (3)$$

where λ is a specified correlation length that we fix equal to 30 km. The a priori variance for the erosion rate, σ_e^2, serves primarily as a weighting factor. It is worth noting that this covariance matrix simply implies that samples close to each other must follow the same erosion history and that samples far apart may follow independent erosion histories.

In turn, it can be shown that the solution to our inverse problem for the erosion rate $\dot{e}$ is given by:

$$\dot{e} = \dot{e}_{pr} + CA^T(ACA^T + C_\varepsilon)^{-1}(z_c - A\dot{e}_{pr}) \quad (4)$$

where $\dot{e}_{pr}$ is the a priori expected value of the erosion rate and C_ε is a diagonal matrix containing the estimated data uncertainty. This corresponds to the common least-squares methods (see page 66 of ref. 36). We note that if the distance between each sample becomes infinitely small, the solution corresponds to a piecewise linear regression over each time interval, as illustrated in great detail in ref. 8.

This formal approach also has the advantage that it enables us to establish resolution by calculating the parameter resolution matrix, R:

$$R = CA^T(ACA^T + C_\varepsilon)^{-1}A \quad (5)$$

It provides us with a means of evaluating the correction to the prior model we obtain[35]. R is derived from the covariance we impose, the temporal discretization and the error in the data. The further away resolution is from identity, the worse the solution is. In this case, we are able to observe only a filtered version of the exact solution (pages 72–73 of ref. 36). For ease of visualization, we integrate R across the spatial dimension[8]. Results at data locations are then interpolated on a regular grid for visualization and to reduce weight due to the sampling density. The influence of various factors such as erosion rates are illustrated below.

Data compilation. We compiled thermochronometric data from across the globe for four systems: apatite (U–Th)/He (AHe), apatite fission track (AFT), zircon (U–Th)/He (ZHe) and zircon fission track (ZFT), which have closure temperatures of approximately 70 °C, 110 °C, 180 °C and 250 °C, respectively[19,37–40]. The data were extracted from the literature, and complemented with unpublished fission-track ages, together making a total of 17,833 ages. A full reference list is provided in Supplementary Information and all thermochronometric data are shown in Extended Data Fig. 1. We note that most fission-track ages were determined using the recommended external-detector method[41]. If they were not reported in the original publication, elevations were interpolated from a digital elevation model using the SRTM data[42] or Google Earth. We did not include track length measurements for the fission-track studies. This implies that we are likely to miss very recent changes in erosion rates, particularly in slowly eroding regions, that would be identified by a small population of long lengths. Further, track-length distributions are less discriminative in rapidly eroding terrains, because of associated generally young AFT ages. Furthermore, we are not trying to fit a single age but rather exploit the information contained in a sequence of ages from different thermochronometric systems and distributed with elevation[8].

Likewise, we did not include grain size for AHe and ZHe in our compilation. Grain size has an effect on He diffusion, because the size of the diffusion domain scales with grain dimensions (see refs 19 and 37 for example). Most grains analysed are typically about 60 μm (sphere-equivalent radius), or larger, to limit alpha-ejection correction[43]. Large grains (100–200 μm), may imply a closure temperature 5° to 8° higher than for 60-μm grains[37], which would lead to older measured cooling ages. Our inversion assumes a grain size of 60 μm, so we may underestimate the travel distance between closure depth and the surface. This does not affect our main conclusions because, in the worst-case scenario, the inferred increase would merely be undervalued.

The compiled data carry a degree of uncertainty that varies between publications. Methods used to estimate this uncertainty are rarely described. To avoid problems raised by the different methods and the associated level of analytical precision, we prescribed uniform uncertainties that are uncorrelated with ages in the inversion (note that using the analytical uncertainties does not modify our conclusions). More importantly, the inversion method we use enables us to treat data of mixed quality and uneven spatial distribution and establish resolution. In turn, it directly propagates the variance in the data into the model variance[8,35,36,44].

Sensitivity to prior erosion rates and initial geotherm. The erosion rate history we obtain using the linear inversion approach may depend on the choice of prior erosion rates (equation (4)). Although we may locally have some independent knowledge of erosion rates, in most cases we do not have any prior information other than from thermochronometric data. Therefore, we performed several inversions using different prior erosion rates. The results are shown in Extended Data Fig. 2a. They show that our inferred increase in erosion rates is weakly dependent on the prior erosion rates, further supporting the robustness of our results. It is also worth pointing out that choosing a prior erosion rate that is substantially different from the actual solution will lead to a wrong solution (not illustrated).

The linear inversion method includes a solution of the transient heat transfer equation (Methods[8]), which defines the depth of closure isotherms. As a result, the choice of thermal parameters may have an impact on the erosion rate history[8,19,45–47], particularly during the latest stage of exhumation. Therefore, we tested several inversions using different initial near-surface geothermal gradients. The results are shown in Extended Data Fig. 2b, which shows that one needs unrealistically high geothermal gradients (over 80 °C km^{-1}) everywhere to erase the increase in erosion rates we observe.

Limitations of using thermochronometry to derive changes in erosion rates. Thermochronology has several limitations for estimating erosion rates and how they vary with time. First, erosion rates inferred from a single thermochronometric age depend on the assumed geotherm, which defines the depth of the closure isotherm. In most cases, the geotherm is poorly known and a thermal model must be used, which may have an influence on the derived erosion rate, as discussed above. This can be circumvented, to some extent, by collecting samples at different elevations. In this case, the slope of the age–elevation relationship gives an estimate of the erosion rate at the timescale fixed by the measured ages[8,19,45–49], at least when heating advection, and therefore erosion rate, is not too large[50,51]. As explained in detail in ref. 8, the inversion scheme we adopt takes advantage of this, accounting for the effects of heat advection. Furthermore, we show above that one needs an anomalously high near-surface geothermal gradient to erase the global increase in erosion rates.

Second, a thermochronometric age only provides an estimate of the erosion rate integrated over the time defined by its apparent age[8,19,45–47]. Given that our objective is to detect changes in erosion rates through time, it is crucial to combine systems of different closure temperatures, in addition to age–elevation profiles. Unfortunately, disparate data sets have been collected for each system. To assess potential problems rising from the compiled data, including paucity of some data sets, we predict ages by running simulations using a one-dimensional thermal model[50] with a prescribed erosion history that varies over 2-Myr time intervals. We then couple this thermal model with a nonlinear inversion algorithm, namely the Neighbourhood algorithm[52,53] (see ref. 54 for details), to investigate whether we can recover the erosion histories using different thermochronometric systems. For

©2013 Macmillan Publishers Limited. All rights reserved

completeness, we also use the linear inversion that we utilize for the global inversion. The results are presented in Extended Data Fig. 3.

The tests consist of four different simple erosion histories. In the first two (Extended Data Fig. 3a and b), we impose a background erosion rate of 0.1 mm yr^{-1} between 20 Myr ago and 2 Myr ago, followed by an increase in erosion rate to 0.9 mm yr^{-1} (Extended Data Fig. 3a) and 1.8 mm yr^{-1} (Extended Data Fig. 3b) over the past 2 Myr. For the two other tests (Extended Data Fig. 3c and d), we use a background erosion rate of 0.9 mm yr^{-1} between 20 Myr ago and 2 Myr ago that increases to 1.3 mm yr^{-1} (Extended Data Fig. 3c) and 1.8 mm yr^{-1} (Extended Data Fig. 3d). The vertical extent of the one-dimensional model is 30 km, with a bottom temperature of 900 °C, a thermal diffusivity of 30 km^2 Myr^{-1}, no radiogenic heat production and an unperturbed linear geotherm as the initial conditions. For each erosion history, we run three subsequent inversions: (1) an optimal case in which we have access to the four thermochronometric systems (AHe, AFT, ZHe and ZFT data), (2) a second case with access only to AFT and AHe data, and (3) a last scenario with AFT data only (which represents the largest amount of data currently available, Extended Data Fig. 1). The results are presented in Extended Data Fig. 3. Both approaches lead to similar erosion rate histories, keeping in mind that the solution of the linear inversion depends on the choice of prior erosion rates[8].

The inversion results show that erosion rates may be underestimated towards the present and overestimated back in the past when the background rates are low (0.1 mm yr^{-1}) and the change in erosion rate is not large (Extended Data Fig. 3a and b). Furthermore, a robust increase is more likely to be found at locations where data from several thermochronometric systems are available. These results imply that we may observe a smoother erosion history when erosion rates are too low, the increase is too small or where we do not have access to several thermochronometric systems. Therefore, regions where we observe a robust increase during the Late Cenozoic correspond mainly to areas where AFT, AHe or more data exist. Importantly, the results also demonstrate that we are more likely to miss an increase in erosion than to infer that one does not exist; the latter has been suggested to be a problem when using sediment accumulation curves as a proxy for erosion[3,4].

In regions where background erosion rates are high (around 1 mm yr^{-1} and higher), we obtain good constraints on erosion rates in the past 2 Myr, but we may have poor constraints on erosion rates in the past if we do not have access to higher-temperature systems (Extended Data Fig. 3c and d). This implies that it may be difficult to constrain erosion rates further back in time in tectonically active areas with sustained very high rates of erosion.

Resolution sensitivity to exhumation rates. Here we illustrate how resolution (Methods and ref. 8) may be used to determine under which conditions one is likely to be able to detect an increase of erosion. We focus on some samples from Patagonia[15]. This region was chosen because it exhibits a large south-to-north gradient in ages, which led the authors of ref. 15 to infer an increase of erosion in response to glaciation in northern Patagonia only. The suite of available AHe, AFT and ZFT data is shown in Extended Data Fig. 1 and 4. We performed two inversions, using the same parameters as for the global inversion. The first inversion includes all the available data and the second includes ZFT ages only.

The first inversion reveals higher erosion rates in northern Patagonia that increase towards the present (upper panels in Extended Data Fig. 5), which corroborates the interpretation of ref. 15. Furthermore, the associated resolution increases towards the present (lower panels in Extended Data Fig. 5). This is important because it implies that resolution degrades backwards in time, as already illustrated for the Dabie Shan example[8]. As a result, we are more likely to resolve changes in erosion rates towards the present than in the past. This is partly why we concentrated only on the recent erosion history (the past 8 Myr), although our global data set spans ages from a few hundred thousand years to several hundred million years.

In addition, we observe low erosion rates in southern Patagonia. In this part of the range, no changes in erosion rates can be resolved, as quantified by the resolution. This is simply because the ages are too old. These results are further illustrated with the second inversion (Extended Data Fig. 6), which includes only ZFT ages. In this case, most of the ages are too old to reveal a robust change in erosion rates. We note that it does not necessarily mean that there was no change in erosion rates. Instead, it may be that the changes were not large enough to be resolved. This is a similar situation to the high-northern-latitude regions, such as western Scandinavia, Baffin Island or Greenland, even though it is clear that glaciation significantly affected these landscapes, as we discuss in the main text. This problem is inherent to thermochronometry and cannot be changed. The advent of recent techniques that give us access to lower temperatures, such as $^4He/^3He$ (ref. 55) or luminescence thermochronometry[56,57], may help us to resolve this issue in the future.

Method sensitivity to changes in exhumation trajectory. Here we assess the potential impact of changes in exhumation trajectory. We present three examples of simulations with exhumation on a thrust fault with a dip angle of 30° and a 25-km-deep flat décollement. The velocity field is defined according to the fault-bend folding method[58]. We first run a three-dimensional thermokinematic model[54] to predict AHe, AFT, ZHe and ZFT ages. The models are run for 20 Myr. The vertical extent of the model is 30 km, the horizontal extent is 120 km long and 60 km wide and includes some topography that remains steady (Extended Data Fig. 7). We use a bottom temperature of 750 °C, a thermal diffusivity of 30 km^2 Myr^{-1}, no radiogenic heat production and an unperturbed linear geotherm as the initial condition. Pre-collisional ages are set to 100 Myr ago. We then select 70 ages randomly and run the linear inversion that we use for the global inversion. The first and second examples have slip rates of 5 mm yr^{-1} and 1 mm yr^{-1}, respectively. The third one has a constant slip rate of 1 mm yr^{-1} that increases to 5 mm yr^{-1} in the past 2 Myr.

The results are shown in Extended Data Fig. 8. First, they illustrate that one cannot constrain erosion rates where the ages are not reset (in general, that is over 20 Myr ago). The scenario with an erosion rate of 5 mm yr^{-1} is an example in which we infer the correct rates between 2 Myr ago and 0 Myr ago but underestimate rates between 6 Myr ago and 4 Myr ago (Extended Data Fig. 8a), as discussed above with the one-dimensional model. However, the resolution is low. In such a situation, the inferred increase would be excluded for our global interpretation. In contrast, if rates have remained relatively low or have increased since 2 Myr ago (Extended Data Fig. 8b and c), the resolution is high enough from 6 Myr ago to 0 Myr ago for us to detect an increase of erosion rates, which is again entirely consistent with the one-dimensional examples shown above.

33. Mancktelow, N. S. & Grasemann, B. Time-dependent effects of heat advection and topography on cooling histories during erosion. *Earth Planet. Sci. Lett.* **270,** 167–195 (1997).
34. Dodson, M. H. Closure temperatures in cooling geochronological and petrological systems. *Contrib. Mineral. Petrol.* **40,** 259–274 (1973).
35. Aster, R., Borchers, B. & Thurber, C. *Parameter Estimation and Inverse Problems* 2nd edn (Elsevier, 2012).
36. Tarantola, A. *Inverse Problem Theory* (SIAM, 2005).
37. Farley, K. A. Helium diffusion from apatite: general behavior as illustrated by Durango fluorapatite. *J. Geophys. Res.* **105,** 2903–2914 (2000).
38. Gleadow, A. J. W. & Duddy, I. R. A natural long-term track annealing experiment for apatite. *Nucl. Tracks Radiat. Meas.* **5,** 169–174 (1981).
39. Green, P. F. *et al.* Thermal annealing of fission tracks in apatite IV: quantitative modelling techniques and extension to geological timescales. *Chem. Geol.* **79,** 155–182 (1989).
40. Hurford, A. J. Uplift and cooling pathways derived from fission track analysis and mica dating: a review. *Geol. Rundsch.* **80,** 349–368 (1991).
41. Hurford, A. J. & Green, P. F. A users' guide to fission track dating calibration. *Earth Planet. Sci. Lett.* **59,** 343–354 (1982).
42. Farr, T. G. *et al.* The Shuttle Radar Topography Mission. *Rev. Geophys.* **45,** RG2004 (2007).
43. Farley, K. A., Wolf, R. & Silver, L. The effect of long alpha-stopping distances on (U-Th)/He dates. *Geochim. Cosmochim. Acta* **60,** 4223–4229 (1996).
44. Menke, W. *Geophysical Data Analysis: Discrete Inverse Theory* MATLAB edn, 3rd edn (Elsevier, 2012).
45. Ehlers, T. A. & Farley, K. A. Apatite (U-Th)/He thermochronometry: methods and applications to problems in tectonic and surface processes. *Earth Planet. Sci. Lett.* **206,** 1–14 (2003).
46. Ehlers, T. A. Crustal thermal processes and thermochronometer interpretation. *Rev. Mineral. Geochem.* **58,** 315–350 (2005).
47. Braun, J., van der Beek, P. A. & Batt, G. *Quantitative Thermochronology: Numerical Methods for the Interpretation of Thermochronological Data* (Cambridge Univ. Press, 2006).
48. Wagner, G. A. & Reimer, G. M. Fission track tectonics: the tectonic interpretation of fission track apatite ages. *Earth Planet. Sci. Lett.* **14,** 263–268 (1972).
49. Gallagher, K., Stephenson, J., Brown, R., Holmes, C. & Fitzgerald, P. Low temperature thermochronology and modeling strategies for multiple samples. 1: Vertical profiles. *Earth Planet. Sci. Lett.* **237,** 193–208 (2005).
50. Mancktelow, N. & Grasemann, B. Time-dependent effects of heat advection and topography on cooling histories during erosion. *Tectonophysics* **270,** 167–195 (1997).
51. Braun, J. *et al.* Quantifying rates of landscape evolution and tectonic processes by thermochronology and numerical modeling of crustal heat transport using PECUBE. *Tectonophysics* **524–525,** 1–28 (2012).
52. Sambridge, M. Geophysical inversion with a neighbourhood algorithm—I. Searching a parameter space. *Geophys. J. Int.* **138,** 479–494 (1999).
53. Sambridge, M. Geophysical inversion with a neighbourhood algorithm—II. Appraising the ensemble. *Geophys. J. Int.* **138,** 727–746 (1999).
54. Herman, F. *et al.* Exhumation, crustal deformation, and thermal structure of the Nepal Himalaya derived from the inversion of thermochronological and thermobarometric data and modeling of the topography. *J. Geophys. Res.* **115,** B06407 (2010).
55. Shuster, D. L., Farley, K. A., Sisteron, J. M. & Burnett, D. S. Quantifying the diffusion kinetics and spatial distributions of radiogenic ^4He in minerals containing proton-induced ^3He. *Earth Planet. Sci. Lett.* **217,** 19–32 (2004).
56. Guralnik, B. *et al.* Effective closure temperature in leaky or saturating thermochronometers. *Earth Planet. Sci. Lett.* **384,** 209–218 (2013).
57. Li, B. & Li, S.-H. Determining the cooling age using luminescence-thermochronology. *Tectonophysics* **580,** 242–248 (2012).
58. Suppe, J. Geometry and kinematics of fault-bend folding. *Am. J. Sci.* **283,** 684–721 (1983).

©2013 Macmillan Publishers Limited. All rights reserved

LETTER

doi:10.1038/nature12715

Attention to eyes is present but in decline in 2–6-month-old infants later diagnosed with autism

Warren Jones[1,2,3] & Ami Klin[1,2,3]

Deficits in eye contact have been a hallmark of autism[1,2] since the condition's initial description[3]. They are cited widely as a diagnostic feature[4] and figure prominently in clinical instruments[5]; however, the early onset of these deficits has not been known. Here we show in a prospective longitudinal study that infants later diagnosed with autism spectrum disorders (ASDs) exhibit mean decline in eye fixation from 2 to 6 months of age, a pattern not observed in infants who do not develop ASD. These observations mark the earliest known indicators of social disability in infancy, but also falsify a prior hypothesis: in the first months of life, this basic mechanism of social adaptive action—eye looking—is not immediately diminished in infants later diagnosed with ASD; instead, eye looking appears to begin at normative levels prior to decline. The timing of decline highlights a narrow developmental window and reveals the early derailment of processes that would otherwise have a key role in canalizing typical social development. Finally, the observation of this decline in eye fixation—rather than outright absence—offers a promising opportunity for early intervention that could build on the apparent preservation of mechanisms subserving reflexive initial orientation towards the eyes.

Autism Spectrum Disorders (ASDs) affect approximately 1 in every 88 individuals[6]. These disorders are lifelong, believed to be congenital, and are among the most highly heritable of psychiatric conditions[7]. However, the genetic heterogeneity of ASD—with estimates suggesting as many as three- to five-hundred distinct genes impacting aetiology[8]—poses a stark challenge for understanding the biology of the condition: with so many different 'causes', a key question is how that genetic heterogeneity can be instantiated into common forms of disability.

One answer is that although the specific biological mechanisms may vary (in genes or pathways affected, in dosage or in timing), any such disruptions will contribute to an individual deviation from normative developmental processes[9,10]; the mechanisms may initially be different, but a divergence from typical development is shared. In this way, widely varying initial liabilities can be converted into similar manifestations of impairment, giving rise to the spectrum of social disability we then call 'autism'.

In typical development, the processes of normative social interaction are extremely early-emerging: from the first hours and weeks of life, preferential attention to familiar voices[11], faces[12], face-like stimuli[13] and biological motion[14] guide typical infants[15]. These processes are highly conserved phylogenetically[16] and lay the foundation for iterative specialization of mind and brain[17], entraining babies to the social signals of their caregivers[11–14,18].

In the current study, we tested the extent to which measures of these early-emerging normative processes may reveal disruptions in ASD at a point prior to the manifestation of overt symptoms. We measured preferential attention to the eyes of others, a skill present in typical infants[12] but significantly impaired in 2-year-olds with ASD[2]. We proposed that in infants later diagnosed with ASD, preferential attention to others' eyes might be diminished from birth onwards[2,3,17].

Data were collected at 10 time points: at months 2, 3, 4, 5, 6, 9, 12, 15, 18 and 24. We studied 110 infants, enrolled as risk-based cohorts: $n = 59$ at high-risk for ASD (full siblings of a child with ASD[19]) and $n = 51$ at low-risk (without first-, second- or third-degree relatives with ASD). Diagnostic status was ascertained at 36 months. For details on study design, clinical characterization of participants, and experimental procedures, see Methods and Supplementary Information.

Of the high-risk infants, 12 met criteria for ASD[20] (10 males, 2 females), indicating a conversion rate of 20.3%[19]. One child from the low-risk cohort was also diagnosed with ASD. Given the small number of girls in the ASD group, we constrained current analyses to males only, 11 ASD (10 from the high-risk cohort and 1 from the low-risk), and 25 typically developing (all from the low-risk cohort).

At each testing session, infants viewed scenes of naturalistic caregiver interaction (Fig. 1a, b) while their visual scanning was measured with eye-tracking equipment. The 36 typically developing and ASD children viewed 2,384 trials of video scenes.

Control comparisons tested for between-group differences in attention to task and completion of procedures. There were no between-group differences in duration of data collected per child (typically developing = 71.25 (27.66) min, ASD = 64.16 (30.77) min, data given as mean (standard deviation), with $t_{34} = 0.685$, $P = 0.498$; two-sample t-test with 34 degrees of freedom, equal variances); or in the distribution of ages at which successful data collection occurred ($k = 0.0759$, $P = 0.9556$; two-sample Kolmogorov–Smirnov test). Calibration accuracy was not significantly different between groups: either cross-sectionally, at any data collection session (all $P > 0.15$, $t < 1.44$; mean $P = 0.428$); or longitudinally, as either a main effect of diagnosis ($F_{1,2968.336} = 0.202$, $P = 0.65$) or as an interaction of diagnosis by time ($F_{1,130.551} = 0.027$, $P = 0.87$) (by hierarchical linear modelling; see Methods, Supplementary Information and Extended Data Fig. 8).

We then measured percentage of visual fixation time to eyes, mouth, body and object regions (Fig. 1c). For each child, during each video, these measures served as the dependent variables for longitudinal analyses. Longitudinal analyses were conducted by functional data analysis (FDA)[21] and principal analysis by conditional expectation (PACE)[22] (examples in Fig. 1d, e), and were repeated with traditional growth curve analysis using hierarchical linear modelling (HLM)[23].

Growth curves for normative social engagement show broad developmental change in typically developing infants during the first 2 years of life (Fig. 2a and Extended Data Figs 2, 4 and 7). From 2 to 6 months, typically developing infants look more at the eyes than at mouth, body, or object regions (all $F_{1,23} > 15.74$, $P < 0.001$, by functional analysis of variance (functional ANOVA)[21]) (Fig. 2a, e). Mouth fixation increases during the first year and peaks at approximately 18 months (Fig. 2a, f). Fixation on body and object regions declines sharply throughout the first year, reaching a plateau between 18 and 24 months (Fig. 2a, g, h), with greater fixation on body than on object regions at all time points ($F_{1,23} = 18.02$, $P < 0.001$).

In infants later diagnosed with ASD, growth curves of social visual engagement follow a different developmental course (Fig. 2b and

[1]Marcus Autism Center, Children's Healthcare of Atlanta, Atlanta, Georgia 30329, USA. [2]Division of Autism & Related Disabilities, Department of Pediatrics, Emory University School of Medicine, Atlanta, Georgia 30022, USA. [3]Center for Translational Social Neuroscience, Emory University, Atlanta, Georgia 30022, USA.

©2013 Macmillan Publishers Limited. All rights reserved

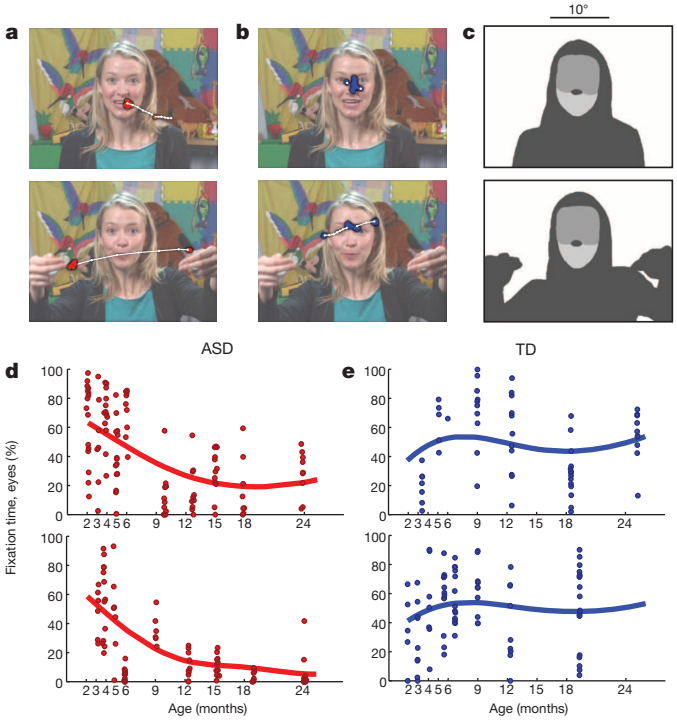


Figure 1 | Example stimuli, visual scanpaths, regions-of-interest, and longitudinal eye-tracking data from 2 until 24 months of age. **a**, Data from a 6-month-old infant later diagnosed with ASD, red. **b**, Data from a typically developing (TD) 6-month-old infant, blue. Two seconds of eye-tracking data are overlaid on each still image, onscreen at the midpoint of the data sample. Saccades are plotted as thin white lines with white dots; fixation data are plotted as larger coloured dots. **c**, Corresponding regions of interest for each image in **a** and **b**, shaded to indicate eye, mouth, body and object regions. **d**, **e**, Trial data with FDA curve fits plotting percentage of total fixation time on eyes, from 2 until 24 months of age, for two children with ASD (**d**) and two TD children (**e**).

Extended Data Figs 2, 5 and 7). From 2 until 24 months of age, eye fixation declines, arriving at a level that is approximately half that of typically developing children by 24 months (Fig. 2e). Fixation on others' mouths increases from month 2 until approximately month 18 (Fig. 2f). Fixation on others' bodies declines in children with ASD, but at less than half the rate of typically developing children, stabilizing at a level 25% greater than typical (Fig. 2g). Object fixation also declines more slowly in children with ASD, and increases during the second year (Fig. 2h), rising by 24 months to twice the level of typical controls.

Between-group comparison of entire 2- to 24-month growth curves by functional ANOVA[21] reveals significant differences in eye fixation (Fig. 2e, $F_{1,34} = 11.90$, $P = 0.002$), in body fixation (Fig. 2g, $F_{1,34} = 10.60$, $P = 0.003$), and in object fixation (Fig. 2h, $F_{1,34} = 12.08$, $P = 0.002$), but not in mouth fixation (Fig. 2f, $F_{1,34} = 0.002$, $P = 0.965$) (Bonferroni corrections for multiple comparisons, $\alpha = 0.0125$). Related analyses, including HLM, are given in Supplementary Information and Extended Data Figs 4, 5, 7, 8 and 9)

Contrary to our initial hypothesis[2], the data for children with ASD show a developmental decline in eye fixation from 2 until 24 months of age (Fig. 2c, d), with average levels of ASD eye-looking that appear to begin in the normative range.

The relationship between longitudinal eye fixation and dimensional level of social-communication disability was tested using regression. As shown in Extended Data Fig. 1, steeper decline in eye fixation is associated with more severe social disability[5]: $r_{(9)} = -0.750$ (-0.27 to -0.93, 95% confidence interval), $P = 0.007$, Pearson r, 9 degrees of freedom. In an exploratory analysis, we also tested sub-sets of the available data: that is, we measured decline in eye fixation using only data collected from month 2 to 6, excluding data collected thereafter, and then using only data collected from month 2 to 9, 2 to 12, 2 to 15, and 2 to 18. The relationship between decline in eye fixation and outcome becomes a statistical trend by the subset of month 2 to 9 ($P = 0.100$), and is statistically significant thereafter. Although these analyses will benefit from replication with larger samples, they offer preliminary indication of the clinical significance of these early behaviours.

Our experimental design densely sampled the first 6 months of life in order to test the relationship between early looking behaviour and later categorical outcome. Extended Data Fig. 2a–c show raw eye-fixation data collected in the first 6 months. Eye-fixation data for both groups show significant associations with chronological age ($F_{1,114.237} = 9.94$, $P = 0.002$ for typically developing eye fixation, $F_{1,41.609} = 9.62$, $P = 0.003$ for ASD eye fixation), but the slopes of the associations are in opposite directions: increasing at +3.6% per month for typically developing (1.3 to 5.9, 95% confidence interval), and decreasing at −4.8% per month for ASD (−7.9 to −1.7, 95% confidence interval). A similar difference is observed for body fixation (Extended Data Fig. 2g–i): body fixation is declining in typically developing children but is not declining in those later diagnosed with ASD (−4.3% per month (−5.4 to −3.1) for typically developing, $F_{1,211.856} = 54.83$, $P < 0.001$; 0.3% per month for ASD (−1.2 to 1.7), $F_{1,241.320} = 0.11$, $P = 0.739$). For both regions, there are significant interactions of diagnosis by age: eyes, $F_{1,787.928} = 9.27$, $P = 0.002$; and body, $F_{1,25.557} = 5.88$, $P = 0.023$ (HLM).

As a control, we tested whether there were between-group differences in levels of looking at the video stimuli, irrespective of content region. There were no between-group differences in levels of fixation or saccading, respectively, either as a main effect of diagnosis ($F_{1,21.652} = 0.958$, $P = 0.339$; $F_{1,27.189} = 0.250$, $P = 0.621$) or as an interaction of diagnosis by age ($F_{1,20.026} = 0.880$, $P = 0.359$; $F_{1,26.430} = 0.561$, $P = 0.460$) (Extended Data Fig. 3).

Given the variability in infant looking, we measured the extent of overlap in distributions for measures of fixation in typically developing infants relative to infants later diagnosed with ASD (Fig. 3a plots individual growth curves for levels of eye fixation, and Fig. 3b plots change in eye fixation). Mean individual levels of change in fixation between 2 and 6 months show minimal overlap between groups (Fig. 3c). However, such estimates (depending as they do on the data used to build the model, with known diagnostic outcomes) are likely to be optimistic[24]; to assess bias, we performed an internal validation.

As an internal validation (Fig. 3d–f), we used leave-one-out cross-validation (LOOCV), partitioning our data into subsamples so that each infant was tested as a validation case (that is, presuming unknown diagnostic outcome) in relation to the remainder of the data set[25]. The results indicate relatively low levels of overlap between groups (Fig. 3f). The same analyses were conducted for rates-of-change in body fixation (Fig. 3g–l). Although the area under each receiver operating characteristic (ROC) curve is smaller (as expected) for the internal validations (Fig. 3f, l) compared to estimates based on known diagnostic outcomes (Fig. 3c, i), the 95% confidence intervals clearly indicate less overlap than expected by chance.

As an external validation, we used the same technique to test six male infants who were not part of the original sample. Two of the six children had reached the age of 36 months, with confirmed ASD diagnosis, and four of the children were low-risk recruits, now at least 22 months of age, with no clinical signs of ASD. In relation to the original sample's change in eye and body fixation (Fig. 3m), these six independent test cases show similar trajectories within the first 6 months (Fig. 3n). Although this validation set is small, the probability of obtaining all six of these results in the predicted direction by chance alone is $P = 0.0156$ (equal to the chance of correctly predicting the outcome, 0.5, on each of 6 occasions, 0.5^6).

As a result of observing these differences between clearly defined extremes of social functioning at outcome (ASD and typically developing), we analysed data from the remaining high-risk males. These siblings were identified clinically as either unaffected at 36 months

©2013 Macmillan Publishers Limited. All rights reserved

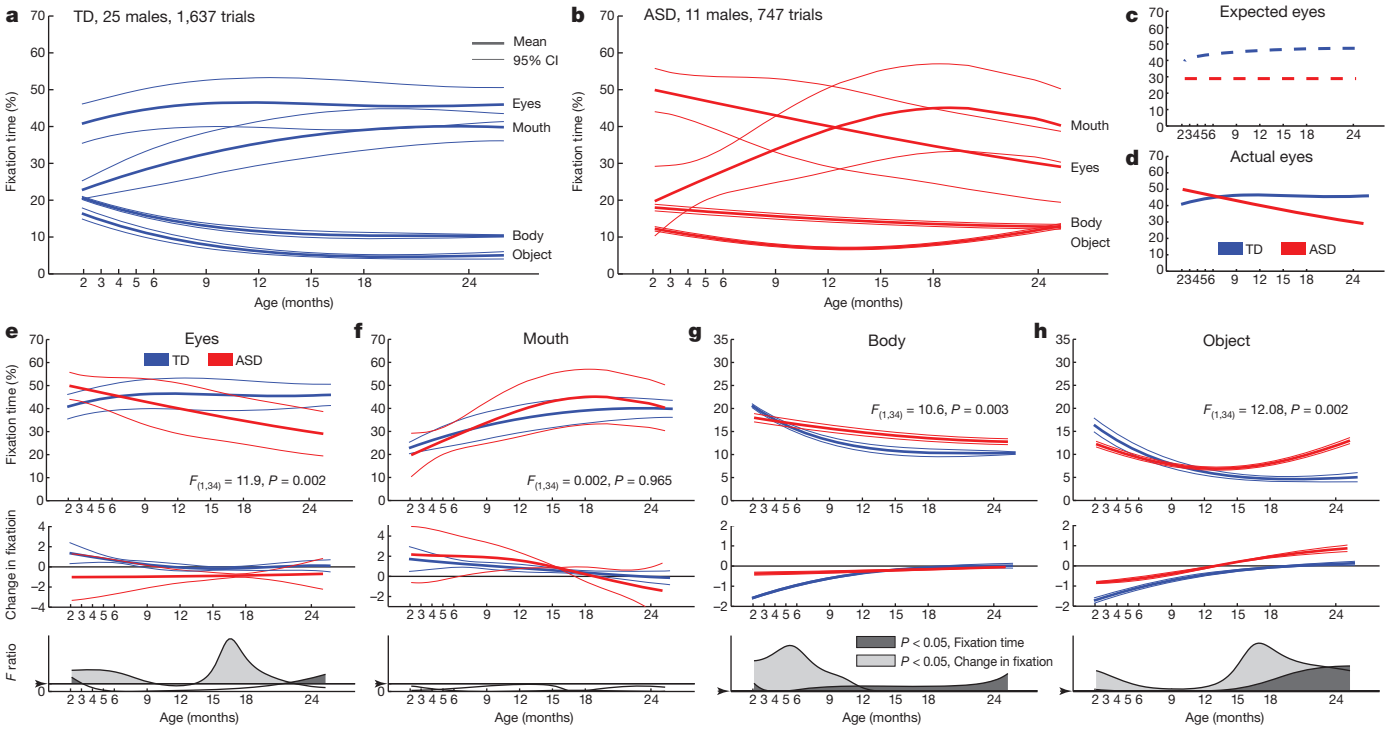


Figure 2 | Growth charts of social visual engagement for typically developing children and children diagnosed with ASD. **a**, **b**, Fixation to eyes, mouth, body and objects from 2 until 24 months in TD (**a**) and ASD (**b**) children. **c**, **d**, Contrary to a congenital reduction in preferential attention to eyes in ASD, children with ASD exhibit mean decline in eye fixation. **e**–**h**, Longitudinal change in fixation to eyes (**e**), mouth (**f**), body (**g**), and object (**h**) regions; between-group comparisons by functional ANOVA. Thick lines indicate mean growth curves, thin lines indicate 95% confidence intervals. Top panels in **e**–**h** plot per cent fixation; middle panels plot change in fixation (the first derivative, in units of % change per month); and bottom panels plot *F* value functions for between-group pointwise comparisons. Significant differences are shaded in medium grey for comparison of fixation data and light grey for comparison of change-in-fixation data, with *F* ratio critical value marked by an arrowhead on the *y* axis.

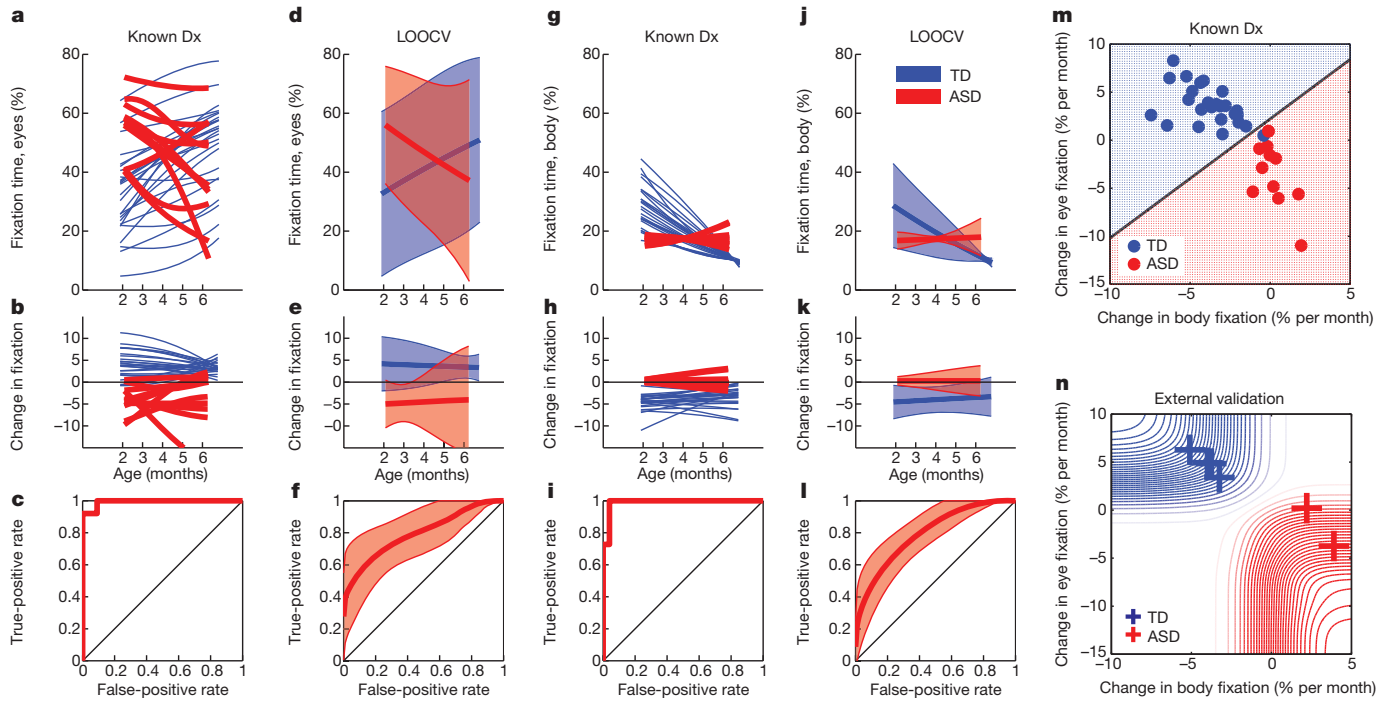


Figure 3 | Visual fixation between 2 and 6 months of age relative to diagnosis at year 3. **a**, **b**, Individual curve fits for eye-fixation data (**a**) and change-in-fixation data (**b**) for TD infants (blue) and infants later diagnosed with ASD (red). **c**, The extent of between-group overlap in distributions of change-in-fixation data with known diagnostic outcomes (Known Dx). For internal validation, each infant was tested as a validation case in relation to the remainder of the data (leave-one-out cross-validation, LOOCV). **d**, **e**, Area plots in **d** and **e** show LOOCV mean and 95% prediction intervals for individual trajectories of eye fixation (**d**) and change-in-fixation (**e**) data. **f**, The extent of between-group overlap in change-in-fixation data (mean and 95% confidence interval). **g**–**l**, The same analyses as **a**–**c** and **d**–**f**, but for body fixation, are shown in **g**–**i** and **j**–**l**. **m**, Plot of the joint distribution of change in eye and body fixation. **n**, Six male infants, not part of the original sample, were tested as an external validation.

©2013 Macmillan Publishers Limited. All rights reserved

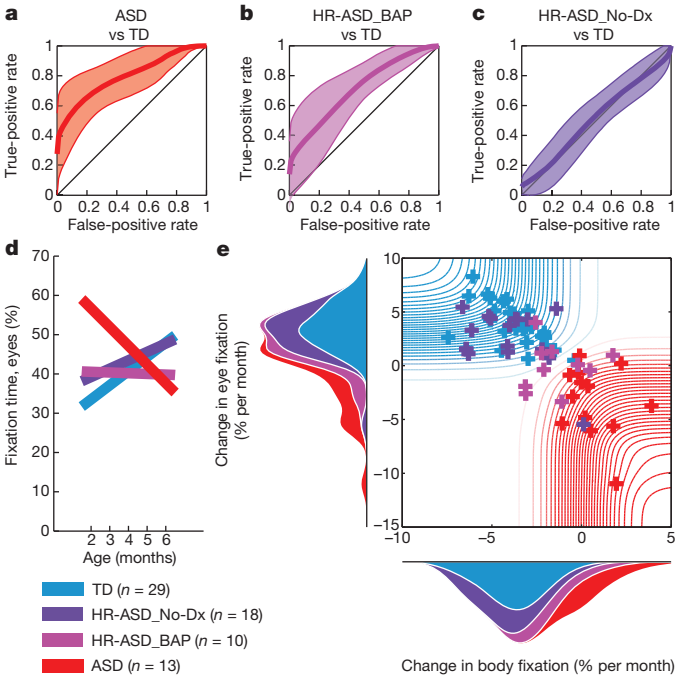


Figure 4 | Visual fixation between 2 and 6 months of age relative to outcome levels of affectedness. **a**–**c**, At 36 months, infant siblings at high risk for ASD were confirmed either as having ASD, as having subthreshold signs of ASD (HR-ASD_BAP), or as unaffected (HR-ASD_No-Dx). ROC curves in **a**, **b**, and **c** quantify overlap in measures of change in eye fixation relative to outcome (95% confidence interval by LOOCV). The behaviour of unaffected siblings overlaps with that of typically developing children (**c**), whereas the behaviour of infants later diagnosed with ASD (**a**) and that of infants with subthreshold signs (**b**) differs significantly from typical children. **d**, Eye fixation varies systematically across all outcome groups, with significant interaction of outcome by age (by HLM). **e**, Individual change in eye and body fixation for 70 infant males (29 typically developing, 25 original sample, 4 external validation; 13 ASD, 11 original sample, 2 external validation; 18 HR-ASD_No-Dx; and $N = 10$ HR-ASD_BAP). Probability density functions on ordinate and abscissa indicate distribution of measures for each outcome group.

(referred to as HR-ASD_No-Dx) or as exhibiting subthreshold signs of ASD (also called the broader autism phenotype (BAP)[26], referred to as HR-ASD_BAP). For change in eye fixation between 2 and 6 months of age, ROC curves in Fig. 4a–c quantify the overlap in measures relative to outcome (95% confidence intervals by LOOCV). The behaviour of unaffected siblings (HR-ASD_NoDx) is highly overlapping with that of typically developing children (Fig. 4c), while the behaviour of infants later diagnosed with ASD (Fig. 4a), and that of infants with subthreshold signs (Fig. 4b), clearly differs from typical controls.

We also considered these data as part of a larger continuum (Fig. 4d and Extended Data Fig. 6). Graded developmental trajectories are evident in the significant interaction of outcome (four levels) by age: $F_{3,133.006} = 6.95$, $P < 0.001$ (HLM). Typically developing children show strongly increasing eye fixation. Unaffected siblings also show increasing eye fixation. Siblings with subthreshold symptoms show neither increasing nor decreasing eye fixation, and infants later diagnosed with ASD show declining eye fixation.

In Fig. 4e, individual results are plotted dimensionally across the full spectrum of social ability to disability. The probability density functions on ordinate and abscissa indicate whole-sample distributions for change in eye and body fixation. The data show gradations from typically developing children to those diagnosed with ASD, with children with ASD showing the largest decline in eye fixation as well as the greatest increase in body fixation. Values for unaffected siblings are fully overlapping with those of typically developing children, whereas children with BAP outcomes show intermediary behaviours.

In summary, the current results indicate that the development of infants later diagnosed with ASD differs already from that of their typical peers during the period from 2 to 6 months of age. These results, although still limited in sample size, document the derailment of skills that would otherwise guide typical socialization[10,17,18], and this early divergence from normative experience suggests a means by which diverse genetic liabilities are instantiated, developmentally, into a spectrum of affectedness. Given the interdependence[9] of individual experience with brain structure and function, and with gene expression and methylation, these results suggest how a single individual's outcome will be shaped not only by initial genotypic vulnerabilities, but also by the atypical experiences that arise as a consequence of those vulnerabilities, instantiating a wide spectrum of affectedness.

In children later diagnosed with ASD, eye looking shows mean decline by at least 2 months. However, unexpectedly, those early levels of eye looking seem to begin at normative levels. This contradicts prior hypotheses of a congenital absence of social adaptive orientation[2,3,17,18] and suggests instead that some social adaptive behaviours may initially be intact in newborns later diagnosed with ASD. If confirmed in larger samples, this would offer a remarkable opportunity for treatment: predispositions that are initially intact suggest a neural foundation that may be built upon, offering far more positive possibilities than if that foundation were absent from the outset. Equally exciting, these data fit well within the framework of long-studied animal models of the neural systems subserving filial orientation and attachment[27]: they highlight a narrow period for future investigation, spanning the transition from experience-expectant to experience-dependent mechanisms[28]. A critical next step will be to measure densely sampled developmental change in gene expression and brain growth, in tandem with detailed quantification of behaviour; in short, measuring gene–brain–behaviour growth charts of infant social engagement to understand the developmental pathogenesis of social disability[29].

METHODS SUMMARY

The research protocol was approved as bearing no significant risk by the Human Investigations Committees at Yale University School of Medicine and at Emory University School of Medicine, and the data collected were used for research purposes only. All aspects of the experimental protocol were performed by personnel blinded to the diagnostic status of the children. All diagnostic measures were administered by trained clinicians blinded to results of experimental procedures. The children were shown, at each of 10 longitudinal testing points between 2 and 24 months of age, video scenes of naturalistic caregiver interaction. We measured percentage of visual fixation time to eyes, mouth, body and object regions, and these measures served as the dependent variables for longitudinal analyses. Planned confirmatory analyses measured longitudinal fixation trajectories relative to both categorical diagnostic outcomes and dimensional levels of social-communication disability. Visual scanning was measured with eye-tracking equipment (ISCAN). Analysis of eye movements and coding of fixation data were performed with software written in MATLAB. Additional details on participants, experimental procedures, data acquisition and analysis are provided in Methods and in Supplementary Information.

Online Content Any additional Methods, Extended Data display items and Source Data are available in the online version of the paper; references unique to these sections appear only in the online paper.

Received 28 January; accepted 24 September 2013.
Published online 6 November 2013.

1. Grice, S. J. *et al.* Neural correlates of eye-gaze detection in young children with autism. *Cortex* **41,** 342–353 (2005).
2. Jones, W., Carr, K. & Klin, A. Absence of preferential looking to the eyes of approaching adults predicts level of social disability in 2-year-olds with autism spectrum disorder. *Arch. Gen. Psychiatry* **65,** 946–954 (2008).
3. Kanner, L. Autistic disturbances of affective contact. *Nerv. Child* **2,** 217–250 (1943).
4. Volkmar, F. R., Lord, C., Bailey, A., Schultz, R. T. & Klin, A. Autism and pervasive developmental disorders. *J. Child Psychol. Psychiatry* **45,** 135–170 (2004).
5. Lord, C., Rutter, M., DiLavore, P. & Risi, S. *Autism Diagnostic Observation Schedule* 2nd edn (Western Psychological Services, 2008).

©2013 Macmillan Publishers Limited. All rights reserved

6. Centers for Disease Control and Prevention. Prevalence of autism spectrum disorders — Autism and Developmental Disabilities Monitoring Network, 14 Sites, United States, 2008. *MMWR Surveillance Summaries* **61,** 1–19 (2012).
7. Constantino, J. N. *et al.* Autism recurrence in half siblings: strong support for genetic mechanisms of transmission in ASD. *Mol. Psychiatry* **18,** 137–138 (2013).
8. State, M. W. & Sestan, N. Neuroscience: the emerging biology of autism spectrum disorders. *Science* **337,** 1301–1303 (2012).
9. Oyama, S. *The Ontogeny of Information: Developmental Systems and Evolution* 2nd edn (Duke Univ. Press, 2000).
10. Jones, W. & Klin, A. Heterogeneity and homogeneity across the autism spectrum: the role of development. *J. Am. Acad. Child Adolesc. Psychiatry* **48,** 471–473 (2009).
11. DeCasper, A. J. & Fifer, W. P. Of human bonding: newborns prefer their mothers' voices. *Science* **208,** 1174–1176 (1980).
12. Haith, M. M., Bergman, T. & Moore, M. J. Eye contact and face scanning in early infancy. *Science* **198,** 853–855 (1977).
13. Johnson, M. H. Subcortical face processing. *Nature Rev. Neurosci.* **6,** 766–774 (2005).
14. Simion, F., Regolin, L. & Bulf, H. A predisposition for biological motion in the newborn baby. *Proc. Natl Acad. Sci. USA* **105,** 809–813 (2008).
15. Johnson, M. H. Functional brain development in humans. *Nature Rev. Neurosci.* **2,** 475–483 (2001).
16. Rosa Salva, O., Farroni, T., Regolin, L., Vallortigara, G. & Johnson, M. H. The evolution of social orienting: evidence from chicks (*Gallus gallus*) and human newborns. *PLoS ONE* **6,** e18802 (2011).
17. Klin, A., Jones, W., Schultz, R. T. & Volkmar, F. The enactive mind — from actions to cognition: lessons from autism. *Phil. Trans. R. Soc. B* **358,** 345–360 (2003).
18. Klin, A., Lin, D. J., Gorrindo, P., Ramsay, G. & Jones, W. Two-year-olds with autism fail to orient towards human biological motion but attend instead to non-social, physical contingencies. *Nature* **459,** 257–261 (2009).
19. Ozonoff, S. *et al.* Recurrence risk for autism spectrum disorders: a Baby Siblings Research Consortium study. *Pediatrics* **128,** e488–e495 (2011).
20. Chawarska, K., Klin, A., Paul, R. & Volkmar, F. R. Autism spectrum disorders in the second year: stability and change in syndrome expression. *J. Child Psychol. Psychiatry* **48,** 128–138 (2007).
21. Ramsay, J. O. & Silverman, B. W. *Functional Data Analysis* 2nd edn (Springer-Verlag, 2006).
22. Yao, F., Müller, H. G. & Wang, J. L. Functional data analysis for sparse longitudinal data. *J. Am. Stat. Assoc.* **100,** 577–590 (2005).
23. Singer, J. D. & Willett, J. B. *Applied Longitudinal Data Analysis* (Oxford Univ. Press, New York, 2003).
24. Mosteller, F. & Tukey, J. W. *Data Analysis and Regression* 37 (Addison-Wesley, 1977).
25. Stone, M. Cross-validatory choice and assessment of statistical predictions. *J. R. Stat. Soc. B* **36,** 111–147 (1974).
26. Steer, C. D., Golding, J. & Bolton, P. F. Traits contributing to the autistic spectrum. *PLoS ONE* **5,** e12633 (2010).
27. Horn, G., Nicol, A. U. & Brown, M. W. Tracking memory's trace. *Proc. Natl Acad. Sci. USA* **98,** 5282–5287 (2001).
28. Johnson, M. H. & Karmiloff-Smith, A. In *Theories of Infant Development* (eds Bremner, G. & Slater, A.) 121–141 (Blackwell, 2004).
29. Abrahams, B. S. & Geschwind, D. H. Advances in autism genetics: on the threshold of a new neurobiology. *Nature Rev. Genet.* **9,** 341–355 (2008).

Supplementary Information is available in the online version of the paper.

Acknowledgements This work was supported by grants from the Simons Foundation and the National Institute of Mental Health (R01 MH083727). Additional support was provided by the Marcus Foundation, the Whitehead Foundation, and the Georgia Research Alliance. We wish to thank the families and children for their time and participation. We also wish to thank S. Habayeb, S. Glazer, M. Ly, T. Tsang, J. Jones, A. Trubanova, J. Borjon, J. Moriuchi, K. Rice, J. Northrup, L. Edwards, J. Xu, S. Shultz, A. Krasno, C. Zampella, K. Knoch, D. Lin, K. Carr and A. Blank for their assistance in data collection and processing; P. Lewis, J. Paredes, P. Gorrindo and M. Ackerman for assistance in designing and building laboratory hardware and software; G. Ramsay and C. McCracken for discussions of data analysis and statistics; I. Zilber, A. Margolis, D. Blum, M. Dye, D. Simeone, A. Smith and K. O'Loughlin for project supervision, coordination, and data collection; T. Babitz for administrative support; and K. Chawarska, C. Saulnier, K. Bearss, S. Macari, R. Paul, A. Carney, T. Goldsmith, A. Steiner, G. Gengoux, D. Goudreau, E. Loring, J. McGrath and A. Gupta for their contributions to the clinical characterization of the samples.

Author Contributions W.J. and A.K. developed the initial idea and design of the study, interpreted data, wrote the final manuscript, had full access to all of the data in the study and take responsibility for the integrity of the data and the accuracy of the data analysis. W.J. and A.K. performed final revision of the manuscript for content. A.K. supervised participant characterization. W.J. supervised technological developments and technical aspects of experimental procedure, data acquisition and analysis.

Author Information Reprints and permissions information is available at www.nature.com/reprints. The authors declare no competing financial interests. Readers are welcome to comment on the online version of the paper. Correspondence and requests for materials should be addressed to W.J. (warren.jones@emory.edu) or A.K. (ami.klin@emory.edu).

©2013 **Macmillan Publishers Limited. All rights reserved**

METHODS

The research protocol was approved as bearing no significant risk by the Human Investigations Committees at Yale University School of Medicine and at Emory University School of Medicine, and the data collected were used for research purposes only. All aspects of the experimental protocol were performed by personnel blinded to the diagnostic status of the children. All diagnostic measures were administered by trained clinicians blind to results of experimental procedures. The children were shown, at each of 10 longitudinal testing points between 2 and 24 months of age, video scenes of naturalistic caregiver interaction. We measured percentage of visual fixation time to eyes, mouth, body and object regions, and these measures served as the dependent variables for longitudinal analyses. Planned confirmatory analyses measured longitudinal fixation trajectories relative to both categorical diagnostic outcomes and dimensional levels of social-communicative disability. Visual scanning was measured with eye-tracking equipment (ISCAN). Analysis of eye movements and coding of fixation data were performed with software written in MATLAB. Additional details on participants, experimental procedures, data acquisition and analysis are provided in Methods and in Supplementary Information.

Stimuli. Children were shown video scenes of a female actor looking directly into the camera and playing the part of a caregiver: entreating the viewing toddler by engaging in childhood games (for example, playing pat-a-cake) (Fig. 1a, b; also described in ref. 2). The actors were filmed in naturalistic settings that emulated the real-world environment of a child's room, with pictures, shelves of toys, and stuffed animals. We used naturalistic stimuli (for example, dynamic rather than static stimuli, and realistic rather than abstracted or reductive scenes) in light of past research indicating that older children with ASD exhibit large discrepancies between their actual adaptive behaviour skills in the real world relative to their cognitive potential in more structured situations[30], larger between-group effect sizes for face-processing deficits with dynamic relative to static stimuli[31], and marked difficulties when attempting to generalize skills from structured, rote environments (in which the skills were initially learned) to environments that are open-ended and rapidly changing[4]. At each data-collection session, videos were drawn in pseudo-random order from a pool of 35 total. Both the 'caregiver' video stimuli analysed here (35 videos), as well as videos of infant and toddler interaction ('peer-play' videos, as described in ref. 32, for another set of experiments not yet analysed) were presented. Video stimuli were presented in pseudo-random order. There were no between-group differences in duration of data collected per child, either in total ($t_{34} = 0.685$, $P = 0.498$) or specifically for the caregiver stimuli ($t_{34} = 0.205$, $P = 0.839$). Successful data collection was achieved in 80.2% of all testing sessions; failed data collection sessions occurred as the result of an infant falling asleep, crying, or becoming too fussy to watch the videos. Reasons for failure were recorded in data collection reports for each session and maintained in a database; no systematic difference in reasons for failure could be discerned between the two groups. At each data collection session, approximately 30% of the videos shown to a child were novel, whereas the remaining 70% were repeated from previous sessions (from both the immediately preceding session as well as from any prior session beginning at month 2 onwards). This balanced the need for repeated measures to the same stimulus video with the need for novelty. To test for learning effects of repeated presentations, we compared end-stage results at 24 months in this longitudinal sample with previous results in a cross-sectional sample at that age (males from ref. 2): tested by 2×2 between-subjects factorial ANOVA, there was no main effect of cohort, longitudinal versus cross-sectional ($F_{1,57} = 0.052$, $P = 0.820$), but there was a significant main effect of diagnosis (ASD versus typically developing, $F_{1,57} = 6.29$, $P = 0.015$).

Caregiver videos were presented as full-screen audiovisual stimuli on a 20-inch computer monitor (refresh rate of 60 Hz noninterlaced); in 32-bit colour; at 640×480 pixels in resolution; at 30 frames per s; with mono-channel audio sampled at 44.1 kHz. Stimuli were sound and luminosity equalized, and were piloted before the start of study in order to optimize engagement for typical infant and toddler viewers. Regions of interest (eye, mouth, body and object) were bitmapped in all frames of video (Fig. 1c). Average sizes of the regions-of-interest are given in Extended Data Table 1c.

Experimental setting and equipment. Two settings for eye-tracking data collection were used in this study. One eye-tracking laboratory was optimized for infants between the ages of 2 and 6 months, and a second setting was optimized for infants and toddlers from 9 to 36 months. The primary distinction between the two settings was the use of a reclined bassinet for younger infants versus the use of a car seat for older infants and toddlers. The eye-tracking data-collection hardware and software were identical in both settings, and all aspects of automated stimuli presentation, data collection and analysis were also identical; these have previously been described in ref. 2. To obtain optimal eye imaging with infants in the reclined bassinet, eye-tracking cameras and an infrared light source were concealed within a teleprompter. In the toddler laboratory, eye-tracking cameras were mounted beneath a computer display monitor. The display monitor was mounted flush within a wall panel. In both laboratories, eye tracking was accomplished by a video-based, dark pupil/corneal reflection technique with hardware and software created by ISCAN, with data collected at 60 Hz. In both laboratories, audio was played through a set of concealed speakers. Infants were placed in a modified travel bassinet, mounted on a table that was raised and lowered at the beginning of each session to standardize the positioning of the infant's eyes relative to the display monitor. In the toddler laboratory, children were seated in a car seat in front of the computer screen on which the videos were presented. As in the infant laboratory, the car seat was raised and lowered so as to standardize the position of each child's eyes relative to the display monitor.

Experimental protocol. Infants and toddlers were accompanied at all times by a parent or primary caregiver. To begin the experimental session, the participant (infant or toddler) and caregiver entered the laboratory room while a popular children's entertainment video played on the display monitor. The child was buckled into the bassinet or car seat. Eye position relative to display monitor was then standardized for each child by adjusting the seat or bassinet location. Viewers' eyes were 28 inches (71.12 cm) from the display monitor, which subtended an approximately $24^\circ \times 32^\circ$ portion of each viewer's visual field. Lights in the room were dimmed so that only content presented on the display monitor could be easily seen. During testing, both experimenter and parent were out of view from the child but were able to monitor the child at all times by means of an eye-tracking camera and by a second video camera that filmed a full-body image of the child.

Visual-fixation patterns were measured with eye-tracking hardware (ISCAN). To begin the process of data collection, after the child was comfortably watching the children's video, calibration targets were presented onscreen by the experimenter. This was done using software that paused the playing video and presented a calibration target on an otherwise blank background. A five-point calibration scheme was used, presenting spinning and/or flashing points of light as well as cartoon animations, ranging in size from 1° to 1.5° of visual angle, all with accompanying sounds. For the infants, calibration stimuli began as large targets, $\geq 10^\circ$ in horizontal and vertical dimensions, which then shrank through animation to their final size of 1° to 1.5° of visual angle. The calibration routine was followed by verification of calibration in which more animations were presented at five on-screen locations. Throughout the remainder of the testing session, animated targets (as used in the calibration process) were shown between experimental videos to measure drift in calibration accuracy. In this way, accuracy of the eye-tracking data was verified before beginning experimental trials and was then repeatedly checked between video segments as the testing continued. In the case that drift exceeded 3°, data collection was stopped and recalibration was carried out before further videos were presented. For additional details and measures of calibration accuracy, please see Supplementary Information and Extended Data Fig. 8.

Analysis of eye movements. Analysis of eye movements and coding of fixation data were performed with software written in MATLAB (MathWorks). The first phase of analysis was an automated identification of non-fixation data, comprising blinks, saccades and fixations directed away from the presentation screen. Saccades were identified by eye velocity using a threshold of 30° per s (ref. 33). We tested the velocity threshold with the 60-Hz eye-tracking system described above and, separately, with an eye-tracking system collecting data at 500 Hz (SensoMotoric Instruments GmbH). In both cases saccades were identified with equivalent reliability as compared with both hand coding of the raw eye-position data and with high-speed video of the child's eyes. Blinks were identified as described in ref. 32. Off-screen fixations (when a participant looked away from the video) were identified by fixation coordinates beyond the stimuli presentation screen.

Eye movements identified as fixations were coded into four regions of interest that were defined within each frame of all video stimuli: eyes, mouth, body (neck, shoulders and contours around eyes and mouth, such as hair) and objects (surrounding inanimate stimuli) (Fig. 1c). The regions of interest were hand traced for all frames of the video and were then stored as binary bitmaps (through software written in MATLAB). Automated coding of fixation time to each region of interest then consisted of a numerical comparison of each child's coordinate fixation data with the bitmapped regions of interest.

Longitudinal data analyses. To examine the longitudinal development of social visual attention, for individual participants and across both ASD and typically developing groups, we used functional data analysis (FDA)[21] and principal analysis by conditional expectation (PACE)[22,34–36] (Fig. 1d, e for example individual fits, and Fig. 2 for group results; also Extended Data Fig. 7). Although we focused on FDA and PACE in order to overcome limitations inherent to cross-sectional analyses, as well as some limitations of traditional growth-curve analyses, we repeated all our analyses using hierarchical linear modelling (HLM) (Extended Data Figs 4, 5 and 6 and Extended Data Table 1b). Although the two methods produced the same pattern of significant between-group differences (described in

©2013 Macmillan Publishers Limited. All rights reserved

main text and in Supplementary Information), we favour the FDA approach because traditional growth-curve analyses can be confounded by individual differences in developmental timescale, and also because traditional growth curve analyses often require correct assumption of an underlying parametric or semi-parametric model (rather than allowing this to be determined in a data-driven fashion[37]). In contrast, FDA methods determine curve shape empirically[22,35] and model statistical variation in both time scale as well as amplitude[34,36]. The PACE method of FDA is also designed specifically to overcome a common problem for longitudinal studies: non-uniform sampling particularly in the case of missing values[22,35]. PACE characterizes statistical ensembles of irregularly sampled longitudinal data in terms of entire curve shapes on the basis of conditional expectation. This maximizes the ability to detect patterns of correlation across trajectories and minimizes the impact of data sampled at discrete intervals with varying number of measurements per participant[36]. This approach notably improves the detection of common features in trajectory shape.

As noted above, as a methodological comparison to FDA, we also analysed the data using hierarchical linear modelling[23]. The presence of linear and curvilinear (quadratic and cubic) patterns was assessed for fixation relative to age using the following model:

$$\text{fixation}_{ij} = \text{intercept}_j + \text{d}_{ij} + B_{1j}(\text{age}_{\text{ij}}) + B_{2j}(\text{age}_{ij})^2 + B_{3j}(\text{age}_{ij})^3 + e_{ij}$$

where d_{ij} represents the normally distributed random effect modelling within-subject dependence (i) by group (j); e_{ij} represents the normally distributed residual error; and the B_1, B_2, and B_3 coefficients indicate how fixation levels change with age and by group. Initial evaluation of the data indicated an inverse relationship between body fixation and age, and was therefore also assessed with the following model:

$$\text{body fixation}_{ij} = d_i + \text{intercept}_j + (B_{1j}/\text{age}_{ij}) + e_{ij}$$

In all cases, the intercept and B terms were modelled as fixed effects but were allowed to vary by group. Degrees of freedom were calculated by the Satterthwaite method (equal variances not assumed). Positively skewed data (for example, body- and object-fixation trials) were log-transformed; plots show untransformed data. *F* tests and log-likelihood ratios were used to determine whether a linear, quadratic, cubic or inverse relationship best described the data. Growth curves from hierarchical linear modelling are plotted in Extended Data Figs 4 and 5, and the regression parameters for eyes, mouth, body and object are given in Extended Data Table 1a.

Throughout our analyses, PACE parameters were selected by generalized cross-validation[22]. Mean fixation curves from Fig. 2 , together with the effects of adding or subtracting principal component functions (following the convention of ref. 21), smoothing kernel bandwidths, and fractions of variance explained per principal component can be found in Extended Data Fig. 7 and Extended Data Table 1b). The Akaike Information Criterion, with likelihood of measurements conditional on estimated random coefficients, was applied for selecting the number of principal components[22]. Derivatives were computed by the PACE-QUO method[35].

30. Klin, A. *et al.* Social and communication abilities and disabilities in higher functioning individuals with autism spectrum disorders. *J. Autism Dev. Disord.* **37,** 748–759 (2007).
31. Speer, L. L., Cook, A. E., McMahon, W. M. & Clark, E. Face processing in children with autism: effects of stimulus contents and type. *Autism* **11,** 265–277 (2007).
32. Shultz, S., Klin, A. & Jones, W. Inhibition of eye blinking reveals subjective perceptions of stimulus salience. *Proc. Natl Acad. Sci. USA* **108,** 21270–21275 (2011).
33. Leigh, R. J. & Zee, D. S. *The Neurology of Eye Movements* 3rd edn (Oxford Univ. Press, 1999).
34. Hall, P., Müller, H.-G. & Yao, F. Estimation of functional derivatives. *Ann. Stat.* **37,** 3307–3329 (2009).
35. Liu, B. & Müller, H. G. Estimating derivatives for samples of sparsely observed functions, with application to online auction dynamics. *J. Am. Stat. Assoc.* **104,** 704–717 (2009).
36. Tang, R. & Müller, H.-G. Pairwise curve synchronization for functional data. *Biometrika* **95,** 875–889 (2008).
37. Burchinal, M., Nelson, L. & Poe, M. In *Best Practices in Quantitative Methods for Developmentalists* (eds McCartney, K.,Burchinal, M. & Bub, K.) *Monogr. Soc. Res. Child Dev.* **71,** 65–87 (2006).

©2013 Macmillan Publishers Limited. All rights reserved

LETTER

doi:10.1038/nature12722

Dysfunctional nitric oxide signalling increases risk of myocardial infarction

Jeanette Erdmann[1,2]*, Klaus Stark[3,4]*, Ulrike B. Esslinger[3,5]*, Philipp Moritz Rumpf[6,7]*, Doris Koesling[8], Cor de Wit[2,9], Frank J. Kaiser[2,10], Diana Braunholz[10], Anja Medack[1], Marcus Fischer[3], Martina E. Zimmermann[3], Stephanie Tennstedt[1], Elisabeth Graf[11,12], Sebastian Eck[11,12], Zouhair Aherrahrou[1,2], Janja Nahrstaedt[1], Christina Willenborg[1,2], Petra Bruse[1], Ingrid Brænne[1], Markus M. Nöthen[13,14], Per Hofmann[13,15], Peter S. Braund[16,17], Evanthia Mergia[8], Wibke Reinhard[6,7], Christof Burgdorf[6], Stefan Schreiber[18], Anthony J. Balmforth[19], Alistair S. Hall[20], Lars Bertram[21], Elisabeth Steinhagen-Thiessen[22], Shu-Chen Li[23,24], Winfried März[25,26,27], Muredach Reilly[28], Sekar Kathiresan[29,30,31], Ruth McPherson[32], Ulrich Walter[33,34], CARDIoGRAM†, Jurg Ott[35,36], Nilesh J. Samani[16,17], Tim M. Strom[11,12], Thomas Meitinger[6,11,12], Christian Hengstenberg[6,7] & Heribert Schunkert[6,7]

Myocardial infarction, a leading cause of death in the Western world[1], usually occurs when the fibrous cap overlying an atherosclerotic plaque in a coronary artery ruptures. The resulting exposure of blood to the atherosclerotic material then triggers thrombus formation, which occludes the artery[2]. The importance of genetic predisposition to coronary artery disease and myocardial infarction is best documented by the predictive value of a positive family history[3]. Next-generation sequencing in families with several affected individuals has revolutionized mutation identification[4]. Here we report the segregation of two private, heterozygous mutations in two functionally related genes, *GUCY1A3* (p.Leu163Phefs*24) and *CCT7* (p.Ser525Leu), in an extended myocardial infarction family. *GUCY1A3* encodes the α1 subunit of soluble guanylyl cyclase (α1-sGC)[5], and *CCT7* encodes CCTη, a member of the tailless complex polypeptide 1 ring complex[6], which, among other functions, stabilizes soluble guanylyl cyclase. After stimulation with nitric oxide, soluble guanylyl cyclase generates cGMP, which induces vasodilation and inhibits platelet activation[7]. We demonstrate *in vitro* that mutations in both *GUCY1A3* and *CCT7* severely reduce α1-sGC as well as β1-sGC protein content, and impair soluble guanylyl cyclase activity. Moreover, platelets from digenic mutation carriers contained less soluble guanylyl cyclase protein and consequently displayed reduced nitric-oxide-induced cGMP formation. Mice deficient in α1-sGC protein displayed accelerated thrombus formation in the microcirculation after local trauma. Starting with a severely affected family, we have identified a link between impaired soluble-guanylyl-cyclase-dependent nitric oxide signalling and myocardial infarction risk, possibly through accelerated thrombus formation. Reversing this defect may provide a new therapeutic target for reducing the risk of myocardial infarction.

The starting point of the present study (work flow in Supplementary Fig. 1) was the identification of a family with 32 members diagnosed with coronary artery disease (CAD), of whom 22 had early onset of the disease (≤60 years of age). Given the high mortality rates of myocardial infarction (MI), DNA was available from only 15 affected family members (Fig. 1 and Supplementary Fig. 2; clinical characteristics in Supplementary Table 1). Microsatellite-based linkage analysis failed to identify any significant single-locus log odds ratio (lod) scores. We decided to sequence the exome in three distantly related family members (III.13, III.24 and III.26; Fig. 1, for statistical and methodological considerations see Supplementary Information). Variants found in any of 800 control exomes from patients with unrelated diseases were excluded. Considering only rare, potentially functional relevant variants (minor allele frequency (MAF) $< 0.5\%$) and a dominant model, all three affected members showed two loss-of-function (*GUCY1A3* and *ETFDH*) and two non-synonymous (*CCT7* and *GCLC*) variants (Supplementary Table 2). These four variants were investigated (1) for presence in further control individuals, (2) for co-segregation pattern in the family assuming single- or two-locus linkage models (primers and PCR conditions in Supplementary Table 3), and (3) for biological links to CAD or MI in the literature (Supplementary Table 2). *ETFDH* and *GCLC* were not considered further, because neither single- nor two-locus linkage analysis produced a signal. Single-locus linkage analyses revealed a maximum lod score of 0.08 at recombination fraction $\theta_3 = 0.33$ for the variant in *GUCY1A3*, and 1.11 at $\theta_1 = 0.19$ in *CCT7*. However, in two-locus analyses, a maximum lod score of 5.68 was

[1]Institut für Integrative und Experimentelle Genomik, Universität zu Lübeck, 23562 Lübeck, Germany. [2]German Centre for Cardiovascular Research (DZHK), partner site Hamburg/Lübeck/Kiel, 23562 Lübeck, Germany. [3]Klinik und Poliklinik für Innere Medizin II, Universitätsklinikum Regensburg, 93053 Regensburg, Germany. [4]Department of Genetic Epidemiology, University of Regensburg, 93053 Regensburg, Germany. [5]Institut National de la Santé et de la Recherche Médicale (INSERM), UMR-S937 Paris, France. [6]Deutsches Herzzentrum München and 1. Medizinische Klinik, Klinikum rechts der Isar, Technische Universität München, 80636 München, Germany. [7]German Centre for Cardiovascular Research (DZHK), partner site Munich Heart Alliance, 80636 Munich, Germany. [8]Department of Pharmacology and Toxicology, Ruhr-University Bochum, 44801 Bochum, Germany. [9]Institut für Physiologie, Universität zu Lübeck, 23562 Lübeck, Germany. [10]Institut für Humangenetik, Universität zu Lübeck, 23562 Lübeck, Germany. [11]Institute of Human Genetics, Helmholtz Zentrum München, German Research Center for Environmental Health, 85764 Neuherberg, Germany. [12]Institute of Human Genetics, Technische Universität München, 81675 München, Germany. [13]Institute of Human Genetics, University of Bonn, 53127 Bonn, Germany. [14]Department of Genomics, Research Center Life & Brain, University of Bonn, 53127 Bonn, Germany. [15]Division of Medical Genetics, University Hospital Basel and Department of Biomedicine, University of Basel, 4003 Basel, Switzerland. [16]Department of Cardiovascular Sciences, University of Leicester, Leicester LE1 7RH, UK. [17]Leicester National Institute for Health Research Biomedical Research Unit in Cardiovascular Disease, Glenfield Hospital, Leicester LE1 7RH, UK. [18]Institute of Clinical Molecular Biology, Christian-Albrecht-Universität, 24105 Kiel, Germany. [19]Division of Cardiovascular and Diabetes Research, Multidisciplinary Cardiovascular Research Centre, Leeds Institute of Genetics, Health and Therapeutics, University of Leeds, Leeds LS2 9JT, UK. [20]Division of Cardiovascular and Neuronal Remodelling, Multidisciplinary Cardiovascular Research Centre, Leeds Institute of Genetics, Health and Therapeutics, University of Leeds, Leeds LS2 9JT, UK. [21]Department of Vertebrate Genomics, Max Planck Institute for Molecular Genetics, 14195 Berlin, Germany. [22]Charité Research Group on Geriatrics, Charité-Universitätsmedizin, 10117 Berlin, Germany. [23]Center for Lifespan Psychology, Max Planck Institute for Human Development, 14195 Berlin, Germany. [24]Department of Psychology, TU Dresden, 01062 Dresden, Germany. [25]Synlab Academy and Business Development, synlab Services GmbH, 68165 Mannheim, Germany. [26]Clinical Institute of Medical and Chemical Laboratory Diagnostics, Medical University of Graz, 8036 Graz, Austria. [27]Medical Clinic V, Medical Faculty Mannheim, University of Heidelberg, 68167 Mannheim, Germany. [28]The Cardiovascular Institute, University of Pennsylvania, Philadelphia, Pennsylvania 19104, USA. [29]Cardiovascular Research Center and Cardiology Division, Massachusetts General Hospital, Boston, Massachusetts 02215, USA. [30]Center for Human Genetic Research, Massachusetts General Hospital, Boston, Massachusetts 02215, USA. [31]Program in Medical and Population Genetics, Broad Institute of Harvard and Massachusetts Institute of Technology (MIT), Cambridge, Massachusetts 02215, USA. [32]University of Ottawa, Heart Institute, Ottawa, Ontario K1Y 4W7, Canada. [33]Centrum für Thrombose und Hämostase (CTH), Universitätsmedizin Mainz, 55131 Mainz, Germany. [34]German Centre for Cardiovascular Research (DZHK), partner site RheinMain, 55131 Mainz, Germany. [35]Institute of Psychology, Chinese Academy of Sciences, Beijing 100864, China. [36]Laboratory of Statistical Genetics, Rockefeller University, New York 10065, USA.

*These authors contributed equally to this work.

†A list of authors and their affiliations appears in the Supplementary Information.

©2013 Macmillan Publishers Limited. All rights reserved

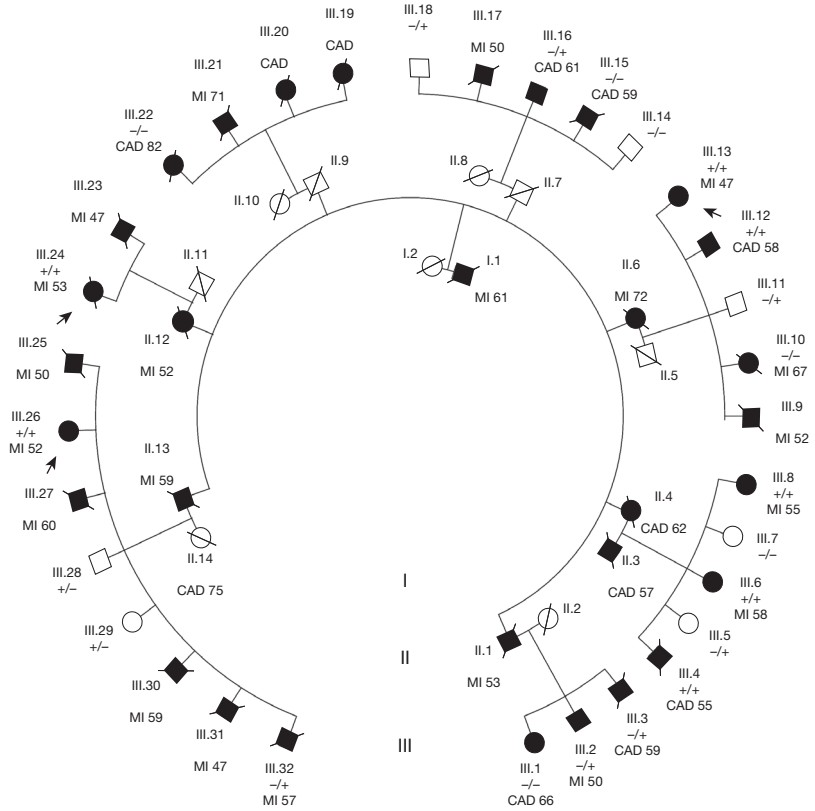


Figure 1 | Pedigree of the extended MI family with several individuals suffering from myocardial infarctions. White symbols denote healthy individuals, black symbols denote affected individuals; squares represent males, circles represent females. Crossed symbols represent deceased individuals. Age of onset is given next to the disease. MI, myocardial infarction; CAD, coronary artery disease. Persons III.13, III.24 and III.26 were exome-sequenced; +/+ denotes double-mutation carriers (p.Leu163Phefs*24^{+}/p.Ser525Leu^{-}); +/− denotes probands carrying only the p.Leu163Phefs*24 mutation in *GUCY1A3*; −/+ denotes probands carrying only the p.Ser525Leu mutation in *CCT7*.

obtained at $\theta_1 = 0.21$, with θ_2 fixed at 0.0001 (Supplementary Fig. 3 and Supplementary Information).

The single nucleotide insertion (T) in exon 6 of *GUCY1A3* (NM_001130683.2: c.488dup, p.Leu163Phefs*24) resulted in a frameshift and a premature stop codon after 24 aberrant amino acids. This variant was present in 7 out of 15 affected and 2 out of 7 unaffected family members for whom DNA was available. The second mutation is a single nucleotide substitution (C>T) in exon 10 of *CCT7* (NM_001166284) leading to a missense mutation at amino acid position 525 (p.Ser525Leu). It was present in 11 out of 15 affected and 3 out of 7 unaffected family members. Notably, all seven carriers of digenic mutations were affected (Fig. 1). Both mutations were absent in 3,150 healthy subjects and 3,842 unrelated MI cases, as determined by TaqMan technology, and are not listed in the current release of the NHLBI Exome Sequencing Project based on 6,503 samples drawn from multiple cohorts (Exome Variant Server, http://evs.gs.washington.edu/EVS/; accessed June 2013).

This finding of digenic inheritance underscores the importance of considering possible interactions between mutant proteins identified by sequencing experiments for understanding segregation patterns within families. It should be noted that some individuals in the family with single mutations had not developed the disease at the time of recruitment, and others had MI without carrying either mutation (Fig. 1). The latter can be expected, from a statistical point of view, for a highly prevalent disease and demonstrates a challenge in analysing the genetics of common conditions (Supplementary Information).

To study the linkage between rare *GUCY1A3* and *CCT7* variants and familial MI risk beyond this index family, the respective coding exons were sequenced (Supplementary Table 4) in 48 patients from 22 additional MI families with >5 affected family members (Supplementary Table 5), and p.Gly537Arg in *GUCY1A3* was identified in one affected family member. This highly conserved variant (Supplementary Fig. 4A) was subsequently found in 3 out of 5 affected members of this family, and was not present in the current 1000 Genome release[8], in the NHLBI Exome Sequencing Project (February 2013), or in 3,150 controls or 3,842 MI cases.

Furthermore, we searched for rare potential deleterious variants in *GUCY1A3* and *CCT7* in 252 young MI cases (age of onset between 24 and 49 years, 24% women) with a positive family history, and 800 individuals affected with other diseases (for example, mental retardation, type 2 diabetes, mitochondriopathy, Charcot–Marie–Tooth disease), for whom full exome sequencing data was available. In *GUCY1A3*, we identified 8 rare missense mutations (5 (2%) in CAD or MI, and 3 (0.37%) in other diseases, Fisher's exact test $P = 0.023$; Supplementary Table 6A). In *CCT7*, we identified 7 different missense mutations (3 (1.2%) in CAD or MI, and 5 (0.62%) in other diseases, $P = 0.12$; Supplementary Table 6B). Notably, p.Ser525Leu in *CCT7* was found in an additional patient suffering from premature MI (age of onset 43 years). No other person carrying mutations in both *GUCY1A3* and *CCT7* genes was found.

We analysed the functional implications of the two newly identified rare variants in *GUCY1A3* (p.Leu163Phefs*24 and p.Gly537Arg), which encodes the α1 subunit of soluble guanylyl cyclase (α1-sGC), by introducing respective point mutations and transfection into human embryonic kidney 293 (HEK 293) cells (Fig. 2). Compared to transfection using a wild-type transgene, the amount of α1-sGC protein was reduced by 96% (p.Leu163Phefs*24) and 80% (p.Gly537Arg) after mutant transfection. This was associated with an almost complete loss of enzyme activity in cells transfected with these mutants (<10% of wild-type cGMP production after nitric oxide (NO) stimulation). The reduced protein content of the p.Gly537Arg mutant is probably due to impaired stability of the mutated protein.

To evaluate the relevance of CCTη for sGC protein integrity, the protein was successfully reduced by short interfering RNA (siRNA) in human aortic smooth muscle cells (HASMC) with three pooled *CCT7*-specific siRNAs (10–20 nM), but remained unchanged in controls (scrambled siRNA), as verified by western blot. Downregulation of CCTη markedly decreased protein levels of the α1 and β1 subunits

©2013 Macmillan Publishers Limited. All rights reserved

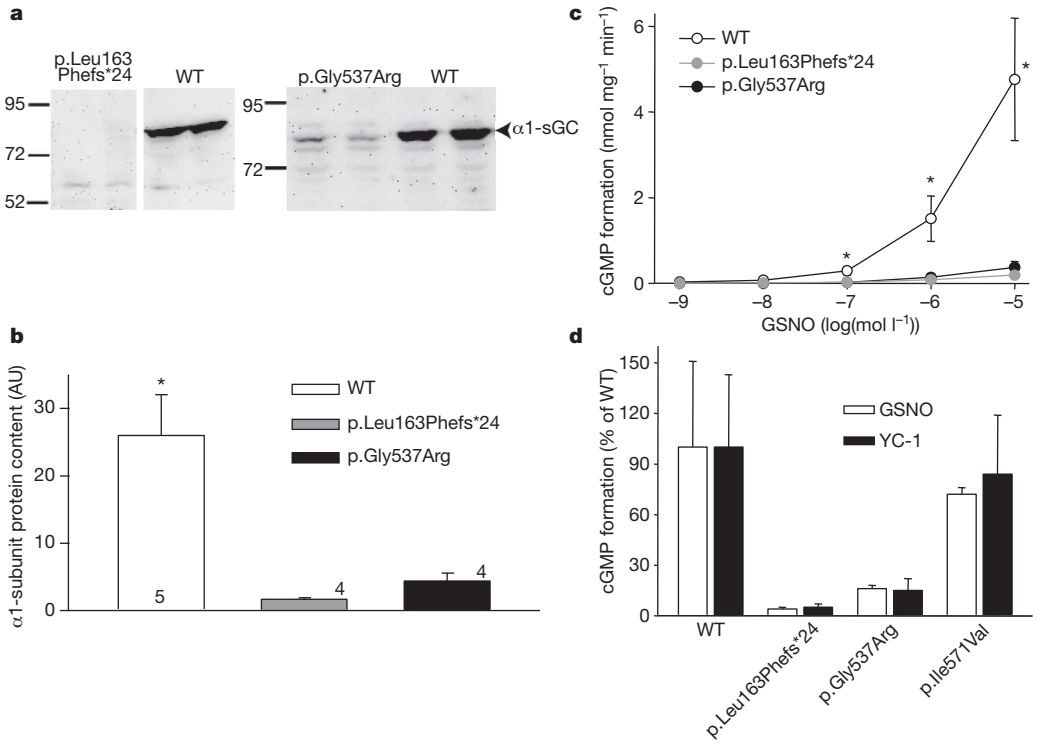


Figure 2 | Reduced expression and enzymatic activity of the identified sGC mutants in HEK 293 cells. **a**, **b**, *GUCY1A3* mutants were expressed together with β1-sGC in HEK 293 cells. Representative western blots of α1-sGC expression are shown (**a**); α1-sGC protein was strongly reduced in mutants (**b**, numbers in bars are independent transfections performed in duplicates). **c**, Accordingly, NO-induced concentration-dependent cGMP formation was significantly attenuated after transfection with mutant proteins ($n = 7$ (wild type; WT) or 4 experiments). **d**, cGMP formation was similarly reduced if sGC was activated by a pharmacological stimulator (YC-1, 100 μM; $n = 3$). GSNO, *S*-nitrosoglutathione; YC-1, 3-(5′-hydroxymethyl-2′-furyl)-1-benzylindazole. $^*P < 0.05$ versus other groups (Mann–Whitney, Bonferroni corrected). AU, arbitrary units. Error bars indicate s.e.m.

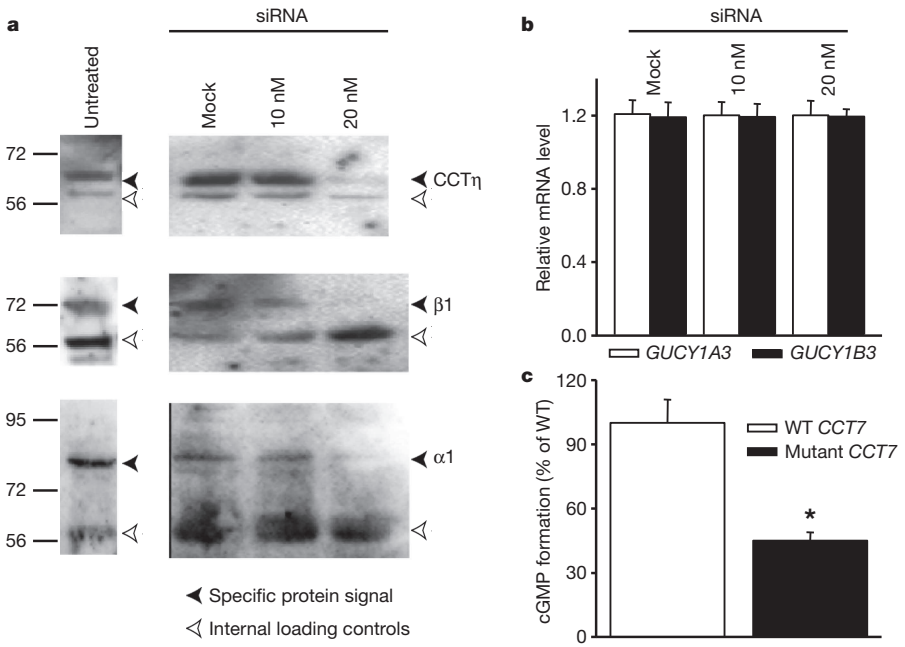


Figure 3 | CCTη is required for sGC expression and function. **a**, Expression of CCT7 was downregulated by transfection of 20 nM *CCT7* siRNAs in HASMC, but unchanged by scrambled (mock, 20 nM) or 10 nM *CCT7* siRNA compared to extracts of untreated HASMC. Reduction of *CCT7* decreased β1-sGC protein levels, and α1-sGC was correspondingly reduced (representative for six experiments). **b**, Quantitative PCR analyses excluded alterations on *GUCY1A3* (α1) and *GUCY1B3* (β1) mRNA levels by siRNA-mediated decrease of CCTη. **c**, NO-stimulated cGMP formation was strongly reduced in HEK 293 cells co-transfected with sGC (α1β1) and mutated CCTη (p.Ser525Leu) compared to wild-type CCTη. $n = 4$, $^*P < 0.05$ versus wild type (paired *t*-test). Error bars indicate s.e.m.

©2013 Macmillan Publishers Limited. All rights reserved

of sGC, whereas the sGC subunits were unaffected in controls (Fig. 3a). However, messenger RNA levels of *GUCY1A3* (α1) and *GUCY1B3* (β1) were not affected by siRNA-mediated *CCT7* knockdown (Fig. 3b). These data identify a functional role for CCTη in maintaining sGC protein levels, presumably by stabilizing the sGC protein complex. The functional effect of the identified mutation in *CCT7* was studied by co-expression of mutant (p.Ser525Leu) or wild-type *CCT7*, together with α1- and β1-sGC in HEK 293 cells. Analysis of NO-stimulated cGMP formation revealed reduced sGC activity (by ~50%) in cells expressing mutant compared to wild-type *CCT7* (Fig. 3c).

We then measured sGC protein and cGMP-forming activity in isolated platelets from family members. Three affected digenic mutation carriers, five mutation carriers with either *GUCY1A3* (p.Leu163Phefs*24) or *CCT7* (p.Ser525Leu) mutation, and four non-carriers were available for this study. Platelets of digenic mutation carriers contained significantly less α1- and β1-sGC, and also produced significantly lower amounts of cGMP after stimulation with NO compared to single-mutation carriers or non-carriers (Fig. 4).

cGMP formation in individuals carrying only the *GUCY1A3* p.Leu163Phefs*24 variant was lower than in non-carriers (2.0 ± 0.0 nmol mg^{-1} min^{-1} versus 3.1 ± 0.4 nmol mg^{-1} min^{-1}). Yet, as only two individuals with just the *GUCY1A3* p.Leu163Phefs*24 variant were available for these measurements, this observation is not statistically significant. cGMP formation in platelets of mice heterozygous for α1-sGC was reduced by roughly 50%, clearly demonstrating that both gene copies contribute to sGC function in mice (Supplementary Fig. 6).

Platelet aggregation represents an important feature of thrombus formation in MI. Several pathways stimulate platelet aggregation, and cGMP inhibits platelet activation[9]. Having observed the effect of *GUCY1A3* and *CCT7* mutations on sGC expression and cGMP production, we directly tested the effect of a loss of *GUCY1A3 in vivo*, and demonstrated that mice lacking α1-sGC had enhanced thrombus formation (Fig. 5), providing a potential mechanistic link between the identified mutations in the sGC pathway and MI through an enhanced thrombotic tendency.

Notably, two recent large-scale genome-wide association studies (GWAS)[10,11] identified a common variant (rs769238) on chromosome 4q32.1 overlapping with the *GUCY1A3* gene, and this variant displayed genome-wide significant association with CAD or MI (the risk allele frequency of rs7692387 is about 80%) (Supplementary Fig. 7a, b). As with any significant GWAS hit, this only indicates a suggestion that the nearby gene is involved. However, our findings of rare variants in two families and in unrelated MI and CAD cases, as well as the *in vitro*/*in vivo* experimental data, now provide substantial evidence for the

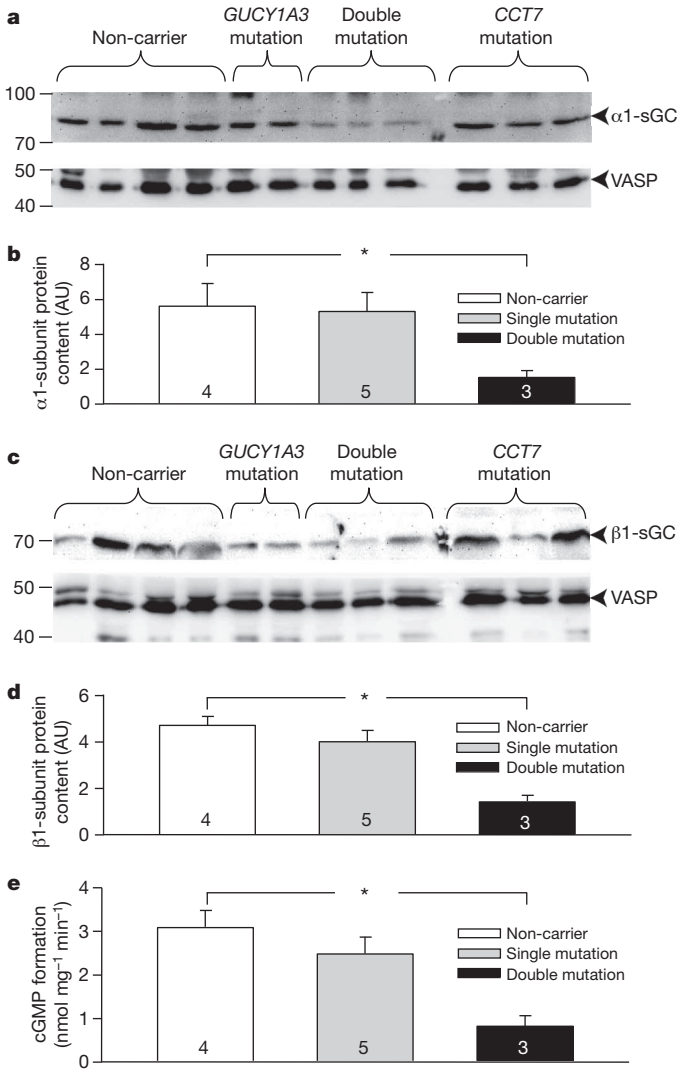


Figure 4 | Reduced sGC expression and activity in platelets of double-mutation carriers. a–d, Expression of α1- and β1-sGC in platelets of members from family 2001 is shown by representative western blot (**a**, **c**) and quantified in quadruplicates (**b**, **d**) (loading control: VASP). Single-mutation carriers are merged in a single group because western blotting did not reveal obvious differences between them. **e**, Only double-mutation carriers exhibited reduced amounts of α1-sGC and attenuated NO-dependent cGMP formation (100 μM GSNO), determined in homogenates of platelets. The dimerizing partner, β1-sGC, was reduced accordingly in double-mutation carriers (**c**, **d**). Numbers in bars denote the number of family members analysed. *$P < 0.05$ (*t*-test, only non-carriers). Error bars indicate s.e.m.

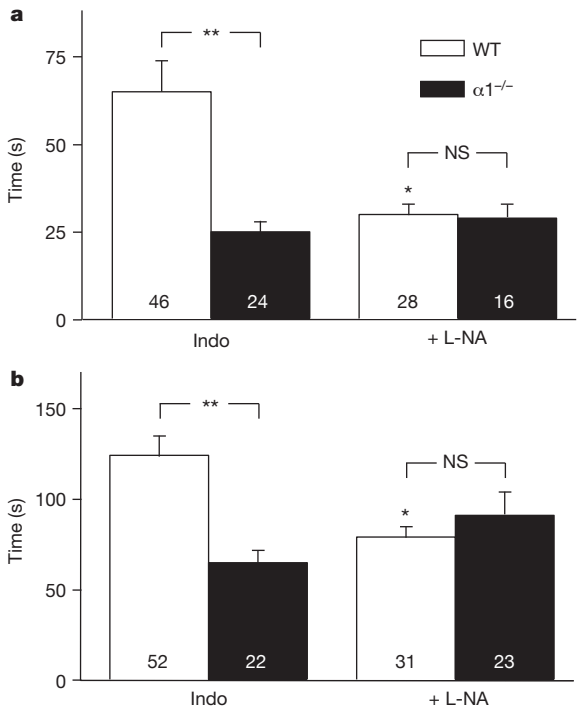


Figure 5 | Thrombus formation in-vivo in mice deficient for the α1-sGC (α1$^{-/-}$). Thrombus formation was initiated in arterioles by photoexcitation. **a**, **b**, Time to visible thrombus formation (**a**) and complete occlusion (**b**) indicated by flow stop were assessed during prostaglandin inhibition (indometacin (indo), 3 μM) and after additional NO synthase inhibition (*N*-nitro-L-arginine (L-NA), 30 μM). Thrombus formation was accelerated in α1$^{-/-}$ mice after indometacin. Inhibition of NO enhanced thrombus formation only in wild type, and abolished differences between genotypes, indicating that endogenous NO counteracts thrombus formation in wild-type, but not in α1$^{-/-}$ mice. Numbers in bars indicate numbers of arterioles studied in 7 α1$^{-/-}$ and 14 wild-type mice. *$P < 0.05$ versus indometacin; **$P < 0.01$ between genotypes (Mann–Whitney). Error bars indicate s.e.m.

©2013 Macmillan Publishers Limited. All rights reserved

causal involvement of guanylyl cyclase variation in the disease process studied in the GWAS[10,11].

One objective of identifying pathways associated with disease risk is to find new therapeutic targets. Further confirmation is required whether variants in *GUCY1A3* and *CCT7* affect MI risk through platelet activation or other mechanisms. Nevertheless, the sGC system is particularly amenable to therapy and a new class of cardiovascular drugs, for example, sGC stimulators or activators, are increasingly recognized as a treatment option for cardiovascular diseases[12]. Our genetic and functional findings provide strong support for further pursuit of this possibility in relation to MI. Furthermore, our study highlights the challenges and opportunities of large-scale sequencing in severely affected families, as novel disease mechanisms (impaired sGC activity causing MI), unexpected contributors to the molecular aetiology (a chaperone), and unusual inheritance patterns (synergistic digenic mutations) may come together and explain a rather private disease entity.

METHODS SUMMARY

Exome sequencing in three affected cousins of a large MI family was performed on a Genome Analyzer IIx system (Illumina). Linkage analysis was carried out using the Affymetrix Human Mapping 10K Array. We assumed a high-penetrance general dominant model and constructed a multiplicative (interaction, epistasis), two-locus model using the LINKAGE (single-locus models) and TLINKAGE (two-locus models) programs. The functional implications of the rare variants were analysed by introducing respective point mutations in α1-sGC encoded by *GUCY1A3* and co-expression with β1-sGC in HEK 293 cells. To evaluate the functional relevance of CCTη, *CCT7* expression was reduced by siRNA in HASMC. The effect of CCTη mutation was assessed by measuring sGC activity in HEK 293 cells co-expressing sGC and mutant or wild-type CCTη. cGMP-forming activity was measured in isolated platelets from family members and mice heterozygous for α1-sGC. We monitored arteriolar thrombus formation in mice deficient for α1-sGC in response to a confined focused trauma (photoexcitation) in the microcirculation *in vivo*.

Online Content Any additional Methods, Extended Data display items and Source Data are available in the online version of the paper; references unique to these sections appear only in the online paper.

Received 22 March 2012; accepted 27 September 2013.
Published online 10 November 2013.

1. World Health Organization. The top 10 causes of death. Fact sheet no. 310; http://www.who.int/mediacentre/factsheets/fs310/en/index.html (2011).
2. Finn, A. V., Nakano, M., Narula, J., Kolodgie, F. D. & Virmani, R. Concept of vulnerable/unstable plaque. *Arterioscler. Thromb. Vasc. Biol.* **30,** 1282–1292 (2010).
3. Lloyd-Jones, D. M. *et al.* Parental cardiovascular disease as a risk factor for cardiovascular disease in middle-aged adults: a prospective study of parents and offspring. *J. Am. Med. Assoc.* **291,** 2204–2211 (2004).
4. Bamshad, M. J. *et al.* Exome sequencing as a tool for Mendelian disease gene discovery. *Nature Rev. Genet.* **12,** 745–755 (2011).
5. Mergia, E., Friebe, A., Dangel, O., Russwurm, M. & Koesling, D. Spare guanylyl cyclase NO receptors ensure high NO sensitivity in the vascular system. *J. Clin. Invest.* **116,** 1731–1737 (2006).
6. Leitner, A. *et al.* The molecular architecture of the eukaryotic chaperonin TRiC/CCT. *Structure* **20,** 814–825 (2012).
7. Zabel, U., Weeger, M., La, M. & Schmidt, H. H. Human soluble guanylate cyclase: functional expression and revised isoenzyme family. *Biochem. J.* **335,** 51–57 (1998).
8. The 1000 Genomes Project Consortium. A map of human genome variation from population-scale sequencing. *Nature* **467,** 1061–1073 (2010).
9. Moro, M. A. *et al.* cGMP mediates the vascular and platelet actions of nitric oxide: confirmation using an inhibitor of the soluble guanylyl cyclase. *Proc. Natl Acad. Sci. USA* **93,** 1480–1485 (1996).
10. Deloukas, P. *et al.* Large-scale association analysis identifies new risk loci for coronary artery disease. *Nature Genet.* **45,** 25–33 (2013).
11. Lu, X. *et al.* Genome-wide association study in Han Chinese identifies four new susceptibility loci for coronary artery disease. *Nature Genet.* **44,** 890–894 (2012).
12. Stasch, J. P., Pacher, P. & Evgenov, O. V. Soluble guanylate cyclase as an emerging therapeutic target in cardiopulmonary disease. *Circulation* **123,** 2263–2273 (2011).

Supplementary Information is available in the online version of the paper.

Acknowledgements We thank all the family members who participated in this research. Without the continuous support of these patients over more than 15 years, the present work would not have been possible. We would like to thank S. Wrobel, S. Stark, A. Liebers, K. Franke, J. Stegmann-Frehse, M. Behrensen, M. Schmid, J. Eckhold, D. Wöllner, U. Krabbe and J. Simon for technical assistance. Furthermore, we would like to thank M. Becker, N. Buchholz, I. Demuth, R. Eckardt, H. Heekeren, U. Lindenberger, M. Lövdén, L. Müller, W. Nietfeld, G. Pawelec, F. Schmiedeck, T. Siedler and G. G. Wagner for their contributions to BASE-II. We also would like to thank S. Herterich and S. Gambaryan for advice, and B. Mayer, U. Hubauer, K.-H. Ameln and A. Großhennig for help with GerMIFS. We thank WTCCC+ and the WTCCC-CAD2 investigators for access to their data. The study is supported by the Deutsche Forschungsgemeinschaft and the German Federal Ministry of Education and Research (BMBF) in the context of the German National Genome Research Network (NGFN-2 (01GS0417) and NGFN-plus (01GS0832)), the FP6 and FP7 EU-funded integrated projects Cardiogenics (LSHM-CT-2006-037593), ENGAGE (201413), and GEUVADIS (261123), the binational BMBF/ANR funded project CARDomics (01KU0908A), the local focus programs 'Kardiovaskuläre Genomforschung' and 'Medizinische Genetik' of the Universität zu Lübeck, and the University Hospital of Regensburg, Germany. The German Federal Ministry for Education and Research provided funding for BASE-II (BMBF; grant no. 16SV5538). Support by NSFC grant 30730057 from the Chinese Government (to J.O.) is gratefully acknowledged. N.J.S. holds a Chair funded by the British Heart Foundation, and is supported by the Leicester NIHR Biomedical Research Unit in Cardiovascular Disease. U.W. is supported by the BMBF (01EO1003). M.M.N. is a member of the DFG-funded Excellence Cluster ImmunoSensation.

Author Contributions J.E., C.H., F.J.K., T.M., N.J.S., H.S. and K.S. designed the study. Z.A., D.B., P.B., C.d.W., S.E., U.B.E., E.G., F.J.K., D.K., A.M., E.M., W.R., P.M.R., T.M.S. and M.E.Z. conducted the experiments. I.B., M.F., J.N., J.O., K.S., T.M.S., S.T. and C.W. analysed the data. A.J.B., L.B., P.S.B., C.B., A.S.H., P.H., S.K., S.-C.L., W.M., R.M., T.M., M.M.N., M.R., N.J.S., S.S., E.S.-T. and U.W. provided material, data and analysis tools. J.E., C.d.W., C.H., F.J.K., N.J.S. and H.S. wrote the paper. C.H. and H.S. contributed equally. See Supplementary Information for Members of CARDIoGRAM.

Author Information Variant data is available in ClinVar (http://www.ncbi.nlm.nih.gov/clinvar/) with accession numbers SCV000083870 for NM_001130683.2:c.488dup and SCV000083871 for NM_001166284.1:c.1313C>T. Reprints and permissions information is available at www.nature.com/reprints. The authors declare no competing financial interests. Readers are welcome to comment on the online version of the paper. Correspondence and requests for materials should be addressed to C.H. (hengstenberg@dhm.mhn.de) or J.E. (jeanette.erdmann@iieg.uni-luebeck.de).

©2013 Macmillan Publishers Limited. All rights reserved

METHODS

Extended MI families and unrelated samples. The ascertainment strategy of MI families is described elsewhere[13,14] and in the Supplementary Information. In brief, index patients had suffered from MI before the age of 60 years. If at least one additional living sibling presented with MI or severe CAD (defined by percutaneous coronary intervention or coronary artery bypass grafting), the entire family (index patient, available parents and all siblings) was contacted and invited to participate in the study. A total of 26 extended families could be recruited, each with more than 5 living CAD or MI patients, and totalling $n = 1{,}001$ individuals. Figure 1 depicts the pedigree of the MI family used for exome sequencing. Clinical and angiographic characteristics are detailed in Supplementary Table 1.

Exome sequencing. Exome sequencing was performed as 54-bp (base pair) paired-end runs on a Genome Analyzer IIx system (Illumina) after in-solution enrichment of exonic sequences (SureSelect Human All Exon 38 Mb kit, Agilent), yielding on average 6.2 gigabases (Gb) of sequence per individual. The average read depth was 78, with between 84.5 and 85.6% of the target regions covered at least 20×. Read alignment was performed with BWA (v. 0.5.8) using the default parameters. We used the human genome assembly hg19 (GRCh37) as reference. A small percentage of duplicate reads (4–5%) were removed. Single nucleotide variants (SNVs) and small insertions and deletions (indels) were detected using SAMtools (v 0.1.7). For the variant filter part of SAMtools, we used the default parameters with the exception of setting a maximum read depth to 9,999. Furthermore, we required putative SNVs to fulfil the following criteria: (1) median base quality of the variant bases of at least 15; (2) a minimum of 15% of reads showing the variant base; and (3) the variant base is indicated by at least 5% of reads coming from different strands. Variant annotation was performed using custom Perl scripts, using data from dbSNP (v131) and the UCSC Genome Browser 'knownGene' track.

Mutation validation. Annotations of SNVs were based on the UCSC database. Mutation validation was performed through PCR and Sanger sequencing of candidate gene region identified via exome sequencing. After confirmation of variants, additional family members were screened considering co-segregation. Primers used for mutation validation and PCR conditions are listed in Supplementary Table 3. We sequenced the coding exons (Supplementary Table 4) of the 2 genes in 48 patients from 22 additional MI families with >5 affected family members (Supplementary Table 5). PolyPhen-2 prediction was done for all non-synonymous SNVs (http://genetics.bwh.harvard.edu/pph2/)[15].

Linkage analysis. Linkage analysis was carried out using the Affymetrix Human Mapping 10K Array. For the genetic linkage analysis, we assumed a high-penetrance general dominant model (for details see Supplementary Table 7). Taking these penetrances as marginal penetrances for each of two loci, we constructed a multiplicative (interaction, epistasis) two-locus model[16]. Analyses were carried out with the Windows versions of the LINKAGE (single-locus models) and TLINKAGE (two-locus models) programs.

For two-locus analysis, we assumed the locus order M_1–D_1–D_2–M_2, in which M refers to marker loci and D to disease loci. Recombination fractions in the three intervals are denoted by θ_1, θ_2 and θ_3, for M_1–D_1, D_1–D_2 and D_2–M_2, respectively. Initially, all three recombination fractions were estimated iteratively, resulting in values of 0.210, 0 and 0.436, respectively. As the two disease loci appeared closely linked, we assumed a fixed recombination fraction of $\theta_2 = 0.0001$ between them, which furnished estimates of $\theta_1 = 0.216$ and $\theta_3 = 0.5$. As marker M_2 appeared essentially unlinked with the other loci, we focused on marker M_1 and its relation with the two-locus cluster D_1–D_2.

Homology modelling. For human CCTη, several homologue X-ray structures are available. We used the yeast T-complex protein 1 subunit η (TCP1-η) as template (PDB accession 3P9G, chain G[17]) for the homology model of human CCTη. The template was received by blast search and allowed us to calculate a human CCTη model containing the amino acid p.Ser525Leu. The model was built with the YASARA 10.8.16 software package by default settings[18]. In this study, we used the hybrid model of 20 generated initial models. The model was energy-minimized by YAMBER3 force field[19,20] to remove bumps and correct the covalent geometry. After removal of conformational stress by a short steep descent minimization, the procedure continued by simulated annealing until convergence was reached. The average quality Z-score after validation with WHAT_CHECK was −1.5. This means that the model is 1.5 standard deviations below average and can be considered as good. For none of the GTP sGCs, NMR data or X-ray structures are available. Therefore, we have built a homology model of human sGC using the theoretical three-dimensional structure of bovine sGC in complex with GTP[21] (PDB accession 1AWN). The resulting model comprises the amino acids p.V472 to p.L627 of *GUCY1A3* in complex with *GUCY1B3* (p.Val412 to p.Leu572) and two GTP molecules. The model was built with the YASARA 10.8.16 software package analogue to CCT7η. The average quality Z-score after validation with WHAT_CHECK was −1.2. A structure file of the models and the alignments are available on request (Supplementary Fig. 5A, B).

sGC and CCTη mutants, platelet homogenates and cGMP-forming activity. The *GUCY1A3* subunit of sGC and CCTη was cloned by standard procedures from a human fetal brain library sub-cloned into pcDNA3.1Zeo(+) (*GUCY1A3*; Invitrogen) or pCMV6 (*CCT7*, OriGene). The *GUCY1A3* construct was co-expressed with the bovine β1 subunit, which only exerts six amino acid differences compared to the human sequence. The respective mutations were introduced with the Quick Change site-directed mutagenesis kit from Stratagene and verified by sequencing. HEK 293 cells cultured in DMEM supplemented with 5% heat-inactivated FCS were seeded at 660,000 cells per flask (25 cm^2). The next day, cells were transfected with 2.6 μg cDNA of each of the sGC subunits with FuGENE6 transfection reagent (Roche Diagnostics) according to the manufacturer's instructions. After transfection (60–70 h), cells were collected, washed and resuspended in 400 μl ice-cold buffer (50 mM NaCl, 50 mM triethanolamine/HCl, pH 7.4, containing 2 mM D,L-dithiothreitol (DTT), 1 mM EDTA, mammalian protease inhibitor cocktail (Sigma-Aldrich)), lysed by sonification (one 5-s pulse) or by passing through a 27-gauge needle (10×). After centrifugation (800*g*, 10 min, 4 °C) to remove cell debris, the protein concentration was determined in the supernatant using the Bradford Protein Assay (Bio-Rad).

Human venous blood samples (20 ml) were immediately mixed with acid citrate dextrose (5 ml, 85 mM trisodium citrate, 70 mM citric acid, 110 mM glucose). After a first centrifugation (200*g*, 15 min, room temperature), the supernatant was collected and centrifuged (1,000*g*, 10 min, room temperature), and the resulting platelet-containing pellet was resuspended in 1 ml WP buffer (5 mM HEPES, pH 7.4, 150 mM NaCl, 0.55 mM NaH_2PO_4, 7 mM $NaHCO_3$, 2.7 mM KCl, 0.5 mM $MgCl_2$, 5.6 mM glucose). Subsequently, cells were lysed by sonification (one 5-s pulse) and samples were centrifuged (20,000*g*, 15 min, room temperature). The protein content was determined in the supernatant (platelet homogenate). Samples (10 μg) were analysed in western blot for the α1 and β1subunit of sGC with specific antibodies[5]. Quantification of the signals was performed by chemiluminescence detection with a CCD camera system.

For the determination of sGC activity, supernatants (10 μg HEK 293 cell or platelet homogenate, see above) were measured at different NO concentrations (0–10 μM GSNO HEK 293 cells, or 100 μM GSNO platelets) in the presence of 300 μM GTP, 3 mM $MgCl_2$, 3 mM DTT, and 50 mM triethanolamine/HCl, pH 7.4, in a total volume of 0.1 ml for 10 min at 37 °C. Subsequently, reactions were stopped and the formed cGMP was measured in a RIA as described in more detail previously[5].

CCT7 knockdown by siRNA. HASMC (GIBCO, C-007-5C) were cultured in smooth muscle cell media 2 (PromoCell). Cells were 50–70% confluent at time of transfection. Lipofectamine RNAiMAX reagent (Invitrogen) was used for transfection according to the manufacturer's instructions. In brief, three pooled *CCT7* siRNAs (Santa Cruz, sc-43449), equivalent to a final concentration of 10–20 nM, were incubated with RNAiMAX reagent in Opti-MEM medium without serum for 20 min at room temperature. Afterwards, RNAi—RNAiMAX complexes were added to the cell cultures and incubated for 40 h at 37 °C in a saturated humidity atmosphere containing 5% CO_2. In parallel, cells were transfected with 20 nM of scrambled RNA as control.

Lysis of the cells was performed in lysis buffer (50 mM HEPES, pH 7.5, 1 mM EDTA, 1% (v/v) Nonidet-P40 (NP 40), 0.5 mM LiCl, and proteinase inhibitor cocktail (Roche)). After the addition of SDS-loading buffer (62 mM Tris, pH 6.8, 2% (w/v) SDS, 10% (v/v) glycerol and 5% (v/v) 2-mercaptoethanol) 0.005% (w/v) protein solutions were separated by SDS–PAGE (10% bisacrylamide/acrylamide) and blotted onto PVDF (polyvinylidene difluoride) membranes (Roche). Anti-CCT7 (Sigma, HPA008425), anti-GUCY1A3 (ref. 5) and GUCY1B3 (ref. 5) antibodies were used for protein detection.

Total RNA was extracted from transfected cells using the RNA easy mini kit (Qiagen) according to manufacturer's instructions. RNA was reverse-transcribed into cDNA with the Super Script First-Strand Synthesis System III (Invitrogen). Expression levels of *CCT7*, *GUCY1A3* and *GUCY1B3* were measured by TaqMan analysis using appropriate probes from Life Technologies (*CCT7*, *Hs00362446_m1*; *GUCY1A3*, *Hs01015574_m1*; and *GUCY1B3*, *Hs00168336_m1*). *HPRT* and *YWHAZ* probes (Life Technologies) served as reference genes. All measurements were performed in duplicates per PCR run. At least three runs were carried out for each sample.

Thrombus formation *in vivo* in mice deficient for α1-sGC ($\alpha1^{-/-}$). The experiments conformed to the guide for the care and use of laboratory animals published by the US National Institutes of Health, were performed in accordance with the German Animal Welfare Act and approved by local authorities (Landwirtschafts- und Umweltministerium Schleswig-Holstein, V312-72241.122-2). Experiments were performed in 3–8-month-old male mice deficient in α1-sGC ($\alpha1^{-/-}$)[5] and respective wild-type animals in a similar genetic background (BL6). Mice were housed at the animal facility of the university with free access to water and food (standard diet, Altromin) under a 12-h light/12-h dark cycle at a room temperature of 20 °C with a maximum of six mice per cage. All surgery was performed

©2013 Macmillan Publishers Limited. All rights reserved

under anaesthesia. Initially, animals were anesthetized by an intraperitoneal injection of fentanyl (0.1 mg kg^{-1}), midazolam (2 mg kg^{-1}) and medetomidin (20 mg kg^{-1}), followed by continuous intravenous application via a catheter placed in the jugular vein. During further preparation and throughout the experiment, mice were regularly pinched in the paw with forceps and also shortly blown on their whiskers to test for reactions as well as level of consciousness, and the rate of anaesthesia infusion was accordingly adjusted. The animals were tracheotomized for artificial ventilation during the experiment and their body temperature was maintained at 37 °C by convective heat. The right cremaster muscle was prepared for intravital microscopy on a custom-made stage as described[22] and continuously superfused with warmed (34 °C) saline solution (in mmol l^{-1}: 143 Na^+, 5 K^+, 2.5 Ca^{2+}, 1.2 Mg^{2+}, 127 Cl^-, 25 HCO^{3-}, 1.2 SO_4^{2-} and 1.2 H_2PO^{4-}), gassed with 5% CO_2 and 95% N_2 ($pCO_2 \approx 40$ mm Hg, $pO_2 \approx 30$ mm Hg) at rate of 8 ml min^{-1}. Arterioles were observed using a microscope (Axioskop 2FS, Zeiss) equipped with a video camera (PCO, XC-77CE, Computer Optics). Images were displayed on a video monitor and recorded on videotape (Panasonic, AG-5700) for later measurement of platelet aggregation and the vessels luminal diameter after image digitization.

In all experiments, indometacin (3 μmol l^{-1}) was added to the superfusion to block prostaglandin production 30 min before the start and throughout the experiment. During this period, 10 arterioles with diameters ranging from 7 to 51 μm (21.7 ± 1.4 and 22.3 ± 1.6 μm in wild-type and $\alpha1^{-/-}$ mice, respectively; $P = 0.80$) were chosen in each animal according to visibility and size. For later photoexcitation, high molecular mass FITC-dextran (MW 150000, TdB Consultancy AB) was injected intravenously (5 μl of a 20% solution per gram body mass) and allowed to circulate for at least 10 min before the start of the experiment. Platelet aggregation was initiated by photoexcitation of the circulating dye at 450–490 nm using a mercury lamp (HBO 100, Zeiss) and appropriate filters (filter set 09, Zeiss) in a circle with a diameter of ~100 μm that contained the arteriole under study. If flow stoppage due to thrombus formation was observed in the arteriole, further excitation was interrupted. Time to visible aggregation (onset) and time to complete arteriolar closure identified by flow stop were assessed. Arterioles with flow cessation without observing a local occluding thrombus were excluded from analysis. After studying about half of the pre-chosen vessels consecutively in the presence of indometacin, the NO-synthase inhibitor L-NA (30 μmol l^{-1}) was also applied to the superfusion solution and the second half of the vessels studied in a similar fashion. Arterioles were allocated to treatment group according to size and location within the network. Hereby, vessels of comparable sizes were assigned to each group. To avoid the examination of an arteriole downstream in the network of a beforehand-studied vessel, the latter were examined first. In some experiments, L-NA and indometacin was applied from the start to balance observation numbers between treatment groups. Therefore, the examiner was aware of the treatment as well as of the genotype of the animal under study. At the end of the experiment, maximal arteriolar diameter was assessed during superfusion of a combination of different dilators (adenosine, SNP and acetylcholine, 30 μmol$^{1-1}$ each) before the animal was killed by injection of pentobarbital.

Association analysis. For the SNP rs7692387, located in intron 6 of the *GUCY1A3* gene, we performed a two-stage analysis: a meta-analysis of GWAS for discovery, and a replication stage in additional cohorts for confirmation. As discovery stage, we used data of 22,233 cases and 64,762 controls from CARDIoGRAM[23], a meta-analysis of 14 GWAS of CAD and MI, and combined these with replication data of an additional 6,500 cases and 10,266 controls from 5 additional studies (Angio-Lueb/KoraF3, PopGen, Luric/Emil, WTCCC-CAD2, and GerMIFS IV/BASE-II). A fixed effect, pooled model was used to estimate the effect size. Details of the design of CARDIoGRAM have been published previously[24]. Only subjects reporting European ancestry were included.

For both stages, we performed analyses in each study separately. Genotyping in all studies except GerMIFS IV was carried out on Affymetrix or Illumina platforms. In GerMIFS IV, SNP rs7692387 was genotyped with TaqMan. Quality control of data was performed centrally according to previously agreed criteria including quality of the imputation, deviation from Hardy–Weinberg equilibrium in the controls, and SNP call rate.

For the CARDIoGRAM studies, a log-additive model frequency test adjusting for age (onset of the first event for cases or time of recruitment for controls) and gender and taking into account the uncertainty of possibly imputed genotypes were performed. For Angio-Lueb/KoraF3, PopGen, Luric_Emil and WTCCC2, logistic regressions were performed adjusting for age (onset of the first event for cases or time of recruitment for controls) and gender. For GerMIFS IV, a chi-squared test was performed. A summary estimate was computed using a fixed-effect model weighting each study by the inverse of its variance. A level of association of $P < 5 \times 10^{-8}$ (Bonferroni correction for 1,000,000 independent SNPs) in the combined analysis of the discovery and replication samples was assumed as significant.

Study information. LUdwigshafen RIsk and Cardiovascular Health (LURIC) study: consists of angiographically confirmed CAD (at least one coronary vessel with a stenosis >50%) cases[25]. The controls included population-based non-case subjects, and were part of a control series (Echinococcus Multilocularis and Internal Diseases in Leutkirch study (EMIL)[26]) that consisted of healthy, unrelated blood donors recruited between May and July 2004 from the south-western area of Germany.

PopGen: PopGen consists of unrelated German patients with CAD recruited in Schleswig-Holstein, through the population-based PopGen biobank with significant CAD (at least a 70% stenosis in one major coronary vessel) and age of onset <55 years, the controls were population-based[27].

Angio-Lueb/KORA F3: Lübeck Registry of Structural Heart Disease[27] consist of consecutive patients referred for coronary angiography, classified as CAD or MI cases based on the coronary angiogram (at least a 50% stenosis in one major coronary vessel) and age of onset (<65 years in males, and <70 years in females). The Kooperative Gesundheitsforschung in der Region Augsburg (KORA) F3 consisted of population-based controls.

GerMIFS IV: cases consists of consecutive patients referred for coronary angiography, classified as CAD or MI cases based on the coronary angiogram (at least a 50% stenosis in one major coronary vessel) and age of onset (<65 years in males, and <70 years in females). Control samples were recruited as part of the Berlin Aging Study II (BASE-II), a multidisciplinary study investigating factors related to human ageing. All subjects were recruited from the Berlin metropolitan area and underwent an extensive phenotypic assessment, including a two-day medical examination. None of the BASE-II subjects included here reported a history of CAD or MI, nor showed any current signs of acute cardiovascular disease. This sample included a total of 1,105 individuals (424 women and 681 men, average age at examination 56.6 years (s.d. 16.5)).

Genotyping and imputation of BASE-II. After applying standard quality-control thresholds (per sample missing rate ≤ 5%, per SNP missing rate ≤ 2%, Hardy–Weinberg equilibrium $P > 1 \times 10^{-6}$), high-quality microarray-based genotypes (using the 'Genome-Wide Human SNP Array 6.0' (Affymetrix, Inc.)) were available for 710,205 autosomal SNPs across 1,125 BASE-II subjects. These were subjected to genome-wide SNP imputations via IMPUTE v2.026 (ref. 28) using precompiled 'HapMap 3 + 1000GP CEU+TSI' panels from the IMPUTE website (Dec 2010 release). These contain HapMap 3 data (from release #2, Feb 2009) and 1,000 Genomes Project data from Phase I (interim_ (based on a sequence freeze in Aug 2010, and haplotype phasing released in Dec 2010) for autosomal SNPs. IMPUTE's average posterior call info and certainty metrices for rs7692387 were 0.966 and 0.986, respectively. For the purpose of this study, genotypes for rs7692387 were hard-coded disregarding dosage data, if individual information and certainty scores were ≥ 0.9 ($n = 1{,}060$), or coded as missing, if one or both metrics fell below 0.9 ($n = 44$).

WTCCC-CAD2. The WTCCC-CAD2 cases ($n = 1{,}213$) comprised patients with a validated history of CAD (92.7% with MI; 19.3% females, mean age at diagnosis 53.5 ± 9.6 years). Controls are from the UK 1958 birth cohort (mean age at recruitment 44 years, 43.9% females). All cases and controls were of white Caucasian origin recruited in the United Kingdom. Further details on the cohorts and genotyping are provided in the Supplementary Information.

Statistical analysis. Means and proportions for clinical characteristics and risk factors at baseline were calculated for CAD and MI cases and controls. Student's *t*-test was used to evaluate differences in means for normally distributed data, otherwise the Wilcoxon and Mann–Whitney test were used. Several comparisons were corrected according to Bonferroni. The chi-squared statistic was used to compare proportions. Conditional logistic regression models were applied after matching for analysis time, age in decades, and gender. Relative risk estimates were obtained in addition to crude models adjusted for several cardiovascular risk factors, including systolic blood pressure, smoking, body mass index, diabetes mellitus, and plasma lipid levels. All *P*-values are two-tailed, and values of less than 0.05 were considered to indicate statistical significance. Confidence intervals were calculated at the 95% level.

All subjects in all studies gave written informed consent before participating. All studies were approved by their local ethics committees.

13. Broeckel, U. *et al.* A comprehensive linkage analysis for myocardial infarction and its related risk factors. *Nature Genet.* **30,** 210–214 (2002).
14. Fischer, M. *et al.* Distinct heritable patterns of angiographic coronary artery disease in families with myocardial infarction. *Circulation* **111,** 855–862 (2005).
15. Adzhubei, I. A. *et al.* A method and server for predicting damaging missense mutations. *Nature Methods* **7,** 248–249 (2010).
16. Risch, N. Linkage strategies for genetically complex traits. III. The effect of marker polymorphism on analysis of affected relative pairs. *Am. J. Hum. Genet.* **46,** 242–253 (1990).
17. Dekker, C. *et al.* The crystal structure of yeast CCT reveals intrinsic asymmetry of eukaryotic cytosolic chaperonins. *EMBO J.* **30,** 3078–3090 (2011).

©2013 Macmillan Publishers Limited. All rights reserved

18. Krieger, E. *et al.* Improving physical realism, stereochemistry, and side-chain accuracy in homology modeling: Four approaches that performed well in CASP8. *Proteins* **77,** 114–122 (2009).
19. Krieger, E., Darden, T., Nabuurs, S. B., Finkelstein, A. & Vriend, G. Making optimal use of empirical energy functions: force-field parameterization in crystal space. *Proteins* **57,** 678–683 (2004).
20. Krieger, E., Nielsen, J. E., Spronk, C. A. & Vriend, G. Fast empirical pK_a prediction by Ewald summation. *J. Mol. Graph. Model.* **25,** 481–486 (2006).
21. Liu, Y., Ruoho, A. E., Rao, V. D. & Hurley, J. H. Catalytic mechanism of the adenylyl and guanylyl cyclases: modeling and mutational analysis. *Proc. Natl Acad. Sci. USA* **94,** 13414–13419 (1997).
22. Wölfle, S. E., Schmidt, V. J., Hoyer, J., Kohler, R. & de Wit, C. Prominent role of $K_{Ca}3.1$ in endothelium-derived hyperpolarizing factor-type dilations and conducted responses in the microcirculation *in vivo*. *Cardiovasc. Res.* **82,** 476–483 (2009).
23. Schunkert, H. *et al.* Large-scale association analysis identifies 13 new susceptibility loci for coronary artery disease. *Nature Genet.* **43,** 333–338 (2011).
24. Preuss, U. W., Koller, G., Zill, P., Bondy, B. & Soyka, M. Alcoholism-related phenotypes and genetic variants of the CB1 receptor. *Eur. Arch. Psychiatry Clin. Neurosci.* **253,** 275–280 (2003).
25. Ritsch, A. *et al.* Cholesteryl ester transfer protein and mortality in patients undergoing coronary angiography: the Ludwigshafen Risk and Cardiovascular Health study. *Circulation* **121,** 366–374 (2010).
26. Haenle, M. M. *et al.* Overweight, physical activity, tobacco and alcohol consumption in a cross-sectional random sample of German adults. *BMC Public Health* **6,** 233 (2006).
27. Schunkert, H. *et al.* Repeated replication and a prospective meta-analysis of the association between chromosome 9p21.3 and coronary artery disease. *Circulation* **117,** 1675–1684 (2008).
28. Marchini, J., Howie, B., Myers, S., McVean, G. & Donnelly, P. A new multipoint method for genome-wide association studies by imputation of genotypes. *Nature Genet.* **39,** 906–913 (2007).

©2013 **Macmillan Publishers Limited. All rights reserved**

LETTER

doi:10.1038/nature12724

Antidiabetic effects of glucokinase regulatory protein small-molecule disruptors

David J. Lloyd[1], David J. St Jean Jr[2], Robert J. M. Kurzeja[2], Robert C. Wahl[2], Klaus Michelsen[2], Rod Cupples[1], Michelle Chen[1], John Wu[1], Glenn Sivits[1], Joan Helmering[1], Renée Komorowski[1], Kate S. Ashton[2], Lewis D. Pennington[2], Christopher Fotsch[2], Mukta Vazir[2], Kui Chen[2], Samer Chmait[2], Jiandong Zhang[2], Longbin Liu[2], Mark H. Norman[2], Kristin L. Andrews[2], Michael D. Bartberger[2], Gwyneth Van[3], Elizabeth J. Galbreath[3], Steven L. Vonderfecht[3], Minghan Wang[1], Steven R. Jordan[2], Murielle M. Véniant[1] & Clarence Hale[1]

Glucose homeostasis is a vital and complex process, and its disruption can cause hyperglycaemia and type II diabetes mellitus[1]. Glucokinase (GK), a key enzyme that regulates glucose homeostasis, converts glucose to glucose-6-phosphate[2,3] in pancreatic β-cells, liver hepatocytes, specific hypothalamic neurons, and gut enterocytes[4]. In hepatocytes, GK regulates glucose uptake and glycogen synthesis, suppresses glucose production[3,5], and is subject to the endogenous inhibitor GK regulatory protein (GKRP)[6–8]. During fasting, GKRP binds, inactivates and sequesters GK in the nucleus, which removes GK from the gluconeogenic process and prevents a futile cycle of glucose phosphorylation. Compounds that directly hyperactivate GK (GK activators) lower blood glucose levels and are being evaluated clinically as potential therapeutics for the treatment of type II diabetes mellitus[1,9,10]. However, initial reports indicate that an increased risk of hypoglycaemia is associated with some GK activators[11]. To mitigate the risk of hypoglycaemia, we sought to increase GK activity by blocking GKRP. Here we describe the identification of two potent small-molecule GK–GKRP disruptors (AMG-1694 and AMG-3969) that normalized blood glucose levels in several rodent models of diabetes. These compounds potently reversed the inhibitory effect of GKRP on GK activity and promoted GK translocation both *in vitro* (isolated hepatocytes) and *in vivo* (liver). A co-crystal structure of full-length human GKRP in complex with AMG-1694 revealed a previously unknown binding pocket in GKRP distinct from that of the phosphofructose-binding site. Furthermore, with AMG-1694 and AMG-3969 (but not GK activators), blood glucose lowering was restricted to diabetic and not normoglycaemic animals. These findings exploit a new cellular mechanism for lowering blood glucose levels with reduced potential for hypoglycaemic risk in patients with type II diabetes mellitus.

To identify compounds that destabilized the GK–GKRP complex, we screened human GK activity in the presence of human GKRP and sorbitol-6-phosphate (S6P) and eliminated compounds that interacted exclusively with GK. In a previous report in which GK activity was screened in the presence of GKRP, only small molecules that acted directly on GK were found[12]. A high-throughput screen using the Amgen chemical library (Extended Data Table 1) identified a thiophene sulphonamidopiperazine (Extended Data Fig. 1), which was optimized to produce the potent functionalized piperazine compound AMG-1694 (Fig. 1a and Extended Data Fig. 1). A glucose-phosphorylation assay demonstrated the inhibitory effect of increasing concentrations of GKRP (half-maximum inhibitory concentration (IC_{50}) = 0.034 μM) on GK activation (Fig. 1b); with this same assay, AMG-1694 (Fig. 1c) was highly effective in restoring the enzymatic activity of GK (half-maximum effective concentration (EC_{50}) = 0.020 μM) in the presence of GKRP. In a direct binding assay, AMG-1694 promoted the dissociation of the GK–GKRP complex (Fig. 1d; IC_{50} = 0.007 μM), indirectly increasing GK enzymatic activity (Fig. 1c).

In surface plasmon resonance (SPR) spectroscopy experiments, S6P enhanced the GK–GKRP complex as reported previously[13–15] (Fig. 1e; dissociation constant (K_d) 0.005 μM; Extended Data Fig. 2a), whereas AMG-1694 destabilized it. S6P and AMG-1694 specifically bound GKRP (K_d = 0.029 μM (Extended Data Fig. 2b) and 0.007 μM (Fig. 1f), respectively) and not GK. In addition, AMG-1694 overrode the stabilizing effect of S6P on GK–GKRP (Fig. 1e). Furthermore, AMG-1694 bound to GKRP irrespective of S6P being pre-bound (Fig. 1f). That a distinct binding site exists for each ligand was confirmed by the 2.35 Å crystal structure of GKRP bound to S6P and AMG-1694 (Fig. 1g, h). As predicted from sequence analysis, the main body of the GKRP protein folds into two sugar isomerase (SIS) domains (Fig. 1g, h, residues 45–248 (purple) and 289–498 (green)). The residues preceding and following the SIS domains form separate domains that sit on top of the SIS domains (Fig. 1g, h, yellow and brown). Clear density was observed for both AMG-1694 and S6P in the initial stages of refinement (Extended Data Fig. 2c, d). S6P bound in the linear conformation in the expected phosphosugar-binding site of the first SIS domain. The AMG-1694-binding site is situated between the first SIS domain (Fig. 1g, h, purple) and the amino-terminal residues 9–34 (Fig. 1g, h, brown). AMG-1694 makes extensive interactions with the protein (Extended Data Fig. 2e, f), with most of the molecule buried, leaving just 6.8% of the ligand surface area exposed (Fig. 1h). The importance of this N-terminal domain was demonstrated with a GKRP truncation lacking the first 19 residues that retains binding to S6P, but not to AMG-1694 (Extended Data Fig. 2g).

The biochemical and biophysical data collectively confirmed that AMG-1694 caused the dissociation of the preformed GK–GKRP complex. We next monitored GK subcellular movement in rat primary hepatocytes (AMG-1694 is equipotent against rat GKRP). In this assay, GK was wholly detected in the nucleus at low glucose concentrations, whereas increasing doses of glucose led to more nuclear loss and cytoplasmic accumulation (Extended Data Fig. 3a, b). Treatment with AMG-1694 led to GK translocation from the nucleus to the cytoplasm (Fig. 2a and Extended Data Fig. 3c), with an IC_{50} = 0.065 μM (Fig. 2b and Extended Data Fig. 3d).

Next, we determined the physiological effect of AMG-1694. We found AMG-1694 increased the cellular content of 2-deoxy-D-glucose (2DG) phosphate in hepatocytes with higher potency than that observed with RO-28-0450, a validated GK activator (GKA)[12] (EC_{50} = 0.053 μM and 5.7 μM, respectively; Fig. 2c). The shallow response curve generated with AMG-1694 was similar to that previously reported with 2DG and sorbitol[16]. The steeper response elicited by the GKA reflects a direct mechanism on GK associated with changes in cooperativity for glucose. The effect of AMG-1694 on GK activity was indirect, leaving GK glucose cooperativity unchanged. These data demonstrate that AMG-1694 dissociates GK from GKRP and increases cellular glucose uptake, consistent with the observed cytoplasmic accumulation of GK. Fructose also causes this redistribution, but high doses are required and the effects are incomplete[17].

[1]Department of Metabolic Disorders, Amgen Inc., One Amgen Center Drive, Thousand Oaks, California 91320, USA. [2]Department of Therapeutic Discovery, Amgen Inc., One Amgen Center Drive, Thousand Oaks, California 91320, USA. [3]Department of Comparative Biology & Safety Sciences, Amgen Inc., One Amgen Center Drive, Thousand Oaks, California 91320, USA.

©2013 Macmillan Publishers Limited. All rights reserved

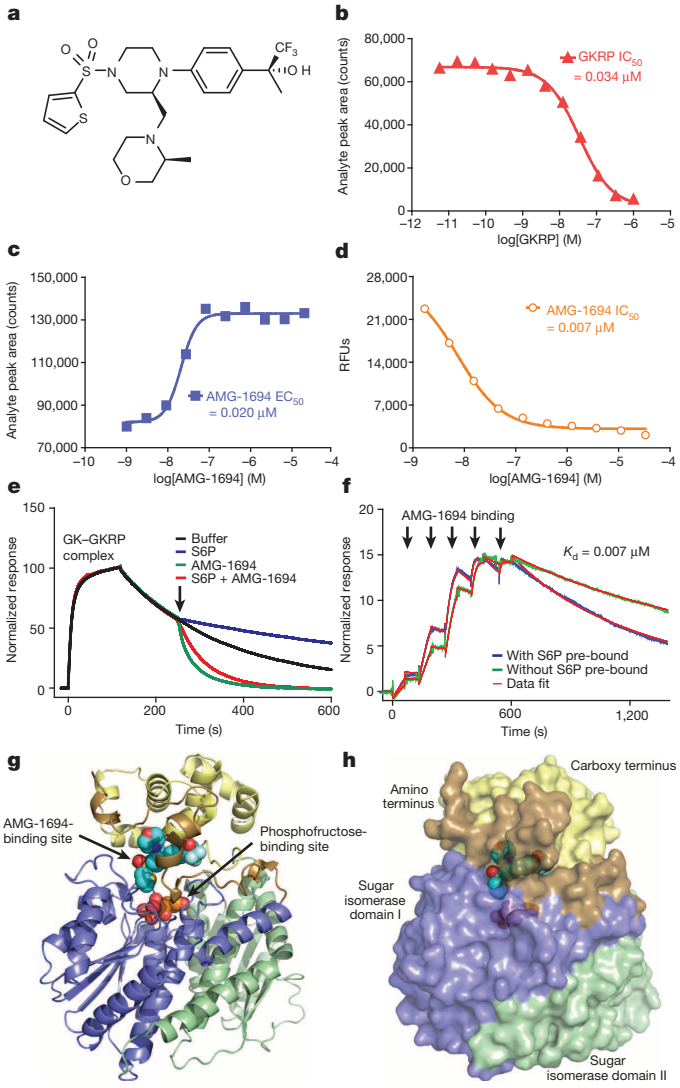


Figure 1 | AMG-1694, potency, binding and GKRP–AMG-1694 co-crystal structure. **a**, AMG-1694 molecular structure. **b**, GK activity (amount of ^{13}C-glucose-6-phosphate formed) with increasing concentrations of GKRP. **c**, GK activity (amount of ^{13}C-glucose-6-phosphate formed) in the presence of GKRP and increasing concentrations of AMG-1694. **d**, GK–GKRP binding dose-response with AMG-1694. AMG-1694 disrupts the preformed GK–GKRP complex, expressed as relative fluorescent units (RFUs). **e**, Effects of S6P, AMG-1694, or both on the GK–GKRP complex (determined by SPR). Immobilized GK on a biosensor surface was incubated with GKRP; during the dissociation phase, buffer with S6P and/or AMG-1694 was injected (arrow). **f**, Binding of AMG-1694 to immobilized GKRP (determined by SPR). Immobilized GKRP on a biosensor surface was exposed to increasing concentrations of AMG-1694 (arrows). **g**, Ribbon diagram of the 2.35 Å resolution co-crystal structure of human GKRP with S6P and AMG-1694 (Extended Data Table 2). **h**, Space-filling diagram of the co-crystal structure of GKRP with S6P and AMG-1694, highlighting the solvent accessibility of AMG-1694. Representative data for **b**, **e** and **f** are from two experiments, and **c** and **d** are from 22 experiments.

An oral dose of AMG-1694 administered at 100 mg kg^{-1} in rats produced free plasma exposure levels sufficient to cover the cellular EC_{50}, which allowed us to monitor GK translocation using immunohistochemistry (IHC) in rat livers from fed and fasted Wistar rats. Figure 3a shows three liver sections from rats dosed with glucose/fructose or with vehicle only; the results are illustrated in Fig. 3b, c with a scoring scheme ranging from 0 to 4 (0 = total nuclear loss; 4 = no GK translocation). In Wistar rats, 30 and 100 mg kg^{-1} of AMG-1694 translocated GK more robustly than glucose and fructose (Extended Data Fig. 4a). A dose-dependent pharmacodynamic response was observed over 24 h after a

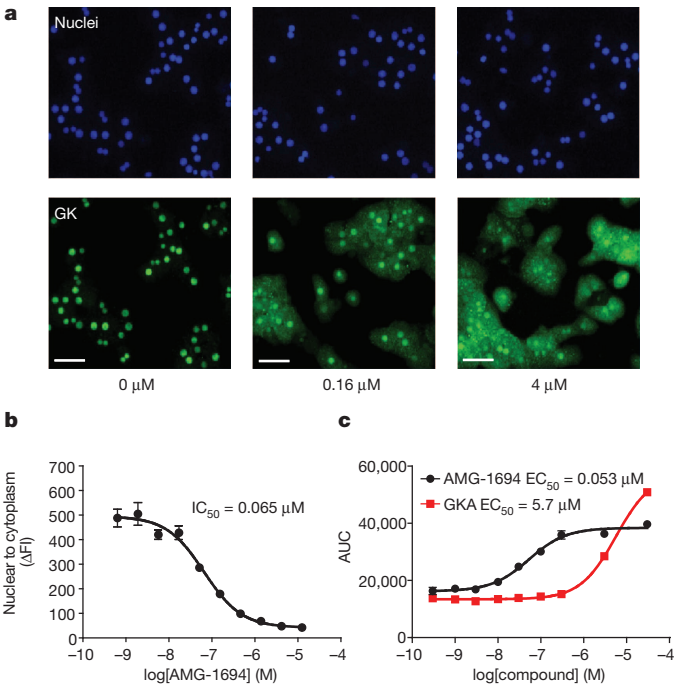


Figure 2 | GK translocation and 2DG phosphorylation in primary rat hepatocytes with AMG-1694. **a**, Nuclei (blue) and GK (green) staining in hepatocytes incubated with AMG-1694. Scale bars, 50 μm. **b**, Nuclear to cytoplasm fluorescence intensity difference (ΔFI) versus increasing concentrations of AMG-1694 using an ArrayScan platform. Representative of six experiments. Error bars denote s.e.m. of two technical replicates. **c**, Formation of 2-deoxy-D-glucose phosphate in rat hepatocytes incubated in the presence of 100 mM 2DG and increasing concentrations of AMG-1694 or a GKA (RO-28-0450)[12]. Representative of two experiments. Error bars denote s.e.m of four technical replicates.

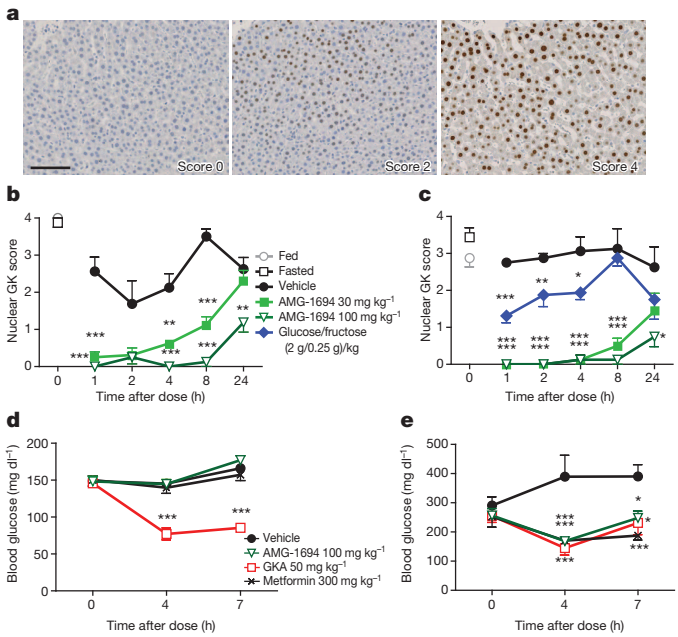


Figure 3 | GK translocation and efficacy in ZDF rats with AMG-1694. **a**, Liver sections from rats dosed with glucose/fructose or vehicle illustrating representative GK IHC scores of 0 (full GK translocation), 2 (partial translocation), and 4 (no translocation). Scale bar, 100 μm. **b**, **c**, GK translocation in Wistar (**b**) and ZDF (**c**) rats dosed with AMG-1694 or glucose/fructose. **d**, **e**, Blood glucose levels in fed Wistar (**d**) and ZDF (**e**) rats after administration of AMG-1694, metformin or a GKA (RO-28-0450)[12]. Error bars denote s.e.m.; $n = 4$ (**b**, **c**) and 6 (**d**, **e**). $^*P < 0.05$, $^{**}P < 0.01$, $^{***}P < 0.001$ versus vehicle (analysis of variance (ANOVA; **b**, **c**) and analysis of covariance (ANCOVA; **d**, **e**)).

©2013 Macmillan Publishers Limited. All rights reserved

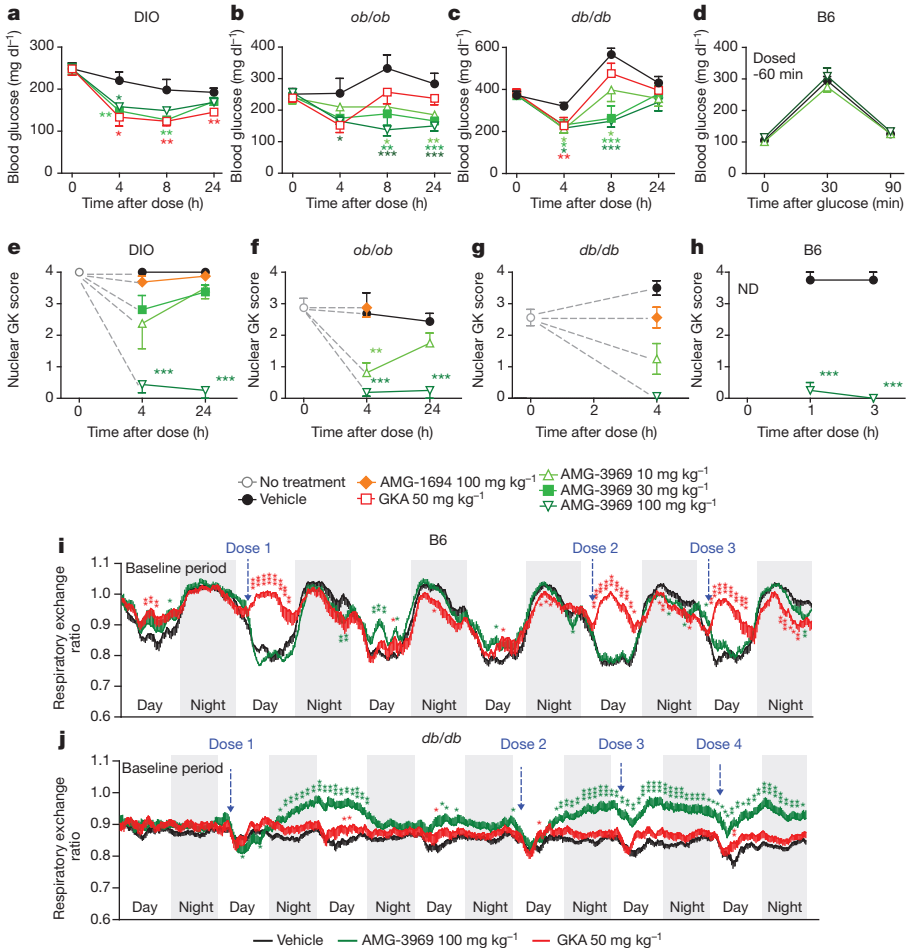


Figure 4 | Efficacy and substrate use in diabetic mice after AMG-3969 administration. **a**–**d**, Blood glucose levels in fed DIO (**a**), *ob/ob* (**b**), *db/db* (**c**) and B6 (**d**) mice administered AMG-3969 or a GKA (RO-28-0450)[12]. B6 mice were challenged with a glucose bolus 1 h after AMG-3969 administration. **e**–**h**, Liver GK translocation in DIO (**e**), *ob/ob* (**f**), *db/db* (**g**) and B6 (**h**) mice administered AMG-3969, AMG-1694 or a GKA (RO-28-0450)[12]. ND, not determined. **i**, **j**, B6 (**i**) and *db/db* (**j**) mice were acclimated to indirect calorimetry housing and baseline readings were obtained to calculate respiratory exchange ratio. Error bars denote s.e.m.; $n = 7$ (**a**, **c**), 8 (**b**, **d**), 4 (**e**–**h**), 6 (vehicle) or 5 (AMG-3969, GKA) (**i**, **j**). $^{*}P < 0.05$, $^{**}P < 0.01$, $^{***}P < 0.001$ versus vehicle (ANCOVA, **a**–**d**; and ANOVA, **e**–**j**).

single dose of AMG-1694 at 30 and 100 mg kg^{-1} (Fig. 3b). We confirmed these effects in Zucker diabetic fatty (ZDF) rats (Fig. 3c) and did not detect increases in plasma insulin levels with AMG-1694, consistent with liver-specific GK activation (Extended Data Fig. 4b–d).

We compared the efficacy of AMG-1694 to a known GKA[12], metformin, or to vehicle in Wistar and ZDF rats. In normoglycaemic Wistar rats, only the GKA decreased blood glucose (Fig. 3d), despite the fact that AMG-1694 led to GK translocation in the same animals. In hyperglycaemic ZDF rats, all compounds effectively lowered blood glucose levels (Fig. 3e), demonstrating that metformin and AMG-1694 are only efficacious in hyperglycaemic animals. Furthermore, the glucose lowering effect of AMG-1694 in ZDF rats was not associated with increased triglycerides, as might have been expected from genome-wide association studies[18] (Extended Data Fig. 4e–g).

We next examined a compound within the piperazine series that was structurally related to AMG-1694 that had improved pharmacokinetic properties in mice (AMG-3969; Extended Data Fig. 5a, b). AMG-3969 demonstrated dose-dependent efficacy in three models of diabetes: diet induced obese (DIO), *ob/ob* and *db/db* mice; however, AMG-3969 was ineffective in lowering blood glucose in normoglycaemic C57BL/6 (B6) mice (Fig. 4a–d). In each model, efficacy was supported by GK translocation, with the exception of B6 mice, in which translocation was observed without a glucose lowering effect (Fig. 4e–h). Because of its low target coverage in mice, AMG-1694 did not lead to GK translocation in mice. The GKA was only minimally efficacious in *ob/ob* and *db/db* mice, whereas AMG-3969 exhibited robust glucose lowering in all diabetic mouse models tested. To establish a mechanism for the observed efficacy of the GK–GKRP disruptors, we used indirect calorimetry to investigate alterations in substrate oxidation. In B6 mice, we observed a marked preference for carbohydrate oxidation with a GKA (MK-0941)[19], whereas no effect was observed with AMG-3969 (Fig. 4i). In *db/db* mice with severe hyperglycaemia, the opposite was found (Fig. 4j); AMG-3969 was highly effective in promoting carbohydrate substrate use whereas the GKA was not. AMG-3969 exhibited extended changes to carbohydrate oxidation as observed by increased respiratory exchange ratio into the next night and day after a single dose.

Our data clearly demonstrate that targeting GKRP improves glucose metabolism in several diabetic rodent models. Paradoxically, mice lacking GKRP exhibit slight impairment in glucose tolerance[20]. This difference may relate to congenital GKRP deficiency and possible developmental adaptation. Alternatively, it is known that GKRP stabilizes and protects GK from degradation. Thus, GKRP deficiency results in reduced GK protein levels, which may give rise to impaired glucose tolerance. Despite what was found in knockout mice, we did not observe reduced GK levels in AMG-1694-treated ZDF rats (Extended Data Fig. 6a).

A liver-specific GKA that promotes hepatic GK activation is alone sufficient for antidiabetic effects, thus avoiding the GK pancreatic activation responsible for hypoglycaemia[21]. Alternatively, GKRP alone can be viewed as a drug target because administration of low concentrations of sorbitol, specifically binding GKRP and not GK, restored GK translocation in ZDF rats and decreased hepatic glucose production[22,23]. Our GKRP crystallization data identified a pocket accessible to small molecule compounds distinct from the sorbitol/fructose-binding site. How AMG-1694 binding disrupts the GK–GKRP complex remains unclear. We do not see large changes of the protein structure after soaking AMG-1694 into preformed GKRP–S6P co-crystals (Extended Data Fig. 6b). A recent report describing the *Xenopus* GK–GKRP co-crystal complex with fructose-6-phosphate[24] identified a GK-binding site on GKRP that is remote to our observed AMG-1694-binding site. Using the *Xenopus* structure, human GKRP (bound to either fructose-1-phosphate or fructose-6-phosphate) was modelled. These models predicted more significant motion of GKRP after binding to each of the different fructose

©2013 Macmillan Publishers Limited. All rights reserved

forms than we observed after binding of AMG-1694. Future investigations will be needed to fully determine the mechanism of GK–GKRP disruption with either phosphofructose or AMG-1694.

AMG-1694 induced GK translocation and decreased blood glucose in ZDF rats, consistent with a previous report using sorbitol[22]. Similar effects of AMG-3969 were observed in hyperglycaemic DIO, *ob/ob* and *db/db* mice. In addition, both AMG-1694 and AMG-3969 caused robust GK translocation in Wistar rats and B6 mice, respectively, without lowering blood glucose levels. This targeted efficacy is advantageous for an antidiabetic therapy because it only lowers blood glucose in the diabetic and not the normoglycaemic state, as is often observed with GKAs[12,16,19]. How AMG-1694 and AMG-3969 physiologically lower glucose has yet to be determined, but may involve increased glucose uptake, increased energy expenditure, and/or decreased hepatic glucose production. We observed a marked preference for carbohydrate use in *db/db* mice administered AMG-3969, suggesting a profound alteration of hepatic energy metabolism. Although GK activators require some endogenous insulin secretory function to produce their hypoglycaemic effects, agents such as AMG-1694 and AMG-3969 would be predicted to work in patients with diabetes regardless of the degree of β-cell reserve.

In conclusion, we have discovered a new mechanism for GK release in the liver, distinct to that of phosphofructose. We have established that the GK–GKRP complex can be modulated with synthetic compounds and, through crystallography, determined that AMG-1694 is mostly buried within the GKRP protein where it is unlikely to block the GK-binding site directly. Furthermore, we showed that disrupting the GK–GKRP complex leads to GK cytosolic translocation both in cells and *in vivo*, and produces antidiabetic effects in rodent models of diabetes. These data describe a class of molecules that affects a new cellular pathway and could potentially treat type II diabetes mellitus while avoiding the hypoglycaemic risk associated with GK activators.

METHODS SUMMARY

Human GK (hepatic) expressed in *Escherichia coli* was purified and labelled with fluorescein. GK was also constructed with an N-terminal AviTag and biotinylated. Human GKRP carboxy-terminal AviTag was expressed in a baculovirus system and biotinylated. SPR spectroscopy was performed on a Biacore T200 instrument. For GK–GKRP complex experiments with S6P and AMG-1694, biotin-GK was captured onto a streptavidin biosensor. For AMG-1694 binding, GKRP-biotin was captured onto the biosensor. GKRP crystals grown for 2 days in the presence of S6P were soaked with 0.5 mM AMG-1694 for 3 days; data were solved and refined to 2.35 Å resolution. The GK–GKRP binding assay was established using GKRP-biotin pre-incubated with compound before the addition of fluorescein-GK and AlphaScreen beads (PerkinElmer), then incubated further before detection on an EnVision Instrument (PerkinElmer). Direct substrate conversion of 5 mM ^{13}C-glucose (Sigma) by GK was measured by monitoring ^{13}C-glucose-6-phosphate. The reaction was incubated for 30 min, stopped, and then injected into a Biobasic AX column for liquid chromatography tandem mass spectrometry (LC–MS/MS). Rat hepatocytes were plated into a 96-well plate, and GK translocation by immunostaining was analysed using an ArrayScan VTI imaging system (Thermo Fisher). For 2-deoxy-D-glucose phosphate experiments, hepatocytes were cultured for 48 h, switched to glucose-free medium for 2 h, and treated with 100 mM 2DG and AMG-1694 or GKA for 2 h; lysates were then analysed using LC–MS/MS to monitor 2-deoxy-D-glucose phosphate. *In vivo* studies were approved by the Institutional Animal Care and Use Committee. Blood glucose values were determined in several mouse and rat models of diabetes. Animals were gavaged with vehicle (2% hydroxypropyl methycellulose and 1% Tween 80), AMG-1694, AMG-3969 or GK activators. For IHC, livers were fixed in cold paraformaldehyde for 3 h, embedded in paraffin and GK was detected using an anti-GK antibody (Santa Cruz Biotechnology).

Online Content Any additional Methods, Extended Data display items and Source Data are available in the online version of the paper; references unique to these sections appear only in the online paper.

Received 18 March; accepted 30 September 2013.
Published online 13 November 2013.

1. Verspohl, E. J. Novel pharmacological approaches to the treatment of type 2 diabetes. *Pharmacol. Rev.* **64,** 188–237 (2012).
2. Agius, L. Glucokinase and molecular aspects of liver glycogen metabolism. *Biochem. J.* **414,** 1–18 (2008).
3. Matschinsky, F. M. Glucokinase as glucose sensor and metabolic signal generator in pancreatic beta-cells and hepatocytes. *Diabetes* **39,** 647–652 (1990).
4. Jetton, T. L. *et al.* Analysis of upstream glucokinase promoter activity in transgenic mice and identification of glucokinase in rare neuroendocrine cells in the brain and gut. *J. Biol. Chem.* **269,** 3641–3654 (1994).
5. Iynedjian, P. B. Mammalian glucokinase and its gene. *Biochem. J.* **293,** 1–13 (1993).
6. Van Schaftingen, E., Vandercammen, A., Detheux, M. & Davies, D. R. The regulatory protein of liver glucokinase. *Adv. Enzyme Regul.* **32,** 133–148 (1992).
7. Vandercammen, A. & Van Schaftingen, E. The mechanism by which rat liver glucokinase is inhibited by the regulatory protein. *Eur. J. Biochem.* **191,** 483–489 (1990).
8. Anderka, O. *et al.* Biophysical characterization of the interaction between hepatic glucokinase and its regulatory protein: impact of physiological and pharmacological effectors. *J. Biol. Chem.* **283,** 31333–31340 (2008).
9. Coghlan, M. & Leighton, B. Glucokinase activators in diabetes management. *Expert Opin. Investig. Drugs* **17,** 145–167 (2008).
10. Grimsby, J., Berthel, S. J. & Sarabu, R. Glucokinase activators for the potential treatment of type 2 diabetes. *Curr. Top. Med. Chem.* **8,** 1524–1532 (2008).
11. Meininger, G. E. *et al.* Effects of MK-0941, a novel glucokinase activator, on glycemic control in insulin-treated patients with type 2 diabetes. *Diabetes Care* **34,** 2560–2566 (2011).
12. Grimsby, J. *et al.* Allosteric activators of glucokinase: potential role in diabetes therapy. *Science* **301,** 370–373 (2003).
13. Detheux, M., Vandercammen, A. & Van Schaftingen, E. Effectors of the regulatory protein acting on liver glucokinase: a kinetic investigation. *Eur. J. Biochem.* **200,** 553–561 (1991).
14. Veiga-da-Cunha, M., Sokolova, T., Opperdoes, F. & Van Schaftingen, E. Evolution of vertebrate glucokinase regulatory protein from a bacterial N-acetylmuramate 6-phosphate etherase. *Biochem. J.* **423,** 323–332 (2009).
15. Veiga-da-Cunha, M. & Van Schaftingen, E. Identification of fructose 6-phosphate- and fructose 1-phosphate-binding residues in the regulatory protein of glucokinase. *J. Biol. Chem.* **277,** 8466–8473 (2002).
16. Fyfe, M. C. *et al.* Glucokinase activator PSN-GK1 displays enhanced antihyperglycaemic and insulinotropic actions. *Diabetologia* **50,** 1277–1287 (2007).
17. Agius, L. & Peak, M. Intracellular binding of glucokinase in hepatocytes and translocation by glucose, fructose and insulin. *Biochem. J.* **296,** 785–796 (1993).
18. Diabetes Genetics Initiative of Broad Institute of Harvard and MIT et al. Genome-wide association analysis identifies loci for type 2 diabetes and triglyceride levels. *Science* **316,** 1331–1336 (2007).
19. Eiki, J. *et al.* Pharmacokinetic and pharmacodynamic properties of the glucokinase activator MK-0941 in rodent models of type 2 diabetes and healthy dogs. *Mol. Pharmacol.* **80,** 1156–1165 (2011).
20. Grimsby, J. *et al.* Characterization of glucokinase regulatory protein-deficient mice. *J. Biol. Chem.* **275,** 7826–7831 (2000).
21. Pfefferkorn, J. A. *et al.* Discovery of (*S*)-6-(3-cyclopentyl-2-(4-(trifluoromethyl)-1*H*-imidazol-1-yl)propanamido)nicotinic acid as a hepatoselective glucokinase activator clinical candidate for treating type 2 diabetes mellitus. *J. Med. Chem.* **55,** 1318–1333 (2012).
22. Fujimoto, Y., Donahue, E. P. & Shiota, M. Defect in glucokinase translocation in Zucker diabetic fatty rats. *Am. J. Physiol. Endocrinol. Metab.* **287,** E414–E423 (2004).
23. Shin, J. S., Torres, T. P., Catlin, R. L., Donahue, E. P. & Shiota, M. A defect in glucose-induced dissociation of glucokinase from the regulatory protein in Zucker diabetic fatty rats in the early stage of diabetes. *Am. J. Physiol. Regul. Integr. Comp. Physiol.* **292,** R1381–R1390 (2007).
24. Choi, J. M., Seo, M. H., Kyeong, H. H., Kim, E. & Kim, H. S. Molecular basis for the role of glucokinase regulatory protein as the allosteric switch for glucokinase. *Proc. Natl Acad. Sci. USA* **110,** 10171–10176 (2013).

Acknowledgements We would like to thank J. Calahan, J. Laubacher, M. Moore and D. Reid for pharmaceutics support, J. Civet for *in vivo* assistance, J. Han and R. Fachini for recombinant protein production, K. Kim for LC–MS/MS technical assistance, N. Nishimura and K. Yang for scale-up of AMG-3969, J. Chen for pharmacokinetic support, and A. Shaywitz and L. Rice for critical reading and editorial support of the manuscript.

Author Contributions D.J.L., S.R.J., M.M.V. and C.H. designed experiments, analysed data and wrote the manuscript. K.M. performed SPR spectroscopy. D.J.S., K.S.A., K.L.A., L.D.P., C.F., L.L., M.D.B. and M.H.N. were responsible for the design and synthesis of AMG-1694 and AMG-3969. R.C. collected data and performed biochemical assays. M.C. developed and collected data for the hepatocyte GK translocation assay. J.W. validated and collected data for the hepatocyte 2DG uptake assay. K.C. and R.C.W. designed, and K.C. performed, the high-throughput screen. R.C.W. developed the GK–GKRP binding assay. M.W. designed experiments. M.V. and R.J.M.K. generated protein reagents. S.C., J.Z. and S.R.J. conducted crystallographic studies. G.V., E.J.G. and S.L.V. performed IHC. G.S., J.H. and R.K. conducted *in vivo* experiments.

Author Information Atomic coordinates and structure factors for the GKRP–AMG-1694 complex are deposited in the Protein Data Bank under accession code 4LY9. Reprints and permissions information is available at www.nature.com/reprints. The authors declare competing financial interests: details are available in the online version of the paper. Readers are welcome to comment on the online version of the paper. Correspondence and requests for materials should be addressed to D.J.L. (dlloyd@amgen.com) or C.H. (chale@amgen.com).

©2013 Macmillan Publishers Limited. All rights reserved

METHODS

Preparation of recombinant GK and GKRP. Recombinant human GK (hepatic), native or with an N-terminal AviTag (avi), was expressed in *Escherichia coli* and purified and formulated in 50 mM Tris, pH 7.5, 150 mM NaCl and 20 mM glucose. A 1:1 ratio of 5-bromomethylfluorescein (Invitrogen) and GK was prepared and the reaction mixture incubated overnight at 4 °C in the dark. Unreacted dye was removed by dialysis into formulation buffer (25 mM Tris, pH 7.2, 150 mM NaCl, 10% glycerol and 2 mM dithiothreitol (DTT)). Human native GKRP (full-length or 20–625 truncation) or with a C-terminal AviTag was expressed in a baculovirus system. Purified avi-GK or GKRP-avi were incubated overnight with recombinant biotin ligase in the presence of D-biotin, ATP and $MgCl_2$. Labelled proteins were isolated from reaction components by chromatography on a Superdex 200 size-exclusion column into 50 mM HEPES, 150 mM NaCl and 5 mM DTT. Untagged native proteins were isolated from their purification tags using caspase 3.

GK–GKRP LC–MS/MS assay. Direct substrate conversion by GK was measured by a liquid chromatography tandem mass spectrometry (LC–MS/MS) assay that monitored mass shift of universally labelled ^{13}C-glucose-6-phosphate (−269→79 *m/z*). The final reaction mixture included 300 μM fructose-6-phosphate, 5 mM ^{13}C-glucose (Sigma), 240 μM ATP, 50 mM Tris, pH 7.5, 4 mM $MgCl_2$, 8% dimethylsulphoxide (DMSO), 6.8 mM DTT, 0.001% Brij-35, 0.01% BSA, 6 nM GK, and either a range (0.05–1,000 nM) of GKRP concentrations, or 28 nM GKRP plus a range (0.009–20 μM) of AMG-1694 concentrations. The reaction was incubated for 30 min at room temperature, stopped with acetonitrile, injected into Biobasic AX column LC–MS/MS and then analyte peak area (counts) was determined. EC_{50} values were calculated using GraphPad Prism software.

GK–GKRP binding assay. GKRP-biotin was incubated with AMG-1694 for 20 min at 5 nM GKRP-biotin, 1 μM S6P, 20 mM Tris, pH 7.5, 0.05% BSA and 1 mM DTT. Afterwards, 1 nM fluorescein-GK and a 1:1,000 dilution of AlphaScreen anti-fluorescein (FITC) acceptor beads and streptavidin donor beads (PerkinElmer) were added followed by an additional 4 h incubation. Using an EnVision Instrument (PerkinElmer), GK–GKRP binding was detected and IC_{50} values were calculated using GraphPad Prism software.

Synthesis of AMG-1694. Unless otherwise noted, all reagents were commercially available and used as received. ^{1}H-, ^{13}C- and ^{19}F-NMR data are reported as follows: chemical shift (p.p.m., δ units) from an internal standard, multiplicity (s = singlet, d = doublet, t = triplet, q = quartet, m = multiplet, and br = broad), coupling constant (Hz), and integration.

A 2-l round-bottomed flask was charged with (*S*)-3-methylmorpholine (10.10 g, 100 mmol), HATU (39.7 g, 104 mmol), (*R*)-1,4-bis(*tert*-butoxycarbonyl)piperazine-2-carboxylic acid (30.0 g, 91 mmol) and 100 ml dimethylformamide. To this was added Hünig's base (20.3 ml, 114 mmol). After stirring at room temperature for 1 h, the mixture was diluted with water (1 l) and extracted with 750 ml of ether. The organic layer was separated and washed with water (4 × 500 ml), saturated aqueous $NaHCO_3$ (250 ml) and brine (250 ml). The organic extracts were dried ($MgSO_4$), filtered and concentrated to give (2*R*)-2-(((3*S*)-3-methyl-4-morpholinyl)-carbonyl)-1,4-piperazinedicarboxylate (33.8 g, 82% yield) as a white solid.

A 1-l round-bottomed flask was charged with (2*R*)-2-(((3*S*)-3-methyl-4-morpholinyl) carbonyl)-1,4-piperazinedicarboxylate (33.8 g, 82.0 mmol), and 100 ml tetrahydrofuran (THF). To this was added borane (1 M in THF, 327 ml, 327 mmol). The mixture was warmed to 50 °C for 2 h and then cooled to 0 °C and slowly quenched with 100 ml methanol. The mixture was concentrated and diluted with 200 ml ethyl acetate.

To this residue was added 100 ml 4 N HCl in dioxane. The mixture was heated at 70 °C for 2.5 h and the resulting white precipitate was collected by filtration to provide the amine HCl salt. This solid was suspended in 200 ml CH_2Cl_2 and triethylamine (57.0 ml, 408 mmol). After cooling to 0 °C, 2-thiophenesulphonyl chloride (14.9 g, 82.0 mmol) was added. The mixture was allowed to warm to room temperature and stirred for 1 h. Water (200 ml) was then added and the mixture was extracted with ethyl acetate. The combined organics were dried ($MgSO_4$), filtered and concentrated to give an oil. Purification via silica gel chromatography (0–10% methanol in CH_2Cl_2) gave (3S)-3-methyl-4-(((2S)-4-(2-thiophenylsulphonyl)-2-piperazinyl)methyl)morpholine (20.2 g, 71% yield) as a white solid.

A 1-l pressure vessel was charged with (*S*)-3-methyl-4-(((*S*)-4-(thiophen-2-ylsulphonyl)piperazin-2-yl)methyl)morpholine (10.50 g, 30.4 mmol), 100 ml toluene, (*R*)-2-(4-bromophenyl)-1,1,1-trifluoropropan-2-ol (ref. 25; 9.81 g, 36.5 mmol) and sodium 2-methylpropan-2-olate (7.30 g, 76 mmol). Oxygen-free nitrogen gas was bubbled through the solution for 3 min. RuPhos precatalyst (1.11 g, 1.52 mmol) and RuPhos (0.709 g, 1.52 mmol) were then added. The vessel was sealed and heated at 60 °C for 12 h. The mixture was diluted with water and extracted with ethyl acetate; the combined organics were dried ($MgSO_4$), filtered, concentrated and purified by silica gel chromatography (0–70% ethyl acetate in hexanes) to deliver (*R*)-1,1,1-trifluoro-2-(4-((*S*)-2-(((*S*)-3-methylmorpholino)methyl)-4-(thiophen-2-ylsulphonyl)-piperazin-1-yl)phenyl)propan-2-ol (AMG-1694) (8.15 g, 50% yield) as a tan foam. This foam was slurried in isopropanol to deliver material with purity >98%. Melting point 188–191 °C; ^{1}H-NMR (400 MHz, DMSO-d_6) δ 8.09 (dd, *J* = 1.0, 4.9 Hz, 1 H), 7.71 (dd, *J* = 1.1, 3.6 Hz, 1 H), 7.38 (d, *J* = 8.6 Hz, 2 H), 7.32 (dd, *J* = 3.9, 4.9 Hz, 1 H), 6.89 (d, *J* = 9.0 Hz, 2 H), 6.36 (s, 1 H), 4.08 (br. d, *J* = 9.8 Hz, 1 H), 3.93 (d, *J* = 10.8 Hz, 1 H), 3.72–3.61 (m, 2 H), 3.56 (dd, *J* = 2.6, 10.9 Hz, 1 H), 3.51–3.39 (m, 2 H), 3.20 (t, *J* = 11.6 Hz, 1 H), 3.14–2.99 (m, 2 H), 2.89 (d, *J* = 11.5 Hz, 1 H), 2.44–2.18 (m, 3 H), 1.96 (dt, *J* = 2.6, 11.0 Hz, 1 H), 1.73–1.56 (m, 4 H), 0.92 (d, *J* = 6.3 Hz, 3 H); ^{13}C-NMR (101 MHz, DMSO-d_6) δ 148.5, 134.1 (2), 133.4, 129.5, 128.4, 127.3 (2), 126.1 (q, *J* = 289 Hz), 114.2 (2), 72.8 (q, *J* = 28 Hz), 72.3, 66.6, 54.8, 51.8, 50.9, 48.0, 46.6, 45.7, 41.2, 22.7, 14.5; ^{19}F-NMR (377 MHz, DMSO-d_6) δ −79.95. HRMS (*m/z*): $[M+H]^+$ calculated for $C_{23}H_{31}F_3N_3O_4S_2$, 533.1708; found, 533.1706.

Synthesis of AMG-3969. A 2-l Erlenmeyer flask was charged with 2-piperazinone (36.5 g, 364 mmol), sodium carbonate (116 g, 1.10 mol), 600 ml dioxane, and 150 ml water at room temperature. To this was slowly added benzyl chloroformate (62.1 g, 364 mmol) over 20 min. After the addition was complete, the mixture was stirred for 2 h, diluted with water and extracted with 2 l of ethyl acetate. The combined organic extracts were dried ($MgSO_4$), filtered and concentrated to give a white solid. To this solid was added 500 ml CH_2Cl_2, triethylamine (92.6 g, 128 ml, 911 mmol), 4-dimethylaminopyridine (4.45 g, 36.4 mmol), and di-*tert*-butyl dicarbonate (119 g, 546 mmol). After 1 h at room temperature, the mixture was diluted with water and the organics were separated, dried ($MgSO_4$), filtered and concentrated to give a brown oil. To this oil was added 100 ml CH_2Cl_2 followed by 1 l hexane. The resulting white solid was collected by filtration to give 4-benzyl 1-*tert*-butyl 2-oxo-1,4-piperazinedicarboxylate (101 g, 81%). ^{1}H-NMR (400 MHz, $CDCl_3$) δ 7.45–7.29 (m, 5 H), 5.15 (s, 2 H), 4.24 (s, 2 H), 3.88–3.74 (m, 2 H), 3.74–3.59 (m, 2 H), 1.54 (s, 9 H).

A 150-ml round-bottomed flask charged with a solution of 4-benzyl 1-*tert*-butyl 2-oxo-1,4-piperazinedicarboxylate (1.41 g, 4.22 mmol) in 5 ml THF was cooled to 0 °C. 1-propynylmagnesium bromide (0.5 M in THF, 20.0 ml, 10.0 mmol) was added dropwise over 15 min. The mixture was stirred at 0 °C for 2 h and then saturated aqueous NH_4Cl (40 ml) was added. The aqueous phase was extracted with ethyl acetate (200 ml, then 2 × 100 ml). The organic extracts were dried (Na_2SO_4), filtered and concentrated. The crude product was purified by silica gel chromatography (0–50% ethyl acetate in hexanes) to afford benzyl (2-((*tert*-butoxycarbonyl)amino) ethyl)(2-oxo-3-pentyn-1-yl)carbamate (1.55 g, 99%) as a clear oil. ^{1}H-NMR (400 MHz, $CDCl_3$) δ 7.39–7.27 (m, 5 H), 5.13 (d, *J* = 19.4 Hz, 2 H), 4.97 (d, *J* = 3.9 Hz, 1 H), 4.18 (s, 1 H), 4.16–4.08 (m, 1 H), 3.44 (td, *J* = 5.8, 11.7 Hz, 2 H), 3.32–3.16 (m, 2 H), 2.00 (d, *J* = 13.3 Hz, 3 H), 1.42 (d, *J* = 4.7 Hz, 9 H).

A 3-l round-bottomed flask was charged with 2-((*tert*-butoxycarbonyl)amino) ethyl)(2-oxo-3-pentyn-1-yl)carbamate (82.2 g, 219 mmol) and 300 ml CH_2Cl_2. After cooling to −10 °C, TFA (169 ml, 2,195 mmol) was added and the resulting dark solution was stirred at room temperature for 15 min. Sodium triacetoxyborohydride (186 g, 878 mmol) was added portion-wise over 10 min. After 2 h, the mixture was concentrated, diluted with ethyl acetate (1 l), and neutralized with 5 N NaOH. The layers were separated and the organic extracts were washed with brine, dried ($MgSO_4$), filtered and concentrated. The resulting orange oil was purified via silica gel chromatography (0–4.5% methanol in CH_2Cl_2) to give benzyl 3-(1-propyn-1-yl)-1-piperazinecarboxylate (43.7 g, 77%) as a brown foam. ^{1}H-NMR (400 MHz, $CDCl_3$) δ 7.43–7.30 (m, 5 H), 5.28–5.04 (m, 2 H), 4.05–3.61 (m, 5 H), 3.37 (br s, 1 H), 3.03 (br s, 1 H), 1.79 (br s, 3 H) (one exchangeable proton was not observed).

A 150-ml reaction vessel was charged with benzyl 3-(prop-1-yn-1-yl)piperazine-1-carboxylate (2.88 g, 11.2 mmol), 2-(4-bromophenyl)-1,1,1,3,3,3-hexafluoro-2-propanol[26] (4.36 g, 13.5 mmol), dicyclohexyl(2′,6′-diisopropoxy-[1,1′-biphenyl]-2-yl) phosphine (RuPhos) (0.530 g, 1.14 mmol), chloro(2-dicyclohexylphosphino-2′,6′-di-*i*-propoxy-1,1′-biphenyl)[2-(2-aminoethylphenyl)]palladium(II), methyl-*tert*-butylether adduct (RuPhos first generation precatalyst) (0.417 g, 0.572 mmol), sodium *tert*-butoxide (2.73 g, 28.4 mmol), and toluene (35 ml). Argon was bubbled through the solution for 10 min. The vessel was sealed and heated at 100 °C for 1.5 h. After the reaction was allowed to cool to room temperature, water (100 ml) was added. The aqueous phase was extracted with ethyl acetate (3 × 100 ml) and the combined organic layers were washed with brine (150 ml), dried (Na_2SO_4), filtered and concentrated. The crude product was purified by silica gel chromatography (0–50% ethyl acetate in hexanes) to afford benzyl 3-(1-propyn-1-yl)-4-(4-(2,2,2-trifluoro-1-hydroxy-1-(trifluoromethyl)ethyl)phenyl)-1-piperazinecarboxylate (3.84 g, 69%) as a yellow solid. ^{1}H-NMR (400 MHz, $CDCl_3$) δ 7.59 (d, *J* = 8.6 Hz, 2 H), 7.44–7.29 (m, 5 H), 6.99 (d, *J* = 9.0 Hz, 2 H), 5.32–5.08 (m, 2 H), 4.48–4.17 (m, 3 H), 3.50–3.02 (m, 5 H), 1.69 (br s, 3 H).

A 500-ml round-bottomed flask was charged with benzyl 3-(1-propyn-1-yl)-4-(4-(2,2,2-trifluoro-1-hydroxy-1-(trifluoromethyl)ethyl)phenyl)-1-piperazinecarboxylate (3.13 g, 6.25 mmol) and TFA (40 ml). Trifluoromethanesulphonic acid (1.25 ml, 14.1 mmol) was added dropwise at room temperature. After 5 min, additional trifluoromethanesulphonic acid (0.45 ml, 5.1 mmol) was added. After an additional

©2013 Macmillan Publishers Limited. All rights reserved

10 min, solid $NaHCO_3$ was carefully added in portions until effervescence ceased. Saturated aqueous $NaHCO_3$ (250 ml) was then slowly to bring the pH to approximately 7. The aqueous phase was extracted with ethyl acetate (100 ml). The organic layers were combined and washed with water (200 ml) and brine (200 ml) then dried (Na_2SO_4), filtered and concentrated to afford a tan solid. To this solid was added CH_2Cl_2 (30 ml) and triethylamine (3.63 g, 5 ml, 35.9 mmol). 6-Chloropyridine-3-sulphonyl chloride[27] (1.58 g, 7.43 mmol) was added in potions at 0 °C. The brown mixture was stirred at 0 °C for 10 min. The reaction mixture was then concentrated and purified by silica gel chromatography (twice, 0–50% ethyl acetate in hexanes) to afford 2-(4-(4-((6-chloro-3-pyridinyl)sulphonyl)-2-(1-propyn-1-yl)-1-piperazinyl)phenyl)-1,1,1,3,3,3-hexafluoro-2-propanol (3.46 g, 100%) as an off-white solid. ^{1}H-NMR (400 MHz, $CDCl_3$) δ 8.84 (d, J = 2.2 Hz, 1 H), 8.06 (dd, J = 2.3, 8.4 Hz, 1 H), 7.60 (d, J = 8.6 Hz, 2 H), 7.52 (d, J = 8.4 Hz, 1 H), 7.01–6.93 (m, 2 H), 4.46 (br s, 1 H), 3.85 (t, J = 11.2 Hz, 2 H), 3.52–3.33 (m, 3 H), 2.95 (dd, J = 3.1, 11.3 Hz, 1 H), 2.81 (dt, J = 3.7, 11.3 Hz, 1 H), 1.78 (d, J = 1.6 Hz, 3 H).

A 20-ml sealed tube was charged with 2-(4-(4-((6-chloro-3-pyridinyl)sulphonyl)-2-(1-propyn-1-yl)-1-piperazinyl)phenyl)-1,1,1,3,3,3-hexafluoro-2-propanol (0.340 g, 0.627 mmol), concentrated ammonium hydroxide (5.00 ml, 38.5 mmol) and ethanol (5 ml). The reaction mixture was heated in a microwave reactor at 120 °C for 1 h. The reaction mixture was heated in a heating block at 110 °C for 5 h and then concentrated and purified by silica gel chromatography (25 g of silica, 30 to 80% ethyl acetate in hexanes) to afford 2-(4-(4-((6-amino-3-pyridinyl)sulphonyl)-2-(1-propyn-1-yl)-1-piperazinyl)phenyl)-1,1,1,3,3,3-hexafluoro-2-propanol (0.289 g, 88%) as a mixture of two enantiomers. ^{1}H-NMR (400 MHz, $CDCl_3$) δ 8.49 (br s, 1 H), 7.80 (dd, J = 2.3, 8.8 Hz, 1 H), 7.59 (d, J = 8.8 Hz, 2 H), 6.97 (d, J = 9.0 Hz, 2 H), 6.55 (d, J = 8.8 Hz, 1 H), 5.05 (s, 2 H), 4.46 (br s, 1 H), 3.85–3.72 (m, 2 H), 3.54 (br s, 1 H), 3.50–3.34 (m, 2 H), 2.83 (dd, J = 3.3, 11.0 Hz, 1 H), 2.69 (dt, J = 3.4, 11.0 Hz, 1 H), 1.80 (s, 3 H); m/z (electrospray ionization (ESI), positive ion) 523.1 $(M + H)^+$.

The individual enantiomers were isolated using chiral SFC (Chiralpak ADH column (21 × 250 mm, 5 μm) eluting with 35% methanol in supercritical CO_2 (total flow was 70 ml min^{-1}). This produced the two analogues with enantiomeric excesses of >98%. The analytical data for 2-(4-((2S)-4-((6-amino-3-pyridinyl)sulphonyl)-2-(1-propyn-1-yl)-1-piperazinyl)phenyl)-1,1,1,3,3,3-hexafluoro-2-propanol (AMG-3969, first eluting peak) are listed below. ^{1}H-NMR (400 MHz, $CDCl_3$) δ 8.48 (d, J = 2.3 Hz, 1 H), 7.77 (dd, J = 2.5, 8.8 Hz, 1 H), 7.57 (d, J = 8.8 Hz, 2 H), 6.95 (d, J = 9.2 Hz, 2 H), 6.52 (d, J = 8.8 Hz, 1 H), 4.94 (s, 2 H), 4.44 (br s, 1 H), 3.82–3.71 (m, 2 H), 3.58–3.33 (m, 3 H), 2.81 (dd, J = 3.2, 11.1 Hz, 1 H), 2.67 (dt, J = 3.9, 11.0 Hz, 1 H), 1.78 (d, J = 2.2 Hz, 3 H); m/z (ESI, positive ion) 523.2 $(M + H)^+$.

Crystallography. Initial GKRP crystals were grown in the presence of S6P. Crystals were grown by vapour diffusion against a well buffer of 100 mM Bis-Tris, pH 7.5, 200 mM NaI and 16% PEG8000. The protein and well buffers were mixed in a 1:1 ratio. The crystal was then soaked into a buffer solution containing 0.5 mM AMG-1694. Previously we determined that soaking and co-crystallizing ligands with GKRP led to similar results.

SPR spectroscopy. SPR experiments were performed on a Biacore T200 instrument (GE Healthcare) at 25 °C. CM5 sensor chips were pre-conditioned with 2 × 6-s pulses of 100 mM HCl, 50 mM NaOH, and 0.5% (*v/v*) SDS. Streptavidin was immobilized at 10,000 response units (RU) using amine coupling chemistry and a buffer consisting of 10 mM HEPES, pH 7.4, and 150 mM NaCl. Immobilization steps: 10 min 800 mM 1-ethyl-3-(3-dimethylaminopropyl) carbodiimide hydrochloride/200 mM *N*-hydroxysuccinimide activation, 15 min 0.5 mg ml^{-1} streptavidin in 10 mM sodium acetate, pH 5.0, and 3 min 1 M ethanolamine HCl, pH 8.5. Buffer was replaced with assay buffer consisting of 50 mM HEPES, pH 7.4, 25 mM KCl, 4 mM $MgCl_2$, 5 mM DTT, 0.002% (*v/v*) Brij35 and 2% (*v/v*) DMSO. To study the effect of S6P and AMG-1694 on the GK–GKRP complex, ~120 RU of biotin-GK were captured, and the complex was formed by injecting 1 μM untagged GKRP for 2 min. During dissociation, buffer, S6P (50 μM), AMG-1694 (2 μM) or a mixture of S6P (50 μM) and AMG-1694 (2 μM) were injected for 10 min. To study AMG-1694 and S6P binding, GKRP-biotin was captured at 6,800–8,100 RU. AMG-1694 was diluted to 2 μM and serially diluted (threefold) five times in buffer without and with 50 μM S6P. S6P was diluted to 5 μM and serially diluted (threefold) five times in buffer without and with 50 μM S6P. AMG-1694 binding to GKRP (full-length or 20–625 truncation) was analysed using a single-site kinetics method with an association time of 60 s, a dissociation time of 900 s and flow rate of 70 μl min^{-1}. To measure the GK–GKRP binding affinity, GKRP-biotin was captured at ~110 RU onto the streptavidin biosensor surface. Untagged GK was diluted to 125 nM and serially diluted (twofold) seven times in a buffer consisting of 50 mM HEPES, pH 7.1, 25 mM KCl, 4 mM $MgCl_2$, 5 mM DTT, 0.2 mM fructose-6-phosphate and 0.002% (v/v) Brij35. GK was injected for 2 min and dissociation observed for 10 min at a flow rate of 50 μl min^{-1}. The data were processed using Biacore T200 Evaluation software and a 1:1 binding model that included mass transfer limitation. Averages and standard deviations were calculated from two biological replicates.

Primary hepatocyte translocation assay. Rat hepatocytes[28] in maintenance media (Williams E, 10% FBS, 1 × PSG, 1 μg ml^{-1} insulin, 100 nM dexamethasone) were plated into a 96-well plate (50,000 cells per well) and incubated overnight. Cells were washed twice (200 μl DMEM no glucose/0.2% BSA), received 100 μl DMEM/0.2% BSA and were then incubated for 3–4 h at 37 °C. Cells were again washed with DMEM only, AMG-1694 diluted in DMEM was added, and the cells were incubated for 20 min at 37 °C. Glucose (10 μl 25 mM) was then added and the cells were further incubated for an additional 40 min at 37 °C. Cells were then fixed (100 μl 8% formaldehyde/PBS) and plates incubated at room temperature for 15 min, washed twice with 200 μl PBS, and then permeabilized (75 μl 0.3% Triton X-100/PBS) for 10 min. After two washes with 200 μl PBS, 50 μl blocking solution (Li-Cor) was added and the cells were incubated for 1 h at room temperature. Cells were washed (100 μl 1% goat serum/0.1% Tween in PBS), incubated with 50 μl anti-GK antibody (H-88, sc7908, Santa Cruz Biotech) diluted 1:125 in 1:1 Li-Cor blocking/wash buffer at 4 °C overnight and, after washing, 50 μl goat anti-rabbit AlexaFluor 555 (goat anti-rabbit IgG, A21429, Life Technologies) diluted 1:100 and 1 μg ml^{-1} of Hoechst 33342 (H3570, Invitrogen) in wash buffer was added to each well and the plates were incubated for 1 h at room temperature. After washing, 200 μl PBS was added to each well. AMG-1694- or glucose-induced nucleus-to-cytoplasmic GK translocation in rat hepatocytes was captured and analysed by Thermo Fisher ArrayScan VTI using Cellomics ArrayScan Software with the built in Molecular Translocation (v.4) protocol to calculate the ratio of cytoplasmic and nuclear intensities. The average intensities of 4,000 cells per well were quantified. An alternative analysis used the Operetta (PerkinElmer) imaging platform equipped with Harmony High Content Imaging and Analysis Software.

Primary hepatocyte 2DG phosphorylation studies. Hepatocytes[28] were plated on collagen-I-coated 96-well tissue culture plates with DMEM/F12 medium containing 10% FBS. Cells were cultured for 48 h, washed twice with PBS, and then transferred to DMEM glucose-free medium/0.2% BSA for starvation. After 2 h, cells were treated with the same medium containing 100 mM 2DG and various concentrations of compounds for 2 h. Plates were washed twice with PBS, and cells lysed with 70% acetonitrile. Lysates were transferred into the assay plate and analysed using LC–MS/MS. EC_{50} values were calculated using GraphPad Prism software using nonlinear regression curve fit analysis selecting the log(agonist) versus response − variable slope (four parameters) equation.

***In vivo* studies.** ZDF and Wistar male rats were purchased from Harlan Laboratories at 6 weeks of age. B6 and *ob/ob* male mice were purchased from Harlan Laboratories at 8 weeks of age, *db/db* male mice were purchased from Jackson Laboratories at 8–9 weeks of age. DIO animals were prepared as B6 mice (4 weeks old) fed a high-fat diet (Research diets D12492 60% kcal fat) for 12 weeks. All animals were cared for in accordance to the US National Research Council Guide for the Care and Use of Laboratory Animals, Eighth Edition. Animals were housed two rats per cage, four *ob/ob* or *db/db* mice per cage, and one B6 or DIO mouse per cage at an AAALAC-International-accredited facility in a ventilated micro-isolator on corn cob bedding. All research protocols were approved by the Amgen Institutional Animal Care and Use Committee. ZDF rats had *ad libitum* access to pelleted Purina 5008 chow, and Wistar rats and mice had access to Harlan Teklad 2020x chow, and were maintained on a 12 h:12 h light:dark cycle with enrichment opportunities. All animals were determined specific pathogen-free. At 08:00, 8-week-old rats were bled via tail venipuncture, and 9-week-old B6 or *ob/ob* mice, 9–10-week-old *db/db* mice, or 16-week-old DIO mice were bled via retroorbital sinus puncture, and blood glucose values were determined (AlphaTRAK glucose meter) and used to randomize the animals in which their group averages were similar and standard deviations minimized. Only ZDF rats with blood glucose ranges between 250 and 350 mg dl^{-1} were included. Animals were excluded from experiments based on pre-established criteria of low body weights or health issues. Because of high variability of blood glucose levels induced by handling stress, groups were sized at 8 animals as determined by historical studies within the laboratory. Minimal variability was observed for liver GK scoring and indirect calorimetry, and groups were sized at 4 animals and 5–6 animals respectively. Animals were gavaged with vehicle (2% hydroxypropyl methycellulose, 1% Tween 80, pH 2.2 adjusted with MSA) or AMG-1694/AMG-3969 or GKA formulations at 09:00. Experimenters were not blinded to treatment group. Blood glucose was measured at 4, 7 or 8, and 24 h after treatment. B6 mice (fasted 11 h) were treated 1 h before a glucose tolerance test was conducted with an intraperitoneal 2 g kg^{-1} glucose challenge. A chronic ZDF rat study was conducted with daily 09:00 dosing and liver collection 8 h after the fourth dose. For IHC studies, animals were not randomized before culling following anaesthesia, and liver samples were immediately excised (2–3 mm thick and 7–8 mm long, from the right medial and the left lateral lobe), fixed in cold paraformaldehyde for 3 h, and transferred to 70% ethanol before processing and embedding in paraffin. Plasma insulin and triglycerides were measured using an ELISA (ALPCO) or Olympus AU400e Chemistry Analyzer (Olympus America). Indirect calorimetry was assessed using the Comprehensive

©2013 Macmillan Publishers Limited. All rights reserved

Laboratory Animal Monitoring System (Columbus Instruments). The animals were acclimatized to the housing for 7 days. A 24-h baseline monitoring was carried out before treatment with either AMG-3969 or GKA at 09:00. The animals were allowed to washout this treatment for 2 days before beginning multiple dosing for 2–3 days. Respiratory exchange ratio was calculated as the ratio of VCO_2 to VO_2.

GK and GKRP immunoblotting. Liver extracts were resolved electrophoretically, transferred to a nitrocellulose membrane and proteins were detected using anti-GK antibody (H-88, sc7908, Santa Cruz Biotech), anti-GKRP antibody (H-300, sc11416, Santa Cruz Biotech), and anti-β actin antibody (Sigma). The bands were visualized by using the FluorChemHD2 system (Alpha Innotech).

Immunohistochemistry. Five-micrometre-thick sections of paraffin-embedded liver were de-paraffinized and hydrated in distilled water. Sections were pre-treated with Diva Decloaker (Biocare Medical) in a pressure cooker, blocked with CAS-Block (Invitrogen), and incubated with rabbit anti-GK antibody (H-88, sc7908, Santa Cruz Biotech) at 1:100 for 1 h at room temperature. Slides were quenched with 3% H_2O_2 followed with EnVision+ horseradish-peroxidase-labelled polymer anti-rabbit (DAKO). Reaction sites were visualized with DAB (DAKO) and slides were counterstained with haematoxylin. Slides were independently evaluated for nuclear GK intensity by two observers without knowledge of treatment group.

25. Ashton, K. *et al.* Preparation of sulfonylpiperazine derivatives that interact with glucokinase regulatory protein for the treatment of diabetes and other diseases. US patent PCT Int. Appl. WO 2012027261 (2012).
26. Frenette, R. *et al.* Substituted 4-(2,2-diphenylethyl)pyridine-*N*-oxides as phosphodiesterase-4 inhibitors: SAR study directed toward the improvement of pharmacokinetic parameters. *Bioorg. Med. Chem. Lett.* **12,** 3009–3013 (2002).
27. Hogan, P. J. & Cox, B. G. Aqueous process chemistry: the preparation of aryl sulfonyl chlorides. *Org. Process Res. Dev.* **13,** 875–879 (2009).
28. Kreamer, B. L. *et al.* Use of a low-speed, iso-density percoll centrifugation method to increase the viability of isolated rat hepatocyte preparations. *In Vitro Cell. Dev. Biol.* **22,** 201–211 (1986).

©2013 **Macmillan Publishers Limited. All rights reserved**

LETTER

doi:10.1038/nature12718

Themis sets the signal threshold for positive and negative selection in T-cell development

Guo Fu[1], Javier Casas[1,2]*, Stephanie Rigaud[1]*, Vasily Rybakin[1,2]*, Florence Lambolez[3], Joanna Brzostek[1,2], John A. H. Hoerter[1], Wolfgang Paster[4], Oreste Acuto[4], Hilde Cheroutre[3], Karsten Sauer[1,5] & Nicholas R. J. Gascoigne[1,2]

Development of a self-tolerant T-cell receptor (TCR) repertoire with the potential to recognize the universe of infectious agents depends on proper regulation of TCR signalling. The repertoire is whittled down during T-cell development in the thymus by the ability of quasi-randomly generated TCRs to interact with self-peptides presented by major histocompatibility complex (MHC) proteins. Low-affinity TCR interactions with self-MHC proteins generate weak signals that initiate 'positive selection', causing maturation of CD4- or CD8αβ-expressing 'single-positive' thymocytes from $CD4^+CD8\alpha\beta^+$ 'double-positive' precursors[1]. These develop into mature naive T cells of the secondary lymphoid organs. TCR interaction with high-affinity agonist self-ligands results in 'negative selection' by activation-induced apoptosis or 'agonist selection' of functionally differentiated self-antigen-experienced T cells[2,3]. Here we show that positive selection is enabled by the ability of the T-cell-specific protein Themis[4–9] to specifically attenuate TCR signal strength via SHP1 recruitment and activation in response to low- but not high-affinity TCR engagement. Themis acts as an analog-to-digital converter translating graded TCR affinity into clear-cut selection outcome. By dampening mild TCR signals Themis increases the affinity threshold for activation, enabling positive selection of T cells with a naive phenotype in response to low-affinity self-antigens.

Themis-deficient mice have severely reduced numbers of single-positive thymocytes and peripheral T cells[4–8], but the mechanism by which Themis controls T-cell development or function remains obscure. Its rapid phosphorylation after TCR stimulation[4,9,10] and subtle signalling defects in *Themis*$^{-/-}$ double-positive thymocytes suggested a role in proximal TCR signalling[4,9,11], although others failed to find any alteration in TCR signalling[5–7,10]. Such mild or undetected signalling defects seemed incompatible with the strong positive selection defect in Themis-deficient mice.

We suspected that activation by antibody-mediated TCR crosslinking may have masked genuine signalling defects that would be revealed with more physiological stimulation. Calcium flux is a hallmark of early TCR signalling and is very sensitive to differences in signal strength[12]. We titrated streptavidin crosslinking for anti-CD3/CD4 antibodies to better mimic graded signal strengths TCRs might generate *in vivo*. Over a broad concentration range, we found only minor reduction in calcium signal in Themis-deficient thymocytes, consistent with our previous observations[4], but of dubious biological relevance (Extended Data Fig. 1). Therefore, we used the well-characterized OT-I TCR-transgenic model[13] to enable thymocyte activation by more physiological MHC proteins ligands. Natural positively selecting and antigen-variant peptides eliciting a full spectrum of signal strengths are well documented (Extended Data Fig. 2a). OT-I *Tap1*$^{-/-}$ mice express low cell-surface MHC-I, so thymocyte development is arrested at the pre-selection double-positive stage. Therefore OT-I *Tap1*$^{-/-}$*Themis*$^{-/-}$ or *Themis*$^{+/+}$ thymocytes are an excellent system to study TCR signalling after stimulation with appropriate antigen H-2K^b (K^b) tetramers. As expected, Themis-sufficient double-positive thymocytes gave very low but sustained Ca^{2+} responses to positively selecting peptides Q4H7, Q7 and G4[12]. Remarkably, Themis-deficient cells responded much stronger than Themis-sufficient cells to these ligands, also giving increased responses to lower-affinity E1 and the natural positive-selector Catnb. Responses to strong agonists OVA (the antigenic peptide for OT-I T cells) and its variant A2 (see Extended Data Fig. 2a) were similar between genotypes (Fig. 1a–c and Extended Data Fig. 2b). Similar results were obtained by stimulation on supported lipid bilayers (Fig. 1d). These results were confirmed by imaging Ca^{2+} in thymocytes recognizing RMA-S cells presenting representative high (OVA)- or low (G4)-affinity peptides. Themis-deficient thymocytes responded more strongly than Themis-sufficient to G4, but similarly to OVA (Fig. 1e, f and Extended Data Fig. 3). The strong, transient Ca^{2+} response to negative-selecting ligands versus low, sustained signal to positively selecting ligands[12], are reflected in differential nuclear translocation of NFATC2[14]. Themis-sufficient thymocytes induced strong, transient NFATC2 translocation in response to K^b–OVA tetramer, and delayed but more sustained translocation in response to K^b–G4 (Fig. 1g, Extended Data Fig. 4). In contrast, in Themis-deficient thymocytes, both K^b–OVA and K^b–G4 tetramers induced nearly identical NFATC2 translocation kinetics, similar to the K^b–OVA response of wild-type thymocytes. These data demonstrate that the role of Themis in thymocyte signalling is manifest in the response to weak ligands, but masked in responses to strong (agonist) ligands. These differences were largest with ligands below the previously described positive-negative selection border[12]. Differences were noticeable for ligands slightly above this threshold (weak agonists), but were completely masked by antibody crosslinking.

Appropriate ERK signalling kinetics are critical for positive selection[15–17]. As shown previously, antibody crosslinking induced slightly weaker ERK phosphorylation in Themis-deficient compared to Themis-sufficient cells[4] (Extended Data Fig. 5). Further analysis of phosphorylated (p)-ERK by flow cytometry showed roughly equal p-ERK responses induced with K^b–OVA tetramer in both genotypes. However, ERK signalling was faster and stronger in Themis-deficient double-positive cells in response to ligands weaker than K^b–OVA (Fig. 2a, b and Extended Data Fig. 6), and confirmed by immunoblot (Extended Data Fig. 5). These data further support the notion that *Themis*$^{-/-}$ cells receive signals induced by classical positive-selecting ligands as activating signals, similar to negative/agonist ligand-induced signals.

The subcellular localization of p-ERK in thymocytes differs with ligand affinity, with negative/agonist-selection stimuli inducing p-ERK more proximal to the plasma membrane than positive-selection stimuli, which induced p-ERK deeper within the cell[12]. To determine whether Themis controls the topology of TCR-induced ERK activation, we

[1]Department of Immunology and Microbial Science, The Scripps Research Institute, 10550 North Torrey Pines Road, La Jolla, California 92037, USA. [2]Department of Microbiology, Yong Loo Lin School of Medicine and Immunology Programme, National University of Singapore, 5 Science Drive 2, Singapore 117545. [3]Developmental Immunology, La Jolla Institute for Allergy and Immunology, 9420 Athena Circle, La Jolla, California 92037, USA. [4]Sir William Dunn School of Pathology, University of Oxford, South Parks Road, Oxford OX1 3RE, UK. [5]Department of Cell and Molecular Biology, The Scripps Research Institute, 10550 North Torrey Pines Road, La Jolla, California 92037, USA.
*These authors contributed equally to this work.

©2013 Macmillan Publishers Limited. All rights reserved

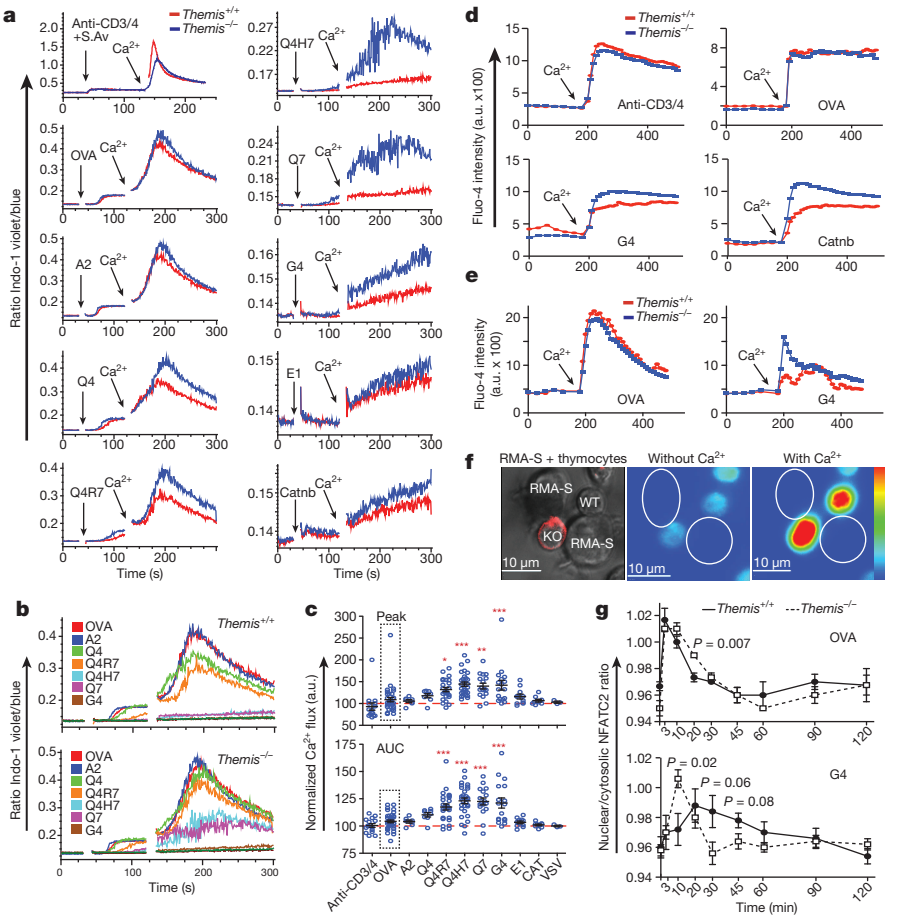


Figure 1 | Differentially regulated Ca^{2+} flux in *Themis*$^{-/-}$ thymocytes. **a**, **b**, *Themis*$^{+/+}$ or *Themis*$^{-/-}$ OT-I pre-selection thymocytes were incubated with indicated stimuli. Results of representative experiment shown in **a**, same-genotype comparisons in **b**. **c**, Summary of Ca^{2+} flux differences. Each dot represents one *Themis*$^{-/-}$ sample normalized to its same-tube *Themis*$^{+/+}$ control[30] (sex and age-matched), thus blinding and randomization was unnecessary. Each paired sample represents a biological and technical replicate[30]. Data obtained from eight litters of each genotype over 10 months. Peak-height (top) and area-under-the-curve (AUC, bottom) shown. Statistical significance determined by one-way analysis of variance Dunnett's test, with OVA as comparison control. $*P < 0.05$, $**P < 0.01$, $***P < 0.001$. Minimal sample size needed to obtain $P = 0.05$, 90% power, estimated based on 1.2-fold difference. a.u., arbitrary units. **d**, Ca^{2+} flux imaging on supported lipid bilayers. Cells settled on K^b-monomer or antibody-coated lipid bilayer were imaged before and after adding $CaCl_2$. Graphs show mean Fluo-4 intensity (wild type (WT): $n = 11, 27, 17, 29$; KO: $n = 20, 14, 24, 23$, for cells stimulated by antibody, OVA, G4 and Catnb, respectively), representative of two experiments. **e**, Live Ca^{2+} imaging of stimulation by RMA-S cells pre-loaded with OVA ($n = 5$) or G4 ($n = 8$) peptide, measured as in **d**. Representative of three experiments. **f**, Representative images of OVA-stimulation of cells analysed in **e**. *Themis*$^{-/-}$ cells identified by Cy5 staining (red on transmitted light image), Ca^{2+} scale on right. **g**, NFATC2 translocation in thymocytes responding to K^b–OVA and K^b–G4 tetramers. Nuclear/cytosolic NFATC2 protein ratios (Extended Data Fig. 4) calculated using CellProfiler, $n = 70$ cells per data-point. Mean ± s.e.m. shown. *P* values from unpaired *t*-test. Representative of two experiments.

compared p-ERK localization in Themis-deficient or Themis-sufficient pre-selection double-positive thymocytes responding to different ligands (Fig. 2c, d and Extended Data Fig. 7). Weak ligands that normally induce intracellular p-ERK in Themis-expressing cells instead gave a relatively high proportion of membrane-proximal p-ERK in *Themis*$^{-/-}$ DPs. In aggregate, these data indicate that, without Themis, the ERK cascade

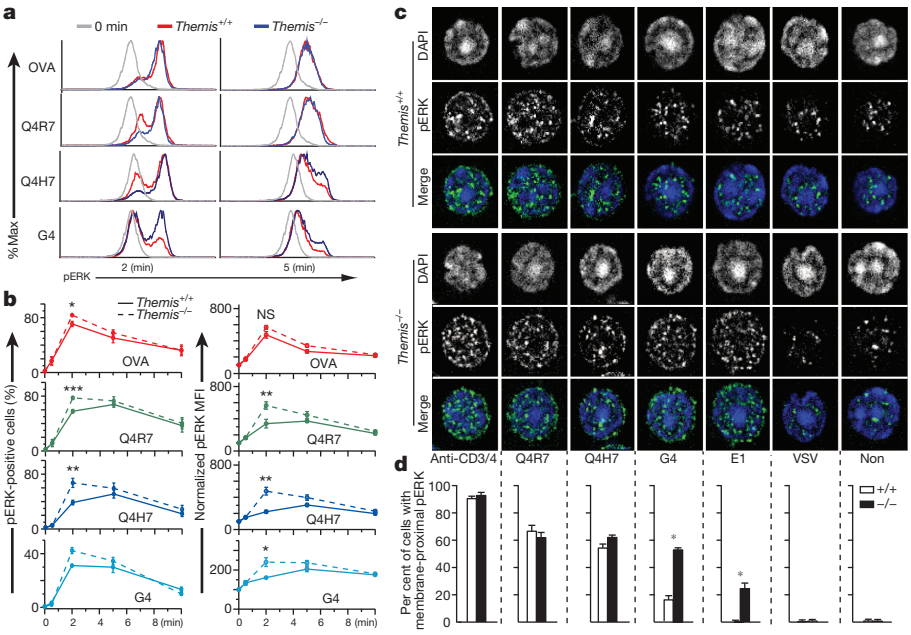


Figure 2 | Themis-deficiency allows low-affinity ligands to elicit negative selection-like characteristics of ERK activation. Themis-sufficient or Themis-deficient pre-selection thymocytes were stimulated with K^b-tetramers. **a**, **b**, ERK phosphorylation detected by flow cytometry following intracellular staining. Representative FACS plots shown in **a** and Extended Data Fig. 6. %Max, per cent of maximum. **b**, Summarized data compiled from multiple experiments ($n = 5$ for OVA, Q4R7 and Q4H7, $n = 8$ for G4), presented as mean ± s.e.m. of percentage p-ERK$^+$ cells (left), MFI, mean fluorescence intensity (right). Sample sizes estimated as Fig. 1. $*P < 0.05$, $**P < 0.01$ and $***P < 0.001$, paired *t*-test. **c**, **d**, Localization of p-ERK determined by staining stimulated thymocytes (2 min) with DAPI and anti-p-ERK[12]. **c**, Representative images. **d**, Percentage of cells with membrane-proximal p-ERK, $n = 20$ for each condition, mean ± s.e.m. Representative of four experiments for each tetramer, two different operators, not blinded. Unpaired *t*-test on two identical experiments, $*P < 0.05$.

©2013 Macmillan Publishers Limited. All rights reserved

was both mis-localized and hyperactivated, so that positive-selecting ligands were mistakenly interpreted as negative/agonist-selectors. Thus, *Themis*$^{-/-}$ double-positive cells seem unable to precisely distinguish low-affinity from high-affinity TCR signalling.

Both the Ca^{2+} response and ERK signalling cascade occur distal to TCR stimulation. We therefore examined more proximal signalling events to determine where these marked changes in signal transduction to low-affinity ligands were initiated. We found substantially elevated phosphorylation of LAT and PLCγ1 (Fig. 3a), although not SLP-76 (Extended Data Fig. 8), in Themis-deficient versus Themis-sufficient cells upon stimulation with low-affinity ligands. This point of action is consistent with previous reports that Themis interacts with PLCγ1 and is part of the LAT signalosome[4,9,11]. These data demonstrate that *Themis*$^{-/-}$ cells mount an augmented response to low-affinity ligands, similar to a wild-type response to high-affinity ligands, indicating that Themis restricts TCR signalling in double-positive cells stimulated by low-affinity ligands. SHP1, a cytoplasmic protein tyrosine phosphatase, is an important negative regulator in TCR signalling (reviewed in ref. 18). It is activated by tyrosine phosphorylation, and reported to control the thresholds for positive and negative selection[18–21]. To test if Themis might limit TCR signalling by controlling SHP1, we analysed SHP1 phosphorylation in *Themis*$^{+/+}$ and *Themis*$^{-/-}$ double-positive cells. Notably, p-SHP1 (but not total protein) was markedly decreased in Themis-deficient cells, clearly opposite to enhanced p-ERK. Indeed p-SHP1 was barely induced in the Themis-deficient cells (Fig. 3b and Extended Data Fig. 9). Moreover, Themis interacted constitutively with SHP1 but p-SHP1 was induced in Themis-SHP1 complexes in response to TCR stimulation (Fig. 3c). Themis–GRB2 binding was constitutive (Fig. 3d)[5–7,9]. Because activated LCK is a SHP1 substrate[18,22], we tested LCK phosphorylation, finding that the activated pY394 form was indeed increased in Themis-deficient thymocytes (Fig. 3e).

These results suggest that Themis 'caps' the signal strength by controlling SHP1 activation, moderating strength and kinetics of responses to relatively low-affinity ligands. This allows these self-antigen-experienced cells to mature into naive T cells. Without Themis, thymocytes receive strong agonist/negative-selection-like signals. To test whether these redirect low-affinity stimulation to induce negative selection, we stimulated pre-selection double-positive thymocytes with K^b-tetramers, and assayed caspase-3 activation, a readout for apoptosis[23]. Indeed, caspase-3 activation was significantly increased in *Themis*$^{-/-}$ versus *Themis*$^{+/+}$ cells in response to ligands that normally induce positive selection, but was similar for ligands that normally induce negative selection (Fig. 4a, left). Reduced activated caspase-3$^+$ cells in OVA-stimulated populations versus weaker ligands is probably due to phagocytosis of dead cells, as OVA signals were clearly stronger based on TCR downmodulation (Fig. 4a, right). Deficiency of the pro-apoptotic protein Bim rescues thymocytes from negative selection[24]. Intriguingly, *Bim* co-disruption rescued the previously reported[4–8] impaired single-positive thymocyte development in *Themis*$^{-/-}$ mice and defective CD8SP thymocyte development in OT-I *Themis*$^{-/-}$ mice (Fig. 4b, c). This indicated that the defect in thymocyte development in *Themis*$^{-/-}$

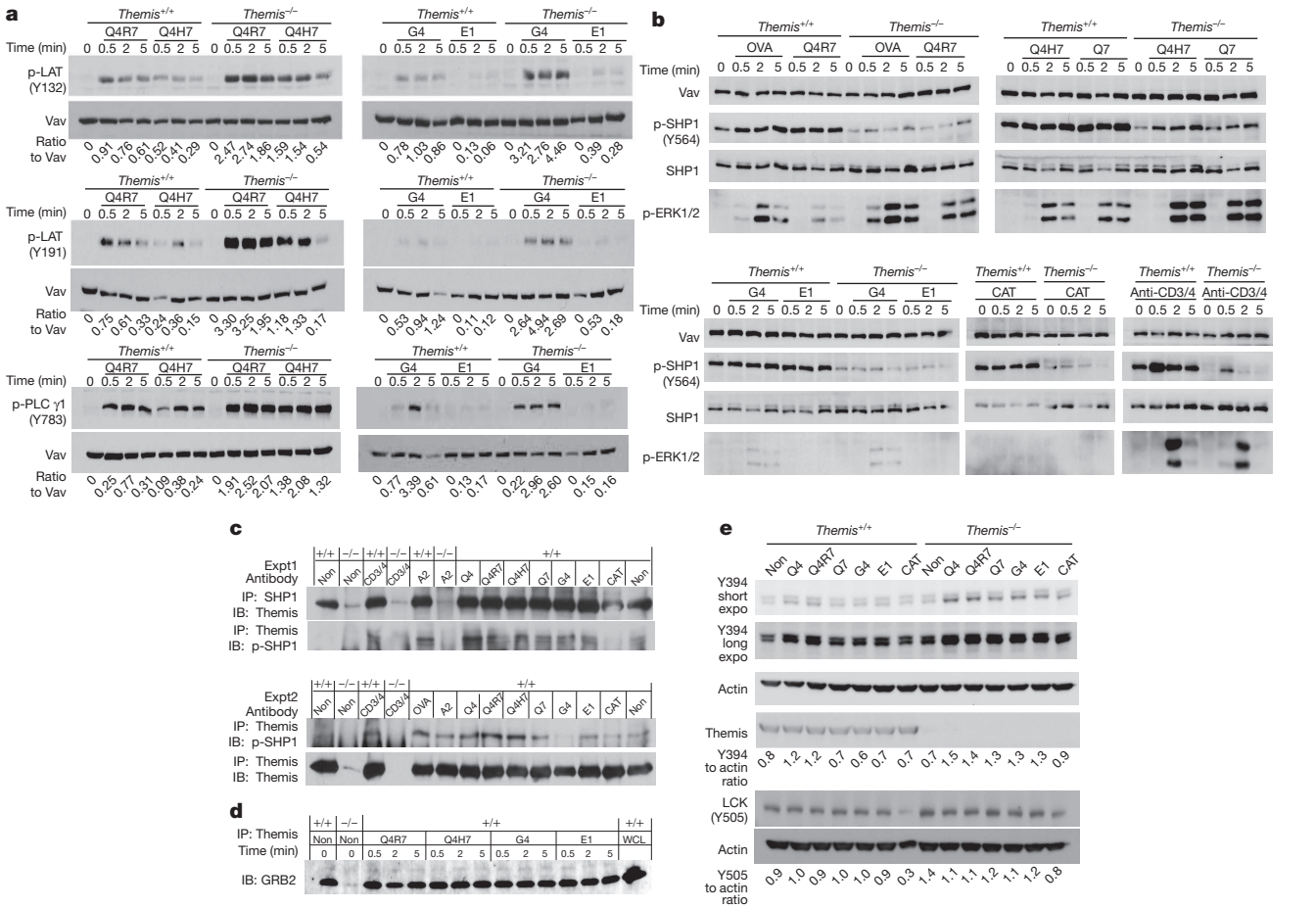


Figure 3 | Proximal TCR signalling in Themis-deficient thymocytes responding to positive selecting ligands. *Themis* KO or WT pre-selection thymocytes were stimulated with indicated tetramers and analysed by immunoblot. **a**, LAT and PLCγ1 phosphorylation. **b**, SHP1 and ERK1/2 phosphorylation. Vav was used as loading control. **c**, Themis interaction with SHP1 and p-SHP1 (Expt, experiment). **d**, Themis interaction with GRB2. IB, immunoblot; IP, immunoprecipitation. **e**, Phosphorylation of LCK in response to different stimuli. The lower molecular weight band in blots probed with anti-p-Y394 is LCK (p56), the higher is FYN (p59). expo, exposure. Representative of 2 (**b**), 3 (**a**, **c**, **e**) and 6 (**d**) experiments, respectively.

©2013 Macmillan Publishers Limited. All rights reserved

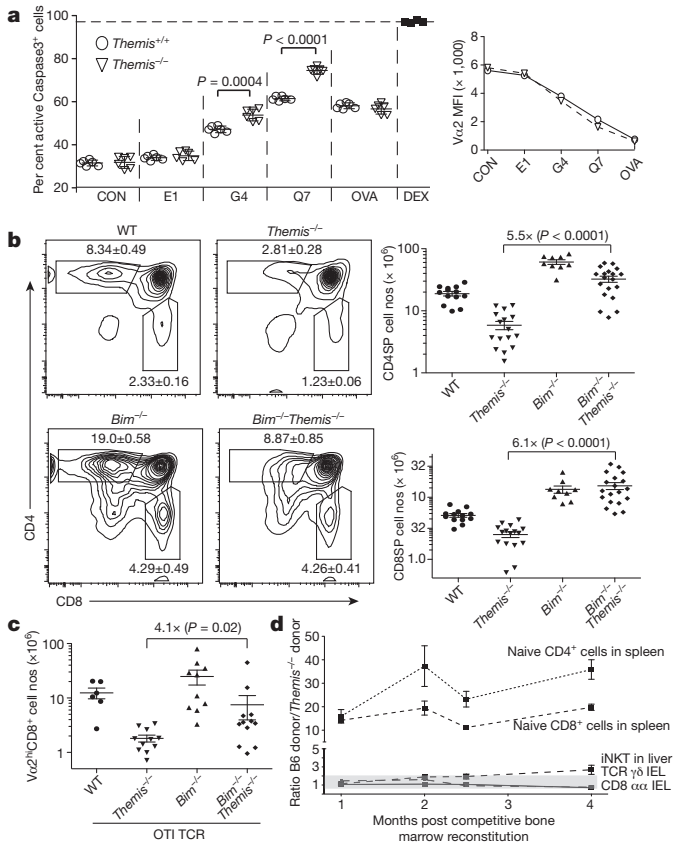


Figure 4 | Themis-deficient mice show enhanced negative selection that can be rescued by Bim deficiency, but normal agonist selection. **a**, Pre-selection thymocytes were stimulated with tetramers for 17 h, then analysed for activated caspase-3[23]. Triplicate measurements for two mice per genotype, showing mean ± s.e.m. Right panel shows TCR down-modulation. Representative of 3 experiments. **b**, Thymocytes were analysed for CD4 and CD8 expression. 4–6-week-old mice of both sexes included, no randomization nor blinding necessary for genetic experiment read by flow cytometry. Sample sizes chosen to obtain $P = 0.01$, 90% power for fivefold difference. Left, representative plots showing mean ± s.e.m. percentage of each subset labelled. Right, summarized data of absolute numbers for each subset. **c**, Mice of indicated genotypes as **b** but expressing OT-I TCR-transgene, analysed for $V\alpha2^{hi}CD8^{+}$ subset. Summarized data of absolute cell numbers shown. In **b** and **c**, each symbol represents a single mouse. Statistics, unpaired *t*-test (**a**) and Mann–Whitney test (**b**, **c**). Fold increases and *P* values between indicated samples shown in each scheme. **d**, Phenotypic analysis of indicated subsets in competitive bone-marrow-reconstituted mice. Data pooled from multiple experiments, shown as mean ± s.e.m. after normalizing $Themis^{+/+}$-derived donor cells to $Themis^{-/-}$ donor cells ($n = 4$ pairs of mice per time point except 2 months, 8 pairs). Grey zone indicates ratio between 0.5 and 2. Group sizes based on prior experience.

mice is caused at least partially by misplaced negative selection (agonist selection would not be affected by Bim-deficiency). This suggested the possibility that, although conventional naive T-cell development requiring weak sustained signalling is severely impaired, agonist-selection of non-conventional T cells by intermediate affinity ligands might be spared or compensated in Themis-deficient mice. To test this, we simultaneously examined development of wild-type and Themis-deficient T cells in mixed bone marrow chimaeras, avoiding potential homeostatic proliferation artefacts (Fig. 4d). $Themis^{+/+}$ vastly outnumbered $Themis^{-/-}$ cells among conventionally selected naive peripheral T cells, but $TCR\gamma\delta^{+}$ intra-epithelial lymphocytes (IEL), $TCR\alpha\beta^{+}$ $CD8\alpha\alpha$ IELs and liver iNKT-cells, which all are selected from double-positive cells by strong TCR signals[2,3,25], showed roughly equal reconstitution by both genotypes. Thus, development of agonist-selected T cells is not, or at most very mildly, affected by the absence of Themis, in contrast to generation of peripheral naive T cells, supporting our notion that the role of Themis differs in relation to ligand strength.

This study shows that Themis acts early in the TCR signalling cascade, reducing signal strength in response to low-affinity but not high-affinity MHC proteins ligands. Without Themis, TCR signalling in response to low-affinity MHC proteins ligands mimics normal signalling responses to negative or agonist-selecting ligands, generating stronger signals that redirect the selection outcome. Themis performs this function through controlling recruitment and activation of the phosphatase SHP1, which limits TCR signalling and reportedly affects the thresholds for positive and negative selection[19–21], as well as helping discriminate between agonist and lower-affinity antagonist ligands[22]. A recent study using a conditional knockout of SHP1, where deletion occurred at the immature double-positive stage of thymocyte development, showed that SHP1 was not required for normal thymocyte development[26]. It is possible that incomplete deletion of SHP1 mediated by transgenic CD4-Cre may mask the requirement of SHP1 in thymocyte development. Alternatively other phosphatases can act redundantly in selection[26]. The dominant negative SHP1 transgenes that appeared to show the involvement of SHP1 in development[19,20] would likely have blocked other phosphatases in addition to SHP1. We therefore tested whether Themis is able to interact with SHP2. We found that Themis indeed interacts constitutively with SHP2 (Extended Data Fig. 10), indicating that the lack of a $Themis^{-/-}$-like phenotype in the conditional SHP1 knockout is probably owing to redundancy between phosphatases, raising the possibility that different phosphatases may be important in TCR signalling in different situations.

Themis acts to enforce the threshold between positive and negative/agonist selection, which occurs over a very narrow range of TCR–MHC protein affinities[12]. Themis causes an analog continuum of TCR affinities to elicit a digital selection outcome—positive versus negative/agonist selection. We speculate that altered Themis expression shifts the selection window, changing the mature TCR repertoire, and therefore affecting disease susceptibility. Indeed, single-nucleotide polymorphisms in the noncoding region between human *THEMIS* and *PTPRK* genes have been associated with susceptibility to coeliac disease and multiple sclerosis[27–29]. More work is needed to understand the connection between these polymorphisms, Themis expression and the aetiology of disease.

METHODS SUMMARY

Animal experiments were performed in accordance with the TSRI Animal Care and Use Committee. Thymocytes from $Themis^{+/+}$ or $Themis^{-/-}$ OT-I $Tap1^{-/-}$ 4–6-week-old mice, both sexes, were used. For *ex vivo* experiments, thymocytes were rested 3 h at 37 °C before assay. For Ca^{2+} assays, knockout cells were pre-labelled with Cy5 and mixed with wild-type cells (or vice versa), loaded with Ca^{2+}-sensitive dye (indo-1-AM for flow cytometry or Fluo-4 for imaging), then washed in Ca^{2+}/Mg^{2+}-free medium, 1 mM EGTA[30]. Cells were stimulated with tetramers for flow cytometry[30], or with antigen-presenting lipid bilayers or peptide-loaded RMA-S cells for imaging. After allowing cells to settle, 1 v/v pre-warmed medium containing 2.5 mM $CaCl_2$ and $MgCl_2$ was added ($t = 0$). For biochemistry, thymocytes were stimulated with tetramers or antibodies, and analysed by western blot as described[4,12]. Rabbit anti-Themis antibody (Millipore 06-1328) was used in immunoprecipitation and blotting.

Online Content Any additional Methods, Extended Data display items and Source Data are available in the online version of the paper; references unique to these sections appear only in the online paper.

Received 26 February; accepted 26 September 2013.
Published online 13 November 2013.

1. Morris, G. P. & Allen, P. M. How the TCR balances sensitivity and specificity for the recognition of self and pathogens. *Nature Immunol.* **13,** 121–128 (2012).
2. Cheroutre, H. & Lambolez, F. The thymus chapter in the life of gut-specific intra epithelial lymphocytes. *Curr. Opin. Immunol.* **20,** 185–191 (2008).
3. Stritesky, G. L., Jameson, S. C. & Hogquist, K. A. Selection of self-reactive T cells in the thymus. *Annu. Rev. Immunol.* **30,** 95–114 (2012).
4. Fu, G. *et al.* Themis controls thymocyte selection through regulation of T cell antigen receptor-mediated signaling. *Nature Immunol.* **10,** 848–856 (2009).

©2013 Macmillan Publishers Limited. All rights reserved

5. Johnson, A. L. *et al. Themis* is a member of a new metazoan gene family and is required for the completion of thymocyte positive selection. *Nature Immunol.* **10,** 831–839 (2009).
6. Lesourne, R. *et al.* Themis, a T cell-specific protein important for late thymocyte development. *Nature Immunol.* **10,** 840–847 (2009).
7. Patrick, M. S. *et al.* Gasp, a Grb2-associating protein, is critical for positive selection of thymocytes. *Proc. Natl Acad. Sci. USA* **106,** 16345–16350 (2009).
8. Kakugawa, K. *et al.* A novel gene essential for the development of single positive thymocytes. *Mol. Cell. Biol.* **29,** 5128–5135 (2009).
9. Brockmeyer, C. *et al.* T cell receptor (TCR)-induced tyrosine phosphorylation dynamics identifies THEMIS as a new TCR signalosome component. *J. Biol. Chem.* **286,** 7535–7547 (2011).
10. Lesourne, R. *et al.* Interchangeability of Themis1 and Themis2 in thymocyte development reveals two related proteins with conserved molecular function. *J. Immunol.* **189,** 1154–1161 (2012).
11. Paster, W. *et al.* GRB2-mediated recruitment of THEMIS to LAT is essential for thymocyte development. *J. Immunol.* **190,** 3749–3756 (2013).
12. Daniels, M. A. *et al.* Thymic selection threshold defined by compartmentalization of Ras/MAPK signalling. *Nature* **444,** 724–729 (2006).
13. Hogquist, K. A. *et al.* T cell receptor antagonist peptides induce positive selection. *Cell* **76,** 17–27 (1994).
14. Oh-Hora, M. *et al.* Dual functions for the endoplasmic reticulum calcium sensors STIM1 and STIM2 in T cell activation and tolerance. *Nature Immunol.* **9,** 432–443 (2008).
15. Mariathasan, S. *et al.* Duration and strength of extracellular signal-regulated kinase signals are altered during positive versus negative thymocyte selection. *J. Immunol.* **167,** 4966–4973 (2001).
16. Fischer, A. M., Katayama, C. D., Pages, G., Pouyssegur, J. & Hedrick, S. M. The role of erk1 and erk2 in multiple stages of T cell development. *Immunity* **23,** 431–443 (2005).
17. McNeil, L. K., Starr, T. K. & Hogquist, K. A. A requirement for sustained ERK signaling during thymocyte positive selection *in vivo*. *Proc. Natl Acad. Sci. USA* **102,** 13574–13579 (2005).
18. Lorenz, U. SHP-1 and SHP-2 in T cells: two phosphatases functioning at many levels. *Immunol. Rev.* **228,** 342–359 (2009).
19. Zhang, J. *et al.* Involvement of the SHP-1 tyrosine phosphatase in regulation of T cell selection. *J. Immunol.* **163,** 3012–3021 (1999).
20. Plas, D. R. *et al.* Cutting edge: the tyrosine phosphatase SHP-1 regulates thymocyte positive selection. *J. Immunol.* **162,** 5680–5684 (1999).
21. Carter, J. D., Neel, B. G. & Lorenz, U. The tyrosine phosphatase SHP-1 influences thymocyte selection by setting TCR signaling thresholds. *Int. Immunol.* **11,** 1999–2014 (1999).
22. Štefanová, I. *et al.* TCR ligand discrimination is enforced by competing ERK positive and SHP-1 negative feedback pathways. *Nature Immunol.* **4,** 248–254 (2003).
23. Rybakin, V. & Gascoigne, N. R. J. Negative selection assay based on stimulation of T cell receptor transgenic thymocytes with peptide-MHC tetramers. *PLoS ONE* **7,** e43191 (2012).
24. Bouillet, P. *et al.* BH3-only Bcl-2 family member Bim is required for apoptosis of autoreactive thymocytes. *Nature* **415,** 922–926 (2002).
25. Moran, A. E. *et al.* T cell receptor signal strength in T_{reg} and iNKT cell development demonstrated by a novel fluorescent reporter mouse. *J. Exp. Med.* **208,** 1279–1289 (2011).
26. Johnson, D. J. *et al.* Shp1 regulates T cell homeostasis by limiting IL-4 signals. *J. Exp. Med.* **210,** 1419–1431 (2013).
27. Dubois, P. C. *et al.* Multiple common variants for celiac disease influencing immune gene expression. *Nature Genet.* **42,** 295–302 (2010).
28. Trynka, G. *et al.* Dense genotyping identifies and localizes multiple common and rare variant association signals in celiac disease. *Nature Genet.* **43,** 1193–1201 (2011).
29. Sawcer, S. *et al.* Genetic risk and a primary role for cell-mediated immune mechanisms in multiple sclerosis. *Nature* **476,** 214–219 (2011).
30. Fu, G. & Gascoigne, N. R. J. Multiplexed labeling of samples with cell tracking dyes facilitates rapid and accurate internally controlled calcium flux measurement by flow cytometry. *J. Immunol. Methods* **350,** 194–199 (2009).

Acknowledgements We thank X. L. Chen and Y. Xing for technical advice. We thank J. Ampudia, S. Vallée, J. Hu and S. Feldstein for help, and the National Institutes of Health (NIH) Tetramer Core Facility for production of MHC-I tetramers. Supported by NIH grants AI073870, DK094173 and GM065230 to N.R.J.G., DP1OD006433 to H.C., GM100785 and AI070845 to K.S.; Wellcome Trust Grant GR076558MA to O.A., and by the National University of Singapore. J.C. was supported by a fellowship from the Spanish Ministerio de Ciencia e Innovacion (MICIIN), J.A.H.H. by the Irving S. Sigal Fellowship of the American Chemical Society and NIH training grant T32AI07244, and K.S. by The Leukemia & Lymphoma Society Scholar Award 1440-11. The content is solely the responsibility of the authors and does not necessarily represent the official views of the National Institute of Allergy and Infectious Diseases, the NIH, or other funding agencies. This is manuscript number 21592 from The Scripps Research Institute.

Author Contributions G.F., J.C., S.R., V.R., F.L., J.B., K.S. and J.A.H.H. performed experiments and analysed data; W.P. and O.A. performed initial experiments on Themis–SHP1/2 interaction, G.F. and N.R.J.G. designed the project with help and insight from W.P., O.A., H.C. and K.S.; G.F. and N.R.J.G. wrote the manuscript with help from the other authors.

Author Information Reprints and permissions information is available at www.nature.com/reprints. The authors declare no competing financial interests. Readers are welcome to comment on the online version of the paper. Correspondence and requests for materials should be addressed to N.R.J.G. (micnrjg@nus.edu.sg).

©2013 **Macmillan Publishers Limited. All rights reserved**

METHODS

Mice. *Themis*$^{-/-}$ mice (B6.129S-*Themis*^{tm1Gasc}) were produced at TSRI and are available from Jackson Laboratory (Stock 010919). C57BL/6 (Thy1.2^{+}CD45.2^{+}) mice were bred at TSRI. OT-I and OT-I *Tap1*$^{-/-}$ animals were obtained from S. Jameson and K. Hogquist and *Bim* knockout mice from L. Sherman. All experiments were performed in accordance with the guidelines of the Animal Care and Use Committee of TSRI.

Antibodies. Anti-CD3 (145-2C11), anti-CD4 (RM4.4, RM4.5 and GK1.5), anti-CD8α (53-6.7), anti-CD8β (H35−17.2)) and anti-Vα2 (B20.1) were from eBioscience or Biolegend. Antibodies against phosphorylated extracellular signal-regulated kinase 1 and 2 (ERK1/2) (T^{202}/Y^{204}, catalogue no. 9101), phosphorylated PLC-γ1 (catalogue no. 2821), phosphorylated LAT (catalogue no. 3584), phosphorylated SHP1 (catalogue no. 8849), VAV (catalogue no. 2502), and NFATC2 (also known as NFAT1) (catalogue no. 5861) were from Cell Signaling Technology. Anti-phosphorylated tyrosine (4G10, catalogue no. 05-1050) and rabbit anti-Themis antibody were from Millipore (catalogue no. 06-1328). Anti-SHP1 antibody was from Santa Cruz Biotechnology (sc-287). Phospho-Src family (Tyr416) antibody (Cell Signaling catalogue no. 2101) cross-reacts with other Src-family kinases phosphorylated at the activating site. As a result probing thymocyte lysates with this monoclonal antibody shows phosphorylated forms of both p56 Lck and p59 Fyn.

Ca^{2+} flux. Ca^{2+} flux measurement by flow cytometry was performed as previously described[30]. Thymocytes from *Themis*$^{+/+}$ or *Themis*$^{-/-}$ OT-I *Tap1*$^{-/-}$ 4–6-week-old mice, both sexes, were used. Briefly, thymocyte suspensions were prepared, put in separate tubes and rested 3 h at 37 °C before assay. One of the two cell types was loaded for 5 min at room temperature with indodicarbocyanine (Cy5; 1 mg ml^{-1}) or was mock treated, followed by washing. Equal numbers of Cy5-labelled cell populations were mixed with the unlabelled sample; for example, OT-I *Tap1*$^{-/-}$*Themis*$^{+/+}$ (mock) plus OT-I *Tap1*$^{-/-}$*Themis*$^{-/-}$ (Cy5). Cells were suspended at a density of 2×10^6–6×10^6 cells per ml in cRPMI (RPMI medium supplemented with 10% (v/v) FCS, 100 U ml^{-1} of penicillin, 10 mg ml^{-1} of streptomycin, 292 mg ml^{-1} of glutamine, 50 mM 2-mercaptoethanol and 25 mM HEPES, pH 7.3) and were incubated for 30 min at 37 °C in 5% CO_2 with the calcium indicator Indo-1-AM (2 mM; Molecular Probes). Cells were washed twice with cRPMI. For antibody stimulation, cells were stained for 20 min on ice with biotin-conjugated anti-CD3 and anti-CD4 (RM4.4), as well as PerCP–Cy5.5-conjugated anti-CD8α and phycoerythrin (PE)-conjugated anti-CD4 (GK1.5) in cRPMI. Cells were washed once with cRPMI and once with cHBSS (Ca^{2+}-free and Mg^{2+}-free Hank's balanced-salt solution supplemented with 1% (v/v) FCS, 1 mM $MgCl_2$, 1 mM EGTA and 10 mM HEPES, pH 7.3) and were resuspended in cHBSS. Cells were prewarmed to 37 °C before analysis and were kept at 37 °C during event collection on an LSR II (Becton Dickinson). For cell stimulation, streptavidin (10 mg ml^{-1}; Jackson ImmunoResearch) was added to crosslink biotinylated antibodies; alternatively, cells were stimulated with tetramers (NIH tetramer core facility). $CaCl_2$ (2 mM) was added during analysis. Mean fluorescence ratio was calculated with FlowJo (TreeStar).

Imaging of Ca^{2+} flux. Knockout cells were prepared and pre-labelled with Cy5 as above[30] then both wild-type and knockout cells were mixed and loaded with 2 μM Ca^{2+}-sensitive dye Fluo-4. After washing in Ca^{2+}/Mg^{2+}-free medium with 1 mM EGTA, cells were mixed and added to the 37 °C imaging chamber containing either the antigen-presenting lipid bilayer or peptide-loaded RMA-S cells. After allowing cells to settle and starting imaging, 1 volume of pre-warmed medium containing 2.5 mM $CaCl_2$ and 2.5 mM $MgCl_2$ was added so that Ca^{2+} influx started at $t = 0$.

p-ERK analysis. For intracellular staining of phosphorylated ERK, stimulated cells were fixed with 4% paraformaldehyde for 12 min at room temperature and then plated in microtitre tubes (for phospho-flow analysis) or in poly-L-lysine-coated LabTek II chambers (for imaging). Cells were permeabilized with 0.3% Triton X-100 for 3 min at room temperature. Cells were then blocked with 5% normal goat serum and incubated with rabbit monoclonal antibody against phospho-ERK, after which they were incubated with Alexa Fluor 488-conjugated Fab fragments against rabbit antibodies (Molecular Probes) for secondary detection (either phospho-flow or microscopy). For flow cytometry analysis, one of the two cell types were pre-labelled with dye Cy5 and the other one was mock labelled. Then the two cell types were mixed in 1:1 ratio and processed for stimulation and staining. Phospho-flow analysis of p-ERK was done on a BD LSR-II digital flow cytometer and the two cell types were distinguished by Cy5 labelling. p-ERK imaging was done as described previously with modification[31]. Briefly, after intracellular staining of p-ERK, nuclei were counterstained with the DNA binding dye 4′,6-diamidino-2-phenylindole (DAPI, Invitrogen). All images were captured with a Zeiss Axiovert 200 M inverted microscope. SlideBook software (Intelligent Imaging Innovations) was used for the capture as well as for deconvolution and image analysis, and ImageJ was used for image presentation.

NFATC2 imaging. Nuclear translocation of NFATC2 (NFAT1) was imaged as described above regarding p-ERK imaging[31], and analysed using CellProfiler software (Broad Institute).

Immunoprecipitation and western blotting analysis. Briefly, cells were stained with antibodies against CD3 and CD4 or tetramers on ice for 15 min and stimulated by rapidly warming to 37 °C with pre-warmed PBS for indicated times. Cells were then lysed and processed for immunoprecipitation or immunoblot analysis as described in detail in ref. 32. In some cases, after primary antibody incubation, membranes were incubated with goat anti-rabbit IgG (H+L), DyLight 800-conjugated (Pierce, catalogue no. 35571) or goat anti-mouse IgG (H+L), DyLight 680-conjugated (Pierce, catalogue no. 35519), and detected and quantified with a LiCor Odyssey infrared imaging system. Human embryonic kidney epithelial cells (HEK293), which express SHP2 but little SHP1[33,34], were transfected by calcium phosphate precipitation and lysates prepared as described[11]. Streptactin-Sepharose beads (IBA BioTAGnology) were used for THEMIS-Strep pull-downs, after which beads were washed three times with lysis buffer. Bound proteins were eluted with 5 mM biotin and subjected to SDS–PAGE[11].

***In vitro* apoptosis assay.** Experiments were performed as described previously[23]. Briefly, pre-selection thymocytes were stimulated with the various tetramers for 17 h. Apoptosis was determined by staining active caspase-3 with fluorescein isothiocyanate (FITC)-conjugated specific antibody following the manufacturer's protocol (APO ACTIVE 3 detection kit, Cell Technology, catalogue no. FAB200-1), and analysed by FACS.

Phenotyping of agonist-selected T cells. Agonist-selected T cells were analysed in bone marrow reconstituted mice. Briefly, *Themis*$^{+/+}$ (CD45.1^{+}/CD45.2^{+}) and *Themis*$^{-/-}$ bone marrow cells (CD45.2^{+}) were mixed 1:1 and injected into lethally irradiated (2 × 5.5 Gy, separated by 3–4 h) B6 recipient mice (CD45.1^{+}). At various times post bone marrow reconstitution, tissues and organs of recipient mice were collected and relevant T-cell subsets were analysed. Splenocytes, IELs and liver mononuclear cells were prepared as previously described[35,36]. Cells were suspended in PBS + 5% FCS + 0.16% azide and anti-CD16/CD32 (2.4G2) Fc-receptor antibody (BD Biosciences) was used to block Fc-antibody binding. The following antibodies were purchased from BD Biosciences: TCRγδ-FITC (GL3), TCRβ-APC-ef780 (H57-597), NK1.1-FITC (PK136), CD8α-PE (53-6.7), CD8β-FITC (53-5.8), CD19-APC (1D3), CD45.2-PercP-Cy5.5 (104). The following antibodies were purchased from eBioscience: CD4-eF450 (RM4-5), CD5-ef450 (53-7.3), CD45.1-PE-Cy7 (A20), CD69-eF450 (H1.2F3), CD90.2-APC (53-2.1). The following antibodies were purchased from Invitrogen: CD8α-PO (5H10). The following antibodies were purchased from Caltag: CD4-PO (RM4-5). All antibodies were directly conjugated to fluorophores. An LSR II cell analyser (BD Biosciences) was used for the flow cytometry, and FlowJo software (TreeStar) was used for analysis.

Statistical testing. Statistics were performed as described in Figure legends using Excel, GraphPad Prism, or Igor Pro (Wavemetrics).

31. Fu, G. *et al.* Protein kinase C η is required for T cell activation and homeostatic proliferation. *Sci. Signal.* **4,** ra84 (2011).
32. Huang, Y. H. *et al.* Positive regulation of Itk PH domain function by soluble IP4. *Science* **316,** 886–889 (2007).
33. Minoo, P., Zadeh, M. M., Rottapel, R., Lebrun, J. J. & Ali, S. A novel SHP-1/Grb2-dependent mechanism of negative regulation of cytokine-receptor signaling: contribution of SHP-1 C-terminal tyrosines in cytokine signaling. *Blood* **103,** 1398–1407 (2004).
34. Simoneau, M. *et al.* Activation of Cdk2 stimulates proteasome-dependent truncation of tyrosine phosphatase SHP-1 in human proliferating intestinal epithelial cells. *J. Biol. Chem.* **283,** 25544–25556 (2008).
35. Hammond, K. J. *et al.* CD1d-restricted NKT cells: an interstrain comparison. *J. Immunol.* **167,** 1164–1173 (2001).
36. Gangadharan, D. *et al.* Identification of pre- and postselection TCRαβ^{+} intraepithelial lymphocyte precursors in the thymus. *Immunity* **25,** 631–641 (2006).
37. Hogquist, K. A., Jameson, S. C. & Bevan, M. J. Strong agonist ligands for the T cell receptor do not mediate positive selection of functional CD8^{+} T cells. *Immunity* **3,** 79–86 (1995).
38. Hogquist, K. A. *et al.* Identification of a naturally occurring ligand for positive selection. *Immunity* **6,** 389–399 (1997).
39. Santori, F. R. *et al.* Rare, structurally homologous self-peptides promote thymocyte positive selection. *Immunity* **17,** 131–142 (2002).
40. Rosette, C. *et al.* The impact of duration versus extent of TCR occupancy on T cell activation: a revision of the kinetic proofreading model. *Immunity* **15,** 59–70 (2001).
41. Huang, J. *et al.* The kinetics of two-dimensional TCR and pMHC interactions determine T-cell responsiveness. *Nature* **464,** 932–936 (2010).
42. Alam, S. M. *et al.* T cell receptor affinity and thymocyte positive selection. *Nature* **381,** 616–620 (1996).
43. Alam, S. M. *et al.* Qualitative and quantitative differences in T cell receptor binding of agonist and antagonist ligands. *Immunity* **10,** 227–237 (1999).
44. Juang, J. *et al.* Peptide-MHC heterodimers show that thymic positive selection requires a more restricted set of self-peptides than negative selection. *J. Exp. Med.* **207,** 1223–1234 (2010).

©2013 Macmillan Publishers Limited. All rights reserved

LETTER

doi:10.1038/nature12721

Commensal microbe-derived butyrate induces the differentiation of colonic regulatory T cells

Yukihiro Furusawa[1,2]*, Yuuki Obata[1,2,3]*, Shinji Fukuda[1,4]*, Takaho A. Endo[1], Gaku Nakato[1], Daisuke Takahashi[1], Yumiko Nakanishi[4], Chikako Uetake[1], Keiko Kato[1,5], Tamotsu Kato[1], Masumi Takahashi[1], Noriko N. Fukuda[4], Shinnosuke Murakami[4], Eiji Miyauchi[1], Shingo Hino[6], Koji Atarashi[1,7], Satoshi Onawa[1], Yumiko Fujimura[2], Trevor Lockett[8], Julie M. Clarke[8], David L. Topping[8], Masaru Tomita[4], Shohei Hori[1], Osamu Ohara[1], Tatsuya Morita[6], Haruhiko Koseki[1,3,5], Jun Kikuchi[5,9], Kenya Honda[1,10], Koji Hase[1,2,7]* & Hiroshi Ohno[1,3,5]

Gut commensal microbes shape the mucosal immune system by regulating the differentiation and expansion of several types of T cell[1–5]. *Clostridia*, a dominant class of commensal microbe, can induce colonic regulatory T (T_{reg}) cells, which have a central role in the suppression of inflammatory and allergic responses[3]. However, the molecular mechanisms by which commensal microbes induce colonic T_{reg} cells have been unclear. Here we show that a large bowel microbial fermentation product, butyrate, induces the differentiation of colonic T_{reg} cells in mice. A comparative NMR-based metabolome analysis suggests that the luminal concentrations of short-chain fatty acids positively correlates with the number of T_{reg} cells in the colon. Among short-chain fatty acids, butyrate induced the differentiation of T_{reg} cells *in vitro* and *in vivo*, and ameliorated the development of colitis induced by adoptive transfer of $CD4^+$ $CD45RB^{hi}$ T cells in *Rag1*$^{-/-}$ mice. Treatment of naive T cells under the T_{reg}-cell-polarizing conditions with butyrate enhanced histone H3 acetylation in the promoter and conserved non-coding sequence regions of the *Foxp3* locus, suggesting a possible mechanism for how microbial-derived butyrate regulates the differentiation of T_{reg} cells. Our findings provide new insight into the mechanisms by which host–microbe interactions establish immunological homeostasis in the gut.

Germ-free mice have an enlarged caecum because of the accumulation of hydrated dietary fibre components. Colonization with chloroform-resistant bacteria (CRB)[6] normalizes caecal size, probably through fermentation of these components by the CRB (Fig. 1a, b). Therefore, CRB-derived dietary fibre metabolites could be responsible for the induction of colonic T_{reg} cells. To assess this possibility, CRB-associated mice were fed either a low-fibre diet (LFD) or a high-fibre diet (HFD). In CRB-associated HFD-fed (CRB-HFD) mice, the expression of neuropilin-1^- and $Helios^-$ (also known as $IKZF2^-$) T_{reg} cells, which represent the peripherally generated T_{reg} cell population[7–9], was significantly increased (Fig. 1c, d and Supplementary Figs 1 and 2). Consistent with previous observations[3], the effect of CRB on T_{reg} cell induction was restricted to the colon and not the mesenteric lymph nodes or spleen (Supplementary Fig. 3). In addition, the expression of $CD103^+$-activated T_{reg} cells was also increased in CRB-HFD mice (Fig. 1d). Notably, a LFD compromised the effects of CRB colonization on T_{reg} cell induction (Fig. 1c, d), despite the comparable number and composition of gut microbes predominantly annotated as *Clostridiales* (Supplementary Figs 4–6). These observations strongly suggest that metabolic differences in gut microbes are responsible for the differential T_{reg} cell inducibility between CRB-HFD and CRB-LFD mice.

Indeed, principal component analysis (PCA) and orthogonal partial least squares discriminate analysis of the NMR-based metabolome data

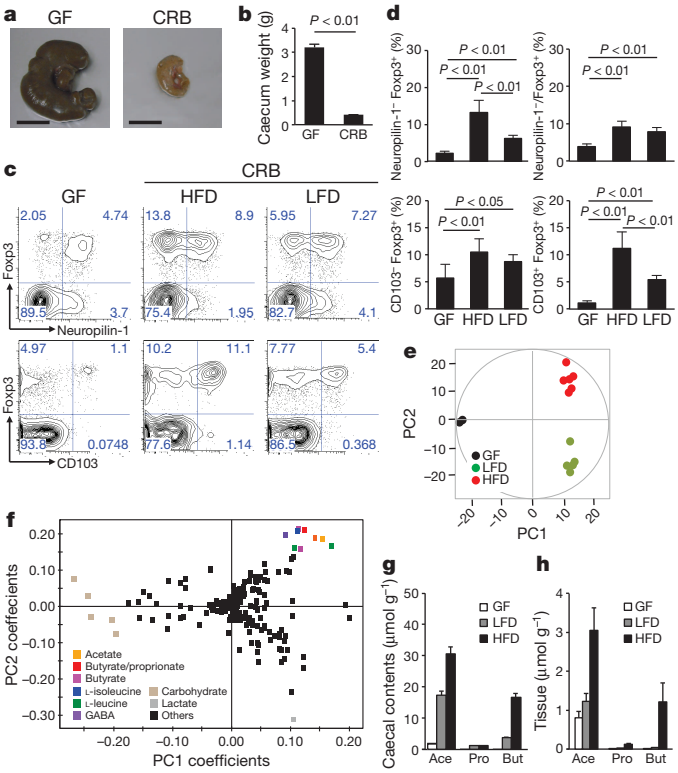


Figure 1 | Gut microbial metabolism is essential for the induction of colonic T_{reg} cells. **a**, **b**, The caecum size of germ-free (GF) and CRB-associated mice. Representative caecum images are shown in **a**. Scale bars, 1 cm. **c**, **d**, The expression of neuropilin-1 and CD103 in $Foxp3^+$ T cells in germ-free and CRB-associated mice fed a HFD or LFD for 4 weeks. Representative FACS plots gated on $CD3^{\varepsilon+}$ $CD4^+$ are shown in **c**. *P* value was determined by one-way analysis of variance (ANOVA) followed by Tukey's post-hoc test. **e**, **f**, Caecal metabolomic profiling by NMR of germ-free and CRB mice fed a HFD or LFD. The results of PCA on the ^{1}H-NMR data (**e**) and loading scatter plot (**f**) are shown. Proportions of the first (PC1) and second (PC2) principal components are 85.1% and 10.3%, respectively. The ellipse denotes the 95% significance limit of the model, as defined by Hotelling's *t*-test. **g**, **h**, Organic acids in caecal contents (**g**) and the proximal colonic tissue (**h**) were measured by gas chromatography–mass spectrometry. Ace, acetate; but, butyrate; pro, propionate. Error bars indicate s.e.m. (**b**, $n = 5$) or s.d. (**d**, $n = 10$; **g**, **h**, $n = 7$). All data are representative of two (**e**–**h**) or three (**a**–**d**) independent experiments.

[1]RIKEN Center for Integrative Medical Sciences (IMS-RCAI), Kanagawa 230-0045, Japan. [2]The Institute of Medical Science, The University of Tokyo, Tokyo 108-8639, Japan. [3]Graduate School of Medicine, Chiba University, Chiba 260-8670, Japan. [4]Institute for Advanced Biosciences, Keio University, Yamagata 997-0052, Japan. [5]Graduate School of Medical Life Science, Yokohama City University, Kanagawa 230-0045, Japan. [6]Faculty of Agriculture, Shizuoka University, Shizuoka 422-8529, Japan. [7]PRESTO, Japan Science and Technology Agency, Saitama 332-0012, Japan. [8]Preventative Health National Research Flagship, CSIRO Food and Nutritional Sciences, South Australia 5000, Australia. [9]RIKEN Center for Sustainable Resource Science, Kanagawa 230-0045, Japan. [10]CREST, Japan Science and Technology Agency, Saitama 332-0012, Japan.
*These authors contributed equally to this work.

©2013 Macmillan Publishers Limited. All rights reserved

indicated that the amount of caecal short-chain fatty acids (SCFAs), namely acetate, propionate and butyrate, was higher in CRB-HFD than in CRB-LFD mice (Fig. 1e, f, Supplementary Fig. 7 and Supplementary Table 1). Quantitative analysis confirmed a significant increase in acetate and butyrate in the caecal content and colonic tissues of CRB-HFD mice (Fig. 1g, h). Luminal GABA (γ-aminobutyric acid), L-leucine and L-isoleucine were also increased in CRB-HFD mice (Fig. 1f and Supplementary Fig. 7). To test whether these metabolites can induce T_{reg} cells *in vitro*, splenic naive ($CD44^{lo}$ $CD62L^{hi}$) $CD4^+$ T cells were cultured in the presence of T-cell antigen receptor and CD28 signalling plus TGF-β with or without each metabolite. Butyrate significantly increased the frequency of $Foxp3^+$ cells (Fig. 2a, b). Propionate showed a moderate effect, whereas the other metabolites, including acetate, did not have any effect on T_{reg} cell induction at physiological concentrations (Fig. 2a, b and Supplementary Fig. 8).

To corroborate the role of butyrate in T_{reg} cell induction *in vivo*, specific pathogen-free (SPF) C57BL/6 mice were fed modified diets containing acetylated, propionylated or butyrylated high-amylose maize starches[10] (HAMSA, HAMSP or HAMSB, respectively) to increase the luminal levels of the corresponding SCFA (Fig. 2c). Consistent with the *in vitro* observations, colonic T_{reg} cells were significantly augmented when the diet contained HAMSB, whereas HAMSP slightly and HAMSA barely induced T_{reg} cells in SPF mice (Fig. 2d, e and Supplementary Fig. 9). The HAMSB diet also increased the number of ovalbumin (OVA)-specific colonic OT-II $Foxp3^+$ cells from adoptively transferred OT-II naive $CD4^+$ T cells (Fig. 2f, g). Because butyrate did not affect the survival or the proliferation of colonic T_{reg} cells (Supplementary Figs 10 and 11), this increase probably reflects a role for this SCFA in regulating T_{reg} cell differentiation. Furthermore, the intake of HAMSB increased colonic T_{reg} cells in germ-free mice mono-associated with *Bacteroides thetaiotaomicron*, an organism devoid of butyrate-producing and T_{reg}-cell-inducing activities per se[3] (Supplementary Fig. 12). Under germ-free conditions, HAMSB did not increase T_{reg} cells, suggesting that the presence of commensal bacteria is a prerequisite for T_{reg} cell induction (Supplementary Fig. 13).

Interleukin (IL)-10 production by T_{reg} cells is well documented to be required for containment of inflammatory responses in mucosal tissues including the colon[11], and the colonization with a mixture of *Clostridiales* is sufficient to induce IL-10-producing T_{reg} cells[3]. Likewise, the intake of HAMSB significantly increased IL-10-producing T_{reg} cells in the colon (Fig. 2h). Collectively, these observations illustrate that butyrate has a key role in the commensal-microbe-mediated differentiation of functional T_{reg} cells in the colon.

We also explored the effect of butyrate on the differentiation of naive T cells into other $CD4^+$ T-cell subsets. Treatment with butyrate or feeding of HAMSB did not affect the induction of T-bet, GATA3 and RORγt, the master regulators of T helper 1 (T_H1), T_H2 and T_H17 cells, respectively (Supplementary Figs 14 and 15). Notably, butyrate promoted the induction of $Foxp3^+$ cells even under T_H1- and T_H17-polarizing conditions. These data strongly suggest that butyrate preferentially induces T_{reg} cell differentiation.

The requirement for the Toll-like receptor (TLR)–MyD88 signalling pathway[12] in commensal microbe-induced T_{reg} cell expansion seems to be variable depending on the type of bacteria involved[3–5,13]. We observed that treatment of SPF *Myd88*$^{-/-}$ *Ticam1*$^{-/-}$ mice with HAMSB induced colonic T_{reg} cells (Supplementary Fig. 16) to the same extent as in wild-type mice (Fig. 2d, e). Therefore, TLR–MyD88 signalling is dispensable for butyrate-dependent T_{reg} cell induction in the colon.

Butyrate is well known to regulate gene expression epigenetically by inhibiting histone deacetylases (HDACs)[14,15], specifically classes IIa and I of the four HDAC classes identified in mammals. Because class IIa HDAC has been reported to suppress T_{reg} cell expansion[16,17], butyrate may influence histone acetylation of gut $CD4^+$ T cells to regulate epigenetically the transcription of the genes responsible for T_{reg} cell induction. To verify this hypothesis, we performed chromatin immunoprecipitation sequencing (ChIP-seq) analysis of naive $CD4^+$ T cells treated with or without butyrate under T_{reg}-cell-polarizing conditions. Butyrate slightly increased genome-wide histone H3 acetylation (Supplementary Fig. 17). Consistently, the histone acetylation status of the promoter regions of most transcription factors was unchanged

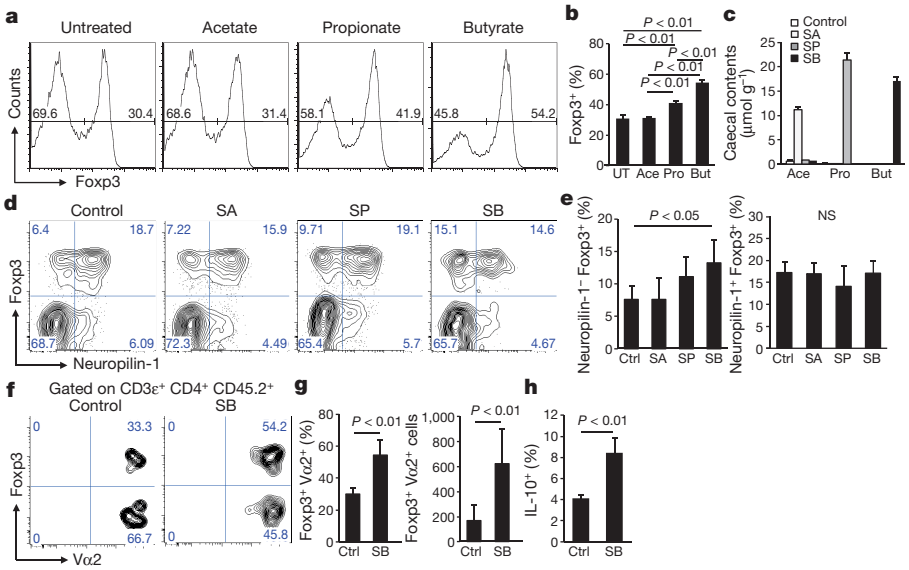


Figure 2 | Butyrate induces the differentiation of T_{reg} cells in the colonic lamina propria. **a**, **b**, Naive $CD4^+$ T cells were stimulated with immobilized anti-CD3 and soluble anti-CD28 monoclonal antibodies in the absence (untreated; UT) or presence of acetate, propionate or butyrate. Representative FACS plots are shown in **a**. **c**, Amount of caecal SCFA in the mice fed with control HAMS diet or diets containing HAMSA, HAMSP or HAMSB (SA, SP or SB, respectively). **d**, **e**, FACS profile of colonic lamina propria cells. The representative FACS plots gated on $CD3\varepsilon^+$ $CD4^+$ cells are shown in **d**. **e**, The frequency of neuropilin-1^- and neuropilin-1^+ $Foxp3^+$ cells among $CD4^+$ T cells. **f**, **g**, The percentage and total number of OVA-induced $Foxp3^+$ cells in mice fed with HAMS control (Ctrl) or HAMSB (SB). Representative FACS plots gated on $CD3\varepsilon^+$ $CD4^+$ $CD45.2^+$ are shown in **f**. $CD45.2^+$ $V\alpha2^+$ $CD4^+$ T cells were sorted and adoptively transferred into $CD45.1^+$ C57BL/6 recipients, followed by administration of drinking water containing 1% ovalbumin (OVA) for 9 days before analysis. **h**, Percentage of IL-10^+ cells among $CD25^+$ $FR4^+$ colonic T_{reg} cells in SPF C57BL/6 mice fed with HAMS or HAMSB. Error bars indicate s.d. (**b**, $n = 3$; **c**, $n = 4$; **e**, $n = 5$; **g**, $n = 4$ for control and $n = 5$ for SB; **h**, $n = 5$). *P* values determined by non-parametrical Mann–Whitney *U* test (**g**, **h**) or one-way ANOVA followed by Tukey's post-hoc test (**b**, **e**). All data are representative of at least two independent experiments. NS, not significant.

©2013 Macmillan Publishers Limited. All rights reserved

or moderately upregulated (Fig. 3a–c), and only 70 transcription factors (4.73% of the genes categorized as a transcription factor), including *Foxp3*, were highly acetylated after butyrate exposure (Fig. 3b, pink area). Importantly, this increased histone acetylation was positively correlated with gene expression (Fig. 3c). *Foxp3* expression is regulated not only by its promoter but also by intragenic enhancer elements termed conserved noncoding sequence (CNS) 1–3 (ref. 18). Butyrate upregulated histone H3 acetylation at both the promoter and CNS3 of the *Foxp3* gene locus 1 day before *Foxp3* induction (Fig. 3a, d). Furthermore, butyrate exposure gradually increased the acetylated histone H3 status of the CNS1 region over the course of T_{reg} cell differentiation. In sharp contrast, no such epigenetic modifications were observed in the *Tbx21*, *Gata3* and *Rorc* genes after butyrate exposure (Supplementary Fig. 18). CNS1, which contains binding motifs for Smad3, NFAT and retinoic acid receptor, is important for the peripheral induction of *Foxp3* (ref. 18). Conversely, CNS3 contains a c-Rel binding motif, which establishes the *Foxp3*-specific enhanceosome and thus greatly enhances the probability of Foxp3 induction[19,20]. We detected little, if any, increase in histone H3 acetylation at the c-Rel, NFAT, Smad3 or Stat5 promoters after butyrate exposure (Supplementary Fig. 19). Correspondingly, expression levels of these genes remained unchanged (Supplementary Fig. 20). On the basis of these observations, we propose that butyrate probably augments the accessibility of these transcriptional regulators to the enhancer elements as well as the promoter region through acetylation of the *Foxp3* gene locus.

Finally, we investigated the function of the butyrate-induced T_{reg} cells in chronic intestinal inflammation by adoptively transferring $CD4^+$ $CD45RB^{hi}$ naive T cells into *Rag1*$^{-/-}$ mice[21]. Over the course of the

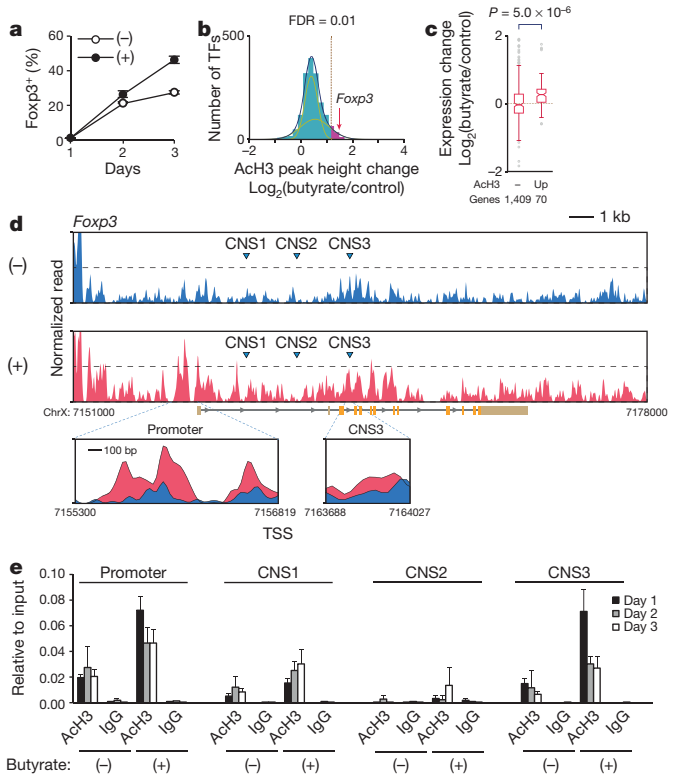


Figure 3 | Chromatin modification at the Foxp3 locus by butyrate. **a**, Time-course analysis on the differentiation of naive T cells into $Foxp3^+$ T_{reg} cells. Naive $CD4^+$ T cells were cultured under T_{reg}-cell-inducing condition in the absence (−) or presence (+) of butyrate. **b**–**d**, Acetylated histone H3 (AcH3) status of transcriptional regulator genes at day 1 after butyrate exposure was determined by ChIP-seq analysis. Distribution of acetylation changes in the gene loci encoding transcription factors (TFs) was fitted using multiple Gaussian distributions with the expectation–maximization algorithm (**b**). Using this analysis, we identified two groups representing upper (highly acetylated) and lower (moderately or not acetylated) transcriptional regulator genes after butyrate treatment. The threshold was set so that the false discovery ratio (FDR) in the upper group was 0.01, where 99% of transcriptional regulators with a high acetylation changes belonged to the upper group (**b**, pink area). Correlation of gene expression changes and the acetylated H3 status in transcriptional regulators is shown in **c**. Gene expression was analysed by microarray at day 2. The normalized number of sequence tags of DNA at the *Foxp3* promoter and gene body is shown in **d**. ChrX, chromosome X. **e**, ChIP quantitative PCR (qPCR) analysis of the *Foxp3* promoter and enhancer regions was performed in $CD4^+$ T cells cultured in the presence or absence of butyrate, using anti-AcH3 antibody or rabbit IgG as a negative control. Error bars indicate s.d (**a**, **e**, $n = 3$).

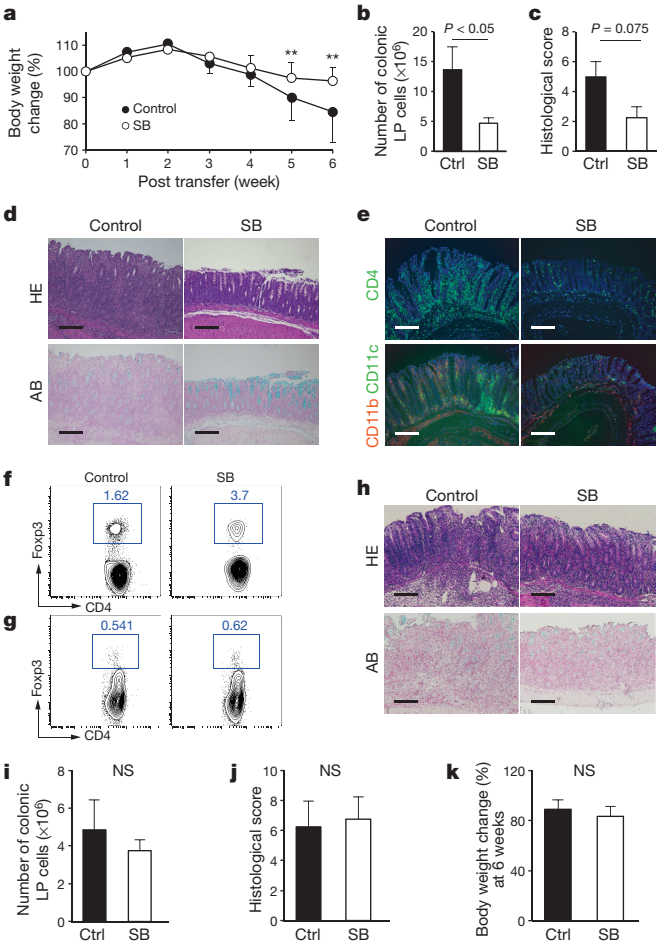


Figure 4 | Butyrate ameliorates T-cell-dependent experimental colitis. **a**–**f**, Experimental colitis was induced by adoptive transfer of $CD4^+$ $CD45RB^{hi}$ T cells in *Rag1*$^{-/-}$ mice fed with HAMS or HAMSB. **a**, Body weight change was monitored. **b**–**f**, The number of colonic lamina propria (LP)-infiltrating mononuclear cells (**b**) and histological score (**c**), representative colonic specimens stained with haematoxylin and eosin (HE) and Alcian blue (AB) (**d**), representative immunofluorescent staining images for CD4, CD11b, CD11c and nuclei (blue) (**e**) and the frequency of $Foxp3^+$ cells in the colonic mucosa (**f**) were analysed at 6 weeks after the cell transfer. **g**–**k**, $CD4^+$ $CD45RB^{hi}$ T cells from *Foxp3*^{hCD2} reporter mice were transferred into *Rag1*$^{-/-}$ recipients, which were injected intravenously with anti-human CD2 monoclonal antibody twice at 4 and 5 weeks after the cell transfer. Depletion of $Foxp3^+$ cells in the colonic lamina propria was confirmed by FACS analysis (**g**). The mice were analysed for colitis development at 6 weeks after transfer (**h**–**k**). Turquoise blue represents goblet cells (**d**, **h**, bottom). Error bars indicate s.d. (**a**, **b**, **c**, **f**, $n = 5$; **i**–**k**, $n = 4$). *P* values were determined by two-way repeated measures ANOVA followed by Tukey's test (**a**) and non-parametrical Mann–Whitney *U* test (**b**, **c**, **i**–**k**). $^{**}P < 0.01$ (**a**). Scale bars, 200 μm (**d**, **e**, **h**). All data are representative of two independent experiments.

©2013 Macmillan Publishers Limited. All rights reserved

experiment, the recipient mice were fed either a control HAMS- or a HAMSB-containing diet. The HAMS-fed group developed wasting disease in association with severe colitis. However, the intake of HAMSB, but not HAMSA or HAMSP, ameliorated the colitis development (Fig. 4a–f and Supplementary Fig. 21). This beneficial effect is at least partly attributed to the induction of colonic T_{reg} cells by butyrate. In support of this notion, depletion of T_{reg} cells abrogated the protective effect of HAMSB (Fig. 4g–k).

The present study demonstrates that butyrate produced by gut microbes induces functional colonic T_{reg} cells, specifically among $CD4^+$ T-cell subsets, via T-cell intrinsic epigenetic upregulation of the *Foxp3* gene. However, we do not formally exclude the possibility that effects of butyrate other than histone acetylation status, or targets of HDAC other than histones, may also be involved in T_{reg} cell differentiation. SCFAs have also been reported to act through cell surface signalling receptors such as G-protein-coupled receptor 43 (GPR43) to execute some of their functions[22]; however, this is unlikely to be the case for the effect of butyrate on T_{reg} cells, because acetate, which is a potent GPR43 ligand[23], failed to ameliorate T-cell-dependent experimental colitis or induce T_{reg} cell differentiation (Fig. 2a–e and Supplementary Fig. 21). In addition, the expression of GPR43 is restricted to myeloid cells among haematopoietic cell lineages. Nevertheless, we do not exclude the possibility that butyrate may stimulate other GPRs on myeloid cells including dendritic cells to facilitate T_{reg} cell differentiation.

Butyrate has been appreciated for its beneficial effects on the host, including trophic and anti-inflammatory effects on epithelial cells[24]. The butyrate transporter is downregulated in the colonic mucosa of patients with inflammatory bowel diseases (IBD)[25]. In addition, butyrate-producing bacteria are decreased in the intestinal microbiota at the gut mucosa and in the faecal samples of patients with IBD compared to control patients[26]. These facts suggest that butyrate insufficiency may be involved in the pathogenesis of IBD. In support of this idea, butyrate enema, alone or as a cocktail of SCFAs, has been shown to ameliorate colonic inflammation in patient with IBD[27,28], although the underlying mechanisms were not fully understood. Our findings not only link butyrate to commensal microbe-mediated induction of functional T_{reg} cells in the colonic mucosa, but also provide molecular insight into the therapeutic application of butyrate and how a metabolite produced by colonic microbial fermentation mediates host–microbial crosstalk for establishment of gut immune homeostasis (Supplementary Fig. 22).

METHODS SUMMARY

Animals. Germ-free IQI mice were housed in germ-free isolators in the animal facility of RIKEN. Eight-to-ten-week-old male or female germ-free mice were orally inoculated with 3% (v/v) chloroform-treated murine faecal suspension (CRB)[6]. Germ-free and CRB-associated mice, which were housed in different isolators, were randomly grouped, and each group was fed with a γ-ray-sterilized CMF chow (Oriental Yeast) as a HFD, or AIN93G-fomula diet (Oriental Yeast) as a LFD for 4 weeks. To generate *B.-thetaiotaomicron*-associated mice, male or female germ-free mice of 8–16 weeks of age were colonized with a single gavage of 10^8 colony-forming units of *B. thetaiotaomicron*, JCM 5827T (Japan Collection of Microorganisms). Ten days after the inoculation, *B.-thetaiotaomicron*-associated mice were randomly grouped and each group was fed with the diet containing 15% (w/w) HAMS and HAMSB as a substitute for corn starch for 4 weeks. C57BL/6 mice and *Myd88*$^{-/-}$ *Ticam1*$^{-/-}$ mice were purchased from CLEA Japan and Oriental Bioservice, respectively. Mice were fed with AIN93G as a control diet for a week, and subsequently a diet containing 15% (w/w) HAMS, HAMSA, HAMSP or HAMSB for 4 weeks. *Foxp3-hCD2-hCD52* knock-in (*Foxp3*^{hCD2}) mice were described previously[29]. OT-II transgenic mice were from the Jackson Laboratory. All animal experiments were performed using protocols approved by Animal Studies Committees of RIKEN Yokohama Institute and Yokohama City University. Sample size was determined based on published studies using similar assays as well as the previous experience of the senior authors. No blinding was done for animal studies.

Adoptive transfer of OT-II T cells. OT-II (Ly5.2) transgenic $CD4^+$ T cells were enriched from the spleen and lymph nodes using the IMag Cell Separation System. $CD3^+$ $CD4^+$ $CD25^-$ $V\alpha2^+$ cells were sorted using FACSAriaII and intravenously transferred into C57BL/6 (Ly5.1) mice. Recipient mice were administered 1% ovalbumin in drinking water for 9 days.

Online Content Any additional Methods, Extended Data display items and Source Data are available in the online version of the paper; references unique to these sections appear only in the online paper.

Received 18 June; accepted 27 September 2013.
Published online 13 November 2013.

1. Chung, H. *et al.* Gut immune maturation depends on colonization with a host-specific microbiota. *Cell* **149,** 1578–1593 (2012).
2. Ivanov, I. I. *et al.* Induction of intestinal Th17 cells by segmented filamentous bacteria. *Cell* **139,** 485–498 (2009).
3. Atarashi, K. *et al.* Induction of colonic regulatory T cells by indigenous clostridium species. *Science* **331,** 337–341 (2011).
4. Geuking, M. B. *et al.* Intestinal bacterial colonization induces mutualistic regulatory T cell responses. *Immunity* **34,** 794–806 (2011).
5. Round, J. L. & Mazmanian, S. K. Inducible $Foxp3^+$ regulatory T-cell development by a commensal bacterium of the intestinal microbiota. *Proc. Natl Acad. Sci. USA* **107,** 12204–12209 (2010).
6. Itoh, K. & Mitsuoka, T. Characterization of clostridia isolated from faeces of limited flora mice and their effect on caecal size when associated with germ-free mice. *Lab. Anim.* **19,** 111–118 (1985).
7. Thornton, A. M. *et al.* Expression of Helios, an Ikaros transcription factor family member, differentiates thymic-derived from peripherally induced $Foxp3^+$ T regulatory cells. *J. Immunol.* **184,** 3433–3441 (2010).
8. Yadav, M. *et al.* Neuropilin-1 distinguishes natural and inducible regulatory T cells among regulatory T cell subsets *in vivo*. *J. Exp. Med.* **209,** 1713–1722 (2012).
9. Weiss, J. M. *et al.* Neuropilin 1 is expressed on thymus-derived natural regulatory T cells, but not mucosa-generated induced $Foxp3^+$ T reg cells. *J. Exp. Med.* **209,** 1723–1742 (2012).
10. Annison, G., Illman, R. J. & Topping, D. L. Acetylated, propionylated or butyrylated starches raise large bowel short-chain fatty acids preferentially when fed to rats. *J. Nutr.* **133,** 3523–3528 (2003).
11. Rubtsov, Y. P. *et al.* Regulatory T cell-derived interleukin-10 limits inflammation at environmental interfaces. *Immunity* **28,** 546–558 (2008).
12. Rakoff-Nahoum, S., Paglino, J., Eslami-Varzaneh, F., Edberg, S. & Medzhitov, R. Recognition of commensal microflora by Toll-like receptors is required for intestinal homeostasis. *Cell* **118,** 229–241 (2004).
13. Mazmanian, S. K., Round, J. L. & Kasper, D. L. A microbial symbiosis factor prevents intestinal inflammatory disease. *Nature* **453,** 620–625 (2008).
14. Candido, E. P., Reeves, R. & Davie, J. R. Sodium butyrate inhibits histone deacetylation in cultured cells. *Cell* **14,** 105–113 (1978).
15. Davie, J. R. Inhibition of histone deacetylase activity by butyrate. *J. Nutr.* **133,** 2485S–2493S (2003).
16. de Zoeten, E. F., Wang, L., Sai, H., Dillmann, W. H. & Hancock, W. W. Inhibition of HDAC9 increases T regulatory cell function and prevents colitis in mice. *Gastroenterology* **138,** 583–594 (2010).
17. Tao, R. *et al.* Deacetylase inhibition promotes the generation and function of regulatory T cells. *Nature Med.* **13,** 1299–1307 (2007).
18. Josefowicz, S. Z., Lu, L.-F. & Rudensky, A. Y. Regulatory T cells: mechanisms of differentiation and function. *Annu. Rev. Immunol.* **30,** 531–564 (2012).
19. Zheng, Y. *et al.* Role of conserved non-coding DNA elements in the *Foxp3* gene in regulatory T-cell fate. *Nature* **463,** 808–812 (2010).
20. Ruan, Q. *et al.* Development of $Foxp3^+$ regulatory T cells is driven by the c-Rel enhanceosome. *Immunity* **31,** 932–940 (2009).
21. Powrie, F., Leach, M. W. M., Mauze, S. S., Caddle, L. B. L. & Coffman, R. L. R. Phenotypically distinct subsets of $CD4^+$ T cells induce or protect from chronic intestinal inflammation in C. B-17 *scid* mice. *Int. Immunol.* **5,** 1461–1471 (1993).
22. Maslowski, K. M. *et al.* Regulation of inflammatory responses by gut microbiota and chemoattractant receptor GPR43. *Nature* **461,** 1282–1286 (2009).
23. Brown, A. J. *et al.* The orphan G protein-coupled receptors GPR41 and GPR43 are activated by propionate and other short chain carboxylic acids. *J. Biol. Chem.* **278,** 11312–11319 (2003).
24. Inan, M. S. *et al.* The luminal short-chain fatty acid butyrate modulates NF-κB activity in a human colonic epithelial cell line. *Gastroenterology* **118,** 724–734 (2000).
25. Thibault, R. *et al.* Down-regulation of the monocarboxylate transporter 1 is involved in butyrate deficiency during intestinal inflammation. *Gastroenterology* **133,** 1916–1927 (2007).
26. Frank, D. N. *et al.* Molecular-phylogenetic characterization of microbial community imbalances in human inflammatory bowel diseases. *Proc. Natl Acad. Sci. USA* **104,** 13780–13785 (2007).
27. Scheppach, W. *et al.* Effect of butyrate enemas on the colonic mucosa in distal ulcerative colitis. *Gastroenterology* **103,** 51–56 (1992).
28. Harig, J. M., Soergel, K. H., Komorowski, R. A. & Wood, C. M. Treatment of diversion colitis with short-chain-fatty acid irrigation. *N. Engl. J. Med.* **320,** 23–28 (1989).
29. Miyao, T. *et al.* Plasticity of $Foxp3^+$ T cells reflects promiscuous Foxp3 expression in conventional T cells but not reprogramming of regulatory T cells. *Immunity* **36,** 262–275 (2012).

Supplementary Information is available in the online version of the paper.

Acknowledgements We would like to thank P. Carninci, Y. Shinkai and M. Yoshida for discussion; Y. Chiba and S. Yamada for technical support; H. Sugahara for technical advice; and P. D. Burrows for critical reading and editing of the manuscript. This work was supported in part by grants from Japanese Ministry of Education, Culture, Sports, Science and Technology (24117524 to S.F.; 21022049 to K.Ha.; 20113003 to H.O.), The Japan Society for the Promotion of Science (24890293 to Y.F.; 252667 to Y.O.;

©2013 Macmillan Publishers Limited. All rights reserved

24380072 and 24658129 to S.F.; 22689017 to K.Ha.; 21390155 to H.O.), The Japan Science and Technology Agency (K.Ha., K.A. and K.Ho.), RIKEN President's Special Research Grant (H.O.), RIKEN RCAI Young Chief Investigator program (K.Ha.), the Institute for Fermentation, Osaka (S.F.), the Mishima Kaiun Memorial Foundation (S.F.), The Takeda Science Foundation (S.F. and H.O.), The Mitsubishi Foundation (H.O.), and The Uehara Memorial Foundation (S.F. and K.Ha.).

Author Contributions S.F., K.Ha., D.L.T., T.M., K.Ho. and H.O. conceived the study; K.Ha. and S.F. designed the experiments and wrote the manuscript with Y.Fur., Y.O. and H.O.; Y. Fur. and Y.O conducted a large part of experiments together with S.F., G.N., D.T., C.U., K.K., T.K., M.Ta., E.M. and K.Ha; S.F, S.O. and K.Ha. prepared germ-free, CRB-associated and gnotobiotic mice. K.A. and K.Ho. were involved in data discussion. S.F., Y.N., C.U. and J.K. performed metabolome analysis. S.F., T.K., S.M. and M.To. performed microbiome analysis. T.A.E. performed bioinformatic analyses. S.Hi. and T.M. performed HPLC analysis. S.F. and N.N.F. performed GC–MS analysis. Y.Fuj. performed histological analysis. T.L., J.M.C., D.L.T. and S.Ho. provided essential materials and contributed to the design of experiments. Y.Fur. and H.K. contributed to the ChIP assay. H.O. directed the study and took primary responsibility for editing the manuscript.

Author Information The microarray and ChIP-seq analysis data have been deposited at the Gene Expression Omnibus (GEO) under accession number GSE49655. The microbiome analysis data have been deposited at the DDBJ database (http://getentry.ddbj.nig.ac.jp/) under accession number DRA001105. Reprints and permissions information is available at www.nature.com/reprints. The authors declare no competing financial interests. Readers are welcome to comment on the online version of the paper. Correspondence and requests for materials should be addressed to H.O. (ohno@rcai.riken.jp), K.Ha. (hase@ims.u-tokyo.ac.jp) or S.F. (sfukuda@sfc.keio.ac.jp).

©2013 Macmillan Publishers Limited. All rights reserved

METHODS

Animals. Germ-free IQI mice were housed in germ-free isolators in the animal facility of RIKEN. Eight-to-ten-week-old male or female germ-free mice were orally inoculated with 3% (v/v) chloroform-treated murine faecal suspension (CRB)[6]. Germ-free and CRB-associated mice, which were housed in different isolators, were randomly grouped, and each group was fed with a γ-ray-sterilized CMF chow (Oriental Yeast) as a HFD, or AIN93G-fomula diet (Oriental Yeast) as a LFD for 4 weeks. To generate *B.-thetaiotaomicron*-associated mice, male or female germ-free mice of 8–16 weeks of age were colonized with a single gavage of 10^8 colony-forming units of *B. thetaiotaomicron*, JCM 5827T (Japan Collection of Microorganisms). Ten days after the inoculation, *B.-thetaiotaomicron*-associated mice were randomly grouped and each group was fed with the diet containing 15% (w/w) HAMS and HAMSB as a substitute for corn starch for 4 weeks. C57BL/6 mice and *Myd88*$^{-/-}$ *Ticam1*$^{-/-}$ mice were purchased from CLEA Japan and Oriental Bioservice, respectively. Mice were fed with AIN93G as a control diet for a week, and subsequently a diet containing 15% (w/w) HAMS, HAMSA, HAMSP or HAMSB for 4 weeks. *Foxp3-hCD2-hCD52* knock-in (*Foxp3*^{hCD2}) mice were described previously[29]. OT-II transgenic mice were from the Jackson Laboratory. All animal experiments were performed using protocols approved by Animal Studies Committees of RIKEN Yokohama Institute and Yokohama City University. Sample size was determined based on published studies using similar assays as well as the previous experience of the senior authors. No blinding was done for animal studies.

Adoptive transfer of OT-II T cells. OT-II (Ly5.2) transgenic CD4$^+$ T cells were enriched from the spleen and lymph nodes using the IMag Cell Separation System. CD3$^+$ CD4$^+$ CD25$^-$ Vα2$^+$ cells were sorted using FACSAriaII and intravenously transferred into C57BL/6 (Ly5.1) mice. Recipient mice were administered 1% ovalbumin in drinking water for 9 days.

Flow cytometry. The following monoclonal antibodies were conjugated with biotin, FITC, AlexaFluor 488, phycoerythrin (PE), PerCP-Cy5.5, PE-Cy7, allophycocyanin (APC), AlexaFluor 647, Alexa700, APC-H7, eFluor450, Brilliant Violet 421 or V500 (from BD Bioscience, eBioscience or Biolegend): anti-human CD2 (RPA-2.10), anti-mouse CD3ε (145-2C11), CD4 (GK1.5), CD25 (PC61), CD44 (IM7), CD45R/B220 (RA3-6B2), CD45RB (16A), CD62L (MEL-14), CD103 (2E7), Gr1 (RB6-8C5), folate receptor 4, FR4 (eBio12A5), Foxp3 (FJK-16 s), Helios (22F6), IL-10 (JES5-16E3) and TER119 (TER-119). Biotinylated anti-mouse/rat neuropilin-1 polyclonal antibodies were from R&D Systems.

For intracellular staining of Foxp3 and Helios, lymphocytes were pre-incubated with FcγR (CD16/CD32)-blocking monoclonal antibody (93; eBioscience) before staining for surface antigens. The cells were then fixed, permeabilized and stained with relevant monoclonal antibodies using the Foxp3 staining set (eBioscience) according to the manufacturer's instructions.

For intracellular IL-10 staining, lamina propria lymphocytes were cultured for 6 h in complete medium (RPMI1640 containing 10% FCS, 100 U ml^{-1} penicillin, 100 μg ml^{-1} streptomycin, 55 μM mercaptoethanol and 20 mM HEPES, pH 7.2) supplemented with 50 ng ml^{-1} phorbol myristate acetate, 500 ng ml^{-1} ionomycin, and Golgi Plug (BD Bioscience) in 12-well plates. The lymphocytes were then stained with monoclonal antibodies against CD3ε, CD4, CD25 and FR4, followed by intracellular staining for IL-10 using a Cytofix/Cytoperm kit (BD Bioscience). Our preliminary experiments demonstrated that the colonic CD3ε$^+$ CD4$^+$ CD25$^+$ FR4$^+$ population exclusively consists of Foxp3$^+$ cells, consistent with a previous report[30]. The stained samples were analysed using FACSCanto II and FACSAria II flow cytometers with DIVA software (BD Biosciences) and FlowJo software version 9.3.2 (Tomy Digital Biology).

Preparation of lymphocytes. Colonic lamina propria lymphocytes were prepared as described previously[31]. In brief, colonic tissues were treated with HBSS (Wako Pure Chemical industries) containing 1 mM dithiothreitol and 20 mM EDTA at 37 °C for 20 min to remove epithelial cells. The tissues were then minced and dissociated with collagenase solution containing 0.5 mg ml^{-1} collagenase (Wako Pure Chemical Industries), 0.5mg ml^{-1} DNase I (Roche Diagnostics), 2% FCS, 100 U ml^{-1} penicillin, 100 μg ml^{-1} streptomycin and 12.5 mM HEPES, pH 7.2, in RPMI 1640 medium (Sigma-Aldrich) at 37 °C for 30 min to obtain single-cell suspensions. After filtering, the single-cell suspensions were washed with 2% FCS in RPMI 1640, and subjected to Percoll gradient separation. The spleen and mesenteric lymph nodes were mechanically disrupted into single-cell suspensions.

***In vivo* EdU-incorporation assay.** To detect proliferating cells *in vivo*, HAMS- or HAMSB-fed mice received intraperitoneal injection of 3 mg EdU in 200 μl PBS, followed by administration of drinking water containing 0.8 mg ml^{-1} EdU for 2 days before the analysis. EdU-incorporated cells in cLP were visualized using Click-it EdU Flow cytometry kit (Invitrogen), following the manufacturer's instructions.

Microbiological analysis. Bacterial genomic DNA was isolated as described previously with some modifications[32]. In brief, faecal samples were lyophilized by using VD-800R lyophilizer (TAITEC) for 24 h. Freeze-dried faeces were disrupted with 3.0 mm Zirconia Beads (Biomedical Science) by vigorous shaking (1,500 r.p.m. for 10 min) using Shake Master (Biomedical Science). Faecal samples (10 mg) were suspended with DNA extraction buffer containing 400 μl 10% (w/v) SDS/TE (10 mM Tris-HCl, 1 mM EDTA, pH 8.0) solution, 400 μl phenol/chloroform/isoamyl alcohol (25:24:1), and 200 μl 3 M sodium acetate. Faeces in mixture buffer were further disrupted with 0.1 mm zirconia/silica beads (BioSpec Products) by vigorous shaking (1,500 r.p.m. for 10 min) using Shake Master (Biomedical Science). After centrifugation at 15,000*g* for 30 min at room temperature, bacterial genomic DNA was purified from the faecal extracts by a phenol/chloroform/isoamyl alcohol method. Adequate amounts of bacterial genomic DNA samples were amplified by the SYBR premix Ex Taq (TAKARA BIO) with the universal primers or *Clostridiales*-specific primers for the genes encoding the bacterial 16S rRNA sequence[33]. The results were calculated as the quantity relative to the copy number detected in the faeces of conventional mice.

454-barcoded pyrosequencing of 16S rRNA genes. The V1–V2 region of the 16S rRNA gene was amplified as described elsewhere[34]. Mixed samples were prepared by pooling approximately equal amounts of PCR amplicons from each sample and subjected to 454 GS JUNIOR (Roche Applied Science) sequencing according to the manufacturer's instructions. 16S rRNA reads were analysed using QIIME(v1.6): fasta, quality files and a mapping file indicating the bar-code sequence corresponding to each sample were used as input. The QIIME pipeline takes this input information and split reads by samples according to the bar code, and classifies all 3,000 filter-passed reads of the 16S V1–V2 sequences obtained from each sample into operational taxonomic units on the basis of sequence similarity. It also performs taxonomical classification using the RDP-classifier (v2.5)[35]. The phylogenetic tree was constructed using ClustalW 2.0 (ref. 36) with 100 bootstrap iterations. The tree was visualized with iTOL[37].

NMR-based metabolomics. Faecal and caecal metabolites were extracted by gentle shaking with 100 mM potassium phosphate buffer containing 90% deuterium oxide and 1 mM sodium 2,2-dimethyl-2- silapentane-5-sulphonate as the chemical shift reference (δ = 0.0 p.p.m.), and then analysed by ^{1}H-NMR and ^{1}H, ^{13}C-NMR (refs 38, 39). PCA and orthogonal partial least squares discriminate analysis on the caecal metabolome data were run with the SIMCA-P+ software (ver 12.0, Umetrics)[40,41]. All NMR experiments were conducted using Bruker DRX-700 spectrometer equipped with a cryogenically cooled probe. The NMR spectra were processed essentially as described[42–44]. In brief, ^{1}H-NMR data were reduced by subdividing the spectra into sequential 0.04 p.p.m. designated regions between ^{1}H chemical shifts of 0.0 to 9.5 p.p.m. After exclusion of water resonance, each region was integrated and normalized to the total of all resonance integral regions. Metabolite annotations were performed using our standard database[45,46].

Mass spectrometry. Organic acid concentrations of caecal contents and colonic tissues were determined by gas chromatography–mass spectrometer (GC–MS)[47]. In brief, 10 mg caecal contents or colonic tissues were disrupted using 3 mm zirconia/silica beads (BioSpec Products) and homogenized with extraction solution containing 100 μl of internal standard (100 μM crotonic acid), 50 μl HCl and 200 μl ether. After vigorous shaking using Shakemaster neo (Bio Medical Science) at 1,500 r.p.m. for 10 min, homogenates were centrifuged at 1,000*g* for 10 min and then the top ether layer was collected and transferred into new glass vials. Aliquots (80 μl) of the ether extracts were mixed with 16 μl *N*-tert-butyldimethylsilyl-*N*-methyltrifluoroacetamide (MTBSTFA). The vials were sealed tightly, heated at 80 °C for 20 min in a water bath, and then left at room temperature for 48 h for derivatization. The derivatized samples were run through a 6890N Network GC System (Agilent Technologies) equipped with HP-5MS column (0.25 mm × 30 m × 0.25 μm) and 5973 Network Mass Selective Detector (Agilent Technologies). Pure helium (99.9999%) was used a carrier gas and delivered at a flow rate of 1.2 ml min^{-1}. The head pressure was set at 97 kPa with split 20:1. The inlet and transfer line temperatures were 250 and 260 °C, respectively. The following temperature program was used: 60 °C (3 min), 60–120 °C (5 °C per min), 120–300 °C (20 °C per min). One microlitre of each sample was injected with a run time of 30 min. Organic acid concentrations were quantified by comparing their peak areas with the standards.

HPLC analysis of faecal organic acids. Faecal and caecal organic acids were measured by the internal standard method using an HPLC equipped with Shim-pack SCR-102H column (Shimadzu) and an electroconductivity detector (CDD-6A, Shimadzu)[48].

***In vitro* cultures.** CD4$^+$ cells were enriched from the spleen and lymph nodes of C57BL/6 mice by a negative selection method with the IMag Cell Separation System (BD Bioscience) using a mixture of biotinylated monoclonal antibodies against B220, CD8α, CD11c, Gr-1 and Ter-119 and Streptavidin Particle Plus-DM (all from BD Bioscience). The enriched CD4$^+$ fraction was subjected to cell sorting with FACSAriaII to isolate CD3$^+$ CD4$^+$CD25$^-$ CD44^{lo} CD62L^{hi} naive T cells. For T_{reg} cell polarization, naive CD4$^+$ T cells (5 × 10^5 cells ml^{-1}) were stimulated with immobilized anti-CD3 monoclonal antibody (10 μg ml^{-1}) and soluble anti-CD28 monoclonal antibody (1 μg ml^{-1}) supplemented with 0.2 ng ml^{-1} TGF-β1

©2013 Macmillan Publishers Limited. All rights reserved

and 10 ng ml^{-1} IL-2 (both from R&D Systems) in the presence or absence of 0.1 mM sodium acetate, sodium propionate or sodium butyrate (Sigma-Aldrich) for 1–3 days (Fig. 3). In the experiments described in Fig. 2a, b and Supplementary Fig. 7, T cells (5×10^5 cells ml^{-1}) were cultured for 3 days and then expanded in complete medium supplemented with TGF-β and IL-2 for 2 days followed by analyses. T cells were polarized to T_H1, T_H2 or T_H17 subtypes *in vitro* by the addition of the following: 10 ng ml^{-1} IL-12 (R&D Systems) and 10 μg ml^{-1} anti-IL-4 monoclonal antibody (clone 11B11) for T_H1 cell polarization; 10 ng ml^{-1} IL-4 (R&D Systems) and 10 μg ml^{-1} anti-IL-12 monoclonal antibody (clone: R4-6A2) for T_H2 cell polarization; and 40 ng ml^{-1} IL-6 (R&D Systems) and 0.2 ng ml^{-1} TGF-β1, along with 10 μg ml^{-1} each of anti-IFN-γ and anti-IL-4 monoclonal antibodies for T_H17 cell polarization. IL-2 was added to the medium 48 h after initial stimulation, and T cell were cultured for 2 days followed by analyses.

ChIP. ChIP assays were performed using the MAGnify ChIP system (Invitrogen) according to the manufacturer's protocol with a few modifications. In brief, 500,000 cells were fixed with 1% formaldehyde (room temperature, 10 min) and the reaction was stopped by the addition of glycine to a final concentration of 125 mM. Crude nuclei were isolated in SDS lysis buffer to obtain the chromatin solution. The chromatin solution was sonicated using a focused-ultrasonicator (Covaris) to reduce the chromatin DNA length to approximately 100–300 base pairs. The acoustic parameters were optimized (Duty cycle: 10%, Intensity: 5, Cycle/Burst: 200, 15 cycles) with monitoring the DNA fragment using Agilent 2100 Bioanalyzer. The sheared chromatin was immunoprecipitated (overnight, 4 °C) with magnetic protein A/G beads with immobilized 3 μg of anti-acetyl histone H3 antibody (Millipore) or rabbit IgG on a rotating wheel. After extensive washing, immune complexes were eluted (55 °C, 30 min) and reverse crosslinking was carried out (65°C, 1 h) in the presence of proteinase K. qPCR analysis was performed following magnetic bead-based DNA purification. For ChIP-seq library construction, immunoprecipitated DNA fragments were ligated with adaptors and amplified by PCR. Amplified libraries were subjected to cluster generation and sequencing analysis with the HiSeq 1000 (Illumina). Sequenced reads were mapped to the mouse genome (v. mm9) with BOWTIE. Peaks for each population were called with MACS with *P* value threshold of less than 1×10^{-5}. The numbers of reads in a section were that of total mapped reads and the length of each section. Because butyrate treatment globally enhances histone acetylation, total mapped reads may be increased in butyrate-treated cells compared to control cells. Therefore, the normalized values within each sample were further subjected to cross-sample adjustment on the basis of read counts of the four genomic regions around transcription start sites of the housekeeping gene *Rpl13a*, whose histone acetylation status remained unchanged between butyrate-treated and untreated cells as confirmed by ChIP-qPCR analysis (data not shown). The normalized reads were calculated within fixed base length for upstream and downstream regions, and relative length for genic regions.

Gene expression profiling. Total RNA was extracted by Trizol reagent (Life Technologies) following a standard protocol, and subjected to microarray analysis using the GeneChip Mouse Gene 1.0 ST Array (Affymetrix). Microarray signals were processed using a standard robust multiarray averaging (RMA) algorithm. Observed signals were normalized using quantile normalization method and genes that had no significant signals were ignored to reduce noise. Butyrate-sensitive transcription factors were selected using annotation provided by Gene Ontology, as they have annotation 'nucleus (GO:0005634)' and 'regulation of transcription, DNA-dependent (GO:0006355)'. Their acetylation was represented by the normalized peak height of ChIP-seq reads from 4 kb upstream to 4 kb downstream of the transcription start site. The distribution of log ratio between control and butyrate treatment could be approximated with two Gaussian distributions and fitted curves were determined using expectation–maximization algorithm. The threshold value was $\log_2 0.5$.

Induction of colitis by adoptive transfer of CD4$^+$ CD45RB^{high} T cells. Colitis was induced in *Rag1*$^{-/-}$ mice by adoptive transfer of CD4$^+$ CD45RB^{high} T cells as described previously[21]. In brief, CD4$^+$ T cells were enriched from splenocytes from C57BL/6 mice by IMag Cell Separation System. Enriched CD4$^+$ T cells were labelled with FITC-conjugated anti-mouse CD3ε (145-2C11), PE-conjugated anti-mouse CD45RB (16A) (all from BD Biosciences), and CD3ε$^+$ CD4$^+$ CD45RB^{high} cells were isolated by cell sorting using FACSAria II flow cytometer (BD Biosciences). The *Rag1*$^{-/-}$ recipients were given 2×10^5 CD4$^+$ CD45RB^{high} T cells via the tail vein, and were euthanized at 6 weeks after transfer. For the T_{reg} cell depletion experiment, CD4$^+$ CD45RB^{high} T cells from *Foxp3*^{hCD2} reporter mice were adoptively transferred into *Rag1*$^{-/-}$ mice. The recipient mice were received intravenous injection of 1 mg anti-human CD2 monoclonal antibody (35.1) at 4 and 5 weeks after the transfer.

Histology. Prefixed colonic tissue sections were deparaffinized, rehydrated and stained with haematoxylin and eosin or with Alcian blue-nuclear fast red. The specimens were examined histologically for scoring the degree of colitis based on the following criteria: inflammatory infiltrates, mucosal hyperplasia and loss of goblet cells.

Immunofluorescent staining. Immunofluorescent staining of cross-sections of colonic tissues was performed as described previously[49].

Immunoblotting. Immunoblotting analysis was performed as described previously[50]. Antibodies against histone H3 (ab1791, Abcam), acetylated histone H3 (06-599, Merck), Stat5 (clone: 3H7, Cell Signaling Technology), Smad3 (clone: C67H9, Cell Signaling Technology), NFAT1 (4389, Cell Signaling Technology), c-Rel (AF2699, R&D systems) and GAPDH (clone: 6C5, MAB374, Merck) were used in this study.

Statistical analyses. Differences between two or more groups were analysed respectively by the Student's *t*-test or ANOVA followed by Tukey's post-hoc test. When variances were not homogeneous, the data were analysed by the non-parametrical Mann–Whitney *U* test or the Kruskal–Wallis test followed by the Scheffé test. The body weight changes of the mice fed with or without HAMSB were analysed using a two-way repeated measures ANOVA followed by Tukey's test. All statements indicating significant differences show at least a 5% level of probability.

30. Yamaguchi, T. *et al.* Control of immune responses by antigen-specific regulatory T cells expressing the folate receptor. *Immunity* **27,** 145–159 (2007).
31. Weigmann, B. *et al.* Isolation and subsequent analysis of murine lamina propria mononuclear cells from colonic tissue. *Nature Protocols* **2,** 2307–2311 (2007).
32. Date, Y. *et al.* New monitoring approach for metabolic dynamics in microbial ecosystems using stable-isotope-labeling technologies. *J. Biosci. Bioeng.* **110,** 87–93 (2010).
33. Bouskra, D. *et al.* Lymphoid tissue genesis induced by commensals through NOD1 regulates intestinal homeostasis. *Nature* **456,** 507–510 (2008).
34. Kim, S. W. *et al.* Robustness of gut microbiota of healthy adults in response to probiotic intervention revealed by high-throughput pyrosequencing. *DNA Res.* **20,** 241–253 (2013).
35. Reyes, A. *et al.* Viruses in the faecal microbiota of monozygotic twins and their mothers. *Nature* **466,** 334–338 (2010).
36. Larkin, M. A. *et al.* Clustal W and Clustal X version 2.0. *Bioinformatics* **23,** 2947–2948 (2007).
37. Letunic, I. & Bork, P. Interactive Tree Of Life (iTOL): an online tool for phylogenetic tree display and annotation. *Bioinformatics* **23,** 127–128 (2006).
38. Fukuda, S. *et al.* Bifidobacteria can protect from enteropathogenic infection through production of acetate. *Nature* **469,** 543–547 (2011).
39. Fukuda, S. *et al.* Evaluation and characterization of bacterial metabolic dynamics with a novel profiling technique, real-time metabolotyping. *PLoS ONE* **4,** e4893 (2009).
40. Kruger, N. J., Troncoso-Ponce, M. A. & Ratcliffe, R. G. ^{1}H NMR metabolite fingerprinting and metabolomic analysis of perchloric acid extracts from plant tissues. *Nature Protocols* **3,** 1001–1012 (2008).
41. Wiklund, S. *et al.* Visualization of GC/TOF-MS-based metabolomics data for identification of biochemically interesting compounds using OPLS class models. *Anal. Chem.* **80,** 115–122 (2008).
42. Kikuchi, J., Shinozaki, K. & Hirayama, T. Stable isotope labeling of *Arabidopsis thaliana* for an NMR-based metabolomics approach. *Plant Cell Physiol.* **45,** 1099–1104 (2004).
43. Tian, C. *et al.* Top-down phenomics of *Arabidopsis thaliana*: metabolic profiling by one- and two-dimensional nuclear magnetic resonance spectroscopy and transcriptome analysis of albino mutants. *J. Biol. Chem.* **282,** 18532–18541 (2007).
44. Sekiyama, Y., Chikayama, E. & Kikuchi, J. Profiling polar and semipolar plant metabolites throughout extraction processes using a combined solution-state and high-resolution magic angle spinning NMR approach. *Anal. Chem.* **82,** 1643–1652 (2010).
45. Akiyama, K. *et al.* PRIMe: a Web site that assembles tools for metabolomics and transcriptomics. *In Silico Biol.* **8,** 339–345 (2008).
46. Chikayama, E. *et al.* Statistical indices for simultaneous large-scale metabolite detections for a single NMR spectrum. *Anal. Chem.* **82,** 1653–1658 (2010).
47. Sannasiddappa, T. H., Costabile, A., Gibson, G. R. & Clarke, S. R. The influence of *Staphylococcus aureus* on gut microbial ecology in an in vitro continuous culture human colonic model system. *PLoS ONE* **6,** e23227 (2011).
48. Morita, T. *et al.* Resistant proteins alter cecal short-chain fatty acid profiles in rats fed high amylose cornstarch. *J. Nutr.* **128,** 1156–1164 (1998).
49. Obata, Y. *et al.* Epithelial cell-intrinsic Notch signaling plays an essential role in the maintenance of gut immune homeostasis. *J. Immunol.* **188,** 2427–2436 (2012).
50. Furusawa, Y. *et al.* DNA double-strand breaks induced by cavitational mechanical effects of ultrasound in cancer cell lines. *PLoS ONE* **7,** e29012 (2012).

©2013 Macmillan Publishers Limited. All rights reserved

LETTER

doi:10.1038/nature12726

Metabolites produced by commensal bacteria promote peripheral regulatory T-cell generation

Nicholas Arpaia[1,2], Clarissa Campbell[1,2], Xiying Fan[1,2], Stanislav Dikiy[1,2], Joris van der Veeken[1,2], Paul deRoos[1,2], Hui Liu[3], Justin R. Cross[3], Klaus Pfeffer[4], Paul J. Coffer[1,2,5] & Alexander Y. Rudensky[1,2]

Intestinal microbes provide multicellular hosts with nutrients and confer resistance to infection. The delicate balance between pro- and anti-inflammatory mechanisms, essential for gut immune homeostasis, is affected by the composition of the commensal microbial community. Regulatory T cells (T_{reg} cells) expressing transcription factor Foxp3 have a key role in limiting inflammatory responses in the intestine[1]. Although specific members of the commensal microbial community have been found to potentiate the generation of anti-inflammatory T_{reg} or pro-inflammatory T helper 17 (T_H17) cells[2–6], the molecular cues driving this process remain elusive. Considering the vital metabolic function afforded by commensal microorganisms, we reasoned that their metabolic by-products are sensed by cells of the immune system and affect the balance between pro- and anti-inflammatory cells. We tested this hypothesis by exploring the effect of microbial metabolites on the generation of anti-inflammatory T_{reg} cells. We found that in mice a short-chain fatty acid (SCFA), butyrate, produced by commensal microorganisms during starch fermentation, facilitated extrathymic generation of T_{reg} cells. A boost in T_{reg}-cell numbers after provision of butyrate was due to potentiation of extrathymic differentiation of T_{reg} cells, as the observed phenomenon was dependent on intronic enhancer CNS1 (conserved non-coding sequence 1), essential for extrathymic but dispensable for thymic T_{reg}-cell differentiation[1,7]. In addition to butyrate, *de novo* T_{reg}-cell generation in the periphery was potentiated by propionate, another SCFA of microbial origin capable of histone deacetylase (HDAC) inhibition, but not acetate, which lacks this HDAC-inhibitory activity. Our results suggest that bacterial metabolites mediate communication between the commensal microbiota and the immune system, affecting the balance between pro- and anti-inflammatory mechanisms.

We explored potential mechanisms of induction of anti-inflammatory T_{reg} cells by commensal microrganisms. We considered the possibility that microbial metabolites facilitate generation of extrathymic T_{reg} cells, and if so, such products are likely to be found in the faeces of specific pathogen-free (SPF) mice with a normal spectrum of commensal microorganisms, but not in that of microbiota-deficient mice treated with broad-spectrum antibiotics (AVNM) or germ-free mice. Indeed, we found that polar solvent extracts of faeces from SPF, but not germ-free or AVNM-treated mice potentiated induction of Foxp3 after stimulation of purified peripheral naive ($CD44^{lo}CD62L^{hi}CD25^{-}$) $CD4^+$ T cells by CD3 antibody in the presence of dendritic cells, interleukin-2 (IL-2), and transforming growth factor-β (TGF-β) (Fig. 1a). Among bacterial metabolites we expected to find short-chain fatty acids (SCFAs), and evaluated their content in faecal extracts from SPF, germ-free or AVNM-treated mice and their ability to affect T_{reg}-cell generation. Analysis of hydrazine-derivatized SCFAs by high-performance liquid chromatography (HPLC) showed a sharp reduction in propionate and butyrate in extracts from germ-free and AVNM-treated versus SPF animals (Fig. 1b). Concentrations of these SCFAs in extracts were within a 5-mM range, corresponding to approximately 100–125 μM in *in vitro* Foxp3 induction assays (data not shown). Furthermore, purified butyrate, and to a lesser degree isovalerate and propionate, but not acetate, augmented TGF-β-dependent generation of $Foxp3^+$ cells *in vitro* (Fig. 1c; data not shown). To exclude the possibility that butyrate allowed for expansion of a few contaminating T_{reg} cells in the starting naive $CD4^+$ T-cell population, we used mice lacking an intronic *Foxp3* enhancer CNS1. These mice are selectively impaired in extrathymic T_{reg}-cell differentiation but have intact thymic differentiation[1,7]. Butyrate failed to rescue the impaired Foxp3 induction in naive $CD4^+$ T cells in the absence of CNS1 (Fig. 1d). Consistent with this result, butyrate did not

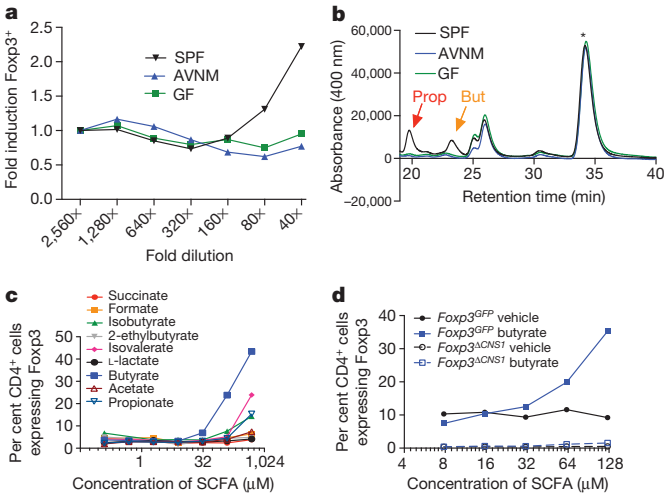


Figure 1 | SCFAs produced by commensal bacteria stimulate *in vitro* generation of T_{reg} cells. **a**, Effect of faecal extracts from specific pathogen-free (SPF), antibiotic-treated (AVNM), or germ-free (GF) mice on *in vitro* induction of Foxp3 expression in naive $CD4^+$ T cells stimulated with CD3 antibody in the presence of Flt3l-elicited dendritic cells and TGF-β. Foxp3 expression was assessed by flow cytometric analysis on day 4 of culture. Naive $CD25^-CD62L^{hi}CD44^{lo}CD4^+$ T cells were FACS-purified from B6 mice. Faecal extracts were prepared in 70% ethanol. Data are shown as fold induction over corresponding dilution of vehicle and are representative of two independent experiments. **b**, HPLC fractionation of 2-nitrophenylhydrazine-HCl-derivatized SCFAs present in indicated faecal extracts. Red and yellow arrows indicate peaks corresponding to propionate (Prop) and butyrate (But), respectively. Asterisk, internal standard peak. The HPLC fractionation profile of faecal extracts pooled from three animals each is representative of two independent experiments. **c**, Effect of indicated purified SCFAs on *in vitro* induction of Foxp3 expression in naive $CD4^+$ T cells isolated from B6 or $Foxp3^{GFP}$ mice as described in **a**. Data are representative of three independent experiments. **d**, Effect of butyrate on Foxp3 induction in CNS1-sufficient and -deficient naive $CD4^+$ T cells from $Foxp3^{GFP}$ and $Foxp3^{\Delta CNS1}$ mice as described in **a**. Data are representative of two or more independent experiments.

[1]Howard Hughes Medical Institute and Ludwig Center at Memorial Sloan-Kettering Cancer Center, New York, New York 10065, USA. [2]Immunology Program, Memorial Sloan-Kettering Cancer Center, New York, New York 10065, USA. [3]Donald B. and Catherine C. Marron Cancer Metabolism Center, Memorial Sloan-Kettering Cancer Center, New York, New York 10065, USA. [4]Institute of Medical Microbiology and Hospital Hygiene, Heinrich-Heine-University Duesseldorf, Duesseldorf 40225, Germany. [5]Department of Cell Biology, University Medical Center Utrecht, 3584 CX Utrecht, The Netherlands.

©2013 Macmillan Publishers Limited. All rights reserved

diminish either qualitatively or quantitatively the TGF-β dependence of Foxp3 induction in CNS1-sufficient $CD4^+$ T cells (data not shown). These data suggest that butyrate promotes extrathymic differentiation of T_{reg} cells.

To determine whether butyrate is capable of promoting extrathymic T_{reg}-cell generation *in vivo*, we administered butyrate in drinking water to AVNM-treated mice, which exhibit a sharp decrease in microbially derived SCFAs, or untreated control SPF mice. Although we detected only very modest changes, if any, in the lymph node and splenic T_{reg}-cell subsets in control mice, provision of butyrate to AVNM-treated animals resulted in a robust increase in peripheral, but not thymic or colonic T_{reg} cells (Fig. 2a, b and Supplementary Fig. 1; data not shown). This increase was not an indirect consequence of an inflammatory response because non-lymphoid tissue histology and production of T_H1, T_H2, and T_H17 cytokines by $Foxp3^-$ $CD4^+$ T cells remained unchanged after butyrate treatment (data not shown; Supplementary Fig. 2). In agreement with the observed CNS1 dependence of *in vitro* Foxp3 induction, provision of butyrate to AVNM-treated CNS1-deficient mice did not increase the proportion or absolute numbers of T_{reg} cells (Fig. 2c; data not shown). Thus, the observed butyrate-mediated increase in the T_{reg} cell subset *in vivo* was due to increased extrathymic generation of T_{reg} cells and not due to their increased thymic output[1,7]. To ensure that butyrate reconstitution did not result in its non-physiologically high levels, we used liquid chromatography–mass spectrometry (LC–MS) to compare amounts of butyrate in the serum of AVNM-treated mice that received butyrate versus amounts found in control SPF mice. Although virtually undetectable in AVNM-treated CNS1-sufficient and -deficient animals, butyrate provision resulted in serum levels comparable to those found in unperturbed SPF mice that did not receive butyrate (Fig. 2d). Consistent with the aforementioned unchanged colonic T_{reg}-cell subset in AVNM-treated mice that received butyrate in their drinking water, levels of butyrate in faecal pellets were not reconstituted in these mice, possibly owing to its uptake in the small intestine or stomach (data not shown). In contrast, delivery of butyrate by enema into the colon of CNS1-sufficient, but not CNS1-deficient mice, led to an increase in the T_{reg}-cell subset in the colonic lamina propria (Fig. 2e). Thus, local provision of butyrate promoted CNS1-dependent extrathymic generation of T_{reg} cells in the colon. Furthermore, feeding mice butyrylated starch, in the absence of antibiotic treatment, increased colonic T_{reg}-cell subsets in comparison to a control starch diet (Supplementary Fig. 3)[8]. In addition to increasing T_{reg}-cell numbers, restoration of butyrate levels in AVNM-treated animals did not decrease, but instead increased intracellular Foxp3 protein amounts on a per-cell basis in both CNS1-sufficient and -deficient mice, suggesting that this bacterial metabolite may also buttress pre-existing T_{reg}-cell populations through stabilization of Foxp3 protein expression (Fig. 2f; data not shown).

In contrast to butyrate's ability to increase T_{reg}-cell generation in the colon only after local, but not systemic delivery, other SCFAs, namely acetate and propionate, were recently shown to promote accumulation of T_{reg} cells in the colon by activating GPR43 (ref. 9). These results suggest discrete modes of action of these three SCFAs. To test this idea we administered AVNM-treated CNS1-sufficient and -deficient mice with propionate and acetate in drinking water. Similarly to butyrate, oral provision of propionate increased T_{reg}-cell subsets in the spleen in AVNM-treated CNS1-sufficient, but not -deficient animals, suggesting that propionate also promotes *de novo* generation of peripheral

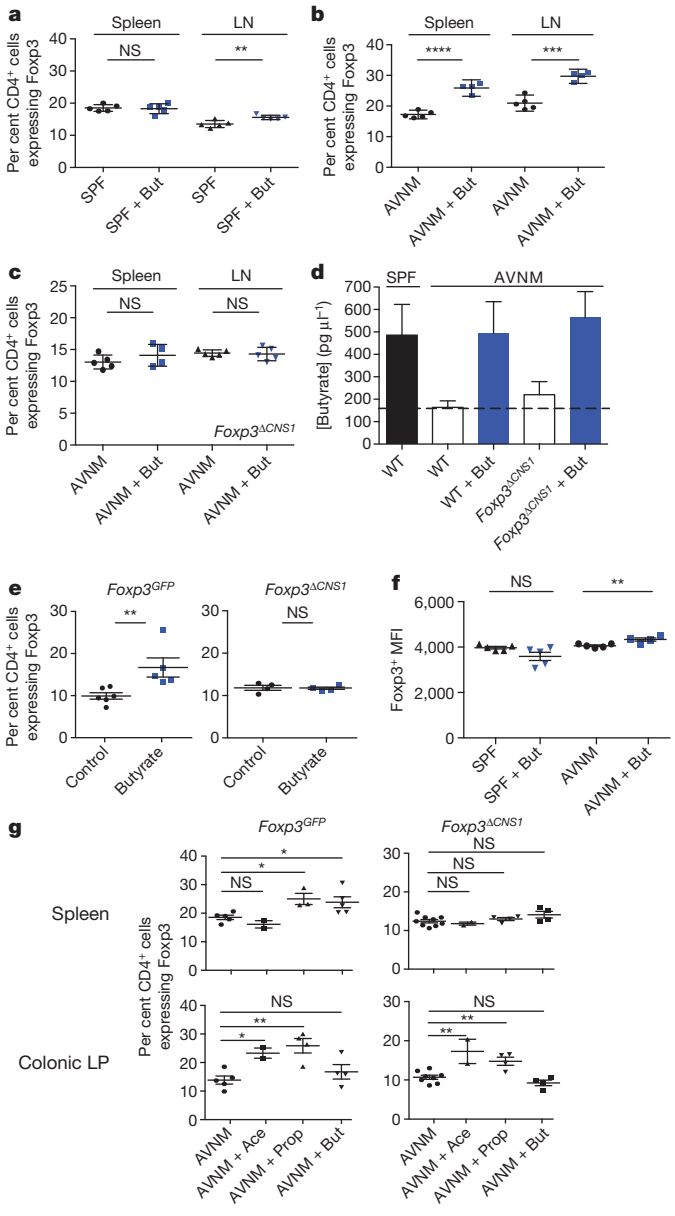


Figure 2 | Butyrate provision promotes extrathymic T_{reg}-cell generation *in vivo*. **a**, **b**, Flow cytometric analysis of $Foxp3^+$ T_{reg}-cell subsets in the spleen and lymph nodes (LNs) of AVNM-treated (AVNM) or untreated (specific pathogen-free; SPF) B6 or $Foxp3^{GFP}$ mice treated with (+But; blue symbols) or without (black symbols) butyrate in drinking water. Data are representative of three independent experiments. **c**, CNS1-deficient mice were treated with AVNM with or without butyrate as in **a** and analysed for Foxp3 expression in splenic and lymph node $CD4^+$ T-cell populations. Data are representative of two independent experiments. **d**, LC–MS analysis of butyrate in serum from CNS1-sufficient B6 (wild-type; WT) and -deficient mice ($Foxp3^{\Delta CNS1}$) treated as in **a**. Serum was derivatized with 2-nitrophenylhydrazine-HCl. Butyrate levels in serum of untreated (SPF) B6 mice are shown in black. AVNM WT and CNS1-deficient animals supplemented with (+But; solid bars) or without (empty bars) butyrate are shown. At least four mice per group; error bars, s.e.m. **e**, Flow cytometric analysis of $Foxp3^+$ T_{reg}-cell populations in colonic lamina propria of $Foxp3^{GFP}$ (left) and CNS1-deficient mice (right). Mice were administered butyrate (blue symbols) or pH-matched water (control; black symbols) by enema for 7 days and analysed for Foxp3 expression in colonic $CD4^+$ T-cell populations. The data represent the combination of two independent experiments; error bars, s.e.m. **f**, Flow cytometric analysis of Foxp3 protein expression on a per-cell basis in splenic $Foxp3^+$ T_{reg} cells in B6 mice treated with butyrate (+But) alone (SPF) or in combination with antibiotics (AVNM) as indicated. The data are shown as mean fluorescence intensity (MFI) ± s.d. Data are representative of at least three independent experiments. **g**, AVNM-treated $Foxp3^{GFP}$ (left) and CNS1-deficient (right) mice were administered acetate (Ace), propionate (Prop), butyrate (But) or no SCFA (AVNM) for a period of 3 weeks. This was followed by analysis of $Foxp3^+$ T_{reg}-cell subsets within $CD4^+$ cells isolated from the colonic lamina propria (top panels) or spleens (bottom panels). Data represent the combination of two independent experiments; error bars, s.e.m. $*P \leq 0.05$, $**P \leq 0.01$, $***P \leq 0.001$,

©2013 Macmillan Publishers Limited. All rights reserved

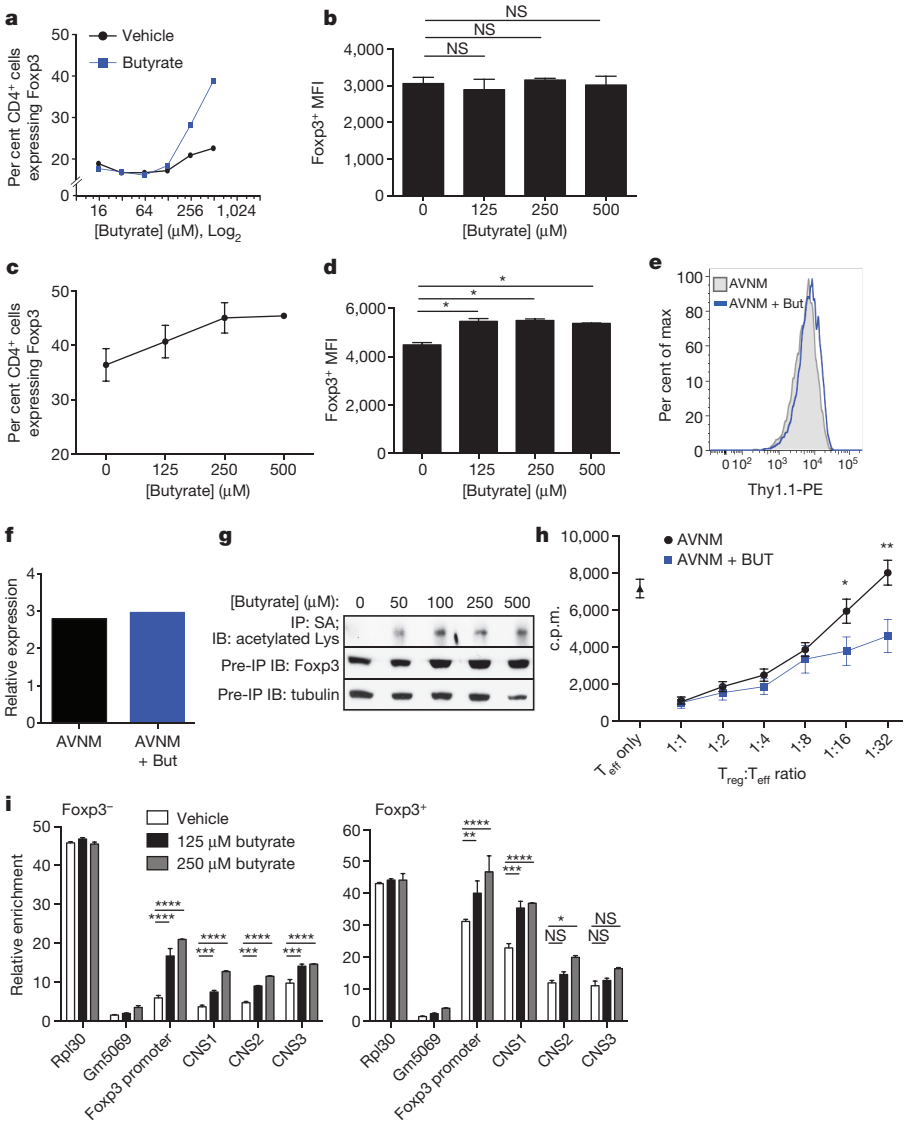


Figure 3 | Butyrate acts within T cells to enhance acetylation of the *Foxp3* locus and Foxp3 protein. a, Induction of Foxp3 expression after stimulation of naive $CD4^+$ T cells by CD3 antibody in the presence of butyrate-treated or untreated Flt3l-elicited dendritic cells (DCs) and TGF-β. DCs were cultured with titrated amounts of butyrate or medium alone for 6 h, washed and co-cultured with FACS-purified naive $CD4^+$ T cells in the presence of CD3 antibody and TGF-β. The data are shown as per cent $CD4^+$ cells expressing Foxp3 after 4 days of culture. Data are representative of at least four independent experiments. **b**, Analysis of Foxp3 protein expression on a per-cell basis in T_{reg} cells generated in the presence of butyrate pre-treated Flt3l-elicited dendritic cells (as in **a**). The data are shown as mean fluorescence intensity (MFI); error bars, s.e.m. **c**, Per cent of $CD4^+$ cells expressing Foxp3 after 4 days in FACS-sorted naive $CD4^+$ T cells incubated with CD3 and CD28 antibody-coated beads under T_{reg}-inducing conditions. Data are representative of two or more independent experiments; error bars, s.e.m. **d**, MFI of Foxp3 expression in $Foxp3^+$ $CD4^+$ cells from **c**. Data are representative of two or more independent experiments; error bars, s.e.m. **e**, Thy1.1 expression in $CD4^+Foxp3^+$ splenocytes isolated from bi-cistronic $Foxp3^{Thy1.1}$ reporter mice treated with AVNM with (+But) or without butyrate as described in Fig. 2a. Cell-surface expression of internal ribosome entry site (IRES)-driven Thy1.1 reporter inserted into the endogenous *Foxp3* locus reflects Foxp3 mRNA levels. The data are representative of at least three mice in each group and of two independent experiments. PE, phycoerythrin. **f**, $CD4^+Foxp3^+$ splenocytes from $Foxp^{GFP}$ reporter mice treated with AVNM with or without butyrate (as in Fig. 2a) were FACS-sorted and analysed for *Foxp3* mRNA expression by qPCR. **g**, AVI (endogenously biotinylated peptide-tagged) Foxp3-expressing TCli hybridoma cells were treated for 15 h with butyrate at the indicated concentrations followed by immunoprecipitation (IP) of tagged Foxp3 protein using streptavidin (SA) beads and immunoblot (IB) analysis for acetylated-lysine residues (top panel), total Foxp3 protein (middle panel) and tubulin (bottom panel) from pre-precipitation whole-cell lysate. Data are representative of two independent experiments. **h**, Analysis of suppressor capacity of GFP^+ T_{reg} cells sorted from antibiotic-treated (AVNM) $Foxp3^{GFP}$ mice administered (+But) or not administered butyrate in drinking water. Data represent two independent experiments combined, with four or more mice per group each. T_{eff}, T effector cells, FACS-sorted $CD4^+$ $Foxp3^-$ naive T cells; error bars, s.e.m. **i**, FACS-sorted naive $CD4^+$ T cells isolated from $Foxp3^{GFP}$ animals were incubated with CD3 and CD28 antibody-coated beads under T_{reg}-inducing conditions in the presence of indicated amounts of butyrate. $Foxp3^+$ and $Foxp3^-$ $CD4^+$ cells were FACS-purified at day 3 of culture and H3K27 acetylation at the *Foxp3* promoter and CNS1, CNS2 and CNS3 enhancers was assessed using ChIP–qPCR. Enrichment over input for each indicated *Foxp3* regulatory region at given concentrations of butyrate is shown. Data in this figure are representative of two or more independent experiments. The data represent mean ± s.e.m. $*P \leq 0.05$, $**P \leq 0.01$, $***P \leq 0.001$, $****P \leq 0.0001$, as determined by Student's *t*-test. NS, not significant.

T_{reg} cells (Fig. 2g). In contrast, acetate did not increase splenic T_{reg}-cell numbers. These results were fully consistent with our *in vitro* T_{reg}-cell differentiation studies (Fig. 1c). However, in the colon, both acetate and propionate, but not butyrate, promoted accumulation of T_{reg} cells in a CNS1-independent manner (Fig. 2g). These results suggest that butyrate promotes *de novo* generation but not colonic accumulation of

©2013 Macmillan Publishers Limited. All rights reserved

T_{reg} cells, whereas acetate has a diametrically opposite activity and propionate is capable of both.

The observation that butyrate facilitates extrathymic differentiation of T_{reg} cells raised a question as to whether butyrate directly affects T cells or dendritic cells (or both) by enhancing their ability to induce Foxp3 expression. To explore these non-mutually exclusive possibilities, we assessed the effects of butyrate on the ability of T cells and dendritic cells to generate T_{reg} cells *in vitro* (Fig. 3a–d). We found that butyrate increased, albeit modestly (<1.5-fold), the numbers of $Foxp3^+$ cells in dendritic cell-free cultures of purified naive $CD4^+$ T cells stimulated by CD3 and CD28 antibody-coated beads and TGF-β (Fig. 3c). Similar to T_{reg} cells isolated from butyrate-treated mice, T_{reg} cells generated in the presence of butyrate *in vitro* expressed not lower, but rather higher amounts of Foxp3 protein on a per-cell basis than those from butyrate-free cultures (Fig. 3d). This effect was not associated with increased Foxp3 messenger RNA levels (Fig. 3e, f). Instead, it is likely to be due to increased Foxp3 protein acetylation observed in the presence of butyrate, a known histone deacetylase (HDAC) inhibitor (Fig. 3g). Foxp3 acetylation confers greater stability and enhanced function[10–13]. Furthermore, the suppressor activity of T_{reg} cells isolated from mice treated with AVNM and butyrate was not attenuated, but was moderately enhanced compared to mice treated with AVNM alone (Fig. 3h).

Previous *in vitro* studies suggested that a synthetic HDAC inhibitor, trichostatin A (TSA), potentiates T_{reg}-cell generation *in vitro* by acting on T cells[14,15]. As butyrate can also boost extrathymic T_{reg}-cell generation by acting directly on T cells in the absence of dendritic cells (Fig. 3c), we assessed the effect of butyrate on histone modification at the *Foxp3* locus. When naive $CD4^+$ T cells from $Foxp3^{GFP}$ mice, which express a green fluorescent protein (GFP) reporter fused to Foxp3, were stimulated by CD3 and CD28 antibody-coated beads and TGF-β with or without butyrate for 3 days, a marked threefold increase in acetylated histone H3 at lysine 27 (acetylated H3K27) at the *Foxp3* promoter and CNS1 enhancer was observed in $Foxp3^-$ cells purified from these cultures (Fig. 3i). In contrast, increases in the acetylated H3K27 occupancy in their $Foxp3^+$ counterparts were expectedly minor (~30%) and inconsequential. Accordingly, *Foxp3* mRNA levels were not different in $Foxp3^+$ cells in the presence or absence of butyrate (Fig. 3e, f). Although we cannot discriminate between the contribution of increased acetylation of histone versus non-histone targets to heightened Foxp3 induction, it is likely to be facilitated by the increase in acetylated H3K27 observed in $Foxp3^-$ T cells.

In addition to its direct T_{reg}-cell differentiation-promoting effects on $CD4^+$ T cell precursors, butyrate endowed dendritic cells with a superior ability to facilitate T_{reg}-cell differentiation. Pre-treatment of dendritic cells with butyrate *in vitro* for 6 h followed by its removal markedly enhanced their ability to induce Foxp3 expression in naive $CD4^+$ T cells stimulated by CD3 antibody and TGF-β in the absence of butyrate (Fig. 3a and Supplementary Fig. 4a, b). This treatment had no detrimental effect on dendritic-cell viability (Supplementary Fig. 4c). The Foxp3 protein expression induced by butyrate-pre-treated and control dendritic cells was comparable, in contrast to a T-cell-intrinsic effect of butyrate leading to increased amounts of Foxp3 protein in T_{reg} cells in mice treated with AVNM and butyrate (Figs 2f and 3b).

We considered butyrate sensing by G-protein-coupled receptors (GPRs) as a potential mechanism for the increase in extrathymic differentiation of T_{reg} cells[16,17]. However, pre-treatment of $Gpr109a^{+/+}$ and $Gpr109a^{-/-}$ dendritic cells with butyrate similarly increased *in vitro* generation of $Foxp3^+$ cells (Supplementary Fig. 5a). Consistent with these results, butyrate-dependent potentiation of Foxp3 induction by dendritic cells remained unchanged after pre-treatment with pertussis toxin (Supplementary Fig. 5b)[18]. Next, we tested HDAC inhibitory activity of butyrate and other SCFAs in dendritic cells using histone H3 acetylation as an indirect readout (Fig. 4a). Trichostatin A (TSA) and valproate, two chemically distinct HDAC inhibitors, and phenylbutyrate, a butyrate derivative with a relatively weak inhibitory activity, were used as controls in these experiments. Relative HDAC inhibitory activity

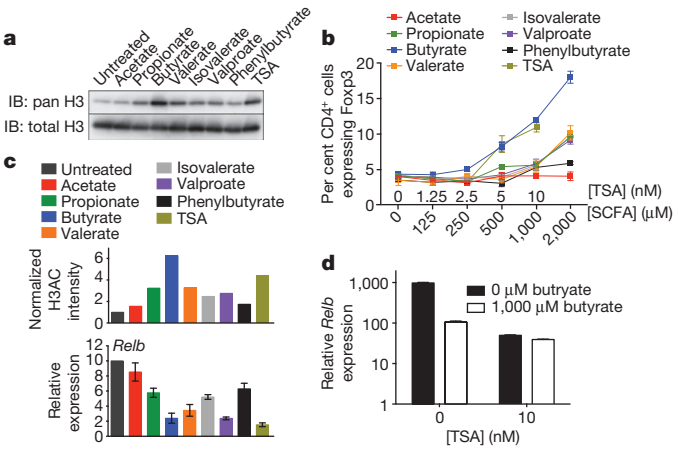


Figure 4 | HDAC-inhibitory activity of butyrate decreases pro-inflammatory cytokine expression within dendritic cells to promote T_{reg} induction. **a**, Histone acetylation in Flt3l-elicited dendritic cells from B6 mice treated with the indicated SCFA (500 μM) or TSA (10 nM) for 6 h followed by acid extraction of histones from isolated nuclei, SDS–PAGE and blotting with antibody for pan-acetylated H3 (pan H3). Total histone H3 served as a loading control. Shown is the relative acetylated H3 band intensity calculated over total H3 and normalized as fold over untreated. **b**, Induction of Foxp3 expression after stimulation of naive $CD4^+$ T cells by CD3 antibody in the presence of SCFA or TSA, Flt3l-elicited dendritic cells and TGF-β. Dendritic cells were cultured with titrated amounts SCFA or TSA for 6 h, washed and co-cultured with FACS-purified naive $CD4^+$ T cells in the presence of CD3 antibody and TGF-β. The data are shown as per cent $CD4^+$ cells expressing Foxp3 after 4 days of culture. Data are representative of two or more independent experiments. **c**, *RelB* gene expression quantified by qPCR in purified Flt3l-elicited dendritic cells from B6 mice treated for 6 h with SCFA or TSA, as in **a**. Data are representative of four independent experiments. **d**, *RelB* gene expression quantified by qPCR in purified Flt3l-elicited dendritic cells from B6 mice treated with or without TSA in combination with, or in the absence of, butyrate at the indicated concentrations. Data in this figure are representative of two or more independent experiments, unless otherwise noted. The data represent mean ± s.e.m.

of SCFAs closely correlated with their ability to potentiate the capacity of dendritic cells to induce T_{reg}-cell differentiation. Dendritic cells briefly exposed to butyrate, TSA, and to a lesser extent propionate, but not acetate, potently induced Foxp3 expression (Fig. 4b). Furthermore, microarray analysis showed that butyrate and TSA induced remarkably similar, if not identical, gene-expression changes in dendritic cells (Supplementary Fig. 6a) with a systemic repression of lipopolysaccharide (LPS) response genes including *Il-12*, *Il-6* and *Relb* (Supplementary Fig. 6b, c). Interestingly, repression of *Relb*, a major inducer of dendritic-cell activation, correlated with the level of HDAC-inhibitory activity of butyrate and other SCFAs (Fig. 4c)[19]. Notably, knockdown of *Relb* expression in dendritic cells promotes their ability to support T_{reg}-cell differentiation[20,21]. To further ascertain whether TSA and butyrate potentiated T_{reg}-cell generation through HDAC inhibition and not through distinct independent mechanisms, we treated dendritic cells with the combination of butyrate and optimal amounts of TSA. If butyrate and TSA were to act through independent mechanisms, they should have exhibited synergistic effects on Foxp3 induction. However, if they acted on identical or related targets (that is, HDACs), additive effects were unlikely. We found that butyrate was unable to further enhance the ability of TSA to down-regulate *Relb* and promote Foxp3 induction (Fig. 4d; Supplementary Fig. 6d), suggesting that they act on identical or related targets. These results are consistent with the idea that the HDAC inhibitory activity of butyrate as well as propionate contributes to the ability of dendritic cells to facilitate extrathymic T_{reg}-cell differentiation.

In conclusion, our studies suggest that butyrate and propionate, produced by commensal microorganisms, increase extrathymic CNS1-dependent differentiation of T_{reg} cells. Our results indicate that metabolic

©2013 Macmillan Publishers Limited. All rights reserved

by-products of commensal microorganisms influence the balance between pro- and anti-inflammatory cells and serve as a means of communication between the commensal microbial community and the immune system.

METHODS SUMMARY

CNS1 knockout (*Foxp3*$^{\Delta CNS1}$), *Foxp3*^{GFP}, *Foxp3*$^{Thy1.1}$ and *Foxp3*^{DTR} mice have been described previously[7,22,23]. Male C57BL/6 mice were purchased from The Jackson Laboratory. All strains were maintained in the Sloan-Kettering Institute animal facility in accordance with institutional guidelines. For antibiotic treatment, mice were given 1 g l^{-1} metronidazole (Sigma-Aldrich), 0.5 g l^{-1} vancomycin (Hospira), 1 g l^{-1} ampicillin (Sigma-Aldrich) and 1 g l^{-1} kanamycin (Fisher Scientific) in drinking water (AVNM). For butyrate, acetate and propionate administration, each SCFA was added to AVNM-containing drinking water at 36 mM and pH-adjusted as needed. Dendritic cells were expanded *in vivo* by subcutaneous injection of B16 melanoma cells secreting FLT3-ligand and purified using CD11c (N418) magnetic beads (Dynabeads, Invitrogen). *In vitro* Foxp3 induction assays were performed by incubating 5.5×10^4 naive CD44^{lo}CD62L^{hi}CD25$^-$CD4$^+$ T cells sorted by FACS, in 1 μg ml^{-1} of CD3 antibody in the presence of dendritic cells in 96-well flat-bottom plates for 4 days. Alternatively, naive CD4$^+$ T cells were stimulated with CD3 and CD28 antibody-coated beads (Dynabeads Mouse T-Activator, Invitrogen) at a 1:1 cell-to-bead ratio. All cultures were supplemented with 1 ng ml^{-1} TGF-β and 100 units ml^{-1} IL-2. Intracellular staining for IL-17, interferon-γ (IFN-γ), IL-4, IL-13 and Foxp3 was performed using the Foxp3 staining kit (eBiosciences). Cytokine staining was performed after re-stimulation of *ex vivo* isolated cells with 5 μg ml^{-1} CD3 antibody and 5 μg ml^{-1} CD28 antibody in the presence of Golgi-plug (BD Biosciences) for 5 h. Stool samples were collected directly into sterile tubes from live mice and snap-frozen before preparation of material for SCFA quantification by HPLC or LC–MS. HPLC analysis of 2-nitrophenylhydrazine HCl-derivatized SCFAs present in stool extracts was performed as described elsewhere[24]. Acetylated H3K27 chromatin immunoprecipitation (ChIP) quantitative polymerase chain reaction (qPCR) was performed as previously described[25].

Online Content Any additional Methods, Extended Data display items and Source Data are available in the online version of the paper; references unique to these sections appear only in the online paper.

Received 20 June; accepted 30 September 2013.

Published online 13 November 2013.

1. Josefowicz, S. Z. *et al.* Extrathymically generated regulatory T cells control mucosal T_H2 inflammation. *Nature* **482,** 395–399 (2012).
2. Round, J. L. & Mazmanian, S. K. Inducible Foxp3$^+$ regulatory T-cell development by a commensal bacterium of the intestinal microbiota. *Proc. Natl Acad. Sci. USA* **107,** 12204–12209 (2010).
3. Ivanov, I. I. *et al.* Induction of intestinal T_H17 cells by segmented filamentous bacteria. *Cell* **139,** 485–498 (2009).
4. Lathrop, S. K. *et al.* Peripheral education of the immune system by colonic commensal microbiota. *Nature* **478,** 250–254 (2011).
5. Atarashi, K. *et al.* Induction of colonic regulatory T cells by indigenous clostridium species. *Science* **331,** 337–341 (2011).
6. Atarashi, K. *et al.* T_{reg} induction by a rationally selected mixture of Clostridia strains from the human microbiota. *Nature* **500,** 232–236 (2013).
7. Zheng, Y. *et al.* Role of conserved non-coding DNA elements in the *Foxp3* gene in regulatory T-cell fate. *Nature* **463,** 808–812 (2010).
8. Annison, G., Illman, R. J. & Topping, D. L. Acetylated, propionylated or butyrylated starches raise large bowel short-chain fatty acids preferentially when fed to rats. *J. Nutr.* **133,** 3523–3528 (2003).
9. Smith, P. M. *et al.* The microbial metabolites, short-chain fatty acids, regulate colonic T_{reg} cell homeostasis. *Science* **341,** 569–573 (2013).
10. van Loosdregt, J. *et al.* Rapid temporal control of Foxp3 protein degradation by sirtuin-1. *PLoS ONE* **6,** e19047 (2011).
11. van Loosdregt, J. *et al.* Regulation of T_{reg} functionality by acetylation-mediated Foxp3 protein stabilization. *Blood* **115,** 965–974 (2010).
12. Zhang, H., Xiao, Y., Zhu, Z., Li, B. & Greene, M. I. Immune regulation by histone deacetylases: a focus on the alteration of FOXP3 activity. *Immunol. Cell Biol.* **90,** 95–100 (2012).
13. Song, X. *et al.* Structural and biological features of FOXP3 dimerization relevant to regulatory T cell function. *Cell Rep.* **1,** 665–675 (2012).
14. Wang, L., de Zoeten, E. F., Greene, M. I. & Hancock, W. W. Immunomodulatory effects of deacetylase inhibitors: therapeutic targeting of FOXP3$^+$ regulatory T cells. *Nature Rev. Drug Discov.* **8,** 969–981 (2009).
15. Tao, R. *et al.* Deacetylase inhibition promotes the generation and function of regulatory T cells. *Nature Med.* **13,** 1299–1307 (2007).
16. Maslowski, K. M. *et al.* Regulation of inflammatory responses by gut microbiota and chemoattractant receptor GPR43. *Nature* **461,** 1282–1286 (2009).
17. Thangaraju, M. *et al.* GPR109A is a G-protein-coupled receptor for the bacterial fermentation product butyrate and functions as a tumor suppressor in colon. *Cancer Res.* **69,** 2826–2832 (2009).
18. Nilsson, N. E., Kotarsky, K., Owman, C. & Olde, B. Identification of a free fatty acid receptor, FFA2R, expressed on leukocytes and activated by short-chain fatty acids. *Biochem. Biophys. Res. Commun.* **303,** 1047–1052 (2003).
19. MacDonald, K. P. *et al.* Effector and regulatory T-cell function is differentially regulated by RelB within antigen-presenting cells during GVHD. *Blood* **109,** 5049–5057 (2007).
20. Zhu, H. C. *et al.* Tolerogenic dendritic cells generated by RelB silencing using shRNA prevent acute rejection. *Cell. Immunol.* **274,** 12–18 (2012).
21. Shih, V. F. *et al.* Control of RelB during dendritic cell activation integrates canonical and noncanonical NF-κB pathways. *Nature Immunol.* **13,** 1162–1170 (2012).
22. Fontenot, J. D. *et al.* Regulatory T cell lineage specification by the forkhead transcription factor Foxp3. *Immunity* **22,** 329–341 (2005).
23. Kim, J. M., Rasmussen, J. P. & Rudensky, A. Y. Regulatory T cells prevent catastrophic autoimmunity throughout the lifespan of mice. *Nature Immunol.* **8,** 191–197 (2007).
24. Torii, T. *et al.* Measurement of short-chain fatty acids in human faeces using high-performance liquid chromatography: specimen stability. *Ann. Clin. Biochem.* **47,** 447–452 (2010).
25. Samstein, R. M. *et al.* Foxp3 exploits a pre-existent enhancer landscape for regulatory T cell lineage specification. *Cell* **151,** 153–166 (2012).

Supplementary Information is available in the online version of the paper.

Acknowledgements This work was supported by the Robert Black Fellowship of the Damon Runyon Cancer Research Foundation DRG-2143-13 (N.A.), Ludwig Center at Memorial Sloan Kettering Cancer Center and the US National Institutes of Health (NIH) grant T32 A1007621 (N.A.) and R37 AI034206 (A.Y.R.). A.Y.R. is an investigator with the Howard Hughes Medical Institute.

Author Contributions N.A., C.C. and X.F. performed experiments and analysed data, with general assistance from S.D. and assistance from P.d. for HPLC, P.J.C. for immunoprecipitation of acetylated Foxp3 and J.v.d.V. for ChIP–qPCR experiments. H.L. and J.R.C. performed LC–MS. N.A., C.C., X.F. and A.Y.R. designed and interpreted experiments. K.P. provided *Gpr109a* mice. N.A. and A.Y.R. wrote the paper.

Author Information Microarray data have been deposited in the Gene Expression Omnibus (GEO) under accession number GSE51263. Reprints and permissions information is available at www.nature.com/reprints. The authors declare no competing financial interests. Readers are welcome to comment on the online version of the paper. Correspondence and requests for materials should be addressed to A.Y.R. (rudenska@mskcc.org).

©2013 Macmillan Publishers Limited. All rights reserved

METHODS

Mice. *Foxp3*$^{\Delta CNS1}$ (CNS1 knockout), *Foxp3*^{GFP}, *Foxp3*$^{Thy1.1}$ and *Gpr109a*$^{-/-}$ mice have been previously described[7,22,23]. Male C57BL/6 (B6) mice were purchased from the Jackson Laboratory and groups of five co-housed mice were randomly assigned to treatment versus control groups after confirmation that age and weight were in accordance between groups. Male mice were used for all experiments. All strains were maintained in the Sloan-Kettering Institute animal facility in accordance with institutional guidelines. Mice were killed by CO_2 asphyxiation then processed for tissue collection thereafter. This was carried with the experimenter blind to the group to which each mouse belonged. For antibiotic treatment, mice at 5 to 6 weeks of age were treated with 1 g l^{-1} metronidazole (Sigma-Aldrich), 0.5 g l^{-1} vancomycin (Hospira), 1 g l^{-1} ampicillin (Sigma-Aldrich) and 1 g l^{-1} kanamycin (Fisher Scientific) dissolved in drinking water. For butyrate, acetate and propionate administration, each SCFA was added to drinking water containing antibiotics (as described above) at a final concentration of 36 mM and pH-adjusted, if needed, to match that of antibiotic-only water. Butyrate was administered to mice after prior treatment with antibiotics for at least 1 week.

Cell isolation and FACS staining. For *in vitro* experiments, CD4$^+$ T cells and CD11c$^+$ dendritic cells were enriched using mouse CD4 (L3T4, Invitrogen) and mouse CD11c (N418, BioLegend) antibodies, respectively, that were biotinylated for use with Streptavidin Dynabeads (Invitrogen). Enriched cells were then sorted on a FACSAria II cell sorter (BD Biosciences) for *in vitro* assays. Intracellular staining for IL-17, IFN-γ, IL-4, IL-13 and Foxp3 was performed using the Foxp3 staining kit (eBiosciences). Cytokine staining was performed after re-stimulation with CD3 antibody and CD28 antibody (5 μg ml^{-1} each) in the presence of Golgiplug (BD Biosciences) for 5 h.

Dendritic-cell generation and isolation. Dendritic cells were expanded *in vivo* by subcutaneous injection of B16 melanoma cells secreting Flt3 ligand into the left hind flank of mice as indicated. Once tumours were visible, spleens from injected animals were dissociated in RPMI 1640 medium containing 1.67 units ml^{-1} liberase TL (Roche) and 50 μg ml^{-1} DNAse I (Roche) for 20 min at 37 °C with shaking. EDTA was then added at a final concentration of 5 mM to stop digestion and the resulting homogenate was processed for CD11c$^+$ cell isolation using the MACS mouse CD11c (N418) purification kit (Miltenyi Biotec).

***In vitro* assays.** *In vitro* Foxp3 induction assays were performed by co-culturing dendritic cells with 5.5×10^4 CD4$^+$CD44^{lo}CD62L^{hi}CD25$^-$ naive T cells in the presence of 1 μg ml^{-1} of CD3 antibody, 1 ng ml^{-1} TGF-β, and 100 units ml^{-1} IL-2, in 96-well flat-bottom plates for 4 days. For Foxp3 induction in the presence of butyrate- or TSA-pre-treated dendritic cells, TGF-β was used at 0.1 ng ml^{-1} final concentration. *In vitro* induction assays in the absence of dendritic cells were performed by incubating 5.5×10^4 naive CD4$^+$ T cells with 1 ng ml^{-1} TGF-β, 100 units ml^{-1} IL-2, and a 1:1 cell-to-bead ratio of CD3 and CD28 T activator Dynabeads (Invitrogen). For *in vitro* suppression assays, 4×10^4 naive CD4$^+$ T cells were FACS-sorted from B6 mice and cultured with graded numbers of CD4$^+$Foxp3$^+$ T_{reg} cells FACS-sorted from *Foxp3*^{GFP} mice treated with antibiotics and with or without butyrate, in the presence of 10^5 irradiated T-cell-depleted splenocytes and 1 μg ml^{-1} CD3 antibody in a 96-well round-bottom plate for 80 h. Proliferation of T cells was assessed by [^{3}H]- thymidine incorporation during the final 8 h of culture.

ChIP–qPCR assays. Acetylated H3K27 ChIP-qPCR was performed as previously described[25]. In brief, fixed cells were lysed and mono- and poly-nucleosomes were obtained by partial digestion with micrococcal nuclease (12,000 units ml^{-1}) for 1 min at 37 °C. EDTA was added to a final concentration of 50 mM to stop the reaction, and digested nuclei were resuspended in nuclear lysis buffer with 1% SDS. After sonication, 1 μg of acetylated-H3K27-specific antibody (Abcam, ab4729) was used to precipitate acetylated-H3K27-bound chromatin. Washing and de-crosslinking was performed as described previously[25].

Stool-sample collection. Stool samples were collected directly into sterile tubes from live mice and snap-frozen before preparation of material for SCFA quantification by HPLC or LC–MS.

HPLC assays. HPLC was carried out for analysis of derivatized stool extracts as previously described[24]. In brief, flash-frozen stool samples were extracted with 70% ethanol and brought to a final concentration of 0.1 μg μl^{-1}. Debris was removed by centrifugation and 300 μl of supernatant was transferred to a new tube and combined with 50 μl of internal standard (2-ethylbutyric acid, 200 mM in 50% aqueous methanol), 300 μl of dehydrated pyridine 3% v/v (Wako) in ethanol, 300 μl of 250 mM *N*-(3-dimethlaminopropyl)-*N*′-ethylcarbodiimide hydrochloride (Sigma-Aldrich) in ethanol, and 300 μl of 20 mM 2-nitrophenylhydrazine hydrochloride (Tokyo Chemical) in ethanol. Samples were incubated at 60 °C for 20 min and 200 μl of potassium hydroxide 15% w/v dissolved 80/20 in methanol was added to stop the derivatization reaction. Samples were incubated again at 60 °C for 20 min and transferred into a glass conical tube containing 3 ml of 0.5 M phosphoric acid. The organic phase was extracted by shaking with 4 ml diethyl ether and transferred to a new glass conical containing water to extract any remaining aqueous compounds. The organic phase containing the derivatized SCFA was transferred into a new 5 ml glass vial and evaporated overnight in a fume hood. Derivatized SCFA were resuspended in 100 μl of mobile phase (below) and 20 μl was chromatographed on a Shimadzu HPLC system equipped with a Vydac 2.1 × 30 mm 300 A C18 column run at 200 μl per min in methanol/acetonitrile/TFA (30%/16%/0.1% v/v) and monitored for absorbance at 400 nm.

LC–MS assays. Methanol (300 μl, 80%) containing deuterated short chain fatty acid internal standards (Cambridge Isotope Laboratories) was added to 70 μl serum and incubated at −80 °C for 30 min. Samples were then centrifuged at 4 °C at 21,000*g* for 15 min to precipitate protein. Pure short chain fatty acid standards (Sigma-Aldrich) were also prepared in 300 μl 80% methanol containing internal standards to produce a calibration curve from 0.25 μM to 50 μM. Methanol (80%) extracts were combined with 300 μl 250 mM *N*-(3-dimethylaminopropyl)-*N*′-ethylcarbodiimide hydrochloride in ethanol, 300 μl 20 mM 2-nitrophenylhydrazine hydrochloride in ethanol and 300 μl 3% pyridine in ethanol in a glass tube and reacted at 60 °C for 20 min. The reaction was quenched with 200 μl potassium hydroxide solution (15% KOH: MeOH, 8:2 v/v) at 60 °C for 20 min. After cooling, the mixture was adjusted to pH 4 with 0.25 M HCl. Derivatized short chain fatty acids were then extracted with 4 ml ether and washed with 4 ml water before drying under a nitrogen stream. The dried sample was dissolved in 150 μl methanol, and 5 μl was injected for LC–MS analysis.

Butyrate enemas. Mice were anaesthetized with isoflurane and injected intrarectally with 200 μl of 50 mM butyric acid (pH 4) or pH-matched water delivered through a 1.2-mm-diameter polyurethane catheter (Access Technologies). Enemas were administered for 7 days.

©2013 Macmillan Publishers Limited. All rights reserved

LETTER

doi:10.1038/nature12723

The heterotaxy gene *GALNT11* glycosylates Notch to orchestrate cilia type and laterality

Marko T. Boskovski[1]*†, Shiaulou Yuan[1]*, Nis Borbye Pedersen[2], Christoffer Knak Goth[2], Svetlana Makova[1], Henrik Clausen[2], Martina Brueckner[1] & Mustafa K. Khokha[1]

Heterotaxy is a disorder of left–right body patterning, or laterality, that is associated with major congenital heart disease[1]. The aetiology and mechanisms underlying most cases of human heterotaxy are poorly understood. In vertebrates, laterality is initiated at the embryonic left–right organizer, where motile cilia generate leftward flow that is detected by immotile sensory cilia, which transduce flow into downstream asymmetric signals[2–6]. The mechanism that specifies these two cilia types remains unknown. Here we show that the *N*-acetylgalactosamine-type *O*-glycosylation enzyme GALNT11 is crucial to such determination. We previously identified *GALNT11* as a candidate disease gene in a patient with heterotaxy[7], and now demonstrate, in *Xenopus tropicalis*, that *galnt11* activates Notch signalling. GALNT11 *O*-glycosylates human NOTCH1 peptides *in vitro*, thereby supporting a mechanism of Notch activation either by increasing ADAM17-mediated ectodomain shedding of the Notch receptor or by modification of specific EGF repeats. We further developed a quantitative live imaging technique for *Xenopus* left–right organizer cilia and show that Galnt11-mediated Notch1 signalling modulates the spatial distribution and ratio of motile and immotile cilia at the left–right organizer. *galnt11* or *notch1* depletion increases the ratio of motile cilia at the expense of immotile cilia and produces a laterality defect reminiscent of loss of the ciliary sensor Pkd2. By contrast, Notch overexpression decreases this ratio, mimicking the ciliopathy primary ciliary dyskinesia. Together our data demonstrate that Galnt11 modifies Notch, establishing an essential balance between motile and immotile cilia at the left–right organizer to determine laterality, and reveal a novel mechanism for human heterotaxy.

Recent genomic analyses have identified candidate genes for congenital heart disease[7–9]; however, determining disease causality and developmental mechanisms remains challenging. In a heterotaxy patient, we identified a copy number deletion of the *GALNT11* gene[7], a polypeptide *N*-acetylgalactosaminyltransferase (GALNT) that controls the initiation of *N*-acetylgalactosamine (GalNAc)-type *O*-glycosylation[10]. GALNTs serve different functions; however, the role of GALNT11 in vertebrate development is unknown.

To investigate the role of GALNT11 in left–right development, we first examined its effects on cardiac looping. Normally, in vertebrates, the initially midline heart tube forms a rightward (D) loop. Aberrant left–right patterning results in abnormal cardiac loops, including leftward (L) and symmetric/midline (A) loops. In *Xenopus*, we first confirmed that *galnt11* knockdown by morpholino oligonucleotide led to abnormal cardiac looping, and that overexpression of human *GALNT11* messenger RNA could rescue this phenotype, demonstrating its specificity (Fig. 1a).

We then examined two early markers of left–right patterning: *coco* (also known as *dand5*, *cerl2*) and *pitx2c*. *coco* is the earliest known asymmetric marker[11]. At the left–right organiser (LRO), *coco* expression is initially symmetric but develops a right-sided bias with the onset of cilia-driven flow, whereas *pitx2c* is expressed in the left lateral plate mesoderm[11]. Both *galnt11* knockdown and *GALNT11* gain of function (GOF; involving the delivery of human *GALNT11* mRNA into *Xenopus* embryos) resulted in abnormal patterns of *coco* and *pitx2c*, indicating that *galnt11* affects left–right patterning upstream of *coco* at the ciliated LRO (Fig. 1b). Consistent with this finding, we previously found *galnt11* mRNA expressed at the LRO[7], and Galnt11 protein is localized in the mouse LRO (node), with enrichment in crown cells compared to pit cells (Extended Data Fig. 1).

Abnormal *coco* expression suggests an abnormality in cilia-dependent signalling at the LRO. We first searched for a ciliary ultrastructural defect in the multiciliated cells on the *Xenopus* epidermis but found no consistent defect (Extended Data Fig. 2). However, we did observe a higher density of multiciliated cells (compare Fig. 1c and d). Conversely, *GALNT11* GOF reduced the number of multiciliated cells (Fig. 1e, f). Interestingly, a similar phenotype is seen with disruptions in Notch signalling[12]. Like *galnt11*, *notch1* knockdown increases, whereas *notch1* GOF (by overexpression of the notch1 intracellular domain (*nicd*)) (Fig. 1k) decreases, the multiciliated cell density (Fig. 1g–j). On the basis of these results, we proposed that Galnt11 may affect the Notch signalling pathway.

We further explored this possibility by examining the effects of Galnt11 and Notch1 on the left–right developmental cascade. *galnt11* and *notch1* knockdown and GOF produced similar left–right patterning defects (Extended Data Fig. 3), suggesting that Galnt11 affects Notch signalling directly or in a parallel pathway. Notch is a key regulator of many aspects of biology[13]. The core components of the Notch pathway include a ligand, Delta or Jagged, the transmembrane Notch receptor, and the CSL (named after CBF1/Su(H)/Lag-1) transcription factor complex (Fig. 1k). Signalling from the Notch receptor requires a number of cleavage steps, S1–S3, culminating in the release of the Notch intracellular domain (NICD), which translocates to the nucleus, interacts with CSL and modulates Notch-responsive genes (Fig. 1k).

To test whether Galnt11 acts directly in the Notch pathway, we attempted to rescue the *galnt11* knockdown phenotype with Notch pathway members. Using *pitx2c* as our assay, we found that *dll1* (hereafter known as *delta*) GOF had little effect on *galnt11* knockdown, but both *nicd* and *su(h)-ank* (a constitutively active CSL protein[14]) efficiently rescued the phenotype (Fig. 1l).

Notch functions are regulated by different *O*-glycosylations in the EGF repeats of the Notch receptor that affect the ligand–receptor interaction[15]. However, GalNAc-type *O*-glycosylation has not been reported previously; given our results, we searched for GalNAc-type *O*-glycosylation of Notch to identify activation mechanisms. First, we confirmed that *Xenopus* and human GALNT11 have identical substrate specificity, similar to the *Drosophila* GALNT11 orthologue compared previously

[1]Program in Vertebrate Developmental Biology, Department of Pediatrics and Genetics, Yale University School of Medicine, 333 Cedar Street, New Haven, Connecticut 06520, USA. [2]Copenhagen Center for Glycomics, Department of Cellular and Molecular Medicine, Faculty of Health Sciences, University of Copenhagen, Building 24.6.30, Blegdamsvej 3, DK-2200 Copenhagen N, Denmark. †Present address: Department of Surgery, Brigham and Women's Hospital, Harvard Medical School, 75 Francis Street, Boston, Massachusetts 02115, USA.
*These authors contributed equally to this work.

©2013 Macmillan Publishers Limited. All rights reserved

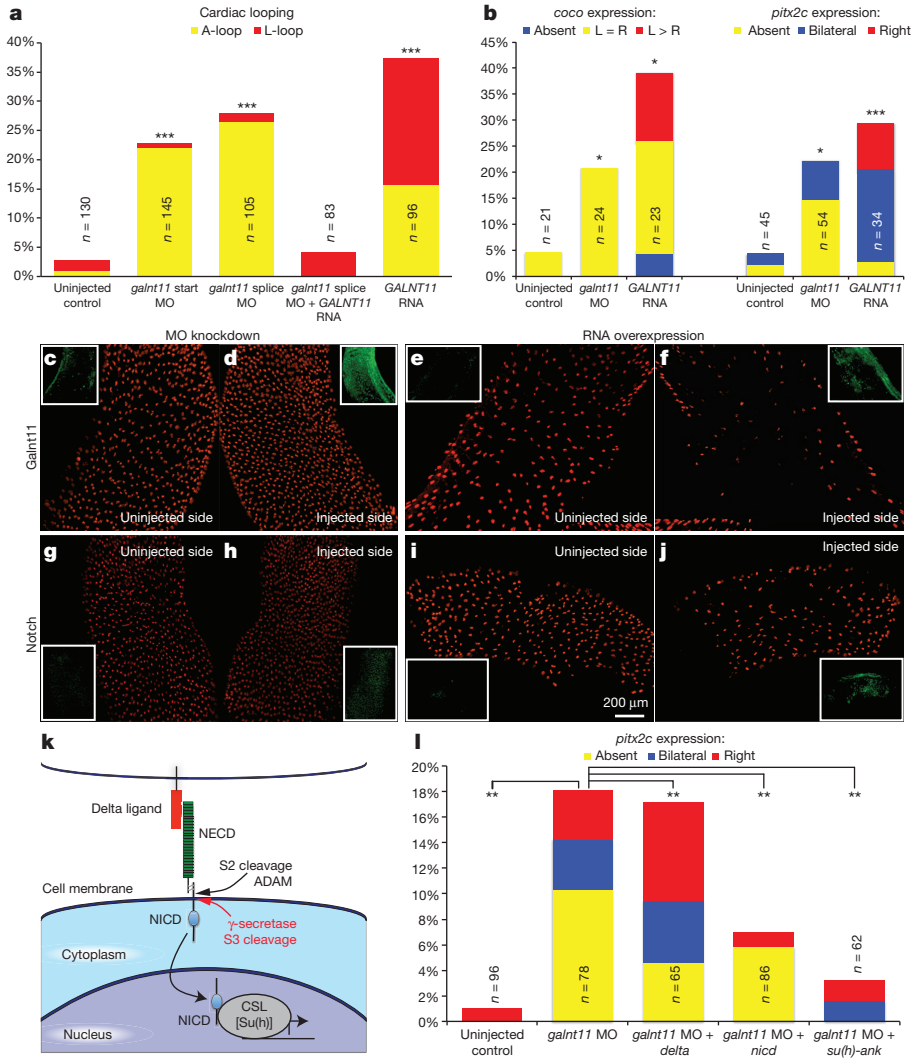


Figure 1 | Galnt11 alters left–right patterning and Notch signalling. **a**, **b**, Percentage of embryos that have abnormal cardiac looping (either A loops or L loops) (**a**) or abnormal *coco* or *pitx2c* expression (**b**). L, left; MO, morpholino oligonucleotide; R, right. **c**–**j**, *Xenopus* epidermal multiciliated cells marked by anti-acetylated α-tubulin (red). Embryos were injected at the two-cell stage targeting the epidermis on either the right or the left side with either *galnt11* morpholino oligonucleotide (**d**), *GALNT11* RNA (**f**), *notch1* morpholino oligonucleotide (**h**) or *nicd* RNA (**j**) and compared to the uninjected side (**c**, **e**, **g**, **i**). Green fluorescent protein (insets) trace the injected side. All views are lateral views with dorsal to the top. **k**, Schematic of the Notch pathway. NECD, Notch extracellular domain. **l**, Percentage of embryos with abnormal *pitx2c* in *galnt11* morphants or *galnt11* morphants co-injected with members of the Notch pathway. Bars depict means. $*P < 0.05$, $**P < 0.01$, $***P < 0.001$, respectively. Additional details can be found in Methods.

to human (Extended Data Table 1)[16]. Using mass spectrometry, we then tested 38 peptides derived from the extracellular domain of human NOTCH1 in an *in vitro* enzyme assay to identify potential substrate sites for GALNT11 *O*-glycosylation. Three peptides were glycosylated by GALNT11, two in EGF repeats 6 and 36 overlapping proposed *O*-fucosylation sites[15] and one in the juxtamembrane region near to the ADAM metalloproteinase ectodomain shedding site (Fig. 2a)[17]. The identified peptide substrates and several others were also glycosylated by other GALNTs (Extended Data Fig. 4).

Our experiments in *Xenopus* indicate that Galnt11 activates the Notch pathway (Fig. 1 and Extended Data Fig. 3). However, the identified *O*-glycosylation site adjacent to the ADAM processing site (Fig. 2a) would be expected to inhibit cleavage (on the basis of numerous previous examples, such as in TNR16; Extended Data Fig. 5a)[18] and thus block Notch receptor activation (Fig. 1k). Surprisingly, but in support of our original hypothesis, GALNT11 *O*-glycosylation enhanced cleavage of the juxtamembrane peptide by ADAM17 (Fig. 2b–d and Extended Data Fig. 5b). We thus propose a model in which site-specific GALNT11 glycosylation of NOTCH1 adjacent to the ADAM cleavage site facilitates shedding and activates the pathway by increasing the amount of NICD. However, alternative models remain possible given the identified glycosylation of extracellular domain peptides, and additional *in vivo* studies are needed. Notably, the catalytic function of GALNT11 is required for mediating left–right development, as mutation of essential catalytic residues from Asp-Ser-His to Asp-Ser-Ala (H247A)[10] eliminates the aberrant effects on *pitx2c* and left–right looping seen with wild-type *GALNT11* GOF (Extended Data Fig. 5c, d).

Next, we focused on how Galnt11 modulation of Notch1 alters left–right development, in which Notch has several possible roles[19]. Our data in *Xenopus* indicate that *galnt11* acts upstream of asymmetric *coco* expression, so we focused our attention on the potential relationship between *galnt11* and cilia function in the LRO.

galnt11 morphants retained bilateral symmetry: a predominance of midline, cardiac A loops and symmetric *coco* and *pitx2* expression (Fig. 1 and Extended Data Fig. 3). Similarly, our patient with *GALNT11* haploinsufficiency had bilateral symmetry, presenting with right atrial isomerism[7]. Finally, mutant *Dll1* or *Notch1/2* mice and mutant *notch1a* (also known as *des*) zebrafish are also predominately symmetric[20,21]. This is reminiscent of the *Pkd2* mutant mice phenotype, which has right isomerism owing to failure of ciliary sensing[4,22]. By contrast, overexpression of human *GALNT11* in *Xenopus* led to L and D loops (Fig. 1a), and randomization across the left–right axis, mimicking the human disorder primary ciliary dyskinesia, in which ineffective ciliary beating fails to generate extracellular fluid flow. On the basis of these two observations, we postulated that GALNT11, via Notch, specifies immotile (sensory) versus motile cilia (Extended Data Fig. 8).

To test this, we developed a live imaging method to simultaneously assay motile and immotile cilia in the LRO of *Xenopus*, the gastrocoel roof plate. Using a fluorophore-tagged ciliary protein, Arl13b–mCherry[23], with confocal microscopy (Fig. 3a and Supplementary Video 1), we

©2013 Macmillan Publishers Limited. All rights reserved

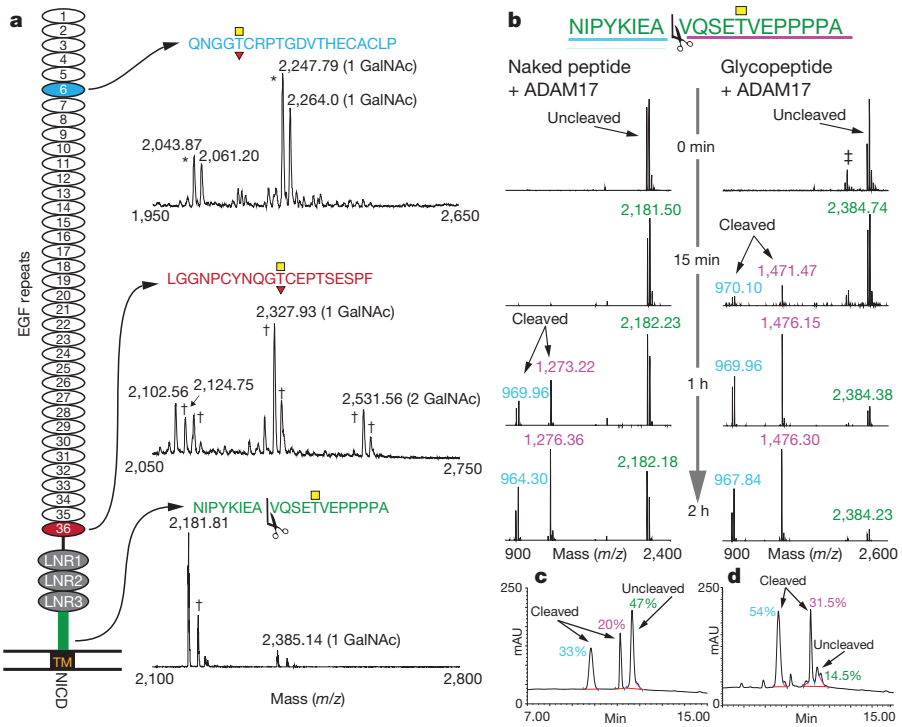


Figure 2 | GALNT11 glycosylation of NOTCH1-derived peptides and effects on ADAM-mediated cleavage. **a**, Depiction of NOTCH1 with matrix-assisted laser desorption/ionization–time of flight (MALDI–TOF) spectra, demonstrating *O*-GalNAc glycosylation of peptides derived from EGF6 (blue), EGF36 (red) and the juxtamembrane region (green). Yellow squares, *O*-GalNAc; red triangles, *O*-fucose; LNR, Lin-12/Notch repeat; TM, transmembrane domain. *Deammoniated peptide; †sodium adducts. **b**, MALDI–TOF time-course analysis of *in vitro* cleavage of the juxtamembrane peptide and glycopeptide by ADAM17. Scissors, cleavage site. ‡Nonspecific amino-terminal degradation of two amino acids. **c**, **d**, High-performance liquid chromatography analysis of the cleavage reactions with naked peptide (**c**) and glycopeptide (**d**) after 2 h (percentages above the peaks) with $P < 0.05$ (two-tailed *t*-test).

spatially mapped motile and immotile cilia. After additive analysis of numerous LROs, we qualitatively and quantitatively analysed cell populations with either cilia type (Extended Data Fig. 6a–d). In wild-type *Xenopus* LRO explants, we found that motile cilia are concentrated in the centre, with relatively more immotile cilia at the periphery, similar to the mouse LRO (or node) pit and crown, respectively (Fig. 3b, c, h (vehicle))[3,4]. In both locations, cilia types are intermixed similar to the mouse LRO.

To evaluate the role of *notch1* signalling, we co-injected *nicd* and *arl13b-mCherry* and analysed cilia types. *nicd* overexpression reduced the ratio of motile to immotile cilia when compared to controls (compare Fig. 3d to b, Fig. 3g, and Supplementary Video 2). Knockdown of *notch1* or *galnt11* had the opposite effect, increasing the ratio of motile to immotile cilia (Fig. 3e–g and Supplementary Videos 3, 4). Previous reports have identified asymmetric RNA expression of Notch ligands at the LRO[24]; however, we failed to observe any significant asymmetry in cilia number or type across the left–right axis of the LRO (Extended Data Fig. 6j, k).

The transcription factors FoxJ1 and Rfx2 are regulators of motile ciliogenesis[25–27], and therefore we evaluated the expression of *rfx2* and *foxj1* at the *Xenopus* LRO in response to Notch activation. *nicd* or *GALNT11* GOF reduced the expression of *foxj1* and *rfx2*, whereas *GALNT11(H247A)* GOF had no effect (Extended Data Fig. 7a–h), suggesting that Notch signalling functions upstream of Foxj1 and Rfx2 in determining ciliary type at the LRO.

Because Galnt11 expression in the mouse node was most prominent in the lateral crown cells (Extended Data Fig. 1), we compared cilia types at the *Xenopus* LRO periphery with the centre (Extended Data Fig. 6a–h). Interestingly, cilia in the periphery, where they are predominantly immotile (Fig. 3b, c), were markedly transformed to the motile type with *galnt11* and *notch1* knockdown (Fig. 3h). Overall, mean total cilia numbers per LRO were not statistically different,

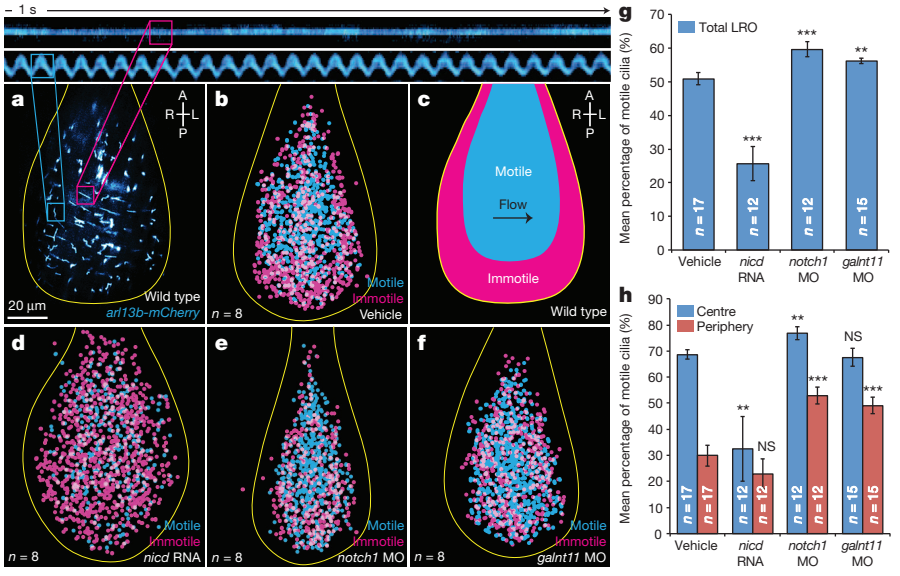


Figure 3 | Galnt11/Notch signalling switches cilia between motile and immotile types. **a**, Wild-type LRO explants expressing *arl13b-mCherry* reveal distinct populations of immotile and motile cilia. Cyan box highlights a single motile cilium, with a corresponding kymograph analysing beating frequency. Magenta box highlights immotile cilium and kymograph. **b**, Analysis of multiple vehicle LROs reveals a specific geography for cilia types: immotile cilia are enriched along the fringes, whereas motile cilia are enriched in the centre. **c**, Schematic of a wild-type LRO. A, anterior; P, posterior; L, left; R, right. **d**, *nicd* overexpressants exhibit a decrease in motile cilia in the centre of the LRO. **e**, **f**, *notch1* (**e**) and *galnt11* (**f**) morphants display a decrease in immotile cilia along the LRO periphery. **g**, **h**, Quantification of motile cilia distribution in total LROs (**g**), and in the centre and along the periphery of the LRO (**h**). Bars depict means and error bars are ± standard error. $^{**}P < 0.01$, $^{***}P < 0.001$; NS, not significant. Additional details are in Methods.

©2013 Macmillan Publishers Limited. All rights reserved

supporting altered cilia identity as the primary mechanism for left–right defects (Extended Data Fig. 6i). To confirm that *galnt11* was not perturbing formation of the LRO periphery, we tested peripheral markers at stages before the stage at which flow alters *coco* and noted no significant differences (Extended Data Fig. 7i–u). We conclude that Galnt11/Notch1 signalling mediates a critical switch between these two cilia types and their spatial distribution within the LRO (Extended Data Fig. 8).

Our results strengthen the two cilia model of left–right patterning by identifying a signalling pathway that modulates the balance between motile and immotile cilia[3] at the LRO (Extended Data Fig. 8). Exactly how many cilia and which types are needed for proper left–right signalling is controversial and may depend on the specific architecture of the LRO found in each organism. For example, in the mouse LRO, a partially open cup-shaped structure, only two motile cilia are needed for left–right patterning[28]. However, in the zebrafish LRO, which is an enclosed spherical structure, there appears to be a greater enrichment of motile cilia relative to frog or mouse[29]. In the frog LRO, which is a shallow indentation inside the gastrocoel cavity, motile cilia are required only on the left for correct left–right patterning[30]. For immotile cilia, there may be a threshold number that also differs depending on the specific architecture of the organism's LRO. Further studies will need to address why two cilia types are needed in the LRO and the mechanisms that convert ciliary sensation of flow to asymmetric gene expression and laterality.

Our findings were prompted by gene discovery in a single disease subject. We had no additional alleles to prove causality using a genetic approach[7]. Instead, we assayed for phenocopy in a high-throughput vertebrate model, *Xenopus*, and then embarked on mechanistic analyses in order to understand the role of GALNT11 in left–right patterning and disease. Our results have led to new insights into the basic biology of GalNAc-type *O*-glycosylation, Notch signalling, left–right patterning and the aetiology of heterotaxy. Because of high locus heterogeneity and severe reduction in fitness, causative gene discovery in children with birth defects has been challenging. However, with the brisk pace of advancing human genomics, these limitations are being broken, and new opportunities are at hand to understand birth defects and their underlying genetic mechanisms, especially when coupled with rapid vertebrate developmental models such as *Xenopus*.

METHODS SUMMARY

Knockdown and overexpression studies were performed in *Xenopus* by microinjection of morpholino oligonucleotides or RNA. Glycosylation of Notch peptides was assayed by MALDI-TOF and electrospray ionization-linear ion trap-Fourier transform mass spectrometry. RNA expression studies were done in *Xenopus* embryos by whole-mount *in situ* hybridization. Cilia were imaged by scanning electron microscopy, transmission electron microscopy and immunofluorescence. We localized the Galnt11 protein using anti-Galnt11 antibodies. We visualized live cilia by explanting the *Xenopus* LRO and imaging with a Zeiss 710 DUO confocal microscope. Additional details are in Methods.

Online Content Any additional Methods, Extended Data display items and Source Data are available in the online version of the paper; references unique to these sections appear only in the online paper.

Received 17 January; accepted 27 September 2013.
Published online 13 November 2013.

1. Sutherland, M. J. & Ware, S. M. Disorders of left–right asymmetry: heterotaxy and situs inversus. *Am. J. Med. Genet. C. Semin. Med. Genet.* **151C,** 307–317 (2009).
2. Nonaka, S. *et al.* Randomization of left–right asymmetry due to loss of nodal cilia generating leftward flow of extraembryonic fluid in mice lacking KIF3B motor protein. *Cell* **95,** 829–837 (1998).
3. McGrath, J., Somlo, S., Makova, S., Tian, X. & Brueckner, M. Two populations of node monocilia initiate left–right asymmetry in the mouse. *Cell* **114,** 61–73 (2003).
4. Yoshiba, S. *et al.* Cilia at the node of mouse embryos sense fluid flow for left-right determination via Pkd2. *Science* **338,** 226–231 (2012).
5. Schweickert, A. *et al.* Cilia-driven leftward flow determines laterality in *Xenopus*. *Curr. Biol.* **17,** 60–66 (2007).
6. Kramer-Zucker, A. G. *et al.* Cilia-driven fluid flow in the zebrafish pronephros, brain and Kupffer's vesicle is required for normal organogenesis. *Development* **132,** 1907–1921 (2005).
7. Fakhro, K. A. *et al.* Rare copy number variations in congenital heart disease patients identify unique genes in left-right patterning. *Proc. Natl Acad. Sci. USA* **108,** 2915–2920 (2011).
8. Greenway, S. C. *et al. De novo* copy number variants identify new genes and loci in isolated sporadic tetralogy of Fallot. *Nature Genet.* **41,** 931–935 (2009).
9. Zaidi, S. *et al. De novo* mutations in histone-modifying genes in congenital heart disease. *Nature* **498,** 220–223 (2013).
10. Bennett, E. P. *et al.* Control of mucin-type O-glycosylation: a classification of the polypeptide GalNAc-transferase gene family. *Glycobiology* **22,** 736–756 (2012).
11. Schweickert, A. *et al.* The nodal inhibitor Coco is a critical target of leftward flow in *Xenopus*. *Curr. Biol.* **20,** 738–743 (2010).
12. Deblandre, G. A., Wettstein, D. A., Koyano-Nakagawa, N. & Kintner, C. A two-step mechanism generates the spacing pattern of the ciliated cells in the skin of *Xenopus* embryos. *Development* **126,** 4715–4728 (1999).
13. Artavanis-Tsakonas, S. & Muskavitch, M. A. Notch: the past, the present, and the future. *Curr. Top. Dev. Biol.* **92,** 1–29 (2010).
14. Wettstein, D. A., Turner, D. L. & Kintner, C. The *Xenopus* homolog of *Drosophila* Suppressor of Hairless mediates Notch signaling during primary neurogenesis. *Development* **124,** 693–702 (1997).
15. Rana, N. A. & Haltiwanger, R. S. Fringe benefits: functional and structural impacts of *O*-glycosylation on the extracellular domain of Notch receptors. *Curr. Opin. Struct. Biol.* **21,** 583–589 (2011).
16. Schwientek, T. *et al.* Functional conservation of subfamilies of putative UDP-*N*-acetylgalactosamine:polypeptide *N*-acetylgalactosaminyltransferases in *Drosophila*, *Caenorhabditis elegans*, and mammals. One subfamily composed of l(2)35Aa is essential in *Drosophila*. *J. Biol. Chem.* **277,** 22623–22638 (2002).
17. Brou, C. *et al.* A novel proteolytic cleavage involved in Notch signaling: the role of the disintegrin-metalloprotease TACE. *Mol. Cell* **5,** 207–216 (2000).
18. Gram Schjoldager, K. T. *et al.* A systematic study of site-specific GalNAc-type *O*-glycosylation modulating proprotein convertase processing. *J. Biol. Chem.* **286,** 40122–40132 (2011).
19. Kato, Y. The multiple roles of Notch signaling during left-right patterning. *Cell. Mol. Life Sci.* **68,** 2555–2567 (2011).
20. Lopes, S. S. *et al.* Notch signalling regulates left-right asymmetry through ciliary length control. *Development* **137,** 3625–3632 (2010).
21. Krebs, L. T. *et al.* Notch signaling regulates left–right asymmetry determination by inducing *Nodal* expression. *Genes Dev.* **17,** 1207–1212 (2003).
22. Pennekamp, P. *et al.* The ion channel polycystin-2 is required for left-right axis determination in mice. *Curr. Biol.* **12,** 938–943 (2002).
23. Duldulao, N. A., Lee, S. & Sun, Z. Cilia localization is essential for *in vivo* functions of the Joubert syndrome protein Arl13b/Scorpion. *Development* **136,** 4033–4042 (2009).
24. Raya, A. *et al.* Notch activity acts as a sensor for extracellular calcium during vertebrate left–right determination. *Nature* **427,** 121–128 (2004).
25. Stubbs, J. L., Oishi, I., Izpisua Belmonte, J. C. & Kintner, C. The forkhead protein Foxj1 specifies node-like cilia in *Xenopus* and zebrafish embryos. *Nature Genet.* **40,** 1454–1460 (2008).
26. Bisgrove, B. W., Makova, S., Yost, H. J. & Brueckner, M. RFX2 is essential in the ciliated organ of asymmetry and an RFX2 transgene identifies a population of ciliated cells sufficient for fluid flow. *Dev. Biol.* **363,** 166–178 (2012).
27. Chung, M. I. *et al.* RFX2 is broadly required for ciliogenesis during vertebrate development. *Dev. Biol.* **363,** 155–165 (2012).
28. Shinohara, K. *et al.* Two rotating cilia in the node cavity are sufficient to break left-right symmetry in the mouse embryo. *Nature Commun.* **3,** 622 (2012).
29. Kamura, K. *et al.* Pkd1l1 complexes with Pkd2 on motile cilia and functions to establish the left-right axis. *Development* **138,** 1121–1129 (2011).
30. Vick, P. *et al.* Flow on the right side of the gastrocoel roof plate is dispensable for symmetry breakage in the frog *Xenopus laevis*. *Dev. Biol.* **331,** 281–291 (2009).

Supplementary Information is available in the online version of the paper.

Acknowledgements We thank the patients and their families, who are the inspiration for this study. We thank S. Kubek and M. Slocum for animal husbandry. We thank U. Mandel, M. Vester-Christensen, T. D. Madsen and S. B. Levery for help with generation of polyclonal antibodies, recombinant GALNT enzymes, *in vitro* glycosylation experiments and mass spectrometry. Thanks to the Center for Cellular and Molecular Imaging at Yale for assistance with SEM/TEM (C. Rahner and M. Graham) and confocal imaging. Thanks to C. Kintner and Z. Sun for reagents. Thanks to R. Harland, K. Liem, R. Lifton, J. McGrath, A. Horwich and Z. Sun for critical reading of the manuscript. M.T.B. was supported by grant number TL 1 RR024137 from the National Center for Research Resources/National Institutes of Health (NIH) and NIH Roadmap for Medical Research. S.Y. was supported by NIH training grant 5T32HD00709436. This work was supported by NIH R01HL093280 to M.B. and NIH DE018825, DE018824 to M.K.K., and the Danish National Research Foundation (DNRF107) to H.C.

Author Contributions M.T.B., S.Y., S.M., M.B. and M.K.K. conceived and designed the embryological experiments in *Xenopus* and mouse. M.T.B., S.Y., S.M. and M.K.K. performed the *Xenopus* experiments and M.B. performed mouse experiments. N.B.P., C.K.G. and H.C. performed and evaluated the glycosylation and ADAM studies. All authors wrote and contributed to the manuscript.

Author Information Reprints and permissions information is available at www.nature.com/reprints. The authors declare no competing financial interests. Readers are welcome to comment on the online version of the paper. Correspondence and requests for materials should be addressed to M.K.K. (mustafa.khokha@yale.edu).

©2013 Macmillan Publishers Limited. All rights reserved

METHODS

Frog husbandry. *X. tropicalis* were housed and cared for in our aquatics facility according to established protocols that were approved by the Yale Institutional Animal Care and Use Committee (IACUC).

Mouse husbandry. Mice were housed and cared for in our animal facility according to established protocols that were approved by Yale IACUC.

Microinjection of morpholino oligonucleotides and mRNA in *Xenopus*. We induced ovulation and collected eggs according to established protocols[31]. Staging of *Xenopus* tadpoles was done according to ref. 32. Morpholino oligonucleotides or mRNA were injected into the one-cell or two-cell embryo as previously described[33]. The following morpholino oligonucleotides were injected: *galnt11* splice blocking (0.5–1 ng 5′-CAGGTCAGAGAGAAGGGCACCTACT-3′), *galnt11* ATG blocking (0.5–1 ng 5′-GCGCTGCCCATCGTCCCCCTAGCA-3′), *notch1* (3 ng 5′-GAACAAGCAGCCCGATCCGATACAT-3′), *dnah9* (2–4 ng 5′-TGGGTCACTCATCTTTCCCCTCATT-3′). Alexa488 (Invitrogen), mini-ruby (Invitrogen) or green fluorescent protein (100 pg) were injected as tracers. We generated *in vitro* capped mRNA using the mMessage machine kit (Ambion) and followed the manufacturer's instructions. We generated human *GALNT11* mRNA by cloning the insert from IMAGE clone 100068224 into the pCSDest vector using Gateway recombination techniques. To generate *arl13b-mCherry* mRNA, we fused zebrafish *arl13b* to *mCherry* into the pCSDest2 vector using Gateway recombination techniques. We injected 6 pg *GALNT11* mRNA for rescue of *galnt11* morphants, 25 pg *GALNT11* mRNA for overexpression to assay left–right patterning and in the ciliated epidermis assay, 25 pg *GALNT11(H247A)*, 12.5 pg *nicd* mRNA for rescue of *galnt11* morphants, 25 pg *nicd* mRNA for overexpression to assay left–right patterning and in the ciliated epidermis assay, 2 pg *su(h)-ank* and 100–200 pg *arl13b-mCherry*.

Cardiac looping in *Xenopus*. Frog embryos at stage 45 were treated with benzocaine and ventrally scored for cardiac looping using a light dissection microscope. Loop direction is defined by the position of the outflow tract relative to the inflow of the heart: outflow to the right, D loop; outflow to the left, L loop; outflow midline, A loop.

Transfection of IMCD3 cells. Cells were transfected with Lipofectamine 2000 (Invitrogen) according to manufacturer's instructions. Cells were fixed in 4% PFA 48 h after transfection and processed for immunofluorescence. Cells were not authenticated nor tested for mycoplasma contamination.

Immunofluorescence and *in situ* hybridization. Embryonic day (E)8.0 mouse embryos were collected from timed pregnancies for node immunofluorescence. Observation of coital plug marks E0.5. For gastrocoel roof plates (GRPs), we collected stage 14 *Xenopus* embryos for *foxj1* and *rfx2*, stage 16 for *coco*, *xnr1 and gdf3*, and stage 19–21 for *coco*. For *pitx2c*, we collected *Xenopus* embryos at stage 28–31. For immunofluorescence of multiciliated epidermal cells, we used stage 28–30 *Xenopus* embryos. GRPs were dissected as described previously[5].

For immunofluorescence, transfected mammalian cells, mouse and *Xenopus* embryos were fixed in 4% paraformaldehyde/PBS overnight at 4 °C. Mouse embryos, *Xenopus* embryos and *Xenopus* GRPs were labelled by immunofluorescence as described previously[3,33]. All embryos were mounted in Pro-Long Gold (Invitrogen) before imaging. Imaging was performed on a Zeiss Axiovert microscope equipped with Apotome optical interference imaging to obtain optical sections. For comparison of left- and right-sided epithelial cilia density, the *Xenopus* embryos were sandwiched between two coverslips and each side of a single embryo was imaged.

RNA *in-situ* hybridization was done as described previously[33]. We detected *coco*[34], *gdf3*, *foxj1*, *pitx2c*, *rfx2* and *xnr1* by generating anti-digoxigenin probes (Roche) using clones TEgg007d24, Tgas141F11, TNeu058M03, TNeu083k20, IMAGE:7680423 and TGas124h10, respectively.

Antibodies. Anti-Arl13b[35] – rabbit anti-Arl13b (1:500, courtesy of T. Caspary); anti-acetylated tubulin (Sigma, no. T-6793)[36] – mouse monoclonal anti-acetylated tubulin, clone 6-11B-1 (1:1,000) (species reactivity: monkey, Protista, mouse, pig, human, bovine, invertebrates, rat, hamster, plant, frog, chicken); Anti-GALNT11 (Santa Cruz, no. sc-68498) – goat polyclonal anti-GALNT11 (K-19) (1:200) (transfected cells) (species reactivity: mouse, rat, human); Anti-GALNT11 (ref. 16) – mouse, monoclonal (undiluted) (mouse LRO).

Live imaging of cilia motility in the GRP. For imaging of cilia motility in the GRP, wild-type embryos were injected with *arl13b-mCherry* mRNA at the 1-cell stage and then cultured until stage 16–17. Vehicle embryos were co-injected with water, whereas *nicd* overexpressants, *notch1* morphants and *galnt11* morphants were co-injected with RNA or morpholino oligonucleotides. GRP explants were prepared in MBSH buffer (88 mM NaCl, 1 mM KCl, 2.4 mM $NaHCO_3$, 0.82 mM $MgSO_4$, 0.33 mM $Ca(NO_3)_2$, 0.41 mM $CaCl_2$, 10 mM HEPES (pH 7.6)) and mounted on a coverglass within a ring of petroleum jelly. High-speed fluorescent imaging was performed on an LSM 710 DUO (Zeiss) microscope equipped with a rapid LIVE linescan detector, a 40× C-Apochromat water objective and a 561-nm laserline. Multiple rapid acquisitions were collected per each embryo at several *Z*-planes within the GRP. All acquisitions were collected at a rate of 240 frames per second with a 512 × 512 pixel resolution using maximal pinhole settings, bidirectional scanning and 0 binning in Zen 2010 (Zeiss). Cilia beating dynamics were analysed and quantified by kymographs in ImageJ (NIH) with an elapsed time of 1 s displayed in Fig. 3. Video clips with overlays were prepared using Final Cut (Apple) and Compressor (Apple).

Spatial analysis of motile and immotile cilia populations in the GRP. Live high-speed acquisitions of GRP explants expressing *arl13b-mCherry* were slowed down, played back and scored for motile and immotile cilia in ImageJ (NIH) onto two overlaying images: one for motile and the second for immotile cilia (Extended Data Fig. 6a–c). Each overlaying image was converted into a binary image and then converted a second time into a false-coloured 8-bit image. Both images were then merged to generate a two-colour map of cilia distribution for an individual GRP (Extended Data Fig. 6d). For each experimental condition, numerous two-colour maps were assembled into an image series and processed into a single composite image using the projection function in ImageJ (Fig. 3b, d–f). For quantification of motile and immotile cilia in the periphery or centre region of the LRO, a two-colour map representing a single GRP was imported into Photoshop CS5 (Adobe). A new layer (named 'layer 1') was created and the edge of the total ciliated population of that GRP was traced using the pencil tool (Extended Data Fig. 6e). A duplicate of the trace layer was created (named 'layer 2'), decreased in area uniformly (to maintain the shape of the original trace) by 50% using the transform tool and aligned at the absolute centre of layer 1 (Extended Data Fig. 6f). By dividing the LRO into two 50% areas while maintaining the specific shape of each GRP, the periphery and centre of the LRO were defined with equal areas, thus minimizing any potential pre-conceived size bias for either zone (Extended Data Fig. 6g, h). Further, this estimate is broadly supported by studies of the crown and pit cells in the mouse LRO[4]. The area within the trace in layer 2 was defined as the centre of the LRO, whereas the area between the traces in layers 1 and 2 was defined as the periphery. Motile cilia, immotile cilia and total cilia (Fig. 3 and Extended Data Fig. 6i) were scored specifically in the centre and then periphery area.

***In vitro* GALNT11 glycosylation and ADAM processing studies.** Glycosylation assays were performed in 25 µl reaction mixtures containing 10 µg peptide substrate, 4 mM UDP-GalNAc, 25 mM cacodylic acid sodium (pH 7.4), 10 mM $MnCl_2$, 0.25% Triton X-100 and purified recombinant GALNT enzymes (0.1 µg). The enzyme reactions in Fig. 2a were performed with GALNT11 by *in vitro* assays for 18–24 h. ADAM cleavage assays were performed with 250 nM ADAM17 (Enzo Life Sciences) with 10 µg of peptide or GalNAc-glycopeptide substrate in 25 mM Tris (pH 9) in a total volume of 25 µl. Reaction for ADAM cleavage assays were sampled at 0 h, 15 min, 1 h and 2 h. All reactions were incubated at 37 °C and product development evaluated by MALDI-TOF in a time-course as described previously[16], except that a Bruker Autoflex MALDI-TOF instrument with accompanying Compass 1.4 FlexSeries software was used for product evaluation. Position of sites were determined by electrospray ionization-linear ion trap-Fourier transform mass spectrometry applying both high energy collision-induced dissociation and electron transfer dissociation enabling peptide sequence analysis by tandem mass spectrometry (MS^2) with retention of glycan site-specific fragments as described in detail previously[37] (data not shown). High-performance liquid chromatography (HPLC) analyses were performed using a multistep gradient on a Dionex Ultimate 3000 LC system (Thermo Scientific) with a Kinetex 2.6u C18 100A 100 × 4.60 mm column (Phenomenex). Area under the curve was calculated using the Chromeleon 6.80 software. Statistical analysis (two-tailed *t*-test) was carried out in Microsoft Excel comparing the averages of full-length glycosylated and unglycosylated peptides from three different sets of cleavage experiments. Statistical analysis showed that the difference in cleavage efficiency between the unglycosylated and glycosylated peptides was significant ($P < 0.05$) in Fig. 2c.

Electron microscopy. Stage 27 *Xenopus* embryos were fixed with Karnovsky fixative for 1 h at 4 °C, washed with 0.1 M sodium cacodylate, pH 7.4, then post-fixed with Palade's osmium for 1 h at 4 °C, shielded from light. Following a second wash, embryos were stained with Kellenburger's solution for 1 h at room temperature (22–23 °C), washed in double distilled water, then put through an ethanol series, propylene oxide, 50/50 propylene oxide/epon, then two incubations in 100% epon. Embedded embryos were sectioned at 400 nm before staining with 2% uranyl acetate. Micrographs were taken on a Zeiss 910 electron microscope.

Statistical analysis. We estimated that for *Xenopus* experiments 20–25 samples per experimental condition were necessary for statistical significance given the magnitude of the changes expected. In most cases, considerably more samples were obtained for each except as noted in the figures. Statistical significance is reported as appropriate. In no cases did we exclude samples except in cases of technical failure (embryos found to be uninjected, *in situ* hybridization failed, etcetera). We did not use any randomization method. For *pitx2c* and *coco* expression, one observer was unblinded but in all cases at least 1–2 other observers were blinded and a high degree of concordance was noted.

©2013 Macmillan Publishers Limited. All rights reserved

For Fig. 1a sample sizes were 130 for uninjected controls, 145 for *galnt11* start morpholino oligonucleotides, 105 for *galnt11* splice morpholino oligonucleotides, 83 for *galnt11* splice morpholino oligonucleotides plus *GALNT11* RNA, and 96 for *GALNT11* RNA. These numbers represent the cumulative total of three biological replicates. For Fig. 1b *coco* expression patterns sample sizes were 21 for uninjected controls, 21 for *galnt11* splice morpholino oligonucleotides and 23 for *GALNT11* RNA. For *pitx2c* expression patterns sample sizes were 45 for uninjected controls, 54 for *galnt11* splice morpholino oligonucleotides and 34 for *GALNT11* RNA. These numbers represent the cumulative total of two biological replicates for *coco* and three for *pitx2* expression patterns. For Fig. 1l sample sizes were 96 for uninjected controls, 78 for *galnt11* morpholino oligonucleotides, 65 for *galnt11* morpholino oligonucleotides plus *delta*, 86 for *galnt11* morpholino oligonucleotides plus *nicd* and 62 for *galnt11* morpholino oligonucleotides plus *su(h)-ank*. These numbers represent the cumulative total of three biological replicates.

For Fig. 2, enzyme reactions were repeated three times, and statistical analysis on HPLC data was done using three biological replicates.

For the entirety of Fig. 3, the data shown represent a cumulative total of 15 biological replicates. Figure 3a is a representative image. For Fig. 3b, d–f, the analysed samples sizes were 8 embryos per each condition. For Fig. 3g, h, analysed sample sizes were 17 embryos for vehicle (dH_20), 12 for *nicd* RNA, 12 for *notch1* morpholino oligonucleotides and 15 for *galnt11* morpholino oligonucleotides. For Fig. 3g, h, statistical significance was analysed by *t*-test (two-tailed, type two); centre values represent averages; errors bars indicate standard error. For quantitative analysis and mapping, embryos were excluded on the following pre-established criteria: (1) only partial labelling of total cilia population in the GRP by Arl13b–mCherry; (2) improper embryonic stage (stages 16/17 were defined as the inclusion criteria).

For Extended Data Fig. 3 *coco* expression patterns sample sizes were 21 for uninjected control, 24 for *galnt11* morpholino oligonucleotides, 30 for *notch* morpholino oligonucleotides, 23 for *galnt11* RNA and 22 for *nicd* RNA. These numbers represent the cumulative total of two biological replicates. For *pitx2c* expression patterns, sample sizes were 45 for uninjected control, 54 for *galnt11* morpholino oligonucleotides, 50 for *notch1* morpholino oligonucleotides, 34 for *galnt11* RNA and 30 for *nicd* RNA. These numbers represent the cumulative total of three biological replicates. For heart looping sample sizes were 276 for uninjected control, 68 for *galnt11* morpholino oligonucleotides, 75 for *notch* morpholino oligonucleotides, 91 for *galnt11* RNA and 50 for *nicd* RNA.

For Extended Data Fig. 4, glycosylations reactions were all repeated a minimum of two times for each glycosylation enzyme.

For Extended Data Fig. 5, panel **a** is a representative spectrum of three independent experiments, and **b** is a representative spectrum of two independent experiments. For panel **c** *pitx2c* expression patterns sample sizes were 45 for uninjected control, 34 for *galnt11* RNA and 40 for *galnt11(H247A)* RNA. These numbers represent the cumulative total of two biological replicates. For heart looping, sample sizes were 276 for uninjected control, 91 for *GALNT11* RNA and 133 for *GALNT11(H247A)* RNA. These numbers represent the cumulative total of three biological replicates.

For the entirety of Extended Data Fig. 6, the data shown represent a cumulative total of 15 biological replicates. Extended Data Fig. 6a–h are representative images. For Extended Data Fig. 6i, analysed sample sizes were 17 embryos for vehicle (dH_20), 12 for *nicd* RNA, 12 for *notch1* morpholino oligonucleotides and 15 for *galnt11* morpholino oligonucleotides. For Extended Data Fig. 6j, k, analysed sample sizes were 17 vehicle ('wild type') embryos. For Extended Data Fig. 6i, j, k, statistical significance was analysed by *t*-test (two-tailed, type two); centre values represent averages; errors bars indicate standard error. For quantitative analysis and mapping, embryos were excluded on the following pre-established criteria: (1) only partial labelling of total cilia population in the GRP by Arl13b–mCherry; (2) improper embryonic stage (stages 16/17 were defined as the inclusion criteria).

In all figures, statistical significance was defined as $P < 0.05$, whereas $P \geq 0.05$ was defined as not significant. $^{*}P < 0.05$, $^{**}P < 0.01$, $^{***}P < 0.001$. Figure 3 and Extended Data Fig. 6 were analysed by *t*-test (two-tailed, type two) presuming a normal distribution. Figure 1, Extended Data Fig. 3 and Extended Data Fig. 5 were analysed by Chi-squared test as described previously[38].

31. del Viso, F. & Khokha, M. Generating diploid embryos from *Xenopus tropicalis*. *Methods Mol. Biol.* **917,** 33–41 (2012).
32. Nieuwkoop, P. D. & Faber, J. *Normal Table of Xenopus laevis (Daudin): a Systematical and Chronological Survey of the Development from the Fertilized Egg Till the End of Metamorphosis* (Garland, 1994).
33. Khokha, M. K. *et al.* Techniques and probes for the study of *Xenopus tropicalis* development. *Dev. Dyn.* **225,** 499–510 (2002).
34. Vonica, A. & Brivanlou, A. H. The left–right axis is regulated by the interplay of Coco, Xnr1 and derriere in *Xenopus* embryos. *Dev. Biol.* **303,** 281–294 (2007).
35. Caspary, T., Larkins, C. E. & Anderson, K. V. The graded response to Sonic Hedgehog depends on cilia architecture. *Dev. Cell* **12,** 767–778 (2007).
36. Piperno, G. & Fulller, M. T. Monoclonal antibodies specific for an acetylated form of alpha-tubulin recognize the antigen in cilia and flagella from a variety of organisms. *J. Cell Biol.* **101,** 2085–2094 (1985).
37. Pedersen, J. W. *et al.* Lectin domains of polypeptide GalNAc transferases exhibit glycopeptide binding specificity. *J. Biol. Chem.* **286,** 32684–32696 (2011).
38. Walentek, P., Beyer, T., Thumberger, T., Schweickert, A. & Blum, M. *ATP4a* is required for Wnt-dependent *Foxj1* expression and leftward flow in *Xenopus* left-right development. *Cell Rep.* **1,** 516–527 (2012).
39. Steentoft, C. *et al.* Mining the O-glycoproteome using zinc-finger nuclease-glycoengineered SimpleCell lines. *Nature Methods* **8,** 977–982 (2011).
40. Steentoft, C. *et al.* Precision mapping of the human *O*-GalNAc glycoproteome through SimpleCell technology. *EMBO J.* **32,** 1478–1488 (2013).

©2013 **Macmillan Publishers Limited. All rights reserved**

LETTER

doi:10.1038/nature12805

Role of Tet1 in erasure of genomic imprinting

Shinpei Yamaguchi[1,2,3], Li Shen[1], Yuting Liu[1,2,3], Damian Sendler[1] & Yi Zhang[1,2,3,4,5]

Genomic imprinting is an allele-specific gene expression system that is important for mammalian development and function[1]. The molecular basis of genomic imprinting is allele-specific DNA methylation[1,2]. Although it is well known that the *de novo* DNA methyltransferases Dnmt3a and Dnmt3b are responsible for the establishment of genomic imprinting[3], how the methylation mark is erased during primordial germ cell (PGC) reprogramming remains unclear. Tet1 is one of the ten-eleven translocation family proteins, which have the capacity to oxidize 5-methylcytosine (5mC)[4–6], specifically expressed in reprogramming PGCs[7]. Here we report that Tet1 has a critical role in the erasure of genomic imprinting. We show that despite their identical genotype, progenies derived from mating between *Tet1* knockout males and wild-type females exhibit a number of variable phenotypes including placental, fetal and postnatal growth defects, and early embryonic lethality. These defects are, at least in part, caused by the dysregulation of imprinted genes, such as *Peg10* and *Peg3*, which exhibit aberrant hypermethylation in the paternal allele of differential methylated regions (DMRs). RNA-seq reveals extensive dysregulation of imprinted genes in the next generation due to paternal loss of Tet1 function. Genome-wide DNA methylation analysis of embryonic day 13.5 PGCs and sperm of *Tet1* knockout mice revealed hypermethylation of DMRs of imprinted genes in sperm, which can be traced back to PGCs. Analysis of the DNA methylation dynamics in reprogramming PGCs indicates that Tet1 functions to wipe out remaining methylation, including imprinted genes, at the late reprogramming stage. Furthermore, we provide evidence supporting the role of Tet1 in the erasure of paternal imprints in the female germ line. Thus, our study establishes a critical function of Tet1 in the erasure of genomic imprinting.

The dynamic expression pattern of Tet1 in PGCs makes it a primary candidate for imprinting erasure[7]. To test this possibility, we generated paternal knockout mice (paternal^{KO}; progenies from *Tet1*$^{-/-}$ male × wild-type female mice) and analysed the effect of paternal Tet1 functional loss on the development of the next generation based on the idea that imprinting defects affect the next generation[1,2]. Unlike the meiotic defects in the oocytes of *Tet1* knockout females[7], *Tet1* knockout testes are morphologically and functionally normal, which makes the generation of paternal^{KO} progeny possible. We found that *Tet1* paternal^{KO} pups show great variability in body size when compared to controls (progeny from *Tet1*$^{+/-}$ male × wild-type female mice) (Fig. 1a, b). In addition, the placental sizes of paternal^{KO} mice are significantly smaller than that of controls (Fig. 1c). Placental size positively correlates with body size ($R = 0.69$) in paternal^{KO} pups, indicating that the growth retardation of the embryos is probably caused by the developmental failure of the placenta, which is already noticeable at embryonic day (E)13.5 and E16.5 (Extended Data Fig. 1a, b). Furthermore, we found that about half of paternal^{KO} pups die within 3 days of birth (Extended Data Fig. 1c). Moreover, about half of survived pups showed marked growth retardation (Fig. 1d, e). This unusually large variation in body size persists to adulthood (Extended Data Fig. 1d).

In addition to growth defects, we found that the litter size of paternal^{KO} mice is also greatly reduced compared to the control crosses (Fig. 2a and Extended Data Fig. 1e). To examine potential embryonic developmental defects of *Tet1* paternal^{KO} pups, we dissected embryos at E13.5 and noticed some absorbed embryos *in utero* (36.4%, $n = 33$ from 4 litters of paternal^{KO}; 2.8%, $n = 36$ from 5 litters of control) (Extended Data Fig. 1f). Although no absorbed embryos were observed at E10.5, about 33.3% ($n = 48$ from 6 litters) of paternal^{KO} embryos exhibited developmental abnormalities, particularly in posterior parts, and no clear somites were observed (Fig. 2b and Extended Data Fig. 1g). Although all of the E9.5 paternal^{KO} embryos analysed were morphologically normal, some

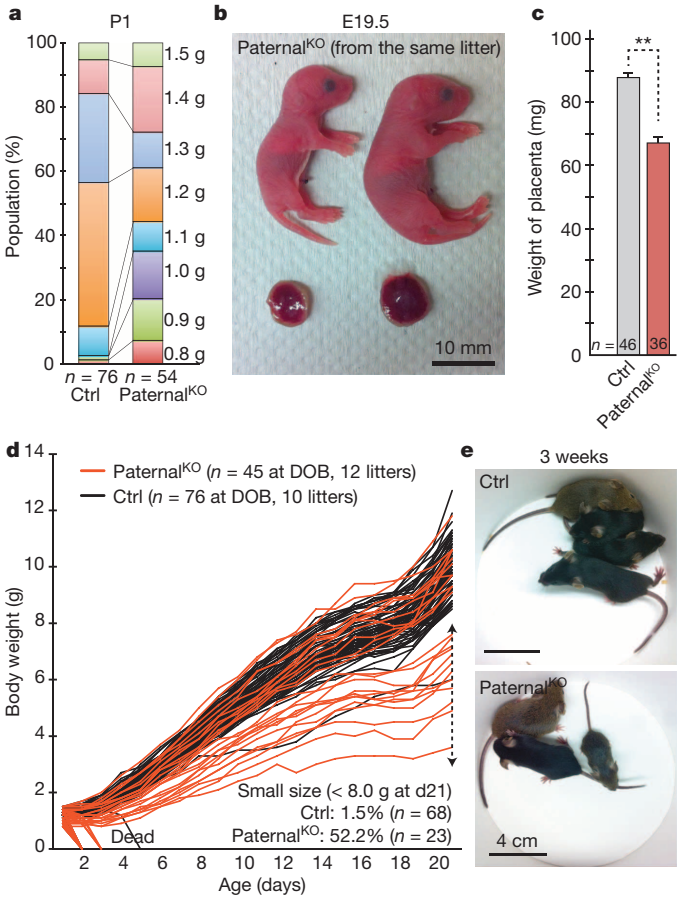


Figure 1 | *Tet1* paternal knockout results in fetal and postnatal growth defects. **a**, Increased variation of body weight at birth in *Tet1* paternal^{KO} pups. Note that pups with weight <1.2 g or >1.3 g account for most of the population in *Tet1* paternal^{KO} mice, whereas most of the control pups are between 1.2–1.3 g at birth. **b**, Representative image of paternal^{KO} pups from the same litter showing big variation in body and placental sizes. Embryos and their placentae were recovered by Caesarean section at the day of birth (E19.5). **c**, Average placental weights at E19.5. Error bars indicate s.e.m. $^{**}P < 0.01$. **d**, Growth curves of individual pups. The lines that drop to zero indicate mice that were found dead at the time indicated. **e**, Representative image of 3-week-old litters from control and paternal^{KO} mice.

[1]Howard Hughes Medical Institute, Boston Children's Hospital, Boston, Massachusetts 02115, USA. [2]Program in Cellular and Molecular Medicine, Boston Children's Hospital, Boston, Massachusetts 02115, USA. [3]Division of Hematology/Oncology, Department of Pediatrics, Boston Children's Hospital, Boston, Massachusetts 02115, USA. [4]Department of Genetics, Harvard Medical School, Boston, Massachusetts 02115, USA. [5]Harvard Stem Cell Institute, WAB-149G, 200 Longwood Avenue, Boston, Massachusetts 02115, USA.

©2013 Macmillan Publishers Limited. All rights reserved

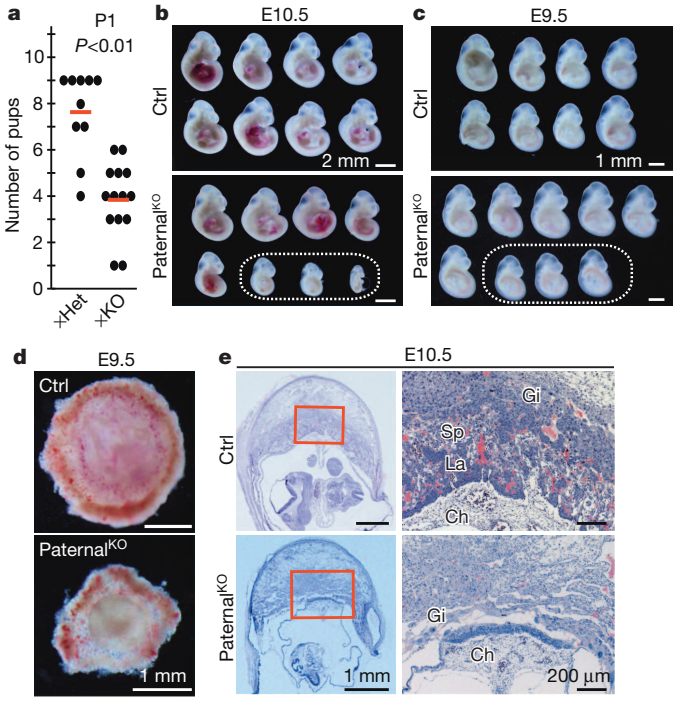


Figure 2 | Early embryonic lethality caused by placental defects in *Tet1* paternal knockout mice. **a**, Mating scores of $Tet1^{+/-}$ male × wild-type female (×Het) and $Tet1^{-/-}$ male × wild-type female (×KO) mice. Black dots indicate the numbers of pups in each litter at the day of birth. Red lines indicate the mean litter size. **b**, E10.5 embryos recovered from a single litter of control and paternal^{KO} mice. The dotted oval indicates morphologically abnormal embryos. **c**, E9.5 embryos recovered from a single litter of control and paternal^{KO} mice. The dotted oval indicates small embryos whose placentae were morphologically abnormal. **d**, Representative images of E9.5 placentae. **e**, Representative images of haematoxylin and eosin staining of E10.5 placentae. Red rectangles indicate the enlarged regions shown in the right panels. Ch, chorionic plate; Gi, trophoblast giant cells; La, labyrinthine zone; Sp, spongioblast.

of them were smaller and had abnormal placentae (34.6%, $n = 26$ from 3 litters) (Fig. 2c, d and Extended Data Fig. 1h). Histological analysis of E9.5 and E10.5 paternal^{KO} placentae revealed a lack of chorionic plate extension and a defect in labyrinthine zone development (Fig. 2e and Extended Data Fig. 1i). Because the frequency of placental abnormality at E9.5 is similar to the frequency of embryo absorption at E13.5, it is likely that the placental defect is one of the major causes of embryonic lethality and reduced litter size of paternal^{KO} embryos. Collectively, the above analyses revealed that loss of Tet1 function in the paternal germ line results in a set of phenotypes that include: (1) early embryonic lethality; (2) placental and embryonic growth defects; and (3) postnatal growth retardation (Extended Data Fig. 1j).

Previous studies have established a critical function of some imprinted genes in embryonic and placental development[1,8]. The phenotypic similarity between *Tet1* paternal^{KO} mice and *Peg10* knockout mice prompted us to examine whether paternal functional loss of Tet1 results in dysregulation of *Peg10* in the paternal^{KO} embryos[9]. Quantitative reverse transcription PCR (qRT–PCR) analysis revealed loss of *Peg10* expression in 33.3% of paternal^{KO} E9.5 embryos ($n = 30$ from 4 litters) (Fig. 3a). In contrast, all of the embryos from controls showed normal *Peg10* expression ($n = 13$ from 2 litters) (data not shown). *Sgce*, a neighbouring imprinted gene of *Peg10*, was simultaneously downregulated in *Peg10*-dysregulated paternal^{KO} embryos (Fig. 3b), indicating co-regulation of these two imprinted genes.

To reveal additional imprinted genes affected by Tet1 deletion, we performed RNA-seq analysis on 10 paternal^{KO} and 3 control E9.5 embryos (Supplementary Table 1). We found that 11–46 out of 81 expressed imprinted genes were dysregulated (fold change (FC) >1.5) in each paternal^{KO} embryo analysed (Fig. 3c and Supplementary Table 2). The dysregulated genes include imprinting gene clusters such as *Mest–Copg2*, *Peg10–Sgce*, *Zim1–Peg3–Usp29*, *Kcnq1ot1–Cdkn1c*, *Ddc–Grb10* and *Impact* (Fig. 3d and Extended Data Fig. 2a, c). Notably, we observed upregulation of maternally expressed genes and downregulation of paternally expressed genes in individual *Tet1* paternal^{KO} embryos (Extended Data Fig. 2b and Supplementary Table 2), indicating that maternalization of the paternal allele of imprinted gene expression pattern is a common phenomenon in *Tet1* paternal^{KO} embryos. In addition to imprinted genes, RNA-seq also identified 1,540 genes for which expression was markedly altered (905 upregulated and 635 downregulated, FC >1.5) in at least two of the ten paternal^{KO} embryos analysed (Extended Data Fig. 3 and Supplementary Table 3). Considering the fact that the paternal^{KO} and half of control embryos have the same heterozygous *Tet1* genotype, many of the gene expression changes are probably caused by either the changes in imprinted gene expression or the consequences of the phenotypes, and not simply an effect of the genotype.

To confirm that dysregulation of imprinted genes is indeed linked to perturbation of DNA methylation, we performed conventional bisulphite sequencing (BS-seq). Whereas the *Peg10* DMR was methylated to ~50% in controls, the DMR is almost fully methylated in *Peg10*-dysregulated *Tet1* paternal^{KO} embryos (Fig. 3e). These data are consistent with previous findings that *Peg10* and *Sgce* are specifically expressed from the unmethylated paternal allele and are silenced at the methylated maternal allele[10]. Thus, our data support the notion that hypermethylation of the paternal allele leads to silencing of *Peg10*, which causes early embryonic lethality of paternal^{KO} embryos through placental malfunction. Similar analysis also revealed hypermethylation of the *Air–Igf2r* cluster and *Impact* loci in *Air–Igf2r*- and *Impact*-dysregulated paternal^{KO} embryos, respectively (Extended Data Fig. 4a–d), further confirming the relationship between DMR hypermethylation and altered imprinted gene expression in *Tet1* paternal^{KO} embryos.

Normal expression of imprinted genes is critical for placental development and fetal growth[8]. To examine whether the growth defects observed in paternal^{KO} embryos are caused by imprinting defects in the placenta, we analysed gene expression in E19.5 paternal^{KO} placentae. qRT–PCR analysis showed that several imprinted genes are dysregulated in smaller placentae of paternal^{KO} mice (Extended Data Fig. 4e, numbers 4–7). The expression level of *Igf2r* in placentae of paternal^{KO} mice numbers 4–6 is about twice as much as that in control, indicating biallelic expression. Similarly, *Peg3*, *Usp29* and *Zim1* are concurrently dysregulated in the placenta of paternal^{KO} number 7. Furthermore, BS-seq analysis revealed that *Peg3* DMR is hypermethylated in *Peg3*-negative placentae of paternal^{KO} mice (Extended Data Fig. 4f). These data indicate that imprinting of the paternal allele at these loci is maternalized, which probably accounts for the placental developmental defects.

The maternalization in imprinted gene expression and DMR methylation of the paternal allele in paternal^{KO} embryos and placentae prompted us to ask whether the aberrant DNA methylation pattern originates from the sperm genome of *Tet1* knockout males. To this end, we performed BS-seq analysis, which revealed that part of the *Peg10* DMR remains methylated in *Tet1* knockout sperm, whereas the same region is nearly completely demethylated in the control sperm (Extended Data Fig. 4g).

To determine whether hypermethylation of imprinted DMRs is a general phenomenon in the *Tet1* knockout germ line, we performed global DNA methylation analysis of E13.5 male PGCs and sperm by reduced representative bisulphite sequencing (RRBS) (Extended Data Fig. 5a, b and Supplementary Table 4). Consistent with our previous report[7], no global change in DNA methylation levels was observed in E13.5 PGCs or sperm (Fig. 4a, b). However, the analysis identified 2,608 (6.8% of commonly covered sites (that is, sites having enough reads of RRBS analysis in both E13.5 PGCs and sperm)) and 422 (1.1% of commonly covered sites) hypermethylated sites in *Tet1* knockout PGCs and sperm, respectively (Supplementary Tables 5 and 6). Among the 422 hypermethylated sites in *Tet1* knockout sperm, 348 (82.5%) of

©2013 Macmillan Publishers Limited. All rights reserved

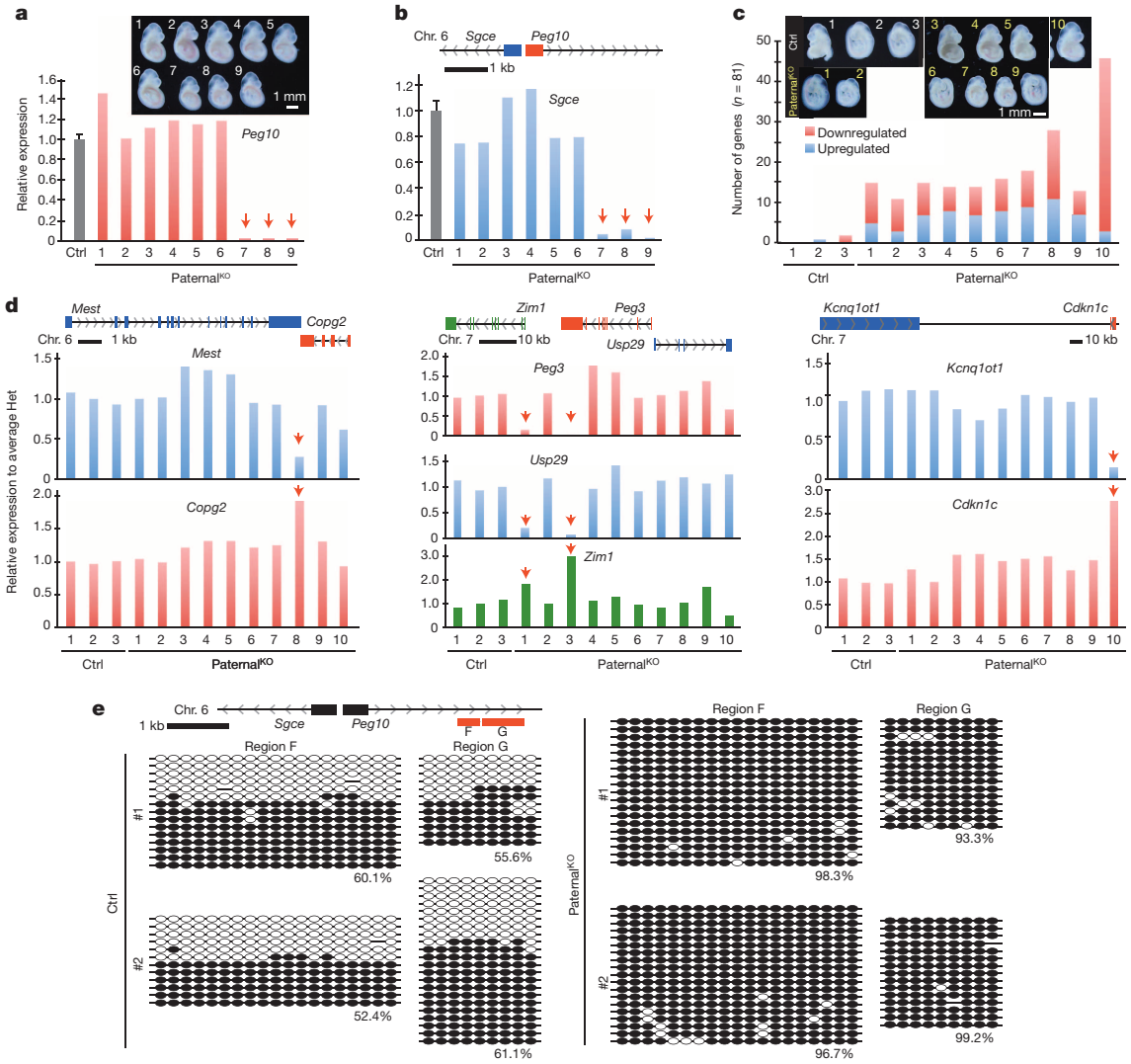


Figure 3 | *Tet1* paternal knockout embryos and placentae exhibit imprinting defects. **a**, **b**, qRT–PCR analysis of *Peg10* (**a**) and *Sgce* (**b**) of E9.5 embryos from a single litter. The pup number corresponds to that in the inserted image in panel **a**. Arrows indicate the samples showing marked reduction in *Peg10* and *Sgce* expression. The average value of control embryos ($n = 13$) is set as 1. Error bars indicate s.e.m. The genomic location of *Peg10* and *Sgce* genes is indicated at the top of panel **b**. **c**, Number of up- and downregulated imprinted genes in each of the paternal^{KO} embryos compared to the average FPKM (fragments per kilobase of exon per million fragments mapped) value of control embryos analysed by RNA-seq (cutoff FC >1.5). A total of 81 autosomal imprinted genes expressed in embryos (FPKM >0.4) was used in this analysis. The pup number corresponds to the inserted images. **d**, Relative expression level of imprinted genes at E9.5 embryos analysed by RNA-seq. Arrows indicate the samples showing marked changes in expression levels. The average FPKM value of three control embryos is set as 1. The genomic locations of each gene are indicated at the top of the diagrams. The pup number corresponds to the inserted images in panel **c**. **e**, Bisulphite sequencing analysis of *Peg10* DMR of E9.5 embryos. The analysed region is indicated at the top of the diagram. Each CpG is represented by a circle with methylation and non-methylation represented by open and filled circles, respectively. The percentages of DNA methylation are indicated.

the sites already exhibited increased DNA methylation in E13.5 male PGCs, and 90 of them exhibited a more than 10% increase (Fig. 4c, Extended Data Fig. 5c and Supplementary Table 7). Notably, a number of imprinted gene loci, including 7 out of 12 commonly covered known germline DMRs, were significantly enriched among these common hypermethylated sites (Fig. 4d, Extended Data Figs 6 and 7, and Supplementary Table 8). This indicates that most of the hypermethylation in the paternal^{KO} embryos can be traced back to sperm and E13.5 PGCs, and clearly demonstrates that hypermethylation in *Tet1* knockout sperm is mainly caused by defective PGC reprogramming. Notably, hypermethylation of meiotic genes was only observed in PGCs, not in sperm (Extended Data Fig. 6a, c). This indicates that passive demethylation and/or other Tet proteins may compensate for the Tet1 deficiency during spermatogenesis, which may explain why the meiotic phenotype is only observed in *Tet1*-null females[7]. Consistent with the Tet1 expression dynamics in PGCs and its capacity to oxidize 5mC to 5hmC, temporal enrichment of 5hmC in DMRs of *Kcnq1ot1*, *Peg3*, *Peg10* and *Igf2r* has been previously reported in reprogramming PGCs[11]. The 5hmC in PGCs generated by Tet1 has probably been diluted via a replication-dependent manner[12,13].

To understand why only a limited number of sites were hypermethylated in response to Tet1 depletion, we analysed the methylation dynamics of these hypermethylated sites during PGC reprogramming. Previous studies have established that PGC demethylation takes place in two stages[14]. The first wave of demethylation completes before E9.5 as more than 70% of CpGs have already been demethylated in E9.5 PGCs. Consistently, most of the RRBS-covered sites have already been demethylated at the early phase of control PGCs, as the average methylation level in E9.5 PGCs dropped to 6.4% (Fig. 4e). Because Tet1 is not upregulated until after E9.5, the first wave of demethylation is Tet1-independent[7,12]. In contrast, Tet1-affected sites remain to be methylated even in E10.5 and E11.5 PGCs, indicating that Tet1 targets are enriched in the

©2013 Macmillan Publishers Limited. All rights reserved

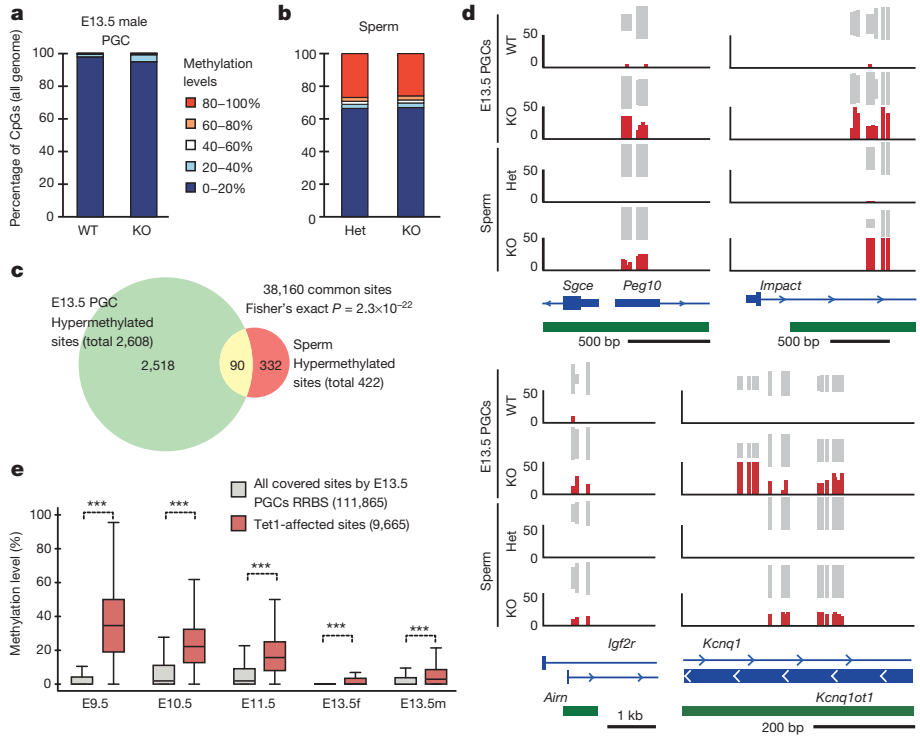


Figure 4 | Locus-specific hypermethylation in *Tet1* knockout PGCs and sperm. **a**, **b**, Genome methylation state of E13.5 PGCs (**a**) and sperm (**b**). **c**, Venn diagram showing the overlap between hypermethylated sites (increased >10%) in *Tet1* knockout PGCs and sperm. **d**, Representative DNA methylation profiles of imprinted genes in E13.5 male PGCs and sperm analysed by RRBS. Vertical grey lines represent the sequence read depth for each cytosine scored, and 30 reads are shown at the most. The vertical red lines represent percentage of methylation for each cytosine scored, which range from 0% to 50%. For each gene, RefSeq exon organization (blue) and location of CGIs (green) are shown at the bottom. **e**, Methylation dynamics of Tet1-affected sites. Methylation level of hypermethylated sites in *Tet1* knockout E13.5 PGCs are analysed based on published data sets[14]. Note that methylation levels of Tet1-affected sites are significantly higher in E9.5 to E11.5 compared to all covered sites. Middle line in the coloured space indicates the median, edges the 25th/75th percentiles, and whiskers the 2.5th/97.5th percentiles. $***P < 1.0 \times 10^{-15}$.

late-demethylated group[14,15] (Fig. 4e and Extended Data Fig. 8a). Indeed, more than 40% of late-demethylated promoters identified previously[14] exhibited hypermethylation in *Tet1* knockout PGCs ($P < 1.0 \times 10^{-15}$, Extended Data Fig. 8b). These data indicate that Tet1 has a major role in the second wave of demethylation in PGCs. Given that these late-demethylated regions affected by Tet1 do not have a consensus DNA sequence motif (data not shown), we believe that instead of being specifically targeted, Tet1 functions to remove the remaining methylation that escaped the first wave of demethylation, including imprinted genes. How the 'late-demethylated regions' are protected from the first wave of DNA demethylation remains to be determined.

During the preparation of this manuscript, one study (ref. 16) reported that some progenies from $Tet1^{-/-}Tet2^{-/-}$ double knockout males crossed with wild-type or $Tet1^{+/-}Tet2^{+/-}$ double-heterozygous females exhibited hypermethylation and dysregulation in a few imprinted genes[16]. To confirm the role of Tet1 in imprinting erasure further, we used the same *Tet1* knockout strain used by ref. 17 and demonstrated similar paternal^{KO} defects (Extended Data Fig. 9), indicating that Tet2 cannot compensate for Tet1's function in imprinting erasure (Supplementary Discussion).

We next asked whether Tet1 also has a role in imprinting erasure in the female germ line. To this end, we generated Tet1 maternal knockout (maternal^{KO}) mice by crossing *Tet1* knockout females with wild-type males. We observed lethality in about 25% of maternal^{KO} embryos with relatively normal placenta (Extended Data Fig. 10a, b). The placentae of the survived embryos were significantly larger compared to that of the control although they had a comparable body size (Extended Data Fig. 10c, d). qRT–PCR analysis revealed silencing of paternally imprinted genes such as *Meg3/Dlk1* and *Mirg* in all of the placentae of dead embryos (Extended Data Fig. 10e). Additionally, *Rasgrf1* was also upregulated in some of the maternal^{KO} placentae (for example, numbers 6, 10 and 11). Consistent with abnormal expression of *Meg3/Dlk1*, *Mirg* and *Rasgrf1*, hypermethylation of both intergenic (IG)-DMR and *Rasgrf1* was observed in abnormal placentae (Extended Data Fig. 10f, g). These results indicate that Tet1 is involved in imprinting erasure of not only maternal DMRs in the male germ line, but also paternal DMRs in the female germ line.

Collectively, our studies clearly demonstrate that Tet1 has an important role in the erasure of genomic imprinting. Although some factors, such as *Aid* and *Tdg*, have been proposed to have a role in imprinting erasure, evidence demonstrating a loss of functional effect at the next generation is still missing[18,19]. As far as we know, our current study is the first that reports a factor critical for imprinting erasure with physiological evidence. Consistent with our study, another study (ref. 20) also revealed that Tet1-mediated oxidation is essential for the erasure of genomic imprinting in cell fusion experiments[20]. The phenotypic variation observed in each *Tet1* paternal^{KO} embryo can be explained by the variable DMR methylation remaining in each *Tet1* knockout sperm (Extended Data Fig. 11 and Supplementary Discussion). It is well known that abnormalities in genomic imprinting can cause various human diseases[1]. The conservation of Tet1 function in humans and mice raises the possibility that human Tet1 may also have an important role in imprinting erasure (Supplementary Discussion). Future studies should reveal whether dysfunction of Tet1 contributes to growth restriction or other imprinting-related syndromes.

METHODS SUMMARY

Animals. *Tet1* gene-trap mice were generated as previously described[7]. *Tet1* paternal^{KO} and control mice were generated by mating littermate males of Tet1-homozygotes or Tet1-heterozygotes with C57BL/6J females.

qRT–PCR and RNA-seq. For expression analysis, cDNAs were synthesized from total RNA by using Superscript III First-Strand synthesis (Invitrogen) with random

©2013 Macmillan Publishers Limited. All rights reserved

primer sets. Quantitative PCR (qPCR) reactions were performed with gene-specific primer sets (Supplementary Table 9). Relative expression levels were calculated on the basis of comparative Ct values after normalizing with *Gapdh*. For RNA-seq, the libraries prepared from purified mRNA were sequenced on an Illumina HISEQ 2500. RNA-seq data analysis was performed with Tophat and Cufflinks using the UCSC mm9 annotation.

Bisulphite sequencing and RRBS. BS-seq was performed using the EZ DNA methylation Gold kit (Zymo Research) following the manufacturer's instructions. Primers for BS-seq are listed in Supplementary Table 9 (refs 21, 22). For RRBS, the libraries were generated from MspI-digested genomic DNA and sequenced on an Illumina Hiseq 2500 as previously described, with some modifications[23]. All obtained reads were trimmed and mapped against the mouse genome (mm9 build) with Bismark v0.7.12, and the methylation call for every single CpG was extracted by bismark methylation extractor script. The CpGs covered by at least 8 reads were analysed. On the basis of the assumption that there should not be any hypomethylated sites in *Tet1* knockout PGCs, the estimated empirical false discovery rate (FDR) of hypomethylated sites in *Tet1* knockout PGCs at a 10% methylation change cutoff is 0.054. At a 20% methylation change cutoff, the FDR is 0.032.

Online Content Any additional Methods, Extended Data display items and Source Data are available in the online version of the paper; references unique to these sections appear only in the online paper.

Received 28 May; accepted 31 October 2013.
Published online 1 December 2013.

1. Bartolomei, M. S. & Ferguson-Smith, A. C. Mammalian genomic imprinting. *Cold Spring Harb. Perspect. Biol.* **3,** a002592 (2011).
2. Li, Y. & Sasaki, H. Genomic imprinting in mammals: its life cycle, molecular mechanisms and reprogramming. *Cell Res.* **21,** 466–473 (2011).
3. Kaneda, M. *et al.* Essential role for *de novo* DNA methyltransferase Dnmt3a in paternal and maternal imprinting. *Nature* **429,** 900–903 (2004).
4. Ito, S. *et al.* Role of Tet proteins in 5mC to 5hmC conversion, ES-cell self-renewal and inner cell mass specification. *Nature* **466,** 1129–1133 (2010).
5. Tahiliani, M. *et al.* Conversion of 5-methylcytosine to 5-hydroxymethylcytosine in mammalian DNA by MLL partner TET1. *Science* **324,** 930–935 (2009).
6. Shen, L. & Zhang, Y. 5-Hydroxymethylcytosine: generation, fate, and genomic distribution. *Curr. Opin. Cell Biol.* **25,** 289–296 (2013).
7. Yamaguchi, S. *et al.* Tet1 controls meiosis by regulating meiotic gene expression. *Nature* **492,** 443–447 (2012).
8. Nelissen, E. C. M., van Montfoort, A. P. A., Dumoulin, J. C. M. & Evers, J. L. H. Epigenetics and the placenta. *Hum. Reprod. Update* **17,** 397–417 (2011).
9. Ono, R. *et al.* Deletion of *Peg10*, an imprinted gene acquired from a retrotransposon, causes early embryonic lethality. *Nature Genet.* **38,** 101–106 (2006).
10. Ono, R. *et al.* Identification of a large novel imprinted gene cluster on mouse proximal chromosome 6. *Genome Res.* **13,** 1696–1705 (2003).
11. Hackett, J. A. *et al.* Germline DNA demethylation dynamics and imprint erasure through 5-hydroxymethylcytosine. *Science* **339,** 448–452 (2013).
12. Kagiwada, S., Kurimoto, K., Hirota, T., Yamaji, M. & Saitou, M. Replication-coupled passive DNA demethylation for the erasure of genome imprints in mice. *EMBO J.* **32,** 340–353 (2013).
13. Yamaguchi, S. *et al.* Dynamics of 5-methylcytosine and 5-hydroxymethylcytosine during germ cell reprogramming. *Cell Res.* **23,** 329–339 (2013).
14. Seisenberger, S. *et al.* The dynamics of genome-wide DNA methylation reprogramming in mouse primordial germ cells. *Mol. Cell* **48,** 849–862 (2012).
15. Kobayashi, H. *et al.* High-resolution DNA methylome analysis of primordial germ cells identifies gender-specific reprogramming in mice. *Genome Res.* **23,** 616–662 (2013).
16. Dawlaty, M. M. *et al.* Combined deficiency of Tet1 and Tet2 causes epigenetic abnormalities but is compatible with postnatal development. *Dev. Cell* **24,** 310–323 (2013).
17. Dawlaty, M. M. *et al.* Tet1 is dispensable for maintaining pluripotency and its loss is compatible with embryonic and postnatal development. *Cell Stem Cell* **9,** 166–175 (2011).
18. Cortellino, S. *et al.* Thymine DNA glycosylase is essential for active DNA demethylation by linked deamination-base excision repair. *Cell* **146,** 67–79 (2011).
19. Popp, C. *et al.* Genome-wide erasure of DNA methylation in mouse primordial germ cells is affected by AID deficiency. *Nature* **463,** 1101–1105 (2010).
20. Piccolo, F. M. *et al.* Different roles for Tet1 and Tet2 proteins in reprogramming-mediated erasure of imprints induced by EGC fusion. *Mol. Cell* **49,** 1023–1033 (2013).
21. Kobayashi, H. *et al.* Bisulfite sequencing and dinucleotide content analysis of 15 imprinted mouse differentially methylated regions (DMRs): paternally methylated DMRs contain less CpGs than maternally methylated DMRs. *Cytogenet. Genome Res.* **113,** 130–137 (2006).
22. Tomizawa, S.-i. *et al.* Dynamic stage-specific changes in imprinted differentially methylated regions during early mammalian development and prevalence of non-CpG methylation in oocytes. *Development* **138,** 811–820 (2011).
23. Gu, H. *et al.* Preparation of reduced representation bisulfite sequencing libraries for genome-scale DNA methylation profiling. *Nature Protocols* **6,** 468–481 (2011).

Supplementary Information is available in the online version of the paper.

Acknowledgements We thank W. Jiang for help with FACS sorting of PGCs; A. Inoue, S. Matoba and D. Cai for critical reading of the manuscript. This project is supported by NIH U01DK089565 (to Y.Z.). S.Y. is supported by a postdoctoral fellowship from the Japan Society for the Promotion of Science (JSPS). Y.Z. is an investigator of the Howard Hughes Medical Institute.

Author Contributions S.Y. and Y.Z. conceived the project, designed the experiments and wrote the manuscript; S.Y., L.S., Y.L. and D.S. performed experiments and analysed the data.

Author Information The accession number for the RNA-seq and RRBS data presented in this study is available from the Gene Expression Omnibus (GEO) database under accession GSE49764. Reprints and permissions information is available at www.nature.com/reprints. The authors declare no competing financial interests. Readers are welcome to comment on the online version of the paper. Correspondence and requests for materials should be addressed to Y.Z. (yzhang@genetics.med.harvard.edu).

©2013 Macmillan Publishers Limited. All rights reserved

METHODS

Mice. All animal studies were performed in accordance with guidelines of the Institutional Animal Care and Use Committee at Harvard Medical School. The *Tet1* knockout mouse strain (B6;129S4-Tet1$^{tm1.1Jae}$/J) was purchased from Jackson Laboratory[17]. All male mice were mated with C57BL/6J female and the mating is timed in the way that appearance of vaginal plug at noon is defined as embryonic day (E) 0.5. E19.5 embryos and placentae were collected by dissecting pregnant females with progesterone injection at E17.5 and E18.5. All data presented were generated by using three or four separate mating pairs as biological replicates.

Histology. Embryos and placentae in the uterus were fixed in 4% paraformaldehyde, dehydrated in ethanol, and embedded in paraffin. For histological analysis, sections (5 μm) were stained with haematoxylin and eosin.

RNA isolation and qRT–PCR. Dissected embryos and placentae were homogenized with a pestle. Total RNAs were isolated with TRizol (Life technologies), and cDNAs were generated with random primer sets and Superscript III first-strand synthesis system (Invitrogen). Real-time qPCR reactions were performed on an ABI ViiA7 sequence detection system (Applied Biosystems) using SYBR green (Applied Biosystems). Relative gene expression levels were calculated using comparative Ct values, in which Ct is the cycle threshold number, and normalized to *Gapdh*. qRT–PCR primers are listed in Supplementary Table 9.

PGC purification for RRBS. E13.5 male PGCs were purified as described previously[7]. Briefly, the transgenic mouse line containing the GOF18DPE-EGFP [Tg(Pou5f1-EGFP)] transgene was purchased from Jackson Laboratory. E13.5 genital ridge cells were dissociated with 0.05% trypsin/EDTA treatment with pipetting. After washing with phosphate buffer medium (PB1)/BSA solution, tissues were incubated in hyaluronidase, washed and then re-suspended in PBS. Germ cells were purified based on the expression of GFP using FACS Aria II flow cytometry (BD Bioscience), and stored in −80 °C until use. Two biological replicates for *Tet1* knockout and wild-type PGCs were combined and split into two as the technical replicates.

RNA-seq library preparation and data analysis. Total RNA was purified with an RNeasy Mini kit (Qiagen), in which an on-column DNase treatment was included. 500 ng of purified RNA was then subjected to mRNA isolation and library preparation using a NEBNext Ultra RNA Directional Library Prep kit for Illumina with the Poly(A) mRNA Magnetic Isolation Module (NEB) following manufacturer's instructions. Libraries were pooled and sequenced on an Illumina HISEQ 2500 (single-end, 50 bp). RNA-seq data analysis was performed with Tophat and Cufflinks using the UCSC mm9 annotation[24]. Functional annotation of the dysregulated genes was performed with DAVID[25].

Bisulphite sequencing and RRBS. BS-seq was performed using the EZ DNA methylation Gold kit (Zymo Research) following the manufacturer's instruction. Primers for BS-seq are listed in Supplementary Table 9 (refs 21, 22). For RRBS, the libraries were generated essentially as previously described[23,26], with some modifications. Briefly, DNA was digested with MspI (NEB), and then subjected to end repair, and ligation of methylated custom adaptors (forward 5′-ACACTCTTTCCCTACACGACGCTCTTCCGATC*T-3′; reverse 5′-/5Phos/GATCGGAAGAGCACACGTCTGAACTCCAGTC-3′, where the asterisk indicates phosphorothioate bond) with a NEBNext Ultra DNA Library Prep kit from Illumina (NEB). Size selection was conducted by purifying the adaptor-ligated DNA twice with 1.5× SPRIselect beads (Beckman Coulter). Size-selected libraries were treated with sodium bisulphite using the EpiTect Fast Bisulphite Conversion kit (Qiagen). After clean-up, the optimal, minimum PCR cycle numbers required to generate the final libraries were determined by qPCR using KAPA 2G Robust HotStart ReadyMix (KAPA) with 0.3× SYBR I. Final libraries were generated by scaled-up PCR reactions (without SYBR I) using the cycles determined above with barcoded primers from the NEBNext Multiplex Oligos kit (NEB), and purified with 1.2× SPRIselect beads. Libraries were pooled and sequenced on an Illumina Hiseq 2500 (single-end, 50 bp).

Adaptor trimming for raw reads from each sample was performed using Trim Galore (Babraham Bioinformatics), and the data quality was examined using FastQC (Babraham Bioinformatics). The trimmed reads were mapped against the mouse genome (mm9 build) with Bismark v0.7.12 (ref. 27), and the methylation call for every single C was extracted by bismark methylation extractor script. All programs were performed with default setting. We only keep the CpGs that were covered by at least 8 reads (common 8x CpGs). The methylation pattern was visualized by Integrative Genomics Viewer (IGV)[7]. For 100-bp tiles and the promoters, reads for the CpGs that were covered at least eight times in each sample were pooled and used to estimate the methylation level by taking the number of reads reporting a C, divided by the total number of reads reporting a C or T. We kept the 100-bp sites and the promoters with at least 2 and 4 common 8× CpGs for subsequent analyses. Repetitive regions were masked before DMR calling. More than 10% methylation level changes were required to be classified as changed sites or promoters. On the basis of the assumption that no hypomethylated sites in *Tet1* knockout PGCs should appear, estimated empirical false discovery rate (FDR) by the number of hypomethylated sites in *Tet1* knockout PGCs was 0.054. At a 20% methylation change cutoff, the FDR is 0.032. Annotation of CpG islands was obtained from a previous report based on pull-down experiments[28]. Promoters were defined as the region −1.5 kb to +1.5 kb of the transcription start site as annotated in Refseq genes. Repeat annotations were extracted from the UCSC Table Browser Repeat-Masker track (mm9 build). DMRs were functionally characterized by GREAT[29] using the Mouse Genome Informatics (MGI) Phenotype ontology[30]. Publically available data sets for whole-genome bisulphite sequencing (WGBS) data sets in PGCs[14,15] were included in this analysis where indicated. For WGBS data analyses, all the informative CpGs were used, and the methylation level in a region was estimated by taking the number of reads reporting a C, divided by the total number of reads reporting a C or T. We required that there were at least 20 methylated or unmethylated cytosine observations in the region for each sample.

24. Trapnell, C. *et al.* Differential gene and transcript expression analysis of RNA-seq experiments with TopHat and Cufflinks. *Nature Protocols* **7,** 562–578 (2012).
25. Huang, D. W., Sherman, B. T. & Lempicki, R. A. Systematic and integrative analysis of large gene lists using DAVID bioinformatics resources. *Nature Protocols* **4,** 44–57 (2009).
26. Boyle, P. *et al.* Gel-free multiplexed reduced representation bisulfite sequencing for large-scale DNA methylation profiling. *Genome Biol.* **13,** R92 (2012).
27. Krueger, F. & Andrews, S. R. Bismark: a flexible aligner and methylation caller for Bisulfite-Seq applications. *Bioinformatics* **27,** 1571–1572 (2011).
28. Illingworth, R. S. *et al.* Orphan CpG islands identify numerous conserved promoters in the mammalian genome. *PLoS Genet.* **6,** e1001134 (2010).
29. McLean, C. Y. *et al.* GREAT improves functional interpretation of cis-regulatory regions. *Nature Biotechnol.* **28,** 495–501 (2010).
30. Blake, J. A. *et al.* The mouse genome database genotypes:phenotypes. *Nucleic Acids Res.* **37,** D712–D719 (2009).

©2013 Macmillan Publishers Limited. All rights reserved

LETTER

doi:10.1038/nature12719

High-resolution Xist binding maps reveal two-step spreading during X-chromosome inactivation

Matthew D. Simon[1,2]*, Stefan F. Pinter[1,3]*, Rui Fang[2]*, Kavitha Sarma[1,3], Michael Rutenberg-Schoenberg[2], Sarah K. Bowman[1], Barry A. Kesner[1,3], Verena K. Maier[1,3], Robert E. Kingston[1] & Jeannie T. Lee[1,3]

The Xist long noncoding RNA (lncRNA) is essential for X-chromosome inactivation (XCI), the process by which mammals compensate for unequal numbers of sex chromosomes[1–3]. During XCI, Xist coats the future inactive X chromosome (Xi)[4] and recruits Polycomb repressive complex 2 (PRC2) to the X-inactivation centre (*Xic*)[5]. How Xist spreads silencing on a 150-megabases scale is unclear. Here we generate high-resolution maps of Xist binding on the X chromosome across a developmental time course using CHART-seq. In female cells undergoing XCI *de novo*, Xist follows a two-step mechanism, initially targeting gene-rich islands before spreading to intervening gene-poor domains. Xist is depleted from genes that escape XCI but may concentrate near escapee boundaries. Xist binding is linearly proportional to PRC2 density and H3 lysine 27 trimethylation (H3K27me3), indicating co-migration of Xist and PRC2. Interestingly, when Xist is acutely stripped off from the Xi in post-XCI cells, Xist recovers quickly within both gene-rich and gene-poor domains on a timescale of hours instead of days, indicating a previously primed Xi chromatin state. We conclude that Xist spreading takes distinct stage-specific forms. During initial establishment, Xist follows a two-step mechanism, but during maintenance, Xist spreads rapidly to both gene-rich and gene-poor regions.

Xist RNA is a prototype lncRNA with global epigenetic function[1–3,6]. The initiation of XCI depends on Xist[7] and loading of the Xist–PRC2 complex at a nucleation site within the *Xic*[8]. Thereafter, Xist RNA forms a "cloud" over the X-chromosome, signalling the initiation of chromosome-wide silencing[4]. Concurrently, PRC2 accumulates broadly along the X-chromosome[9]. Although Xist RNA coats the Xi at cytological resolution, whether and where Xist binds at molecular resolution remains unknown. In one model, Xist targets PRC2 to the *Xic*, but outward spreading of PRC2 does not involve Xist. Alternatively, both nucleation and spread involve Xist, in which case Xist and PRC2 would co-migrate at a molecular scale.

We mapped genome-wide binding locations of Xist RNA by performing CHART-seq (capture hybridization analysis of RNA targets with deep sequencing), a technique to localize lncRNAs on chromatin using complementary oligonucleotides to enrich for DNA targets[10] (Extended Data Fig. 1a). We designed a cocktail of 11 complementary oligonucleotides for Xist CHART based on conserved or functional Xist domains[7,11–13] and RNase H mapping for accessibility (Extended Data Fig. 1b, c and Extended Data Table 1). Allele-specific CHART-seq was performed at four developmental stages (Extended Data Fig. 1d): before XCI in undifferentiated female mouse embryonic stem (ES) cells (d0; <1% of nuclei XCI positive, showing an Xist cloud or H3K27me3 focus), early-XCI (d3; <10% positive), mid-XCI (d7; 40–50% positive), and post-XCI (mouse embryonic fibroblast (MEF) clone, >95% positive). About 600,000 sequence polymorphisms between the *Mus musculus* (mus) and *Mus castaneus* (cas) X-chromosomes enabled ~35% allele-specific mapping to Xi and Xa (active X chromosome), respectively[9]. Disabling the mus *Tsix* allele in the female ES cells ensured that the mus X will be Xi[14]. We validated results by comparing two independent capture oligonucleotide sub-mixtures and an alternative 40-oligonucleotide cocktail targeting across the length of Xist (Extended Data Fig. 2a–e and Extended Data Table 1). Regions with significant Xist enrichment localized almost exclusively to Xi (>99% X-linked, $P < 0.001$; >90% Xi-skewed, $P < 0.05$, Extended Data Fig. 2f, g, i). On autosomes, binding was minimal and of questionable significance. Enriched segments were not complementary to capture-oligonucleotides and showed minimal enrichment on Xa of d0, d3, d7 and MEF cells. Enrichment was not observed using sense control oligonucleotides (Extended Data Fig. 2a, c). These experiments excluded artefactual enrichment, validating Xist CHART-seq specificity.

The dominant CHART peak was in *Xist* exon 1 and was specific to Xi (Fig. 1a). A developmental time course demonstrated a progression in Xist density, with enriched segments increasing from <0.1% coverage of the X in pre-XCI cells to approximately 20% in early- and mid-XCI, and approximately 54% in post-XCI cells (Fig. 1b, c and Extended Data 2h). Thus, Xist RNA not only forms a cytological cloud but also binds broad swaths of the Xi at molecular resolution. Xist could either spread uniformly along the Xi or target specific regions. Intriguingly, in cells undergoing XCI (d3, d7), Xist preferentially targeted multi-megabase domains (Fig. 1c). In post-XCI MEFs, Xist spread into intervening gene-poor regions throughout the Xi. The d3 and d7 patterns were more similar to each other than to MEF patterns (Fig. 1d, e and Extended Data Fig. 3a). Furthermore, comparative analysis identified MEF-specific domains not found during XCI (Fig. 1e). Despite heterogeneity in the onset of XCI in the *ex vivo* ES differentiation system, the highly similar d3 and d7 distributions show that Xist targets gene-rich domains first. Extension of ES differentiation to d10 showed statistically significant filling in of gene-poor domains (Extended Data Fig. 3b, c), although not to the extent observed in somatic cells (MEFs). We infer that full spreading across Xi may only be achieved later in development, once differentiation into somatic lineages occurs. Thus, during *de novo* XCI in the embryo, Xist probably follows a two-step pattern of spreading, first targeting gene-rich clusters (hereafter, 'early' domains) and eventually spreading to intervening gene-poor regions ('late' domains). Throughout the process, gene bodies of escapees[15,16] were depleted of Xist, but occasionally demonstrated Xist enrichment in flanking regions (Fig. 1f and Extended Data Fig. 4), indicating boundaries that sequester Xist and prevent spreading into neighbouring privileged escapee loci.

We investigated what might target Xist to early domains by comparisons with various chromatin features (see Methods)[9,17–22]. Interestingly, Xist is more likely to target genes in regions of active chromatin in ES cells. Allele-specific RNA sequencing analysis demonstrated the preference of Xist for genes that are active (for example, on the Xa and in d0 and d7 cells) and showed skewed expression in d7 ES cells and in MEFs

[1]Department of Molecular Biology, Massachusetts General Hospital, and Department of Genetics, Harvard Medical School, Boston, Massachusetts 02114, USA. [2]Department of Molecular Biophysics and Biochemistry, and Chemical Biology Institute, Yale University, West Haven, Connecticut 06516, USA. [3]Howard Hughes Medical Institute, Massachusetts General Hospital, Harvard Medical School, Boston, Massachusetts 02114, USA.

*These authors contributed equally to this work.

©2013 Macmillan Publishers Limited. All rights reserved

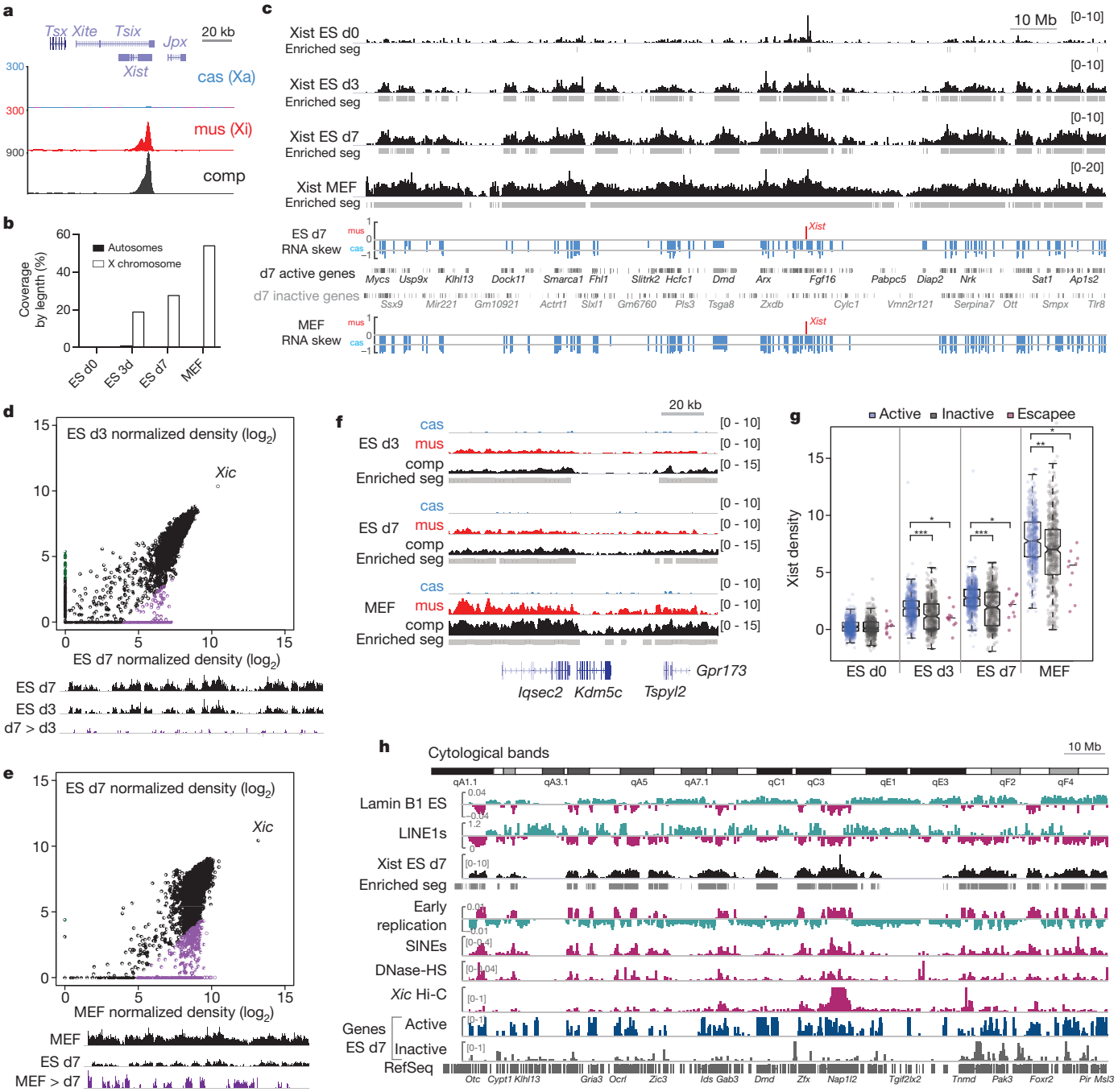


Figure 1 | CHART-seq reveals a two-step mechanism of Xist spreading during *de novo* XCI. **a**, Xist RNA is enriched on Xi. Normalized read densities displayed in mus, cas and composite (comp) tracks. **b**, Coverage of enriched segments on the X chromosome and the autosomes. **c**, Xist coverage at indicated time points relative to gene silencing. Enriched segments shown beneath in grey. Brackets, *y*-axis scale of normalized Xist density as in all figures. Xist peaks at d0 have less amplitude and density, but reflect d3 and d7 patterns, and are Xi-enriched (Extended Data Fig. 2f), consistent with initial Xist spreading to local regions, suggesting initial differentiation in a subfraction of cells. RNA-seq of d7 and MEF is shown below. Skewed allelic expression consistent with Xi-silencing (value −0.5 = threefold expression difference between Xi and Xa). **d**, **e**, Xist CHART signals (40-kilobase bins) from d7 correlate with d3 (**d**) and MEF (**e**) (see Extended Data Fig. 3). Regions showing more than tenfold differences after normalization are coloured purple and displayed on the X chromosome in screenshot panels below. **f**, Depletion of Xist at a representative escapee. **g**, Xist preferentially targets genes in active chromatin (H3K4me3-marked on d7). Xist densities shown for gene bodies of active ($n = 532$), inactive ($n = 475$) and escapee genes ($n = 10$). Medians are indicated. Individual data points overlaid on boxplot; error bars, 1.5-fold interquartile range. $^{*}P < 0.05$, $^{**}P < 10^{-8}$, $^{***}P < 2.2 \times 10^{-16}$, Mann–Whitney *U* tests. **h**, Xist RNA distribution from d7 cells relative to 200-kb binned chromatin features (*y*-scale is fraction of binned sequence unless otherwise indicated): SINEs, LINE1s (multiple LINE1 annotations from RepeatMasker included, fraction of SINE/LINE1 nucleotides in 200-kb windows; LINE1s with chosen midpoint of 0.6 to highlight anti-correlation), DNase hypersensitive sites (DNase-HS), *Xic* Hi-C (*y*-scale is normalized Hi-C signal from 40-kb *Xic* bin containing *Xist*), active/inactive genes (classification based on presence of H3K4me3 at Xa promoters in d7 ES cells), and lamin B1 association and replication timing (*y*-scale is normalized microarray probe intensities).

©2013 Macmillan Publishers Limited. All rights reserved

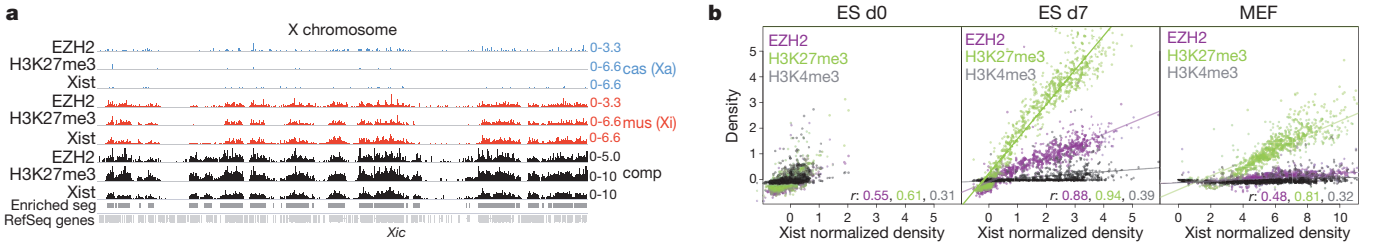


Figure 2 | Co-spreading of Xist RNA and PRC2. **a**, Normalized read densities of Xist, EZH2 and H3K27me3 on the X chromosome in d7 cells. **b**, Xist densities (200-kb bins) correlated with EZH2, H3K27me3 and H3K4me3 signals at different stages of XCI. Pearson's r displayed. EZH2/H3K27me3 R^2 values: 0.3/0.37 for d0, 0.77/0.88 for d7, and 0.23/0.66 for MEFs, respectively. H3K4me3 R^2 values: < 0.15 across all samples.

(Fig. 1c, g and Extended Data Fig. 5a; $P < 2.2 \times 10^{-16}$; Pearson's $r = 0.46$). Furthermore, there were positive correlations with DNase I hypersensitive sites (Pearson's $r = 0.43$), short interspersed elements (SINEs; $r = 0.55$), and early replicating regions ($r = 0.45$; Fig. 1h and Extended Data Fig. 5b). Strong anti-correlations were observed with long terminal repeat retrotransposons (LTRs; $r = -0.39$), long interspersed

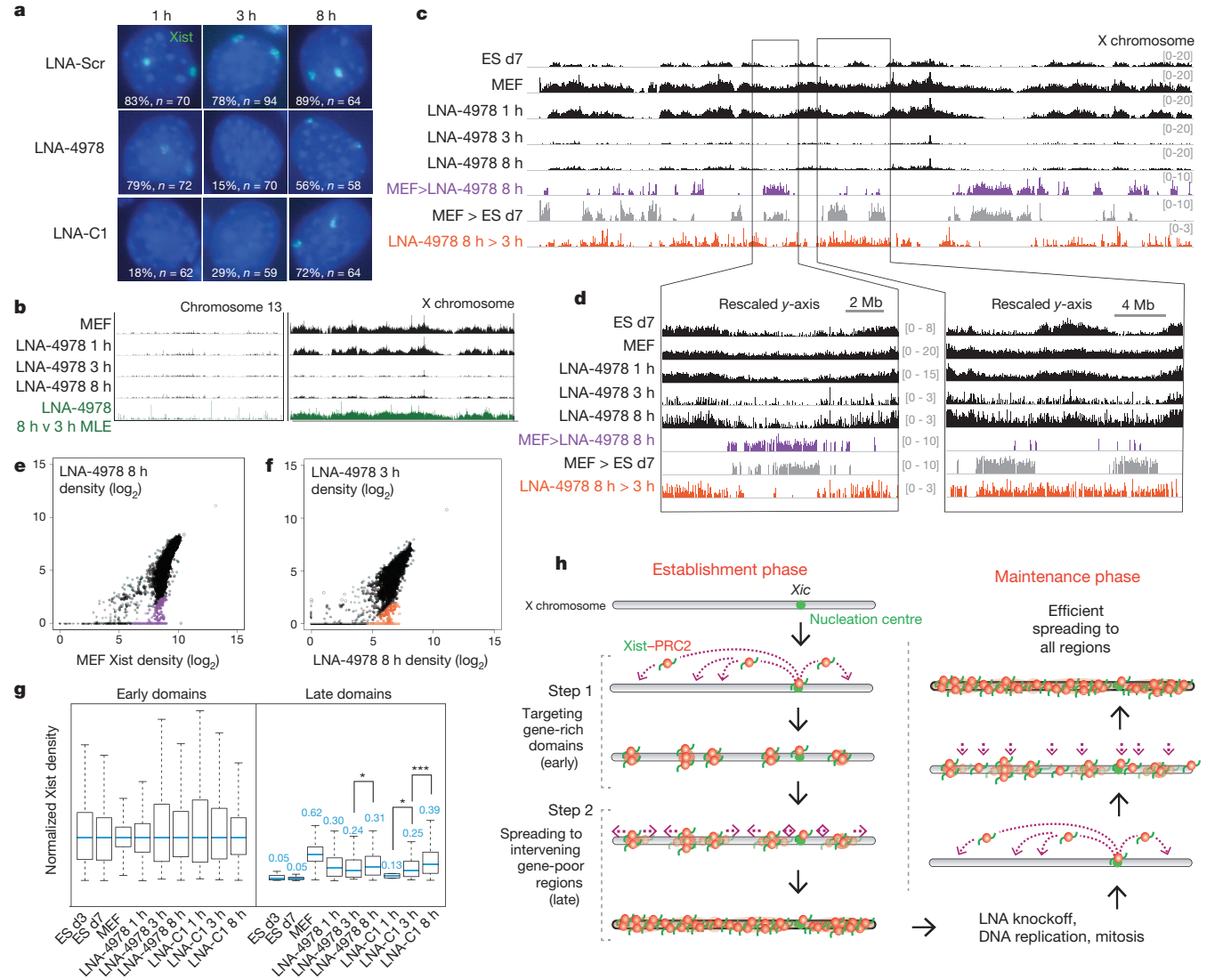


Figure 3 | Xist knockoff uncovers a distinct spreading method during the maintenance phase. **a**, RNA FISH shows depletion and recovery of Xist RNA (green) in MEF cells after Xist knockoff. Per cent of nuclei with Xist clouds and sample size (n) shown. Scr, scrambled LNA. **b**, Chromosome-wide recovery of Xist after LNA-4978 knockoff on chromosomes X and 13. Regions of recovery comparing 8 h over 3 h LNA-4978 were determined using a maximum likelihood enrichment (MLE) estimate[29]. **c**, **d**, Xist knockoff and recovery across the X chromosome. Coloured regions show more than tenfold median-normalized differences between samples. **d**, Expanded view of one region with more late domain recovery (right) than the other (left). **e**, **f**, Xist CHART signals (40-kb bins) from LNA-4978 8 h correlated with MEF (**e**); LNA-4978 3 h correlated against LNA-4978 8 h (**f**). Regions showing more than tenfold differences after normalization are coloured as shown in **d**. **g**, Xist recovery in indicated samples, with 40-kb-binned Xist densities normalized to median levels of early domains of each sample, to determine how early and late domains recover from knockoff compared to during *de novo* XCI. Normalized median values for each sample indicated above box. $*P < 0.05$; $***P < 10^{-8}$, Wilcoxon test, as in Extended Data Figs 7c and 3c. **h**, Model, distinct methods of Xist spreading during establishment and maintenance.

©2013 Macmillan Publishers Limited. All rights reserved

element-1 (LINE1) ($r = -0.54$), and lamin-associated domains (LADs, $r = -0.48$)[23]. Xist partitioning did not correlate with cytogenetic banding on the X chromosome (Fig. 1h)[19,24]. LINE1s have been proposed as spreading elements[25], but repetitive reads from Xist CHART-seq aligning to LINE1 were not enriched over input (Extended Data Fig. 5c). The localization of Xist showed modest positive correlation with *Xic* looping contacts inferred from HiC (high-throughput chromosome conformation capture)[18] through an anchor within the *Xist* locus (Fig. 1h and Extended Data Fig. 5b). Together, these data support a role for open chromatin in guiding Xist, with Xist coming into contact with gene-rich regions (early domains) first, and spreading secondarily to more distal gene-poor inter-regions (late domains).

Given co-nucleation of Xist and PRC2 at the *Xic*[8], we asked whether Xist continues to associate with PRC2 during spreading. Comparison of Xist, EZH2 and H3K27me3 enrichment revealed strikingly similar chromosome profiles across time (Fig. 2a and Extended Data Fig. 6a–c). By contrast, PRC2 and H3K27me3 densities on Xa did not correlate with Xist, nor did those on chromosome 13, a representative autosome (Extended Data Fig. 6a). Consistent with the idea that Xist directs PRC2 localization onto Xi[5], Xist densities demonstrated an extensive linear relationship with EZH2 and its product H3K27me3 across the X chromosome in mid-XCI but not pre-XCI cells (Fig. 2b). Correlation with the H3K4me3 control (active mark) was poor. In MEFs, densities of H3K27me3 and Xist remained highly correlated, whereas reduced densities of PRC2 were observed during maintenance. Interestingly, Xist densities were not necessarily greater at previously defined "PRC2 strong sites"[9] (Extended Data Fig. 6d, e); instead, Xist densities showed a general correlation with Xi-specific PRC2 enrichment (Extended Data Figs 5b and 6d, h). This supports the idea that strong sites are Xist-independent (as indeed they are present in d0 cells[9]) and indicate that Xist and PRC2 co-migrate to new regions within the early domains on the Xi.

We then asked if localization mechanisms were inherent to Xist RNA or chromatin context. In perturbation experiments, we stripped away Xist RNA and observed recovery on the Xi of MEFs at 1 h, 3 h and 8 h. Locked nucleic acids (LNA) directed against repeat C of Xist RNA prevented nucleation and therefore spreading[13]. RNA fluorescence *in situ* hybridization (FISH) showed that LNA-4978 did not overtly perturb Xist at 1 h, but led to full Xist displacement by 3 h, with Xist reassociation at 8 h (Fig. 3a). As reassociation requires newly synthesized Xist rather than relocalization of displaced Xist[13], reassociation must depend on outward spreading of new RNA from the *Xic*, just as during XCI establishment.

Interestingly, however, CHART-seq revealed a pattern not evident cytologically by RNA FISH. At 1 h, when Xist was still visualized on Xi (Fig. 3a), CHART-seq demonstrated a relative loss in late domains (Fig. 3b–d), indicating that Xist binds more weakly to gene-poor than to gene-rich regions, and consistent with the banded pattern of Xist on the metaphase Xi observed cytologically[24]. At 3 h, Xist was strongly depleted from both regions. At 8 h, partial recovery was evident in both regions. However, unlike spreading during *de novo* XCI (d3, d7), spreading of Xist during the somatic maintenance phase (MEF) did not follow a two-step process, as Xist reassociation in early and late domains occurred simultaneously (Fig. 3b–d). Therefore, spreading during *de novo* XCI was restricted to early domains and occurred on a timescale of days in the *ex vivo* system. In contrast, recovery and re-spreading in post-XCI cells occurred more generally in both domains and on a timescale of hours. This quantitative difference is significant, with accumulation in late domains appearing on the same timescale as early domains during the recovery period after Xist knockoff (Fig. 3e–g and Extended Data Figs 7 and 8). Similar results were observed using an independent LNA, LNA-C1, targeted to a different sequence in the repeat C region and in multiple replicates (Fig. 3a and Extended Data Figs 2d, 3a, 7 and 8). Despite LNA-C1 being faster acting[13] (Fig. 3a), LNA-C1 and LNA-4978 treatment resulted in remarkably similar Xist knockoff and recovery on Xi.

Taken together, these data provide evidence for distinct mechanisms of Xist spreading during establishment (*de novo* XCI) in early embryonic cells, when spreading occurs in a two-step fashion (early to late domains), and during maintenance in somatic cells, when Xist spreads more generally into both early and late domains (Fig. 3h). The Xi may retain an epigenetic memory of Xist[26], enabling more efficient spreading during maintenance. As Xist mostly dissociates from the Xi during mitosis[4], epigenetic memory could facilitate the resynthesis of Xist and re-spreading in G1, and duplication of Xist patterns after DNA replication. Indeed, the continued action of Xist is essential for maintenance of XCI[27]. In summary, we have illuminated the mechanism by which Xist spreads on a 150-Mb scale. Comparing localization dynamics of Xist relative to other lncRNAs (E. Hasiculeyman and J. Rinn, personal communication) and three-dimensional conformations[28] may prove highly informative for understanding general mechanisms of RNA-directed chromatin change.

METHODS SUMMARY

Cells were grown as previously described[9]. RNA was isolated and sequenced using a modified adaptor ligation protocol, and Xist localization determined by CHART[10] with several modifications as detailed in the extended Methods. LNAs (Exiqon) that target Xist were previously described[13].

Online Content Any additional Methods, Extended Data display items and Source Data are available in the online version of the paper; references unique to these sections appear only in the online paper.

Received 28 May; accepted 2 October 2013.
Published online 27 October 2013.

1. Disteche, C. M. Dosage compensation of the sex chromosomes. *Annu. Rev. Genet.* **46,** 537–560 (2012).
2. Wutz, A. Gene silencing in X-chromosome inactivation: advances in understanding facultative heterochromatin formation. *Nature Rev. Genet.* **12,** 542–553 (2011).
3. Lee, J. T. Epigenetic regulation by long noncoding RNAs. *Science* **338,** 1435–1439 (2012).
4. Clemson, C. M., McNeil, J. A., Willard, H. F. & Lawrence, J. B. XIST RNA paints the inactive X chromosome at interphase: evidence for a novel RNA involved in nuclear/chromosome structure. *J. Cell Biol.* **132,** 259–275 (1996).
5. Zhao, J., Sun, B. K., Erwin, J. A., Song, J. J. & Lee, J. T. Polycomb proteins targeted by a short repeat RNA to the mouse X chromosome. *Science* **322,** 750–756 (2008).
6. Pontier, D. B. & Gribnau, J. Xist regulation and function eXplored. *Hum. Genet.* **130,** 223–236 (2011).
7. Brown, C. J. *et al.* The human *XIST* gene: analysis of a 17 kb inactive X-specific RNA that contains conserved repeats and is highly localized within the nucleus. *Cell* **71,** 527–542 (1992).
8. Jeon, Y. & Lee, J. T. YY1 tethers Xist RNA to the inactive X nucleation center. *Cell* **146,** 119–133 (2011).
9. Pinter, S. F. *et al.* Spreading of X chromosome inactivation via a hierarchy of defined Polycomb stations. *Genome Res.* **22,** 1864–1876 (2012).
10. Simon, M. D. *et al.* The genomic binding sites of a noncoding RNA. *Proc. Natl Acad. Sci. USA* **108,** 20497–20502 (2011).
11. Brockdorff, N. *et al.* The product of the mouse *Xist* gene is a 15 kb inactive X-specific transcript containing no conserved ORF and located in the nucleus. *Cell* **71,** 515–526 (1992).
12. Wutz, A., Rasmussen, T. P. & Jaenisch, R. Chromosomal silencing and localization are mediated by different domains of *Xist* RNA. *Nature Genet.* **30,** 167–174 (2002).
13. Sarma, K., Levasseur, P., Aristarkhov, A. & Lee, J. T. Locked nucleic acids reveal sequence requirements and kinetics of Xist RNA localization to the X chromosome. *Proc. Natl Acad. Sci. USA* **107,** 22196–22201 (2010).
14. Ogawa, Y., Sun, B. K. & Lee, J. T. Intersection of the RNA interference and X-inactivation pathways. *Science* **320,** 1336–1341 (2008).
15. Berletch, J. B., Yang, F., Xu, J., Carrel, L. & Disteche, C. M. Genes that escape from X inactivation. *Hum. Genet.* **130,** 237–245 (2011).
16. Carrel, L. & Willard, H. F. X-inactivation profile reveals extensive variability in X-linked gene expression in females. *Nature* **434,** 400–404 (2005).
17. Splinter, E. *et al.* The inactive X chromosome adopts a unique three-dimensional conformation that is dependent on Xist RNA. *Genes Dev.* **25,** 1371–1383 (2011).
18. Dixon, J. R. *et al.* Topological domains in mammalian genomes identified by analysis of chromatin interactions. *Nature* **485,** 376–380 (2012).
19. Chadwick, B. P. & Willard, H. F. Multiple spatially distinct types of facultative heterochromatin on the human inactive X chromosome. *Proc. Natl Acad. Sci. USA* **101,** 17450–17455 (2004).
20. Chadwick, B. P. & Willard, H. F. Chromatin of the Barr body: histone and non-histone proteins associated with or excluded from the inactive X chromosome. *Hum. Mol. Genet.* **12,** 2167–2178 (2003).

©2013 Macmillan Publishers Limited. All rights reserved

21. Marks, H. *et al.* High-resolution analysis of epigenetic changes associated with X inactivation. *Genome Res.* **19,** 1361–1373 (2009).
22. Calabrese, J. M. *et al.* Site-specific silencing of regulatory elements as a mechanism of X inactivation. *Cell* **151,** 951–963 (2012).
23. Bickmore, W. A. & van Steensel, B. Genome architecture: domain organization of interphase chromosomes. *Cell* **152,** 1270–1284 (2013).
24. Duthie, S. M. *et al. Xist* RNA exhibits a banded localization on the inactive X chromosome and is excluded from autosomal material *in cis*. *Hum. Mol. Genet.* **8,** 195–204 (1999).
25. Lyon, M. F. The Lyon and the LINE hypothesis. *Semin. Cell Dev. Biol.* **14,** 313–318 (2003).
26. Kohlmaier, A. *et al.* A chromosomal memory triggered by *Xist* regulates histone methylation in X inactivation. *PLoS Biol.* **2,** e171 (2004).
27. Yildirim, E. *et al.* Xist RNA is a potent suppressor of hematologic cancer in mice. *Cell* **152,** 727–742 (2013).
28. Engreitz, J. M. *et al.* The Xist lncRNA exploits three-dimensional genome architecture to spread across the X chromosome. *Science* **341,** 1237973 (2013).
29. Kharchenko, P. V., Tolstorukov, M. Y. & Park, P. J. Design and analysis of ChIP-seq experiments for DNA-binding proteins. *Nature Biotechnol.* **26,** 1351–1359 (2008).

Acknowledgements We thank J. Overton, I. Tikhonova and A. Lopez, and the MGH Bioinformatics Core. We also acknowledge funding from Yale University start-up funds to M.D.S., the Deutsche Forschungsgemeinschaft to S.F.P. and V.K.M., the MGH Fund for Medical Discovery to S.F.P., and the National Institutes of Health (grant F32-GM090765 to K.S., RO1-GM043901 to R.E.K., and RO1-GM090278 to J.T.L.). J.T.L. is an Investigator of the Howard Hughes Medical Institute.

Author Contributions R.E.K., J.T.L., M.D.S. and S.F.P. designed the experiments; S.F.P., K.S. and R.F. performed cell culture; R.F. and M.D.S. established CHART conditions and performed CHART; S.K.B. prepared CHART-seq libraries; K.S. performed LNA knockoffs; S.F.P. and V.K.M. performed RNA-seq; S.F.P. performed bioinformatic analyses with M.D.S., M.R.-S., R.F. and B.A.K.; M.D.S., S.F.P., R.F., J.T.L. and R.E.K. interpreted the results; J.T.L, M.D.S, R.E.K, S.F.P. and R.F. wrote the manuscript.

Author Information CHART-seq and RNA-seq datasets have been deposited in GEO (accession number GSE48649). Reprints and permissions information is available at www.nature.com/reprints. The authors declare no competing financial interests. Readers are welcome to comment on the online version of the paper. Correspondence, queries and requests for materials should be addressed to M.D.S. (matthew.simon@yale.edu, CHART protocols), R.E.K. (kingston@molbio.mgh.harvard.edu, CHART protocols) or J.T.L. (lee@molbio.mgh.harvard.edu, biological materials and bioinformatics protocols).

©2013 Macmillan Publishers Limited. All rights reserved

METHODS

Capture oligonucleotides. Capture oligonucleotides were designed based either on repetitive sequences in Xist RNA (X.A, X.C, Extended Data Fig. 1b and Extended Data Table 1), or by using RNase H mapping[10] of functional regions of Xist[12] to identify sites in Xist RNA available for hybridization in crosslinked chromatin extracts (Extended Data Fig. 1c and Extended Data Table 1). Regions of sensitivity were further interrogated by BLAST to identify oligonucleotides both with minimal cross-hybridization potential to other RNAs and genomic sites, as well as similar melting temperatures. Oligonucleotides were either synthesized as previously described on an Expedite Oligo synthesizer and purified using reverse phase cartridges (Poly-Pak II, Glen Research)[10], or ordered commercially (IDT, 3′-biotin-TEG, iSp18 spacer modified, salt free) and used without further purification.

Alternative capture oligonucleotides. Alternative capture oligonucleotides (CO40; see Extended Data Fig. 2a, c, d) were designed using the oligowiz software[30] limiting lengths to 22–28 nucleotides and otherwise default parameters. Mouse (mm9) transcripts were screened to minimize cross-hybridization to off-target transcripts and 40 oligonucleotides (out of 263 candidates) were picked manually to cover the length of the Xist transcript in ~300–500 nucleotide intervals where possible (Extended Data Table 1). Standard unmodified desalted oligonucleotides were ordered commercially (IDT), resuspended and pooled. 3′ biotinylation of pooled oligonucleotides was carried out as previously described[31] using biotin-16-UTP, and biotinylated oligonucleotides recovered after a single chloroform extraction and nucleotide removal (Qiagen).

Xist CHART enrichment. Clonal female MEFs[32] and female Tsix^{STOP} ES cells[14] were cultured as previously reported[9], including differentiation of ES cells by LIF withdrawal. Xist CHART enrichment was performed as previously reported[10] with minor modifications. Briefly, 10^8 cells were crosslinked initially with 1% formaldehyde for 10 min at room temperature. The crosslinking reaction was stopped by adding 0.125 M glycine. After washing 3 times with PBS, crosslinked cells were re-suspended in 10 ml sucrose buffer, dounced 20 times with a tight pestle, and kept on ice for 10 min. Nuclei were collected by centrifugation at 1,500*g* for 10 min on top of a cushion of 25 ml glycerol buffer. Nuclei were further crosslinked with 3% formaldehyde for 30 min at room temperature. After washing three times with PBS, nuclei were extracted once with 50 mM HEPES pH 7.5, 250 mM NaCl, 0.1 mM EGTA, 0.5% N-lauroylsarcosine, 0.1% sodium deoxycholate, 5 mM DTT, 100 U ml^{-1} SUPERasIN (Invitrogen) for 10 min on ice, and centrifuged at 400*g* for 5 min at 4 °C. Nuclei were resuspended in 1.5 ml 50 mM HEPES pH 7.5, 75 mM NaCl, 0.1 mM EGTA, 0.5% N-lauroylsarcosine, 0.1% sodium deoxycholate, 5 mM DTT, 100 U ml^{-1} SUPERasIN, and sonicated in microtubes using Covaris E210 sonicator at 10% duty cycle, 200 bursts per cycle, intensity 3 for 5 min. The median size of chromatin fragments was ~3 kb as determined by agarose gel electrophoresis with ethidium bromide post-staining. For each CHART enrichment, 120 µl of cleared chromatin extract was incubated overnight with 36 pmol capture oligonucleotides in a total volume of 360 µl 33 mM HEPES pH 7.5, 808 mM NaCl, 0.17% N-lauroylsarcosine, 2.5 mM DTT, 0.33% SDS, 5× Denhardt's, 5 mM EDTA, 1× protease inhibitor cocktail (Roche), 100 U ml^{-1} SUPERasIN at room temperature. The hybridized material was captured after 3 h of incubation with 240 µl MyOne streptavidin beads (Invitrogen), washed sequentially once with 30 mM HEPES pH 7.5, 240 mM NaCl, 2 M urea, 1.5 mM EDTA, 0.75 mM EGTA, 0.65% SDS, 0.75% N-lauroylsarcosine, four times with 10 mM HEPES pH 7.5, 250 mM NaCl, 2 mM EDTA, 1 mM EGTA, 0.2% SDS, 0.1% N-lauroylsarcosine and once with RNase H elution buffer (50 mM HEPES pH 7.5, 75 mM NaCl, 0.125% N-lauroylsarcosine, 0.5% Triton X-100, 0.5 M urea, 10 mM DTT), and eluted by 10 µl RNase H (5 U µl^{-1}, New England Biolabs) digestion in 100 µl RNase H elution buffer for 10 min at room temperature. Eluent was subjected to crosslink reversal by treatment with SDS (1% final), proteinase K (1 mg ml^{-1} final) and Tris pH 7.5 (100 mM final) and heating for 1 h at 55 °C and 1–3 h at 65 °C. The enriched DNA was purified using the Qiagen PCR purification kit per manufacturer's instructions. Prior to preparing libraries for high throughput sequencing, CHART-enriched DNA was treated with RNase cocktail (Roche) and further sheared to below 500 base pairs (Covaris E210 sonicator, at 5% duty cycle, 200 bursts per cycle, intensity 5 for 4 min total process time).

qPCR analysis and validation. The Xist CHART enrichment at several DNA loci was determined using real-time PCR (Bio-Rad iTaq Universal SYBR Green Supermix) under standard conditions for both conventional and allele-specific PCR using the primers listed in Extended Data Table 2. Enrichment values were calculated as $2^{-\Delta C_t}$ relative to input. The real-time PCR experiments were from biologically independent CHART samples (that is, not the samples used for CHART-seq) as independent confirmation of the sequencing results (Extended Data Figs 2e, 4d).

Library preparation, replicates and sequencing. Sequencing libraries were either constructed by standard ChIP-seq protocols by the Yale Center for Genomic Analysis (YCGA), or as described previously[33]. Briefly, sequencing libraries were prepared by first repairing DNA-ends, A-tailing, ligating to universal adapters, and amplifying for 12 cycles with indexed primers. Excess adapters were removed by purification with Agencourt AMPureXP beads (Beckman Coulter) before sequencing. Sequencing was performed at the YCGA on Illumina HiSeq 2500 instruments. To confirm Xist distribution on the X chromosome, we produced biological replicates for d0, d7, MEF, and technical replicates for d3 and LNA knockoff experiments. Except for d0 where Xist CHART-seq showed mostly background signals, all replicates showed excellent positive correlation (Pearson's $r \approx 0.9$, Extended Data Fig. 2d). In addition, the replicates of ES d3 and d7 confirmed the specific enrichment in early domains and depletion at late domains. For LNA knockoff experiments, recovery profiles of Xist were confirmed by re-CHART replicates of LNA-4798 at 3 h and 8 h. We further confirmed our LNA knockoff results with a time course for LNA C1, which targets a different sequence within the repeat C region of Xist (see Fig. 3 and Extended Data Figs 7 and 8).

RNA-seq library. RNAs greater than 200 nucleotides from d7 cells and MEFs were purified using the mirVana RNA extraction kit (Ambion), cleared of ribosomal RNA (Ribozero, Epicentre) and sheared to a median size of 200 nucleotides using the Covaris S2 sonicator. After treatment with T4 polynucleotide kinase, a commercial 5′ adenylated linker (miRNA Cloning Linker 1, IDT) was ligated to the 3′ end of RNAs using T4 RNA ligase 2 (truncated, NEB) followed by reverse transcription (SuperScriptIII, Invitrogen) using a primer (CCGATCTATTGATGGTGCCTACAG) matching the linker. After reverse transcription, RNA was hydrolysed in 10 mM Tris pH 10, 5 mM $MgCl_2$ at 95 °C for 15 min and cDNA products greater than 100 nucleotides size selected and purified on AMPureXP. A barcoded (NNNNNN) 5′ phosphorylated linker (GATCGGAAGAGCACACGTCTGAACTCCAGTCACCNNNNNNATCTCGTATGCCGTCTTCTGCTTGddC) matching Illumina adapters was ligated to the 3′ end of the cDNA using T4 RNA ligase 1 (NEB) and directly amplified using custom forward (AATGATACGGCGACCACCGAGATCTACACTCTTTCCCTACACGACGCTCTTCCGATCTATTGATGGTGCCTACA*G) and reverse (CAAGCAGAAGACGGCATACGA*G) primers (* denotes phosphorothioate bond at 3′ terminal nucleotides), matching the Illumina TruSeq primers. Sequencing of purified libraries was carried out on an Illumina HiSeq instrument for either paired or single-end 50 nucleotides reads. Reads were aligned allele-specifically to 129S1/SvJm (mus) and CAST/EiJ (cas) genomes using Tophat2[43] with the "b2-sensitive" preset and otherwise default parameters (further described in 'Allele-specific alignments'). After removal of PCR duplicates, all unique reads mapping to gene bodies were summed for cas, mus and comp tracks. Read numbers over genes in the allelic tracks were used to calculate skew (mus − cas/mus + cas) and genes skewed significantly ($P < 0.01$, cumulative binomial probability) in d7 cells and MEFs were plotted (Fig. 1c and Extended Data Fig. 5a). A skew of −0.5 corresponds to threefold difference in inferred expression between Xa and Xi, equal to 67% inactivation of the Xi gene.

LNA displacement. LNAs synthesized by Exiqon were introduced into mouse embryonic fibroblasts (MEFs) as previously described[13]. Briefly, 2×10^6 cells were resuspended in 100 µl MEF nucleofector solution with LNAs at a final concentration of 2 µM and nucleofected using a T-20 program. Fresh culture medium was added to the cells and they were collected and formaldehyde crosslinked at the time points indicated.

Allele-specific alignments. Paired-end sequencing data from CHART-seq were aligned allele-specifically as previously described[9]. Briefly, each data set was aligned to variant CAST/EiJ and 129S1/SvJm genomes constructed using high quality polymorphisms[34] to the C57/Bl6 reference genome (mm9 build). Pairs aligning to only one variant genome and pairs aligning better to one variant genome (in number of nucleotide edits to reference) than the other were retained (allele-specific), as were pairs aligning equally well (non-allele-specific). Only unique pairs were used for this analysis and approximately half of all pairs in the CHART-seq data provided allelic information.

Generation of normalized coverage tracks. Xist CHART-seq reads were filtered for quality and repetitive alignments; low-quality alignments and duplicate reads were removed. The resulting files were analysed using SPP software[29]. In this analysis, all tags were included and the coverage generated with smoothing using 1-kb bins every 500 bp to generate input-subtracted, normalized read densities. To account for different read depths across data sets, each coverage file was scaled using the total positive read density on an autosome (chromosome 4) from the corresponding composite track (that is, the mus, cas and comp tracks were all scaled using the same factor). These data were visualized with either the IGV[35] or UCSC genome browser[36] displaying all tracks using a mean windowing function and scales indicated in each figure. We note that other methods to generate normalized coverage files, including the generation of conservative enrichment and maximum likelihood estimates, resulted in similar distribution patterns, but did not aid in comparisons across data sets with diverse read depths. To determine regions of Xist recovery after LNA treatment, in addition to the normalization and analysis described above, we separately subjected data from 8 h LNA-4978 treatment and 8 h LNA-C1 (time points with partial recovery of Xist density) to

©2013 Macmillan Publishers Limited. All rights reserved

normalization using 3 h LNA-4978 and 1 h LNA-C1 reads, respectively (the time point where most of Xist has been removed from the chromatin). The recoveries were determined using the maximum likelihood estimate function in SPP (Fig. 3b, Extended Data Fig. 7b, indicated by "MLE").

Identification of Xist-enriched segments. Significant segments of Xist enrichment were determined using Epicentre software[37] using a whole-genome semi-dynamic 5-kb window scan, and selecting only windows with $P < 0.001$ from an exact-rate ratio test. The distribution of the overlap between enriched segments and genomic features (Extended Data Fig. 2h) was determined using CEAS[38].

Meta-site and meta-gene analysis. Smoothed normalized read density for ChIP and CHART experiments generated as described above, (with the exception that these were calculated with 2,000-bp windows recorded every 50 bp to avoid aliasing difficulties) were used to calculate average density profiles using CEAS software[38].

Definition and significance estimation of allelic skew. The definition of allelic skew is based on the distribution of unique fragments (excluding PCR duplicates) in the allele-specific experimental and input tracks. Allele-specific coverage tracks were queried for a given interval and the cumulative binomial probability estimated by normal approximation from the number of effective fragments based on the interval length and the median sequenced fragment size (200 bp). Skew is then defined as ranging from −1 (fully cas) to +1 (fully mus) and as shown in Fig. 1c and Extended Data Fig. 5a. For example, a threefold difference between alleles is expressed as a skew of (±) 0.5.

Correlation analyses and significance estimates. Coverage densities over all tracks were tabulated for non-overlapping 40-kb, 200-kb and 1-Mb bins across the chromosome. For analysis and presentation of 40-kb bins that display differential enrichment between samples (Figs 1d, e and 3e, f, Extended Data Figs 7 and 8), bins were identified where the average median-normalized sum was greater than tenfold enriched. These enriched bins were displayed as coloured data on $\log_2$ enrichment plots. The location of these bins were identified and displayed as a separate browser track using the intensities from the enriched coverage file (Figs 1d, e and 3c, d, Extended Data Fig. 8). Correlations between Xist CHART samples were evaluated using Pearson's r and presented as scatterplots or heat maps. Pairwise comparisons of Xist, EZH2, H3K27me3 and H3K4me3 coverage densities were also used for linear regressions shown in scatter plots (Fig. 2b). For correlation of Xist segment density maps with various genomic features (Fig. 1h), the density of each feature was calculated for the same 40-kb, 200-kb and 1-Mb bins and Pearson's r was determined for all pairwise comparisons and displayed as a heat map (Extended Data Fig. 5b). Dendrograms are shown where hierarchical clustering was performed based on distance matrices, and the resulting clusters were consistent across a range of bin sizes. Genomic features annotated in the mm9 reference were obtained via the UCSC table browser and included genes (RefSeq), repeats (RepeatMasker), GC%, CpG islands and conservation[39]. In addition, peaks of DNase hypersensitivity[40], replication timing[41], lamin-association[42] and HiC data from the Xist locus viewpoint[18] were queried for correlation with Xist segment density maps in this fashion. LINE1s were queried using all annotations (Fig. 1h, Pearson's $r = -0.54$ with Xist CHART d7 ES) or single, merged annotations ($r = -0.56$). Moreover, repetitive sequences were aligned to the full murine RepeatMasker database and fraction of all hits compared between Xist d7 cells and corresponding input sample (Extended Data Fig. 5c).

Comparison of Xist spreading patterns. To assess the degree of Xist spreading and compare spreading patterns across samples, we focused on chromosomal regions where fully differentiated MEF cells had tenfold greater Xist signal (defined above) than d7 cells, which represent the intermediate stage of Xist spreading. We refer to these regions as "late" domains, and to other chromosomal regions as "early" domains. For each sample, we normalized both early and late domain signals to the median of the early domain signal. We then plotted these normalized early and late domain signals (Fig. 3g, Extended Data Fig. 7c), and evaluated differences between samples were assessed using the one-sided Wilcoxon test.

30. Wernersson, R. & Nielsen, H. B. OligoWiz 2.0–integrating sequence feature annotation into the design of microarray probes. *Nucleic Acids Res.* **33,** W611–W615 (2005).
31. Flickinger, J. L., Gebeyehu, G., Buchman, G., Haces, A. & Rashtchian, A. Differential incorporation of biotinylated nucleotides by terminal deoxynucleotidyl transferase. *Nucleic Acids Res.* **20,** 2382 (1992).
32. Yildirim, E., Sadreyev, R. I., Pinter, S. F. & Lee, J. T. X-chromosome hyperactivation in mammals via nonlinear relationships between chromatin states and transcription. *Nature Struct. Mol. Biol.* **19,** 56–61 (2012).
33. Bowman, S. K. *et al.* Multiplexed Illumina sequencing libraries from picogram quantities of DNA. *BMC Genomics* **14,** 466 (2013).
34. Keane, T. M. *et al.* Mouse genomic variation and its effect on phenotypes and gene regulation. *Nature* **477,** 289–294 (2011).
35. Thorvaldsdottir, H., Robinson, J. T. & Mesirov, J. P. Integrative Genomics Viewer (IGV): high-performance genomics data visualization and exploration. *Brief. Bioinform.* **14,** 178–192 (2013).
36. Kuhn, R. M. *et al.* The UCSC genome browser database: update 2007. *Nucleic Acids Res.* **35,** D668–D673 (2007).
37. Huang, W. *et al.* Efficiently identifying genome-wide changes with next-generation sequencing data. *Nucleic Acids Res.* **39,** e130 (2011).
38. Ji, X., Li, W., Song, J., Wei, L. & Liu, X. S. CEAS: cis-regulatory element annotation system. *Nucleic Acids Res.* **34,** W551–W554 (2006).
39. Davydov, E. V. *et al.* Identifying a high fraction of the human genome to be under selective constraint using GERP++. *PLOS Comput. Biol.* **6,** e1001025 (2010).
40. John, S. *et al.* Chromatin accessibility pre-determines glucocorticoid receptor binding patterns. *Nature Genet.* **43,** 264–268 (2011).
41. Hiratani, I. *et al.* Global reorganization of replication domains during embryonic stem cell differentiation. *PLoS Biol.* **6,** e245 (2008).
42. Peric-Hupkes, D. *et al.* Molecular maps of the reorganization of genome-nuclear lamina interactions during differentiation. *Mol. Cell* **38,** 603–613 (2010).
43. Kim, D. *et al.* TopHat2: accurate alignment of transcriptomes in the presence of insertions, deletions and gene fusions. *Genome Biol.* **14,** R36 (2013).

©2013 Macmillan Publishers Limited. All rights reserved

CORRECTIONS & AMENDMENTS

CORRIGENDUM

doi:10.1038/nature12794

Corrigendum: Membrane potential dynamics of grid cells

Cristina Domnisoru, Amina A. Kinkhabwala & David W. Tank

Nature **495,** 199–204 (2013); doi:10.1038/nature11973

In this Article, tetrode recordings from mice navigating in real environments and on virtual reality linear tracks were used to develop a classifier that was subsequently used to identify grid cells within our set of intracellular whole-cell recordings. Owing to an error in the way the analogue angular encoder signal detecting rotation of the treadmill was digitized and post-processed, the distances run by the mice along the one-dimensional virtual reality tracks during the tetrode recordings are approximately 5% to 30% longer than reported. (Track lengths for whole-cell recordings in virtual reality are unaffected.) Correct track lengths for tetrode recordings by date are provided in Table 1 of this Corrigendum. Track lengths affect the *x* axes in Fig. 2d–f, Supplementary Fig. 6b, and the one-dimensional virtual reality portion of Supplementary Fig. 9. Because the majority of one-dimensional virtual reality tracks were about 30% longer, we corrected the classifier to require three in-field to out-of-field switches per 5.2 m of linear track. As expected, the correct classifier makes the same decisions as the original for both whole-cell and tetrode recordings. The new track lengths lead to small changes in the mean field width (40 ± 11 cm), peak firing rate (12 ± 6 Hz) and number of fields per metre (0.7 ± 0.3) for tetrode virtual reality data in Supplementary Fig. 6d–f. In addition, two cells in Supplementary Fig. 9 part 5 should have been labelled 'T10_20100805_t2_c6' (third cell from top, left panel) and 'T10_20100811_t2_c2' (fourth cell from top, left panel), and the Supplementary Methods should state that when two clusters were identified as the same cell due to the use of both positive and negative thresholds, we kept only one of the clusters. These corrections have no impact on the results, conclusions and interpretation of this Article. The errors have been corrected in Fig. 2 of the HTML and PDF versions online and in Supplementary Figs 6 and 9 of the original Supplementary Information.

Table 1 | Corrected track lengths

Date	Track length
2010-07-23	411 cm
2010-07-24	429 cm
2010-07-28	872 cm
2010-08-05	803 cm
2010-08-08	814 cm
2010-08-09	820 cm
2010-08-11	861 cm
2010-08-12	822 cm
2010-08-20	812 cm
2010-08-24	814 cm
2010-08-25	815 cm
2010-09-14	1,035 cm
2010-10-20	614 cm
2010-11-03	648 cm
2010-11-04	652 cm

RETRACTION

doi:10.1038/nature12728

Retraction: Dance reveals symmetry especially in young men

William M. Brown, Lee Cronk, Keith Grochow, Amy Jacobson, C. Karen Liu, Zoran Popović & Robert Trivers

Nature **438,** 1148–1150 (2005); doi:10.1038/nature04344

We retract this Letter, which reported strong positive associations between symmetry and dancing ability in a group of young Jamaican men. K.G. could not be contacted.

©2013 Macmillan Publishers Limited. All rights reserved

CAREERS

EQUALITY Lack of female academic leaders misrepresents faculty and students **p.473**

RECESSION Basic research increasingly targets societal outcomes **p.473**

NATUREJOBS For the latest career listings and advice **www.naturejobs.com**

VANDERBILT PHOTO/DANIEL DUBOIS



Vanderbilt University, Tennessee, is the leading US producer of minority graduates with PhDs in astronomy, physics and materials science.

HIGHER EDUCATION

On the lookout for true grit

With the right mix of persistence and support structures, scholars from minority groups can thrive as they pursue their PhDs.

BY KENDALL POWELL

Jedidah Isler had always dreamed of attending an Ivy League graduate school. She had a stellar record as an undergraduate at Norfolk State University in Virginia, one of many US universities that traditionally enrol mostly African American students. She earned her bachelor's degree in physics there in 2003. But a two-year break after college, taken for personal reasons, left her shaky and unsure. "In physics, there are so many things you have to have at the top of your head, like formulae, and I was feeling out of the loop," she says.

However, an e-mail from the American Physical Society encouraging people from minority groups to study physics showed her an avenue back to graduate school. In a follow-up e-mail exchange, she learned about a joint programme starting in Nashville, Tennessee, called the Fisk–Vanderbilt Masters-to-PhD Bridge Program. Six weeks later, Isler threw her possessions into a rental car and drove to Nashville to start a master's degree at Fisk University, an historically black institution less than 2 kilometres from Vanderbilt University, the programme's partner.

Isler was part of the second cohort of students in the Fisk–Vanderbilt programme, which helps students from minority groups that are under-represented in the sciences to pursue doctorates in astronomy, biology, chemistry, physics and materials science. After launching in 2004 with just four students, it has emerged as one of the most successful initiatives aimed at minority scientists in the United States. Fisk University is now the United States' biggest producer of black students with master's degrees in physics, and Vanderbilt is the biggest producer of minority scholars receiving doctorates in astronomy, physics and materials science. Where other programmes have tried and failed, this one seems to have a winning formula.

Boosting the number of minority-scholars science PhDs has been a major challenge in the United States, despite university programmes and government incentives. In 2010, African Americans were awarded just 3% of all science and engineering doctorates; Hispanics ▶

© 2013 Macmillan Publishers Limited. All rights reserved

received 3.6% and Native Americans 0.3%.

Leaders of the Fisk–Vanderbilt programme see it as a problem at the entry level. Programmes such as the US National Institutes of Health Minority Access to Research Careers graduate fellowships and other minority-specific funding schemes help only minority students who have already succeeded in getting into a graduate programme. "Our goal is fundamentally different," says Keivan Stassun, the co-director of the Fisk–Vanderbilt programme. "If we are going to move the needle at a national level, we have to engage individuals from a larger pool." This unorthodox approach — which includes intensive mentoring and eliminating standardized test scores as a criterion for admission — is already boosting minority numbers in some of the least diverse fields, such as astronomy and physics.

The Fisk–Vanderbilt programme's success is clear. Since 2004, it has admitted 67 students. It awarded its first PhD in 2009, and will see its eighth PhD granted by the end of this year. That number includes mostly Vanderbilt graduates and a few students who choose to pursue a PhD at another university. Stassun expects that about five doctorates will be awarded each year in future. He notes that an average US PhD-granting programme in the sciences awards a doctorate to a minority scholar about once every 5–10 years.

BUILDING RELATIONSHIPS

From his very first associations with Vanderbilt, Stassun had been clear about his passion for boosting minority scholarship. In his 2003 job interview for a tenure-track astronomy position, he presented his vision for a programme that would address the low numbers. Himself a minority scientist, he saw the potential for synergy in connecting Fisk, an institution that was already producing smart, capable, master's-level scientists, with the research resources of the PhD-granting departments at Vanderbilt.

During his job-offer negotiations, he asked for extra financing for the programme and found that he had ample support from his department and Vanderbilt administrators. Faculty members including physicist Arnold Burger, Stassun's co-director and counterpart at Fisk, were equally invested in the idea.

The programme is designed for students who are dedicated to pursuing graduate studies in science but who may need additional coursework, training or research experience before beginning a doctorate. Students benefit from individualized mentoring, a seminar series on professional development and a seamless transition between master's and PhD research. By the time students formally apply to a Vanderbilt PhD programme, they have already taken classes at Vanderbilt, worked on a research collaboration between a Fisk and a Vanderbilt laboratory for two years and established relationships with the faculty members who will become their thesis advisers. To Stassun, science undergraduate degree-holders are at the ideal academic level from which to recruit. "These students have already stood up and said: 'I want to be a physicist'," he says.

So far, 81% of the 67 students admitted to the programme have advanced to doctoral studies. That flips another statistic on its head: typically, 80% of minorities who complete US science, technology, engineering or maths (STEM) bachelor's degrees do not continue on to graduate school. One-fifth continue to master's programmes and about 2% continue on to a doctorate.



"You climb as high as you can, and then you guide the next person, who may go higher."
Jedidah Isler

In meetings with faculty members from minority-serving undergraduate institutions, Stassun heard one potentially unsettling reason why many of these students might fall out of the academic science pipeline: advisers at minority-serving undergraduate institutions sometimes actively discourage students from pursuing graduate degrees. Instead, they steer students towards scientific and technical industry careers that already have better minority mentoring and support networks in place. One report suggests additional barriers: greater financial needs and being more location-bound owing to finances or family obligations (K. G. Stassun *Bull. Am. Astr. Soc.* **35,** 1448–52; 2003).

In building their programme, Burger and Stassun considered the problem of the leaky pipeline. They knew from statistics that nearly 40% of white or Asian students proceed to a PhD straight from a bachelor's degree, compared to about 27% of minority students. They knew what they needed to do — provide a stepping-stone to the PhD. "The data were there. Students who were successful did it slowly. Now we are giving them that vehicle," says Burger.

The approach resonated with Erica Tross, now in her second year of a biology master's degree at Fisk. Like many bachelor's biology-degree holders, she did not know whether she wanted to pursue a career in medicine or research when she graduated from what she calls the "itty-bitty" Oakwood University in Huntsville, Alabama. "I had research experience, but not that much. This would be a perfect transition; in two years you have your master's and I could decide then to go to medical school or go on to Vanderbilt," she says.

The master's portion also gives students time to fill holes in their undergraduate education. "I was afraid of graduate school," says Fabienne Bastien, a fifth-year astronomy PhD candidate in the programme. "I thought I had to be much more prepared." Bastien, a first-generation American, unfavourably compared herself with undergraduate peers who had their own telescopes, had taken high-school science classes that were more difficult and had an astronomy vocabulary that, to her ear, sounded "like a completely different language".

GRITTY REALITY

The programme also had to confront another trend in the data from minority STEM graduates — an elephant in the room that was far more worrisome and controversial. Students applying to graduate school must take the Graduate Record Examination (GRE), and median maths GRE scores for Hispanic, Native American, black and female students are consistently lower than those for Asian, white and male students. Many graduate departments use a cut-off score to narrow applicant pools, which automatically limits minority numbers. "If someone wanted to intentionally shut the door to minority students, the GRE is the filter they would use," says Burger. So the Fisk–Vanderbilt programme uses an entirely different measure of persistence in the face of adversity — what Burger and Stassun call 'fire in the belly' or 'grit'.

Grit is, in fact, a metric in the social sciences, based largely on work by Angela Duckworth, a psychology researcher at the University of Pennsylvania in Philadelphia. She defines it as a predisposition for pursuing long-term, challenging goals with passion and perseverance. To measure grit, the Fisk–Vanderbilt programme developed an interview during which applicants describe what intrigues them about science, a challenging experience or obstacle, their fears, how they pulled through and the resources or relationships on which they relied. At least two faculty members score interviewees' answers on a grit scale, and the programme uses that number and the professors' qualitative assessment of the student's interview for selection.

In Bastien's interview, her self-awareness and determination to become an astronomer were clear. Stassun describes her GRE

STEPHEN SARTORI/SYRACUSE UNIV.



FISK UNIV.

Arnold Burger measures applicants on their 'grit'.

© 2013 Macmillan Publishers Limited. All rights reserved

scores as "reflective of what's typical of her ethnicity and gender", but her grit score as off the charts. "That's a person who will start graduate school way ahead of the game, with all the resources and skills that go beyond smarts: self-discipline, organization, follow-through," says Stassun. "Far too often, graduate programmes ignore that." Bastien's grit has paid off: this year she appeared as the first author of a *Nature* paper defining a new, relatively easy and more precise way to calculate a star's evolutionary age (F. A. Bastien *et al. Nature* **500,** 427–430; 2013).

Duckworth cautions that assessing grit in such high-stakes settings as graduate admissions is tricky. "The grittiest people are often the least willing to say they are gritty," she says. Moreover, she adds, the higher the stakes, the greater the incentive the interviewee has to provide phony or insincere answers. "You can interview for social intelligence on the spot," Duckworth says. "But I don't know that you can assess whether [the candidate] will be awake at 6 a.m. the next morning — or if after their first major screw-up, they are going to give up." She still thinks that screening for grit might be worthwhile, but how best to measure it remains uncertain.



STEVE GREEN, VANDERBILT CREATIVE SERVICES

"I was afraid of graduate school. I thought I had to be much more prepared."
Fabienne Bastien

Regardless, the Fisk–Vanderbilt students exemplify the grit quality, and they say that the programme's focus on character building sets it apart from other minority initiatives. Tross is currently struggling in a Vanderbilt class on advanced molecular genetics. She is relying on her grit to get her through. "I've cried my tears. I've weighed whether I'm going to pass or not. But I'll keep doing the work," she says.

EXPANDING HORIZONS

Other universities are taking note of the Fisk–Vanderbilt success. Abigail Stewart, who has been involved in setting up the programmes at the University of Michigan in Ann Arbor, says that all science-graduate admissions committees could learn from the Fisk–Vanderbilt model. "In general, we are eager to use simple tests or cut-offs to limit applications to a manageable number, and that means that, too often, we rely on indicators that are not actually indicators of what we care about," she says.

Although the University of Michigan is not particularly close to any minority-serving institutions, four campus departments have started master's programmes, based on the Fisk–Vanderbilt model, in ecology and environmental biology, molecular, cellular and developmental biology, applied mathematics and applied physics. In addition, the American Physical Society now funds similar bridge-to-PhD programmes at Ohio State University in Columbus and the University of South Florida in Tampa.

Edmund Bertschinger, institute community and equity officer at the Massachusetts Institute of Technology in Cambridge, which has its own physics bridge programme, says that the Fisk–Vanderbilt programme has amazingly dedicated faculty members and staff that watch out for and support one another. "They don't let students slip through the cracks."

Bertschinger and Stewart say that all graduate programmes could boost the pipeline persistence of alumni by taking a closer look at the 'grit factor' and other personality measurements when deciding which students to admit. After all, persistence in the face of adversity describes most successful academic science endeavours. For all types of STEM graduate students entering US PhD programmes, only 50–65% (depending on ethnicity, gender and discipline) complete their doctorates — a miserably low return on investment for the time and money spent training students.

Participation in the bridge programme does not provide automatic admission to Vanderbilt — students must apply formally and meet all of the requirements. Isler decided to apply to other PhD programmes as well and was admitted to the astronomy programme at Yale University in New Haven, Connecticut. Stassun gently but firmly encouraged her to leave the bridge programme and follow her Ivy League dream. "That was the most generous thing anyone has ever done for me," she says.

On her first day at Yale, she felt out of place as the sole black woman, and also for her acute lack of pedigree. No one in her class knew what a historically black institution was, and no one had heard of Norfolk State or Fisk. "At a different time in my life, that would have crushed me," she says. But her time in the Fisk–Vanderbilt programme had given her the confidence to keep going. And her bridge family was never more than a phone call away.

In October, Isler defended her thesis work on blazars — hyperactive supermassive black holes that spew out accelerated particles. She became the first black woman to graduate from Yale with a PhD in astronomy and has already begun a Chancellor's Faculty Fellowship at Syracuse University in New York, a post that provides a transition to a tenure-track faculty position. "You climb as high as you can," she says, "and then you guide the next person, who may go higher." ■

Kendall Powell *is a science writer based in Lafayette, Colorado.*

EQUALITY

Lack of female leaders

Women chair just 12% of all UK higher-education governing bodies and lead 17% of UK institutions as vice-chancellors, says a study. *Leaders in Higher Education 2013*, released by the non-profit group WomenCount in Cardiff, says that the low numbers of women in leadership roles at institutions do not accurately reflect the proportion of female faculty members and students. Unconscious bias might be partly to blame for the numbers because people often appoint and promote others who are like themselves, the report suggests. Author Norma Jarboe, director of WomenCount, says that women must seek sponsors who will help them to get promotions, and pursue a position on the board of a company or charity. "Cross-sector knowledge and powerful contacts can be door openers," she says.

RECESSION

Focus on outcomes

The global recession has led government-funded academic science to focus increasingly on 'targeted outcomes' with a clear societal or economic impact, finds a report. *The State of Higher Education 2013*, released on 1 December by the Organisation for Economic Co-operation and Development in Paris, polled presidents and rectors at 34 higher-education institutions across 29 nations. Researchers are also spending a lot of time on public outreach, it finds. "If taxpayers understand the value of the research, they're more likely to agree to fund it," says report co-author Ellen Hazelkorn, vice-president of research and enterprise at the Dublin Institute of Technology. She suggests that early-career researchers polish their communication skills and focus on interdisciplinary work.

COMMUNICATION

Internet freedom

US faculty members are entitled to discuss issues relevant to the public on social media, argues a draft report. *Academic Freedom and Electronic Communications*, released on 3 December by the American Association of University Professors in Washington DC, notes that faculty members in some states have been suspended or dismissed for writing on Facebook or Twitter about controversial issues such as religion and gun control. Academics should be involved in creating social-media policies, the report says.

© 2013 Macmillan Publishers Limited. All rights reserved

to Western ingredients. In New York City, the Momofuku restaurant group's Culinary Lab has focused on miso- and tamari-like pastes and sauces made from non-soya bases such as cashews, pistachios, chickpeas and spelt. Copenhagen's renowned Noma and the affiliated Nordic Food Lab have had good results with a yellow-pea 'peaso', a barley *koji* roasted to a chocolate brown and versions of fish sauces made from grasshoppers and from *koji*-treated beef.

These experiments with fusion fermentation are probably just a taste of things to come. The James Beard Foundation, a New York-based organization of professional chefs, gave its award for the best reference book of 2013 to Sandor Ellix Katz's 500-page *The Art of Fermentation* (Chelsea Green Publishing), a jaw-dropping survey of possibilities from abará (Nigerian steamed or boiled fermented cowpeas) to zur (Polish sour rye porridge soup).

"Provocation rather than flavour has motivated experiments with what might be called personal fermentation."

Outside the restaurant world, provocation rather than flavour has motivated experiments with what might be called personal fermentation. After the Rogue Ales brewery in Newport, Oregon, failed to find beerworthy wild yeasts in its hop yard, it turned to a different local niche: a strain cultured from the brewmaster's hair follicles now goes into the making of its speciality Beard Beer. And noting that we regularly devastate our own microbiome to suppress its production of the same odours that we enjoy in fermented foods, biologist Christina Agapakis and artist Sissel Tolaas have developed an exhibit to help us to better appreciate our unsanitized selves: cheeses made from milk inoculated with swabs of volunteers' hands, feet, noses and armpits (see A. King *Nature* **503,** 196; 2013).

After a centuries-long stationary phase during which traditional food cultures slowly developed in isolation from each other, the world crock has been stirred and things are really bubbling. Will new fermentations grace our future holiday spreads? Even the possibility is worth toasting. ■

Harold McGee *is the author of* McGee On Food & Cooking *and* Keys to Good Cooking, *both published by Hodder & Stoughton.*
e-mail: harold@curiouscook.com



CALIFORNIA DIGITAL LIB.

A forest of the Carboniferous period as depicted in *The Fairy-Land of Science*.

EDUCATION

Fairylands of science

Melanie Keene revisits two Victorian children's science primers that harnessed interest in the supernatural.

© 2013 Macmillan Publishers Limited. All rights reserved

Plum puddings, stockings and trees were not all of the Christmas thrill for American and British children in the second half of the nineteenth century. Many were given gifts of a special kind: primers that propelled them into a fairyland of science. These books inspired the young to imagine vast families of fairies at work beneath the visible world, building frosty forms on windowpanes and setting the fire crackling.

That fantastical construct was stoked by the then-widespread interest in the supernatural and folklore. It also complemented contemporary research in science, technology and medicine that was busy revealing or harnessing the previously unseen: from the vanished species of prehistory to the tantalizing promises of electricity; information that travelled at light-speed across the Universe to be captured in laboratories; and the 'monster soup' of disease lurking within a water pump. A handful of educators saw an opportunity to meld these two trends — notably Arabella Buckley and Lucy Rider Meyer, two women of science who, on opposite sides of the Atlantic, encouraged youthful enthusiasm for the wonders of nature.

Buckley and Meyer were part of a new generation of writers and educators who urged that science was for everyone. Their works emphasized hands-on investigations in the child's own home and environs — an approach that still permeates children's science publications. Although instructional books for juvenile audiences had existed for more than a century by the late 1800s, they were lampooned as dry fact-crammers. British and US publishers instead sought new genres that combined science with characters, illustrations, narratives and writing styles similar to those in children's fiction, then in a golden age dominated by the likes of Lewis Carroll. By the 1870s and 1880s, a range of genres — from autobiographies and object lessons to animal stories and voyages — were enlivening science for the young. At the same time, the writing, translation and collection of fairy tales was booming. This form was seen as ideal for revealing the hidden mysteries and histories of nature. As Buckley and Meyer masterfully showed, the real magic of nature surpassed the fictions of old.

Buckley's *The Fairy-Land of Science* was the best known of the fairy science books (she wrote many other popular-science works, including two on evolution). She drew on impeccable connections: she was geologist Charles Lyell's secretary for more than a decade, and was acquainted with the biologists Alfred Russel Wallace, Charles Darwin and Thomas Henry Huxley.

Buckley based this book on ten lectures she had delivered to children in London in 1878, touching on areas from animal behaviour to atmospheric science. It retains a charming conversational style, and includes black-and-white illustrations of experiments that Buckley performed live. It begins by describing objects that are familiar to the young reader: a primrose, a bee, a sunbeam, a drop of water. These constituents of the quotidian world, she argues, are protagonists in the fairy tales of nature; they provide transformations and revelations as astonishing as those wrought by imaginary sprites. In Buckley's layered text, her science fairies sometimes equate with the "forces" of nature, such as gravity, portrayed as a giant; elsewhere, they represent natural processes such as crystallization or cohesion.

Nature reviewed *The Fairy-Land of Science* in January 1879 (*Nature* **19,** 265; 1879), praising the book's goal of "showing how things far more wonderful than those related in fairy-tales are daily happening around us". This realm, the reviewer wrote, "may be entered by any one with eyes": a common argument of elementary educators, who were eager to extend scientific training to wider audiences. Acquiring the observational and technical skills necessary for understanding the sciences would, they wrote, be akin to developing superior senses and glimpsing the structures and forces hidden beneath the surfaces of things.



CHEMICAL HERITAGE FOUNDATION

In *Real Fairy Folks*, water is shown as an oxygen fairy holding hands with two hydrogen fairies.

The *Nature* reviewer felt, however, that Buckley should have focused on just one area of science. Meyer's 1887 book *Real Fairy Folks* took this route, exploring elementary chemistry in its most literal sense. Meyer had studied chemistry at the Massachusetts Institute of Technology in Cambridge in the late 1870s, and from 1879 to 1881 was a professor of chemistry at McKendree College in Lebanon, Illinois.

She, too, chose the domestic environment as the domain of wonder-working creatures. An avuncular Professor leads his young charges on a playful exploration of the "Fairy Land of Chemistry" (the book's alternative title). Meyer's main conceit was to present chemical elements as "fairy-tribes" — families of beings whose physical attributes mimic their chemical properties. Particular groups of elements are even termed cousins, and introduced in quasi-genealogical tables that convey their characteristics — such as "bad smell" for bromine and "violets" for iodine — as well as their masses in "fairy-pounds".

How slowly or quickly the fairies move reflects their frozen or gaseous chemical states and, as illustrated (supposedly by the Professor), the number of their limbs determines their propensity to form chemical bonds. Water is portrayed as the oxygen fairy clasping hands with two hydrogen fairies: "Oxygen has two hands, and every hand must be full." All flowing dresses and liquid tresses, the image capitalized on its audience's familiarity with depictions of fairies at the time, and neatly represented watery properties.

Meyer layers different types of explanation. These range from the "story" of balancing chemical equations to basic experiments that, like Buckley's, could be recreated by young readers ("the Professor held the edge of a white china plate in the flame a moment. On it the black fairies appeared in great numbers"). Importantly, Meyer urges the need for "imitative experiments" involving everyday objects such as candles, sugar or vinegar. These were easy to replicate and taught ordinary realities: chlorine, for instance, could disinfect a hospital ward.

The interplay between the fantastical and the familiar in these works converted homes and gardens into magical realms. This sense of wonder, both authors hoped, would remain with their readers when, as in Buckley's sequel *Through Magic Glasses* (D. Appleton; 1890), it was time to leave domestic fairyland and enter the laboratory.

Children today, unwrapping sophisticated chemistry sets or animatronic dinosaur models, are immersed in science. But as Buckley and Meyer emphasized, a sense of wonder is still the best start for seeing beneath and beyond the everyday world — to glimpse the marvellous processes, genes, forces, elements and particles that make up the Universe. ■

The Fairy-Land of Science
ARABELLA BUCKLEY
Edward Stanford (1st edn): 1879.

Real Fairy Folks: Explorations in the World of Atoms
LUCY RIDER MEYER
D. Lothrop and Company: 1887.

Melanie Keene *is a senior research fellow in the history of science and a graduate tutor at Homerton College, University of Cambridge, UK. Her book* Science in Wonderland *will be published by Oxford University Press.*
e-mail: mjk32@cam.ac.uk

© 2013 Macmillan Publishers Limited. All rights reserved

A SOON AND DISTANT CHRISTMAS

It's all in the delivery.

BY NATHAN INSEL

The parking lot is a field of frustration. We get lucky: a pod unexpectedly pulls out in front of us and we zip in. Another pod coming from the other direction had apparently been waiting for the spot, and when we get out the driver gives us the finger.

"Mum, did you see what he did!" Masson is excited.

"Just ignore him," Cheryl says.

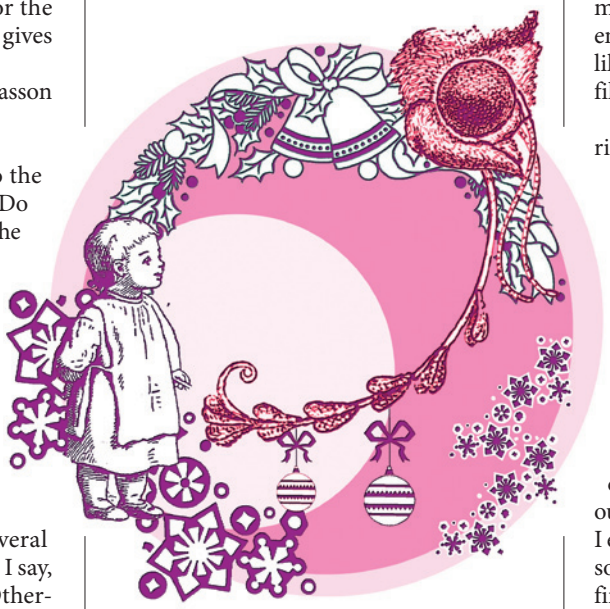
I ask Masson if he wants to jog to the entrance, but Cheryl gives me a look. "Do you want to get run over?" Sensors on the pods make that nearly impossible but we agree to walk together, happy to have escaped the competitive prowl for parking.

The relief is short-lived: the inside of the mall is busier than a water station on Sunday. We don't get ten paces before Cheryl is distracted by a stylish winter vest. I'm more impressed by the mannequin wearing it, which cycles through several moderately seductive poses. "Honey," I say, "let's stay focused. Keep to the list. Otherwise …" I look at Masson, "we may become mall rats and spend the rest of our lives hunting for cheese in the food court." He laughs.

We split up so that I can take care of Masson's gifts. His list isn't long. There's a video game and two movies that can be downloaded from the Internet. There's a set of mutant wrestler action figures that can be built with the 3-D printer. But what he wants more than anything can only be found at the toy store — a caterpillar-like robot with the label *AIBUG!*.

The toy store feels like a mosh pit. I push myself through and take a number. An hour and three v-pings with Cheryl later, the store runs out of *AIBUG!*s. What a mess. It's yet another reminder that society hasn't recovered from the collapse of the postal system. Saturated with technology and yet we can't seem to reorganize a simple package-delivery system. In progress we regress, and tumble into the future.

Two hundred years later: a new generation of workers emerge from pupae and fan out in flight from caverns beneath Greenland. It is their first exposure to wind, but the nervous system quickly fills in details left blank by genetic memory. Although it is only their first flight, it is also their last. By the next rotation of Earth, each worker will have liquefied into a blanket of mulch, providing sustenance to the next generation. In this way the colony propagates itself. The unsuccessful workers, those who fail to return engorged with digestible compounds, will pass on only starved, frozen eggs that mark the terminus of a lineage.



JACEY

But thoughts beyond this night have no purpose. Tonight the worker hunts. Internal molecular dances crescendo into physiological combustion. The worker's 32 ventral, rope-like extensions crawl forward, tasting the air and stabilizing flight. Its dorsal extensions form a rigid, branching meshwork, which triangulates light from stars while integrating code-embedded radio waves.

Two weeks after the shopping-mall mishap, I'm at home with Cheryl, my hands rolling around an *AIBUG!* box delivered by a stranger moments earlier. The toy arrived in the final hour, and I can't completely halt the inertia of my worry.

"Yes, we got it," I say. "But the fact is that crowdsourced delivery doesn't work, at least not during the holidays. It takes too long, things get lost. It's a crummy system. We need something more, well, sustainable."

"Sustainable?" Cheryl says. "I thought your big issue was 'adaptability'. Are you saying that the two are the same?"

"Well, no. Or maybe it's unsustainable that we don't automatically adapt. Postal delivery is one of the oldest social structures we have, how could it reach this level of dysfunction?"

"And you think having to wait two weeks for a toy is dysfunctional? Here's an idea: make it your next grant proposal, to bioengineer a package-delivery system. Seems like the logical step after your biotic water-filtration system, don't you think so?"

I chuckle, she's got me. "Of course. I'll get right on that."

I continue to stare at the *AIBUG!* package in my hands. The solution to everything: mix together some nucleotides, bake with speeded reproductive rates, voilà! Instant biological package-delivery system. Dot com. As if making bacteria to purify water didn't require decades, multiple labs and millions of dollars. I am good friends with a DARPA rep, this will give him a laugh. I still have a dozen things to finish before bed, but instead I continue to stare at the robot toy, drawing out details of an absurd engineering project. I eat the plate of cookies for Santa that Masson had set out, and by the time I go to bed I find myself thinking: "Maybe …"

One worker flies west. The atmosphere compels it towards large structures filled with strange, complex composites. The worker's red proboscis creeps delicately but with unnatural speed, binding and engulfing the objects. From the largest structures it then targets the smaller; its ventral extensions optimize silence during the abrupt landings. White sensory cilia guide its proboscis down through the structure towards a unique and unmistakable combination of sugars and fats. But before reaching these, the organism is arrested by an allergy that forces it to regurgitate some of its gut contents.

Once in a while, the worker isn't fast enough. One time in a million, the landing is too loud, or the proboscis stalls too long by the allergenic pine. A bipedal child strays near the red, cilia-draped proboscis and then stops, awed. The worker reacts reflexively — not in attack, but to soothe the smaller organism with a low-frequency, calming call: "Ho, ho, ho." ■

NATURE.COM
Follow Futures:
@NatureFutures
go.nature.com/mtoodm

Nathan Insel *claims to be a neuroscientist studying how the brain uses expectations to motivate behaviour. He also teaches at the University of Toronto and now apparently writes science fiction.*

© 2013 Macmillan Publishers Limited. All rights reserved